Light Modulation of Properties of Arylazoisoxazole Photoswitches and their Benzene-1,3,5-tricarboxamide (BTA) Functionalized Derivatives

Pravesh Kumar

A thesis submitted for the partial fulfillment of

the degree of Doctor of Philosophy

Department of Chemical Sciences

Indian Institute of Science Education and Research Mohali

Knowledge city, Sector 81, SAS Nagar, Manauli PO, Mohali 140306, Punjab, India.

September 2022

DEDICATED **to**

MY BELOVED FAMILY

Declaration

The work presented in this thesis has been carried out by me under the guidance of Dr. Sugumar Venkataramani at the Indian Institute of Science Education and Research Mohali. This work has not been submitted in part or in full for a degree, a diploma, or a fellowship to any other university or institute. Whenever contributions of others are involved, every effort is made to indicate this clearly, with due acknowledgement of collaborative research and discussions. This thesis is a bona fide record of original work done by me and all sources listed within have been detailed in the bibliography.

Pravesh Kumar

In my capacity as the supervisor of the candidate's thesis work, I certify that the above statements by the candidate are true to the best of my knowledge.

Dr. Sugumar Venkataramani

Acknowledgements

First and foremost, I would like to express my sincere gratitude to my supervisor Dr. Sugumar Venkataramani for his guidance, continued support, and enthusiasm during my research work. The completion of my work would not have been possible without his kind support and guidance. He gave me the freedom to work free-handedly, without any restrictions. His advice and suggestions helped me to grow academically and non-academically. Under his guidance, I have never felt frustrated even after many failures in these years because of his encouragement, positive attitude, and friendly behavior. He has been the backbone of my Ph.D. journey with his care during my health issues and financial support from time to time. My words can never express my gratitude to him.

Besides my supervisor, I would also like to thank my Doctoral Committee members: Dr. Santanu Kumar Pal and Dr. S. Arulananda Babu for their invaluable suggestions and insightful comments during the annual assessments. My sincere thanks to Prof. J Gowrishankar, present director of IISER Mohali and former director Prof. N. Sathyamurthy, Prof. Debi P. Sarkar, Prof. Arvind, and Prof. Siva Umapathy for providing the facilities and infrastructure to carry out my research work smoothly. I am sincerely thankful to the Head of the chemistry department Dr. Sanjay Singh and former heads of the chemistry departments: Dr. S. Arulananda Babu and Prof. K. S. Viswanathan for making the various departmental facilities available for use.

I would also like to thank our collaborators Dr. Santanu Kumar Pal, Dr. S. S. V. Ramasastry, and Prof. V. Ramamurthy for providing me the opportunity to explore my work in diverse areas which helped me to learn many new and diverse things. I am also thankful to other research group members: Sai from Dr. S. Rakshit's group for helping in microscopic studies, Shaina and Sumit from Dr. Arijit Kumar De's group for transient spectroscopic studies and holographic studies, and Dr. Mayank and Labhini from Dr. A. R. Chaudhary's group for single crystal data collection, Prashant from Dr. S. S. V. Ramasastry's group, for helping in photophysical studies and Amal from Prof. V. Ramamurthy's group, for doing host-guest studies. I would especially like to thank Dr. Indu Bala from Dr. Santanu Kumar Pal's group for doing LC studies.

My sincere thank also goes to all the faculty members of the department of chemical sciences of IISER Mohali for their teachings during course work, guidance and

encouragement. I am also thankful to the research facilities of the chemistry department as well as the central research facilities of IISER Mohali: NMR, HRMS, FT-IR, UV-Vis Spectrophotometer, etc. I also want to thank the funding agencies of IISER Mohali and CSIR for the fellowship.

I thank my senior Dr. Sudha Devi and present group members of the Physical Organic Chemistry (POC) group: Ankit Kumar Gaur, Himanshu Kumar, Piyush, Gayathri, Navneet Kaur, Ramanpreet Kaur, Surbhi Grewal, Debapriya Gupta, Anjali Srivastava, Sapna Singh, Anjali Mahadevan, Roshan, Hrishikesh, Sajal, Dhanyaj, and past group members: Dr. Mayank Saraswat, Dr. Chitranjan Sah, Amandeep, Amal, Vaitheesh, Irin, for sharing their skills, knowledge and providing a friendly environment in the lab. I would like to appreciate my labmates for all the celebrations and fun we have had in the last five years and thanks to Himanshu (BTech) for showing his technical skills in repairing lab instruments. Thanks to Dr. Chitranjan (Changoo Bhai) for entertaining time to time during research by mimicking everyone. My thank also goes to Dr. Mayank (Mangoo Bhai) for his valuable advice and suggestions during the last five years. Thanks to Ankit (yar) for sharing and suggesting new ideas daily during my research.

I would also like to thank Mrs. Manju Ma'am for her care and best wishes during my research work and covid time. I also thank my labmates for their care, help, and providing whatever I needed when I was found corona positive and was quarantined. Thanks to Anjali Srivastava for providing healthy food during my quarantine period.

I am also thankful to all the staff of the library for providing very nice facilities for access to books, sci-finder, readings, etc. I am also thankful to all the staff of the stores, the account section, the administrative office, the computing facility, and lab assistants of the chemistry teaching lab, for their help and cooperation.

Finally, I would like to give a special thanks to my family members for their love, and support throughout my research.

Research contributions:

Part of the thesis:

- **P. Kumar**, A. Srivastava, C. Sah, S. Devi, S. Venkataramani,* Arylazo-3,5-dimethylisoxazoles: Azoheteroarene Photoswitches Exhibiting High *Z*–Isomer Stability, Solid-State Photochromism, and Reversible Light–Induced Phase Transition, *Chem*. *Eur*. *J*. **2019**, *25*, 11924–11932.

- D. Gupta,‡ A. K. Gaur,‡ **P. Kumar**,‡ H. Kumar,‡ A. Mahadevan,‡ S. Devi, S. Roy, S. Venkataramani,* Tuning of Bistability, Thermal Stability of the Metastable States, and Application Prospects in the C_3–Symmetric Designs of Multiple Azo(hetero)arenes Systems, *Chem*. *Eur*. *J*. **2021**, *27*, 3463–3472. (‡ = equally contributed)

- **P. Kumar**,‡ I. Bala,‡ S. K. Pal,* S. Venkataramani,* Light modulated reversible "On-Off" transformation of arylazoheteroarene based discotics in smectic organization (**Manuscript Submitted**). (‡ = equally contributed)

- C. Sah, A. Mahadevan, **P. Kumar**, S. Venkataramani,* The curious case of the photochemistry of 2-hydroxyphenylazo-3,5-dimethylisoxazole: unraveling the process among tautomerization, photoisomerization, and conformational changes, *Phys*. *Chem*. *Chem*. *Phys*. **2022**, *24*, 7848–7855.

- S. Devi, I. Bala, S. P. Gupta, **P. Kumar**, S. K. Pal,* S. Venkataramani,* Reversibly photoswitchable alkoxy azobenzenes connected benzenetricarboxamide discotic liquid crystals with perpetual long-range columnar assembly, *Org*. *Biomol*. *Chem*. **2019**, *17*, 1947–1954.

- **P. Kumar**,‡ D. Gupta,‡ S. Grewal,‡ A. Srivastava,‡ A. K. Gaur,‡ S. Venkataramani,* Multiple Azoarenes Based Systems–Photoswitching, Supramolecular Chemistry and Application Prospects, *The Chemical Record*, (**https://doi.org/10.1002/tcr.202200074**). (‡ = equally contributed)

Other contributions

- S. Grewal,‡ **P. Kumar**,‡ S. Roy, I. Bala, C. Sah, S. K. Pal,* S. Venkataramani,* Deciphering Internal and External π-Conjugation in C_3–Symmetric Multiple Azobenzene Connected Systems in Self–Assembly, *Chem*. *Eur*. *J*. **2022**, *28*, e202104602. (‡ = equally contributed).

- P. Kumar, **P. Kumar**, S. Venkataramani*, S. S. V. Ramasastry,* Pd–Catalyzed Formal [3 + 3] Heteroannulation of Allylic gem–Diacetates: Synthesis of Chromene–Based Natural Products and Exploration of Photochromic Properties, *ACS Catal*. **2022**, *12*, 963–970.

Index

List of tables

List of Figures

Abstract

Azobenzenes undergo reversible photoisomerization between two isomeric states, namely *trans* (*E*) (thermodynamically more stable) and *cis* (*Z*) isomers. Forward (*E*-*Z*) isomerization occurs with light (UV or visible), and reverse (*Z*-*E*) occurs through light (visible light) or under thermal conditions. Among the various classes of photoswitches reported so far, azobenzene is one of them exhibiting robustness and high stability and is easily accessible through simple synthetic steps. Apart from this, azobenzenes can be easily functionalized and utilized in various applications such as molecular machines, data storage, molecular recognition, liquid crystals, etc. In recent times, the resurgence of azoarene chemistry is being witnessed mainly due to the emergence of azoheteroarenes, where one of the aryl rings in azobenzene is replaced by five-membered heterocyclic rings. Depending on the heteroaryl ring, they have shown comparatively better forward and reverse bidirectional photoswitching, variable *cis* (*Z*) isomer stability, and exhibit a wide range of applications in photochemical, photobiological, optochemical, data storage devices, energy storage materials, etc.

In this relevance, we have introduced arylazo-3,5-dimethyl isoxazole as a new class of photoswitches. We synthesized 37 derivatives with different aryl substituents using a simple synthetic strategy. To understand the effect of substitution on the photoswitching properties and *Z*-isomer stability, we performed UV-vis and ^{1}H NMR spectroscopic studies. They all showed good to excellent reversible photoswitching in solution and solid state, and high thermal stability of *Z*-isomeric state. For the unsubstituted aryl derivative, we have estimated the $t_{1/2}$ as 45.5 days in [D_6]DMSO, making it one of the long-lived *Z*-isomeric forms. Activation parameters (E_a, $\Delta H^{\ddagger}$, $\Delta G^{\ddagger}$, $\Delta S^{\ddagger}$) have also been estimated from Eyring and Arrhenius plots using the thermal reverse isomerization kinetics data of *Z*-isomer at variable temperatures that showed consistency with the literature reports on stable *Z*-isomers. Apart from this, we also observed a light-induced phase transition in the parent phenylazo-3,5-dimethylisoxazole which is followed by POM, DSC, and further supported by the crystal packing.

In the next part of the work, we functionalized the *o*-, *m*-, and *p*-aminophenylazoisoxazoles and their *N*-methylated analogues into a C_3-symmetric benzene-1,3-5-tricarboxamide (BTA) core. The resulting tripodal photoswitches were explored for their photoswitching characteristics and supramolecular assemblies. Particularly, the possibilities of multistate photochromic properties, concentration dependency in photoswitching, and estimation of PSS

composition of individual photoisomers have been obtained through UV-vis and ^{1}H-NMR spectroscopic studies. The results revealed the existence of bistability between all-*trans* and all-*cis* isomers with excellent and reversible photoswitching and high thermal stability of *ZZZ*-isomeric state, which are the salient features of these tripodal molecules. Activation parameters have also been obtained through variable temperature kinetics studies and Eyring and Arrhenius plots. Interestingly, a reversible light-induced sol-gel phase transition has also been observed in the case of benzene1,3,5-tricarboxamide derivatives, which was supported by POM studies.

In the last part of the work, we synthesized C_3-symmetric molecules for photoswitchable liquid crystalline properties where phenylazoisoxazole units are present at terminal positions and separated from the core part through alkoxy spacer units of variable lengths (C_8, C_{10}, C_{12}). All three molecules showed discotic liquid crystalline (DLC) properties in a nematic manner at room temperature, confirmed by POM (Polarized optical microscopy), SAXS/WAXS (Small angle/wide angle X-ray scattering), and DSC (Differential scanning calorimetry) studies. Besides this, excellent and reversible photoswitching has been observed in the solution state, solid state, and thin film state by using UV-vis, POM, ^{1}H NMR, and AFM studies. Also, high *Z*-isomer stability and photostability are the other salient features of these functional molecules. Furthermore, activation parameters for the reverse thermal isomerization step have been estimated from Eyring and Arrhenius plots. Interestingly, we also observed a reversible light-induced mesophase change that was confirmed by POM and SAXS/WAXS studies.

Chapter 1. General Introduction

1.1 Photoswitches

Photoswitches are molecules, which can switch between two or more states in the presence of light as external stimuli. Typically, photoswitches exhibit an intriguing property called photochromism. "Photochromism" is the term that first was suggested by Hirshberg in 1950 where *phos* refers to light and *chroma* refers to the color.[1] Photochromism is the light-induced reversible transformation of a chemical species between two isomeric states A and B, which differ in their absorption properties.[1b,2] Owing to the different structures, both the isomeric species differ in their color and physicochemical properties such as refractive index, dielectric constant, oxidation/reduction potential, etc.

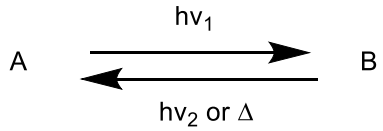

The thermodynamically stable form A transforms into the less stable form B in the presence of light, which in turn can revert to A either photochemically (P-type) or thermally (T-type).[1b] There are several main classes of organic photochromic molecules such as spiropyrans, diarylethenes, stilbenes, fulgides, azobenzenes, etc. Out of these, spiropyrans, stilbenes, and azobenzenes belong to the T type, and fulgides and diarylethene are examples of P-type photoswitches.

1.1.1 Spiropyran[3]

Ring-opening of spiropyran (SP) (mostly colorless) happens after irradiation at 365 nm UV light leading to an extended π-conjugated ring opened merocyanine (MC) with brightly colored form, which is short-lived, and undergoes *cis* to *trans* isomerization into a long-lived transoid isomer, i.e., *trans*-MC (**Scheme 1.1**).

1.1.2 Fulgides[4]

Photoisomerization in fulgide occurs via electrocyclic ring-closing and opening reactions. After irradiation at UV light colorless or faintly colored *E*-isomer converts into a deeply colored isomer C (**Scheme 1.1**).

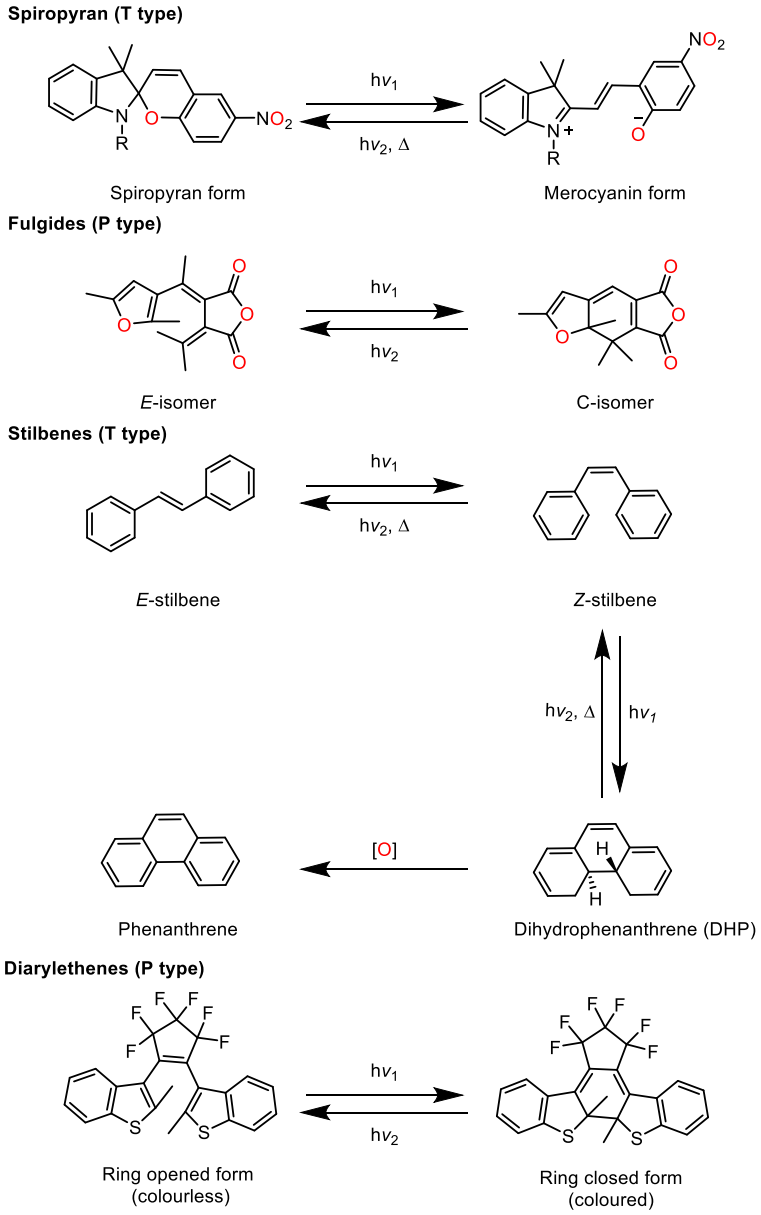

Scheme 1.1. Photoisomerization in different classes of photoswitches

1.1.3 Stilbenes[5]

In stilbene, *trans* to *cis* reversible photoisomerization happens through the rotation of C=C double bond using UV light (for unsubstituted stilbene, 313 nm). The energy barrier between *cis* to *trans* thermal isomerization relative to ground state *cis* configuration was determined to be in the range of 41 to 46 kcal mol^{-1} (**Scheme 1.1**). Due to this high barrier, the *cis* isomer is more stable. However, under photochemical conditions, the *cis* isomer can undergo a 6π electrocyclic ring closure to form dihydrophenanthrene, which on slow oxidative aromatization leads to phenanthrene. Such side reactions can cause fatigues in the photochemical and reversible *trans-cis* isomerization in stilbene.

1.1.4 Diarylethenes[6]

The ring opened isomer of diarylethene undergoes 6π photochemical electrocyclic ring-closing to give the ring closed and more conjugated isomer. The most striking features of this class of compounds are high sensitivity, high fatigue resistance, thermal stability of the two isomers, rapid response, and reactivity in a solid state (**Scheme 1.1**).

1.2 Azobenzenes

Azobenzene is known as a diazene (NH=NH) derivative where both of the hydrogen atoms have been replaced by two phenyl rings.[7] Azobenzene undergoes *trans* (thermodynamically stable state) to *cis* (less stable state) photoisomerization upon irradiation with UV light whereas reverse isomerization happens either thermally in dark or photochemically under irradiation conditions (T-type photoswitch).

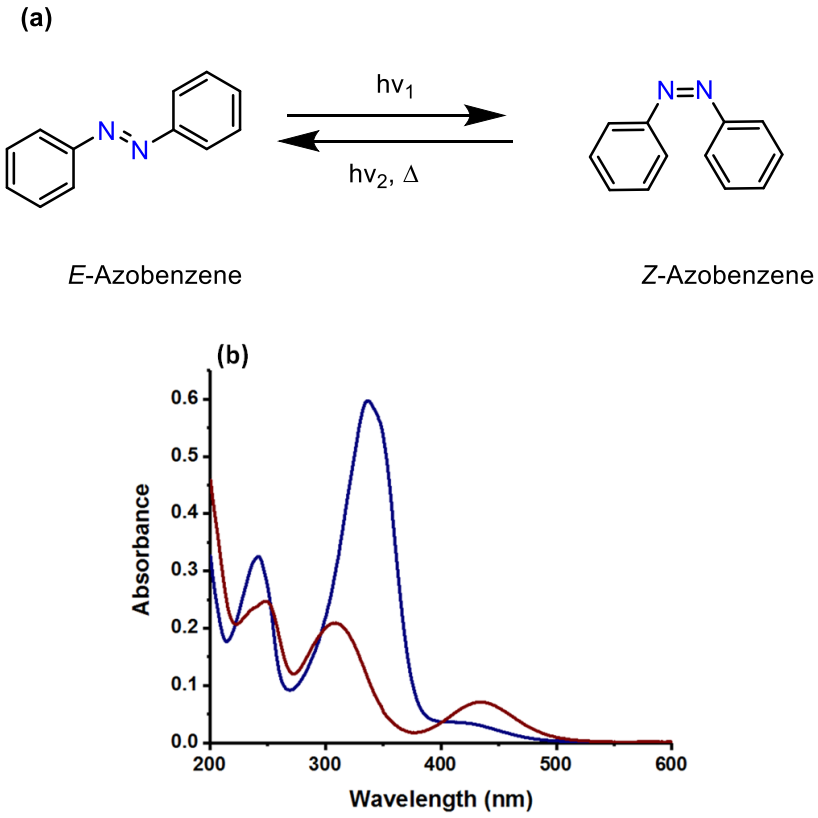

Scheme 1.2. (a) Photoisomerization in azobenzene, and (b) the electronic absorption spectral data depicting the contrasting spectral profiles in the *trans* (blue trace) and *cis* (brown trace) isomers.

Trans (*E*) azobenzene is a planar molecule with C_{2h} symmetry, whereas the *cis* (*Z*) isomer of it has a non-planar structure with a twisted shape and C_2 symmetry, both of which were confirmed from the X-ray crystal structure and computational data.[7,8] In the UV-vis

region, the *trans* (*E*) isomer exhibits two important absorption bands due to the azo chromophore. These include a strong band corresponding to the π–π* absorption (λ_{max} = 320 nm, ε = 22000 M^{-1} cm^{-1}) and a weak feature attributed to the n–π* (λ_{max} = 450 nm, ε = 400 M^{-1} cm^{-1}) transition. Upon photoisomerization, the resulting *cis* (*Z*) isomer exhibits a variation in the absorption bands in the UV-vis region. Two features with reasonably higher intensity corresponding to the π–π* (λ_{max} = 270 nm, ε = 5000 M^{-1} cm^{-1}; λ_{max} = 250 nm, ε = 11000 M^{-1} cm^{-1}) and a third one belongs to the n–π*, which is comparatively more intense than *trans* isomer (λ_{max} = 450 nm, ε = 1500 M^{-1} cm^{-1}). Both the blue shift and lowering of intensity in the π–π* feature and enhancement in the n–π* bands of the azo group are significant indicators for following the photoisomerization process in azobenzene.

1.2.1 Photoisomerization mechanism in azobenzenes[7]

Azobenzene generally follows four possible pathways for photoisomerization, which are rotation, inversion, concerted inversion, and inversion-assisted rotation (**Scheme 1.3**).

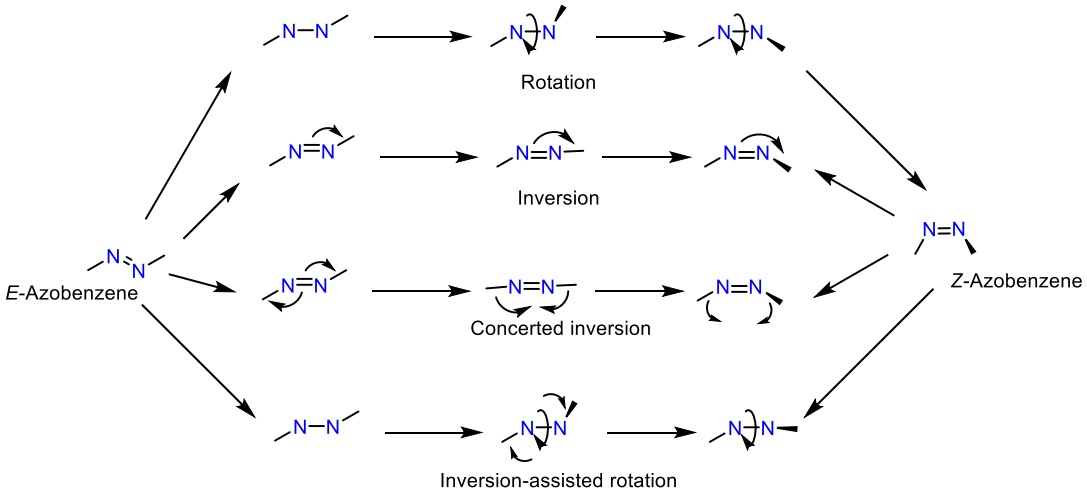

Scheme 1.3. Photoisomerization mechanism in azobenzene (for clarity phenyl ring has been omitted)

In the rotation mechanism, the N=N π bond weakens and behaves similarly to the free N-N bond and undergoes free rotation around it. During free rotation, the N=N-C bond angle remains constant at 120°, while the C-N=N-C dihedral angle changes. In the inversion mechanism, one of the N=N-C bond angles changes to 180°, while the dihedral angle around C-N=N-C remains constant at 0°, which generates a transition state (TS) with sp-hybridized N atom. The concerted inversion mechanism deals with the change in both the N=N-C angles to 180°, which causes a linear transition state, while the dihedral angle around the C-N=N-C bond is constant here. However, in the case of inversion-assisted rotation, two processes are

taking place simultaneously, one is a large change in the C-N=N-C dihedral angle and another one is a more or smaller change in the dihedral angle around the N=N-C bond. However, it has been a topic of debate which path is followed during photochemical or thermal reverse isomerization.[9]

Azobenzenes are divided further into the following three classes: azobenzenes, aminoazobenzenes, and pseudostilbenes (**Scheme 1.4**). This classification is based on the π–π* and n-π* energy gap variation. Many substituted azobenzenes show similar absorption features as simple azobenzene, where the two absorption bands are well separated. However, aminoazobenzenes exhibit overlapping bands (π–π* and n–π* are merged) due to the electron donation by the NH_2 group and red shifting in π–π*. Pseudostilbenes, on the other hand, are the protonated azobenzenes and push-pull azobenzenes, where the π–π* and n–π* bands degenerate. All these variations exhibit an impact on both photoswitching and the thermal stability of the *cis* isomers.

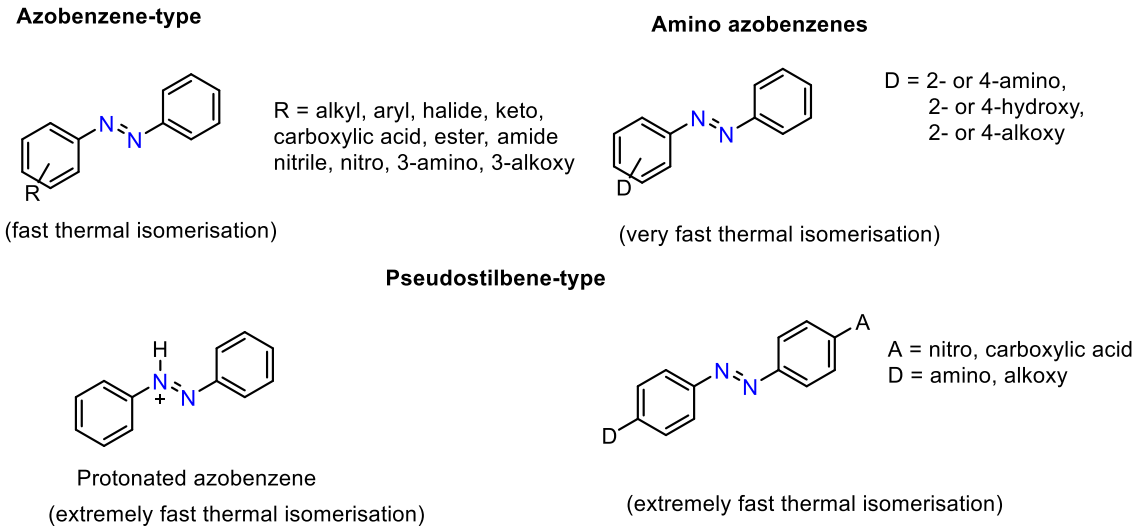

Scheme 1.4. Different types of azobenzenes

1.2.2 Thermal stability of *cis* (*Z*) azobenzenes[7]

Thermal stability of *cis* (*Z*) isomeric states is defined in terms of activation energy (Ea) or the barrier associated with the ground state isomerization process. The activation energy of *cis* (*Z*) isomer strongly depends on the medium and the phase. For instance, in the solution phase, the activation energy of azobenzene is 95 kJ mol^{-1} (half-life 2 days at rt),[10] which increases to 105 kJ mol^{-1} in the molten state, and becomes 233 kJ mol^{-1} in the crystalline state, which is significantly very high. Also, substitution at azobenzene alters electronically the thermal stability of *cis* (*Z*) isomer. Strong electron-withdrawing substituents such as NO_2 or COOH decrease the thermal stability for *cis* (*Z*) isomer more significantly.[11]

Moreover, a decrease in thermal stability is observed when electron-donating substituent such as NH_2 or OMe is present at the *para* position of one of the azobenzene. These groups donate very effectively to the π* orbital leading to a red shift in absorption maximum, and so overlap with n–π* orbital. 2-hydroxyazobenzenes however, behave differently. 2-hydroxyazobenzenes forms intramolecular H-bonds with an azo nitrogen atom and transfer of the H atom takes place to azo nitrogen, which results in the formation of phenylhydrazone that leads to fast thermal reverse isomerization.[12] The rate of thermal reverse isomerizations is extremely fast in the case of the push-pull type of azobenzenes, which lies in the range of milliseconds to seconds. However, there are examples where substitutions can slow down the thermal isomerization rates (e.g. tetra *ortho* fluorination at azobenzene can increase the thermal half-life of *cis*-isomer up to 700 days at room temperature.[13] Computationally it was observed that σ electron-withdrawing effect of the four fluorine atoms stabilizes the *Z*-isomer.

1.3 Introduction to azoheterocycles

The journey of the development of new azo-based dyes led to the discovery of novel azoheteroarenes.[14] The photoisomerization behavior in azoheteroarenes has been established based on the understanding of the photoisomerization behavior in azobenzenes. Le Fèvre, in 1951, demonstrated the *E-Z* photoisomerization behavior of 2,2'-azopyridine in sunlight, based on the resemblance in absorption properties with non-heterocyclic azoarenes.[15] Tayler and co-workers prepared two derivatives *cis* 2,2' and 3,3'-azopyridine and made further attempts to characterize them by measuring their melting points (M.P.), X-ray powder photographs, UV-vis absorption, dipole moments, and confirmed the *trans-cis* isomerization behavior[16]. Although, photoisomerization behaviour of heterocyclic azopyridine analogs was discovered, yet photoswitching behavior of other azoheterocycles remained undiscovered. Most of the reports on azoheteroarenes are related to their therapeutic action[17] in medicinal chemistry and for coloration in the dye industry.[18] Various synthetic strategies have been developed for accessing various azoheteroarenes. One of the synthetic strategies adopted was the synthesis of hydrazone derivatives, followed by an oxidation step leading to the access of a variety of azoheteroarenes.[19] Apart from this, azoheteroarenes find use in diverse fields such as they have been used as a heterogeneous catalyst in Mistnobu reaction,[20] in non-linear optics,[21] and as a directing group[22] through C-H activation strategy, etc. On the other hand, heteroatoms in the rings can coordinate with the metal

centers [23] (as a monodentate or bidentate) or they can form Hydrogen bonds/or other non-covalent interactions.[24]

1.3.1 Classification

Types of azoheteroarenes [34]

A lot of heterocycles-based azoarenes have been reported in the literature, which differs in terms of the ring size, a number of heteroatoms, nature of heteroatom, nature of ring, etc (**Scheme 1.5**). In a broader perspective, Grewal *et al* have made classification such systems into 4 different classes as follows:

1. Monoheteroaromatic ring containing azoheteroarenes (class I)
2. Bisheteroaromatic rings containing azoheteroarenes (class II)
3. Fused heteroaromatic ring(s) containing azoheteroarene (class III)
4. Partially or fully saturated heterocyclic ring containing/miscellaneous azoheteroarenes (class IV)

Monoheteroaromatic ring containing azoheteroarenes (class I)

This class includes the azoheteroarenes, which are formed after the replacement of one of the phenyl rings of azobenzene with 5/6 membered azoheterocycle. These, 5/6 membered rings may have one, two, three, or four heteroatoms. This class includes the most abundant 5-membered azoheterocycles (**Scheme 1.5**).

Bisheteroaromatic rings containing azoheteroarenes (class II)

This class includes the heterocycles, which are obtained after the replacement of both rings of azobenzenes with either 5/6-membered heterocyclic ring. These two heterocyclic rings may be connected either in a symmetric way or unsymmetric fashion. The number of atoms in a particular ring may differ from 1-4 (**Scheme 1.5**).

Fused heteroaromatic ring(s) containing azoheteroarene (class III)

This class includes the heterocycles, which are obtained after the replacement of both rings of azobenzenes with either 5/6 membered fused heterocycles. The fused heterocycle may also have a combination of one heteroaromatic ring and a simple phenyl ring, which may further differ in the connectivity to the azo group. Both heterocyclic rings may be connected

such that the resulting system may be either symmetrical or unsymmetrical azoheteroarene (**Scheme 1.5**).

Partially or fully saturated heterocyclic ring containing/miscellaneous azoheteroarenes (class IV)

This class includes the heterocycles where out of the two rings of azobenzenes, one of the rings has been replacement with either 5/6 membered saturated or partially saturated heterocycles. The such class also includes the azoheterocycles where one of the nitrogen atoms from the ring is connected directly to the azo group nitrogen making a triazene link. This category also includes some miscellaneous azoheterocycles (**Scheme 1.5**).

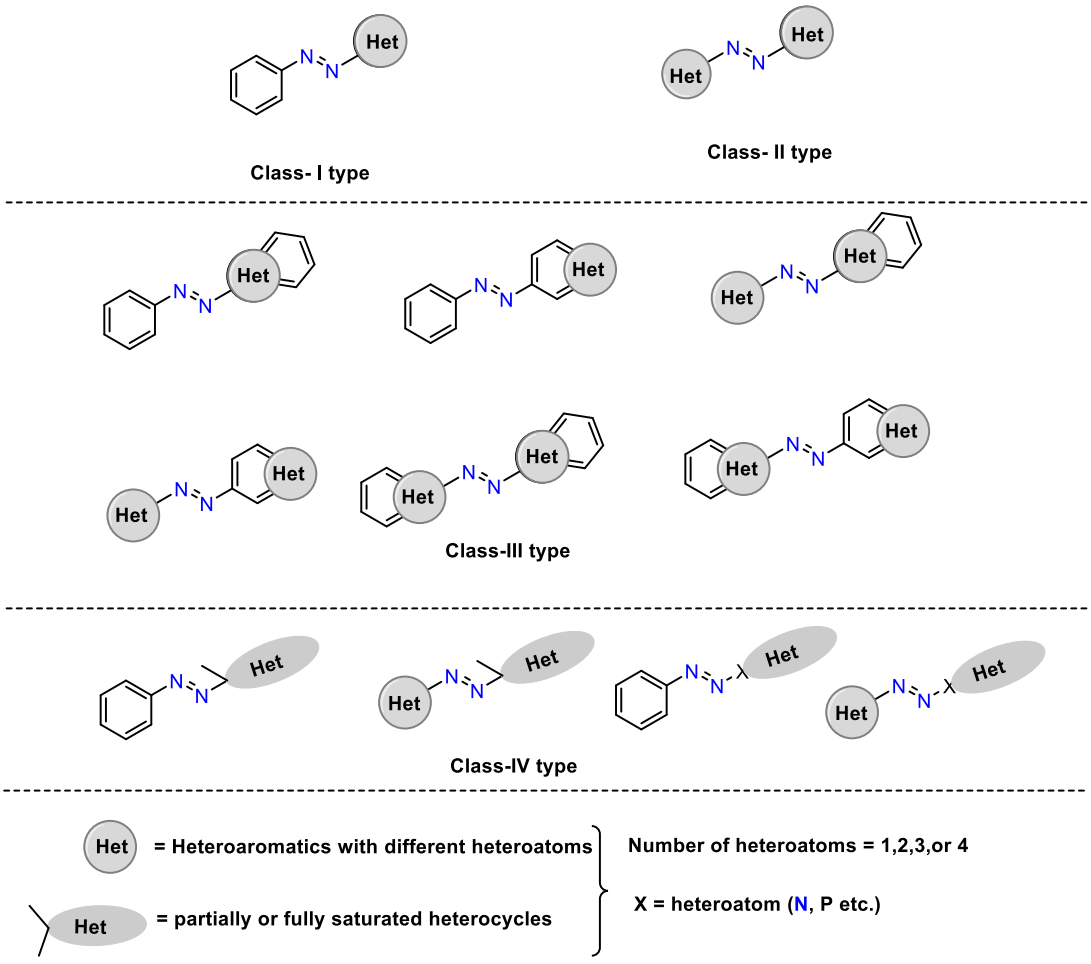

Scheme 1.5. Classification of azoheteroarenes

1.3.2 Five-membered heteroazoarenes

In recent decades, azoheteroarene analogs of azoarenes have attracted the attention of scientists and attempts have been made to improve photoswitching characteristics, and thermal stability of *cis* isomers, bringing tunability to these properties and applications.[25]

Herges' group demonstrated the role of azopyridine photoswitching in magnetic resonance imaging applications where azopyridine is tethered to a nickel porphyrin complex.[25a] While searching for such novel magnetic bistable compounds, the same group also reported the synthesis of several new phenylazoimidazoles, which showed excellent *E*-*Z* photoisomerization, however, reverse *Z*-*E* was incomplete.[25b,c] Indeed, this report kick-started the exploration of five-membered heterocycles-based azophotoswitches. Following this, in 2014 and 2017, Fuchter and co-workers designed and synthesized a five-membered ring containing arylazopyrazoles, which showed tremendous improvement in the photoswitching efficiencies (quantitative and bidirectional photoswitching, i.e., light-induced isomerization in the forward and reverse directions), and high thermal stability of *cis* (*Z*) isomer.[26] The importance of five-membered heterocycles, tuning of photoswitching, and thermal stability have also been demonstrated by utilizing different five-membered heterocycles with or without methyl group and changing the number and position of nitrogen as the heteroatom(s) in the ring.[26] Devi *et al* investigated the importance of electronic effects, steric effects, and H-bonding in tuning *Z*-isomer stability in arylazopyrazoles, and also revealed solvent-assisted tautomerism as an important factor that decreases the thermal stability of *Z*-isomer.[27] Such tautomerism was previously reported in azoimidazoles by Otsuki *et al*.[28] In 2018, arylazoindole core has been introduced by König and co-workers, where substitution at indole core provided the importance of tautomerism in tuning the thermal half-life of *Z*-isomer from days to nanosecond[29] Several other heterocycles such as Wegner (thiophene),[30] Ortega-Alfaro (pyrrole),[31] Olson (triazole),[32] Velasco (thiazole),[33] etc., have also been utilized in azoheteroarenes, which showed intriguing properties. Due to the continuous explorations in this direction, azoheteroarenes (particularly with five-membered heterocycles) have attained a different status in terms of their photoswitching behavior, the thermal stability of *Z*-isomer, and tuning of these properties as well as application prospects.[34]

1.3.3 Applications of azoheteroarenes

Recently, a variety of azoheteroarenes have been developed and also functionalized further to get a variety of applications in diverse fields such as medicinal chemistry, catalysis, photoswitchable contrast agents, spin cross etc. Due to the emergence and better understanding of several azoheteroarenes as photoswitches, the research focus has been shifted to utilize them in novel applications, which have not been imagined before. The

development of new azoheteroarenes and their functionalized systems are crucial to such applications.

Azoheteroarenes have found important applications in medicinal chemistry as photopharmcology agents and photoswitchable drugs. For instance, heteroazoarene based molecules installed with sulphonyl urea have targeted pancreatic beta cells (responsible for the release of insulin hormone), whose function can be controlled optically by using yellow-green light (**Scheme 1.6**).[35] The problem of bacterial resistance has been addressed by Feringa and co-workers by using light as stimuli and photoswitchable quinolone-based heteroazoarenes as antibacterial agents, which have been used for controlling the growth of bacteria by light.[36] Recently, Fuchter and co-workers reported the azobenzenes and arylazopyrazoles as photoswitchable inhibitors for the bacterial human histone deacetylases (HDACs) homologs. Although both exhibited very good and similar inhibitory activity, aryazopyrazoles exhibited an enhanced inhibitory activity performance over azobenzene, owing to its complete photoswitching and high thermal stability in the *cis* isomeric state (**Scheme 1.6**). The activity difference in *E* and *Z* isomeric forms was found to be promising (10-fold).[37] Not only are simple azoheteroarenes, but their metal complexes also have been utilized in medicinal chemistry such as in photodynamic therapy (PDT), where an azo-ruthenium complex has been used as a photosensitizer activated by glutathione (GSH). The complex exhibited high phototoxicity against cancer cells under two-photon excitation (810 nm).[38]

Photoswitching of properties led to the generation of very important applications such as light modulation of catalysis. Azoheteroarene, owing to its very interesting photoswitching properties, has been utilized in catalysis. Hecht and co-workers developed a photoswitchable catalyst, where a basic *N*-alkylated heterocyclic piperidine moiety is connected to a 3,5-disubstituted azobenzene. The lone pair of electrons on the Nitrogen atom is shielded by the substituent present on azobenzene. By switching on (*cis*) and off (*trans*) using light, the reactivity of reactive sight (N lone pair) can be controlled reversibly by shielding and deshielding of Nitrogen lone pair (**Scheme 1.6**). They proved the concept by demonstrating a general base that catalyzed Henry's reaction.[39] Several other photoswitchable catalysts with different *modus operandi* have also been reported.[40]

Data storage is another important application of azoheteroarenes, where an external stimulus such as light or pH can induce isomerization and this leads to change in the

associated properties (molecular logic gate). Herges and co-workers synthesized a record player molecule where azopyridine tethered to a metal porphyrin complex exhibited photoswitching from *E* to *Z* configuration. By changing the pH (high/low) and using the light (430/500nm) as an input, the record player molecule changed its magnetic properties (diamagnetic/paramagnetic) as an output. Coordination of pyridine Nitrogen to the Ni atom in the presence of light leads to the coordination-induced spin state switch (LD-CISSS) (**Scheme 1.6**). Association and dissociation of azopyridine ligand cause the change in the spin state of metal from high spin (paramagnetic) to low spin (diamagnetic).[41,42] In yet another work from the same group, they demonstrated the application of magnetic resonance imaging (MRI) as a contrast agent.[42]

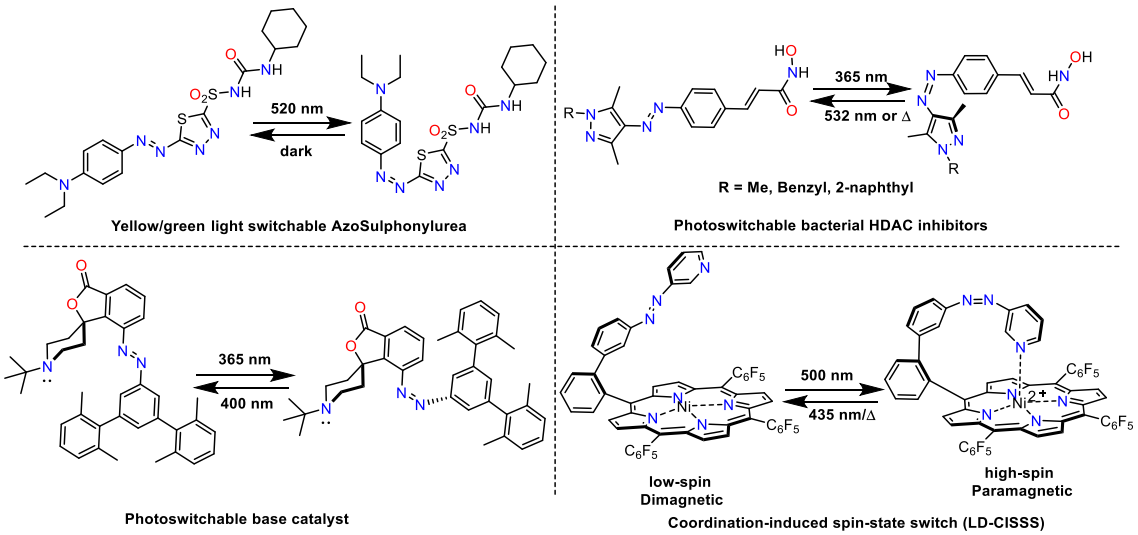

Scheme 1.6. Representative examples for the diverse applications of azoheteroarenes

1.4 Photochromism and light-induced phase transition

Phase transition by heat is a very common phenomena that can be induced by varying temperatures, which is a physical process. For example, ice can be melted into the water by heating, and it can be reverted by cooling.[43] In contrast to this, there are some chemical processes, where photochromic materials such as azobenzenes undergo reversible *trans* to *cis* isomerization induced by light, which leads to solid to liquid or liquid to the solid phase transition. Such phase transitions can be used to modulate the properties such as LC phases, sol-gel transitions, fluidity changes in thin film surfaces, etc.[43b]

In azobenzenes, *trans* and *cis* isomers exhibit different melting points (T_m). In principle, light is switching the melting point (T_m)/glass transition temperature (T_g) of *cis* and *trans* isomers.[43] If T_m/T_g of *trans* and *cis* isomers are above or below room temperature

respectively, then such materials undergo light-induced solid to the liquid phase transition. Reversible light-induced solid to liquid phase transitions have been observed in small molecular weight azobenzene compounds and polymers with photoswitchable T_m and T_g, respectively. Such phenomena also attracted various applications. Okui and Han reported amphiphilic *ortho*-alkylated azobenzenes incorporated with hydrophilic tetra(ethylene glycol) units, which showed UV light-induced crystalline to isotropic photo melting.[44] It was suggested that weak intermolecular π–π interactions due to the *ortho*-alkylation could be responsible for low phase transition temperature. Akiyama and co-workers synthesized multiazobenzene sugar alcohol derivatives for photochemical and reversible liquefaction and solidification properties by using UV and visible light,[45] and their application to reworkable adhesives.[45b] Norikane and co-workers reported macrocycles incorporated with two and three azobenzene units, which showed light-induced phase transition from LC to isotropic phase.[46a] The bis-azobenzene-containing macrocycle exhibited light-induced solid to liquid phase transition with the involvement of two crystalline phases.[46b] Furthermore, in the same molecule photoinduced crystal to melt transition has also been observed.[46c]

Norikane *et al* reported small azobenzene molecules for the photoinduced crystal to liquid phase transitions and their applications in photolithography.[47a] Molecular symmetry breaking by the substitution of methyl group was found to be important in solid to liquid phase transition. In the photolithographic process, azobenzene has been used as a photoresist, which was removed after irradiation by UV light and by washing with a propanol solution. In another report, the same group investigated the influence of chain length variation on photoinduced solid to the liquid phase transition, and adhesion properties.[47b] It has been observed that compounds with medium chain length (n = 6-10) showed faster photoinduced solid to liquid phase transition than their shorter or longer chain analogs. Green light triggered phase transition from solid to liquid also reported by Yin and co-workers for azobenzene incorporated binaphthols having long alkoxy chains.[48] They demonstrated that phase transition happens due to the photothermal effect in the solid state after irradiation with green light. However, the reverse liquid to solid transition requires thermal conditions. Using these properties they also demonstrated the reversible adhesion behavior of the molecule with green light.

Apart from small molecules, azopolymers with chain-like architectures are also reported for reversible light-induced phase transition and studied for various applications. These azopolymers exhibit photoswitching of glass transition temperature (T_g) due to solid to

the liquid phase transition.[49] Furthermore, the latter process has been utilized in applications such as the healing of hard coatings, fabrication of smooth surfaces, and transfer printing as a result of photoswitchable adhesion.

Apart from azobenzenes, recently azoheteroarenes also exhibited light-induced phase transition properties and showed interesting applications. In 2020, Fuchter, Han, and co-workers reported arylazopyrazoles functionalized with dodecanoate groups, which can store energy for a longer time and release as a result of visible-light-triggered crystallization at −30 ^{o}C.[50a] In 2020, Ravoo and co-workers also reported low molecular weight arylazoisoxazoles for photoreversible adhesives applications.[50b]

1.4.1 Multiphotochromism and multiphotochromic azoarenes

The photochromic property of azobenzene has been used for the modulation of functions of chemical systems by using clean, highly selective, noninvasive, spatiotemporally precise light sources.[51-53] Monophotoswitches such as azobenzenes undergo reversible *E* to *Z* and *Z* to *E* photoisomerization when irradiated with light with two isomeric states. However, when two or more photoswitches are incorporated into a molecular design, then the resulting molecules exhibit multiphotochromic nature.[51] These molecules can exist up to 2^n number of states (n is the number of photochromic units) and exhibit more complex photoswitching behavior with multistate (more than two isomeric states) when the photochromic units are unsymmetric. However, symmetry may reduce the complexities. The multistate photoswitching properties allow such molecules useful in applications such as data storage or multi-responsive materials and logic gate devices, etc. The contrasting photoswitching in those systems can lead to bistability, where end-to-end photoswitching can be seen without involving the intermediate isomers. One of the major driving forces for bistability can be cooperative photoswitching, which may lead to large geometrical changes that are useful for macroscopic functions.[51] One possible strategy to achieve bistability is electronic decoupling between the photoswitches. In general, interchromophoric interaction or electronic coupling in a multichromophoric molecule can be minimized by *meta* connections, introducing sterically bulky groups, and utilizing alkyl spacers.

1.4.2 Structural variations in multiphotochromic azoarenes

Several multiphotochromic azoarenes have been reported with a wide range of designs. Such architecturally distinct molecules can be broadly classified based on shape, mode of connections, and symmetry, as linear, bent, tripodal, and cyclic systems, etc.

In linear or bent-shaped multiazobenzene incorporated systems, two or more azobenzene photoswitches are functionalized and the role of electronic decoupling on photoswitching and thermal reverse isomerization properties has been investigated. In bis-azobenzene incorporated systems, it was found that electronic decoupling increased the photoswitching efficiency when they are *meta* (1,3) to each other, whereas when they are *para* (1,4), electronic coupling reduced the photoswitching efficiency.[51,53] Wegner and co-workers also showed that connectivity at the *ortho* (1,2) position results in a high rate of thermal relaxation (half-life 1.6 ms).[53a] Robertus *et al* showed that in *meta*-connected isomers during thermal reverse isomerization photochromic units behave independently of each other.[53b] In another approach for electronic decoupling, Hecht and co-workers showed that the introduction of the sterically congested methyl group at *ortho* positions of a biphenyl connection led to electronic decoupling and an improvement in photoswitching.[53c] A wavelength selective photoswitching of possible photoisomers (*EZ*/*ZE*, *ZZ*, and *EE*) in a bis-azobenzene incorporated system has been achieved in a unique molecular design. However, *ZE* was accessed using only electrons.[53e] In molecular designs to achieve orthogonal photoswitching and multistate, a visible light photoswitchable tetraorthofluoro substituted azobenzene and a simple azobenzene (photoswitchable in UV light) have been incorporated.

Various multiple (two or more) azobenzenes incorporated azomacrocycles have also been synthesized and studied for their multistate photoswitching and thermal stability aspects.[54] Wegner and co-workers reported an efficient synthesis of cyclotrisazobiphenyls. It was observed that by changing the solvent/irradiation wavelength, a selective control on photoisomeric ratio at PSS can be achieved.[54a] In yet another report, they synthesized a chiral cyclotrisazobiphenyl, which showed different PSSs at different wavelengths. These PSSs were accessed by using CD spectroscopy.[54b] The same group further reported highly strained cyclotrisazobenzene, in which photoswitchable azobenzenes unit didn't isomerize. However, the energy absorbed by photoswitchable units is released in the form of thermal energy on ultrafast time scales and they envisioned these systems as a UV-B light absorbers.[54c] Moreover, they also revealed that macrocyclic ring strain is very crucial in designing multistate photoswitches and provides opportunities for designing multistate photoresponsive materials.[54d] Furthermore, they discussed the synthesis of bis-azobenzenophanes, in which *ZZ* isomeric form is more stable than *EE*-isomeric form.[54e] Wager-wysiecka *et al* reported a review on selected macrocyclic compounds where they

discussed the relationship between compounds, their structure, and properties such as guest complexation, supramolecular chemistry, switching, motion, etc.[54f]

Other important multiazo(hetero)arenes incorporated systems include the C_3-symmetric or branched systems. Multiphotochromic C_3-symmetric tripodal systems are enormously popular and exhibit diverse applications. Broadly these systems can be categorized based on core structures, linkers, or spacers.[52,54] Core may include aliphatic, aromatic, heteroaromatic, or a single atom, whereas spacers or linkers can be alkyl, amide, ether, ester, etc. For constructing C_3-symmetric tripodal systems, the 1,3,5-connection strategy at the central phenyl ring has been profoundly used. One of the advantages of 1,3,5-connection is that photochromic units remain electronically decoupled, which improves the photoswitching efficiency and thermal stability of such systems. Besides this, the functionalization at 1,3,5-positions results in a C_3-symmetric system that makes the spectroscopic analysis less complex. Samorì and co-workers reported a unique C_3-symmetric tris-azobenzenes incorporated molecule, in which tris-azobenzenes are connected at 1,3,5-positions to a central phenyl ring.[55] Weak electronic coupling in between photoswitches, led to efficient photoisomerization, even in 2D self-assembly. Interestingly, during thermal reverse isomerization photochromic units were found to behave independently. The 1,3,5-benzene-tricarboxamide (BTA) core-based C_3-symmetric molecules have been explored extensively.[56] Thiele and co-workers synthesized a BTA core-based tris-azobenzene functionalized molecule.[56] Weak electronic coupling during *trans* to *cis* photoisomerization led to the formation of photoisomers (*EEE*, *EEZ*, *EZZ*, *ZZZ*) at PSS, which were distinguished by *in-situ* irradiation NMR spectroscopy, and the photochromic units isomerize independently during thermal relaxation of the *cis* isomer. Wegner and co-workers reported an unsymmetrical triad system for wavelength selective control on photoswitching.[57] Although the computational designs predicted multistate photoswitching,[58] however, no wavelength selectivity has been achieved due to the overlapping signals in spectroscopy. Atomic core (C, N, P) based C_3-symmetric tripodal systems have also been reported.[59] Bahrenburg *et al* reported Nitrogen atom-based tris-azobenzene incorporated systems, where photochromic units were found to be electronically coupled that decreased the photoswitching efficiency.[59a] They also concluded that the number of azo units or the overall shape of the molecule has an impact on *cis* isomer stability.

Apart from photoswitching and thermal stability prospects at the molecular level, these C_3-symmetric molecules as a result of intermolecular non-covalent interactions undergo

self-assembly to generate supramolecular architectures such as LCs, sol-gel systems, etc. These non-covalent interactions are weaker and can be tuned by light, which can bring phase transitions. Particularly, the BTA core is known for intermolecular H-bonding and drives the molecules to self-assemble, which is further reinforced by π–π the stacking of flat and planar azobenzenes. In this regard, Kim and co-workers demonstrated the self-assemblies (fibers, gels, and hollow spheres) in different solvents, which undergo a reversible light-induced phase transition.[60] Huang and co-workers synthesized a cyclohexyl core-based tris-azobenzene functionalized gelator molecule, which gelled most of the organic solvents and showed light-induced gel to the sol phase transition.[61] Recently Grewal *et al* synthesized two π-extended molecules, which formed different self-assemblies depending on the internal and external position of the group enabling conjugation.[62]

1.4.3 Applications of multiphotochromic azoarenes

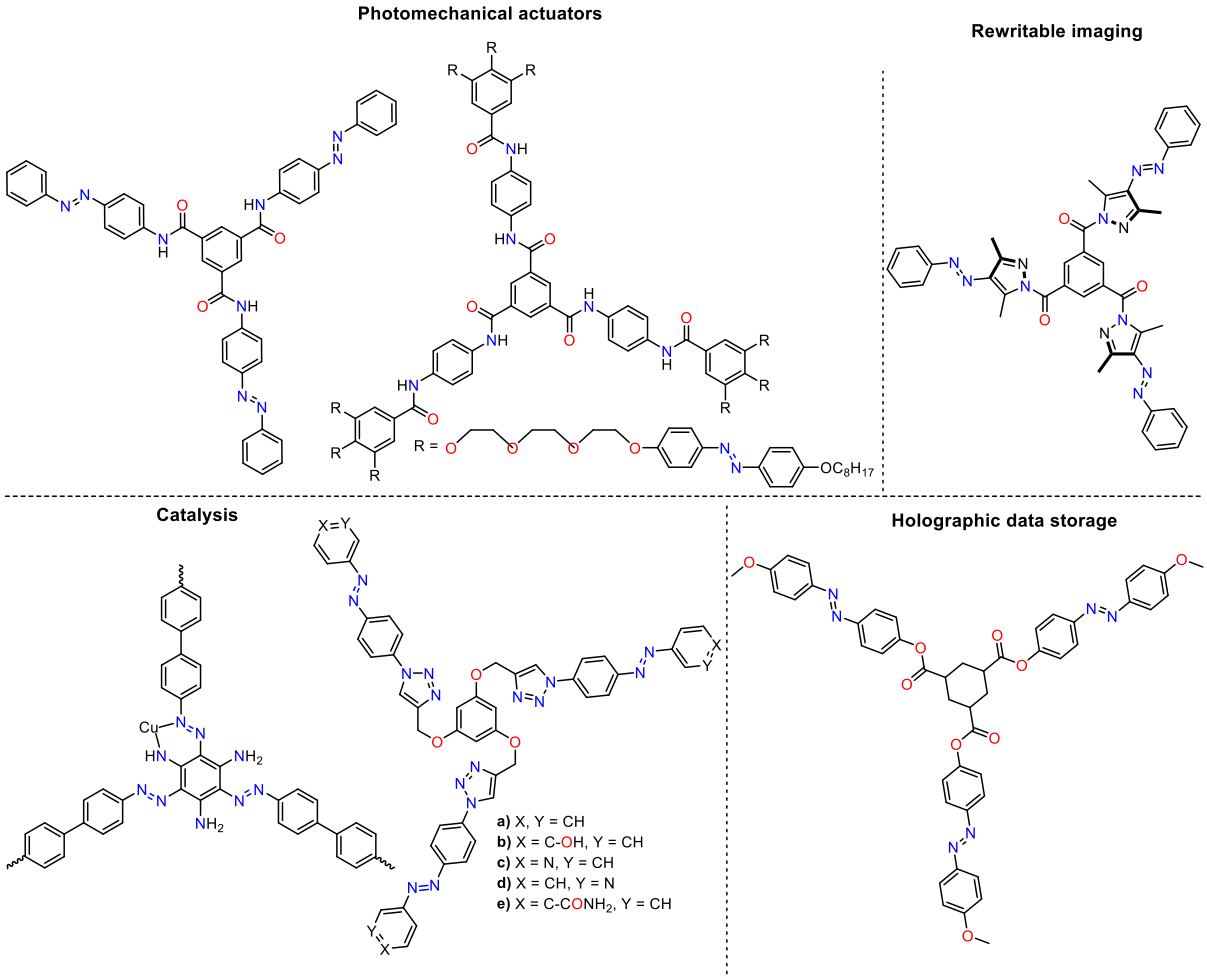

Scheme 1.7. Representative examples of C_3-symmetric molecules showing diverse applications

The C_3-symmetric multiazo(hetero)arenes incorporated designs at the molecular level as well as supramolecular level and showed the variety of properties. Light modulation of these properties also offers the possibilities for diverse applications such as catalysis, actuators, data storage, rewritable imaging, etc.

One of the important applications is in photomechanical actuators. A BTA core-based azobenzene tri-carboxamide molecules have been grown vertically in the form of nanowires (**Scheme 1.7**).[63a] The vertically grown nanowires undergo reversible light-induced photomechanical three dimensional (3D) movements (bending and unbending). This bending behavior followed the kinetics of first order. Jeong and co-workers demonstrated the 3D photomechanical actuation behavior in a thin film, which was controlled remotely using light (**Scheme 1.7**).[63b]

Another important application is catalysis. A C_3-symmetric, functional porous organic polymers (POPs) have been synthesized with mesopores and a high percentage of nitrogen and triamino-triphenylazobenzene as a subunit (**Scheme 1.7**).[64a] It was demonstrated that it removes 85% copper ions from water. The resulting functional Cu@Azo-POP-4 behaved as a heterogeneous catalyst and catalyzed the aerobic C-H oxidation into organic substrates with high reactivity, selectivity, and reusability. A tripodal heteroazoarene and triazole incorporated systems have been designed and synthesized for light-controlled catalysis of tritylation reaction. Owing to the triazole and chloride ion interactions, it was observed that the all-*trans* (*EEE*) form of the catalysis accelerated the rate of reaction, whereas the photoswitched state decelerated it.[64b]

Another application is based on heterocyclic arylazopyrazole functionalized tripodal molecules, which showed a light-induced contrasting color change in solid-state and demonstrated for rewritable imaging applications (**Scheme 1.7**).[65]

Another important application is in data storage. Holographic data storage provides the solution to a data storage problem where a large amount of data can be stored in 3D, whereas in digital storage data is stored in 2D.[66] Photoswitchable azobenzene-based polymers have been used for holographic data storage but they are lacking fast holographic data writing speed, which got improved after adding a tripodal tris-azobenzene incorporated system (**Scheme 1.7**).[66b]

1.5 C_3-symmetric tripodal photoswitchable liquid crystals

1.5.1 Introduction to liquid crystals (LCs)

Liquid crystal (LC) is a different phase of matter, which is an intermediate state to crystalline solid and amorphous isotropic liquid and possesses the properties of a crystalline solid such as anisotropy and fluidity of an isotropic liquid.[67] Owing to its appearance in between two phases, it is also called a mesophase or fourth state of matter. LCs were first discovered by F. Reinitzer in 1888.[67c] But the term liquid crystal was first given by Lehman in 1889. Since then, LCs have been studied in diverse fields such as chemistry, physics, biophysics, and engineering with outstanding achievements in basic science and technologies.

1.5.2 Classification

LC phases are generally classified into two classes' i.e thermotropic and lyotropic.[67b,68] In the case of thermotropic LCs, the mesophases are obtained by temperature variation, whereas the lyotropic mesophases are obtained by changing solvents and concentration. Based on the molecular shape or geometry of the constituent molecules, thermotropic LCs are further divided into calamitics and discotic mesophases.[68b] Calamatics are LCs, which consist of rigid rod-like molecules and flexible long alkyl or alkoxy chains at terminal positions, whereas discotic are made of disc-shaped molecules connected with alkyl or alkoxy chains at the periphery.[68b] Based on the changes in positional or orientational order, the calamitic LCs are further subdivided into nematic, smectic, and cholesteric mesophases, classified by Friedel in 1922.[68a]

Nematic LC phases are the mesophases where the long rod-like molecules are oriented in the direction of a general director axis while they are lacking positional order. In nematics, molecules are free to move throughout the whole liquid while maintaining their orientational order. It possesses the least degree of order than other LC phases.[67a,68b] While in smectic mesophase, molecules have both orders due to positional as well as orientation. Molecules form layers in which their positions and orientations are fixed. Moreover, in smectics, other classes have also been observed such as smectic A, smectic B, smectic C, smectic D, smectic E, etc. The cholesteric phase and nematic phase are similar except that in the cholesteric phase the direction of the director varies regularly throughout the medium.[67a,68b]

Discotic LCs can be of three type's nematics, columnar and lamellar. Nematics includes the discotic nematic (N_D) phases, which are very less common and least ordered, whereas, in the case of columnar DLCs, molecules have flat, rigid, π-conjugated cores that are connected with long alkyl chains at the periphery. These disc-shaped cores self-assemble through π–π stack to form a 1D columnar structure. These 1D columns further self-assemble and gives rise to different lattices such as columnar hexagonal (Col_h), columnar rectangular (Col_r), columnar oblique (Col_{ob}), columnar plastic (Col_p), and helical (*H*) lattices. However, the structure of discotic lamellar (D_L) lattices, where the molecules are arranged in layers, is not fully understood.[69]

1.5.3 Stimuli responsiveness in LCs

Materials that undergo a change in their properties in a controlled and reversible fashion using external stimuli such as temperature, pressure, light, pH, electric or magnetic field, etc are known as smart or responsive materials. The stimuli-responsive functional materials are gaining interest for their realization as a smart materials [70] owing to their widespread use in a variety of applications such as artificial muscles,[71] photomechanical actuators,[72] light-activated shape memory change,[73] nanoporosity,[74], etc. The property of stimuli responsiveness at the molecular level can be manifested to bring a large change at the macroscopic level.[75] Light as stimuli is highly preferable over other stimuli as it is non-invasive, ubiquitous, and provides high spatiotemporal resolution with remote control. For example, macroscopic properties such as supramolecular self-assembly property in solution state (sol-gel, etc.), on surfaces (such as adhesion, catalysis, etc.), and in the bulk state (polymers, LCs, OLEDs, etc.) can be reversibly photo controlled.[75] To modulate such supramolecular functions at the macroscopic level, it is necessary to incorporate photo-responsive groups in such systems.

1.5.4 Photoswitchable LCs

A dual combination of photochromic property and LC property in a molecular design led to the development of highly fascinating photoswitchable LC functional materials.[76] These photoswitchable soft organic materials have a great wealth of research in diverse areas. One of the research areas includes the development of soft actuators at nano- to centimeter scales where LC polymeric materials (liquid crystal polymers (LCPs), liquid crystal elastomers (LCEs), and liquid crystal polymer networks (LCNs) have been used.[77] These polymeric materials have been used in shape memory (fixing of shape)[78] and artificial

muscles.[79] Another research area is their ability to modulate the properties in response to light reversibly which is very interesting from the technological point of view. To bring the property of photo responsiveness to an LC molecule, various photochromic molecules such as spiropyrans, spirooxazines, dithienylcyclopentenes, fulgimide, naphthopyrans, azobenzene, etc. have been incorporated into the design and studied for the photo modulation of properties, which makes these materials highly suitable candidates for the applications in optics, photonics, adaptive materials, nanotechnology, etc.[80]

1.5.5 Azobenzene-based LCs

Among these photochromic materials, photochromic azobenzene-based LC systems are highly fascinating and extensively studied for a wide range of applications.[80,81] Azobenzenes, owing to its unique reversible *trans* to *cis* photoisomerization behavior associated with large structural changes, offers photocontrol over the dynamic supramolecular self-assembled property of LC molecules, which in turn, leads to control over supramolecular function at the macroscopic level. The incorporation of photochromic azobenzenes into LC materials offers the modulation of properties such as photoinduced phase transitions, photo orientation, photoalignment, photomodulation etc.[80a] Photochromic azobenzene either in doped form or as an integral part of LC molecules underwent photochemical phase transitions, which causes either reversible modulation of properties or applications such as reversible optical control on transmittance,[82a] amplified image recording,[82b] rapid optical switching,[82c] nematic to isotropic phase transition in low molar LCs,[82d] mesophase transition from Col_r to S_mA to isotropic,[82e] surface relief gratings,[82f] refractive index modulation, etc.[82g] In photoalignment photochromic azobenzenes have been used as a command surface to photoalign the LC materials,[83] where azobenzenes derivatives were coated in a monolayer on surfaces and LC materials used to be sandwiched in between the cells that change alignment from homeotropic to planar.[83] In the photo orientation process, the photochromic azobenzene itself is an integral part of the design. Azobenzene is typically part of an LC (co)polymer, in which upon irradiation photosensitive group follows the cooperative photo orientation leading to an optical anisotropy in LC thin films.[84] The thin films of azobenzene copolymers upon irradiation with linearly polarized light undergo an enhancement in birefringence as a result of cooperative motions. In photo modulation, chiral azobenzene as guest (dopants) has been added to nematic phases (host) to induce the cholesteric liquid crystals (CLCs), where light induces *trans* to *cis* reversible

photoisomerization causing the pitch modulation, phase transition, and handedness inversion, etc, which enable various applications.[85]

1.5.6 Different types of LCs (based on the number of photoswitches)

More than one photochromic azobenzene unit can be functionalized into various designs and geometries such as linear branched, or cyclic, whereas based on the number of photoswitchable units, LC molecules may adopt various geometry or shapes such as linear, bent, tripodal, tetrameric, pillararene type etc.

Out of these, tripodal C_3-symmetric systems have their unique advantages. The molecular design consists of core/linker/spacers and photoswitchable units. The commonly used cores are triazine, benzene-1,3,5-tricarboxamide (BTA), hydroxy phenols etc. The linkers or spacers involved are alkyl chains, amide, ether, ester, etc. For example, Giese and co-workers designed and synthesized H-bonded LCs using 1,3,5-trihydroxy phenol and H-bond acceptor azopyridines, which showed light-induced phase transition as a result of the breaking of H-bonding interactions.[86] Li and co-workers reported unsymmetric, fully rigid tripodal molecules for lyotropic LC behavior in water which formed hexagonal columnar LC mesophase.[87] Liu and co-workers reported star-shaped highly conjugated, rigid 1,3,5-tri(azobenzeneethynyl)benzene derivatives, which exhibited thermotropic DLC properties, and optical limiting behavior.[88] Janietz and co-workers designed and synthesized triazine core-based two and three alkoxyazobenzene incorporated molecules, which showed the different structures of mesophases.[89] Recently, Detert and co-workers reported trisazolotriazines a heterocyclic core incorporated with tris-azobenzenes, which showed solvatochromic, acidochromic, and DLC behavior.[90] Haino and co-workers reported C_3-symmetric molecules which self-assemble to form toroidal nanostructures and exhibited mesomorphic properties.[91]

1.5.7 Applications

Tunability of properties of photoresponsive supramolecular functional LC materials opens the door for various applications. One of the important applications of C_3-symmetric molecules is in optical data storage.

Tripodal small molecular tris-azobenzene functionalized molecular systems were reported for stable holographic volume gratings by Schmidt and co-workers (**Scheme 1.8**).[92] LC property was induced by incorporating a long alkyl chain as spacer units. It was observed that molecules with decoupling spacers as well as polar end groups display stable holographic

grating properties. In another report, they observed that by using linearly polarized light and annealing in between glass transition temperature (T_g) and isotropic temperature, the alignment of tris-azobenzene units in the LC phase can further be amplified. The same group further explored one of the molecules for patterned photoalignment of LC material.

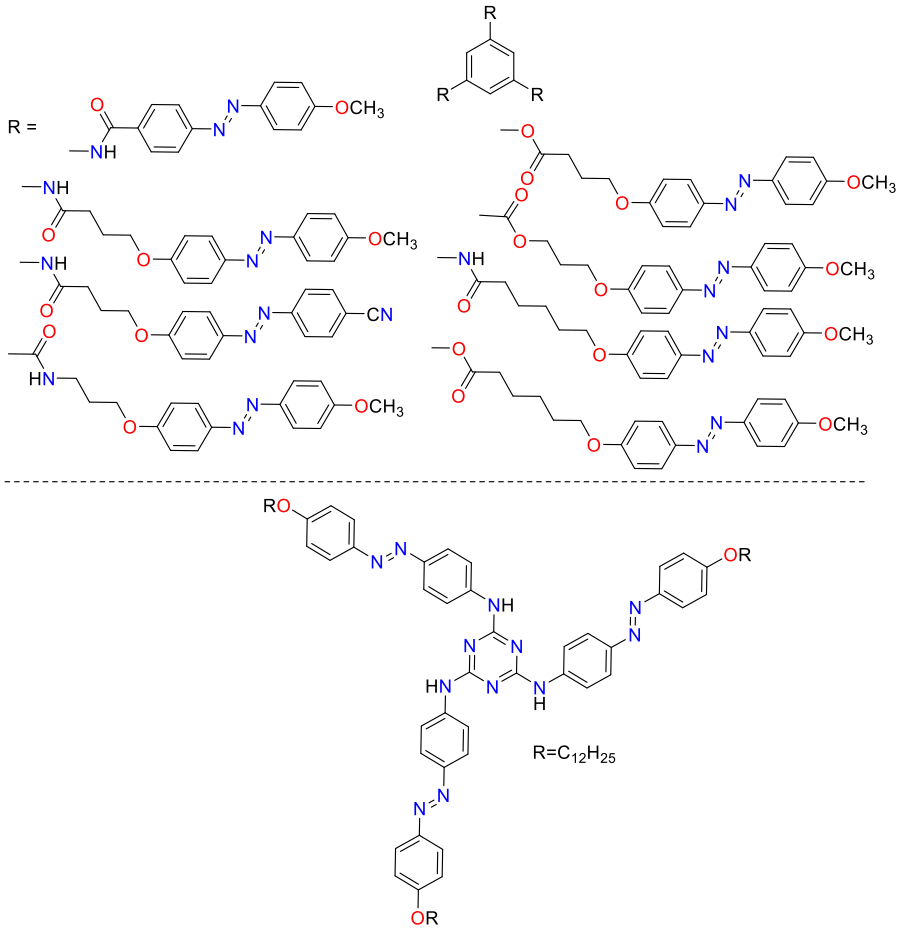

Scheme 1.8. C_3-symmetric tripodal LC molecules showing applications in holographic data storage

Wendorff and co-workers reported triazine core-based tris-azobenzene incorporated molecules for optical storage in smectic mesophase (**Scheme 1.8**).[93] It was observed that the efficiency of photoinduced surface relief gratings (SRG) can further be improved by thermal development (i.e., heating in between T_g and isotropic temperature). They proved that the enhancement in gain effect is a consequence of surface relief patterns formation and their amplification during thermal treatment.

1.6 Motivation and Objectives of the thesis

Recently, azoheteroarenes photoswitches are increasingly gaining importance over simple azobenzenes. This is owing to their improved photoswitching properties, tunable and

exceptional *cis* (*Z*) isomer stability, and their interesting properties as well as potential applications. In our group's previous investigations on arylazopyrazoles, the interplay of hydrogen bonding, solvent-assisted tautomerism through the free *N*-H part of pyrazole, and electronic effects in the photoswitching and thermal relaxation of the *Z*-isomer have been reported.[27] This motivated us to design photoswitches of a similar kind without such free *N*-H so that they can exhibit better photoswitching and extended half-life without the hindrance due to hydrogen bonding. One possible strategy is the *N*-alkylation, which has been previously reported by Fuchter and co-workers.[26a] At this stage, we decided on an alternative strategy to replace *N*-H with O, which results in azoisoxazole-based photoswitches. During the investigation of the parent and its aryl-substituted derivatives of azoisoxazole photoswitches, we unraveled a lot of intriguing properties. This made way to design and construct multiple azoarene-containing systems that can switch even in the solid-state. Also, the utility of core moieties such benzene-1,3,5-tricarboxamide (BTA) can facilitate supramolecular assemblies. In this regard, we decide to incorporate the azoisoxazole photoswitches in a tripodal C_3-symmetric fashion. To understand the propensity towards supramolecular assembly, the connectivity (*ortho*, *meta*, and *para* orientation of azo group relative to the amide functionality of the BTA core) and *N*-methylation strategies were considered. Additionally, the effects of such designs on various physicochemical and photoswitching characteristics as well as the supramolecular properties were also investigated. Furthermore, an extension of such supramolecular assemblies towards making photoswitchable discotic LCs was also considered. To achieve this, the BTA core-based design with azoisoxazole photoswitches in tripodal C_3-symmetric designs was tethered by alkoxy spacers. The exploration of the LC properties and the changes upon photoswitching was the main objective in this regard.

After introducing various concepts and topics related to the entire thesis in this current general introduction chapter, the next three chapters are mainly dealt with the results and discussion part.

In chapter two, the introduction to azoisoxazole photoswitches, the synthesis, characterization, and photoswitching studies are discussed. Also, the comparison of photoswitching properties and thermal stability of metastable *Z*-isomers has been discussed. Apart from that, this class of photoswitches is also studied for the light-induced reversible phase transition between the solid state and liquid phase.

In chapter three, the design, synthesis, and studies on azoisoxazole photoswitchable systems functionalized to a benzene1,3,5-tricarboxamides (BTA) core in tripodal C_3-symmetric design are discussed. Apart from photoswitching and thermal relaxation studies, their propensities towards supramolecular assemblies, in particular, sol-gel properties are demonstrated too. Furthermore, investigations on the effect of *N*-methylation at the BTA core are also included.

In chapter four, explorations of the designed systems based on azoisoxazoles-BTA analogs tethered through alkoxy spacer units for photoswitchable LC properties are discussed.

Chapter five provides overall conclusions from the results that are discussed in chapters two, three, and four. Also, brief future directions have been included as perspectives.

Chapter six deals with the materials and methods, where the technical aspects and the instruments used for all the studies are listed.

All the supporting data such as spectral characterization, photoswitching, kinetics studies, etc. are included in the Appendix at the end of chapters two, three, and four.

1.7 References

[1] a) Y. Hirshberg. *Compt. Rend. Acad. Sci*. **1950**, Paris, *231*, 903; b) H. Bouas-Laurent, H. Dürr, *Pure Appl. Chem*. **2001**, *73*, 639–665.

[2] a) M. Irie, *Chem. Rev*. 2000, 100, 5, 1683–1684; b) S. Kobatake, M. Irie, *Annu. Rep. Prog. Chem. Sect. C*, **2003**, *99*, 277–313.

[3] R. Klajn, *Chem. Soc. Rev*. **2014**, *43*, 148−184.

[4] a) A. Santiago, R. S. Becker, *J. Am. Chem. Soc*. **1968**, *90*, 3654−3658; b) Y. Yokoyama, In Molecular Switches; B. L. Feringa, Ed.; Wiley-VCH GmbH: Weinheim, Germany, **2001**, 107−121; c) Y. Yokoyama, *Chem. Rev*. **2000**, *100*, 1717−1739.

[5] a) W. M. Moore, D. D. Morgan, F. R. Stermitz, *J. Am. Chem. Soc*. **1963**, *85*, 829; b) F.B. Mallory, C.S. Wood, J.T. Gordon, *J. Am. Chem. Soc*. **1964**, *86*, 3094−3102; c) F.B. Mallory, C.W. Mallory, *Org. React*. **1984**, *30*, 1−456.

[6] M. Irie, *Chem. Rev*. **2000**, *100*, 1685−1716.

[7] H. M. D. Bandara, S. C. Burdette, *Chem. Soc. Rev*. **2012**, *41*, 1809–1825.

[8] a) C. J. Brown, *Acta Crystallogr*. **1966**, *21*, 146–152; b) C. R. Crecca, A. E. Roitberg, *J. Phys. Chem. A*, **2006**, *110*, 8188–8203; c) A. Mostad, C. Roemming, *Acta Chem. Scand*. **1971**, *25*, 3561–3568; d) L. Gagliardi, G. Orlandi, F. Bernardi, A. Cembran, M. Garavelli, *Theor. Chem. Acc*. **2004**, *111*, 363–372.

[9] a) Y. Dou, Y. Hu, S. Yuan, W. Wu, H. Tang, *Mol. Phys*. **2009**, *107*, 181–190; b) C. R. Crecca, A. E. Roitberg, *J. Phys. Chem. A* **2006**, *110*, 8188–8203; c) I. Conti, M. Garavelli, G. Orlandi, *J. Am. Chem. Soc*. **2008**, *130*, 5216–5230.

[10] a) E. V. Brown, G. R. Granneman, *J. Am. Chem. Soc*. **1975**, *97*, 621–627.

[11] J. Dokic, M. Gothe, J. Wirth, M. V. Peters, J. Schwarz, S. Hecht, P. Saalfrank, *J. Phys. Chem. A* **2009**, *113*, 6763–6773.
[12] a) W. R. Brode, J. H. Gould, G. M. Wyman, *J. Am. Chem. Soc.* **1952**, *74*, 4641–4646; b) M. Emond, T. Le Saux, S. Maurin, J.-B. Baudin, R. Plasson, L. Jullien, *Chem. Eur. J.* **2010**, *16*, 8822–8831.
[13] D. Bléger, J. Schwarz, A. M. Brouwer, S. Hecht, *J. Am. Chem. Soc.* **2012**, *134*, 20597–20600.
[14] a) G. B. El-Hefnawy, M. A. El-Borai, E. S. A. Aly, A. A. Gabr, *Indian J. Fibre Text. Res.* **1992**, *17*, 87–91; b) A. Ben-Bassat, S. Dershowitz, *J. Soc. Dyers Colour*. **1979**, *95*, 143–7; c) H. E. Gaffer, M. E. Khalifa, *Molecules* **2015**, *20*, 21982–21991; d) H. Balli, H. Ritter, *Dyes Pigm.* **1981**, *2*, 93–124; e) S. M. Fahmy, A. H. Badran, M. H. Elnagdi, *J. Chem. Technol. Biotechnol.* **1980**, *30*, 390–395.
[15] R. J. W. Le. Fèvre, C. V. Worth, *J. Chem. Soc.* **1951**, 1814–1817.
[16] N. Campbell, A. W. Henderson, D. Taylor, *J. Chem. Soc.* **1953**, 1281–1285.
[17] a) S. J. Dougan, M. Melchart, A. Habtemariam, S. Parsons, P. J. Sadler, *Inorg. Chem.* **2006**, *45*, 10882–10894; b) M. Ortiz, M. Torréns, J. L. Mola, P. J. Ortiz, A. Fragoso, A. Díaz, R. Cao, P. Prados, J. de Mendoza, A. Otero, A. Antiñolo, A. Lara, *Dalton Trans.* **2008**, 3559–3566; c) P. Manojkumar, T. K. Ravi, S. Gopalakrishnan, *Eur. J. Med. Chem.* **2009**, *44*, 4690–4694.
[18] a) Towns, A. D. *Dyes Pigm.* **1999**, *42*, 3–28; b) M. A. Weaver, L. Shuttleworth, *Dyes Pigm.* **1982**, *3*, 81–121.
[19] a) P. Sharma, A. Kumar, S. Upadhyay, J. Singh, V. Sahu, *Med. Chem. Res.* **2010**, *19*, 589-602; b) J. Marten, W. Seichter, E. Z. Weber, *Anorg. Allg. Chem.* **2005**, *631*, 869–877; c) J. Kunitomo, M. Yoshikawa, M. Fushimi, A. Kawada, J. F. Quinn, H. Oki, H. Kokubo, M. Kondo, K. Nakashima, N. Kamiguchi, K. Suzuki, H. Kimura, T. J. Taniguchi, *Med. Chem.* **2014**, *57*, 9627–9643.
[20] N. Iranpoor, H. Firouzabadi, D. Khalili, *Org. Biomol. Chem.* **2010**, *8*, 4436–4443.
[21] T. Jaunet-Lahary, A. Chantzis, K. J. Chen, A. D. Laurent, D. J. Jacquemin, *Phys. Chem. C* **2014**, *118*, 28831–28841.
[22] Z. Wang, Z. Yin, F. Zhu, Y. Li, X.-F. Wu, *ChemCatChem* **2017**, *9*, 3637–3640.
[23] a) A. Garci, A. A. Dobrov, T. Riedel, E. Orhan, P. J. Dyson, V. B. Arion, B. Therrien, *Organometallics* **2014**, *33*, 3813–3822; b) Y. Fu, M. J. Romero, L. Salassa, X. Cheng, A. Habtemariam, G. J. Clarkson, I. Prokes, A. Rodger, G. Costantini, P. J. Sadler, *Angew. Chem. Int. Ed.* **2016**, *55*, 8909–8912; c) Q.-X. Zhou, Y. Zheng, T.-J. Wang, Y.-J. Chen, K. Li, Y.-Y. Zhang, C. Li, Y.-J. Hou, X.-S. Wang, *Chem. Commun.* **2015**, *51*, 10684–10686; d) A. E. Rudenko, N. E. Clayman, J. K. MacLaren, R. M. Waymouth, *ChemistrySelect* **2016**, *1*, 3491–3496; e) A. Eskandari, A. Kundu, C. Lu, S. Ghosh, K. Suntharalingam, *Dalton Trans.* **2018**, *47*, 5755–5763; f) A. Telleria, P. W. N. M. van Leeuwen, Z. Freixa, *Dalton Trans.* **2017**, *46*, 3569–3578; g) K. Ghebreyessus, S. M. Cooper, *Organometallics* **2017**, *36*, 3360–3370.
[24] a) K. M. Hutchins, D. K. Unruh, F. A. Verdu, R. H. Groeneman, *Cryst. Growth Des.* **2018**, *18*, 566–570; b) C. M. Santana, E. W. Reinheimer, H. R. Krueger, L. R. MacGillivray, R. H. Groeneman, *Cryst. Growth Des.* **2017**, *17*, 2054–2058; c) O. Drath, R. W. Gable, B. Moubaraki, K. S. Murray, G. Poneti, L. Sorace, C. Boskovic, *Inorg. Chem.* **2016**, *55*, 4141–4151; d) G. L. Perlovich, *CrystEngComm* **2015**, *17*, 7019–7028; e) P. Ravat, S. SeethaLekshmi, S. N. Biswas, P. Nandy, S. Varughese, *Cryst. Growth Des.* **2015**, *15*, 2389–2401; f) O. S. Bushuyev, T. C. Corkery, C. J. Barrett, T. Friščić, *Chem. Sci.* **2014**, *5*, 3158–3164.

[25] a) M. Dommaschk, M. Peters, F. Gutzeit, C. Schütt, C. Näther, F. D. Sönnichsen, S. Tiwari, C. Riedel, S. Boretius, R. Herges, *J. Am. Chem. Soc.* **2015**, *137*, 7552–7555; b) G. Heitmann, C. Schütt, R. Herges, *Eur. J. Org. Chem.* **2016**, 3817–3823; c) T. Wendler, C. Schütt, C. Näther, R. Herges, *J. Org. Chem.* **2012**, *77*, 3284–3287.

[26] a) C. E. Weston, R. D. Richardson, P. R. Haycock, A. J. P. White, M. J. Fuchter, *J. Am. Chem. Soc.* **2014**, *136*, 11878–11881; b) J. Calbo, C. E. Weston, A. J. P. White, H. S. Rzepa, J. Contreras-García, M. J. Fuchter, *J. Am. Chem. Soc.* **2017**, *139*, 1261–1274.

[27] S. Devi, M. Saraswat, S. Grewal, S. Venkataramani, *J. Org. Chem.* **2018**, *83*, 4307–4322.

[28] J. Otsuki, K. Suwa, K. Narutaki, C. Sinha, I. Yoshikawa, K. Araki, *J. Phys. Chem. A* **2005**, *109*, 8064–8069.

[29] N. A. Simeth, S. Crespi, M. Fagnoni, B. König, *J. Am. Chem. Soc.* **2018**, *140*, 2940–2946.

[30] a) A. H. Heindl, H. A. Wegner, *Chem. Eur. J.* **2020**, *26*, 13730–13737; b) C. Slavov, C. Yang, A. H. Heindl, H. A. Wegner, A. Dreuw, J. Wachtveitl, *Angew. Chem. Int. Ed.* **2020**, *59*, 380–387.

[31] a) J. A. Balam-Villarreal, B. J. López-Mayorga, D. Gallardo-Rosas, R. A. Toscano, M. P. Carreón-Castro, V. A. Basiuk, F. Cortés-Guzmán, J. G. López-Cortés, M. C. Ortega-Alfaro, *Org. Biomol. Chem.* **2020**, *18*, 1657–1670; b) L. Muñoz-Rugeles, D. Gallardo-Rosas, J. Durán-Hernández, R. López-Arteaga, R. A. Toscano, N. Esturau-Escofet, J. G. López-Cortés, J. Peon, M. C. Ortega-Alfaro, *ChemPhotoChem* **2019**, *3*, 1–12.

[32] a) J. R. Tuck, R. J. Tombari, N. Yardeny, D. E. Olson, *Org. Lett.* **2021**, *23*, 4305−4310; b) Y.-C. Li, C. Qi, S.-H. Li, H.-J. Zhang, C.-H. Sun, Y.-Z. Yu, S.-P. Pang, *J. Am. Chem. Soc.* **2010**, *132*, 12172–12173.

[33] a) J. Garcia-Amorós, M. C. R. Castro, P. Coelho, M. M. M. Raposo, D. Velasco, *Chem. Commun.* **2013**, *49*, 11427–11429; b) C. Boga, S. Cino, G. Micheletti, D. Padovan, L. Prati, A. Mazzanti, N. Zanna, *Org. Biomol. Chem.* **2016**, *14*, 7061–7068.

[34] a) S. Grewal, D. Gupta, A. K. Gaur, M. Saraswat, S. Venkataramani in *Photoisomerization: Causes, Behavior and Effects* (Ed.: D. Sampedro, Nova Publishers, USA, **2019**; b) S. Crespi, N. A. Simeth, B. König, *Nat. Rev. Chem.* **2019**, *3*, 133−146; c) H. Chen, W. Chen, Y. Lin, Y. Xie, S. H. Liu, J. Yin, *Chin. Chem. Lett.* **2021**, *32*, 2359−2368.

[35] J. Broichhagen, J. A. Frank, N. R. Johnston, R. K. Mitchell, K. Šmid, P. Marchetti, M. Bugliani, G. A. Rutter, D. Trauner, D. J. Hodson, *Chem. Commun.* **2015**, *51*, 6018–6021.

[36] W. A. Velema, J. P. van der Berg, M. J. Hansen, W. Szymanski, A. J. M. Driessen, B. L. Feringa, *Nat. Chem.* **2013**, *5*, 924–928.

[37] C. E. Weston, A. Kramer, F. Colin, O. Yildiz, M. G. J. Baud, F.-J. Meyer-Almes, M. J. Fuchter, *ACS Infect. Dis.* **2017**, *3*, 152–161.

[38] L. Zeng, S. Kuang, G. Li, C. Jin, L. Ji, H. Chao, *Chem. Commun.* **2017**, *53*, 1977–1980.

[39] a) M. V. Peters, R. S. Stoll, A. Kuehn, S. Hecht, *Angew. Chem. Int. Ed.* **2008**, *47*, 5968–5972; b) C. E. Weston, R. D. Richardson, M. J. Fuchter, *Chem. Commun.* **2016**, *52*, 4521–4524.

[40] S. Erbas-Cakmak, D. A. Leigh, C. T. McTernan, A. L. Nussbaumer, *Chem. Rev.* **2015**, 115, 10081–10206.

[41] M. Dommaschk, C. Schütt, S. Venkataramani, U. Jana, C. Näther, F. D. Sönnichsen, R. Herges, *Dalton Trans*. **2014**, *43*, 17395–17405.
[42] S. Venkataramani, U. Jana, M. Dommaschk, F. D. Sönnichsen, F. Tuczek, R. Herges, *Science* **2011**, *331*, 445–448.
[43] W.-C. Xu, S. Sun, S. Wu, *Angew*. *Chem*. *Int*. *Ed*. **2019**, *58*, 9712–9740.
[44] Y. Okui, M. Han, *Chem*. *Commun*. **2012**, *48*, 11763–11765.
[45] a) H. Akiyama, M. Yoshida, *Adv*. *Mater*. **2012**, *24*, 2353–2356; b) H. Akiyama, S. Kanazawa, M. Yoshida, H. Kihara, H. Nagai, Y. Norikane, R. Azumi, *Mol*. *Cryst*. *Liq*. *Cryst*. **2014**, *604*, 64–70; c) H. Akiyama, S. Kanazawa, Y. Okuyama, M. Yoshida, H. Kihara, H. Nagai, Y. Norikane, R. Azumi, *ACS Appl*. *Mater*. *Interfaces* **2014**, *6*, 7933−7941.
[46] a) Y. Norikane, Y. Hirai, M. Yoshida, *Chem*. *Commun*. **2011**, *47*, 1770–1772; b) E. Uchida, K. Sakaki, Y. Nakamura, R. Azumi, Y. Hirai, H. Akiyama, M. Yoshida, Y. Norikane, *Chem*. *Eur*. *J*. **2013**, *19*, 17391–17397; c) M. Hoshino, E. Uchida, Y. Norikane, R. Azumi, S. Nozawa, A. Tomita, T. Sato, S.-i. Adachi, S.-y. Koshihara, *J. Am. Chem. Soc.* **2014**, *136*, 9158–9164.
[47] a) Y. Norikane, E. Uchida, S. Tanaka, K. Fujiwara, E. Koyama, R. Azumi, H. Akiyama, H. Kihara, M. Yoshida, *Org*. *Lett*. **2014**, *16*, 5012−5015; b) Y. Norikane, E. Uchida, S. Tanaka, K. Fujiwara, H. Nagai, H. Akiyama, *Photopolym. Sci. Technol.* **2016**, *29*, 149–157.
[48] Z. Wu, C. Ji, X. Zhao, Y. Han, K. Müllen, K. Pan, M. Yin, *J. Am. Chem. Soc.* **2019**, *141*, 7385–7390.
[49] H. Zhou, C. Xue, P. Weis, Y. Suzuki, S. Huang, K. Koynov, G. K. Auernhammer, R. Berger, H.-J. Butt, S. Wu, *Nature Chemistry* **2017**, *9*, 145–151.
[50] a) M. A. Gerkman, R. S. L. Gibson, J. Calbo, Y. Shi, M. J. Fuchter, G. G. D. Han, *J. Am. Chem. Soc.* **2020**, *142*, 8688–8695; b) L. Kortekaas, J. Simke, D. W. Kurka, B. J. Ravoo, *ACS Appl. Mater. Interfaces* **2020**, *12*, 32054–32060.
[51] F. Cisnetti, R. Ballardini, A. Credi, M. T. Gandolfi, S. Masiero, F. Negri, S. Pieraccini, G. P. Spada, *Chem*. *Eur*. *J*. **2004**, *10*, 2011–2021.
[52] A. Galanti, V. Diez-Cabanes, J. Santoro, M. Valášek, A. Minoia, M. Mayor, J. Cornil, P. Samorì, *J*. *Am*. *Chem*. *Soc*. **2018**, *140*, 16062–16070.
[53] a) C. Slavov, C. Yang, L. Schweighauser, C. Boumrifak, A. Dreuw, H. A. Wegner, J. Wachtveitl, *Phys*. *Chem*. *Chem*. *Phys*. **2016**, *18*, 14795–14804; (b) J. Robertus, S. F. Reker, T. C. Pijper, A. Deuzeman, W. R. Browne, B. L. Feringa, *Phys. Chem. Chem. Phys.* **2012**, *14*, 4374–4382; c) D. Bléger, J. Dokić, M. V. Peters, L. Grubert, P. Saalfrank, S. Hecht, *J. Phys*. *Chem*. *B* **2011**, *115*, 9930–9940; d) Á. Moneo, G. C. Justino, M. F. N. N. Carvalho, M. C. Oliveira, A. M. M. Antunes, D. Bléger, S. Hecht, J. P. Telo, *J*. *Phys*. *Chem*. *A* **2013**, *117*, 14056–14064; (e) F. Zhao, L. Grubert, S. Hecht, D. Bléger, *Chem*. *Commun*. **2017**, *53*, 3323–3326.
[54] a) R. Reuter, H. A. Wegner, *Chem*. *Eur*. *J*. **2011**, *17*, 2987–2995; (b) R. Reuter, H. A. Wegner, *Org*. *Lett*. **2011**, *13*, 5908–5911; (c) C. Slavov, C. Yang, L. Schweighauser, H. A. Wegner, A. Dreuw, J. Wachtveitl, *ChemPhysChem* **2017**, *18*, 2137–2141; d) A. H. Heindl, J. Becker, H. A. Wegner, *Chem*. *Sci*. **2019**, *10*, 7418–7425; (e) A. H. Heindl, L. Schweighauser, C. Logemannb, H. A. Wegner, *Synthesis* **2017**, *49*, 2632–2639; (f) E. Wagner-Wysiecka, N. Łukasik, J. F. Biernat, E. Luboch, *J*. *Incl*. *Phenom*. *Macrocycl*. *Chem*. **2018**, *90*, 189–257.
[55] a) A. Galanti, V. Diez-Cabanes, J. Santoro, M. Valášek, A. Minoia, M. Mayor, J. Cornil, P. Samorì, *J. Am. Chem. Soc*. **2018**, *140*, 16062–16070; b) A. Galanti, J. Santoro, R. Mannancherry, Q. Duez, V. Diez-Cabanes, M. Valášek, J. D. Winter, J. Cornil, P. Gerbaux, M. Mayor, P. Samorì, *J. Am*. *Chem*. *Soc*. **2019**, *141*, 9273–9283;

[56] J. Kind, L. Kaltschnee, M. Leyendecker, C. M. Thiele, *Chem. Commun*. **2016**, *52*, 12506–12509;
[57] A. H. Heindl, H. A. Wegner, Beilstein *J. Org. Chem*. **2020**, *16*, 22–31
[58] C. Yang, C. Slavov, H. A. Wegner, J. Wachtveitl, A. Dreuw, *Chem. Sci*. **2018**, *9*, 8665–8672.
[59] a) J. Bahrenburg, C. M. Sievers, J. B. Schönborn, B. Hartke, F. Renth, F. Temps, C. Näther, F. D. Sönnichsen, *Photochem. Photobiol. Sci*. **2013**, *12*, 511–518; b) J. Strueben, M. Lipfert, J.-O. Springer, C. A. Gould, P. J. Gates, F. D. Sönnichsen, A. Staubitz, *Chem. Eur. J*. **2015**, *21*, 11165–11173; c) M. D. Segarra-Maset, P. W. N. M. v. Leeuwen, Z. Freixa, *Eur. J. Inorg. Chem.* **2010**, 2075–2078; d) A. Telleria, P. W. N. M. v. Leeuwenb, Z. Freixa, *Dalton Trans*. **2017**, *46*, 3569–3578.
[60] S. Lee, S. Oh, J. Lee, Y. Malpani, Y.-S. Jung, B. Kang, J. Y. Lee, K. Ozasa, T. Isoshima, S. Y. Lee, M. Hara, D. Hashizume, J. M. Kim, *Langmuir* **2013**, *29*, 5869–5877.
[61] Y. Zhou, M. Xu, J. Wu, T. Yi, J. Han, S. Xiao, F. Li, C. Huang, *J. Phys. Org. Chem*. **2008**, *21*, 338–343.
[62] S. Grewal, P. Kumar, S. Roy, I. Bala, C. Sah, S. K. Pal, S. Venkataramani, *Chem. Eur. J*. **2022**, *28*, e20210460.
[63] a) J. Lee, S. Oh, J. Pyo, J.-M. Kim, J. H. Je, *Nanoscale* **2015**, *7*, 6457–6461; b) Y.-J. Choi, D.-Y. Kim, M. Park, W.-J. Yoon, Y. Lee, J.-K. Hwang, Y.-W. Chiang, S.-W. Kuo, C-H. Hsu, K.-U. Jeong, *ACS Appl. Mater. Interfaces* **2016**, *8*, 9490–9498.
[64] a) X. Liu, X.-S. Luo, H.-L. Deng, W. Fan, S. Wang, C. Yang, X.-Y. Sun, S.-L. Chen, M.-H. Huang, *Chem. Mater*. **2019**, *31*, 5421–5430; b) S. Grewal, S. Roy, H. Kumar, M. Saraswat, N. K. Bari , S. Sinha, S. Venkataramani, *Catal. Sci. Technol.* **2020**, *10*, 7027–7033.
[65] S. Devi, A. K. Gaur, D. Gupta, M. Saraswat, S. Venkataramani, *ChemPhotoChem* **2018**, *2*, 806–810.
[66] a) A. S. Matharu, S. Jeevaa, P. S. Ramanujam, *Chem. Soc. Rev*. **2007**, *36*, 1868–1880; b) C. Probst, C. Meichner, H. Audorff, R. Walker, K. Kreger, L. Kador, H.-W. Schmidt, *J. Polym. Sci. Part B* **2016**, *54*, 2110–2117.
[67] a) M. J. Stephen, J. P. Straley, *Rev. Mod. Phys*. **1974**, *46*, 617–704. b) D. Andrienko, *J. Mol. Liq*. **2018**, *267*, 520–541; c) T. Kato, J. Uchida, T. Ichikawa, T. Sakamoto, *Angew. Chem. Int. Ed*. **2018**, *57*, 4355–4371; d) P. Collings, M. Hird, An Introduction to Liquid Crystals: Chemistry and Physics (Taylor and Francis, **1997**).
[68] a) M. Sargazia, M. R. Linford, M. Kaykhaii, *Crit. Rev. Anal. Chem*. **2019**, *49*, 243–255; b) I. Dierking, Wiley-VCH Verlag GmbH & Co. KGaA, **2003**, pp. i–xi. b) J.-G. An, S. Hina, Y. Yang, M. Xue, Y. Liu, *Rev. Adv. Mater. Sci*. **2016**, *44*, 398–406.
[69] M. Kumar, S. Varshney, S. Kumar, *Polym. J*. **2021**, *53*, 283–297.
[70] a) P. Xie, R. Zhang, *J. Mater. Chem*. **2005**, *15*, 2529; b) Z. Yang, Z. Liu, L. Yuan, Asian *J. Org. Chem*. **2021**, *10*, 74; c) J. S. M. Lee, H. Sato, *Nat. Chem*. **2020**, *12*, 584; d) Y.–S. Meng, T. Liu, *Acc. Chem. Res*. **2019**, *52*, 1369; e) Z. L. Pianowski. *Chem. Eur. J*. **2019**, *25*, 5128.
[71] a) P. Rothemund, N. Kellaris, S. K. Mitchell, E. Acome, C. Keplinger, *Adv. Mater.* **2020**, e2003375; b) M. Kanik, S. Orguc, G. Varnavides, J. Kim, T. Benavides, D. Gonzalez, T. Akintilo, C. C. Tasan, A. P. Chandrakasan, Y. Fink, P. Anikeeva, *Science* **2019**, *365*, 145.
[72] a) H. Yu, T. Ikeda, *Adv. Mater.* **2011**, *23*, 2149–2180; b) Z. Jiang, M. Xu, F. Li, Y. Yu, *J. Am. Chem. Soc*. **2013**, *135*, 16446−16453; c) D.-Y. Kim, S. Shin, W.-J. Yoon, Y.-J. Choi, J.-K. Hwang, J.-S. Kim, C.-R. Lee, T.-L. Choi, K.-U. Jeong, *Adv. Funct.*

Mater. **2017**, *27*, 1606294; d) Y. Yu, T. Ikeda, *Angew. Chem. Int. Ed.* **2006**, *45*, 5416–5418; e) Y. Yu, M. Nakano, T. Ikeda, *Nature*, **2003**, *425*, 145; f) L. Qin, X. Liu, Y. Yu, *Adv. Optical Mater.* **2021**, *9*, 2001743; g) X. Lu, C. P. Ambulo, S. Wang, L. K. R.-Tarazona, H. Kim, K. Searles, T. H. Ware, *Angew. Chem. Int. Ed.* **2021**, *60*, 5536–5543.

[73] a) K. M. Lee, H. Koerner, R. A. Vaia, T. J. Bunning, T. J. White, *Soft Matter* **2011**, *7*, 4318–4324; b) Z. Wen, K. Yang, J.-M. Raquez, *Molecules* **2020**, *25*, 1241; c) A. Lendlein, H. Jiang, O. Juenger, R. Langer, *Nature*, **2005**, *434*, 879–882.

[74] a) J. A. M. Lugger, P. P. M. S. Roman, C. C. E. Kroonen, R. P. Sijbesma, *ACS Appl. Mater. Interfaces* **2021**, *13*, 3, 4385–4392; b) A. B. Grommet, L. M. Lee, R. Klajn, *Acc. Chem. Res.* **2020**, *53*, *11*, 2600–2610; c) Z. Wang, K. Müller, M. Valášek, S. Grosjean, S. Brase, C. Wöll, M. Mayor, L. Heinke, *J. Phys. Chem. C* **2018**, *122*, 19044−19050.

[75] M.-M. Russew, S. Hecht, *Adv. Mater*. **2010**, *22*, 3348–3360.

[76] A. Eremin, *Liq. Cryst. Rev*. **2020**, *8*, 29–43.

[77] L. Hines, K. Petersen, G. Zhan, Lum, M. Sitti, *Adv. Mater*. **2017**, *29*, 1603483.

[78] I. A. Rousseau, P. T. Mather, *J. Am. Chem. Soc.* **2003**, *125*, 15300–15301.

[79] M.-H. Li, P. Keller, *Phil. Trans. R. Soc. A* **2006**, *364*, 2763–2777.

[80] a) H. K. Bisoyi, Q. Li, *Chem. Rev*. **2016**, *116*, 15089−15166; b) T. Kosa, L. Sukhomlinova, L. Su, B. Taheri, T. J. White, T. J. Bunning, *Nature*, **2012**, *485*, 347; c) M. J. Moran, M. Magrini, D. M. Walba, I. Aprahamian, *J. Am. Chem. Soc.* **2018**, *140*, 13623; d) M. Frigoli, G. H. Mehl, *Eur. J. Org. Chem*. **2004**, 636; e) M. Lahikainen, K. Kuntze, H. Zeng, S. Helantera, S. Hecht, A. Priimagi, *ACS Appl. Mater. Interfaces*, **2020**, *12*, 47939; f) J. Boelke, S. Hecht, *Adv. Optical Mater*. **2019**, *7*, 1900404; g) M. Irie, T. Fukaminato, K. Matsuda, S. Kobatake, *Chem. Rev*. **2014**, *114*, 12174.

[81] a) J. A. Delaire, K. Nakatani, *Chem. Rev*. **2000**, *100*, 1817; b) T. Ikeda, O. Tsutsumi, *Science*, **1995**, *268*, 1873; c) K. Ichimura, *Chem. Rev*. **2000**, *100*, 1847.

[82] a) H.-K. Lee, A. Kanazawa, T. Shiono, T. Ikeda, T. Fujisawa, M. Aizawa, B. J. Lee, *Appl. Phys*. **1999**, *86*, 5927−5934; b) S. Tazuke, S. Kurihara, T. Ikeda, *Chem. Lett*. **1987**, *16*, 911−914; c) A. Shishido, O. Tsutsumi, A. Kanazawa, T. Shiono, T. Ikeda, N. Tamai, *J. Am. Chem. Soc*. **1997**, *119*, 7791−7796; d) J. Garcia-Amoros, A. Szymczyk, D. Velasco, *Phys. Chem. Chem. Phys*. **2009**, *11*, 4244−4250; e) D. Tanaka, H. Ishiguro, Y. Shimizu, K. Uchida, *J. Mater. Chem*. **2012**, *22*, 25065−25071; f) N. Zettsu, T. Ogasawara, R. Arakawa, S. Nagano, T. Ubukata, T. Seki, *Macromolecules* **2007**, *40*, 4607−4613; g) H. Yu, A. Shishido, T. Ikeda, *Appl. Phys. Lett*. **2008**, *92*, 103117.

[83] a) K. Ichimura, Y. Suzuki, T. Seki, A. Hosoki, K. Aoki, *Langmuir* **1988**, *4*, 1214−1216; b) T. Seki, M. Sakuragi, Y. Kawanishi, Y. Suzuki, T. Tamaki, R. Fukuda, K. Ichimura, *Langmuir* **1993**, *9*, 211−218; c) K. Ichimura, M. Han, S. Morino, *Chem. Lett*. **1999**, *28*, 85−86; d) S. Furumi, M. Nakagawa, S. Morino, K. Ichimura, *J. Mater. Chem*. **2000**, *10*, 833−837.

[84] a) L. Lasker, T. Fischer, J. Stumpe, S. Kostromin, S. Ivanov, V. Shibaev, R. Ruhmann, *Mol. Cryst. Liq. Cryst. Sci. Technol. Sect. A* **1994**, *253*, 1−10; b) T. Fischer, L. Lasker, M. Rutloh, S. Czapla, J. Stumpe, *Mol. Cryst. Liq. Cryst. Sci. Technol. Sect. A* **1997**, *299*, 293−299; c) R. Rosenhauer, Th. Fischer, J. Stumpe, R. Gimenez, M. Pinol, J. L. Serrano, A. Vinuales, D. Broer, *Macromolecules* **2005**, *38*, 2213−2222.

[85] a) C. Ruslim, K. Ichimura, *J. Phys. Chem. B* **2000**, *104*, 6529−6535; b) S. Kurihara, S. Nomiyama, T. Nonaka, *Chem. Mater.* **2000**, *12*, 9−12; c) C. Ruslim, K. Ichimura, *J. Mater. Chem.* **2002**, *12*, 3377−3379.
[86] a) M. Pfletscher, C. Wölper, J. S. Gutmann, M. Mezger, M. Giese, *Chem. Commun.* **2016**, *52*, 8549; b) M. Pfletscher, S. Hölscher, C. Wölper, M. Mezger, M. Giese, *Chem. Mater.* **2017**, *29*, 8462−8471.
[87] D. Wang, Y. Huang, J. Li, L. Xu, M. Chen, J. Tao, L. Li, *Chem. Eur. J.* **2013**, *19*, 685–690.
[88] Z. Xie, H. He, Y. Deng, X. Wang, C. Liu, *J. Mater. Chem. C* **2013**, *1*, 1791–1797.
[89] D. Goldmann, D. Janitz, *Liq. Cryst.* **1998**, *25*, 711–719.
[90] M. Sperner, N. Tober, H. Detert, *Eur. J. Org. Chem.* **2019**, 4688–4693.
[91] H. Adachi, Y. Hirai, T. Ikeda, M. Maeda, R. Hori, S. Kutsumizu, T. Haino, *Org. Lett.* **2016**, *18*, 924−927.
[92] a) K. Kreger, P. Wolfer, H. Audorff, L. Kador, N. Stingelin-Stutzmann, P. Smith, H.-W. Schmidt, *J. Am. Chem. Soc.* **2010**, *132*, 509–516; b) P. Wolfer, H. Audorff, K. Kreger, L. Kador, H.-W. Schmidt, N. Stingelin, P. Smith, *J. Mater. Chem.* **2011**, *21*, 4339–4345; c) P. Wolfer, K. Kreger, H.-W. Schmidt, N. Stingelin, P. Smith, *Mol. Cryst. Liq. Cryst.* **2012**, *562*, 133–140.
[93] a) A. Stracke, J. H. Wendorff, D. Goldmann, D. Janietz, B. Stiller, *Adv. Mater.* **2000**, *12*, 282−285; b) A. Stracke, J. H. Wendorff, D. Goldmann, D. Janietz, *Liq. Cryst.* **2000**, *27*, 1049–1057.

Chapter 2. Arylazo-3,5-dimethylisoxazole photoswitches

2.1 Introduction to arylazo-3,5-dimethylisoxazoles

Azobenzene is an exciting class of photoswitches. Due to its photoswitching property, extensive investigations have been done on azobenzenes that resulted in diverse applications. The replacement of the phenyl group by heterocycle rings led to an interesting subclass of azobenzenes, namely, azoheteroarenes. Although they are known for quite some time, azoheteroarenes attracted a lot of attention in recent times owing to their improved and tunable photoswitching properties. Indeed, the introduction of five-membered heterocycles in such systems revived the importance of azoarenes. Considering the increasing importance of azoheteroarenes towards applications in different fields, several attempts have been made to develop novel photoswitches. In this regard, the contributions by Herges (imidazole),[1] Fuchter (pyrazole)[2], and other nitrogen-based heterocycles),[3] Wegner (thiophene),[4] König (indole),[5] Olson (triazole),[6] Ortega-Alfaro (pyrrole),[7] Velasco (thiazole),[8] etc. are some of the important milestones. Along the line, a tremendous improvement in photoswitching behavior and tunable thermal stability of *cis* (*Z*) isomers have been achieved. For instance, Fuchter's group demonstrated the variation in thermal stability of *cis* (*Z*) isomer between 10 and 1000 days by using a simple substitution of methyl group and the connectivity of five-membered heterocylces.[2] In a similar line, Koenig and co-workers exploited the presence and absence of methyl group in indole-based azoheterarenes to tune the half-life of the *Z*-isomer from nanosecond (ns) to days [5] In yet another work, Devi *et al* reported that pyrazole *N*-H decreased the thermal stability of *Z*-isomer through hydrogen bonding and solvent-assisted tautomerism.[9] Indeed, the electronic and steric factors also play a crucial role along with the above-mentioned factors in dictating the *Z*-isomer stability of such azopyrazoles, and also affect the photoswitching characteristics.

Furthermore, *N*-methylation of pyrazole *N*-H can improve the *Z*-isomer thermal stability tremendously in phenylazopyrazoles. The hydrogen bonding through dimerization of azopyrazoles and solvent-assisted tautomerism were key in diminishing the photoswitching ability and the lowering of *Z*-isomer stability in the systems with *N*-H-pyrazoles. The *N*-methylation prevents both these channels and enhanced the Z-isomer stability, as well as efficiency in the photoswitching. An alternative strategy to induce a similar impact is a simple replacement of 3,5-dimethylpyrazole *N*-H with O which can lead to the generation of 3,5-dimethylisoxazole-based photoswitches. Despite, the fact that such compounds were

investigated for their medicinal effects, their photoswitching aspects have never been attempted.[10,11]

The impact of the isoxazole moiety on photoswitching behavior and thermal stability aspects of *Z*-isomers is the focus of this contribution. Besides, the aryl substituent effects and the added benefits of utilizing such photoswitches were also considered. The advantage of isoxazole unit is that hydrogen bonding and tautomeric channels are cut off, so steric and electronic influences of the substituents can be realized. In this regard, we synthesized arylazo-3,5-dimethylisoxazole derivatives with different *ortho*, *meta*, and *para* substituents. A few selected disubstituted derivatives were also synthesized. Photoswitching studies and UV-vis spectroscopic analysis were carried out for all of the azo compounds. The stability of the *Z*-isomer was estimated by monitoring the first-order kinetics of thermal reverse isomerization through NMR and UV-vis spectroscopic techniques. To determine the effects of substituents on electronic-structural aspects of both *E*- and *Z*-isomers, as well as the stability aspects underpinning the reverse thermal isomerization, extensive computations were performed.

During our investigations, apart from photoswitching, we also observed photochromic behavior accompanied by the light-induced phase transition in the majority of the derivatives. The native solid state of the compound underwent partial to complete melting on exposure to UV light. Such room temperature phase transitions have a variety of applications such as photolithography, reversible adhesives, photoresists, etc.[12] Indeed, the parent phenylazo-3,5-dimethylisoxazole **1d** was found to be one of the simplest azo derivatives exhibiting such reversible light-induced phase transition. For understanding, this phenomenon, differential scanning calorimetry (DSC), polarized optical microscopy (POM), IR spectroscopy, and computations were carried out. Overall, the investigations of arylazo-3,5-dimethylisoxazoles revealed that they are indeed an interesting class of photoswitches with several salient features. The details of the synthesis, photoswitching, kinetics studies, and reversible light-induced phase transition through spectroscopic studies on arylazo-3,5-dimethylisoxazole photoswitches are described in this chapter in detail.

2.2 Synthesis

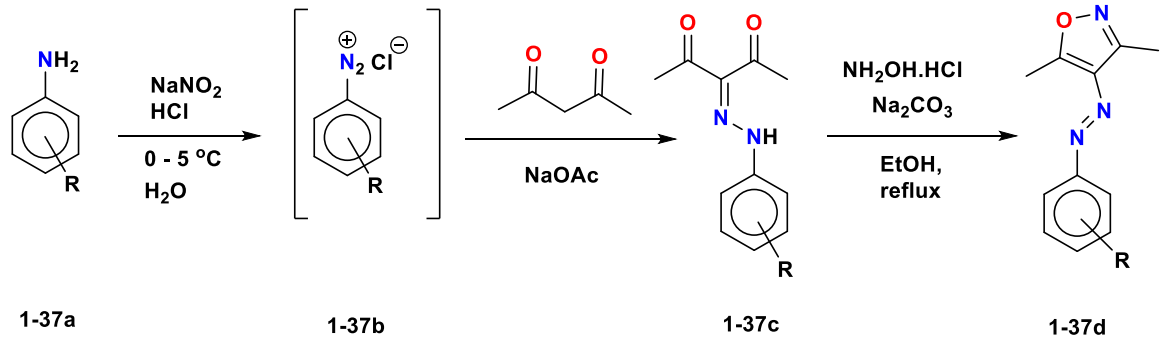

1-37a 1-37b 1-37c 1-37d

Scheme 2.1. Synthesis of arylazoisoxazole derivatives **1-37d**

A common diazonium-salt strategy was adopted for synthesizing the parent phenylazo-3,5-dimethylisoxazole and the majority of the 36 substituted derivatives (**Scheme 2.1** and **Table 2.1**). Commercially available aniline derivatives were used as starting materials. Both the generation of hydrazone derivatives **1**–**37c** and the consecutive cyclization step with hydroxylamine hydrochloride to access the target isoxazole-based derivatives **1**–**37d** adopted the literature procedure.[9] However, the presence of a base provided good to excellent yields in the cyclization step. The 2-amino derivative **32d** was synthesized by reduction of corresponding nitro derivative **20d**.[13] On the other hand, 3- and 4-amino derivatives **33d** and **34d** were obtained by the hydrolysis of **23d** and **24d**, respectively (**Experimental Section 2.8** and **Appendix 2I**).

To understand the effects of substituents and also to evaluate their impact on photoswitching characteristics, we compared the electronic spectral properties of the native *E*- and *Z*-isomers of all 37 arylazoisoxazole derivatives **1-37d** (**Figure 2.1a**, **Table 2.2** and **Appendix 2A**). Electronic spectral analysis in a common solvent (acetonitrile) was carried out for all derivatives. All derivatives were subjected to 365 nm UV irradiation in the same solvent to induce *E*–*Z* photoisomerization. Despite the observation of changes in the spectral features, the relative isomerization conversion was found to vary from one derivative to another. A few derivatives, such as **14d**, **15d**, **16d**, **20d**, **27d**, **30d**, **36d**, and **37d**, exhibited poor isomerization conversion, inferred from the subtle lowering of intensity without a significant blueshift, a key signature for the π–π* transition corresponding to the *E*–*Z* isomerization process. However, we observed an enhancement in the n–π* feature indicating isomerization. Moreover, the presence of isosbestic points confirmed interconversion between the two isomers without any intermediate. On the other hand, excellent

Table 2.1. Synthesis of arylazoisoxazole derivatives **1-37d**

S. No.	Substituent	Step 2[a]			Step 3			
		Product	Time, h	Yield (%)	Product	Condition	Time, h	Yield (%)
1	Nil	**1c**	5	88	**1d**	A	10	88
2	2-F	**2c**	10	99	**2d**	A	10	96
3	3-F	**3c**	6	97	**3d**	A	6	89
4	4-F	**4c**	13	99	**4d**	A	8	50
5	2-Cl	**5c**	3	98	**5d**	A	6	54
6	3-Cl	**6c**	3	98	**6d**	A	6	84
7	4-Cl	**7c**	5	95	**7d**	A	6	85
8	2-Br	**8c**	7	96	**8d**	A	7	67
9	3-Br	**9c**	7	95	**9d**	A	8	72
10	4-Br	**10c**	6	73	**10d**	A	6	75
11	4-I	**11c**	6	73	**11d**	A	6	94
12	2-OH	**12c**	5	98	**12d**	A	10	93
13	3-OH	**13c**	10	60	**13d**	A	8	71
14	4-OH	**14c**	12	94	**14d**	A	8	79
15	3-CF_3	**15c**	5	91	**15d**	A	7	89
16	4-CF_3	**16c**	5	91	**16d**	A	15	62
17	2-OMe	**17c**	8	82	**17d**	A	10	78
18	3-OMe	**18c**	8	87	**18d**	A	8	75
19	4-OMe	**19c**	10	95	**19d**	A	12	80
20	2-NO_2	**20c**	13	87	**20d**	A	24	60
21	4-NO_2	**21c**	8	82	**21d**	A	8	97
22	4-CH_3	**22c**	3	63	**22d**	A	10	87
23	3-$NHCOCH_3$	**23c**	3	87	**23d**	A	6	82
24	4-$NHCOCH_3$	**24c**	3	67	**24d**	A	8	80
25	R-Ph = α-Np	**25c**	3	66	**25d**	A	15	78
26	2,5, di-Cl	**26c**	14	54	**26d**	A	12	54
27	2,6, di-Cl	**27c**	3	62	**27d**	A	10	71
28	2,4, di-F	**28c**	3	99	**28d**	A	9	78
29	2,5, di-F	**29c**	5	99	**29d**	A	8	54
30	2,6, di-F	**30c**	10	98	**30d**	A	10	53
31	3,5, di-F	**31c**	4	99	**31d**	A	11	87
32	2-NH_2	-	-	-	**32d**	B	8	78
33	3-NH_2	-	-	-	**33d**	C	6	82
34	4-NH_2	-	-	-	**34d**	C	8	73
35	2-CN	**35c**	3	90	**35d**	A	12	51
36	R-Ph = 3-Pyridyl	**36c**	3	95	**36d**	A	7	78
37	R-Ph = 4-(Ph-N=N-Ph)	**37c**	5	92	**37d**	A	8	69

Step-1 corresponds to *in situ* diazonium salt formation; [a]Temperature = RT; α-Np = α-Naphthyl, **Condition-A:** Na_2CO_3 (1.5 eq.), $NH_2OH.HCl$ (1.5 eq.), EtOH, reflux; **Condition-B: 20d**, $Na_2S.9H_2O$ (7.5 eq.), 1,4-dioxane, ethanol, H_2O (10:2.6:1), reflux, 4h; **Condition-C: 23d**/**24d**, conc. HCl, EtOH, reflux.

photoswitching was observed in many derivatives, revealed by both the variation in the intensity and blueshifts of the π-π* band.

2.3 Absorption properties and photoswitching in solution and the solid-state

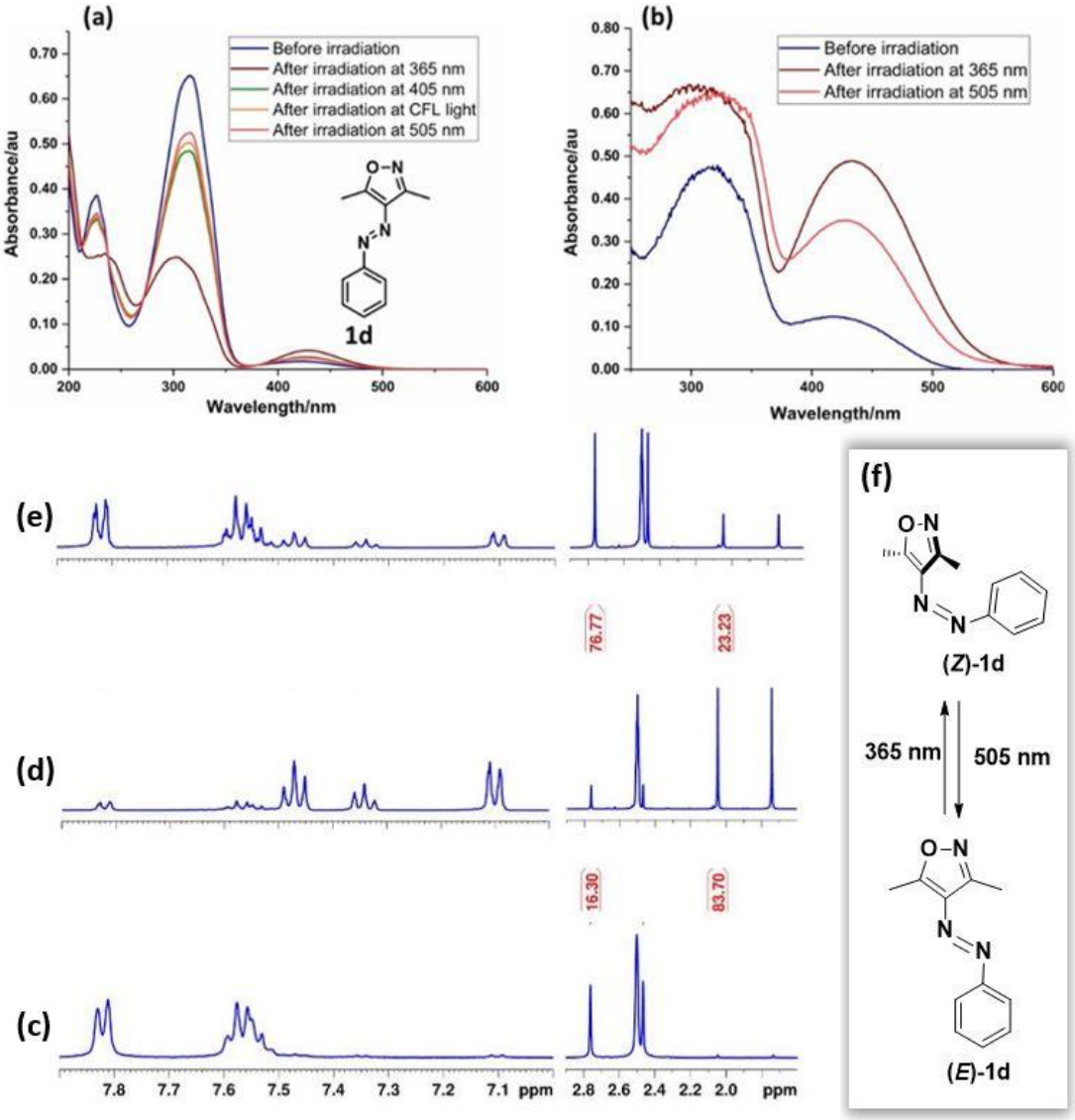

Figure 2.1. Photoisomerization of phenylazo-3,5-dimethylisoxazole (**1d**). Analysis of reversible *E*–*Z* photoisomerization in **1d** by UV/Vis spectroscopy in a) the solution phase (solvent: CH_3CN, 35.8 μM) and b) in the solid phase (medium: KBr). Analysis of photoswitching by ^1H NMR spectroscopy (solvent: $[D_6]$DMSO, 9.9 mM) c) Before irradiation, d) after 365 nm irradiation, and e) after 505 nm irradiation. f) Reversible photoisomerization of **1d**.

Table 2.2. UV-Vis spectroscopic and photoswitching data of (*E*)- and (*Z*)- isomers of phenylazo-3,5-dimethylisoxazole derivatives **1-37d**.

S. No	Compound	R	***E*-isomer[a]**				***Z*-isomer[a]**				$\Delta\lambda_{conjugation}$ [d]	Concentration [μM]
			π–π* λ_{max}, (ε)	**n–π* λ_{max}, (ε)**	$\Delta\lambda_{trans}$	***E*-*Z* PSS[b] (%*Z*)**	**π–π* λ_{max}, (ε)**	**n–π* λ_{max}, (ε)**	$\Delta\lambda_{cis}$	***Z*-*E* PSS[c] (%*E*)**		
1	**1d**	H	315 (18162±117)	422 (481±17)	107	65 ***59***	302 (15100)	428 (1428)	126	81 ***76***	13	36
2	**2d**	2-F	321 (14301±183)	416 (609±7)	95	48	313 (16782)	422 (1345)	109	80	8	42
3	**3d**	3-F	315 (8340±753)	421 (336±36)	106	36	309 (7741)	428 (916)	119	91	6	56
4	**4d**	4-F	318 (16360±153)	421 (481±8)	103	68 **80**	296 (6857)	428 (1378)	132	80 **82**	22	37
5	**5d**	2-Cl	321 (12124±220)	424 (383±40)	103	62	304 (8889)	426 (1186)	122	74	17	51
6	**6d**	3-Cl	315 (17731±71)	425 (425±15)	110	70	294 (6181)	429 (1605)	135	81	21	39
7	**7d**	4-Cl	323 (22789±269)	423 (670±16)	100	82 **94**	294 (7780)	429 (2301)	135	78 **62**	29	28
8	**8d**	2-Br	321 (9830±688)	428 (418±7)	107	58	310 (15503)	428 (1112)	118	88	11	56
9	**9d**	3-Br	315 (7822±744)	423 (388±35)	108	50 **89**	306 (11094)	429 (1750)	123	84 **76**	9	41
10	**10d**	4-Br	325 (21083±89)	421 (679±14)	96	85	295 (13767)	432 (1976)	137	77	30	32
11	**11d**	4-I	330 (23665±614)	424 (830±35)	94	87	295 (11728)	432 (4530)	137	77	35	28
12	**12d**	2-OH	316 (17128±549)	-	-	46	316 (20660)	-	316	73	-	39
13	**13d**	3-OH	313 (16908±46)	418 (596±15)	105	80 **87**	288 (8317)	432 (1948)	144	76 **80**	25	36
14	**14d**	4-OH	340	-	-	-	-	-	-	-	-	48
15	**15d**	3-CF_3	314 (19730±419)	418 (569±54)	104	39	308 (32445)	426 (1081)	118	77	6	34
16	**16d**	4-CF_3	312 (8744±757)	425 (384±8)	113	35	309 (20332)	429 (817)	120	83	3	62
17	**17d**	2-OMe	311 (10598±419)	414 (1036±36)	103	76	285 (6732)	426 (2296)	141	69	26	64
18	**18d**	3-OMe	312 (14802±133)	423 (604±16)	111	76	289 (7002)	430 (1813)	141	75	23	46
19	**19d**	4-OMe	337 (21570±319)	403 (1314±138)	66	81 **98**	309 (20332)	434 (3187)	125	82 **92**	28	28

20	**20d**	2-NO_2	318 (17241±110)	421 (640±19)	103	16	318 (91429)	415 (1037)	97	92	-	35
21	**21d**	4-NO_2	332 (22095±113)	431 (905±30)	99	75	295 (18140)	436 (2393)	141	86	37	28
22	**22d**	4-CH_3	323 (12333±1450)	420 (973±34)	97	47	308 (23450)	430 (2220)	122	93	15	41
23	**23d**	3-NHAc	315 (18797±1328)	429 (573±48)	114	75	295 (8842)	429 (2171)	134	78	20	33
24	**24d**	4-NHAc	342 (25152±129)	416 (1336±28)	74	82	315 (14035)	437 (8817)	122	79	27	27
25	**25d**	R-Ph = α-Np	362 (6789±354)	439 (881±10)	77	59	342 (4876)	440 (1970)	98	79	20	70
26	**26d**	2,5-diCl	320 (10850±556)	430 (452±16)	110	53	298 (10045)	427 (1267)	129	85	22	50
27	**27d**	2,6-diCl	297 (10893±31)	429 (409±8)	132	24	292 (36409)	421 (809)	129	82	5	60
28	**28d**	2,4-diF	324 (20900±443)	420 (766±53)	96	44	323 (27197)	420 (1818)	97	72	1	36
29	**29d**	2,5-diF	328 (16027±77)	417 (583±12)	89	84	287 (8405)	422 (2222)	135	69	41	38
30	**30d**	2,6-diF	309 (16809±155)	419 (882±28)	110	31	305 (26476)	419 (1646)	114	73	4	38
31	**31d**	3,5-diF	315 (16104±19)	417 (427±10)	102	64	297 (10953)	429 (1324)	132	81	18	36
32	**32d**	2-NH_2	310 (11667±1227)	-	-	56 ***61***	304 (14387)	438 (7566)	134	47 ***92***	6	34
33	**33d**	3-NH_2	315 (18293±113)	373 (3212±14)	58	72	290 (9804)	428 (2590)	138	72	25	36
34	**34d**	4-NH_2	371 (17176±378)	-	-	68	348 (15207)	439 (4988)	91	69	23	38
35	**35d**	2-CN	325 (16353±1035)	431 (499±39)	106	65 **90**	304 (8317)	434 (1501)	130	78 **83**	21	52
36	**36d**	R-Ph = 3-Pyridine	316 (7810±1340)	421 (376±7)	105	19	311 (40431)	429 (741)	118	98	5	83
37	**37d**	R-Ph = 4-(Ph-N=N-Ph)	358 (37483±309)	428 (3041±60)	70	43	348 (65006)	434 (4051)	86	70	10	17

[a]λ_{max} is given in nm and ε in L mol^{-1} cm^{-1}.[b]PSS for *E*–*Z* isomerization was estimated at 365 nm (roman: UV/Vis (CH_3CN); bold: ^{1}H NMR (italics: $CDCl_3$ (**1d** and **32d**); roman: [D_6]DMSO); [c]PSS for *Z*–*E* isomerization was estimated at the appropriate wavelengths of light, as indicated in the **Table 2D.1** of the **Appendix 2D** with 2–5% uncertainty[2] (normal: UV/Vis (CH_3CN); bold: ^{1}H NMR (bold + italics: $CDCl_3$ (**1d** and **32d**); bold + normal: [D_6]DMSO); [d]The difference in the π–π* absorptions for *E*- and *Z*-isomers was estimated by considering the degree of conjugation breaking on isomerization. The ε values for *Z*-isomers were estimated based on the PSS composition in the *E*–*Z* isomerization step; α-Np=α-naphthyl.

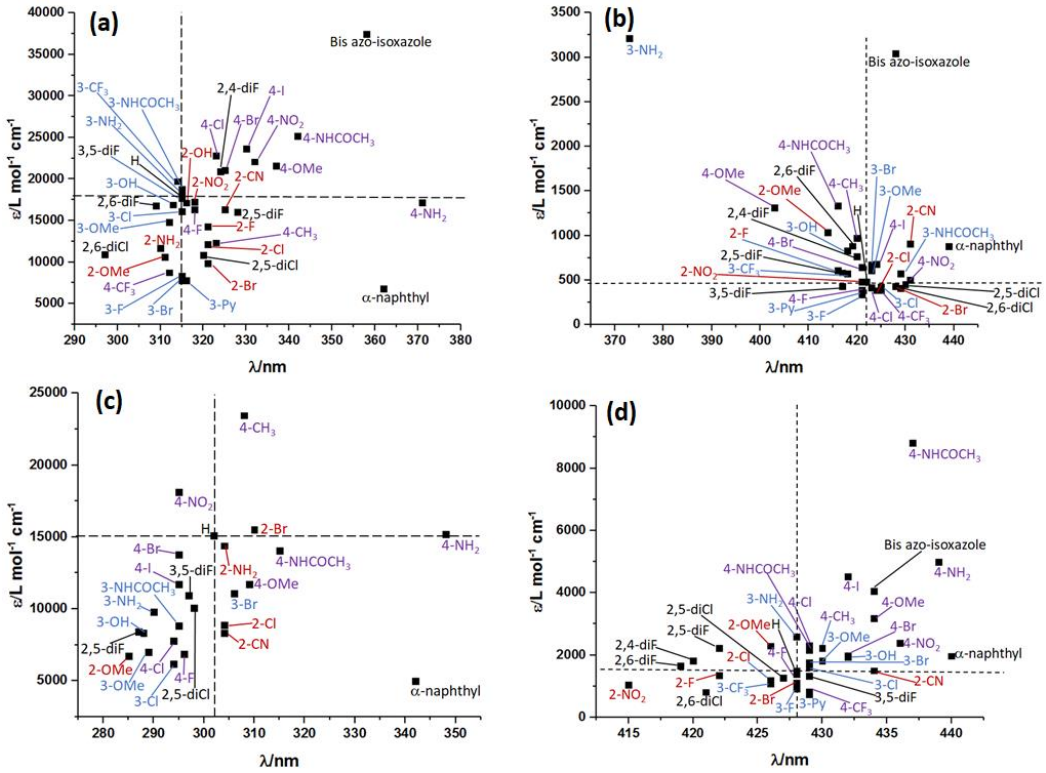

Figure 2.2. Effect of substituents on the absorption properties of *E*- and *Z*-isomers of the substituted phenylazo-3,5-dimethylisoxazoles: (a) π–π* absorption of *E*-isomers (b) n–π* absorption of *E*-isomers (c) π–π* absorption of *Z*-isomers, and (d) n–π* absorption of *Z*-isomers. The variation in absorption in terms of ε and λ_{max} shifts is separated into four quadrants to that of parent **1d**, which was taken as the origin.

For a better understanding of the substituent effects on the *E*- and *Z*-isomers, the electronic- spectral characteristics were utilized in the form of λ_{max} vs ε plots (**Figure 2.2**). First, both the π–π* and n–π* absorption features of the *E*- and *Z*-isomers of all the compounds were plotted around those of parent **1d** using the ε versus λ_{max} plot. The plots were split into four quadrants by using the corresponding λ_{max} and ε values of parent compound **1d** (unsubstituted) as the origin. **Figure 2.2** plot (a) depicts the effect of substitution in the π–π* band of the *E*-isomer. Based on the distribution, it is apparent that *para* and *ortho* substitutions significantly influence both the $\lambda_{max(\pi-\pi^*)}$ with bathochromic shifts relative to the parent. Whereas the para substituents in *E*-isomer exhibit higher ε than that of *ortho* and *meta* substituted systems. Interestingly, the *meta* substitution affects only the ε. Based on the spread in the plot (b), it is clear that the substituent effects are very small in the λ_{max} and ε values in the *E*-isomer, however, a slight influence has been observed for *para* and *ortho* substitutions. Upon isomerization, a majority of the substituents significantly decrease the λ_{max} and ε values of π–π* band that can be understood from panel (c). Unlike

the *E*-isomer case, the substituents in the *Z*-isomers strongly influence the λ_{max} and ε values (**Figure 2.2d**). This revealed that both the π–π* and n–π* absorption maxima are more sensitive to the substituents in the *Z*- than in the *E*-isomers. In general, *para* substitution influences λ_{max}, whereas *meta* and *ortho* substituents affect the molar absorptivity of the π–π* absorption in both *E*- and *Z*-isomers. This observation may be due to the interplay of inductive and mesomeric electronic effects. Indeed, the role of the steric effect can clearly be understood from the shifts of 2-substituted analogs, for which n–π* bands were found to be more susceptible.

The solution-phase photoswitching showed minimal concentration dependence in the forward isomerization step. Even at a very high concentration (1.6 mM), the *E*–*Z* isomerization was found to show 40% isomerization (**Appendix 2B**). This supported our understanding, based on the earlier studies on azopyrazoles, that the photoisomerization step can be limited by hydrogen bonding.[9]

Surprisingly, the 2-hydroxy- and 2-amino-substituted derivatives (**12d** and **32d**, respectively) were also found to undergo photoswitching (**Figure 2.6**, **Table 2.2,** and **Appendix 2A**). This is contrary to many azoarenes and azoheteroarenes with such functional groups at the *ortho* position, which has been attributed to the intramolecular hydrogen bonding and the resulting tautomeric equilibrium.[14] However, at higher concentrations, **12d** did not show any photoswitching, which indicates that either the reverse isomerization step is faster or intermolecular hydrogen bonding dominates. Compare to the hydroxy derivative, the amino derivative indeed showed better photoswitching. Indeed, **32d** exhibited visible-light photoswitching as well (**Appendix 2A**). For obtaining better insight, both compounds were subjected to photoswitching and monitored by NMR spectroscopy. The ^{1}H NMR signal of the hydroxyl protons in **12d** at 11.94 ppm indicated the possibility of intramolecular hydrogen bonding with the azo nitrogen atom (**Appendix 2I**). On the other hand, the amino protons in **32d** were not strongly influenced by hydrogen bonding, as inferred from the appearance of a single broad signal around 5.35 ppm (**Figure 2C.8** in **Appendix 2C**). In the case of bis-azo derivative **37d**, we observed photoswitching in which four different species were involved, due to the unsymmetrical environment between the two azo groups. Since photoisomerization takes place only to a limited extent, both forward and reverse isomerization steps lead to a mixture of photo products. For the best photoswitching derivatives, the composition of the photostationary state (PSS) was estimated by ^{1}H NMR spectroscopy, which revealed good to

excellent photoswitching for both forward and reverses isomerization steps (**Table 2.2** and **Appendix 2C**). Furthermore, UV/Vis spectroscopic studies on selected derivatives by repeating the forward and reverse photoswitching over five cycles revealed the photoswitching stability without any fatigue (**Figure 2.3**).

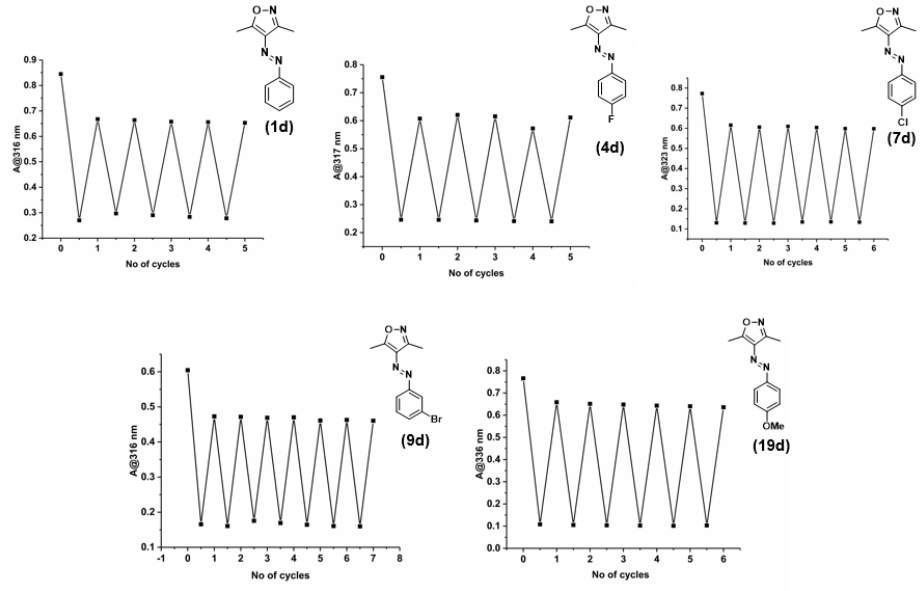

Figure 2.3. Photoswitching stability of selected and better photoswitching arylazo-3,5-dimethylisoxazole derivatives. For the forward isomerization step, 365 nm light was used, whereas for the reverse isomerization step, 470 nm light was used; Both the irradiation steps were repeated over five. (Solvent: Acetonitrile.)

Apart from solution-phase photoisomerization, solid-state photoswitching of all 37 arylazoisoxazole derivatives was studied (**Appendix 2A**). To this end, we studied their reversible photoisomerization in the KBr medium. Despite showing excellent *E–Z* photoisomerization, the reverse step was found to be partial in the majority of the derivatives. To understand the photoisomerization efficiency, the isomerization conversion was estimated at their respective PSSs for the forward *E–Z* and reverse *Z–E* steps in the solid state and the solution phase. The PSS compositions were estimated by literature methods [15a,b,2,9], and the results were tabulated (**Table 2.2** and **Table 2D.1** in **Appendix 2D**).

2.4 Thermal stability of *Z*-isomers

Apart from the efficient photoswitching in the forward *E–Z* and the reverse *Z–E* isomerization steps, the stability of the *Z*-isomer is a decisive factor in many practical applications. Often the thermal reverse isomerization is a crucial step in influencing the utility. In this regard, we utilized NMR spectroscopy.[16] The room-temperature (25 ± 2 ^{o}C) kinetics showed a slow rate of isomerization with a half-life of 45.5 d in [D_6]DMSO (**Table 2.3, Figure 2.4, Table 2.4**). On the other hand, the half-lives were estimated to be 111, 48,

and 16 min by monitoring the kinetics at 70 ± 2, 80 ± 2, and 90 ± 2 ^{o}C, respectively (**Figure 2.4**, **Table 2.4** and **Appendix 2E**).[17a] From these variable-temperature kinetics data, the activation parameters for the thermal reverse isomerization step were estimated (**Figure 2.5**, **Table 2.5,** and **Appendix 2E**). The activation barrier for the reaction of **1d** was found to be

Table 2.3. Thermal reverse isomerization kinetics data of **1d** in [D_6]DMSO at 25 ± 2 ^{o}C using NMR spectroscopy

S. No.	Time (min)	%Z	S. No.	Time (min)	%Z
1	0	82.56	15	71828	42.65
2	1353	80.13	16	76055	41.93
3	2875	78.11	17	81921	39.85
4	4270	77.85	18	86222	38.81
5	5725	76.32	19	96341	35.20
6	10131	73.67	20	106320	32.97
7	11381	70.60	21	113611	32.55
8	25696	61.33	22	116728	30.82
9	31540	60.81	23	132325	27.58
10	35906	58.76	24	172630	21.00
11	40199	56.41	25	193090	18.49
12	53143	50.07	26	214593	16.74
13	56282	49.72	27	253576	15.27
14	60380	47.48			

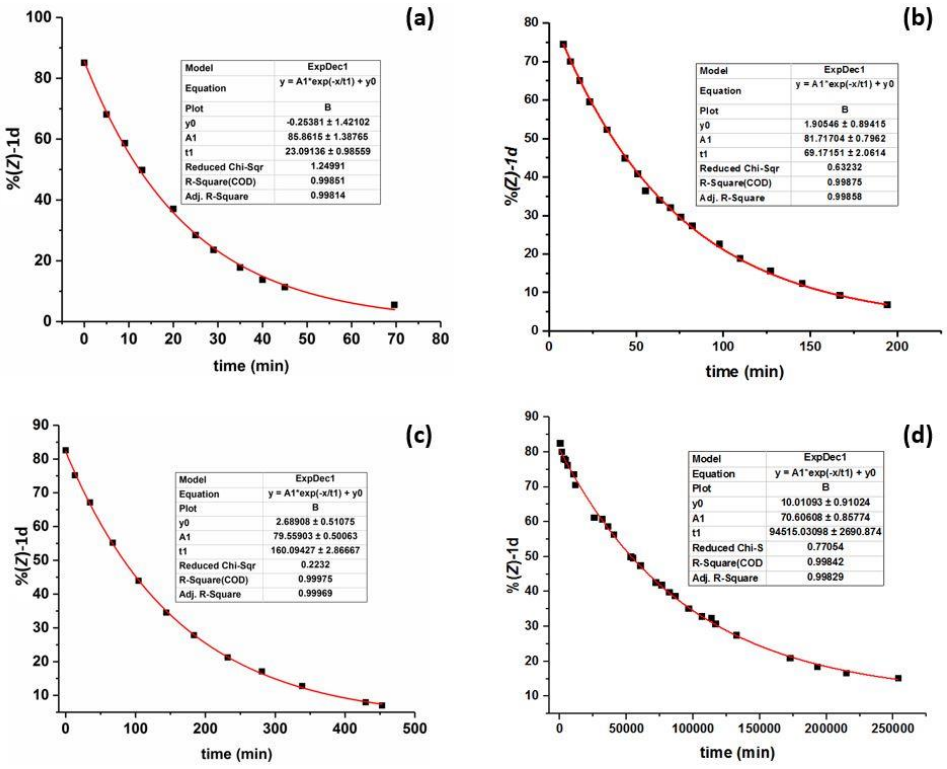

Figure 2.4. Thermal reverse isomerization kinetics plots of **1d** in [D_6]DMSO at (a) at 90 ± 2 ^{o}C; (b) 80 ± 2 ^{o}C (c) 70 ± 2 ^{o}C and (d) 25 ± 2 ^{o}C using ^{1}H-NMR spectroscopy.

116 ± 3 kJ mol^{-1}, which is comparable to those of the few known thermally long-lived *Z*-isomers of azoarenes and azoheteroarenes.[2,17b,18] For the selected candidates showing better photoswitching, we performed the thermal reverse isomerization kinetics at 80 ^{o}C in DMSO, and the kinetics was followed by UV-Vis spectroscopy. Using these data, the rate constants and the thermal half-lives have been estimated. The results indeed showed high thermal stability for those selected arylazo-3,5-dimethylisoxazoles in *Z*-isomeric form (**Table 2.6** and **Figure 2E.3** in **Appendix 2E**).

Table 2.4. Thermal reverse isomerization kinetics data of **1d** using ^{1}H-NMR spectroscopy

S. No.	Solvent	Temp. (^{o}C)	$t_{½}$ (min)	k (min^{-1})	Conc. [mM]
1	[D_6]DMSO	90 ± 2	16	4.3 x 10^{-2} ± 1.8 x 10^{-3}	12.1
2	[D_6]DMSO	80 ± 2	48	1.4 x 10^{-2} ± 4.3 x 10^{-4}	9.9
3	[D_6]DMSO	70 ± 2	111	6.2 x 10^{-3} ± 1.1 x 10^{-4}	14.9
4	[D_6]DMSO	25 ± 2	61987	1.1 x 10^{-5} ± 3.0 x 10^{-7}	9.9
3	$CDCl_3$	25 ± 2	30826	2.2 x 10^{-5} ± 8.0 x 10^{-7}	9.9

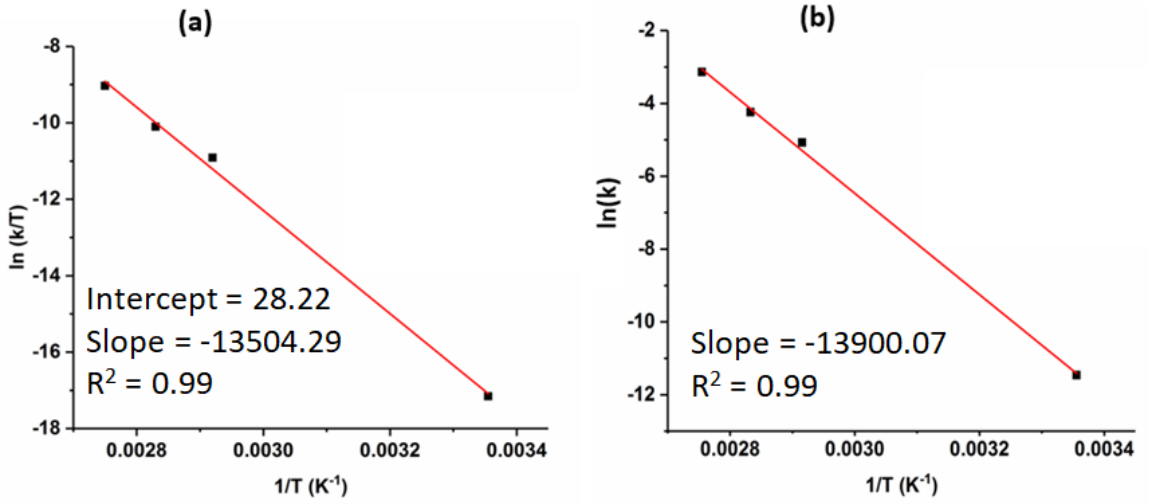

Figure 2.5. Reverse thermal isomerization of **1d** in [D_6]DMSO: (a) Eyring plot (b) Arrhenius plot.

Table 2.5. Activation parameters derived from Eyring and Arrhenius plots (at 298 K)

E_a	$\Delta H^{‡}$	$\Delta S^{‡}$	$\Delta G^{‡}$
116 ± 3 kJ.mol^{-1}	**112 ± 4** kJ.mol^{-1}	**30 ± 12** J.K^{-1}mol^{-1}	**103 ± 6** kJ.mol^{-1}
27.7 ± 0.8 kcal.mol^{-1}	27.0 ± 1.0 kcal.mol^{-1}	7.0 ± 2.9 cal.K^{-1}mol^{-1}	25.0 ± 1.3 kcal.mol^{-1}

Table 2.6. Thermal reverse isomerization (*Z*-*E*) kinetics data of selected arylazo-3,5-dimethylisoxazole derivatives using UV-Vis spectroscopy in (DMSO)

S. No.	Comp.	Substituent	Temp. (^{o}C)	$t_{½}$ (min)	k (min^{-1})	Conc. [μM]
1	**4d**	4-F	80 ± 2	52	$1.3x10^{-2} \pm 3.6 \times 10^{-4}$	18.2
2	**7d**	4-Cl	80 ± 2	43	$1.6x10^{-2} \pm 5.1x\ 10^{-4}$	25.5
3	**9d**	3-Br	80 ± 2	53	$1.3x10^{-2} \pm 5.4 \times 10^{-4}$	21.4
4	**19d**	4-OCH_3	80 ± 2	30	$2.3x10^{-2} \pm 2.0x\ 10^{-3}$	41.2

2.5 Photochemistry of *o*-hydroxy phenylazoisoxazole (12d)

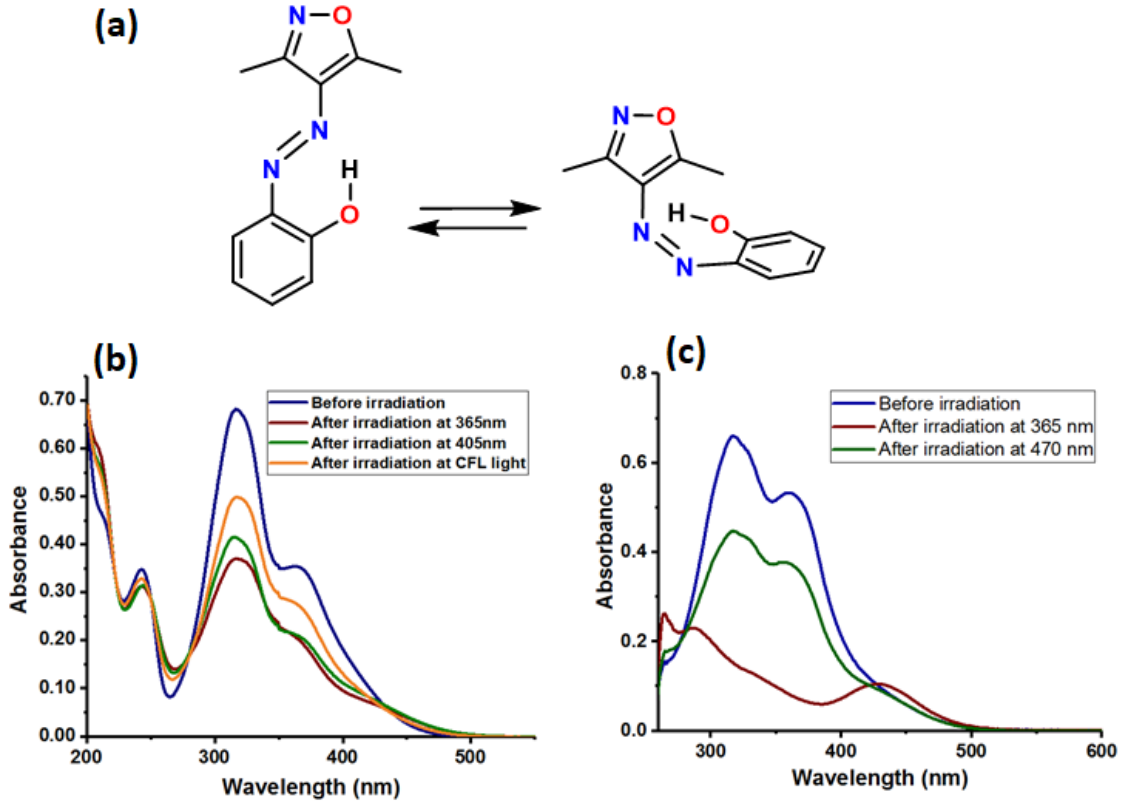

Figure 2.6. (a) Photoisomerization process in 2-hydroxy phenylazoisoxazole **12d** (b) and (c) UV-vis spectral data depicting the photoswitching in **12d** at different irradiation conditions in solvents acetonitrile and DMSO respectively

Typically, in *o*-hydroxyazobenzenes photoswitching is not observed due to intramolecular H-bonding leading to hydrazone formation as a result of tautomerism.[14,19] Indeed, the rate of thermal reverse isomerization is very fast, and so often photoswitching cannot be monitored. However, we observed that when *o*-hydroxy phenylazoisoxazole **12d** was subjected to photoswitching studies in DMSO under continuous irradiation with 365 nm, we observed prominent spectral changes with a decrease in the absorption maxima from the initial state.

However, in acetonitrile, only a few changes in the absorption profile were observed. Such observations indeed motivated us to understand the exact changes due to irradiation at 365 nm among the possibilities, photoswitching between *trans* (*E*) and *cis* (*Z*) isomers, tautomerism, and light-induced conformation changes. Interestingly, the spectral signatures of the initial state reverted partially upon irradiation at 470 nm at room temperature (**Figure 2.6c** and **Appendix 2F**). Furthermore, if the species obtained after irradiation at 365 nm is left standing at room temperature, it also spontaneously converts into its native state completely in minutes. This behavior allowed us to perform kinetics of thermal decay of the

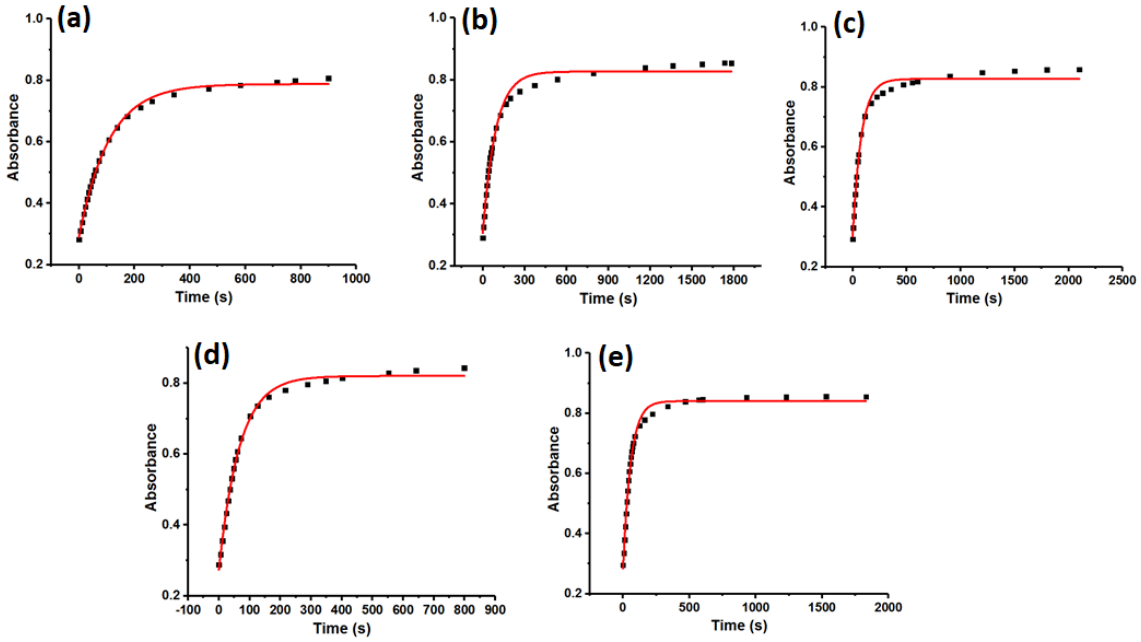

Figure 2.7. Kinetics data for the thermal reverse isomerization of **12d** at (a) 25 ^{o}C, (b) 30 ^{o}C, (c) 35 ^{o}C, (d) 40 ^{o}C and (e) 45 ^{o}C in DMSO (152 μM). Kinetics data have been followed by the absorption changes at $\lambda_{max}(\pi-\pi*)$ = 317 nm of *E*-isomer.

new species at various temperatures viz 25, 30, 35, 40, and 45 ^{o}C. Based on these variable temperature kinetics data, we estimated the activation parameters *E*a, $\Delta H^{\ddagger}$, $\Delta G^{\ddagger}$, and $\Delta S^{\ddagger}$ using Arrhenius and Eyring plots (**Figure 2.7, Table 2.7, Figure 2.8,** and **Table 2.8**). A low activation energy barrier (*E*a = 5.7 kcal mol^{-1}) was estimated, which is about 4 to 5 times lower than the thermal *Z*-*E* reverse isomerization of unsubstituted phenylazoisoxazole derivative **1d** (Ea = 27.7 kcal mol^{-1}, [D_6]DMSO). The lower activation energy barrier indicates the possibility of tautomerism due to intramolecular H-bonding between *o*-hydroxy proton and azo-nitrogen. To unravel this anomalous behavior computations and matrix isolation infrared spectroscopic studies were performed in cryogenic conditions in argon matrices at 4 K.[20] The experiments revealed that out of the three possibilities, viz.

photoswitching, tautomerism, and *E* to *E* conformation changes, photoswitching was found to be the observed channel. It is noteworthy to mention that a few plots corresponding to the thermal reverse isomerization step have poor fitting (monoexponential fit), we also attempted biexponential fits, and the results are updated in the Appendix (**Figure 2F.2** and **Table 2F.1** in **Appendix 2F**).

Table 2.7. Half-lives and rate constants for the thermal reverse isomerization of **12d** at variable temperature

Compound	Temperature (^{o}C)	Rate constant (s^{-1})	Half-life (s)	Conc. [μM]
12d	25	$9.3 \times 10^{-3} \pm 2.5 \times 10^{-4}$	75	152
	30	$1.1 \times 10^{-2} \pm 5.8 \times 10^{-4}$	64	152
	35	$1.3 \times 10^{-2} \pm 7.8 \times 10^{-4}$	55	152
	40	$1.5 \times 10^{-2} \pm 5.0 \times 10^{-4}$	46	152
	45	$1.7 \times 10^{-2} \pm 5.7 \times 10^{-4}$	40	152

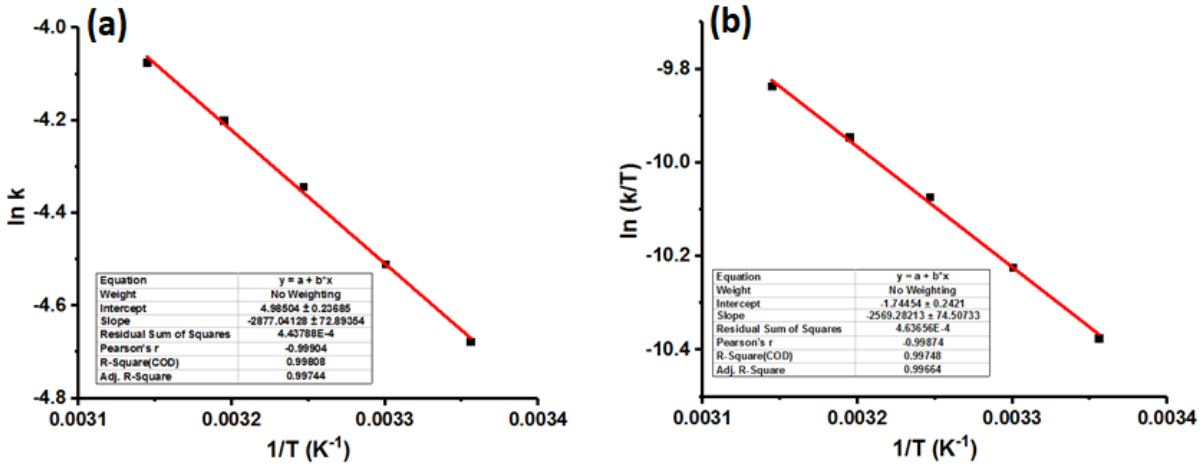

Figure 2.8. Arrhenius plot (a) and Eyring plot (b) for the thermal reverse isomerization of **12d**.

Table 2.8. Activation parameters derived from Arrhenius and Eyring plots for **12d**

Compound	E_a kcal mol^{-1}	$\Delta G^{\ddagger}$ (298K) kcal mol^{-1}	$\Delta H^{\ddagger}$ kcal mol^{-1}	$\Delta S^{\ddagger}$ cal K^{-1}
12d	5.7 ± 0.1	20.2 ± 0.2	5.1 ± 0.1	-50.7 ± 0.5

2.6 Light-induced phase transition

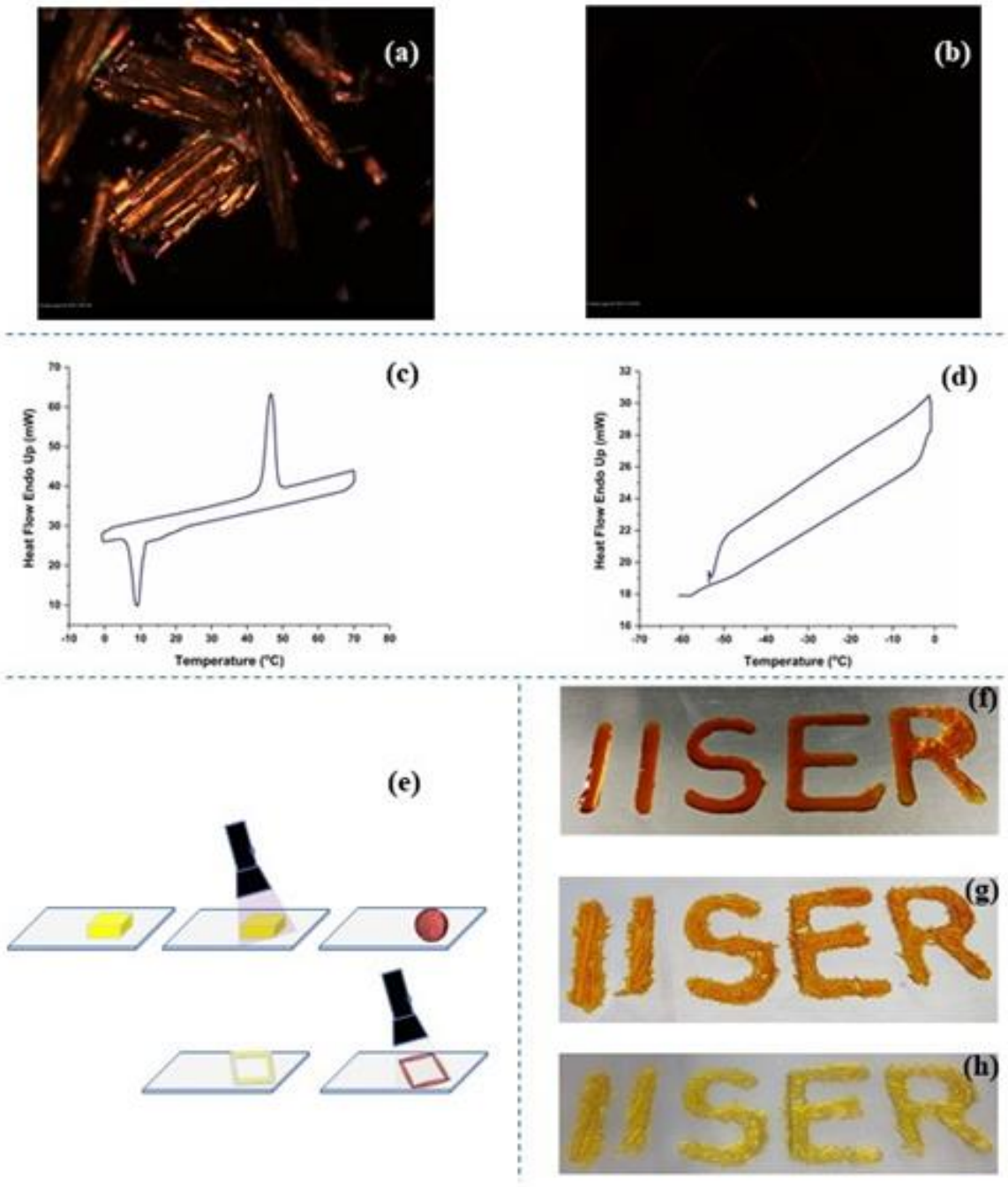

Figure 2.9. Light-induced phase transition in phenylazo-3,5-dimethylisoxazole. POM image (magnification: x200) of **1d** a) before UV irradiation and b) after 30 s of irradiation at 365 nm (RT); DSC curves obtained c) before irradiation and d) after irradiation at 365 nm (heating rate: 10 ^{o}C/min); e) Diagram showing the application of photo melting in molding a desired crystalline shape; f) Photographs depicting photo melting under UV light and patterning of the molten sample in the middle and at the end of crystallization under white-light irradiation (CFL bulb), respectively (g and h).

One of the salient features of the arylazoisoxazole derivatives is a light-induced phase transition. Many of the derivatives exhibited minimal to partial melting on solid-state UV

irradiation (365 nm) accompanied by contrasting color changes. Remarkably, parent compound **1d** showed complete melting. To obtain further insight, we monitored this phenomenon using POM. The phase transition was observed as a change in the birefringence pattern, which gradually turned dark, as a result of the conversion of crystalline (*E*)-**1d** to an isotropic molten phase on irradiation at 365 nm (**Figure 2.9a-b**, **Figure 2G.1** in **Appendix 2G**). As expected, differential scanning calorimetry (DSC) studies revealed a clear difference in the phase transition behavior for both the *E*-isomer and the molten material. The native sample of **1d** exhibited both solid-to-liquid phase transitions on heating and liquid-to-solid phase transition on cooling. Indeed, the molten sample did not change its phase even after cooling to -60 ^{o}C (**Figure 2.9c-d, Figure 2G.2** in **Appendix 2G**). To understand whether the heating effect of the light source induces the melting, aliquots were kept under water and irradiated. Still, we observed the melting phenomenon.[21] Furthermore, IR spectroscopic studies and inspection of the ^{1}H NMR spectrum of the molten sample revealed a small amount of the *Z*-isomer (**Figure 2G.5-G.7** in **Appendix 2G**).[22,23] Presumably, the presence of the *Z*-isomer and its high thermal stability prevents the freezing of the molten sample. On the other hand, irradiation of the molten sample with white light led to phase change and induced crystallization (**Figure 2.9f-h**). Interestingly, color changes were prominent during this reverse step. An initial orange-colored crystalline phase started to appear and ultimately led to a yellow-colored crystalline phase. Through white-light irradiation, we were able to crystallize the sample in 2 h, whereas crystallization was much slower if the same sample was kept at room temperature and took a few days. By using this reversible light-induced phase transition, we were able to demonstrate patterned crystallization of **1d** (**Figure 2.9e**).

To shed light on this phase transition, we considered the crystal structure of **1d**, computational data on the possible dimers of **1d**, and accompanying changes in the non-covalent interactions on isomerization (**Figure 2.10** and **Appendix 2H**).

According to the XRD data, the packing was mainly held together by several cooperative weak contacts such as π–π interactions, N···H–C interactions, and interactions of azo N atoms with the aryl rings. Presumably, the absence of strong intermolecular interactions provides the necessary conditions for phase transition on irradiation in **1d**.

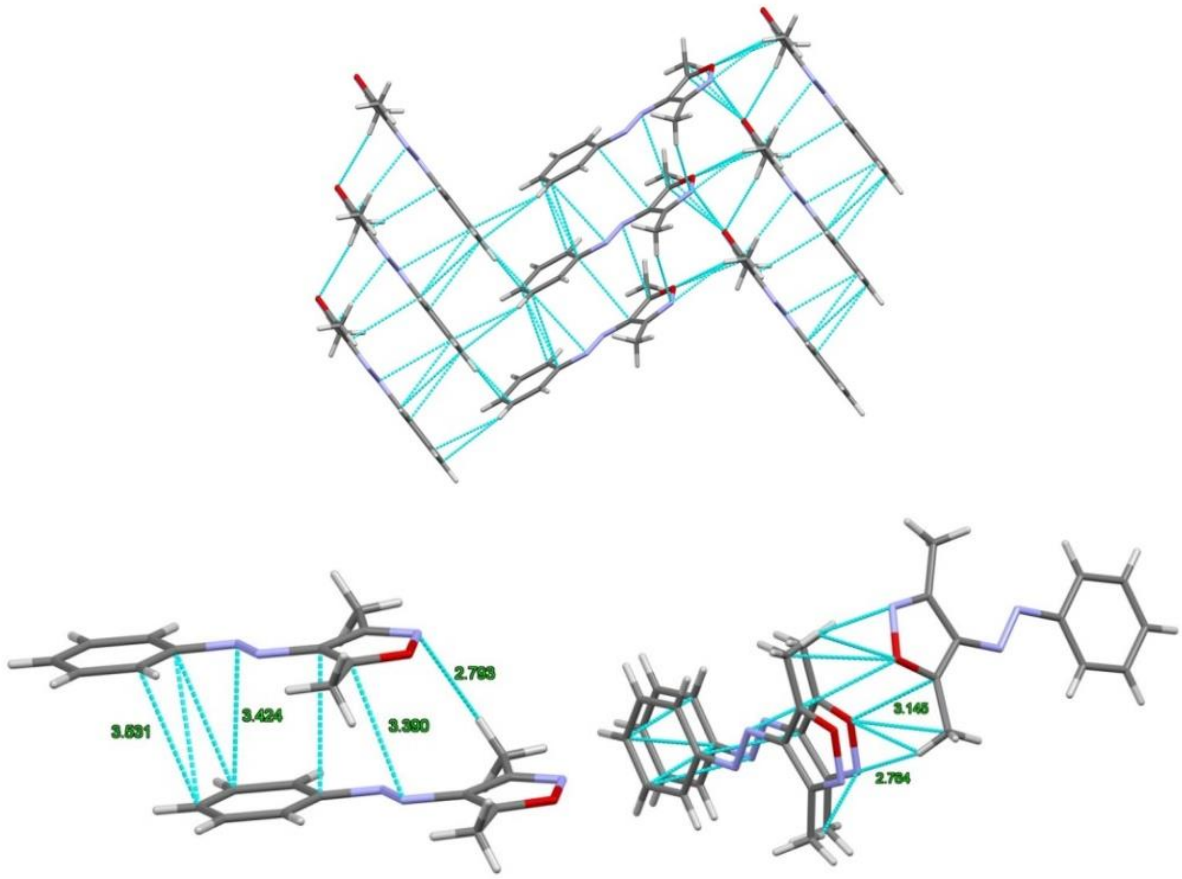

Figure 2.10. Crystal packing in **1d** from the single crystal XRD data (The dominant interactions and the internuclear distances in "Å" are indicated).

2.7 Summary

We have demonstrated the utility of arylazo-3,5-dimethylisoxazole derivatives as a new class of azoheteroarene-based photoswitches. The ease of synthesis, high yields, excellent photoswitching in solution, and long half-life of the *Z*-isomer make them robust photoswitchable systems. By means of extensive photoswitching studies and estimation of PSS composition using ^{1}H NMR spectroscopy, we found that parent **1d (**in $CDCl_3$, $\%Z_{PSS\text{-}E\text{-}Z}$ = 59, $\%E_{PSS\text{-}Z\text{-}E}$ = 76, in [D_6]DMSO, $\%Z_{PSS\text{-}E\text{-}Z}$ = 84, $\%E_{PSS\text{-}Z\text{-}E}$ = 77), 4-fluoro-derivative **4d (**in [D_6]DMSO, $\%Z_{PSS\text{-}E\text{-}Z}$ = 80, $\%E_{PSS\text{-}Z\text{-}E}$ = 82), 3-bromo-derivative **9d** (in [D_6]DMSO, $\%Z_{PSS\text{-}E\text{-}Z}$ = 89, $\%E_{PSS\text{-}Z\text{-}E}$ = 76), and 4-methoxy- derivative **19d** (in [D_6]DMSO, $\%Z_{PSS\text{-}E\text{-}Z}$ = 98, $\%E_{PSS\text{-}Z\text{-}E}$ = 92) are the best photoswitches among the 37 derivatives. On the other hand, most of the other derivatives exhibited moderate to good photoswitching. The studies on the photoswitching stability of the better photoswitching candidates revealed no fatigue over five cycles. The reverse thermal isomerization kinetics revealed long half-lives for *Z*-isomers. Besides, these compounds showed photoswitching in the solid state. Parent compound **1d**

was found to exhibit a reversible light-induced phase transition with contrasting colors that can potentially be useful in patterned crystallization. All these salient features make them ideal for many applications.

2.8 Experimental section

General procedure for the synthesis of arylazoacetylacetone derivatives (1-37c)

In a 50 ml round bottom flask aniline or substituted aniline (5.0 mmol) in distilled water was taken and cooled to 0 ^{o}C. Then concentrated HCl (37%, 1.6 ml) was added dropwise with continuous stirring to get a clear solution. A cold aqueous solution of $NaNO_2$ (5.5 mmol) dissolved in 5 ml of distilled water was added dropwise to the reaction mixture. The reaction mixture was stirred at 0 ^{o}C for half an hour until the diazonium salt intermediate was completely formed. Separately, in another flask, a solution of sodium acetate (17.5 mmol) and acetylacetone (5.0 mmol) in 25 ml of water and 3 ml of methanol was cooled to 0 ^{o}C, and was charged into the diazonium salt intermediate dropwise. The reaction was then stirred at room temperature for 2 hours and monitored for completion by TLC. The resulting yellow to orange precipitate was filtered and washed with water and dried in a vacuum to get the desired product.

General procedure for the synthesis of arylazoisoxazole derivatives (1-37d)

A mixture of arylazoacetylacetone derivative (1.0 mmol), hydroxylamine hydrochloride (1.5 mmol), and sodium carbonate (1.5 mmol) was refluxed in 10 ml ethanol. The reaction was monitored by TLC and upon completion, the solvent was evaporated and purified by column chromatography using (1:50) ethylacetate/hexane mixture.

Synthesis of *(E)*-2-((3,5-dimethylisoxazole-4-yl)diazenyl)aniline (32d)

In a round bottom flask, a mixture of *2*-nitro phenylazo-3,5-dimethylisoxazle (1.7 mmol) and $Na_2S.9H_2O$ (13.1 mmol) have been charged. To this, 1,4-dioxane (30 ml), ethanol (8 ml), and water (3 ml) were added. The resulting mixture was refluxed at 90 ^{o}C. The reaction was monitored by TLC and continued up to completion. The reaction mixture was concentrated in a vacuum and extraction was done using ethyl acetate and water. The organic layer was washed with brine, and water and dried under anhydrous Na_2SO_4. After evaporation of the solvent, purification was done by column chromatography using an 8-10% ethyl acetate-hexane mixture.

Synthesis of *(E)*-3- and *(E)*-4-((3,5-dimethylisoxazole-4-yl)diazenyl)aniline (33d and 34d)

Hydrolysis of 3- and 4-acetamido derivatives **23d** and **24d** (24.7 mmol) has been done using conc. HCl (12 ml, 37%) in ethanol (90 ml) by refluxing the resulting mixture for 6-8 hours. Reaction progress was monitored by TLC. After completion, the reaction mixture was neutralized by adding aqueous $NaHCO_3$ and concentrated. Afterward, extraction was done by using ethyl acetate and was washed with brine, and water and dried under anhydrous Na_2SO_4. Purification was done by column chromatography using an 8-10% ethyl acetate-hexane mixture.

(*E*)-3,5-dimethyl-4-(phenyldiazenyl)isoxazole (1d): yellow solid, mp = 55-57 ^oC, 718.0 mg, 88% yield; ^1H NMR (400 MHz, $CDCl_3$) δ 2.53 (s, 3H), 2.75 (s, 3H), 7.44-7.51 (m, 3H), 7.80-7.82 (m, 2H); ^{13}C NMR (100 MHz, $CDCl_3$) δ 11.77, 12.23, 122.27, 129.14, 130.80, 132.52, 152.93, 153.78, 169.52; HRMS (ESI-TOF) calcd for $C_{11}H_{11}N_3O$ $[M+H]^+$ 202.0980, found 202.0973; IR (ATR, cm^{-1}) 3041, 2923, 1613, 1411, 1061, 763.

***(E)*-4-((2-fluorophenyl)diazenyl)-3,5-dimethylisoxazole (2d):** yellow solid, mp = 96-97 ^oC, 210.3 mg, 96% yield; ^1H NMR (400 MHz, $CDCl_3$) δ 2.53 (s, 3H), 2.76 (s, 3H), 7.18-7.26 (m, 2H), 7.39-7.43 (m, 1H), 7.65-7.69 (td, *J* = 7.8, 1.6 Hz, 1H); ^{13}C NMR (100 MHz, $CDCl_3$) δ 11.85, 12.17, 116.97, 117.15 (d, *J* = 19.6 Hz), 124.31 (d, *J* = 3.8 Hz), 132.28 (d, *J* = 8.2 Hz), 133.31, 140.88 (d, *J* = 6.9 Hz), 153.92, 159.92 (d, *J* = 255.9 Hz), 170.10; HRMS (ESI-TOF) calcd for $C_{11}H_{10}FN_3O$ $[M+H]^+$ 220.0886, found 220.0896; IR (ATR, cm^{-1}) 3070, 2929, 1405, 1224, 757.

***(E)*-4-((3-fluorophenyl)diazenyl)-3,5-dimethylisoxazole (3d):** yellow solid, mp = 79-81 ^oC, 196.0 mg, 89% yield; ^1H NMR (400 MHz, $CDCl_3$) δ 2.52 (s, 3H), 2.76 (s, 3H), 7.13-7.17 (td, *J* = 8.1, 1.7 Hz, 1H), 7.44-7.49 (m, 2H), 7.63-7.65 (d, *J* = 7.9 Hz, 1H); ^{13}C NMR (100 MHz, $CDCl_3$) δ 11.85, 12.27, 107.37 (d, *J* = 22.8 Hz), 117.56 (d, *J* = 21.9 Hz), 120.13 (d, *J* = 2.9 Hz), 130.39 (d, *J* = 8.5 Hz), 132.53, 153.69, 154.48 (d, *J* = 6.9 Hz), 163.41 (d, *J* = 247.8 Hz), 170.38; HRMS (ESI-TOF) calcd for $C_{11}H_{10}FN_3O$ $[M+H]^+$ 220.0886, found 220.0876; IR (ATR, cm^{-1}) 3075, 2923, 1591, 1405, 1224, 785.

***(E)*-4-((4-fluorophenyl)diazenyl)-3,5-dimethylisoxazole (4d):** yellow solid, mp = 66-67 ^oC, 110.0 mg, 50% yield; ^1H NMR (400 MHz, $CDCl_3$) δ 2.51 (s, 3H), 2.73 (s, 3H), 7.13-7.19 (m, 2H), 7.79-7.84 (m, 2H); ^{13}C NMR (100 MHz, $CDCl_3$) δ 11.77, 12.23, 116.11 (d, *J* = 22.7 Hz), 124.22 (d, *J* = 8.8 Hz), 132.34, 149.47 (d, *J* = 3.03 Hz), 153.63, 164.26 (d, *J* = 244.7

Hz), 169.54; HRMS (ESI-TOF) calcd for $C_{11}H_{10}FN_3O$ $[M+H]^+$ 220.0886, found 220.0877; IR (ATR, cm^{-1}) 3075, 2923, 1591, 1219, 840.

***(E)*-4-((2-chlorophenyl)diazenyl)-3,5-dimethylisoxazole (5d):** yellow solid, mp = 117-118 ^oC, 130.0 mg, 54% yield; ^1H NMR (400 MHz, $CDCl_3$) δ 2.56 (s, 3H), 2.78 (s, 3H), 7.30-7.39 (m, 2H), 7.55 (dd, *J* = 7.9, 1.5 Hz), 7.66 (dd, *J* = 7.8, 2.0 Hz); ^{13}C NMR (100 MHz, $CDCl_3$) δ 11.92, 12.34, 116.79, 127.25, 130.81, 131.57, 133.47, 135.30, 148.94, 154.01, 170.37; HRMS (ESI-TOF) calcd for $C_{11}H_{10}ClN_3O$ $[M+H]^+$ 236.0591, found 236.0584; IR (ATR, cm^{-1}) 2917, 1613, 1411, 1054, 756.

***(E)*-4-((3-chlorophenyl)diazenyl)-3,5-dimethylisoxazole(6d):** yellow solid, mp = 78-80 ^oC, 399.9 mg, 84% yield; ^1H NMR (400 MHz, $CDCl_3$) δ 2.52 (s, 3H), 2.76 (s, 3H), 7.40-7.45 (m, 2H), 7.70-7.73 (m, 1H), 7.77 (br, 1H); ^{13}C NMR (100 MHz, $CDCl_3$) δ 11.86, 12.28, 121.26, 121.84, 130.24, 130.53, 132.58, 135.23, 153.63, 153.77, 170.47; HRMS (ESI-TOF) calcd for $C_{11}H_{10}ClN_3O$ $[M+H]^+$ 236.0591, found 236.0601; IR (ATR, cm^{-1}) 3076, 2923, 1411, 785.

***(E)*-4-((4-chlorophenyl)diazenyl)-3,5-dimethylisoxazole(7d):** yellow solid, mp = 61-62^oC, 401.3 mg, 85% yield; ^1H NMR (400 MHz, $CDCl_3$) δ 2.51 (s, 3H), 2.74 (s, 3H), 7.45 (d, *J* = 8.6 Hz, 2H), 7.75 (d, *J* = 8.6 Hz, 2H); ^{13}C NMR (100 MHz, $CDCl_3$) δ 11.83, 12.26, 123.55, 129.41, 132.46, 136.65, 151.26, 153.79, 169.96; HRMS (ESI-TOF) calcd for $C_{11}H_{10}ClN_3O$ $[M+H]^+$ 236.0591, found 236.0580; IR (ATR, cm^{-1}) 2923, 1603, 1089, 824.

***(E)*-4-((2-bromophenyl)diazenyl)-3,5-dimethylisoxazole(8d):** yellow solid, mp = 123-124 ^oC, 189.3 mg, 67% yield; ^1H NMR (400 MHz, $CDCl_3$) δ 2.59 (s, 3H), 2.75 (s, 3H), 7.29 (t, *J* = 7.8 Hz, 1H), 7.38 (t, *J* = 7.4 Hz, 1H), 7.65 (d, *J* = 8.0 Hz, 1H), 7.74 (d, *J* = 7.9 Hz, 1H); ^{13}C NMR (100 MHz, $CDCl_3$) δ 11.98, 12.54, 117.10, 125.72, 128.13, 131.86, 133.31, 133.89, 149.88, 153.88, 170.57; HRMS (ESI-TOF) calcd for $C_{11}H_{10}BrN_3O$ $[M+H]^+$ 280.0085, found 280.0079; IR (ATR, cm^{-1}) 2923, 1607, 1405, 763.

***(E)*-4-((3-bromophenyl)diazenyl)-3,5-dimethylisoxazole** (**9d**): yellow solid, mp = 97-98 ^oC, 200.9 mg, 72% yield; ^1H NMR (400 MHz, $CDCl_3$) δ 2.52 (s, 3H), 2.76 (s, 3H), 7.37 (t, *J* = 7.9 Hz, 1H), 7.56 (d, *J* = 8.0 Hz, 1H), 7.76 (d, *J* = 7.9 Hz, 1H), 7.93 (s, 1H); ^{13}C NMR (100 MHz, $CDCl_3$) δ 11.89, 12.30, 122.34, 123.23, 124.19, 130.57, 132.60, 133.44, 153.65, 153.88, 170.51; HRMS (ESI-TOF) calcd for $C_{11}H_{10}BrN_3O$ $[M+H]^+$ 280.0085, found 280.0097; IR (ATR, cm^{-1}) 2923, 1603, 1393, 824, 779.

***(E)*-4-((4-bromophenyl)diazenyl)-3,5-dimethylisoxazole (10d):** yellow solid, mp = 82-83 ^{o}C, 209.7 mg, 75% yield; ^{1}H NMR (400 MHz, $CDCl_3$) δ 2.52 (s, 3H), 2.74 (s, 3H), 7.65 (dd, *J* = 27.7, 8.6 Hz, 2H); ^{13}C NMR (100 MHz, $CDCl_3$) δ 11.87, 12.29, 123.82, 125.10, 132.42, 132.60, 151.71, 153.72, 170.06; HRMS (ESI-TOF) calcd for $C_{11}H_{10}BrN_3O$ $[M+H]^+$ 280.0085, found 280.0077; IR (ATR, cm^{-1}) 2964, 1265, 1016, 785.

***(E)*-4-((4-iodophenyl)diazenyl)-3,5-dimethylisoxazole (11d):** Light orange solid, mp = 130 ^{o}C, 309.1 mg, 94% yield; ^{1}H NMR (400 MHz, $CDCl_3$) δ 2.50 (s, 3H), 2.73 (s, 3H), 7.51-7.54 (m, 2H), 7.80-7.83 (m, 2H); ^{13}C NMR (100 MHz, $CDCl_3$) δ 11.87, 12.29, 97.29, 123.93, 132.57, 138.40, 152.26, 153.67, 170.09; HRMS (ESI-TOF) calcd for $C_{11}H_{10}IN_3O$ $[M+H]^+$ 327.9947, found 327.9931; IR (ATR, cm^{-1}) 2923, 1603, 970, 828.

***(E)*-2-((3,5-dimethylisoxazole-4-yl)diazenyl)phenol (12d):** yellow solid, mp = 114 ^{o}C, 201.9 mg, 93% yield; ^{1}H NMR (400 MHz, $CDCl_3$) δ 2.53 (s, 3H), 2.70 (s, 3H), 7.01 (dd, *J* = 8.3, 1.1 Hz, 1H), 7.05 (td, *J* = 8.0, 1.2 Hz, 1H), 7.31-7.366 (m, 1H), 7.82 (dd, *J* = 7.9 Hz, 1.6 Hz, 1H), 11.94 (s, 1H); ^{13}C NMR (100 MHz, $CDCl_3$) δ 12.11, 12.12, 118.24, 120.23, 130.80, 132.21, 133.15, 137.67, 152.13, 154.11, 167.41; HRMS (ESI-TOF) calcd for $C_{11}H_{11}N_3O_2$ $[M+H]^+$ 218.0930, found 218.0923; IR (ATR, cm^{-1}) 3510, 3178, 1591, 1220, 779.

***(E)*-3-((3,5-dimethylisoxazole-4-yl)diazenyl)phenol (13d):** yellow solid, mp = 162-163 ^{o}C, 1400.0 mg, 71% yield; ^{1}H NMR (400 MHz, $CDCl_3$) δ 2.53 (s, 3H), 2.74 (s, 3H), 5.95 (br, 1H), 6.96 (dd, *J* = 7.8 Hz, 1.8 Hz, 1H), 7.29 (t, *J* = 1.8 Hz, 1H), 7.36 (t, *J* = 7.9 Hz, 1H), 7.42 (d, *J* = 7.8 Hz, 1H); ^{13}C NMR (100 MHz, $CDCl_3$) δ 11.82, 12.22, 107.40, 116.67, 118.11, 130.17, 132.50, 153.96, 154.30, 156.65, 169.66; HRMS (ESI-TOF) calcd for $C_{11}H_{11}N_3O_2$ $[M+H]^+$ 218.0930, found 218.0925; IR (ATR, cm^{-1}) 3510, 3178, 1591, 1220, 779.

***(E)*-4-((3,5-dimethylisoxazole-4-yl)diazenyl)phenol (14d):** yellow solid, mp = 180 ^{o}C, 63.2 mg, 29% yield; ^{1}H NMR (400 MHz, $CDCl_3$) δ 2.52 (s, 3H), 2.73 (s, 3H), 5.57 (br, 1H), 6.93 (d, *J* = 8.7 Hz, 2H), 7.76 (d, *J* = 8.7 Hz, 2H); ^{13}C NMR (100 MHz, $CDCl_3$) δ 11.81, 12.24, 115.91, 124.35, 139.61, 147.51, 154.11, 158.27, 168.44; HRMS (ESI-TOF) calcd for $C_{11}H_{11}N_3O_2$ $[M+H]^+$ 218.0930, found 218.0920; IR (ATR, cm^{-1}) 3121, 2923, 1581, 1242, 840.

***(E)*-3,5-dimethyl-4-((3-(trifluoromethyl)phenyl)diazenyl)isoxazole (15d):** yellow solid, mp = 124 ^{o}C, 269.2 mg, 89% yield; ^{1}H NMR (400 MHz, $CDCl_3$) δ 2.54 (s, 3H), 2.78 (s, 3H), 7.62 (t, *J* = 7.8 Hz, 1H), 7.70 (d, *J* = 7.7 Hz, 1H), 7.99 (d, *J* = 7.9 Hz, 1H), 8.05 (br, 1H); ^{13}C

NMR (100 MHz, $CDCl_3$) δ 11.90, 12.33, 119.19 (q, *J* = 3.8 Hz), 122.59, 125.30, 125.52 (d, *J* = 0.8 Hz), 127.05 (q, *J* = 3.6 Hz), 128.01, 129.18, 129.81, 130.25, 131.80 (q, *J* = 32.6 Hz), 132.67, 153.25 (d, *J* = 69.0 Hz), 170.80; HRMS (ESI-TOF) calcd for $C_{12}H_{10}F_3N_3O$ $[M+H]^+$ 270.0854, found 270.0841; IR (ATR, cm^{-1}) 2963, 1607, 1326, 1111, 1054, 824.

***(E)*-3,5-dimethyl-4-((4-(trifluoromethyl)phenyl)diazenyl)isoxazole (16d):** yellow solid, mp = 56-57 ^oC, 167.4 mg, 62% yield; ^1H NMR (400 MHz, $CDCl_3$) δ 2.54 (s, 3H), 2.78 (s, 3H), 7.75 (d, *J* = 8.4 Hz, 2H), 7.89 (d, *J* = 8.3 Hz, 2H); ^{13}C NMR (100 MHz, $CDCl_3$) δ 11.90, 12.31, 122.52, 125.37, 126.41 (q, *J* = 3.6 Hz), 132.07 (d, *J* = 32.4 Hz,) 132.85, 153.57, 154.79, 170.98; HRMS (ESI-TOF) calcd for $C_{12}H_{10}F_3N_3O$ $[M+H]^+$ 270.0854, found 270.0852; IR (ATR, cm^{-1}) 2923, 1607, 1322, 1105, 1067, 840.

***(E)*-4-((2-methoxyphenyl)diazenyl)-3,5-dimethylisoxazole (17d):** yellow solid, mp = 134-135 ^oC, 181.3 mg, 78% yield; ^1H NMR (400 MHz, $CDCl_3$) δ 2.54 (s, 3H), 2.75 (s, 3H), 3.99 (s, 3H), 7.00 (t, *J* = 7.6 Hz, 1H), 7.07 (d, *J* = 8.3 Hz, 1H), 7.42 (t, *J* = 8.1 Hz, 1H), 7.58 (d, *J* = 8.0 Hz, 1H); ^{13}C NMR (100 MHz, $CDCl_3$) δ 11.85, 12.03, 56.46, 112.98, 116.19, 120.83, 132.31, 133.42, 142.56, 154.20, 156.88, 168.75; HRMS (ESI-TOF) calcd for $C_{12}H_{13}N_3O_2$ $[M+H]^+$ 232.1086, found 232.1079; IR (ATR, cm^{-1}) 3009, 2923, 1587, 1157, 1016, 744.

***(E)*-4-((3-methoxyphenyl)diazenyl)-3,5-dimethylisoxazole (18d):** yellow solid, mp = 75-76 ^oC, 350.0 mg, 75% yield; ^1H NMR (400 MHz, $CDCl_3$) δ 2.53 (s, 3H), 2.75 (s, 3H), 3.88 (s, 3H), 7.00 (dq, *J* = 7.9, 1.3 Hz, 1H), 7.33 (t, *J* = 2.1 Hz, 1H), 7.37-7.45 (m, 2H); ^{13}C NMR (100 MHz, $CDCl_3$) δ 11.80, 12.25, 55.72, 114.29, 124.08, 132.36, 137.38, 154.04, 161.90, 168.37; HRMS (ESI-TOF) calcd for $C_{12}H_{13}N_3O_2$ $[M+H]^+$ 232.1086, found 232.1079; IR (ATR, cm^{-1}) 3019, 2935, 1242, 1038, 779.

***(E)*-4-((4-methoxyphenyl)diazenyl)-3,5-dimethylisoxazole (19d):** yellow solid, mp = 110-111 ^oC, 184.8 mg, 80% yield; ^1H NMR (400 MHz, $CDCl_3$) δ 2.52 (s, 3H), 2.73 (s, 3H), 3.88 (s, 3H), 6.98 (d, *J* = 8.8 Hz, 2H), 7.80 (d, *J* = 8.9 Hz, 2H); ^{13}C NMR (100 MHz, $CDCl_3$) δ 11.80, 12.25, 55.72, 114.29, 124.08, 132.36, 147.38, 154.04, 161.90, 168.37; HRMS (ESI-TOF) calcd for $C_{12}H_{13}N_3O_2$ $[M+H]^+$ 232.1086, found 232.1090; IR (ATR, cm^{-1}) 2916, 1581, 1028, 840.

***(E)*-3,5-dimethyl-4-((2-nitrophenyl)diazenyl)isoxazole (20d):** orange solid, mp = 133-134^oC, 178.0 mg, 60% yield; ^1H NMR (400 MHz, $CDCl_3$) δ 2.46 (s, 3H), 2.76 (s, 3H), 7.53-7.57 (m, 1H), 7.64-7.68 (m, 2H), 7.87 (d, *J* = 7.9 Hz, 2H); ^{13}C NMR (100 MHz, $CDCl_3$) δ

11.92, 12.13, 117.91, 123.99, 130.64, 132.87, 133.34, 145.33, 147.76, 153.69, 171.72; HRMS (ESI-TOF) calcd for $C_{11}H_{10}N_4O_3$ $[M+H]^+$ 247.0831, found 247.0819; IR (ATR, cm^{-1}) 3472, 3341, 1513, 1365, 857.

***(E)*-3,5-dimethyl-4-((4-nitrophenyl)diazenyl)isoxazole (21d):** orange solid, mp = 161-162 ^oC, 238.7 mg, 97% yield; ^1H NMR (400 MHz, $CDCl_3$) δ 2.54 (s, 3H), 2.80 (s, 3H), 7.92 (d, *J* = 8.9 Hz, 2H), 8.36 (d, *J* = 9.0 Hz, 2H); ^{13}C NMR (100 MHz, $CDCl_3$) δ 11.98, 12.35, 122.95, 124.88, 133.20, 148.57, 153.36, 156.12, 172.00; HRMS (ESI-TOF) calcd for $C_{11}H_{10}N_4O_3$ $[M-H]^+$ 245.0675, found 245.0683; IR (ATR, cm^{-1}) 3098, 2923, 1513, 1332, 869.

***(E)*-3,5-dimethyl-4-(p-tolyldiazenyl)isoxazole (22d):** yellow solid, mp = 81-82^oC, 188.7mg, 87% yield; ^1H NMR (400 MHz, $CDCl_3$) δ 2.43 (s, 3H), 2.53 (s, 3H), 2.74 (s, 3H), 7.28 (d, *J* = 8.1 Hz, 2H), 7.71 (d, *J* = 8.1 Hz, 2H); ^{13}C NMR (100 MHz, $CDCl_3$) δ 11.81, 12.25, 21.61, 122.28, 129.83, 132.48, 141.36, 151.12, 153.96, 169.00; HRMS (ESI-TOF) calcd for $C_{12}H_{13}N_3O$ $[M+H]^+$ 216.1137, found 216.1133; IR (ATR, cm^{-1}) 2929, 1613, 1416, 824.

***(E)*-N-(3-((3,5-dimethylisoxazol-4-yl)diazenyl)phenyl)acetamide (23d):** yellow solid, mp = 185-186^oC, 211.7 mg, 82% yield; ^1H NMR (400 MHz, $CDCl_3$) δ 2.21 (s, 3H), 2.49 (s, 3H), 2.71 (s, 3H), 7.41 (t, *J* = 7.9 Hz, 1H), 7.55 (d, *J* = 7.8 Hz, 1H), 7.61 (d, *J* = 7.8 Hz), 7.77 (br, 1H), 7.97 (s, 1H); ^{13}C NMR (100 MHz, $CDCl_3$) δ 11.81, 12.25, 24.73, 113.17, 118.73, 122.02, 129.64, 132.49, 138.89, 153.46, 153.79, 168.82, 169.89; HRMS (ESI-TOF) calcd for $C_{13}H_{14}N_4O_2$ $[M+H]^+$ 259.1195, found 259.1202; IR (ATR, cm^{-1}) 3268, 3139, 2929, 1677, 155.

***(E)*-N-(4-((3,5-dimethylisoxazol-4-yl)diazenyl)phenyl)acetamide (24d):** yellow solid, mp = 178-179 ^oC, 206.5 mg, 80% yield; ^1H NMR (400 MHz, $CDCl_3$) δ 2.23 (s, 3H), 2.52 (s, 3H), 2.74 (s, 3H), 7.35 (br, 1H), 7.65 (d, *J* = 8.5 Hz, 2H), 7.80 (d, *J* = 8.7 Hz, 2H); ^{13}C NMR (100 MHz, $CDCl_3$) δ 11.83, 12.28, 24.92, 119.82, 123.37, 132.48, 140.31, 150.20, 153.93, 168.61, 169.12; HRMS (ESI-TOF) calcd for $C_{13}H_{14}N_4O_2$ $[M+H]^+$ 259.1195, found 259.1182; IR (ATR, cm^{-1}) 3319, 2923, 1693, 1591, 1150, 840.

***(E)*-3,5-dimethyl-4-(naphthalen-1-yldiazenyl)isoxazole (25d):** Yellow-orange solid, mp = 145-146 ^oC, 196.1 mg, 78% yield; ^1H NMR (400 MHz, $CDCl_3$) δ 2.68 (s,3H), 2.83 (s,3H), 7.54-7.67 (m, 3H), 7.78 (d, *J* = 7.5 Hz, 1H), 7.93 (d, *J* = 8.1 Hz, 2H), 7.97 (d, *J* = 8.1 Hz, 2H), 8.73 (d, *J* = 8.4 Hz, 1H); ^{13}C NMR (100 MHz, $CDCl_3$) δ 11.94, 12.72, 111.26, 123.25, 125.69, 126.59, 127.09, 128.16, 131.17, 131.24, 133.58, 134.43, 148.14, 153.55, 170.12;

HRMS (ESI-TOF) calcd for $C_{15}H_{13}N_3O$ $[M+H]^+$ 252.1137, found 252.1129; IR (ATR, cm^{-1}) 2917, 971, 802, 773.

***(E)*-4-((2,5-dichlorophenyl)diazenyl)-3,5-dimethylisoxazole (26d):** yellow solid, mp = 150-151^oC, 147.2 mg, 54% yield; ^1H NMR (400 MHz, $CDCl_3$) δ 2.55 (s, 3H), 2.80 (s, 3H), 7.34 (dd, *J* = 8.5, 2.4 Hz, 1H), 7.48 (d, *J* = 8.6 Hz, 1H), 7.64 (d, *J* = 7.6 Hz, 1H); ^{13}C NMR (100 MHz, $CDCl_3$) δ 12.00, 12.38, 117.02, 131.18, 131.65, 133.51, 133.57, 133.58, 149.23, 153.75, 171.32; HRMS (ESI-TOF) calcd for $C_{11}H_9Cl_2N_3O$ $[M+H]^+$ 270.0201, found 270.0192; IR (ATR, cm^{-1}) 3092, 2922, 1597, 1411, 818.

***(E)*-4-((2,6-dichlorophenyl)diazenyl)-3,5-dimethylisoxazole (27d):** red solid, mp = 103-104 ^oC, 386.3 mg, 71% yield; ^1H NMR (400 MHz, $CDCl_3$) δ 2.53 (s, 3H), 2.76 (s, 3H), 7.18 (t, *J* = 8.3 Hz, 1H), 7.40 (d, *J* = 8.1 Hz, 2H); ^{13}C NMR (100 MHz, $CDCl_3$) δ 11.78, 12.21, 127.38, 128.63, 129.31, 133.29, 148.02, 153.34, 171.89; HRMS (ESI-TOF) calcd for $C_{11}H_9Cl_2N_3O$ $[M+H]^+$ 270.0201, found 270.0194; IR (ATR, cm^{-1}) 3075, 2922, 1607, 1364, 971, 767.

***(E)*-4-((2,4-difluorophenyl)diazenyl)-3,5-dimethylisoxazole (28d):** yellow solid, mp = 113-114 ^oC, 184.9 mg, 78% yield; ^1H NMR (400 MHz, $CDCl_3$) δ 2.51 (s, 3H), 2.75 (s, 3H), 6.92-7.01 (m, 2H), 7.71 (td, *J* = 8.8, 2.4 Hz, 1H); ^{13}C NMR (100 MHz, $CDCl_3$) δ 11.84, 12.14, 105.22 (dd, *J* = 25.8, 23.3 Hz), 111.85 (dd, *J* = 22.5, 3.8 Hz), 118.22 (dd, *J* = 10.2, 1.5 Hz), 133.19, 137.81 (q, *J* = 3.9 Hz), 153.86, 160.30 (dd, *J* = 258.9, 12.2 Hz), 164.43 (dd, *J* = 252.6, 11.4), 170.07; HRMS (ESI-TOF) calcd for $C_{11}H_9F_2N_3O$ $[M+H]^+$ 238.0792, found 238.0788; IR (ATR, cm^{-1}) 3070, 2929, 1275, 1089.

***(E)*-4-((2,5-difluorophenyl)diazenyl)-3,5-dimethylisoxazole (29d):** yellow solid, mp = 135-136 ^oC, 128.0 mg, 54% yield; ^1H NMR (400 MHz, $CDCl_3$) δ 2.52 (s, 3H), 2.77 (s, 3H), 7.09-7.15 (m, 1H), 7.21 (td, *J* = 9.2, 4.6 Hz, 1H), 7.36-7.41 (m, 1H); ^{13}C NMR (100 MHz, $CDCl_3$) δ 11.91, 12.19, 103.38 (d, *J* = 24.8 Hz), 118.09 (dd, *J* = 22.4, 8.6 Hz), 118.62 (dd, *J* = 25.0, 8.1 Hz), 133.30, 141.29 (dd, *J* = 8.8, 5.9 Hz), 153.81, 156.30 (dd, *J* = 252.4, 2.7 Hz), 158.95 (dd, *J* = 243.3, 2.6 Hz), 170.94; HRMS (ESI-TOF) calcd for $C_{11}H_9F_2N_3O$ $[M+H]^+$ 238.0792, found 238.0786; IR (ATR, cm^{-1}) 3082, 2929, 1242, 1185.

***(E)*-4-((2,6-difluorophenyl)diazenyl)-3,5-dimethylisoxazole (30d):** yellow solid, mp = 106-107 ^oC, 125.6 mg, 53% yield; ^1H NMR (400 MHz, $CDCl_3$) δ 2.47 (s, 3H), 2.72 (s, 3H), 6.99 (t, *J* = 8.7 Hz, 2H), 7.23-7.30 (m, 1H); ^{13}C NMR (100 MHz, $CDCl_3$) δ 11.75, 12.15,

112.47-112.71 (m), 130.14 (t, *J* = 10.2 Hz), 131.36 (t, *J* = 9.7 Hz), 133.98, 153.31, 155.90 (dd, *J* = 257.7, 4.4 Hz), 171.12; HRMS (ESI-TOF) calcd for $C_{11}H_9F_2N_3O$ $[M+H]^+$ 238.0792, found 238.0786; IR (ATR, cm^{-1}) 2969, 1367, 1230, 1089.

***(E)*-4-((3,5-difluorophenyl)diazenyl)-3,5-dimethylisoxazole (31d):** yellow solid, mp = 107-108 ^oC, 206.3 mg, 87% yield; ^1H NMR (400 MHz, $CDCl_3$) δ 2.51 (s, 3H), 2.77 (s, 3H), 6.90 (tt, *J* = 8.4, 2.2 Hz, 1H), 7.33-7.37 (m, 2H); ^{13}C NMR (100 MHz, $CDCl_3$) δ 11.88, 12.23, 105.37-105.89 (m, 2C), 132.52, 153.55, 154.91 (t, *J* = 9.0 Hz), 163.39 (dd, *J* = 247.9, 13.1 Hz), 171.15; HRMS (ESI-TOF) calcd for $C_{11}H_9F_2N_3O$ $[M+H]^+$ 238.0792, found 238.0783; IR (ATR, cm^{-1}) 3076, 2923, 1597, 1111, 828, 642.

***(E)*-2-((3,5-dimethylisoxazole-4-yl)diazenyl)aniline (32d):** yellow solid, mp = 99-100 ^oC, 281.5 mg, 70% yield; ^1H NMR (400 MHz, $CDCl_3$) δ 2.52 (s, 3H), 2.71 (s, 3H), 5.35 (br, 2H), 6.77-6.81 (m, 2H), 7.18-7.23 (m, 1H), 7.67-7.70 (m, 1H); ^{13}C NMR (100 MHz, $CDCl_3$) δ 11.93, 12.39, 117.14, 117.80, 123.86, 132.29, 132.66, 137.87, 143.43, 153.81, 167.35; HRMS (ESI-TOF) calcd for $C_{11}H_{12}N_4O$ $[M+H]^+$ 217.1089, found 217.1081; IR (ATR, cm^{-1}) 3476, 3341, 2923, 1607, 1485, 1265, 757.

***(E)*-3-((3,5-dimethylisoxazole-4-yl)diazenyl)aniline (33d):** yellow solid, mp = 108-109 ^oC, 4967.8 mg, 82% yield; ^1H NMR (400 MHz, $CDCl_3$) δ 2.52 (s, 3H), 2.74 (s, 3H), 3.82 (br, 2H), 6.77-6.79 (m, 1H), 7.12 (t, *J* = 1.9 Hz, 1H), 7.23-7.30 (m, 2H); ^{13}C NMR (100 MHz, $CDCl_3$) δ 11.81, 12.23, 107.19, 114.16, 117.67, 129.92, 132.49, 147.29, 153.90, 154.07, 169.28; HRMS (ESI-TOF) calcd for $C_{11}H_{12}N_4O$ $[M+H]^+$ 217.1089, found 217.1082; IR (ATR, cm^{-1}) 3425, 3353, 1591, 1416, 785.

***(E)*-4-((3,5-dimethylisoxazole-4-yl)diazenyl)aniline (34d):** yellow solid, mp = 105-106 ^oC, 3900.0 mg, 73% yield; ^1H NMR (400 MHz, $CDCl_3$): δ 2.51 (s, 3H), 2.70 (s, 3H), 4.03 (br, 2H), 6.72 (d, *J* = 7.8 Hz, 2H), 7.69 (d, *J* = 7.8 Hz, 2H); ^{13}C NMR (100 MHz, $CDCl_3$) δ 11.76, 12.19, 114.73, 124.37, 132.27, 145.93, 149.40, 154.24, 167.32; HRMS (ESI-TOF) calcd for $C_{11}H_{12}N_4O$ $[M+H]^+$ 217.1089, found 217.1084; IR (ATR, cm^{-1}) 3335, 2929, 1591, 1411, 1144, 834.

***(E)*-2-((3,5-dimethylisoxazol-4-yl)diazenyl)benzonitrile (35d):** yellow solid, mp = 152-154^oC, 115.6 mg, 51% yield; ^1H NMR (400 MHz, $CDCl_3$) δ 2.60 (s, 3H), 2.81 (s, 3H), 7.51-7.55 (t, *J* = 7.7 Hz, 1H), 7.66-7.70 (t, *J* = 7.9 Hz, 1H), 7.81-7.83(d, *J* = 8.2 Hz, 2H); ^{13}C NMR (100 MHz, $CDCl_3$) δ 12.07, 12.41, 112.63, 116.59, 117.14, 130.78, 133.32, 133.43, 133.65,

153.84, 153.97, 171.78; HRMS (ESI-TOF) calcd for $C_{10}H_{10}N_4O$ $[M+H]^+$ 227.0933, found 227.0924; IR (ATR, cm^{-1}) 2917, 2229, 1411, 965.

***(E)*-3,5-dimethyl-4-(pyridin-3-yldiazenyl)isoxazole (36d):** yellow solid, mp = 86-87 ^oC, 159.0 mg, 78% yield; ^1H NMR (400 MHz, $CDCl_3$) δ 2.53 (s, 3H), 2.77 (s, 3H), 7.41-7.44 (m, 1H), 8.03-8.05 (d, *J* = 8.2 Hz, 1H), 8.66-8.68 (d, *J* = 4.6 Hz, 1H), 9.07 (s, 1H); ^{13}C NMR (100 MHz, $CDCl_3$) δ 11.89, 12.31, 124.05, 126.48, 132.96, 146.78, 148.23, 151.55, 153.57, 170.73; HRMS (ESI-TOF) calcd for $C_{10}H_{10}N_4O$ $[M+H]^+$ 203.0933, found 203.0930; IR (ATR, cm^{-1}) 2923, 1603, 1246, 1185, 818.

***(E)*-3,5-dimethyl-4-((*E*)-(4-((*E*)-phenyldiazenyl)phenyl)diazenyl)isoxazole (37d):** orange-red solid, mp = 133-134 ^oC, 423.9 mg, 69% yield; ^1H NMR (400 MHz, $CDCl_3$) δ 2.57 (s, 3H), 2.79 (s, 3H), 7.57-7.51 (m, 3H), 7.97-7.95 (m, 4H), 8.06-8.04 (m, 2H); ^{13}C NMR (100 MHz, $CDCl_3$) δ 11.93, 12.35, 123.18, 123.23, 123.89, 129.31, 131.58, 132.96, 152.78, 153.60, 153.74, 154.10, 170.33; HRMS (ESI-TOF) calcd for $C_{17}H_{15}N_5O$ $[M+H]^+$ 306.1355, found 306.1367; IR (ATR, cm^{-1}) 2923, 1607, 1411, 840, 677.

2.9 References

[1] a) T. Wendler, C. Schütt, C. Näther, R. Herges, *J. Org. Chem.* **2012**, *77*, 3284–3287; b) G. Heitmann, C. Schütt, R. Herges, *Eur. J. Org. Chem.* **2016**, 3817–3823; c) J. Otsuki, K. Suwa, K. Narutaki, C. Sinha, I. Yoshikawa, K. Araki, *J. Phys. Chem. A* **2005**, *109*, 8064–8069.

[2] C. E. Weston, R. D. Richardson, P. R. Haycock, A. J. P. White, M. J. Fuchter, *J. Am. Chem. Soc.* **2014**, *136*, 11878−11881.

[3] J. Calbo, C. E. Weston, A. J. P. White, H. S. Rzepa, J. Contreras-García, M. J. Fuchter, *J. Am. Chem. Soc.* **2017**, *139*, 1261−1274.

[4] a) A. H. Heindl, H. A. Wegner, *Chem. Eur. J.* **2020**, *26*, 13730–13737; b) C. Slavov, C. Yang, A. H. Heindl, H. A. Wegner, A. Dreuw, J. Wachtveitl, *Angew. Chem. Int. Ed.* **2020**, *59*, 380–387.

[5] N. A. Simeth, S. Crespi, M. Fagnoni, B. König, *J. Am. Chem. Soc.* **2018**, *140*, 2940–2946.

[6] a) J. R. Tuck, R. J. Tombari, N. Yardeny, D. E. Olson, *Org. Lett.* **2021**, *23*, 4305−4310; b) Y.-C. Li, C. Qi, S.-H. Li, H.-J. Zhang, C.-H. Sun, Y.-Z. Yu, S.-P. Pang, *J. Am. Chem. Soc.* **2010**, *132*, 12172–12173.

[7] a) J. A. Balam-Villarreal, B. J. López-Mayorga, D. Gallardo-Rosas, R. A. Toscano, M. P. Carreón-Castro, V. A. Basiuk, F. Cortés-Guzmán, J. G. López-Cortés, M. C. Ortega-Alfaro, *Org. Biomol. Chem.* **2020**, *18*, 1657–1670; b) L. Muñoz-Rugeles, D. Gallardo-Rosas, J. Durán-Hernández, R. López-Arteaga, R. A. Toscano, N. Esturau-Escofet, J. G. López-Cortés, J. Peon, M. C. Ortega-Alfaro, *ChemPhotoChem* **2019**, *3*, 1–12.

[8] a) J. Garcia-Amorós, M. C. R. Castro, P. Coelho, M. M. M. Raposo, D. Velasco, *Chem*. *Commun*. **2013**, *49*, 11427–11429; b) C. Boga, S. Cino, G. Micheletti, D. Padovan, L. Prati, A. Mazzanti, N. Zanna, *Org*. *Biomol*. *Chem*. **2016**, *14*, 7061–7068.

[9] S. Devi, M. Saraswat, S. Grewal, S. Venkataramani, *J*. *Org*. *Chem*. **2018**, *83*, 4307−4322.

[10] a) M. H. Elnagdi, M. R. H. Elmoghayar, E. A. A. Hafez, H. H. Alnima, *J*. *Org*. *Chem*. **1975**, *40*, 2604-2607; b) M. A. Al-Shiekh, A. M. S. El-Din, E. A. Hafez, M. H. Elnagdi, *J*. *Het*. *Chem*. **2004**, *41*, 647-654; c) W. U. Malik, H. G. Garg, V. Arora, *J*. *Pharm*. *Sci*. **1971**, *60*, 1738-1740.

[11] C. Bustos, E. Molins, J. G. Carcamo, M. N. Aguilar, C. Sanchez, I. Moreno-Villoslada, H. Nishide, A. Mesias-Salazar, X. Zarate, E. Schott, *New J*. *Chem*. **2015**, *39*, 4295−4307.

[12] a) H. Zhou, C. Xue, P. Weis, Y. Suzuki, S. Huang, K. Koynov, G. K. Auernhammer, R. Berger, H.-J. Butt, S. Wu, *Nat*. *Chem*. **2017**, *9*, 145–151; b) Y. Yue, Y. Norikane, R. Azumi, E. Koyama, *Nat*. *Commun*. **2018**, *9*, 3234; c) Z. Wu, C. Ji, X. Zhao, Y. Han, K. Mellen, K. Pan, M. Yin, *J*. *Am*. *Chem*. *Soc*. **2019**, *141*, 7385–7390; d) O. Tsutsumi, T. Kitsunai, A. Kanazawa, T. Shiono, T. Ikeda, *Macromolecules* **1998**, *31*, 355–359; e) Y. Norikane, E. Uchida, S. Tanaka, K. Fujiwara, E. Koyama, R. Azumi, H. Akiyama, H. Kihara, M. Yoshida, *Org*. *Lett*. **2014**, *16*, 5012–5015; f) F. Fernandez-Palacio, M. Poutanen, M. Saccone, A. Siiskonen, G. Terraneo, G. Resnati, O. Ikkala, P. metrangolo, A. Priimagi, *Chem*. *Mater*. **2016**, *28*, 8314–8321; g) J. Hu, X. Li, Y. Ni, S. Ma, H. Yu, *J*. *Mater*. *Chem*. *C* **2018**, *6*, 10815–10821; h) S. Ma, X. Li, S. Huang, J. Hu, H. Yu, *Angew*. *Chem*. *Int*. *Ed*. **2019**, *58*, 2655–2659; *Angew*. *Chem*. **2019**, *131*, 2681–2685; i) Y. Hao, S. Huang, Y. Guo, L. Zhou, H. Hao, C. J. Barrett, H. Yu, *J*. *Mater*. *Chem*. *C* **2019**, *7*, 503–508; j) W.-C. Xu, S. Sun, S. Wu, *Angew*. *Chem*. *Int*. *Ed*. **2019**, *58*, 9712–9740; *Angew*. *Chem*. **2019**, *131*, 9814–9843.

[13] J. Vappaavuori, A. Goulet-Hanssens, I. T. S. Heikkinen, C. J. Barrett, A. Priimagi, *Chem*. *Mater*. **2014**, *26*, 5089–5096.

[14] H. M. D. Bandara, S. C. Burdette, *Chem*. *Soc*. *Rev*. **2012**, *41*, 1809–1825.

[15] a) K. Ghebreyessus, S. M. Cooper, *Organometallics* **2017**, *36*, 3360–3370; b) S. Devi, A. K. Gaur, D. Gupta, M. Saraswat, S. Venkataramani, *ChemPhotoChem* **2018**, *2*, 806–810.

[16] To elucidate the thermal stability of the *Z*-isomer, we monitored the *Z*–*E* reverse isomerization kinetics of a few derivatives using UV/Vis spectroscopy. The preliminary results suggested that the room-temperature thermal isomerization is extremely slow. Hence, the experiments were performed at higher temperature (80 ^{o}C) in DMSO to determine the rate constants for the selected derivatives (**Table 2.6**, **Figure 2E.3** in **Appendix 2E**).

[17] a) Reverse thermal isomerization was also monitored at room temperature (25 ± 2 ^{o}C) in $CDCl_3$. The rate constant was found to be $2.2 \times 10^{-5} \pm 8.0 \times 10^{-7}$ min^{-1}, and the half-life was estimated to be 30826 min (21.4 d), which is nearly half of the values observed in [D_6]DMSO. The corresponding rate constants in [D_6]DMSO at RT (25 ± 2 ^{o}C) and 80 ± 2 ^{o}C were found to be $1.1 \times 10^{-5} \pm 3.0 \times 10^{-7}$ min^{-1} and $1.4 \times 10^{-2} \pm 4.3 \times 10^{-4}$ min^{-1}, respectively (**Figure 2.4**, **Table 2.4** and **Appendix 2E**); b) The activation parameters $\Delta H^{\ddagger}$ and $\Delta S^{\ddagger}$ for the *Z*–*E* thermal reverse isomerization reaction were found to be 112 ± 4 $kJ.mol^{-1}$, and 30 ± 12 $J.K^{-1}.mol^{-1}$, respectively (**Table 2.5**). The reason for the positive entropy factor may be the relief of steric strain due to the 3,5-dimethyl groups (isoxazole unit) in the *Z*-isomer on attaining the transition state.

[18] D. Bléger, J. Schwarz, A. M. Brouwer, S. Hecht, *J. Am. Chem. Soc.* **2012**, *134*, 2059–20600.
[19] a) M. Emond, T. Le Saux, S. Maurin, J.-B. Baudin, R. Plasson, L. Jullien, *Chem. Eur. J.* **2010**, *16*, 8822–8831; b) W. R. Brode, J. H. Gould, G. M. Wyman, *J. Am. Chem. Soc.* **1952**, *74*, 4641–4646.
[20] C. Sah, A. Mahadevan, P. Kumar, S. Venkataramani, *Phys. Chem. Chem. Phys.* **2022**, *24*, 7848–7855.
[21] Relaxation process following photoexcitation of the azo compounds may liberate heat through nonradiative decay, which can increase the temperature locally. However, as mentioned by Norikane *et al*. (ref. [12e]) the local heating alone may not be sufficient for the phase transition.
[22] Both the native yellow solid and the molten red liquid of **1d** were subjected to IR spectroscopic studies by the ATR method. Minor broadening of few of the signals and splitting of one of the bands were observed. On comparing with the computed IR spectral data, possible formation of the *Z*-isomer has been envisaged. The spectral data are available in the **Figure 2G.5, Figure 2G.6** in **Appendix 2G**.
[23] ^{1}H NMR spectral data of the molten sample (from 4 mg of **1d** after irradiation for 30 s) obtained after exposure to 365 nm irradiation showed 16% *Z*-isomer. The spectral data are available in the **Figure 2G.7** in **Appendix 2G**.

Appendix 2A

Photoswitching experiments in all the arylazoisoxazole derivatives **1-37d** have been performed and analyzed using UV-vis spectroscopy. In the following pages the data related to those experiments are given in the following sequence: (a) in solution phase (solvent: acetonitrile at 25±1 ^{o}C; (b) in solid state (KBr medium); The molar absorption coefficients of the *E*-isomers have been estimated for (c) π–π* and (d) n-π* absorption bands.

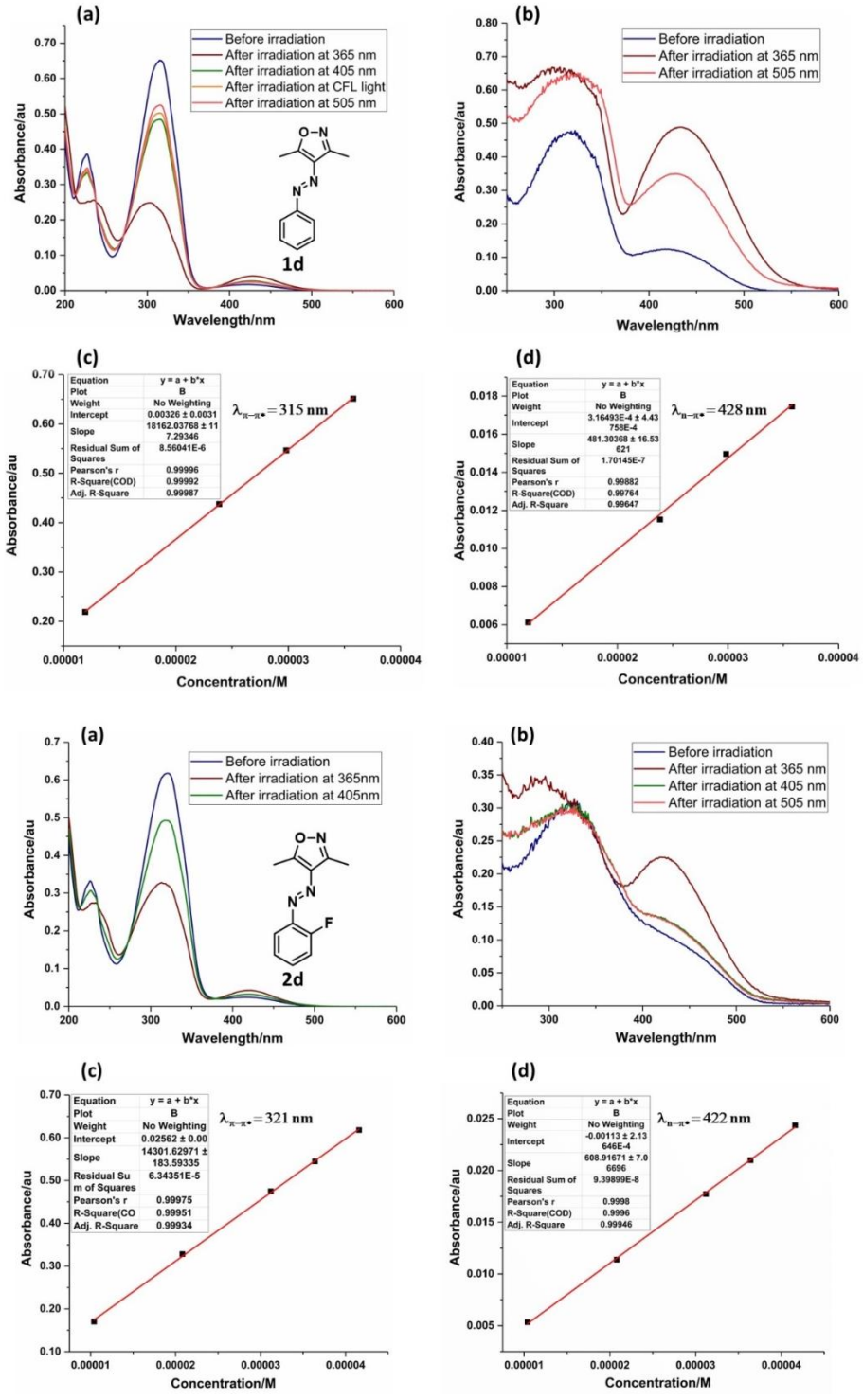

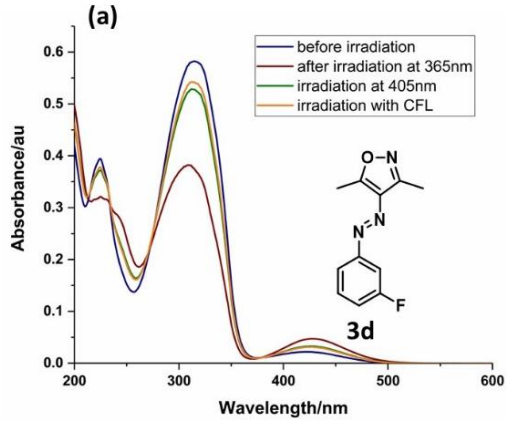
(a)
before irradiation
after irradiation at 365nm
irradiation at 405nm
irradiation with CFL
3d
Absorbance/au
Wavelength/nm

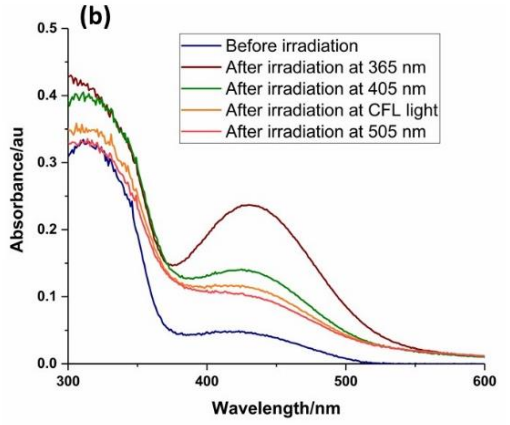
(b)
Before irradiation
After irradiation at 365 nm
After irradiation at 405 nm
After irradiation at CFL light
After irradiation at 505 nm
Absorbance/au
Wavelength/nm

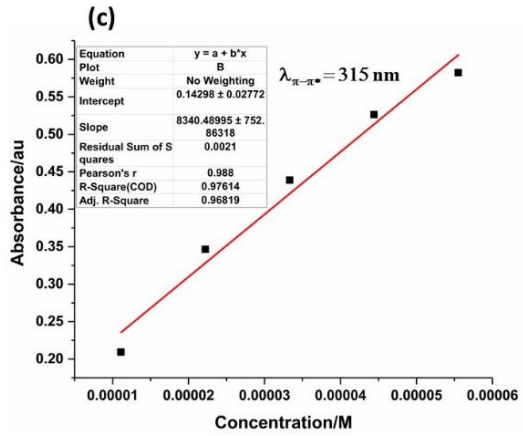
(c)
Equation y = a + b*x
Plot B
Weight No Weighting
Intercept 0.14298 ± 0.02772
Slope 8340.48995 ± 752.86318
Residual Sum of Squares 0.0021
Pearson's r 0.988
R-Square(COD) 0.97614
Adj. R-Square 0.96819
λπ–π* = 315 nm
Absorbance/au
Concentration/M

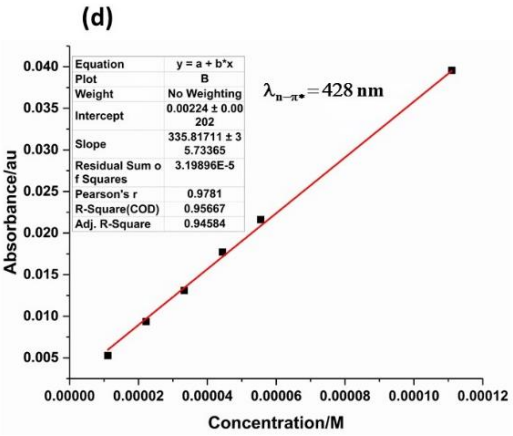
(d)
Equation y = a + b*x
Plot B
Weight No Weighting
Intercept 0.00224 ± 0.00202
Slope 335.81711 ± 3.73365
Residual Sum of Squares 3.19896E-5
Pearson's r 0.9781
R-Square(COD) 0.95667
Adj. R-Square 0.94584
λn–π* = 428 nm
Absorbance/au
Concentration/M

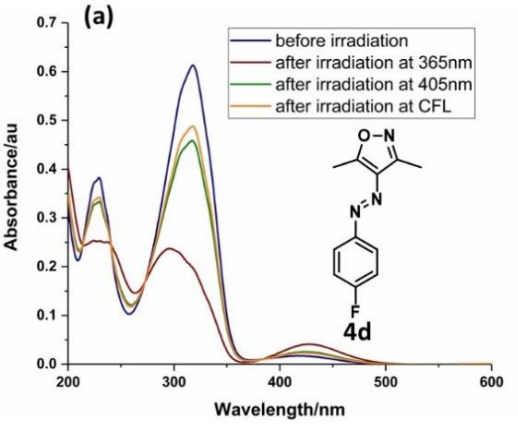
(a)
before irradiation
after irradiation at 365nm
after irradiation at 405nm
after irradiation at CFL
4d
Absorbance/au
Wavelength/nm

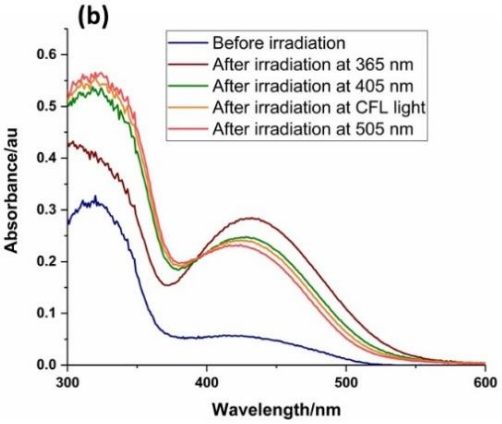
(b)
Before irradiation
After irradiation at 365 nm
After irradiation at 405 nm
After irradiation at CFL light
After irradiation at 505 nm
Absorbance/au
Wavelength/nm

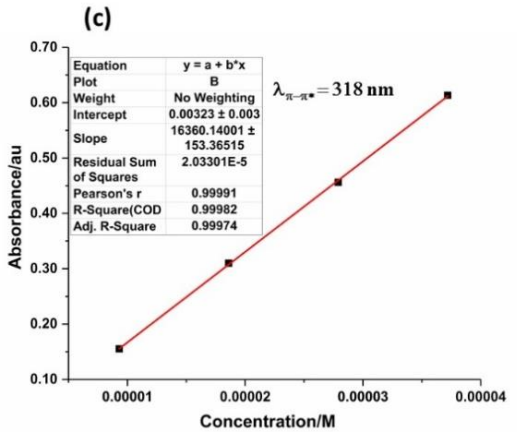
(c)
Equation y = a + b*x
Plot B
Weight No Weighting
Intercept 0.00323 ± 0.003
Slope 16360.14001 ± 153.36515
Residual Sum of Squares 2.03301E-5
Pearson's r 0.99991
R-Square(COD 0.99982
Adj. R-Square 0.99974
λπ–π* = 318 nm
Absorbance/au
Concentration/M

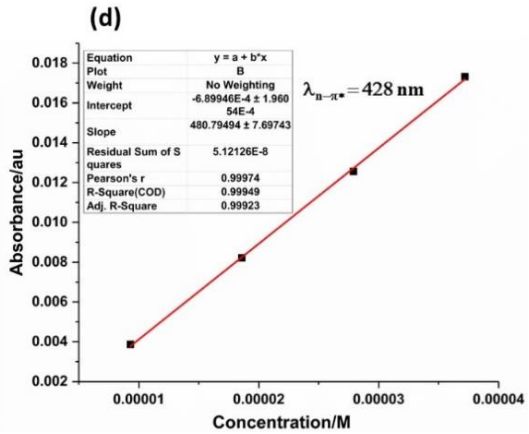
(d)
Equation y = a + b*x
Plot B
Weight No Weighting
Intercept -6.89946E-4 ± 1.96054E-4
Slope 480.79494 ± 7.69743
Residual Sum of Squares 5.12126E-8
Pearson's r 0.99974
R-Square(COD) 0.99949
Adj. R-Square 0.99923
λn–π* = 428 nm
Absorbance/au
Concentration/M

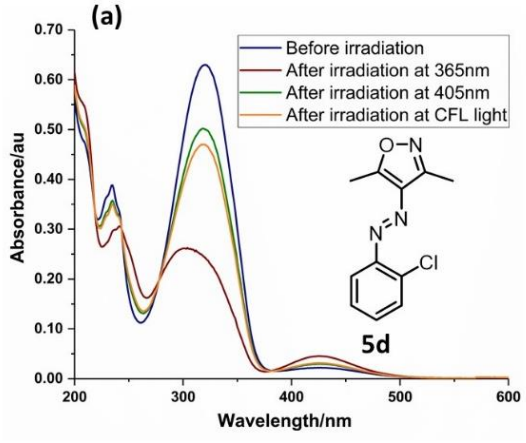
(a)
Before irradiation
After irradiation at 365nm
After irradiation at 405nm
After irradiation at CFL light
Absorbance/au
Wavelength/nm
5d

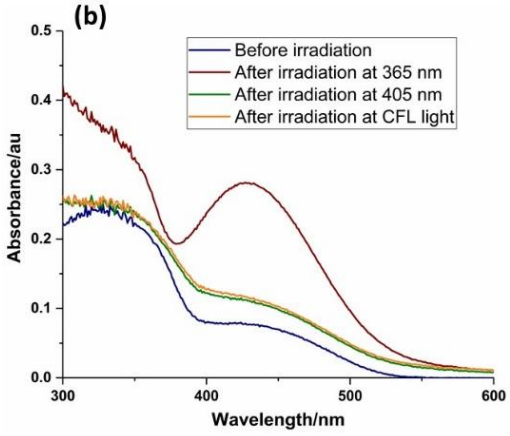
(b)
Before irradiation
After irradiation at 365 nm
After irradiation at 405 nm
After irradiation at CFL light
Absorbance/au
Wavelength/nm

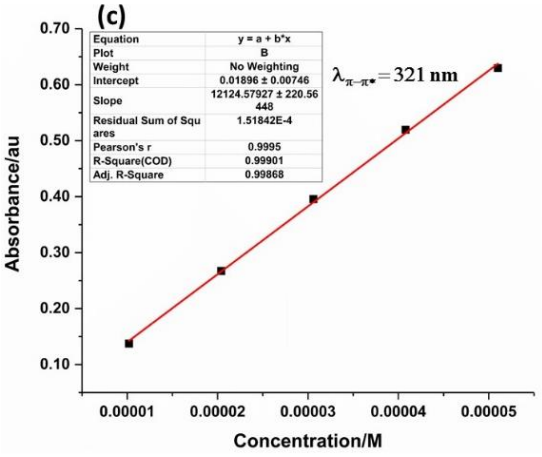
(c)
Equation y = a + b*x
Plot B
Weight No Weighting
Intercept 0.01896 ± 0.00746
Slope 12124.57927 ± 220.56448
Residual Sum of Squares 1.51842E-4
Pearson's r 0.9995
R-Square(COD) 0.99901
Adj. R-Square 0.99868
λπ–π* = 321 nm
Absorbance/au
Concentration/M

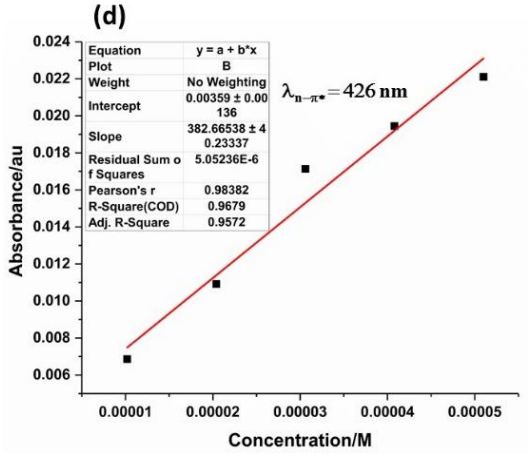
(d)
Equation y = a + b*x
Plot B
Weight No Weighting
Intercept 0.00359 ± 0.00136
Slope 382.66538 ± 4.23337
Residual Sum of Squares 5.05236E-6
Pearson's r 0.98382
R-Square(COD) 0.9679
Adj. R-Square 0.9572
λn–π* = 426 nm
Absorbance/au
Concentration/M

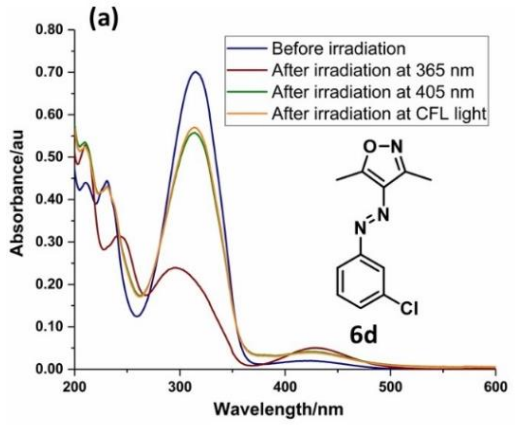
(a)
Before irradiation
After irradiation at 365 nm
After irradiation at 405 nm
After irradiation at CFL light
Absorbance/au
Wavelength/nm
6d

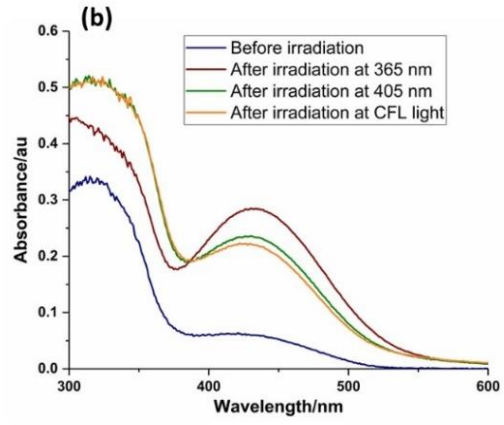
(b)
Before irradiation
After irradiation at 365 nm
After irradiation at 405 nm
After irradiation at CFL light
Absorbance/au
Wavelength/nm

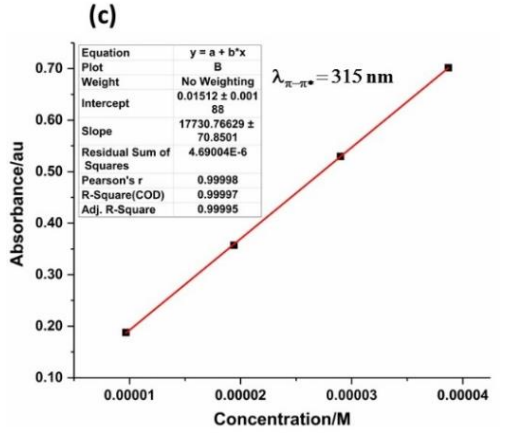
(c)
Equation y = a + b*x
Plot B
Weight No Weighting
Intercept 0.01512 ± 0.00188
Slope 17730.76629 ± 70.8501
Residual Sum of Squares 4.69004E-6
Pearson's r 0.99998
R-Square(COD) 0.99997
Adj. R-Square 0.99995
λπ–π* = 315 nm
Absorbance/au
Concentration/M

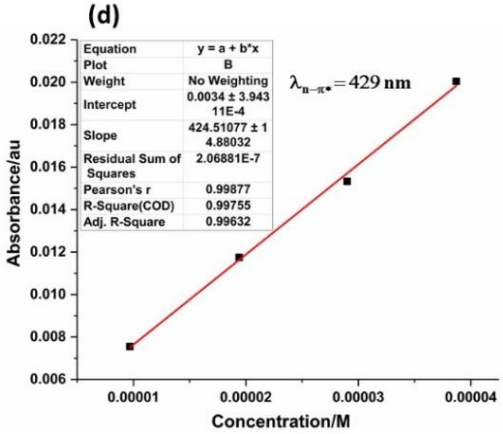
(d)
Equation y = a + b*x
Plot B
Weight No Weighting
Intercept 0.0034 ± 3.94311E-4
Slope 424.51077 ± 4.88032
Residual Sum of Squares 2.06881E-7
Pearson's r 0.99877
R-Square(COD) 0.99755
Adj. R-Square 0.99632
λn–π* = 429 nm
Absorbance/au
Concentration/M

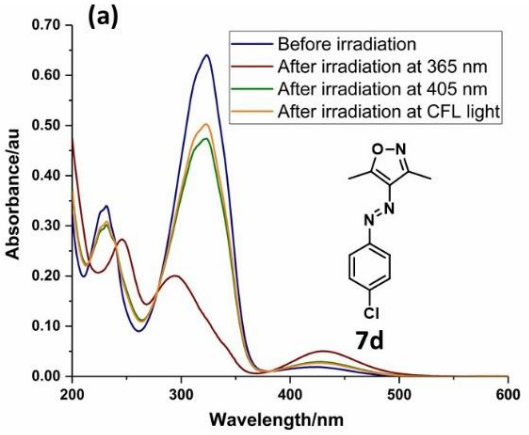
(a)
Before irradiation
After irradiation at 365 nm
After irradiation at 405 nm
After irradiation at CFL light
Absorbance/au
Wavelength/nm
7d

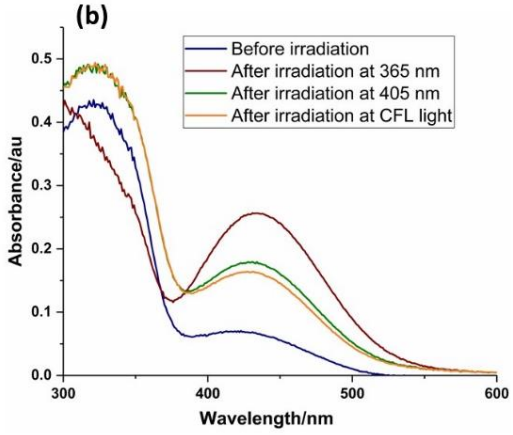
(b)
Before irradiation
After irradiation at 365 nm
After irradiation at 405 nm
After irradiation at CFL light
Absorbance/au
Wavelength/nm

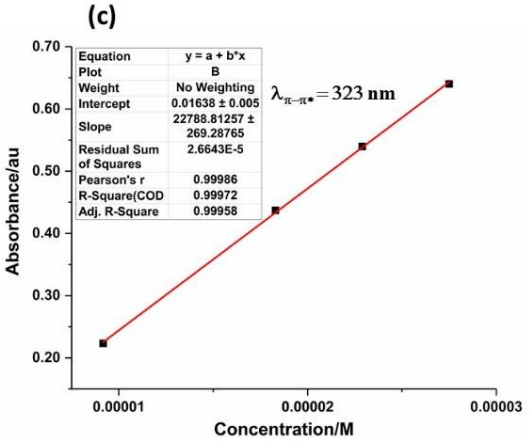
(c)
Equation y = a + b*x
Plot B
Weight No Weighting
Intercept 0.01638 ± 0.005
Slope 22788.81257 ± 269.28765
Residual Sum of Squares 2.6643E-5
Pearson's r 0.99986
R-Square(COD 0.99972
Adj. R-Square 0.99958
λπ–π* = 323 nm
Absorbance/au
Concentration/M

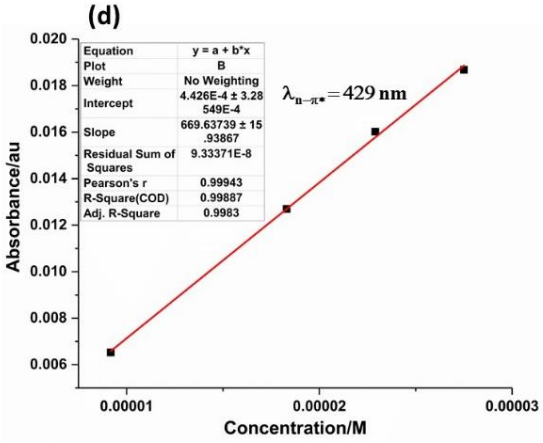
(d)
Equation y = a + b*x
Plot B
Weight No Weighting
Intercept 4.426E-4 ± 3.28549E-4
Slope 669.63739 ± 15.93867
Residual Sum of Squares 9.33371E-8
Pearson's r 0.99943
R-Square(COD) 0.99887
Adj. R-Square 0.9983
λn–π* = 429 nm
Absorbance/au
Concentration/M

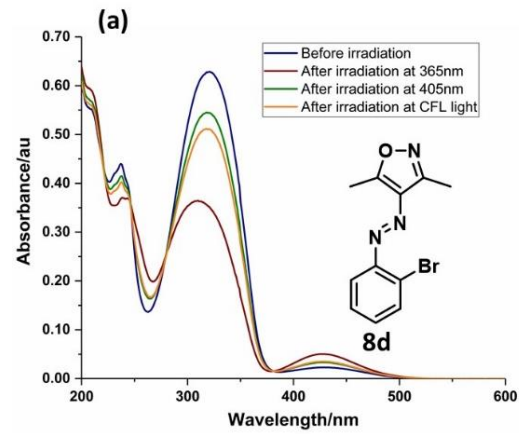
(a)
Before irradiation
After irradiation at 365nm
After irradiation at 405nm
After irradiation at CFL light
Absorbance/au
Wavelength/nm
8d

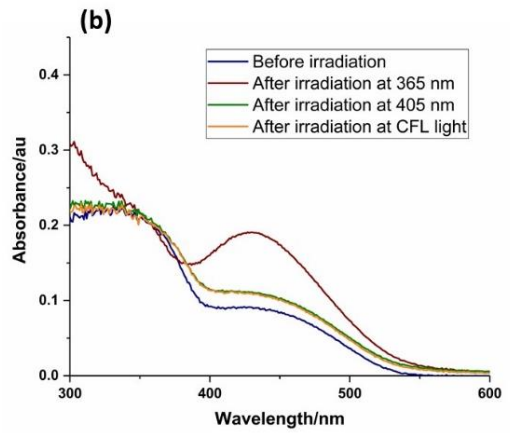
(b)
Before irradiation
After irradiation at 365 nm
After irradiation at 405 nm
After irradiation at CFL light
Absorbance/au
Wavelength/nm

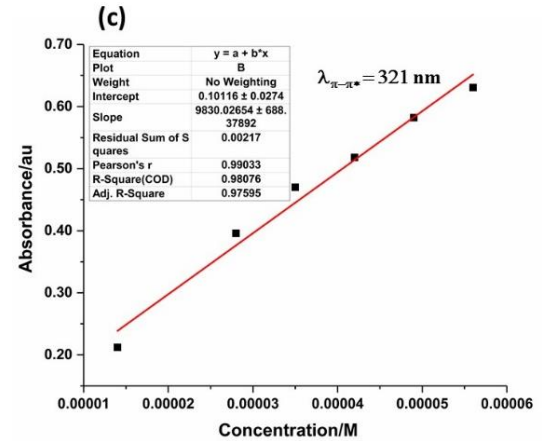
(c)
Equation y = a + b*x
Plot B
Weight No Weighting
Intercept 0.10116 ± 0.0274
Slope 9830.02654 ± 688.37892
Residual Sum of Squares 0.00217
Pearson's r 0.99033
R-Square(COD) 0.98076
Adj. R-Square 0.97595
λπ–π* = 321 nm
Absorbance/au
Concentration/M

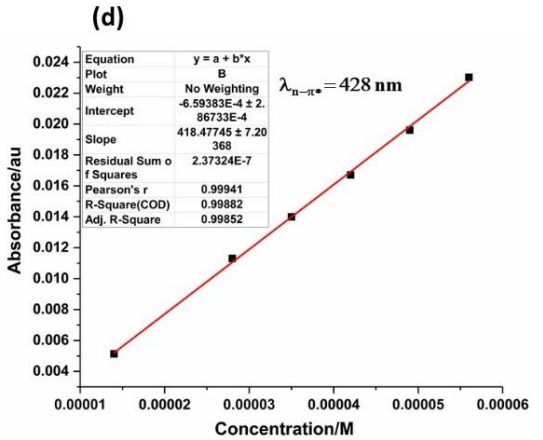
(d)
Equation y = a + b*x
Plot B
Weight No Weighting
Intercept -6.59383E-4 ± 2.86733E-4
Slope 418.47745 ± 7.20368
Residual Sum of Squares 2.37324E-7
Pearson's r 0.99941
R-Square(COD) 0.99882
Adj. R-Square 0.99852
λn–π* = 428 nm
Absorbance/au
Concentration/M

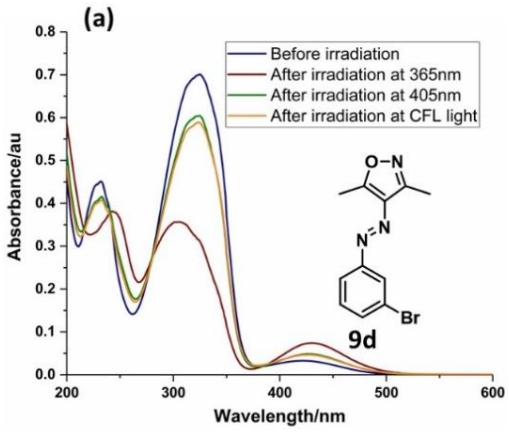
(a)
Before irradiation
After irradiation at 365nm
After irradiation at 405nm
After irradiation at CFL light
Absorbance/au
Wavelength/nm
9d

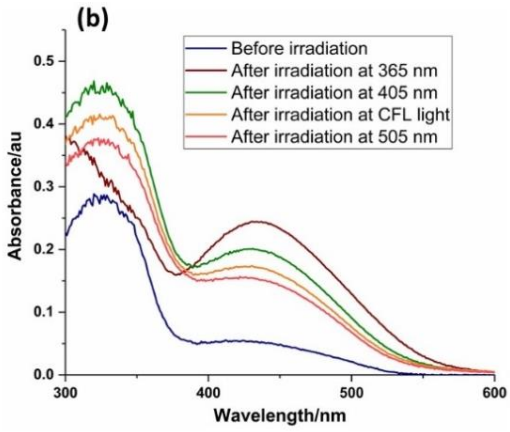
(b)
Before irradiation
After irradiation at 365 nm
After irradiation at 405 nm
After irradiation at CFL light
After irradiation at 505 nm
Absorbance/au
Wavelength/nm

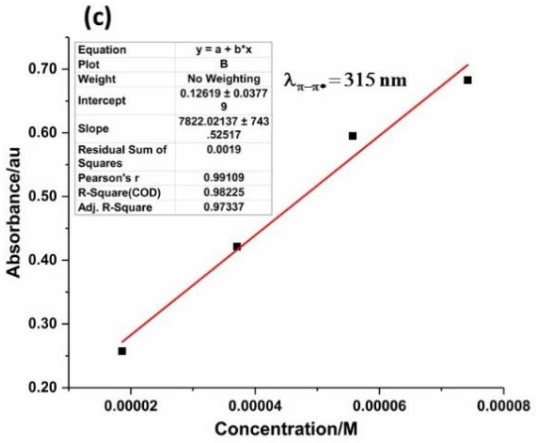
(c)
Equation y = a + b*x
Plot B
Weight No Weighting
Intercept 0.12619 ± 0.03779
Slope 7822.02137 ± 743.52517
Residual Sum of Squares 0.0019
Pearson's r 0.99109
R-Square(COD) 0.98225
Adj. R-Square 0.97337
λπ–π* = 315 nm
Absorbance/au
Concentration/M

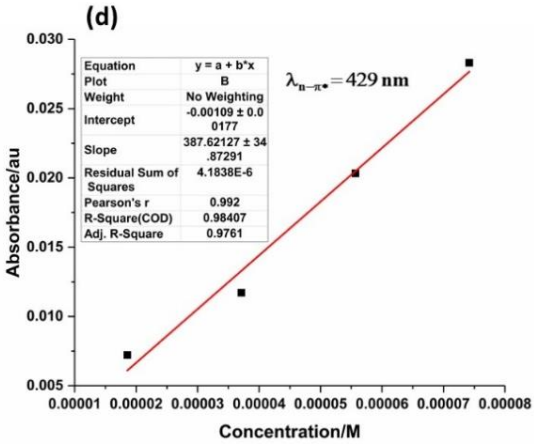
(d)
Equation y = a + b*x
Plot B
Weight No Weighting
Intercept -0.00109 ± 0.00177
Slope 387.62127 ± 34.87291
Residual Sum of Squares 4.1838E-6
Pearson's r 0.992
R-Square(COD) 0.98407
Adj. R-Square 0.9761
λn–π* = 429 nm
Absorbance/au
Concentration/M

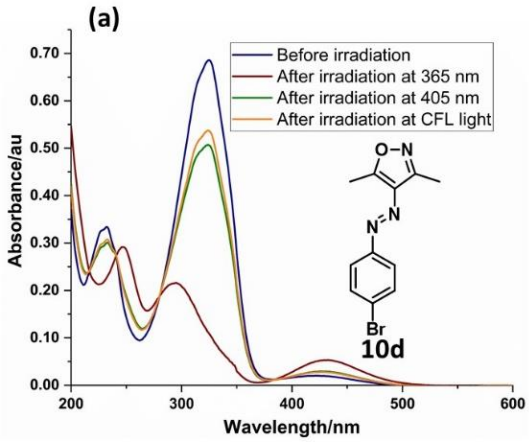
(a)
Before irradiation
After irradiation at 365 nm
After irradiation at 405 nm
After irradiation at CFL light
Absorbance/au
Wavelength/nm
10d

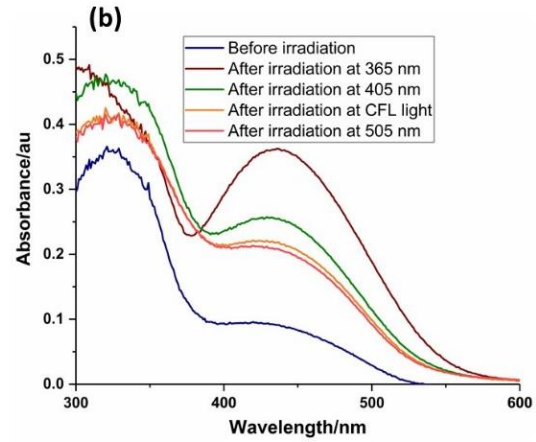
(b)
Before irradiation
After irradiation at 365 nm
After irradiation at 405 nm
After irradiation at CFL light
After irradiation at 505 nm
Absorbance/au
Wavelength/nm

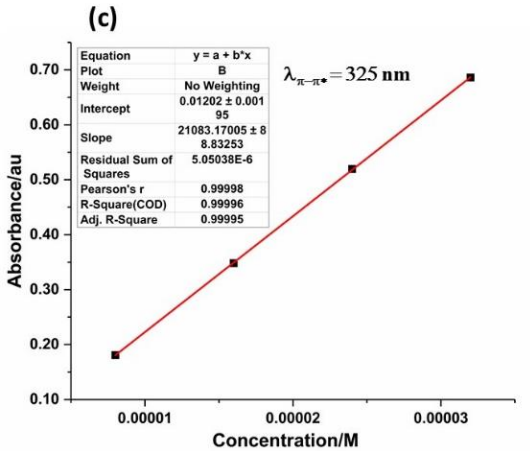
(c)
Equation y = a + b*x
Plot B
Weight No Weighting
Intercept 0.01202 ± 0.00195
Slope 21083.17005 ± 88.83253
Residual Sum of Squares 5.05038E-6
Pearson's r 0.99998
R-Square(COD) 0.99996
Adj. R-Square 0.99995
λπ–π* = 325 nm
Absorbance/au
Concentration/M

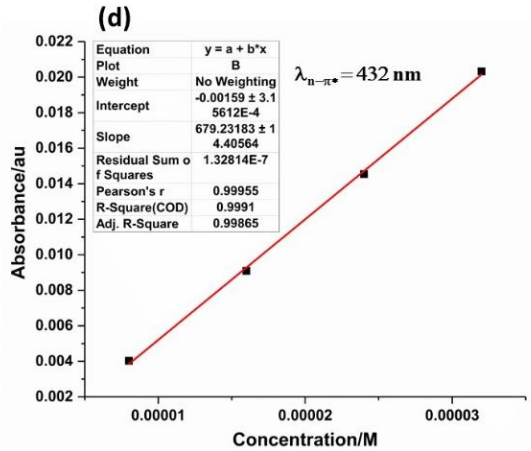
(d)
Equation y = a + b*x
Plot B
Weight No Weighting
Intercept -0.00159 ± 3.15612E-4
Slope 679.23183 ± 14.40564
Residual Sum of Squares 1.32814E-7
Pearson's r 0.99955
R-Square(COD) 0.9991
Adj. R-Square 0.99865
λn–π* = 432 nm
Absorbance/au
Concentration/M

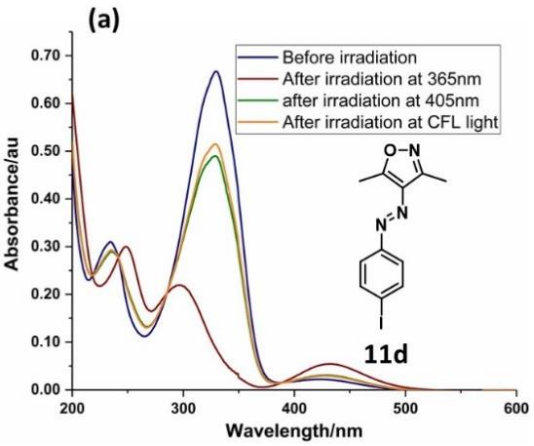
(a)
Before irradiation
After irradiation at 365nm
after irradiation at 405nm
After irradiation at CFL light
11d
Absorbance/au
Wavelength/nm

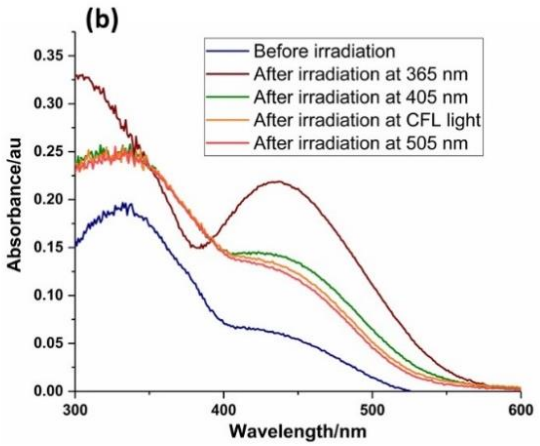
(b)
Before irradiation
After irradiation at 365 nm
After irradiation at 405 nm
After irradiation at CFL light
After irradiation at 505 nm
Absorbance/au
Wavelength/nm

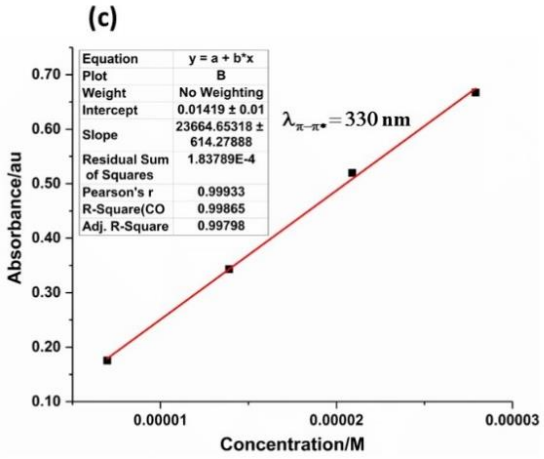
(c)
Equation y = a + b*x
Plot B
Weight No Weighting
Intercept 0.01419 ± 0.01
Slope 23664.65318 ± 614.27888
Residual Sum of Squares 1.83789E-4
Pearson's r 0.99933
R-Square(CO 0.99865
Adj. R-Square 0.99798
λπ–π* = 330 nm
Absorbance/au
Concentration/M

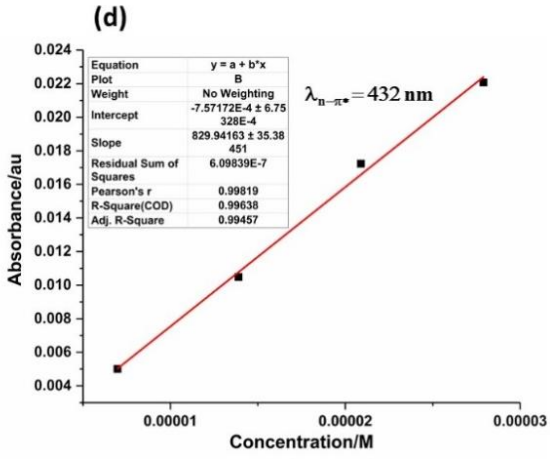
(d)
Equation y = a + b*x
Plot B
Weight No Weighting
Intercept -7.57172E-4 ± 6.75328E-4
Slope 829.94163 ± 35.38451
Residual Sum of Squares 6.09839E-7
Pearson's r 0.99819
R-Square(COD) 0.99638
Adj. R-Square 0.99457
λn–π* = 432 nm
Absorbance/au
Concentration/M

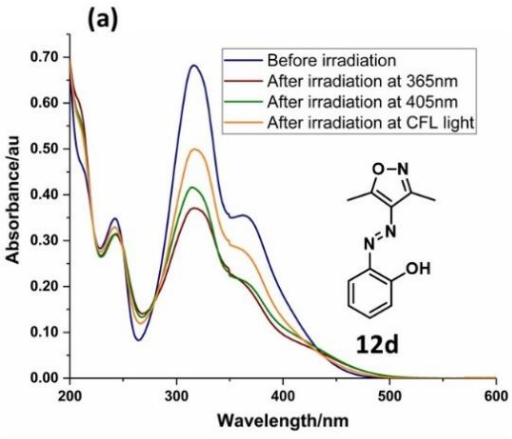
(a)
Before irradiation
After irradiation at 365nm
After irradiation at 405nm
After irradiation at CFL light
12d
Absorbance/au
Wavelength/nm

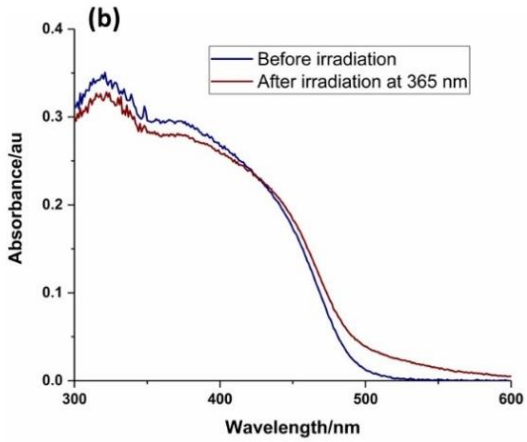
(b)
Before irradiation
After irradiation at 365 nm
Absorbance/au
Wavelength/nm

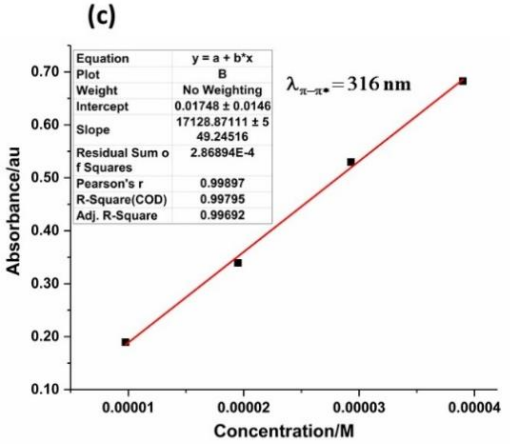
(c)
Equation y = a + b*x
Plot B
Weight No Weighting
Intercept 0.01748 ± 0.0146
Slope 17128.87111 ± 549.24516
Residual Sum of Squares 2.86894E-4
Pearson's r 0.99897
R-Square(COD) 0.99795
Adj. R-Square 0.99692
λπ–π* = 316 nm
Absorbance/au
Concentration/M

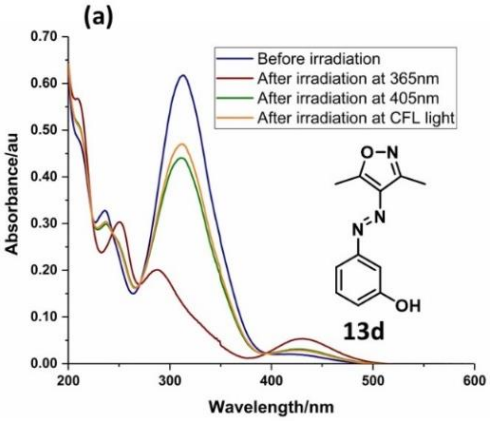
(a)
Before irradiation
After irradiation at 365nm
After irradiation at 405nm
After irradiation at CFL light
13d
Absorbance/au
Wavelength/nm

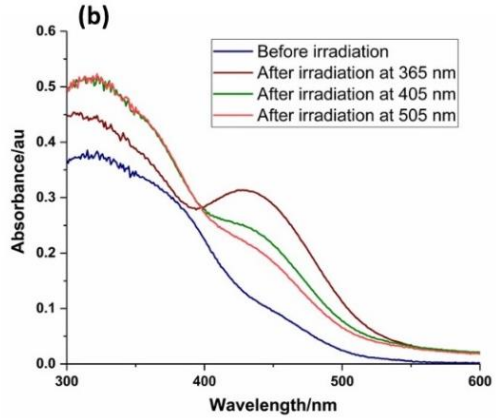
(b)
Before irradiation
After irradiation at 365 nm
After irradiation at 405 nm
After irradiation at 505 nm
Absorbance/au
Wavelength/nm

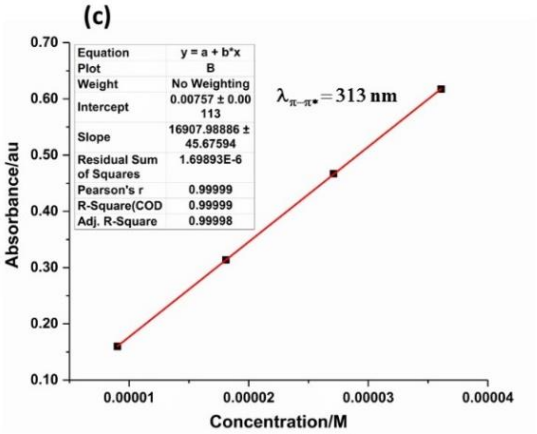
(c)
Equation y = a + b*x
Plot B
Weight No Weighting
Intercept 0.00757 ± 0.00113
Slope 16907.98886 ± 45.67594
Residual Sum of Squares 1.69893E-6
Pearson's r 0.99999
R-Square(COD 0.99999
Adj. R-Square 0.99998
λπ→π*=313 nm
Absorbance/au
Concentration/M

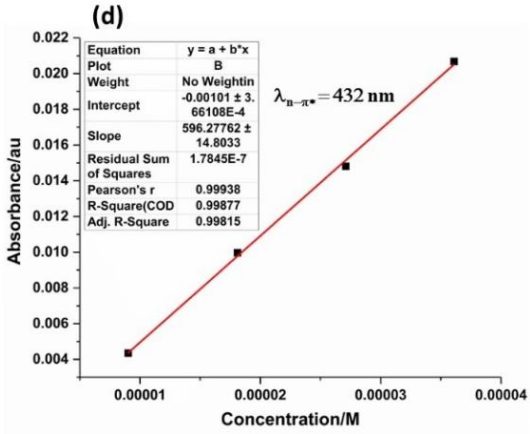
(d)
Equation y = a + b*x
Plot B
Weight No Weightin
Intercept -0.00101 ± 3.66108E-4
Slope 596.27762 ± 14.8033
Residual Sum of Squares 1.7845E-7
Pearson's r 0.99938
R-Square(COD 0.99877
Adj. R-Square 0.99815
λn→π*=432 nm
Absorbance/au
Concentration/M

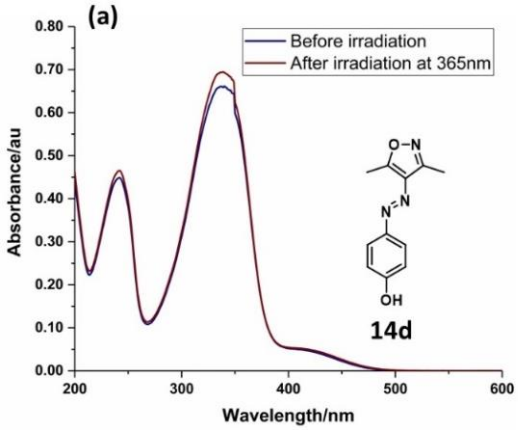
(a)
Before irradiation
After irradiation at 365nm
14d
Absorbance/au
Wavelength/nm

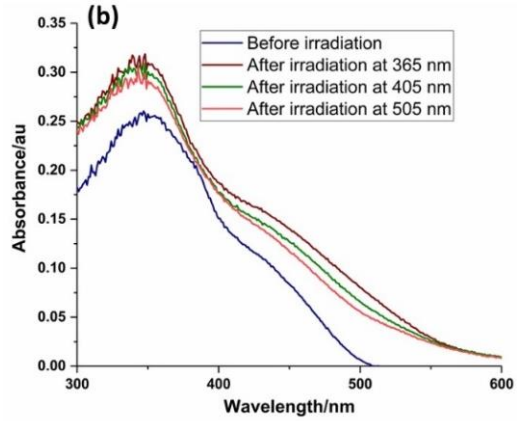
(b)
Before irradiation
After irradiation at 365 nm
After irradiation at 405 nm
After irradiation at 505 nm
Absorbance/au
Wavelength/nm

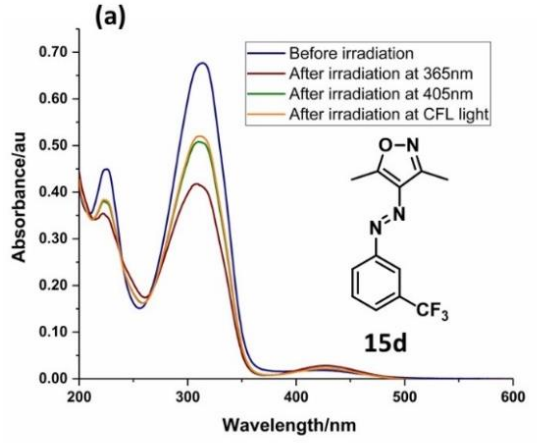
(a)
Before irradiation
After irradiation at 365nm
After irradiation at 405nm
After irradiation at CFL light
15d
Absorbance/au
Wavelength/nm

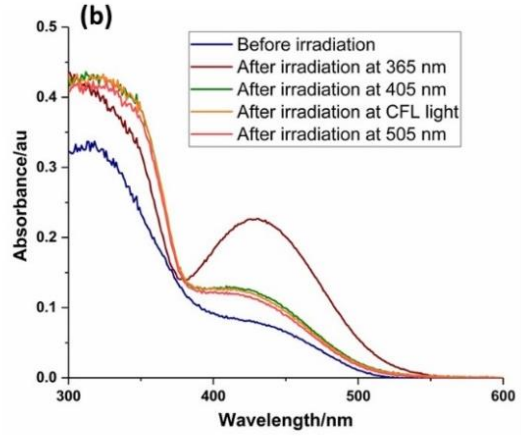
(b)
Before irradiation
After irradiation at 365 nm
After irradiation at 405 nm
After irradiation at CFL light
After irradiation at 505 nm
Absorbance/au
Wavelength/nm

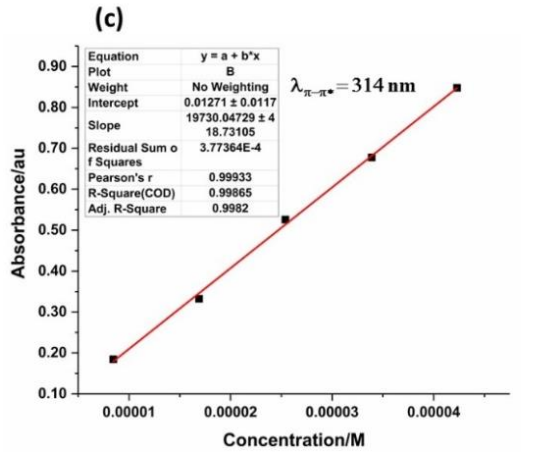
(c)
Equation y = a + b*x
Plot B
Weight No Weighting
Intercept 0.01271 ± 0.0117
Slope 19730.04729 ± 418.73105
Residual Sum of Squares 3.77364E-4
Pearson's r 0.99933
R-Square(COD) 0.99865
Adj. R-Square 0.9982
λπ–π* = 314 nm
Absorbance/au
Concentration/M

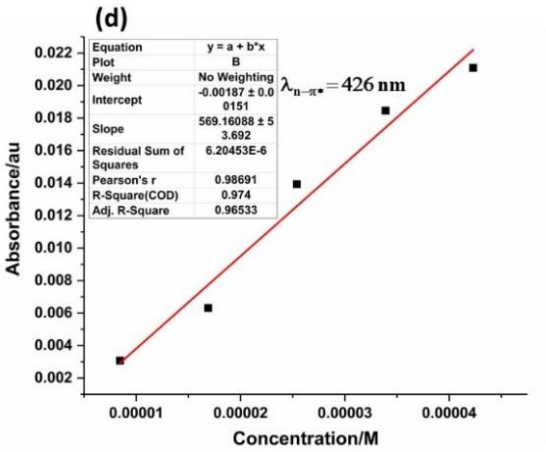
(d)
Equation y = a + b*x
Plot B
Weight No Weighting
Intercept -0.00187 ± 0.00151
Slope 569.16088 ± 53.692
Residual Sum of Squares 6.20453E-6
Pearson's r 0.98691
R-Square(COD) 0.974
Adj. R-Square 0.96533
λn–π* = 426 nm
Absorbance/au
Concentration/M

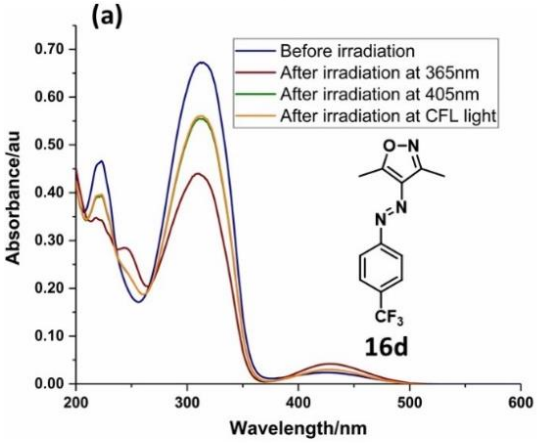
(a)
Before irradiation
After irradiation at 365nm
After irradiation at 405nm
After irradiation at CFL light
16d
Absorbance/au
Wavelength/nm

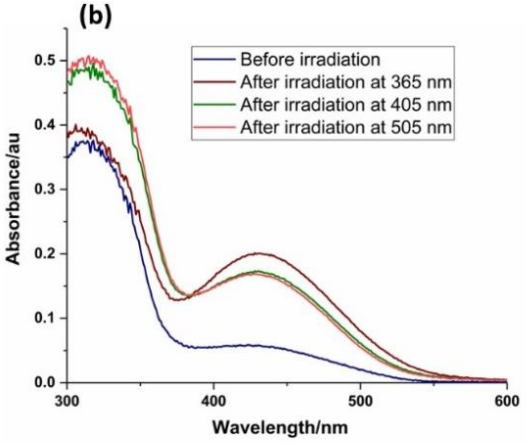
(b)
Before irradiation
After irradiation at 365 nm
After irradiation at 405 nm
After irradiation at 505 nm
Absorbance/au
Wavelength/nm

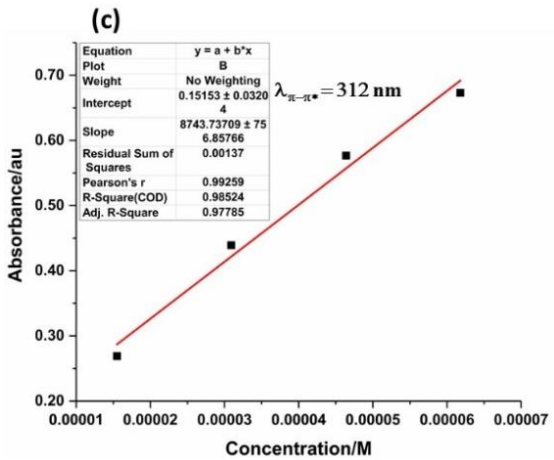
(c)
Equation y = a + b*x
Plot B
Weight No Weighting
Intercept 0.15153 ± 0.03204
Slope 8743.73709 ± 75.85766
Residual Sum of Squares 0.00137
Pearson's r 0.99259
R-Square(COD) 0.98524
Adj. R-Square 0.97785
λπ–π* = 312 nm
Absorbance/au
Concentration/M

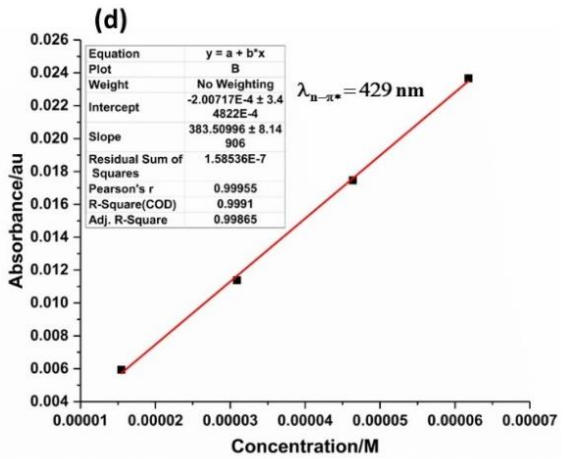
(d)
Equation y = a + b*x
Plot B
Weight No Weighting
Intercept -2.00717E-4 ± 3.44822E-4
Slope 383.50996 ± 8.14906
Residual Sum of Squares 1.58536E-7
Pearson's r 0.99955
R-Square(COD) 0.9991
Adj. R-Square 0.99865
λn–π* = 429 nm
Absorbance/au
Concentration/M

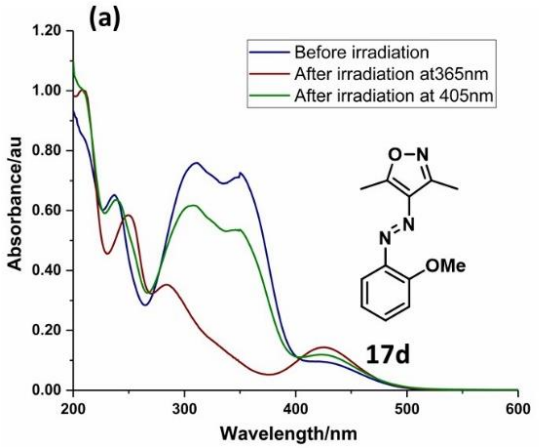
(a)
Before irradiation
After irradiation at365nm
After irradiation at 405nm
17d
Absorbance/au
Wavelength/nm

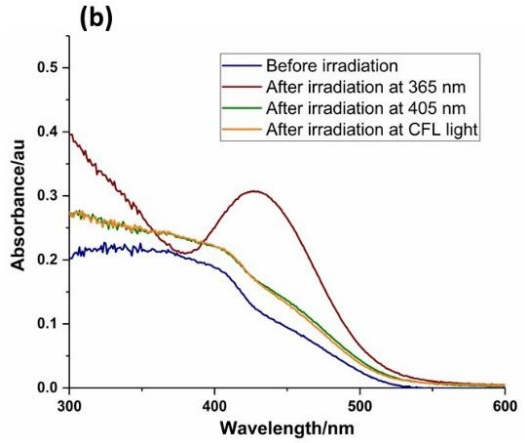
(b)
Before irradiation
After irradiation at 365 nm
After irradiation at 405 nm
After irradiation at CFL light
Absorbance/au
Wavelength/nm

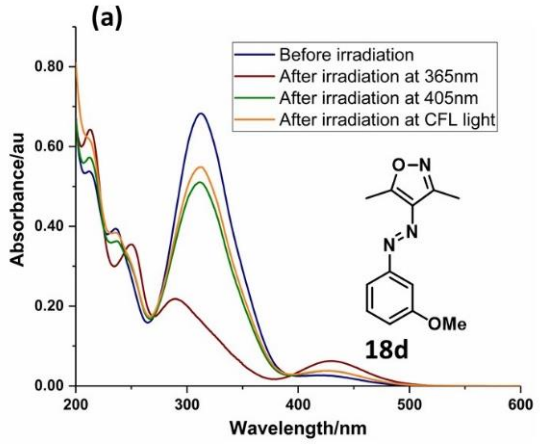
(a)
Before irradiation
After irradiation at 365nm
After irradiation at 405nm
After irradiation at CFL light
18d
Absorbance/au
Wavelength/nm

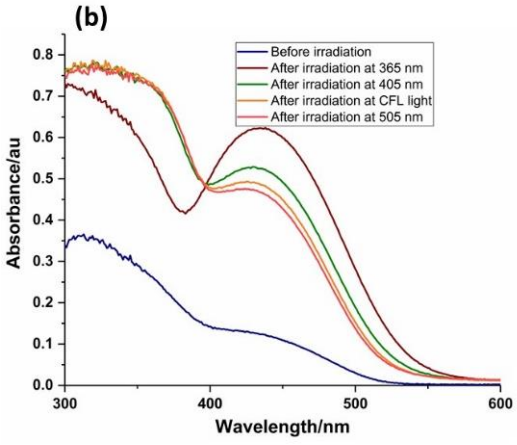
(b)
Before irradiation
After irradiation at 365 nm
After irradiation at 405 nm
After irradiation at CFL light
After irradiation at 505 nm
Absorbance/au
Wavelength/nm

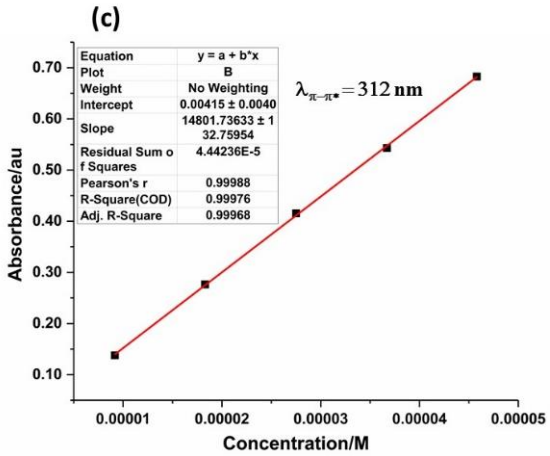
(c)
Equation y = a + b*x
Plot B
Weight No Weighting
Intercept 0.00415 ± 0.0040
Slope 14801.73633 ± 1 32.75954
Residual Sum o f Squares 4.44236E-5
Pearson's r 0.99988
R-Square(COD) 0.99976
Adj. R-Square 0.99968
λπ–π* = 312 nm
Absorbance/au
Concentration/M

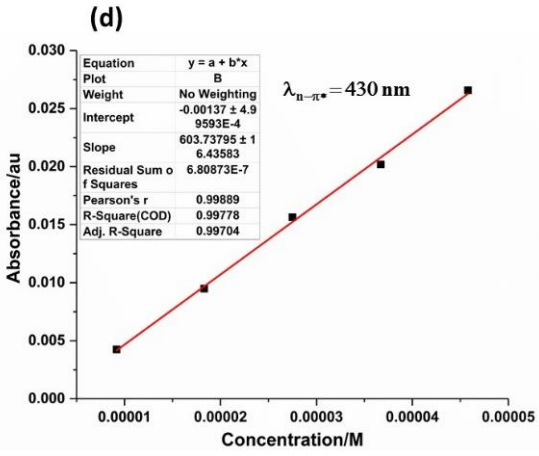
(d)
Equation y = a + b*x
Plot B
Weight No Weighting
Intercept -0.00137 ± 4.9 9593E-4
Slope 603.73795 ± 1 6.43583
Residual Sum o f Squares 6.80873E-7
Pearson's r 0.99889
R-Square(COD) 0.99778
Adj. R-Square 0.99704
λn–π* = 430 nm
Absorbance/au
Concentration/M

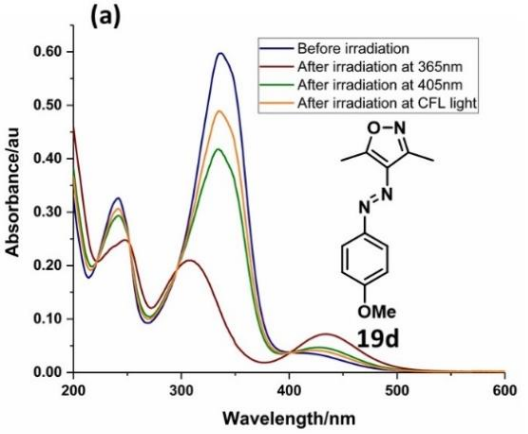
(a)
Before irradiation
After irradiation at 365nm
After irradiation at 405nm
After irradiation at CFL light
O–N
N=N
OMe
19d
Absorbance/au
Wavelength/nm

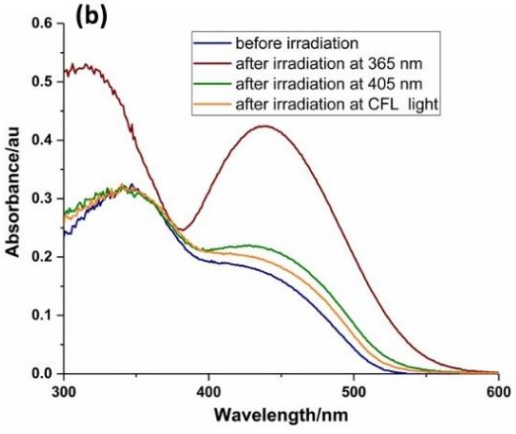
(b)
before irradiation
after irradiation at 365 nm
after irradiation at 405 nm
after irradiation at CFL light
Absorbance/au
Wavelength/nm

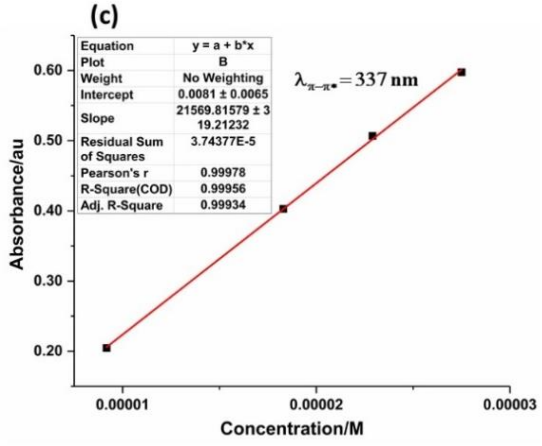
(c)
Equation y = a + b*x
Plot B
Weight No Weighting
Intercept 0.0081 ± 0.0065
Slope 21569.81579 ± 319.21232
Residual Sum of Squares 3.74377E-5
Pearson's r 0.99978
R-Square(COD) 0.99956
Adj. R-Square 0.99934
λπ–π* = 337 nm
Absorbance/au
Concentration/M

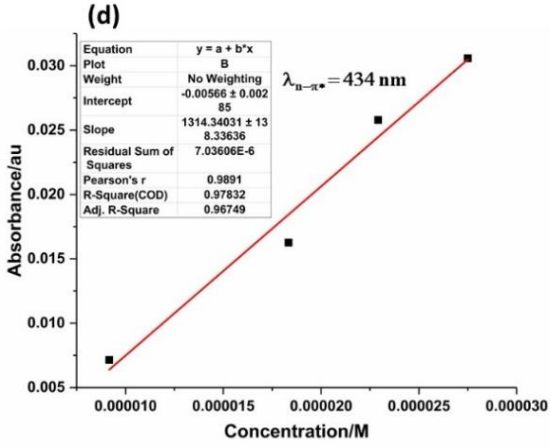
(d)
Equation y = a + b*x
Plot B
Weight No Weighting
Intercept -0.00566 ± 0.00285
Slope 1314.34031 ± 138.33636
Residual Sum of Squares 7.03606E-6
Pearson's r 0.9891
R-Square(COD) 0.97832
Adj. R-Square 0.96749
λn–π* = 434 nm
Absorbance/au
Concentration/M

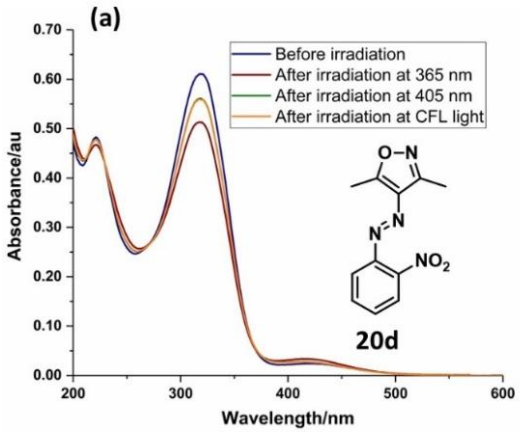
(a)
Before irradiation
After irradiation at 365 nm
After irradiation at 405 nm
After irradiation at CFL light
O–N
N=N
NO2
20d
Absorbance/au
Wavelength/nm

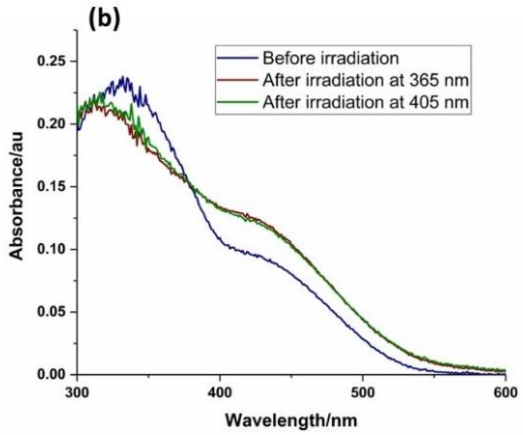
(b)
Before irradiation
After irradiation at 365 nm
After irradiation at 405 nm
Absorbance/au
Wavelength/nm

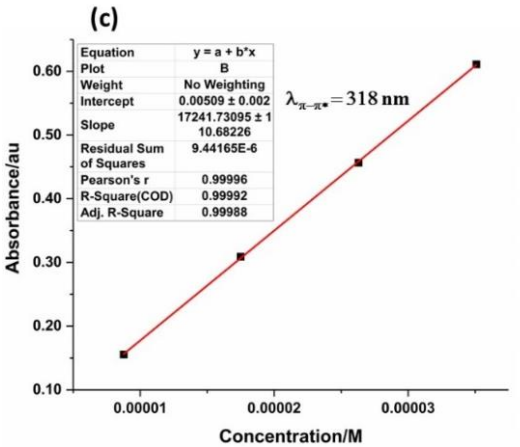
(c)
Equation y = a + b*x
Plot B
Weight No Weighting
Intercept 0.00509 ± 0.002
Slope 17241.73095 ± 110.68226
Residual Sum of Squares 9.44165E-6
Pearson's r 0.99996
R-Square(COD) 0.99992
Adj. R-Square 0.99988
λπ–π* = 318 nm
Absorbance/au
Concentration/M

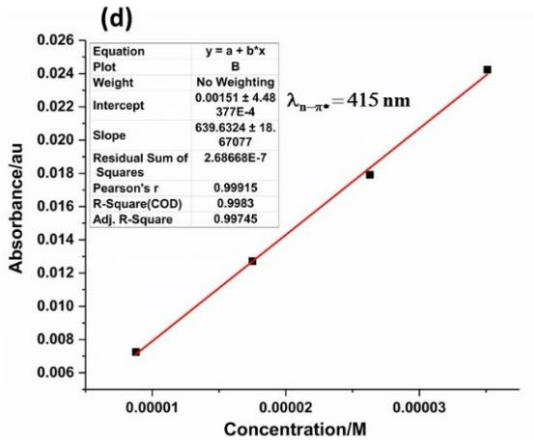
(d)
Equation y = a + b*x
Plot B
Weight No Weighting
Intercept 0.00151 ± 4.48377E-4
Slope 639.6324 ± 18.67077
Residual Sum of Squares 2.68668E-7
Pearson's r 0.99915
R-Square(COD) 0.9983
Adj. R-Square 0.99745
λn–π* = 415 nm
Absorbance/au
Concentration/M

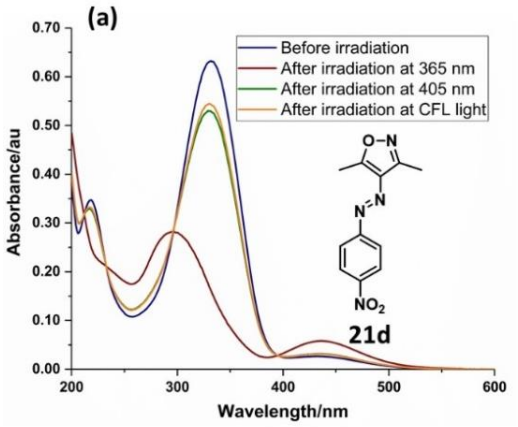
(a)
Before irradiation
After irradiation at 365 nm
After irradiation at 405 nm
After irradiation at CFL light
21d
Absorbance/au
Wavelength/nm

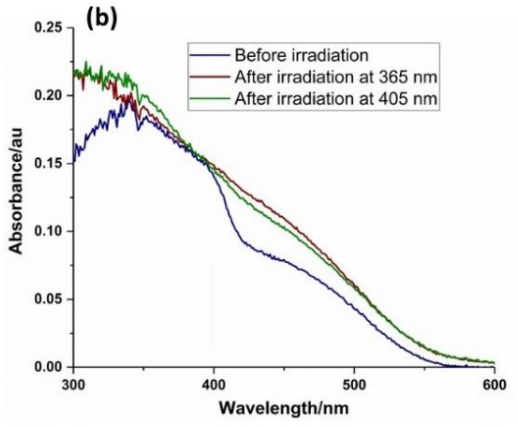
(b)
Before irradiation
After irradiation at 365 nm
After irradiation at 405 nm
Absorbance/au
Wavelength/nm

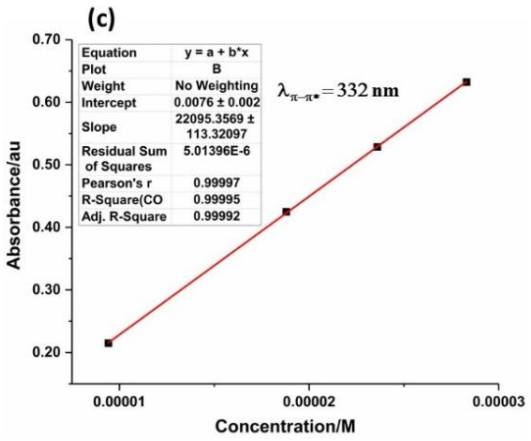
(c)
Equation y = a + b*x
Plot B
Weight No Weighting
Intercept 0.0076 ± 0.002
Slope 22095.3569 ± 113.32097
Residual Sum of Squares 5.01396E-6
Pearson's r 0.99997
R-Square(CO 0.99995
Adj. R-Square 0.99992
λπ–π* = 332 nm
Absorbance/au
Concentration/M

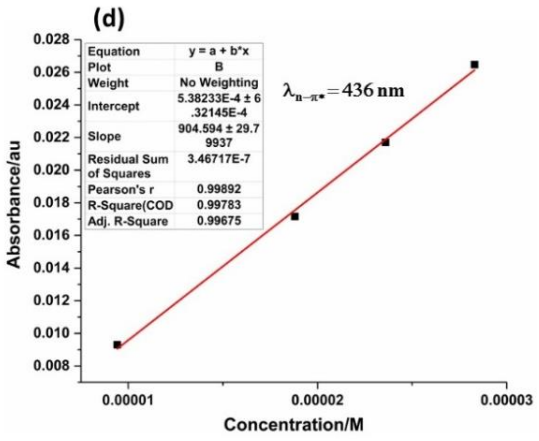
(d)
Equation y = a + b*x
Plot B
Weight No Weighting
Intercept 5.38233E-4 ± 6.32145E-4
Slope 904.594 ± 29.79937
Residual Sum of Squares 3.46717E-7
Pearson's r 0.99892
R-Square(COD 0.99783
Adj. R-Square 0.99675
λn–π* = 436 nm
Absorbance/au
Concentration/M

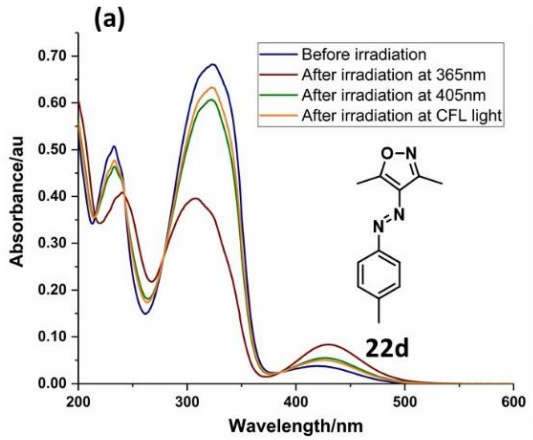
(a)
Before irradiation
After irradiation at 365nm
After irradiation at 405nm
After irradiation at CFL light
22d
Absorbance/au
Wavelength/nm

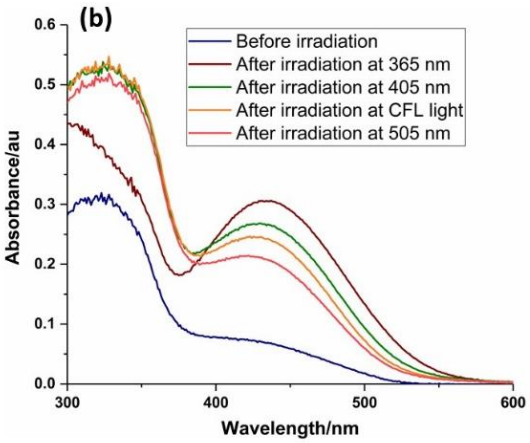
(b)
Before irradiation
After irradiation at 365 nm
After irradiation at 405 nm
After irradiation at CFL light
After irradiation at 505 nm
Absorbance/au
Wavelength/nm

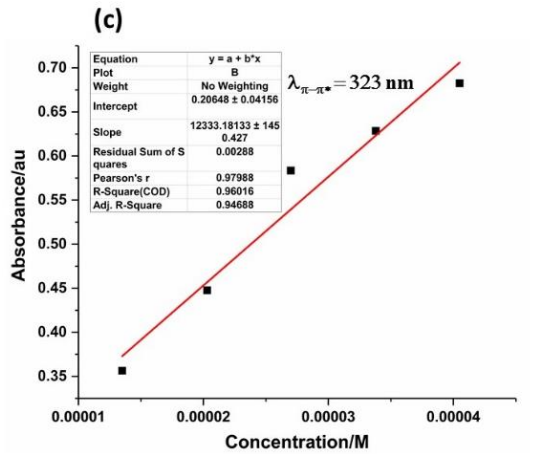
(c)
Equation y = a + b*x
Plot B
Weight No Weighting
Intercept 0.20648 ± 0.04156
Slope 12333.18133 ± 145.427
Residual Sum of Squares 0.00288
Pearson's r 0.97988
R-Square(COD) 0.96016
Adj. R-Square 0.94688
λπ–π* = 323 nm
Absorbance/au
Concentration/M

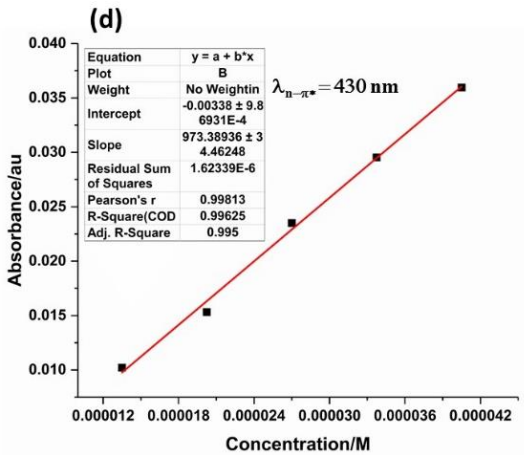
(d)
Equation y = a + b*x
Plot B
Weight No Weightin
Intercept -0.00338 ± 9.86931E-4
Slope 973.38936 ± 34.46248
Residual Sum of Squares 1.62339E-6
Pearson's r 0.99813
R-Square(COD 0.99625
Adj. R-Square 0.995
λn–π* = 430 nm
Absorbance/au
Concentration/M

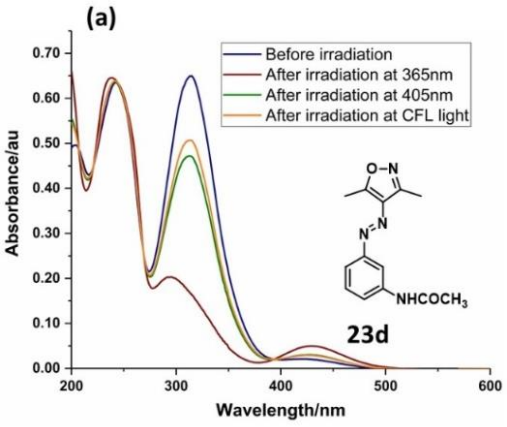
(a)
Before irradiation
After irradiation at 365nm
After irradiation at 405nm
After irradiation at CFL light
NHCOCH3
23d
Absorbance/au
Wavelength/nm

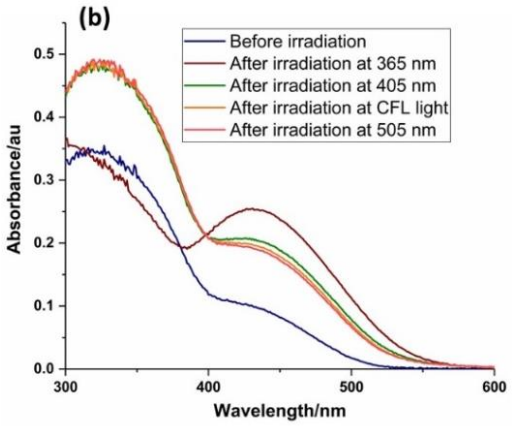
(b)
Before irradiation
After irradiation at 365 nm
After irradiation at 405 nm
After irradiation at CFL light
After irradiation at 505 nm
Absorbance/au
Wavelength/nm

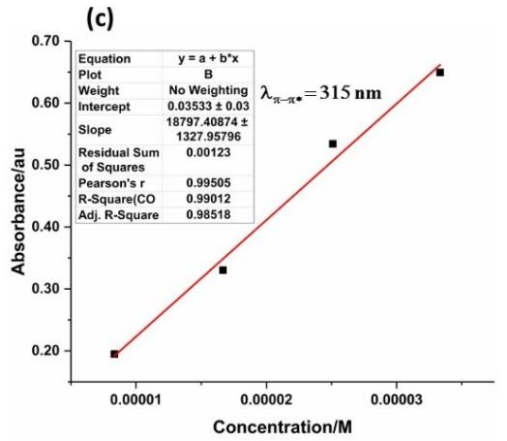
(c)
Equation y = a + b*x
Plot B
Weight No Weighting
Intercept 0.03533 ± 0.03
Slope 18797.40874 ± 1327.95796
Residual Sum of Squares 0.00123
Pearson's r 0.99505
R-Square(CO 0.99012
Adj. R-Square 0.98518
λπ–π* = 315 nm
Absorbance/au
Concentration/M

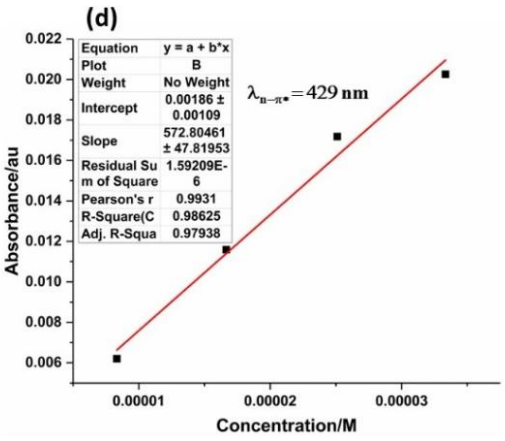
(d)
Equation y = a + b*x
Plot B
Weight No Weight
Intercept 0.00186 ± 0.00109
Slope 572.80461 ± 47.81953
Residual Sum of Square 1.59209E-6
Pearson's r 0.9931
R-Square(C 0.98625
Adj. R-Squa 0.97938
λπ–π* = 429 nm
Absorbance/au
Concentration/M

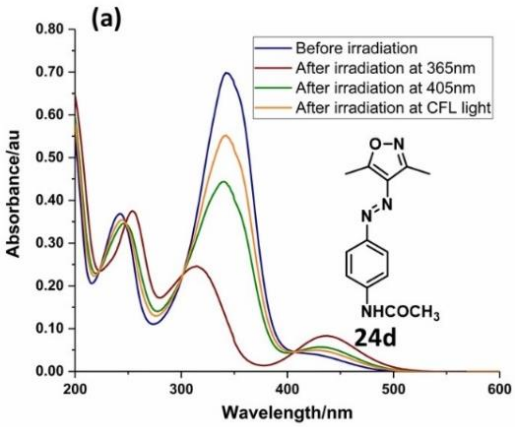
(a)
Before irradiation
After irradiation at 365nm
After irradiation at 405nm
After irradiation at CFL light
NHCOCH3
24d
Absorbance/au
Wavelength/nm

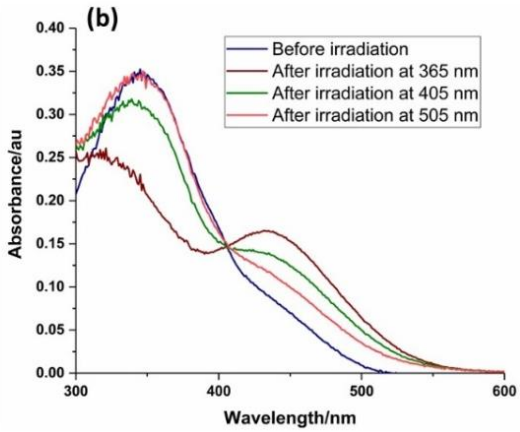
(b)
Before irradiation
After irradiation at 365 nm
After irradiation at 405 nm
After irradiation at 505 nm
Absorbance/au
Wavelength/nm

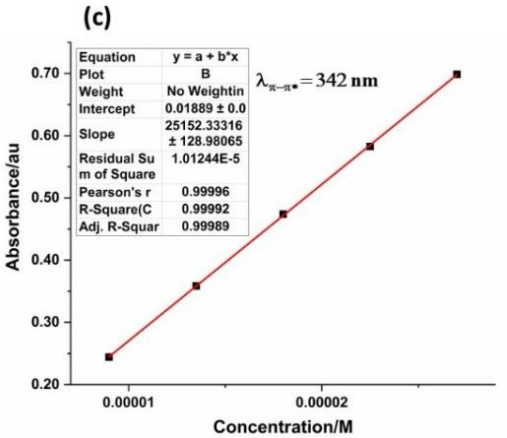
(c)
Equation y = a + b*x
Plot B
Weight No Weightin
Intercept 0.01889 ± 0.0
Slope 25152.33316 ± 128.98065
Residual Sum of Square 1.01244E-5
Pearson's r 0.99996
R-Square(C 0.99992
Adj. R-Squar 0.99989
λπ–π* = 342 nm
Absorbance/au
Concentration/M

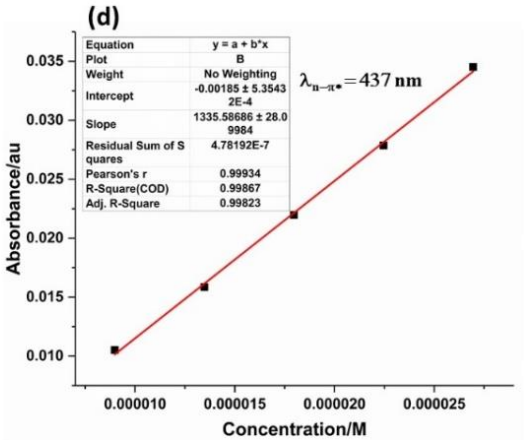
(d)
Equation y = a + b*x
Plot B
Weight No Weighting
Intercept -0.00185 ± 5.35432E-4
Slope 1335.58686 ± 28.09984
Residual Sum of Squares 4.78192E-7
Pearson's r 0.99934
R-Square(COD) 0.99867
Adj. R-Square 0.99823
λπ–π* = 437 nm
Absorbance/au
Concentration/M

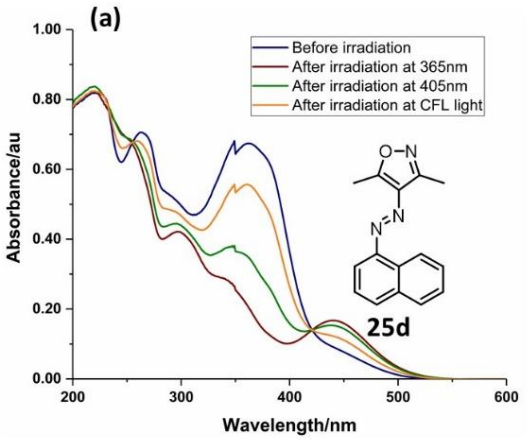
(a)
Before irradiation
After irradiation at 365nm
After irradiation at 405nm
After irradiation at CFL light
25d
Absorbance/au
Wavelength/nm

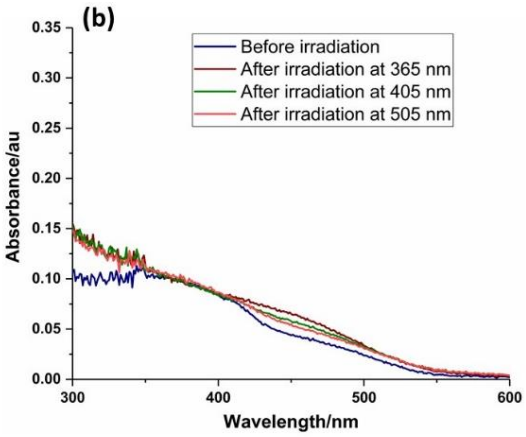
(b)
Before irradiation
After irradiation at 365 nm
After irradiation at 405 nm
After irradiation at 505 nm
Absorbance/au
Wavelength/nm

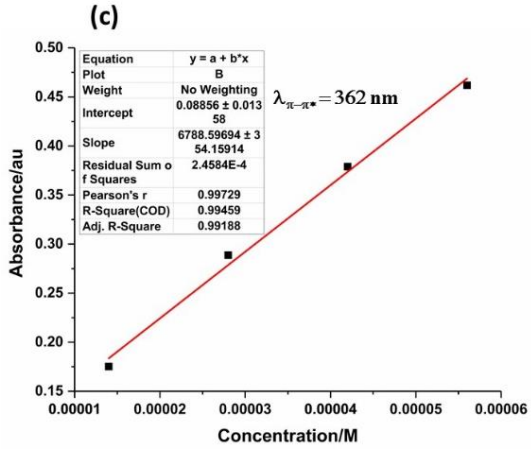
(c)
Equation y = a + b*x
Plot B
Weight No Weighting
Intercept 0.08856 ± 0.01358
Slope 6788.59694 ± 354.15914
Residual Sum of Squares 2.4584E-4
Pearson's r 0.99729
R-Square(COD) 0.99459
Adj. R-Square 0.99188
λπ–π* = 362 nm
Absorbance/au
Concentration/M

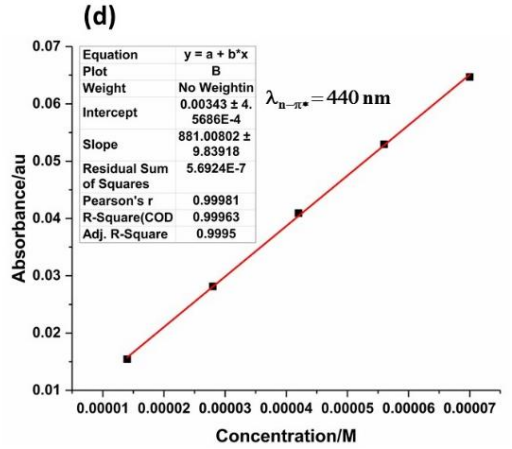
(d)
Equation y = a + b*x
Plot B
Weight No Weightin
Intercept 0.00343 ± 4.5686E-4
Slope 881.00802 ± 9.83918
Residual Sum of Squares 5.6924E-7
Pearson's r 0.99981
R-Square(COD 0.99963
Adj. R-Square 0.9995
λn–π* = 440 nm
Absorbance/au
Concentration/M

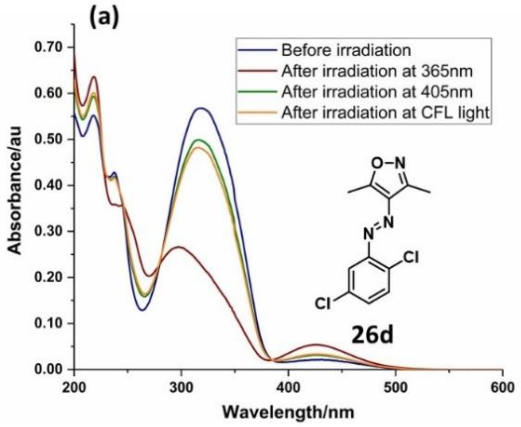
(a)
Before irradiation
After irradiation at 365nm
After irradiation at 405nm
After irradiation at CFL light
26d
Absorbance/au
Wavelength/nm

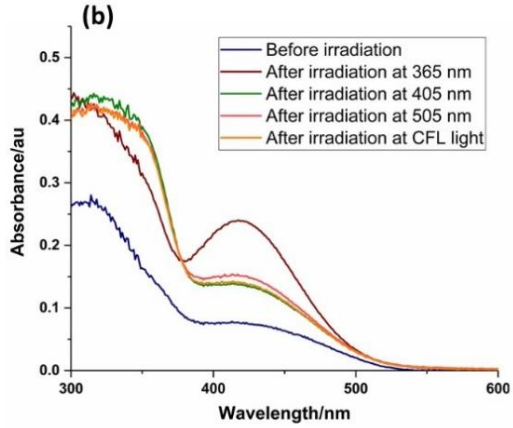
(b)
Before irradiation
After irradiation at 365 nm
After irradiation at 405 nm
After irradiation at 505 nm
After irradiation at CFL light
Absorbance/au
Wavelength/nm

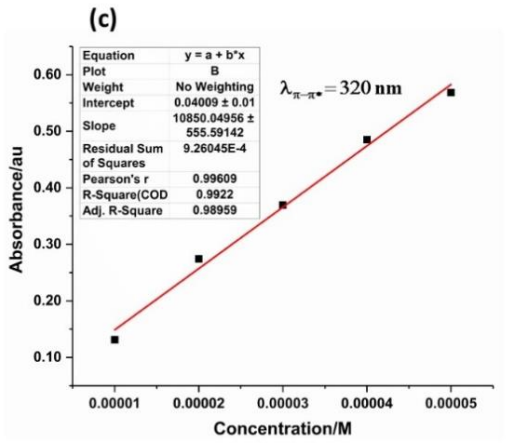
(c)
Equation y = a + b*x
Plot B
Weight No Weighting
Intercept 0.04009 ± 0.01
Slope 10850.04956 ± 555.59142
Residual Sum of Squares 9.26045E-4
Pearson's r 0.99609
R-Square(COD 0.9922
Adj. R-Square 0.98959
λπ–π* = 320 nm
Absorbance/au
Concentration/M

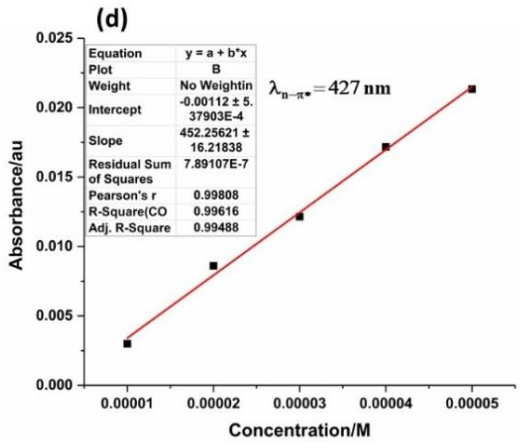
(d)
Equation y = a + b*x
Plot B
Weight No Weightin
Intercept -0.00112 ± 5.37903E-4
Slope 452.25621 ± 16.21838
Residual Sum of Squares 7.89107E-7
Pearson's r 0.99808
R-Square(CO 0.99616
Adj. R-Square 0.99488
λn–π* = 427 nm
Absorbance/au
Concentration/M

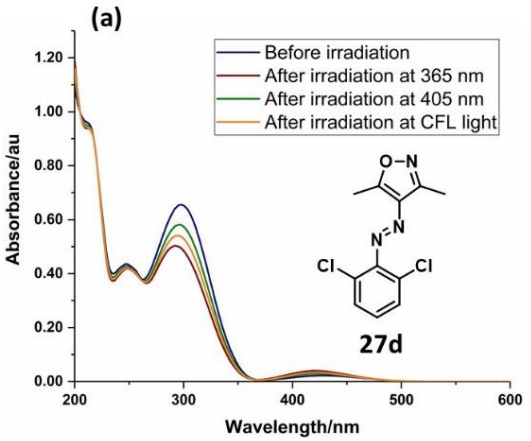
(a)
Before irradiation
After irradiation at 365 nm
After irradiation at 405 nm
After irradiation at CFL light
Absorbance/au
Wavelength/nm
27d

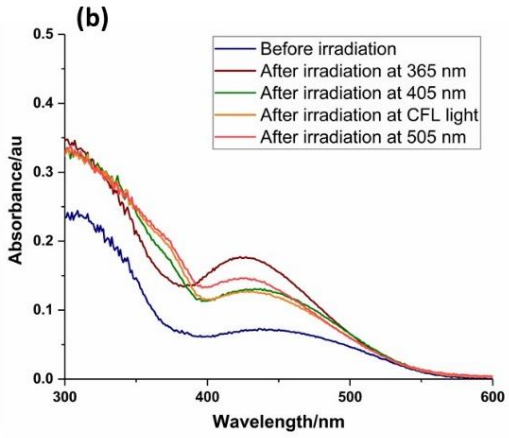
(b)
Before irradiation
After irradiation at 365 nm
After irradiation at 405 nm
After irradiation at CFL light
After irradiation at 505 nm
Absorbance/au
Wavelength/nm

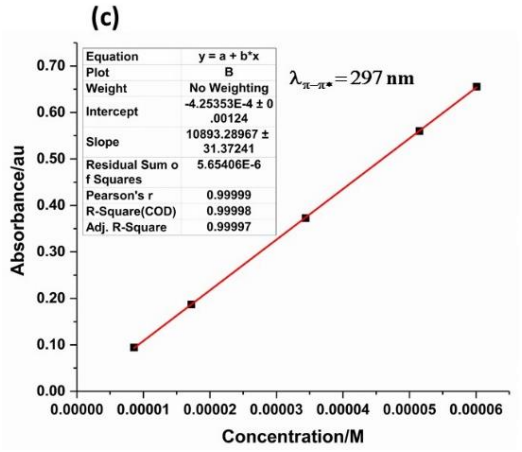
(c)
Equation y = a + b*x
Plot B
Weight No Weighting
Intercept -4.25353E-4 ± 0.00124
Slope 10893.28967 ± 31.37241
Residual Sum of Squares 5.65406E-6
Pearson's r 0.99999
R-Square(COD) 0.99998
Adj. R-Square 0.99997
λπ–π* = 297 nm
Absorbance/au
Concentration/M

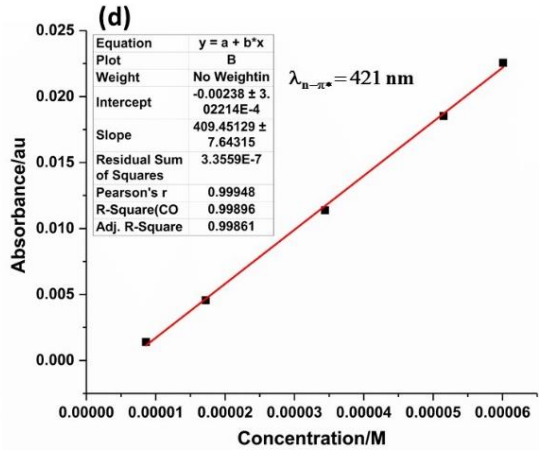
(d)
Equation y = a + b*x
Plot B
Weight No Weightin
Intercept -0.00238 ± 3.02214E-4
Slope 409.45129 ± 7.64315
Residual Sum of Squares 3.3559E-7
Pearson's r 0.99948
R-Square(CO 0.99896
Adj. R-Square 0.99861
λn–π* = 421 nm
Absorbance/au
Concentration/M

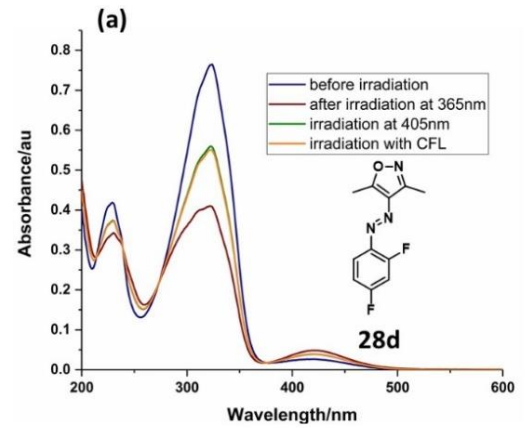
(a)
before irradiation
after irradiation at 365nm
irradiation at 405nm
irradiation with CFL
28d
Absorbance/au
Wavelength/nm

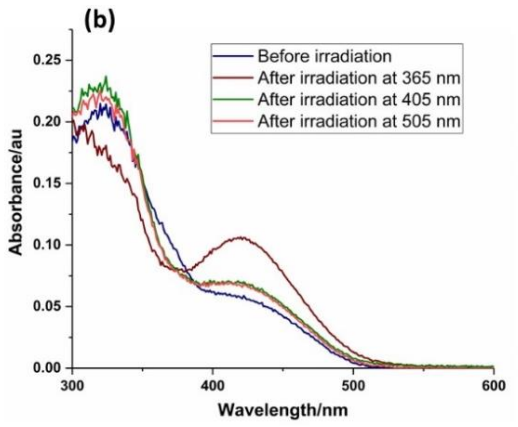
(b)
Before irradiation
After irradiation at 365 nm
After irradiation at 405 nm
After irradiation at 505 nm
Absorbance/au
Wavelength/nm

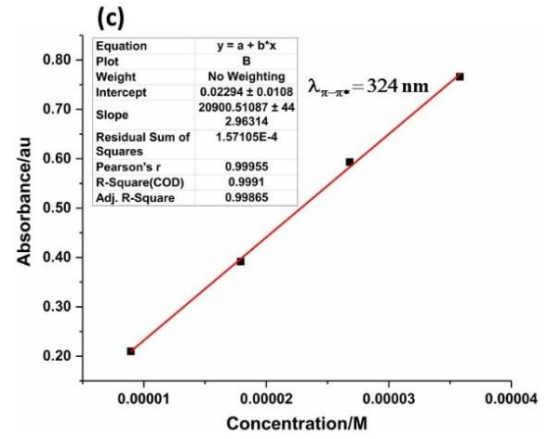
(c)
Equation y = a + b*x
Plot B
Weight No Weighting
Intercept 0.02294 ± 0.0108
Slope 20900.51087 ± 44 2.96314
Residual Sum of Squares 1.57105E-4
Pearson's r 0.99955
R-Square(COD) 0.9991
Adj. R-Square 0.99865
λπ–π* = 324 nm
Absorbance/au
Concentration/M

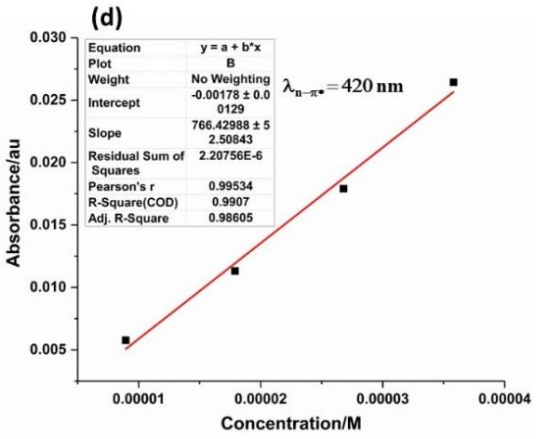
(d)
Equation y = a + b*x
Plot B
Weight No Weighting
Intercept -0.00178 ± 0.00129
Slope 766.42988 ± 52.50843
Residual Sum of Squares 2.20756E-6
Pearson's r 0.99534
R-Square(COD) 0.9907
Adj. R-Square 0.98605
λn–π* = 420 nm
Absorbance/au
Concentration/M

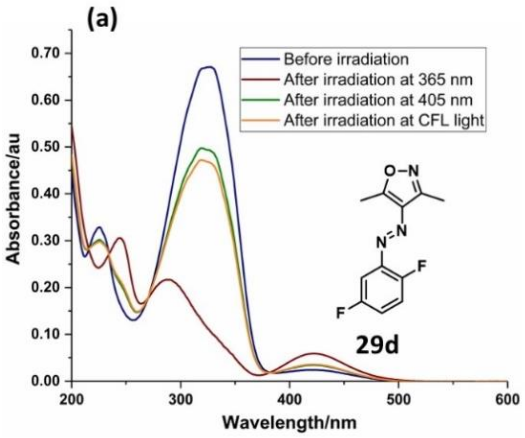
(a)
Before irradiation
After irradiation at 365 nm
After irradiation at 405 nm
After irradiation at CFL light
29d
Absorbance/au
Wavelength/nm

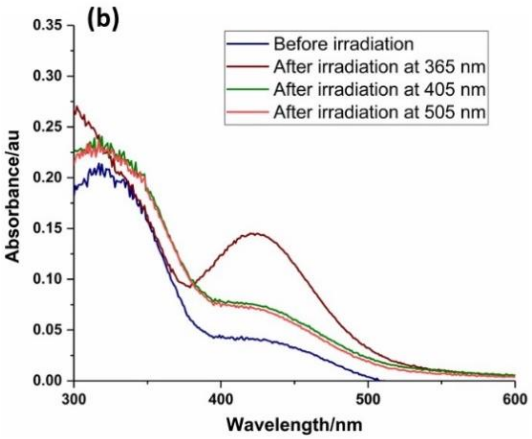
(b)
Before irradiation
After irradiation at 365 nm
After irradiation at 405 nm
After irradiation at 505 nm
Absorbance/au
Wavelength/nm

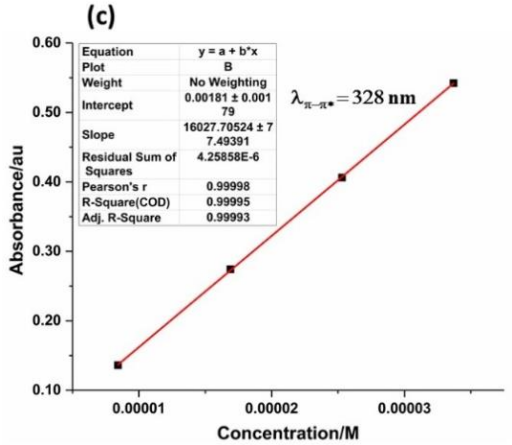
(c)
Equation y = a + b*x
Plot B
Weight No Weighting
Intercept 0.00181 ± 0.00179
Slope 16027.70524 ± 77.49391
Residual Sum of Squares 4.25858E-6
Pearson's r 0.99998
R-Square(COD) 0.99995
Adj. R-Square 0.99993
λπ–π* = 328 nm
Absorbance/au
Concentration/M

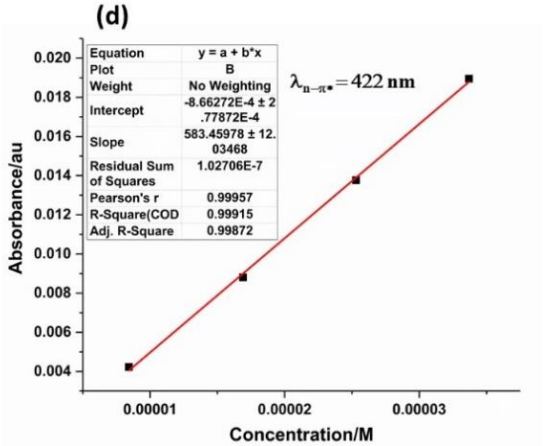
(d)
Equation y = a + b*x
Plot B
Weight No Weighting
Intercept -8.66272E-4 ± 2.77872E-4
Slope 583.45978 ± 12.03468
Residual Sum of Squares 1.02706E-7
Pearson's r 0.99957
R-Square(COD 0.99915
Adj. R-Square 0.99872
λn–π* = 422 nm
Absorbance/au
Concentration/M

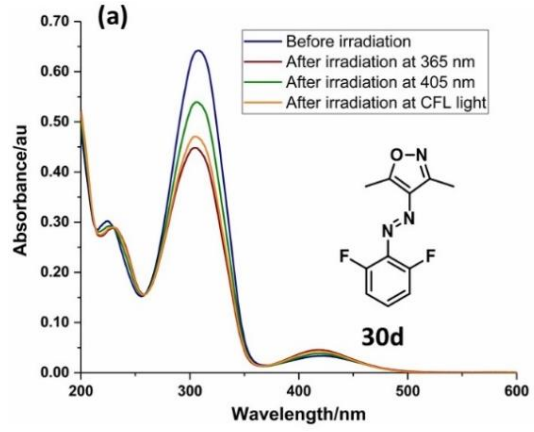
(a)
Before irradiation
After irradiation at 365 nm
After irradiation at 405 nm
After irradiation at CFL light
30d
Absorbance/au
Wavelength/nm

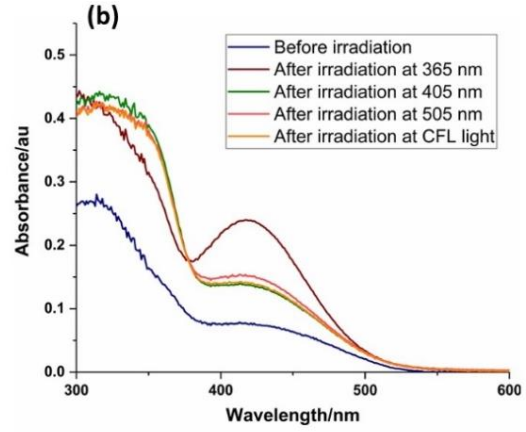
(b)
Before irradiation
After irradiation at 365 nm
After irradiation at 405 nm
After irradiation at 505 nm
After irradiation at CFL light
Absorbance/au
Wavelength/nm

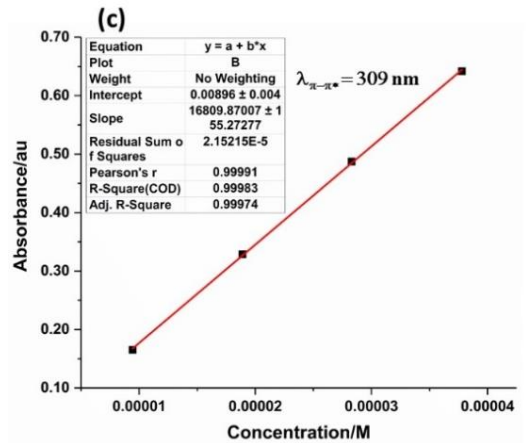
(c)
Equation y = a + b*x
Plot B
Weight No Weighting
Intercept 0.00896 ± 0.004
Slope 16809.87007 ± 155.27277
Residual Sum of Squares 2.15215E-5
Pearson's r 0.99991
R-Square(COD) 0.99983
Adj. R-Square 0.99974
λπ–π* = 309 nm
Absorbance/au
Concentration/M

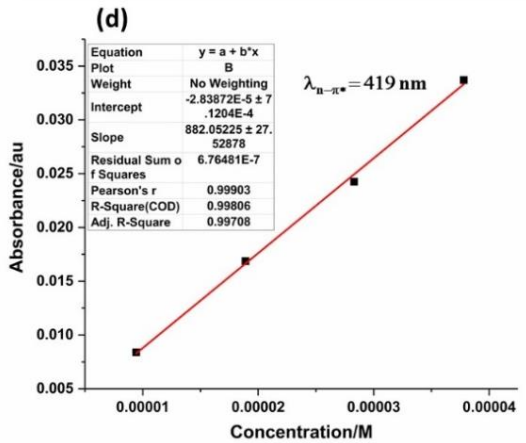
(d)
Equation y = a + b*x
Plot B
Weight No Weighting
Intercept -2.83872E-5 ± 7.1204E-4
Slope 882.05225 ± 27.52878
Residual Sum of Squares 6.76481E-7
Pearson's r 0.99903
R-Square(COD) 0.99806
Adj. R-Square 0.99708
λn–π* = 419 nm
Absorbance/au
Concentration/M

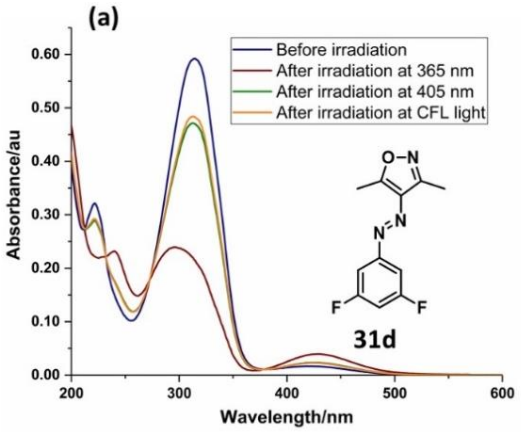
(a)
Before irradiation
After irradiation at 365 nm
After irradiation at 405 nm
After irradiation at CFL light
Absorbance/au
Wavelength/nm
31d

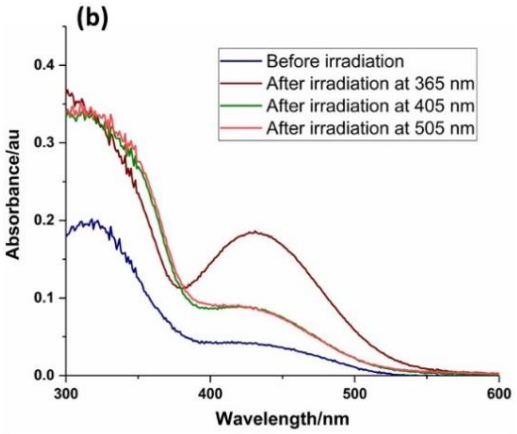
(b)
Before irradiation
After irradiation at 365 nm
After irradiation at 405 nm
After irradiation at 505 nm
Absorbance/au
Wavelength/nm

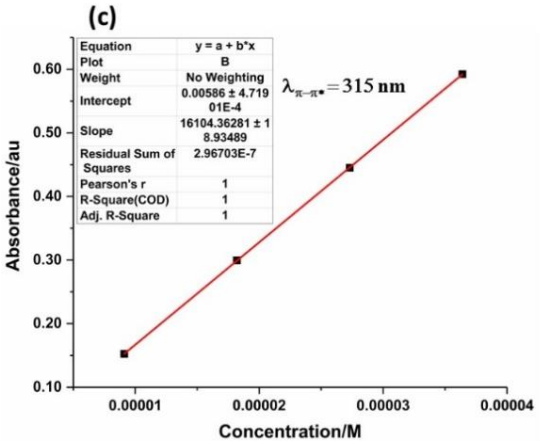
(c)
Equation y = a + b*x
Plot B
Weight No Weighting
Intercept 0.00586 ± 4.719 01E-4
Slope 16104.36281 ± 18.93489
Residual Sum of Squares 2.96703E-7
Pearson's r 1
R-Square(COD) 1
Adj. R-Square 1
λπ–π* = 315 nm
Absorbance/au
Concentration/M

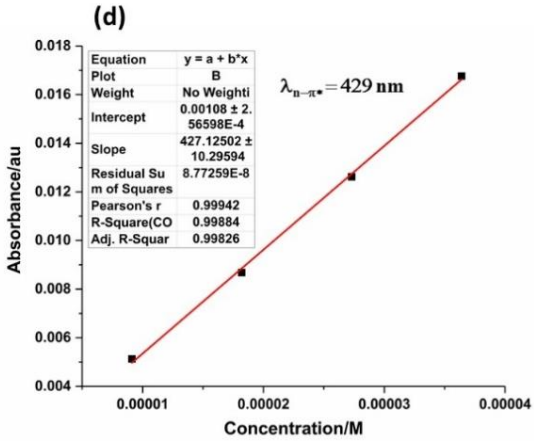
(d)
Equation y = a + b*x
Plot B
Weight No Weighti
Intercept 0.00108 ± 2.56598E-4
Slope 427.12502 ± 10.29594
Residual Sum of Squares 8.77259E-8
Pearson's r 0.99942
R-Square(CO 0.99884
Adj. R-Squar 0.99826
λn–π* = 429 nm
Absorbance/au
Concentration/M

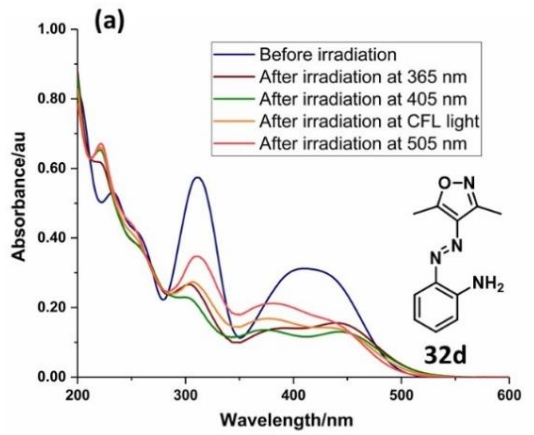
(a)
Before irradiation
After irradiation at 365 nm
After irradiation at 405 nm
After irradiation at CFL light
After irradiation at 505 nm
NH2
32d
Absorbance/au
Wavelength/nm

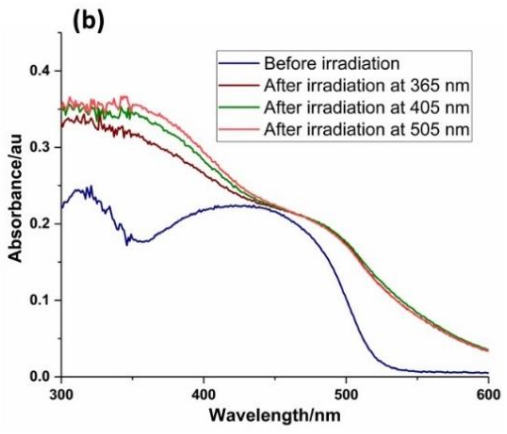
(b)
Before irradiation
After irradiation at 365 nm
After irradiation at 405 nm
After irradiation at 505 nm
Absorbance/au
Wavelength/nm

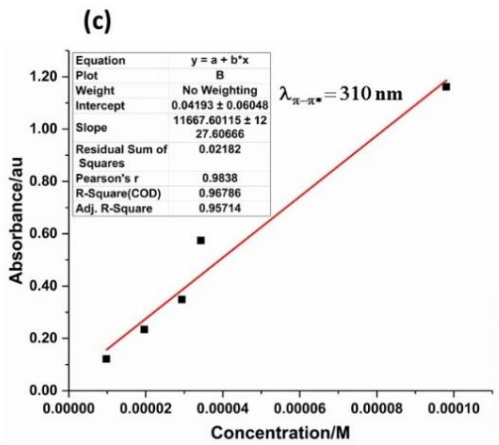
(c)
Equation y = a + b*x
Plot B
Weight No Weighting
Intercept 0.04193 ± 0.06048
Slope 11667.60115 ± 12 27.60666
Residual Sum of Squares 0.02182
Pearson's r 0.9838
R-Square(COD) 0.96786
Adj. R-Square 0.95714
λπ–π* = 310 nm
Absorbance/au
Concentration/M

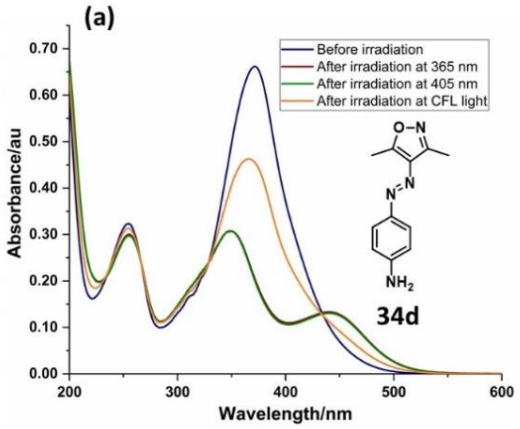
(a)
Before irradiation
After irradiation at 365 nm
After irradiation at 405 nm
After irradiation at CFL light
34d
Absorbance/au
Wavelength/nm

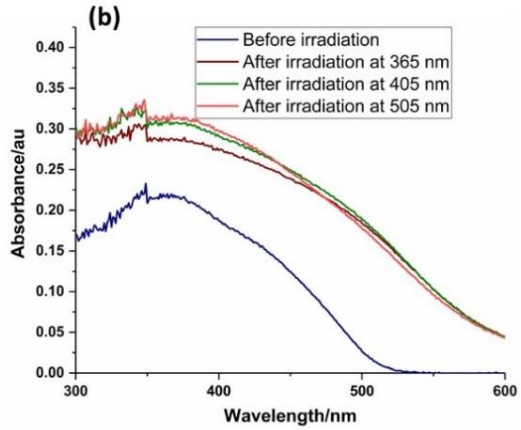
(b)
Before irradiation
After irradiation at 365 nm
After irradiation at 405 nm
After irradiation at 505 nm
Absorbance/au
Wavelength/nm

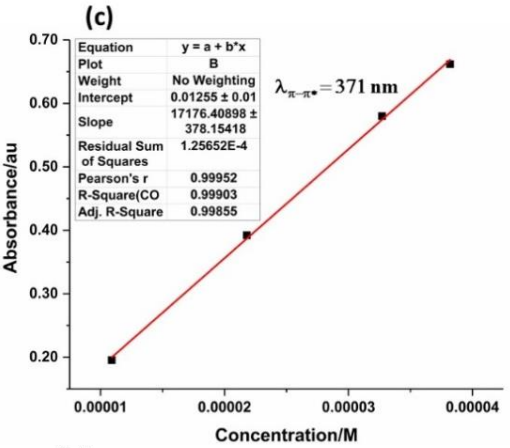
(c)
Equation y = a + b*x
Plot B
Weight No Weighting
Intercept 0.01255 ± 0.01
Slope 17176.40898 ± 378.15418
Residual Sum of Squares 1.25652E-4
Pearson's r 0.99952
R-Square(CO 0.99903
Adj. R-Square 0.99855
λπ–π* = 371 nm
Absorbance/au
Concentration/M

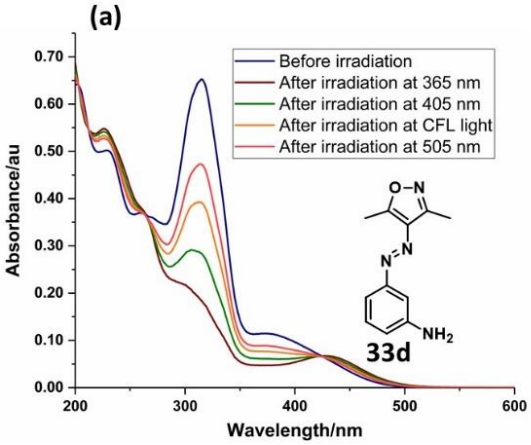
(a)
Before irradiation
After irradiation at 365 nm
After irradiation at 405 nm
After irradiation at CFL light
After irradiation at 505 nm
33d
Absorbance/au
Wavelength/nm

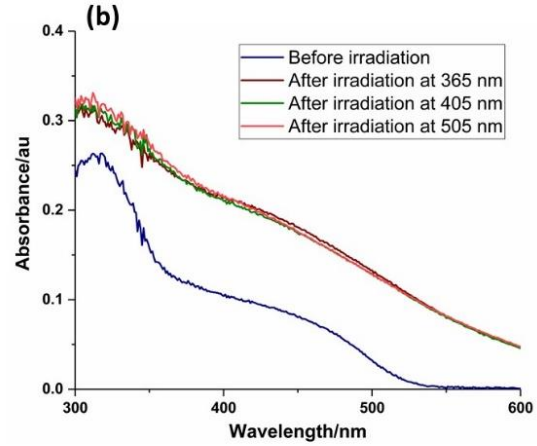
(b)
Before irradiation
After irradiation at 365 nm
After irradiation at 405 nm
After irradiation at 505 nm
Absorbance/au
Wavelength/nm

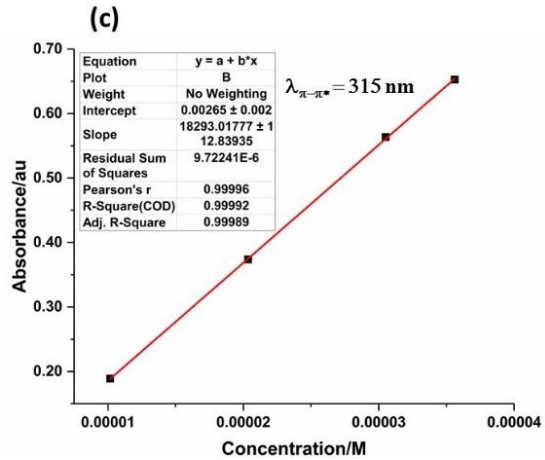
(c)
Equation y = a + b*x
Plot B
Weight No Weighting
Intercept 0.00265 ± 0.002
Slope 18293.01777 ± 12.83935
Residual Sum of Squares 9.72241E-6
Pearson's r 0.99996
R-Square(COD) 0.99992
Adj. R-Square 0.99989
λπ–π* = 315 nm
Absorbance/au
Concentration/M

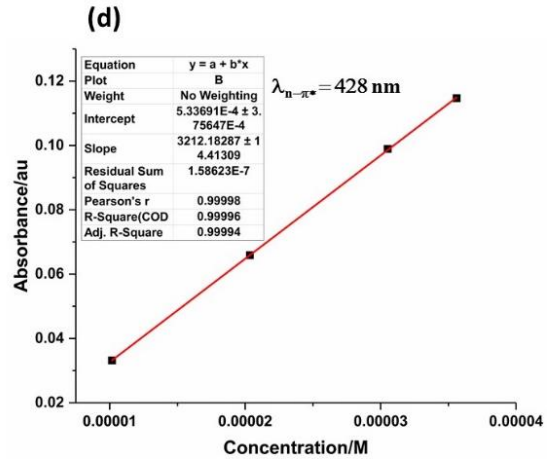
(d)
Equation y = a + b*x
Plot B
Weight No Weighting
Intercept 5.33691E-4 ± 3.75647E-4
Slope 3212.18287 ± 14.41309
Residual Sum of Squares 1.58623E-7
Pearson's r 0.99998
R-Square(COD 0.99996
Adj. R-Square 0.99994
λn–π* = 428 nm
Absorbance/au
Concentration/M

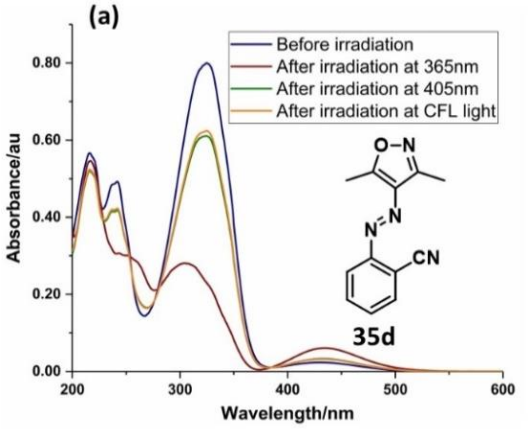
(a)
Before irradiation
After irradiation at 365nm
After irradiation at 405nm
After irradiation at CFL light
O–N
N
N
CN
35d
Absorbance/au
Wavelength/nm

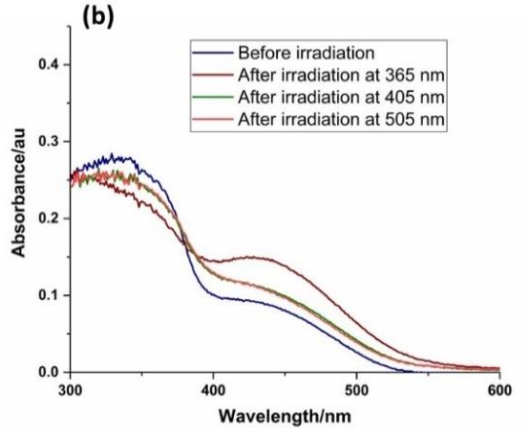
(b)
Before irradiation
After irradiation at 365 nm
After irradiation at 405 nm
After irradiation at 505 nm
Absorbance/au
Wavelength/nm

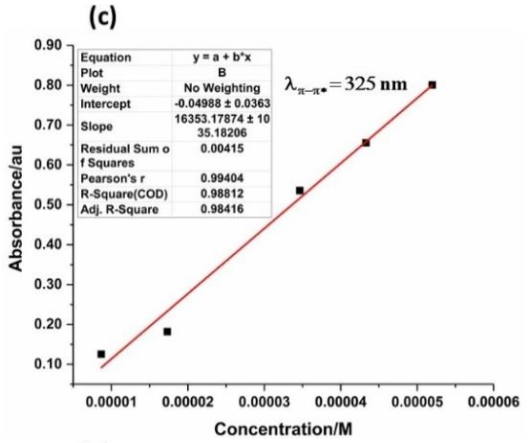
(c)
Equation y = a + b*x
Plot B
Weight No Weighting
Intercept -0.04988 ± 0.0363
Slope 16353.17874 ± 10 35.18206
Residual Sum o f Squares 0.00415
Pearson's r 0.99404
R-Square(COD) 0.98812
Adj. R-Square 0.98416
λπ–π* = 325 nm
Absorbance/au
Concentration/M

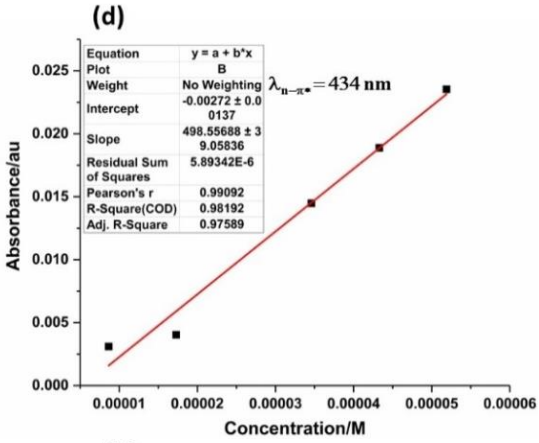
(d)
Equation y = a + b*x
Plot B
Weight No Weighting
Intercept -0.00272 ± 0.0 0137
Slope 498.55688 ± 3 9.05836
Residual Sum of Squares 5.89342E-6
Pearson's r 0.99092
R-Square(COD) 0.98192
Adj. R-Square 0.97589
λn–π* = 434 nm
Absorbance/au
Concentration/M

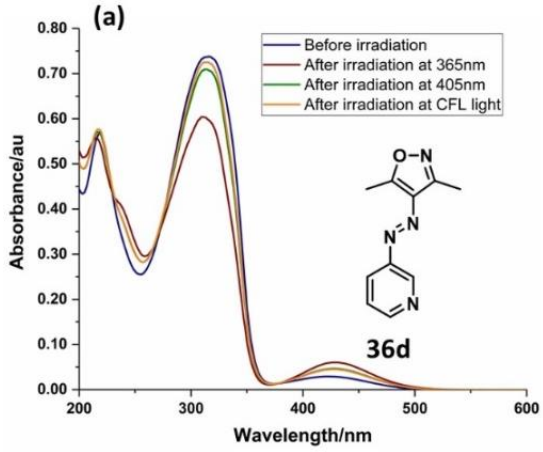
(a)
Before irradiation
After irradiation at 365nm
After irradiation at 405nm
After irradiation at CFL light
O–N
N
N
N
36d
Absorbance/au
Wavelength/nm

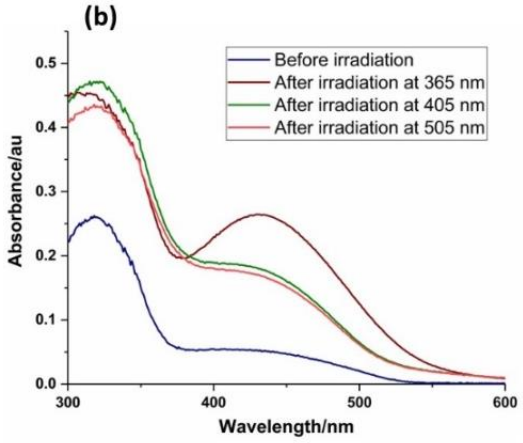
(b)
Before irradiation
After irradiation at 365 nm
After irradiation at 405 nm
After irradiation at 505 nm
Absorbance/au
Wavelength/nm

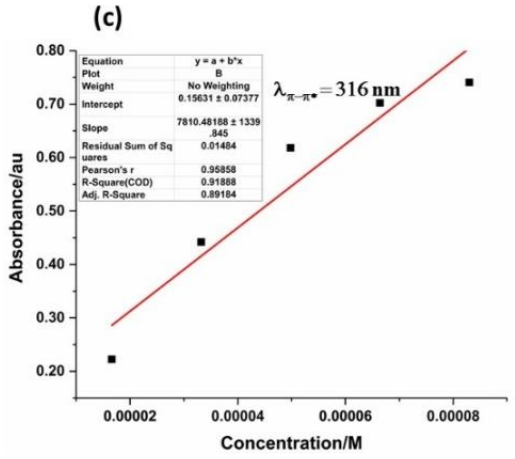
(c)
Equation y = a + b*x
Plot B
Weight No Weighting
Intercept 0.15631 ± 0.07377
Slope 7810.48188 ± 1339 .845
Residual Sum of Squares 0.01484
Pearson's r 0.95858
R-Square(COD) 0.91888
Adj. R-Square 0.89184
λπ–π* = 316 nm
Absorbance/au
Concentration/M

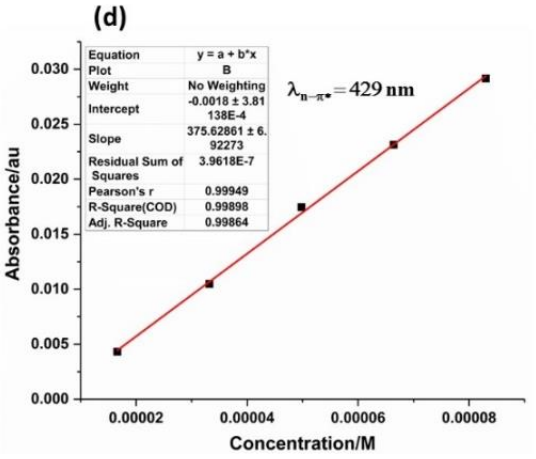
(d)
Equation y = a + b*x
Plot B
Weight No Weighting
Intercept -0.0018 ± 3.81 138E-4
Slope 375.62861 ± 6. 92273
Residual Sum of Squares 3.9618E-7
Pearson's r 0.99949
R-Square(COD) 0.99898
Adj. R-Square 0.99864
λn–π* = 429 nm
Absorbance/au
Concentration/M

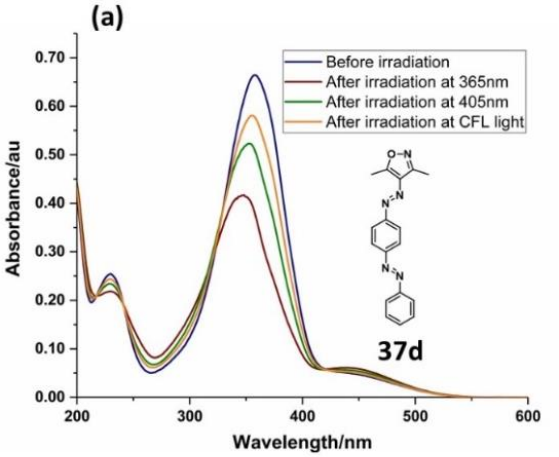
(a)
Before irradiation
After irradiation at 365nm
After irradiation at 405nm
After irradiation at CFL light
37d
Absorbance/au
Wavelength/nm

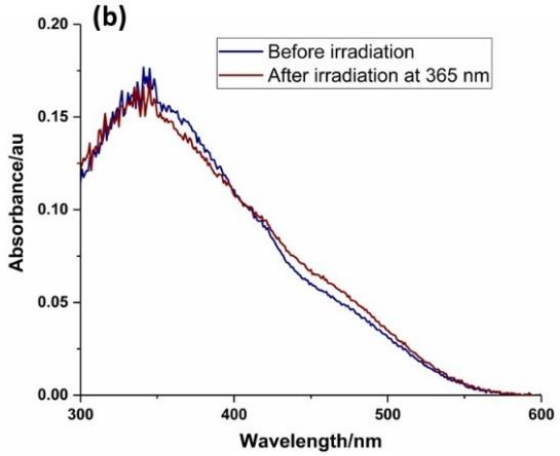
(b)
Before irradiation
After irradiation at 365 nm
Absorbance/au
Wavelength/nm

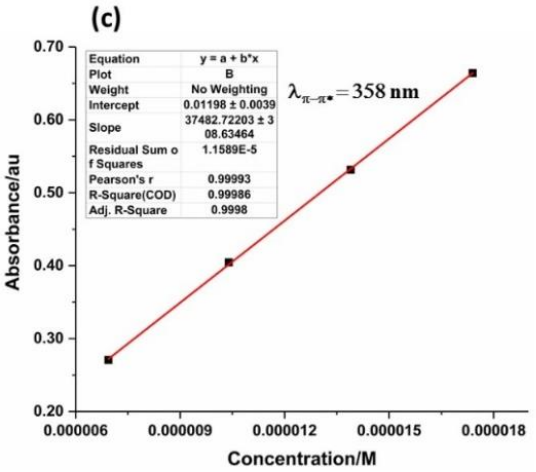
(c)
Equation y = a + b*x
Plot B
Weight No Weighting
Intercept 0.01198 ± 0.0039
Slope 37482.72203 ± 308.63464
Residual Sum of Squares 1.1589E-5
Pearson's r 0.99993
R-Square(COD) 0.99986
Adj. R-Square 0.9998
λπ→π* = 358 nm
Absorbance/au
Concentration/M

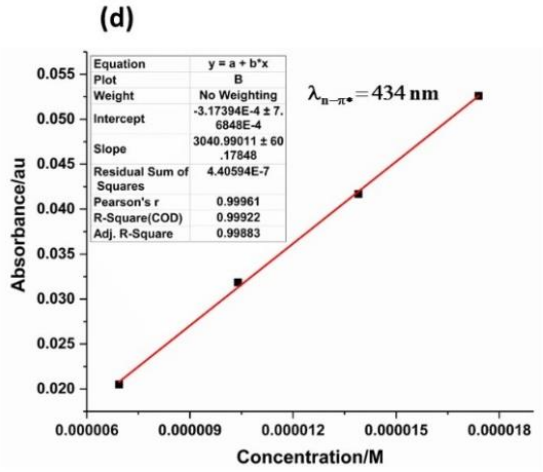
(d)
Equation y = a + b*x
Plot B
Weight No Weighting
Intercept -3.17394E-4 ± 7.6848E-4
Slope 3040.99011 ± 60.17848
Residual Sum of Squares 4.40594E-7
Pearson's r 0.99961
R-Square(COD) 0.99922
Adj. R-Square 0.99883
λn→π* = 434 nm
Absorbance/au
Concentration/M

Appendix 2B
Concentration dependency in the photoswitching (UV-Vis spectroscopic studies)

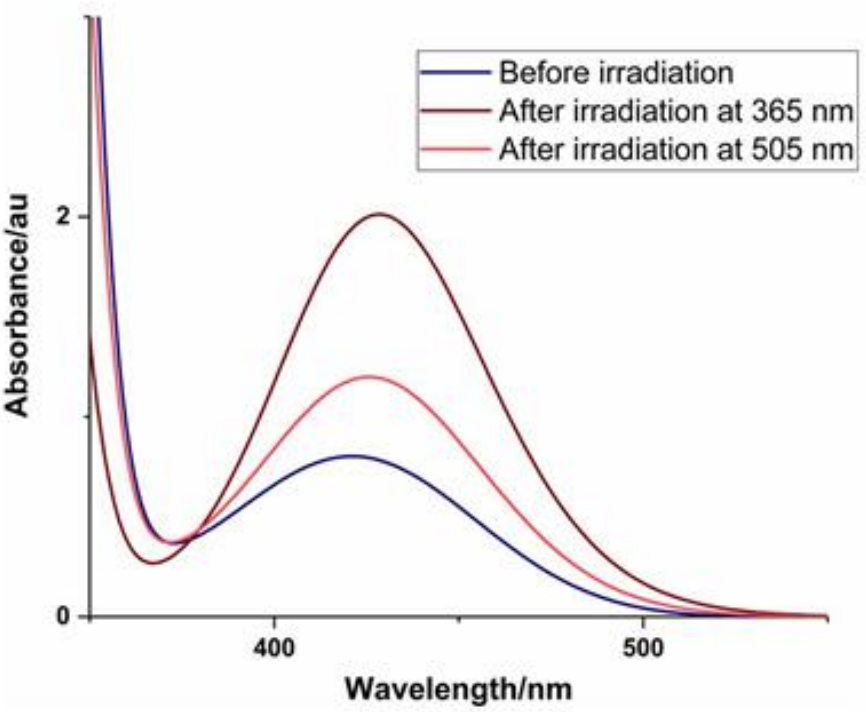

Figure 2B.1. Photoisomerization in phenylazo-3,5-dimethylisoxazole **1d**. Analysis of reversible *E*-*Z* photoisomerization in **1d** using UV-Vis spectroscopy in (a) solution phase (Solvent: CH_3CN, 1.6 mM). At this concentration, the PSS for forward and reverse isomerization steps in terms of *E*-isomer are 60% and 33%, respectively.

Table 2B.1. PSS table for Phenylazoisoxazole in solution phase (CH_3CN) (**1d**)

S. No.	**PSS at Low concentration (36 μM)**		**PSS at a high concentration (1.6 mM)**	
	***E*-*Z* PSS (%*Z*)**	***Z*-*E* PSS (%*E*)**	***E*-*Z* PSS (%*Z*)**	***Z*-*E* PSS (%*E*)**
1	46	78	40	33

Appendix 2C

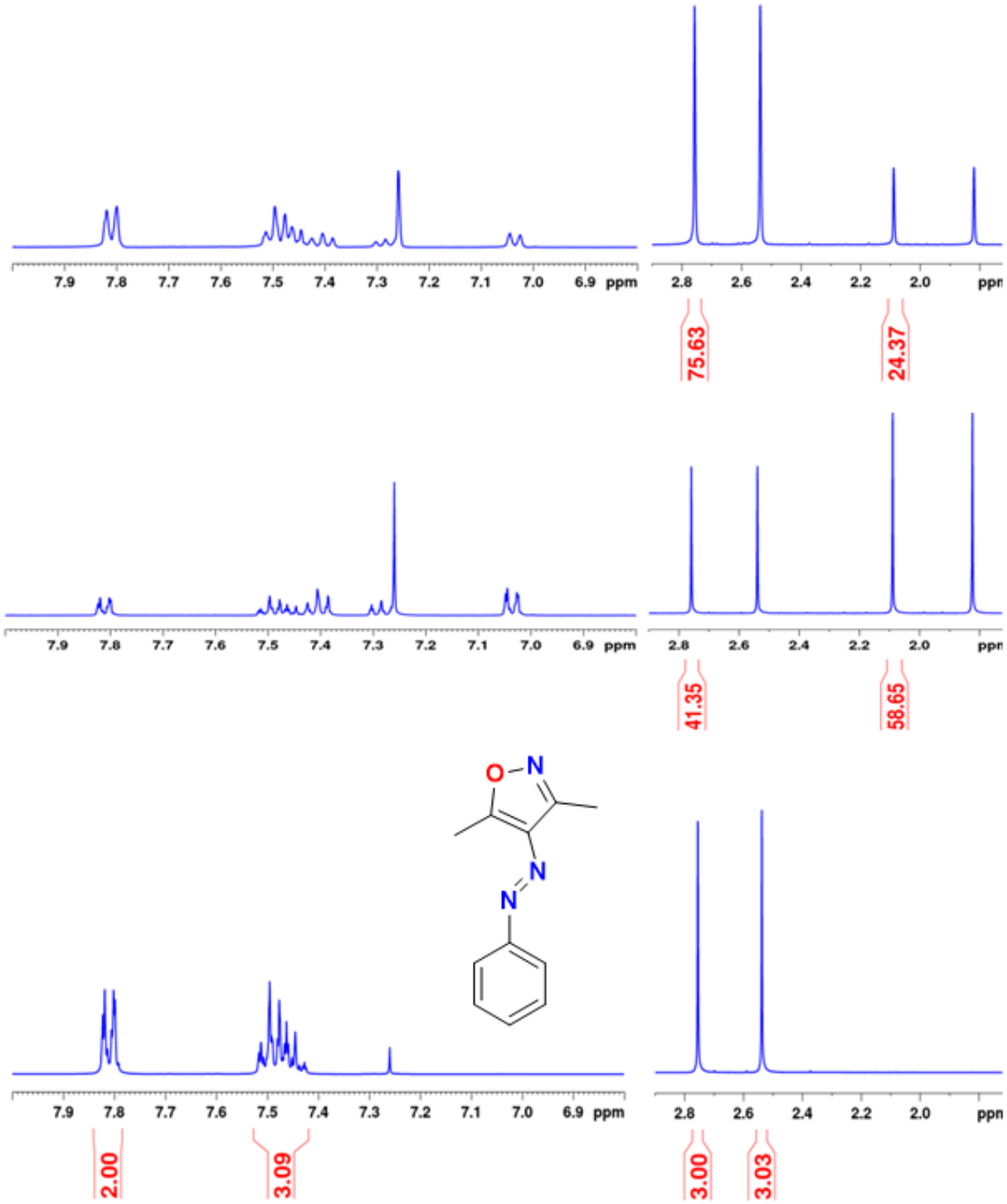

Figure 2C.1. (*E*)-3,5-dimethyl-4-(phenyldiazenyl)isoxazole (**1d**) ($CDCl_3$): (bottom) before irradiation; (middle) after irradiation at 365 nm and (top) after irradiation at 505 nm.

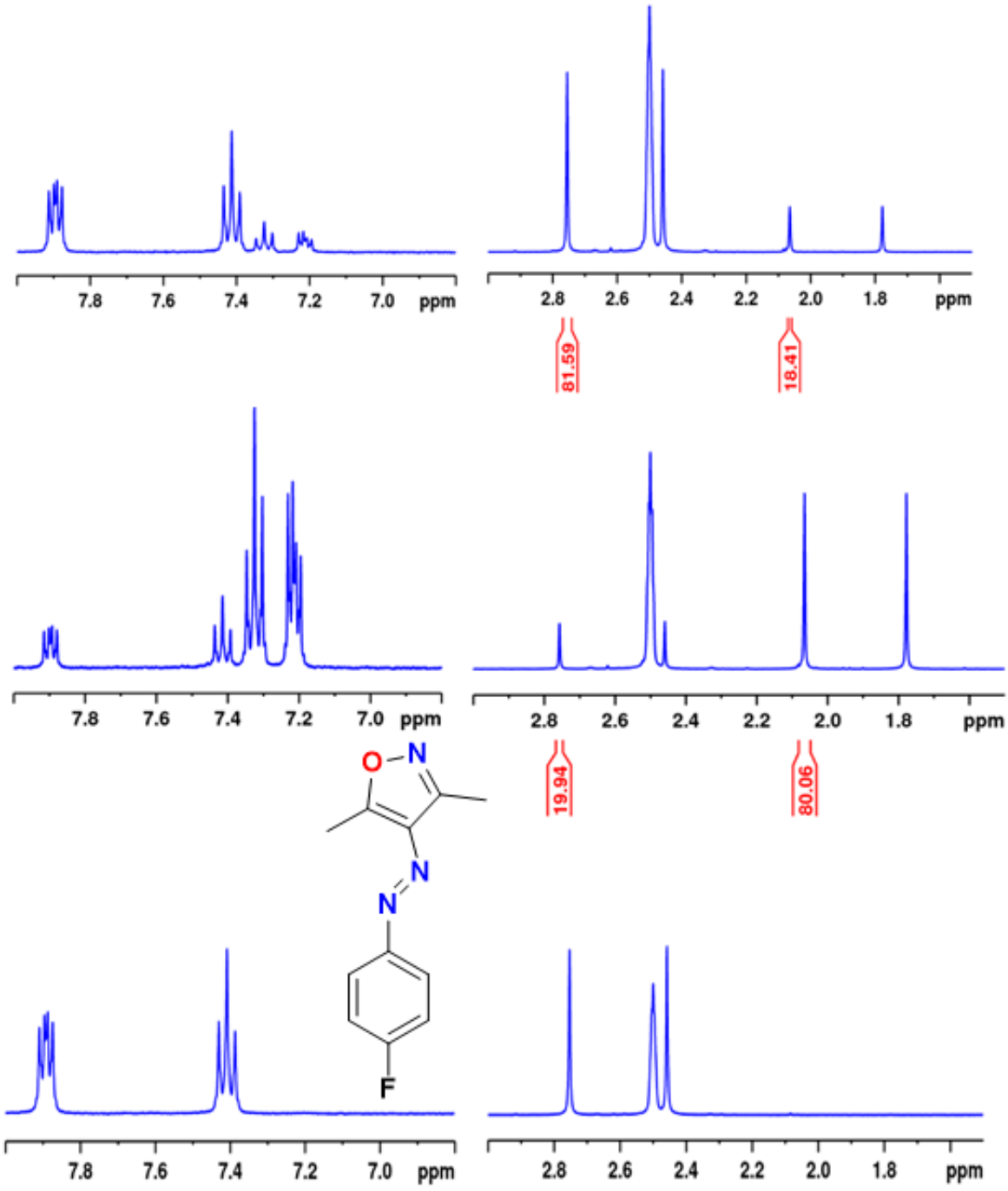

Figure 2C.2. (*E*)-4-((4-fluorophenyl)diazenyl)-3,5-dimethylisoxazole **(4d)** [D_6]DMSO: (bottom) before irradiation; (middle) after irradiation at 365 nm and (top) after irradiation at 470 nm.

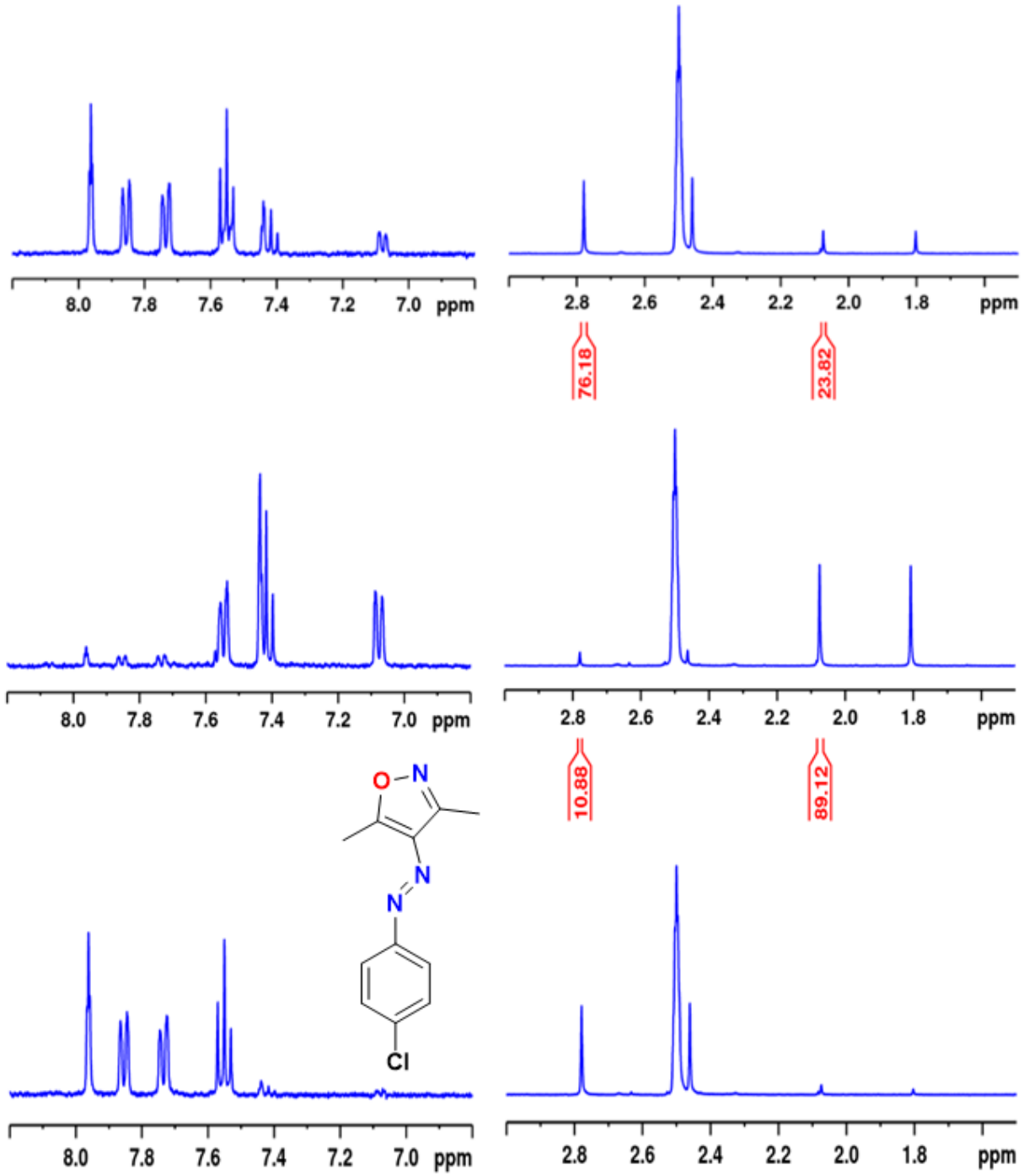

Figure 2C.3. (*E*)-4-((4-chlorophenyl)diazenyl)-3,5-dimethylisoxazole **(7d)** [D_6]DMSO: (bottom) before irradiation; (middle) after irradiation at 365 nm and (top) after irradiation at 470 nm.

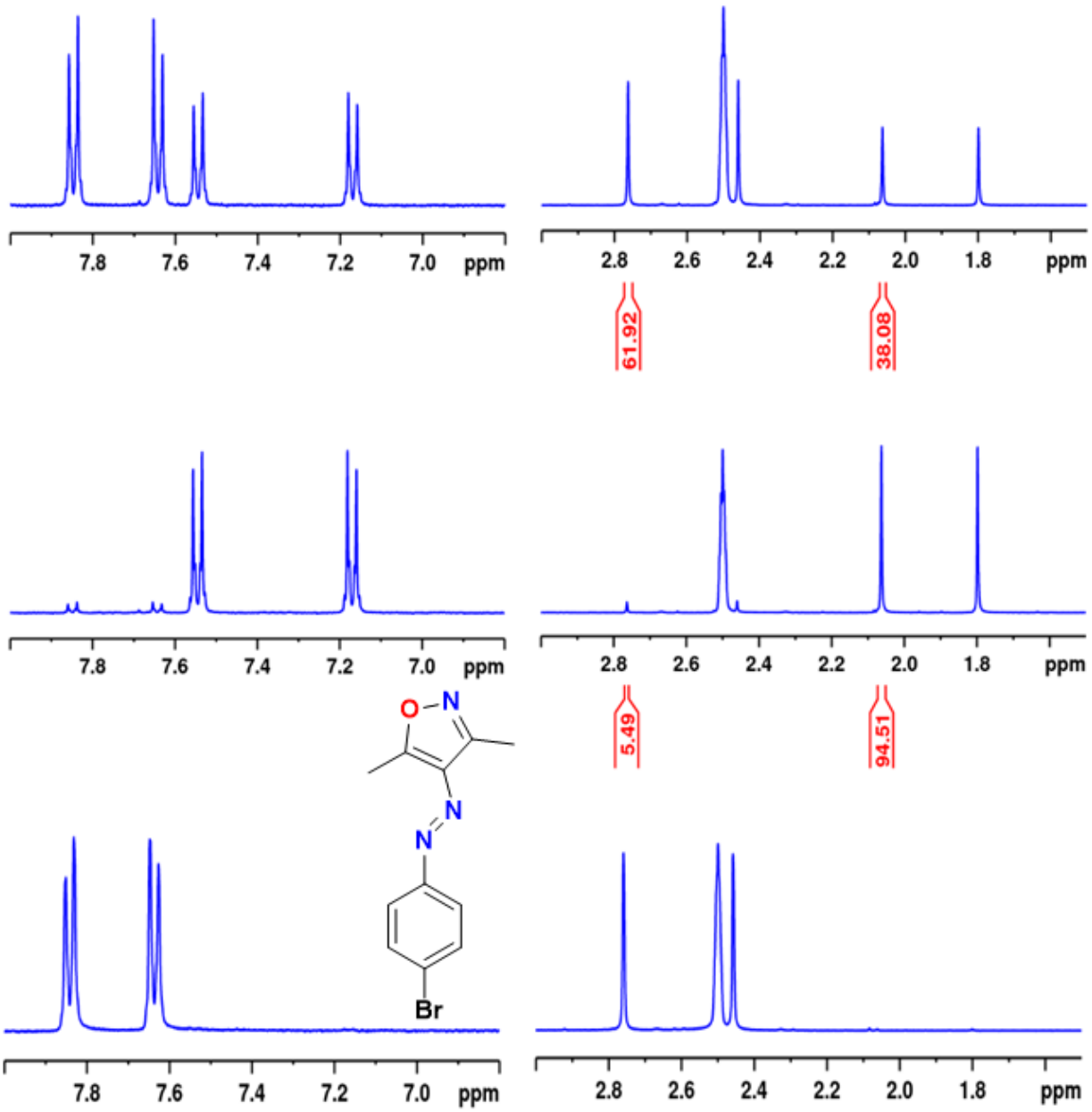

Figure 2C.4. (*E*)-4-((3-bromophenyl)diazenyl)-3,5-dimethylisoxazole **(9d)** [D_6]DMSO: (bottom) before irradiation; (middle) after irradiation at 365 nm and (top) after irradiation at 470 nm.

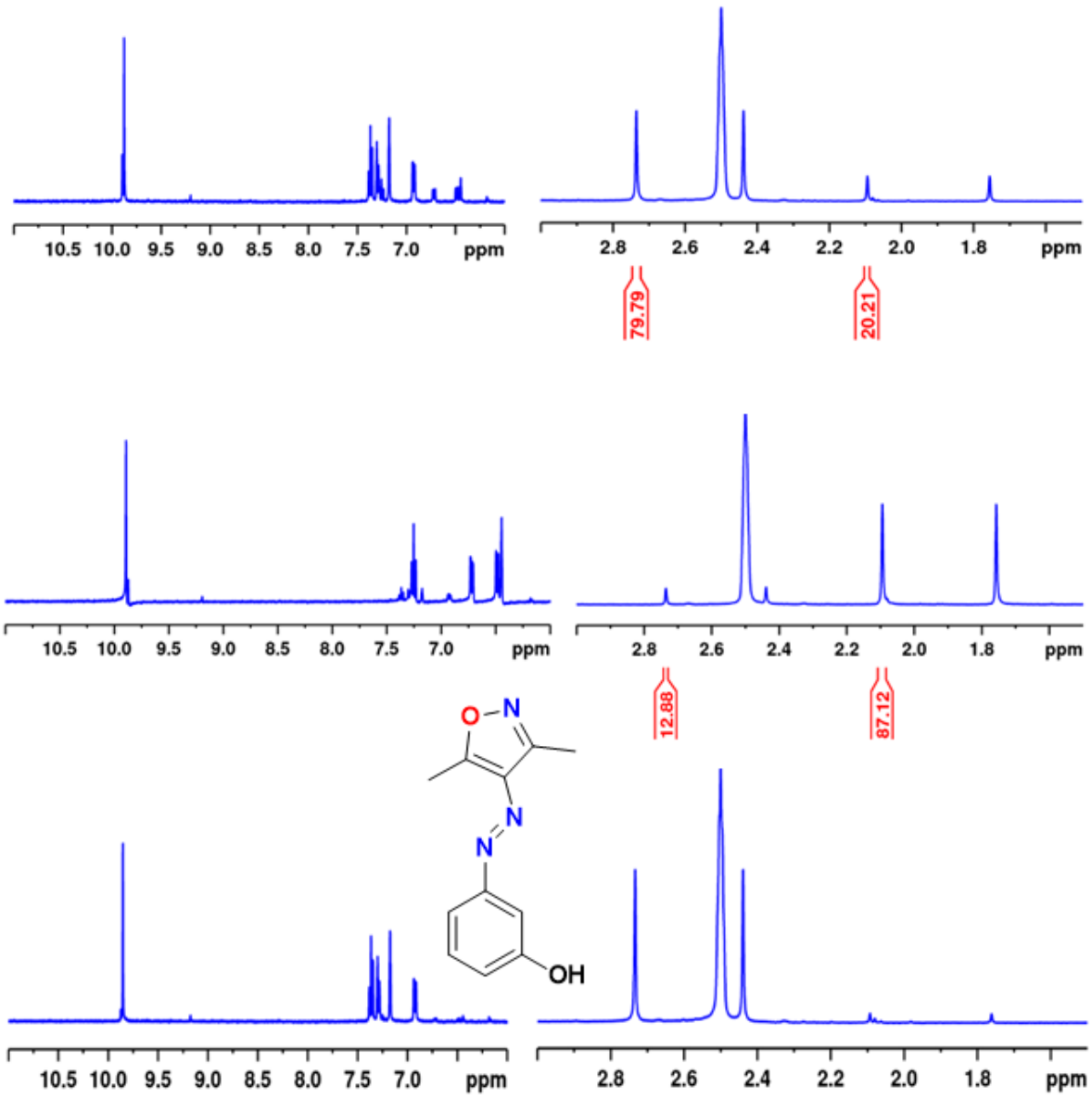

Figure 2C.5. (*E*)-3-((3,5-dimethylisoxazole-4-yl)phenol **(13d)** [D_6]DMSO: (bottom) before irradiation; (middle) after irradiation at 365 nm and (top) after irradiation at 470 nm.

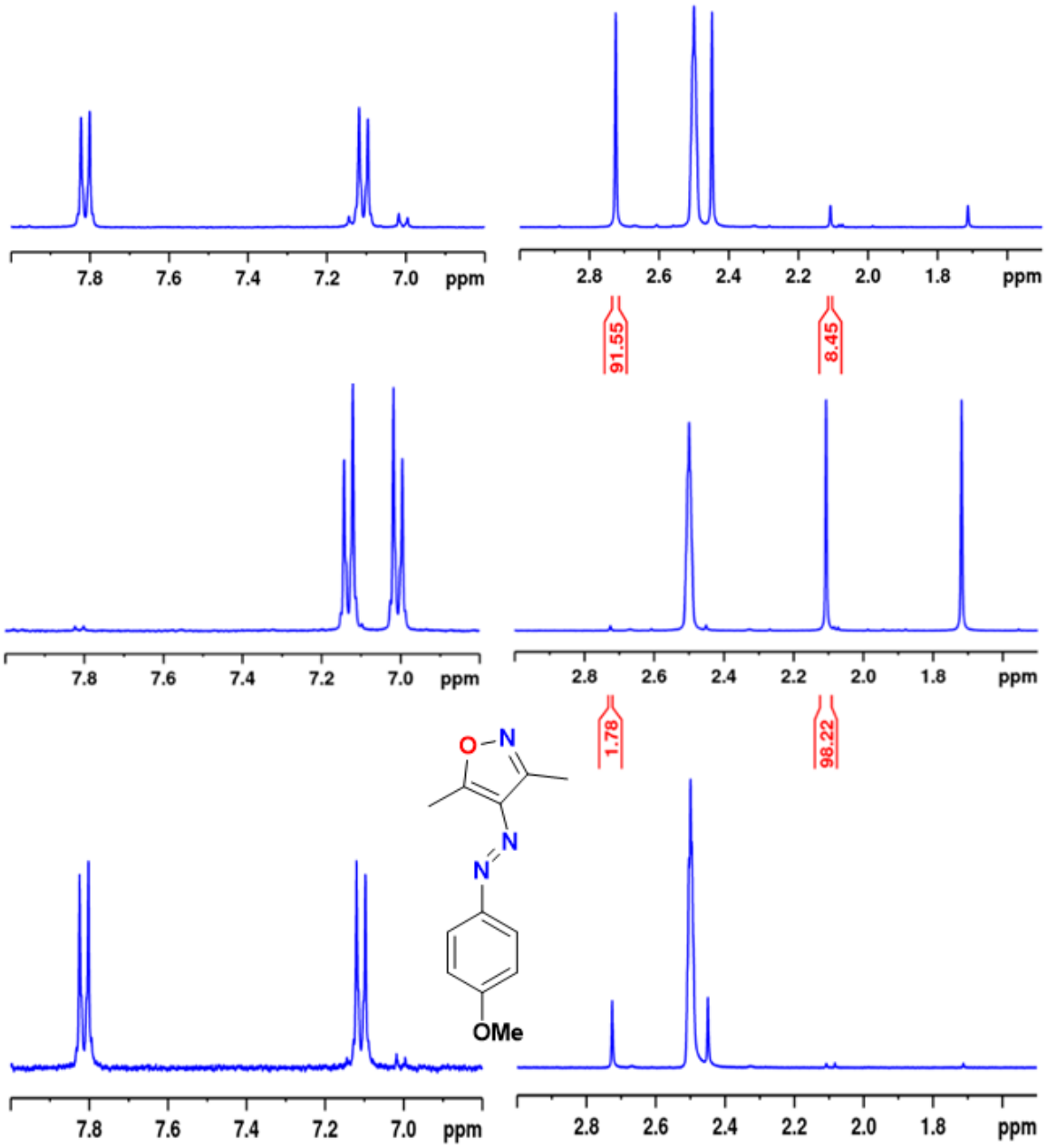

Figure 2C.6. (*E*)-4-((4-methoxyphenyl)diazenyl)-3,5-dimethylisoxazole **(19d)** [D_6]DMSO: (bottom) before irradiation; (middle) after irradiation at 365 nm and (top) after irradiation at 470 nm.

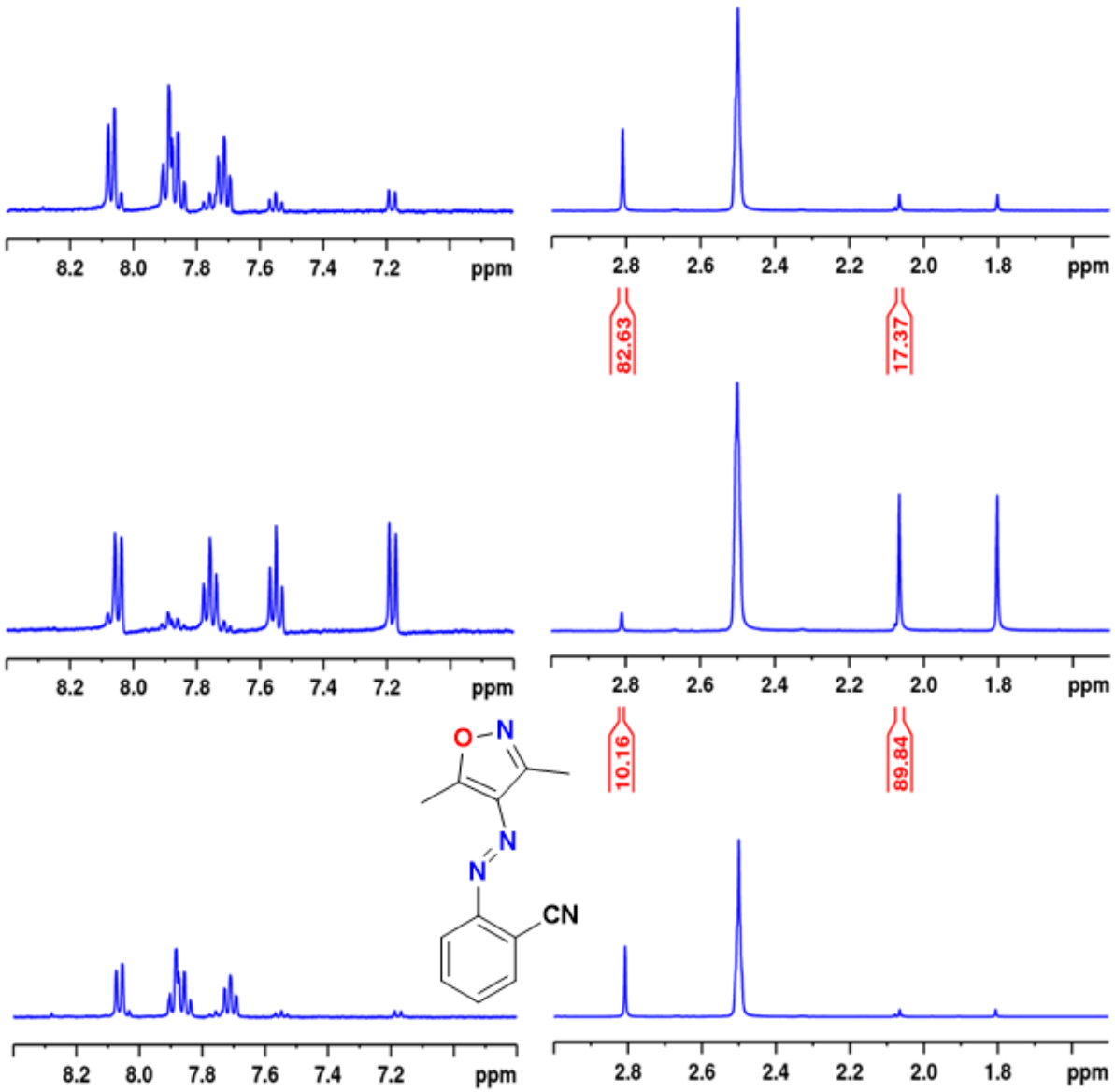

Figure 2C.7. (*E*)-2-((3,5-dimethylisoxazol-4-yl)diazenyl)benzonitrile (**35d)** [D_6]DMSO: (bottom) before irradiation; (middle) after irradiation at 365 nm and (top) after irradiation at 470 nm.

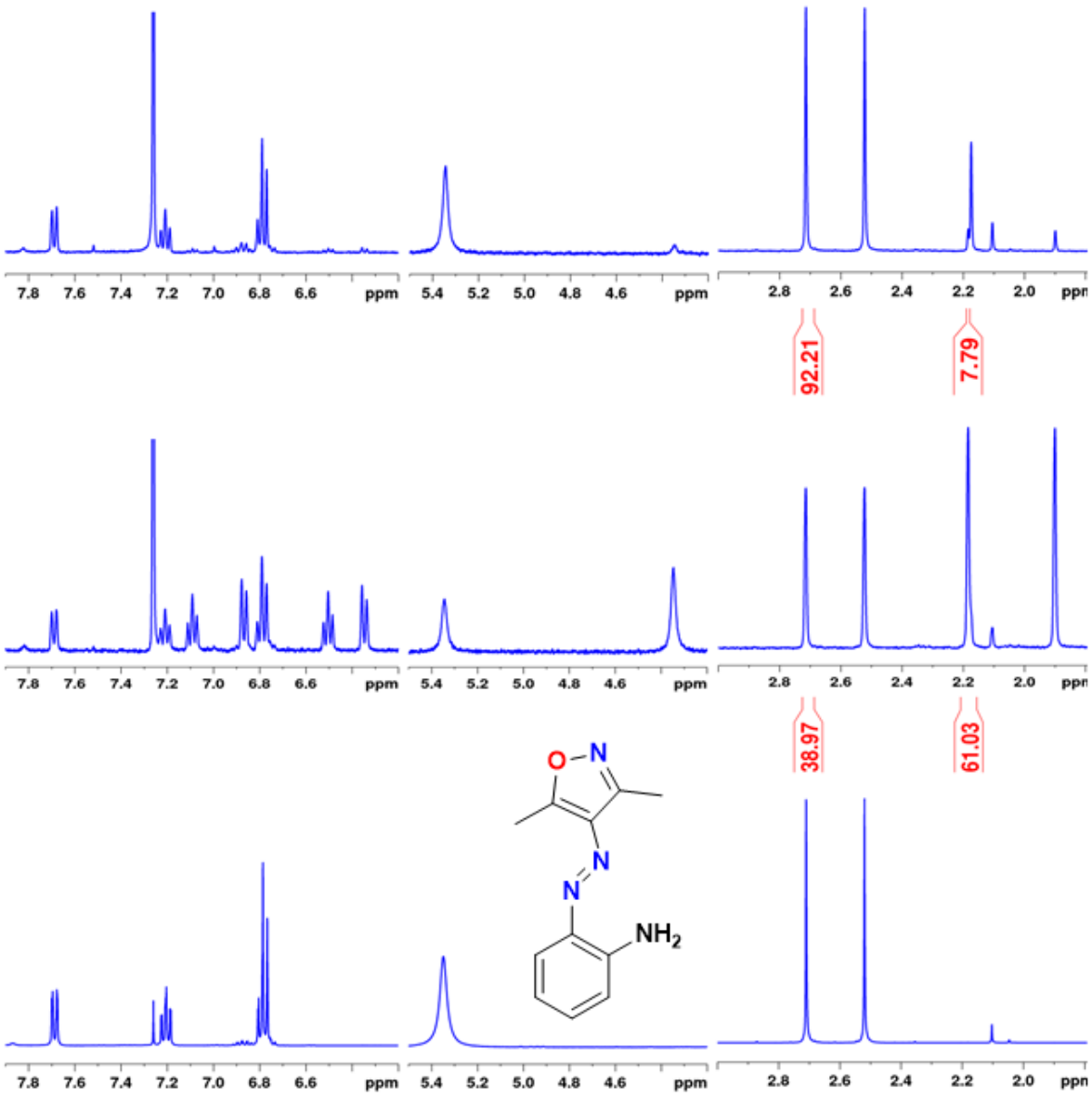

Figure 2C.8. *(E)*-2-((3,5-dimethylisoxazole-4-yl)diazenyl)aniline (**32d)** ($CDCl_3$): (bottom) before irradiation; (middle) after irradiation at 405 nm and (top) after irradiation at 505 nm.

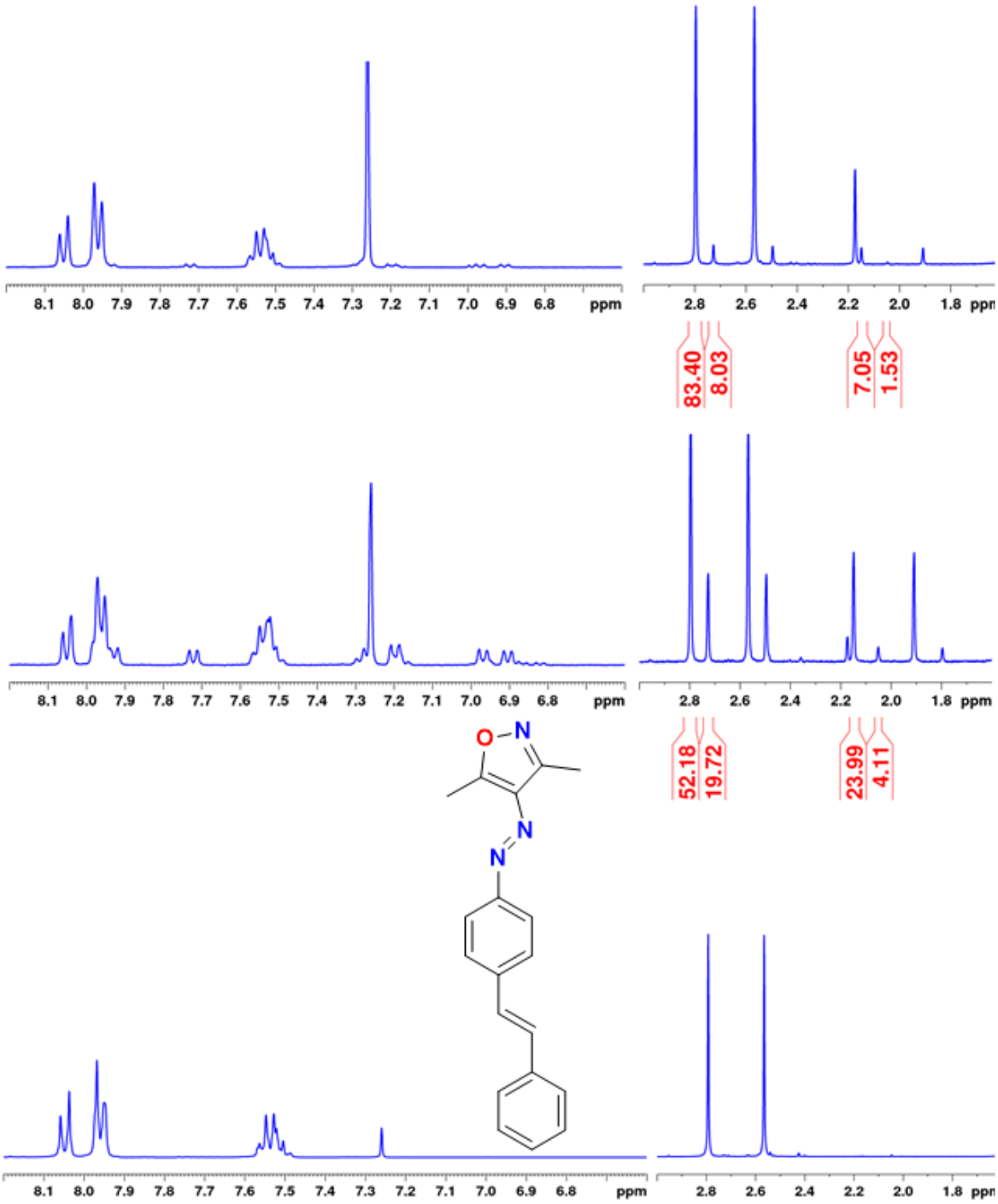

Figure 2C.9. (*E*)-3,5-dimethyl-4-((*E*)-(4-((*E*)-phenyldiazenyl)phenyl)diazenyl)isoxazole (**37d**) ($CDCl_3$): (bottom) before irradiation; (middle) after irradiation at 365 nm and (top) after irradiation at 505 nm.

Appendix 2D

The composition of individual isomers at the photostationary states corresponding to forward (at 365 nm) and reverse isomerization steps have been estimated using UV-vis spectral data. These estimations have been done for both solution phase as well as for the solid state.

Table 2D.1 PSS data in the forward and the reverse photoisomerization in **1-37d** in KBr medium

S. No.	Comp.	R=	PSS in solid state (KBr)[a]			PSS in solution phase (CH_3CN)[b]			
			***E*-isomer**	***Z*-*E***	***Z*-isomer**	***E*-isomer**	***Z*-*E***	***Z*-isomer**	**Conc. μmol.L^{-1}**
			***E*-*Z* PSS (%*Z*)**	**Wavelength (nm)**	***Z*-*E* PSS (%*E*)**	***E*-*Z* PSS (%*Z*)**	**Wavelength (nm)**	***Z*-*E* PSS (%*E*)**	
1.	**1d**	H	75	505	64	65	505	81	36
2.	**2d**	2-F	50	505	16	48	405	80	42
3.	**3d**	3-F	79	505	55	36	[c]	91	56
4.	**4d**	4-F	80	505	77	68	[c]	80	37
5.	**5d**	2-Cl	72	[c]	33	62	[c]	74	51
6.	**6d**	3-Cl	78	[c]	71	70	[c]	81	39
7.	**7d**	4-Cl	73	[c]	57	82	[c]	78	28
8.	**8d**	2-Br	83	[c]	71	58	[c]	88	56
9.	**9d**	3-Br	77	505	65	50	[c]	84	41
10.	**10d**	4-Br	74	505	55	85	[c]	77	32
11.	**11d**	4-I	86	505	75	87	[c]	77	28
12.	**12d**	2-OH	[d]	[d]	[d]	46	[c]	73	39
13.	**13d**	3-OH	58	505	41	80	[c]	76	36
14.	**14d**	4-OH	[d]	505	[d]	[d]	[d]	d	48
15.	**15d**	3-CF_3	66	505	30	39	[c]	77	34
16.	**16d**	4-CF_3	71	505	65	35	[c]	83	62
17.	**17d**	2-OMe	59	[c]	25	76	405	69	64
18.	**18d**	3-OMe	80	505	74	76	[c]	75	46
19.	**19d**	4-OMe	59	[c]	11	81	[c]	82	28
20.	**20d**	2-NO_2	[d]	405	[d]	16	[c]	92	35

21.	**21d**	4-NO_2	[d]	405	[d]	75	[c]	86	28
22.	**22d**	4-CH_3	78	505	67	47	[c]	93	41
23.	**23d**	3-NHAc	57	505	44	75	[c]	78	33
24.	**24d**	4-NHAc	[d]	505	[d]	82	[c]	79	27
25.	**25d**	R-Ph = α- Np	[d]	505	[d]	59	[c]	79	70
26.	**26d**	2,5-diCl	72	[c]	45	53	[c]	85	50
27.	**27d**	2,6-diCl	71	505	45	24	[c]	82	60
28.	**28d**	2,4-diF	46	505	15	44	[c]	72	36
29.	**29d**	2,5-diF	72	505	44	84	[c]	69	38
30.	**30d**	2,6-diF	68	[c]	46	31	[c]	73	38
31.	**31d**	3,5-diF	77	505	52	64	[c]	81	36
32.	**32d**	2-NH_2	[d]	505	[d]	56	505	47	42
33.	**33d**	3-NH_2	[d]	505	[d]	72	505	72	56
34.	**34d**	4-NH_2	[d]	505	[d]	68	[c]	69	37
35.	**35d**	2-CN	37	505	18	65	[c]	78	51
36.	**36d**	R-Ph = 3-Pyridyl	80	505	69	18	[c]	98	39
37.	**37d**	R-Ph = 4-(Ph-N=N-Ph)	[d]	[c]	[d]	43	[c]	70	28

[a,b]The exact method for estimation has been followed as in the literature; [c]CFL bulb irradiation; [d]Unclear spectral data for predicting the PSS; Estimation of %*E*/%*Z* conversion at PSS in solid state and solution phases was done by UV-vis spectroscopy using the following expressions, respectively:

$$\%\ \text{conversion of } E\text{-isomer} = 1 - \frac{\text{A}(\text{n}-\pi*)\ \text{absorption before irradiation}}{\text{A}(\text{n}-\pi*)\ \text{absorption after irradiation at 365 nm}}$$

$$\%\ \text{conversion of } E\text{-isomer} = 1 - \frac{\text{A}(\pi-\pi*)\ \text{absorption after irradiation at 365 nm}}{\text{A}(\pi-\pi*)\ \text{absorption before irradiation}}$$

Appendix 2E

Thermal reverse isomerization (*Z*-*E*) kinetics of phenylazoisoxazole 1d and its selected derivatives

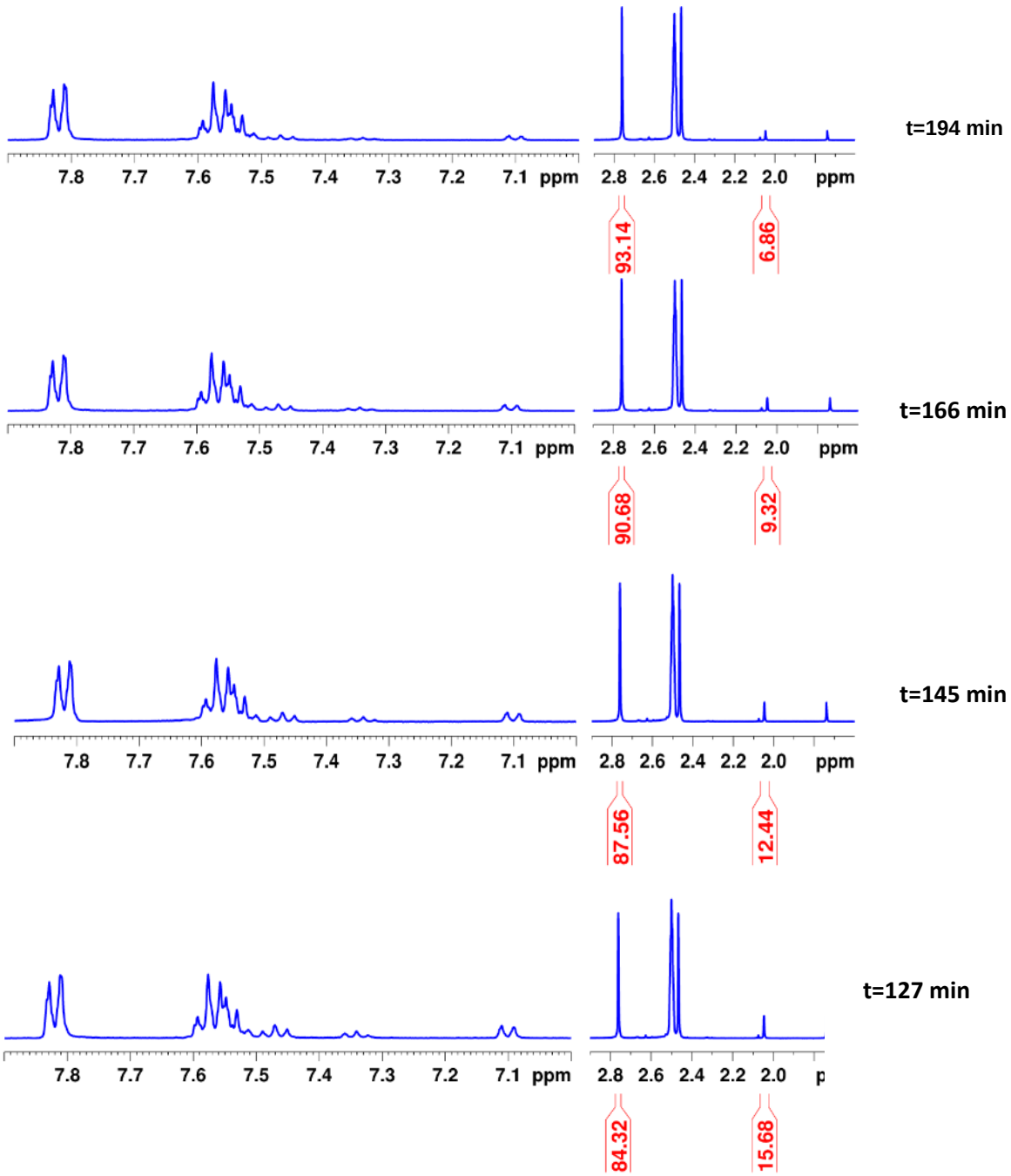

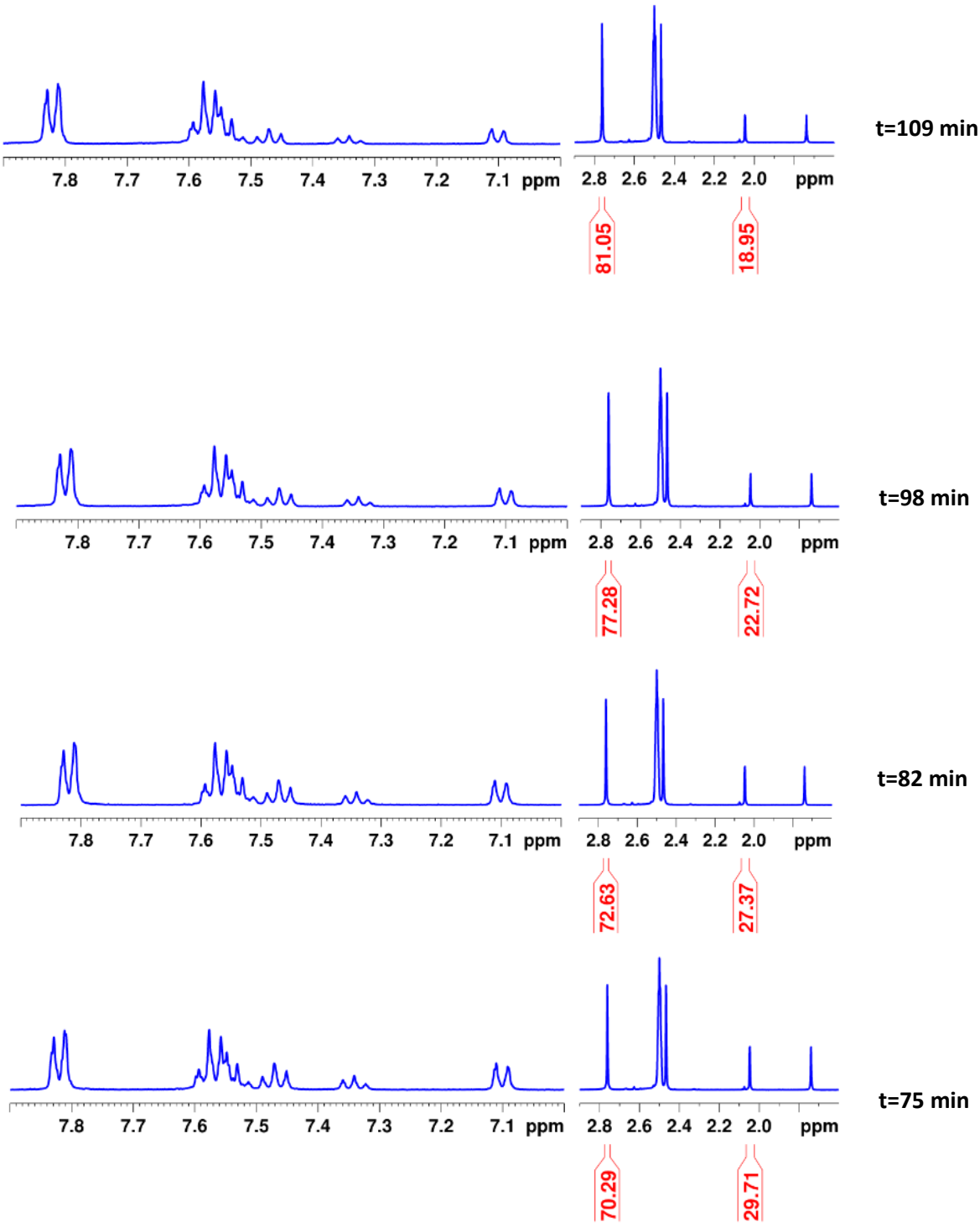
7.8 7.7 7.6 7.5 7.4 7.3 7.2 7.1 ppm
2.8 2.6 2.4 2.2 2.0 ppm
81.05
18.95
t=109 min
7.8 7.7 7.6 7.5 7.4 7.3 7.2 7.1 ppm
2.8 2.6 2.4 2.2 2.0 ppm
77.28
22.72
t=98 min
7.8 7.7 7.6 7.5 7.4 7.3 7.2 7.1 ppm
2.8 2.6 2.4 2.2 2.0 ppm
72.63
27.37
t=82 min
7.8 7.7 7.6 7.5 7.4 7.3 7.2 7.1 ppm
2.8 2.6 2.4 2.2 2.0 ppm
70.29
29.71
t=75 min

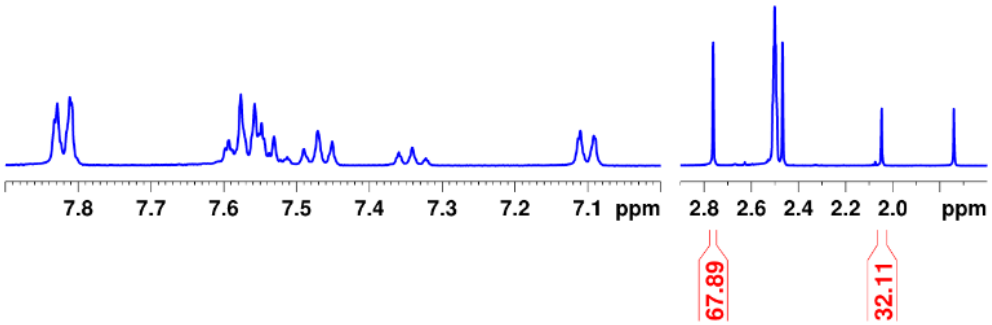

t=69 min

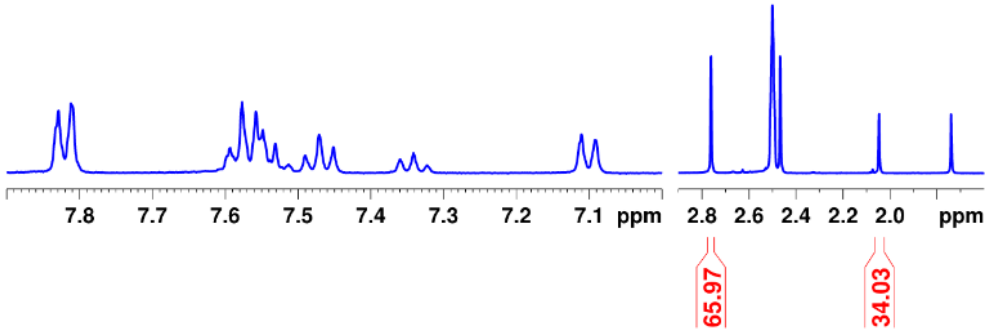

t=63 min

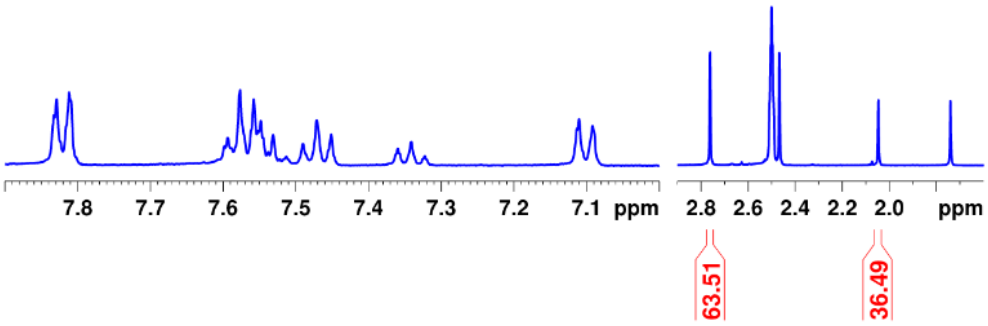

t=55 min

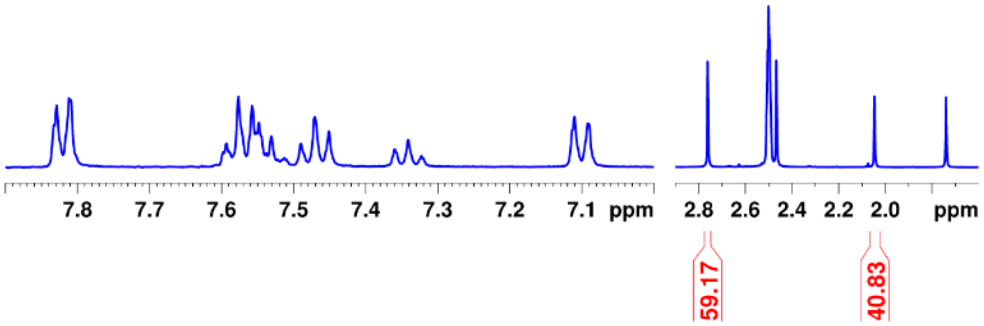

t=50 min

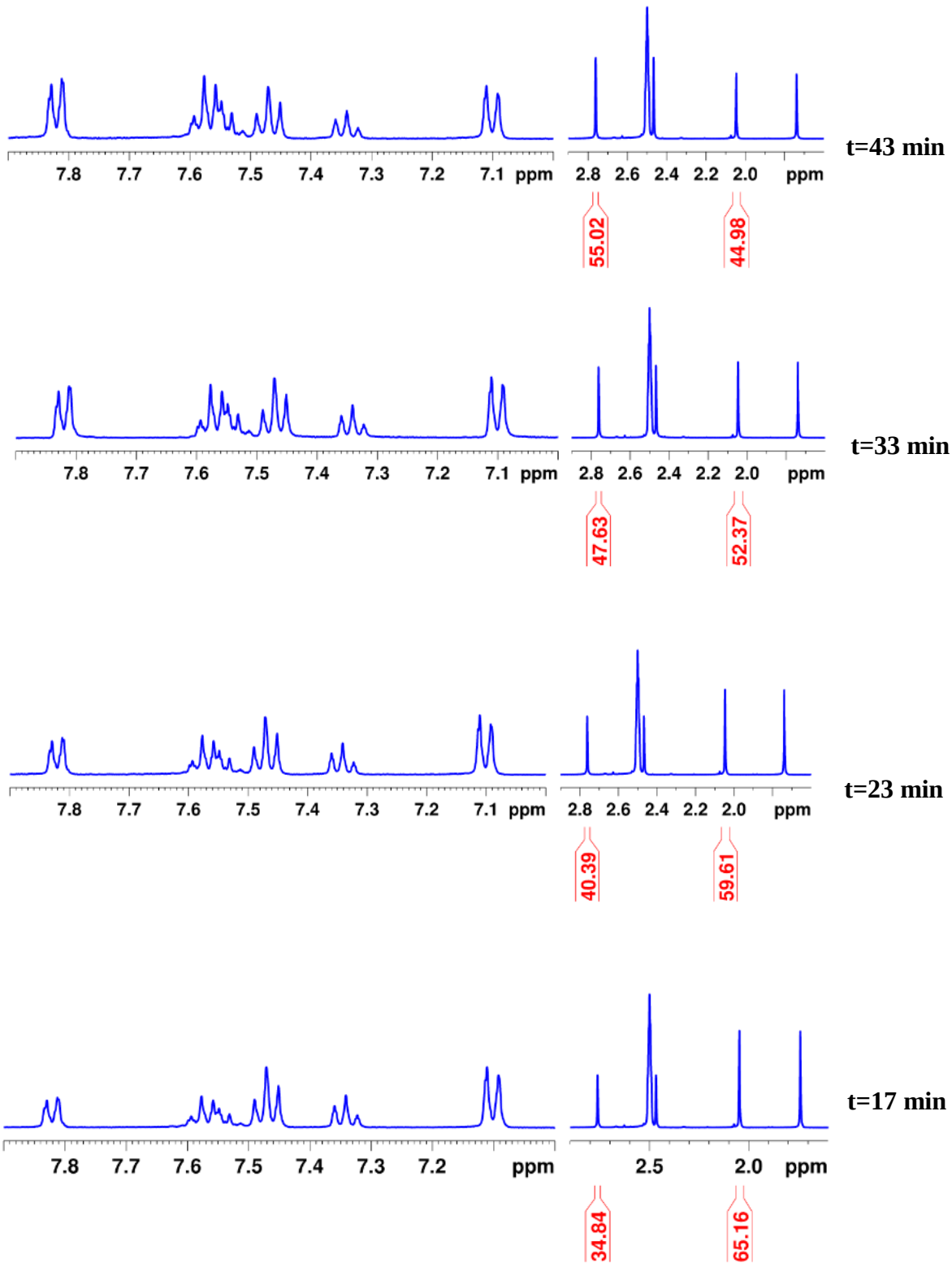
7.8 7.7 7.6 7.5 7.4 7.3 7.2 7.1 ppm
2.8 2.6 2.4 2.2 2.0 ppm
55.02
44.98
t=43 min
7.8 7.7 7.6 7.5 7.4 7.3 7.2 7.1 ppm
2.8 2.6 2.4 2.2 2.0 ppm
47.63
52.37
t=33 min
7.8 7.7 7.6 7.5 7.4 7.3 7.2 7.1 ppm
2.8 2.6 2.4 2.2 2.0 ppm
40.39
59.61
t=23 min
7.8 7.7 7.6 7.5 7.4 7.3 7.2 ppm
2.5 2.0 ppm
34.84
65.16
t=17 min

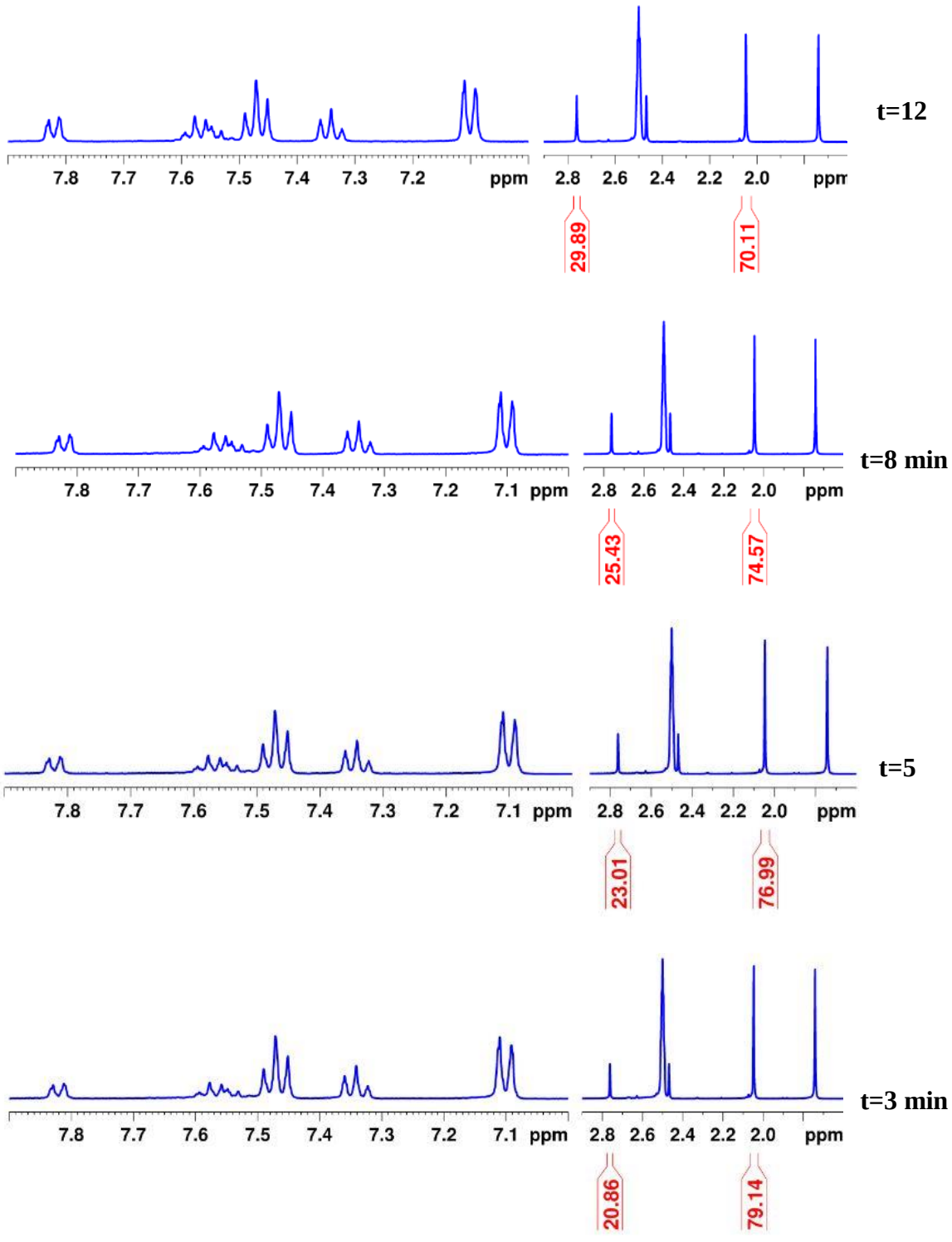
t=12
7.8 7.7 7.6 7.5 7.4 7.3 7.2 ppm
2.8 2.6 2.4 2.2 2.0 ppm
29.89
70.11
t=8 min
7.8 7.7 7.6 7.5 7.4 7.3 7.2 7.1 ppm
2.8 2.6 2.4 2.2 2.0 ppm
25.43
74.57
t=5
7.8 7.7 7.6 7.5 7.4 7.3 7.2 7.1 ppm
2.8 2.6 2.4 2.2 2.0 ppm
23.01
76.99
t=3 min
7.8 7.7 7.6 7.5 7.4 7.3 7.2 7.1 ppm
2.8 2.6 2.4 2.2 2.0 ppm
20.86
79.14

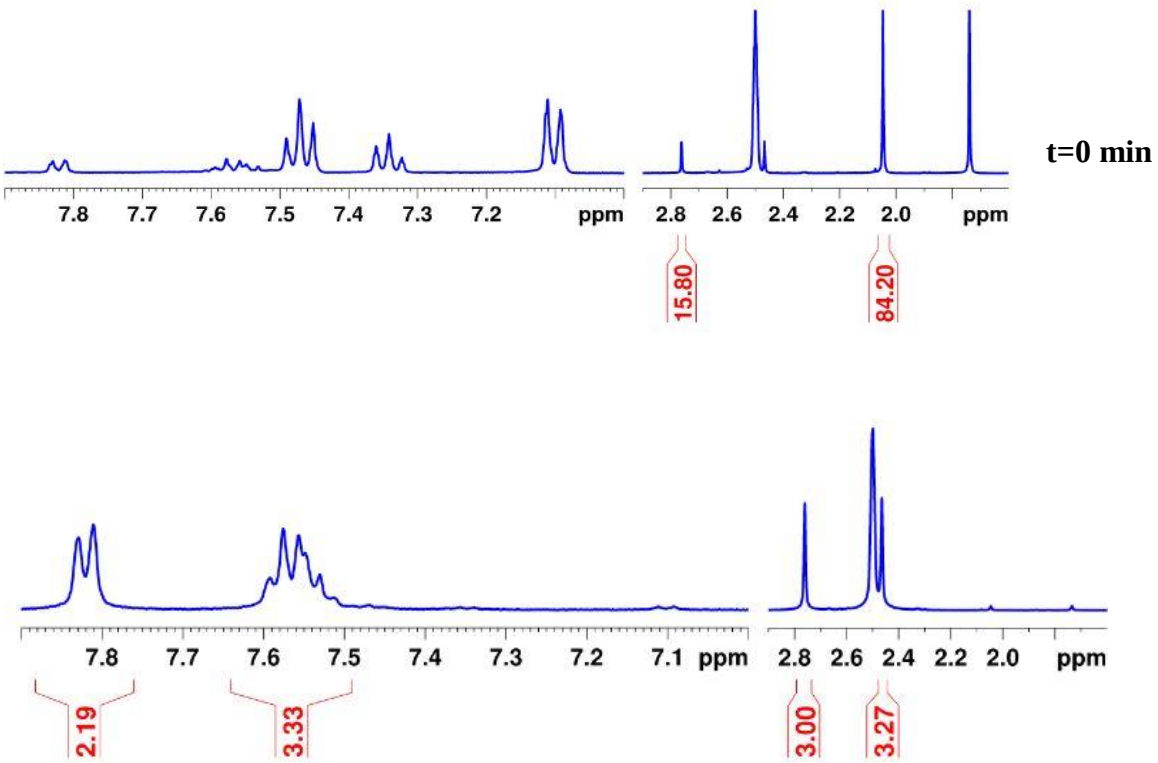

Figure 2E.1. NMR spectral data at different intervals of time for a sample of **1d** in [D_6]DMSO (9.9 mM). The sample was irradiated at 365 nm to obtain the (*Z*)-**1d** and the thermal reverse isomerization kinetics was followed by maintaining the sample at 80 ± 2 ^{O}C using NMR spectroscopy (measurements were done at 298 K).

Table 2E.1. Thermal reverse isomerization kinetics data of **1d** in [D_6]DMSO at 80 ± 2 ^{O}C using NMR spectroscopy

S. No.	Time (min)	%*Z*	S. No.	Time (min)	%*Z*
1	0	84.20	12	63.3	34.03
2	3.3	79.14	13	69.5	32.11
3	5.1	76.99	14	75.5	29.71
4	8.1	74.57	15	82.0	27.37
5	12.0	70.10	16	97.7	22.72
6	17.4	65.15	17	109.5	18.90
7	23.1	59.61	18	127.2	15.68
8	33.2	52.37	19	145.2	12.44
9	43.3	44.98	20	166.7	9.32
10	50.7	40.83	21	193.9	6.86
11	55.0	36.49			

Table 2E.2. Thermal reverse isomerization kinetics data of **1d** in [D_6]DMSO at 90 ± 2 ^{O}C using NMR spectroscopy

S. No.	Time (min)	%*Z*	S. No.	Time (min)	%*Z*
1	0	85.10	12	29.0	23.59
2	5.0	68.10	13	35.0	17.81
3	9.1	58.65	14	40.0	13.77
4	13.0	49.85	15	45.0	11.35
5	20.0	37.02	16	69.6	5.50
6	25.0	28.41	17	109.5	18.90

Table 2E.3. Thermal reverse isomerization kinetics data of **1d** in [D_6]DMSO at 70 ± 2 ^{O}C using NMR spectroscopy

S. No.	Time (min)	%*Z*	S. No.	Time (min)	%*Z*
1	0	82.58	8	232.0	21.25
2	13.4	75.16	9	281.0	17.09
3	34.8	67.13	10	338.7	12.77
4	67.4	55.20	11	429.5	7.94
5	104.5	43.93	12	453.0	6.99
6	144.2	34.53			
7	183.6	27.84			

Table 2E.4. Thermal reverse isomerization kinetics data of **1d** in $CDCl_3$ at 25 ± 2 ^{O}C using NMR spectroscopy

S. No.	Time (min)	%*Z*	S. No.	Time (min)	%*Z*
1	0	57.92	18	41607	27.17
2	1303	56.76	19	44637	25.30
3	2802	54.40	20	50418	23.71
4	4204	52.82	21	51815	22.70
5	5537	53.03	22	54746	21.55
6	10012	49.63	23	60500	19.39
7	11337	48.88	24	61935	18.84
8	14414	42.70	25	63372	18.72
9	15645	41.45	26	64832	18.00
10	20190	38.58	27	71821	16.79
11	24419	36.05	28	73411	16.04
12	25971	35.20	29	80658	14.62
13	30182	32.86	30	82238	14.26
14	33094	31.51	31	84953	14.17
15	34611	30.11	32	92205	12.82
16	35768	29.85	33	96234	12.00
17	40281	26.08	34	100647	12.19

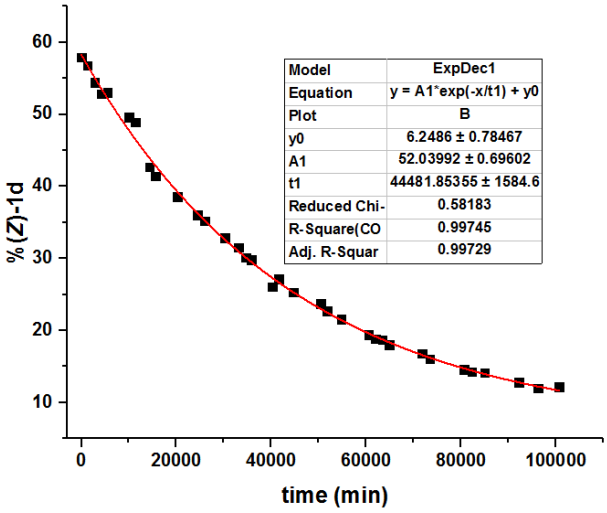

Figure 2E.2. Thermal reverse isomerization kinetics plot of **1d** in $CDCl_3$ at 25 ± 2 ^{O}C using ^{1}H-NMR spectroscopy.

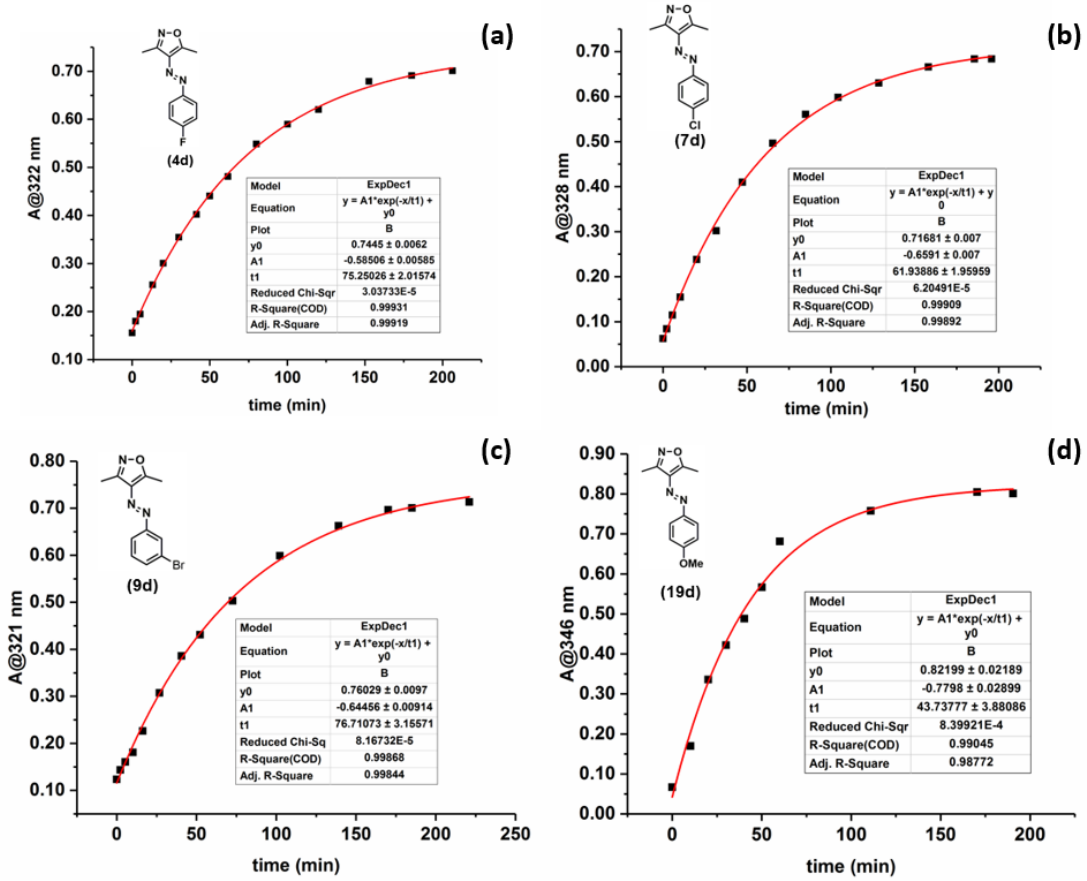

Figure 2E.3. Thermal reverse isomerization (*Z*-*E*) kinetics plots of selected arylazo-3,5-dimethylisoxazole derivatives using UV-Vis spectroscopy: (a) **4d**; (b) **7d**; (c) **9d** and (d) **19d**. All the experiments have been performed in DMSO at 80 ^{o}C.

Appendix 2F

Solution phase photoswitching and kinetics data: UV-Vis spectroscopic studies

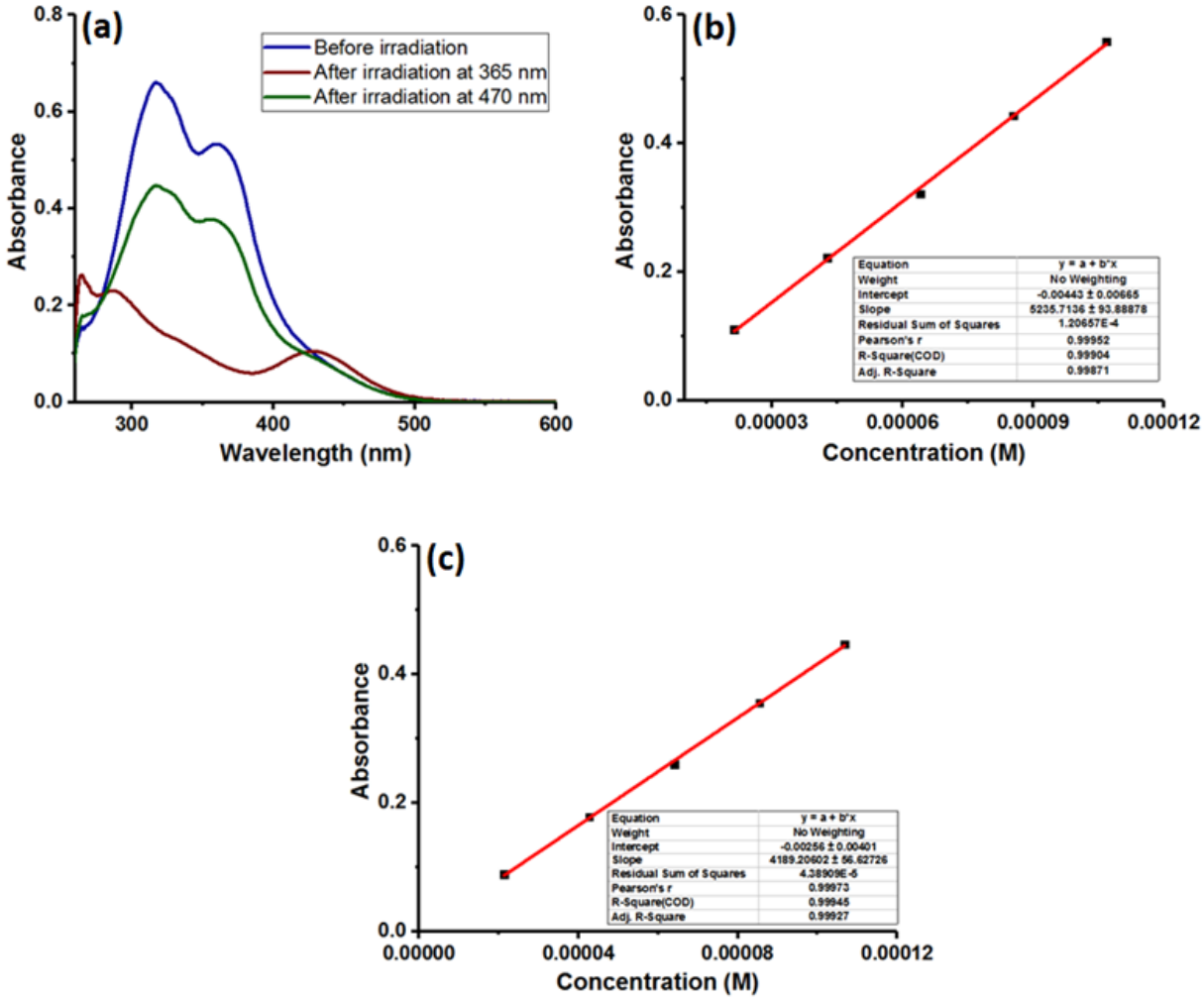

Figure 2F.1. (a) UV-Vis spectral data depicting the photoswitching in **12d** (126 μM, DMSO) at different irradiation conditions; Estimation of molar absorption coefficient corresponding to the $\lambda_{max}(\pi-\pi*)$: (b) 317 nm (ε, 5236 ± 94 M^{-1} cm^{-1}), and (c) 360 nm (ε, 4189 ± 57 M^{-1} cm^{-1}) in DMSO.

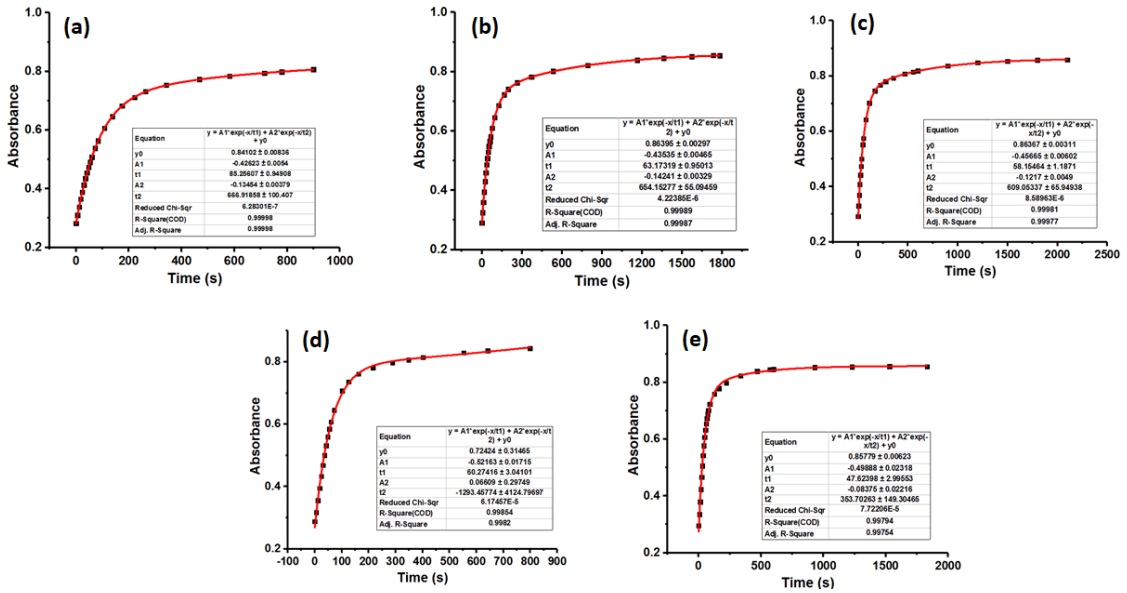

Figure 2F.2. Kinetics data for the thermal reverse isomerization with bi-exponential fit of **12d** at (a) 25 ^{o}C, (b) 30 ^{o}C, (c) 35 ^{o}C, (d) 40 ^{o}C and (e) 45 ^{o}C in DMSO (152 μM). Kinetics data have been followed by the absorption changes at $\lambda_{max}(\pi-\pi*)$ = 317 nm of *E*-isomer.

Table 2F.1. Kinetics data for the thermal reverse isomerization with the biexponential fit of **12d**

S. No.	Temperature (^{o}C)	Rate constant, k_1 (s^{-1})	Rate constant, k_2 (s^{-1})
1	25	$1.2 \times 10^{-2} \pm 1.3 \times 10^{-4}$	$1.5 \times 10^{-3} \pm 2.3 \times 10^{-4}$
2	30	$1.6 \times 10^{-2} \pm 2.4 \times 10^{-4}$	$1.5 \times 10^{-3} \pm 1.3 \times 10^{-4}$
3	35	$1.7 \times 10^{-2} \pm 3.5 \times 10^{-4}$	$1.6 \times 10^{-3} \pm 1.8 \times 10^{-4}$
4	40	$1.7 \times 10^{-2} \pm 8.4 \times 10^{-4}$	$7.7 \times 10^{-4} \pm 2.1 \times 10^{-3}$
5	45	$2.1 \times 10^{-2} \pm 1.3 \times 10^{-3}$	$2.8 \times 10^{-3} \pm 1.2 \times 10^{-3}$

Appendix 2G

Light-induced phase transition (POM images of 1d)

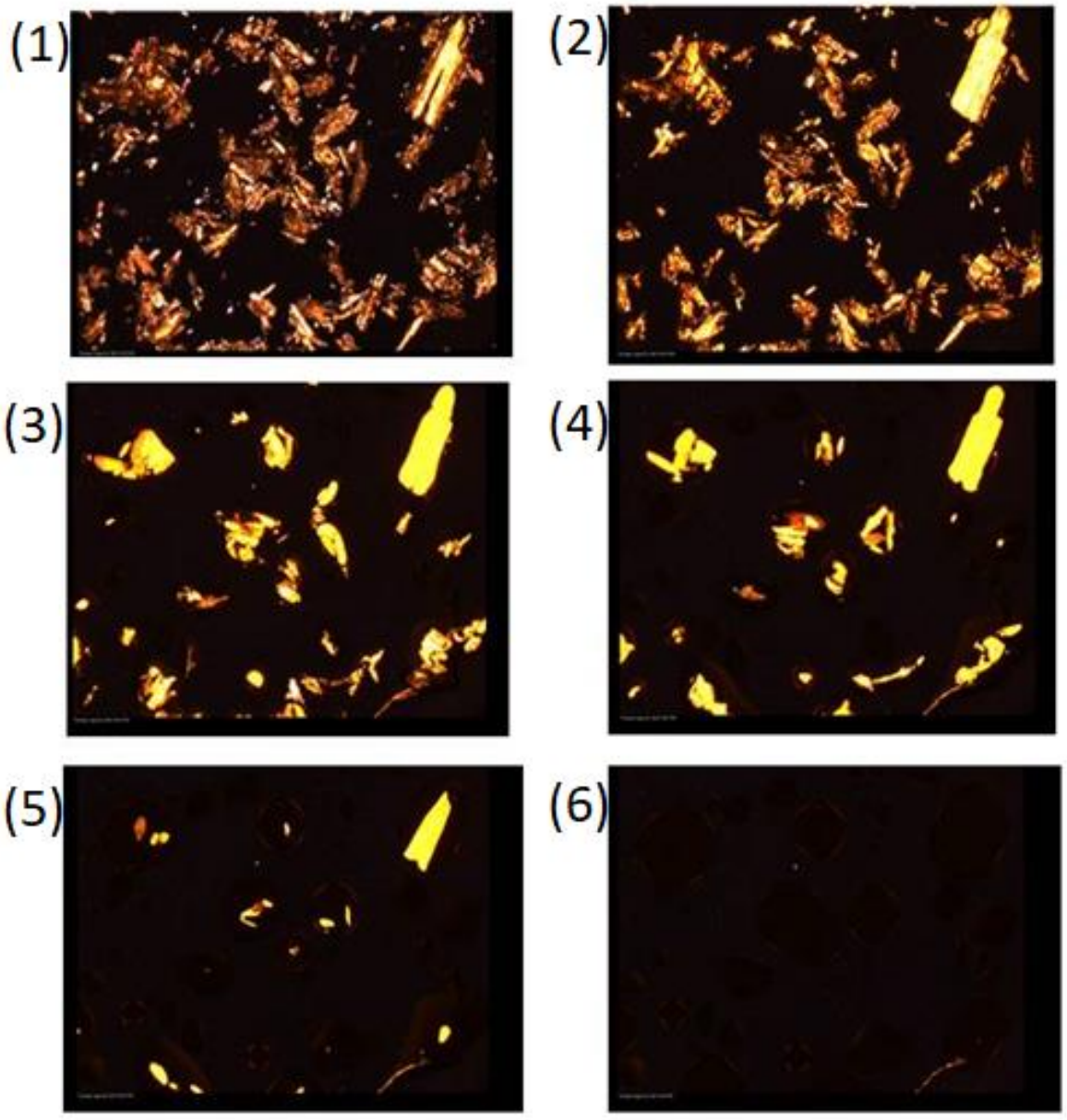

Figure 2G.1. POM images during the light-induced phase transition in **1d**. The sample was subjected to irradiation at 365 nm and the images were recorded simultaneously for 4 seconds. (The sequence of events is numbered in the images; magnification: x500)

DSC data

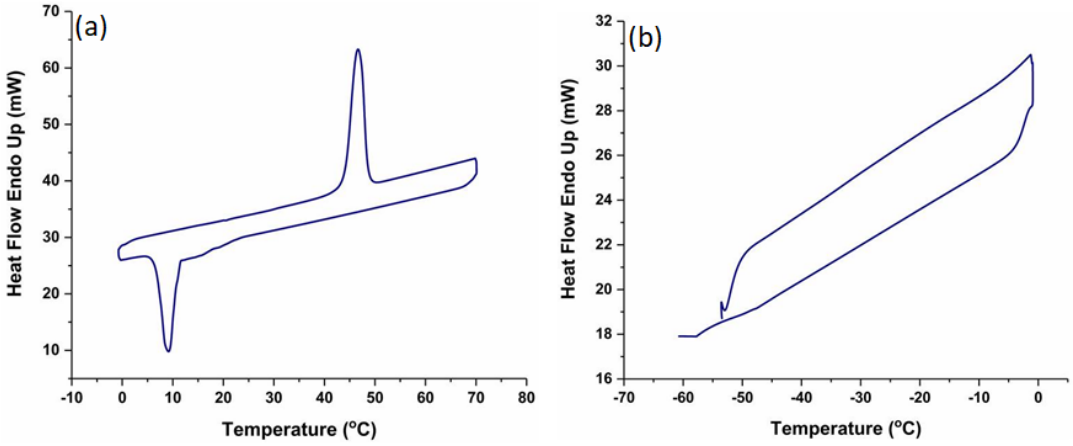

Figure 2G.2. DSC thermograms of **1d** (a) before irradiation and (b) after irradiation at 365 nm

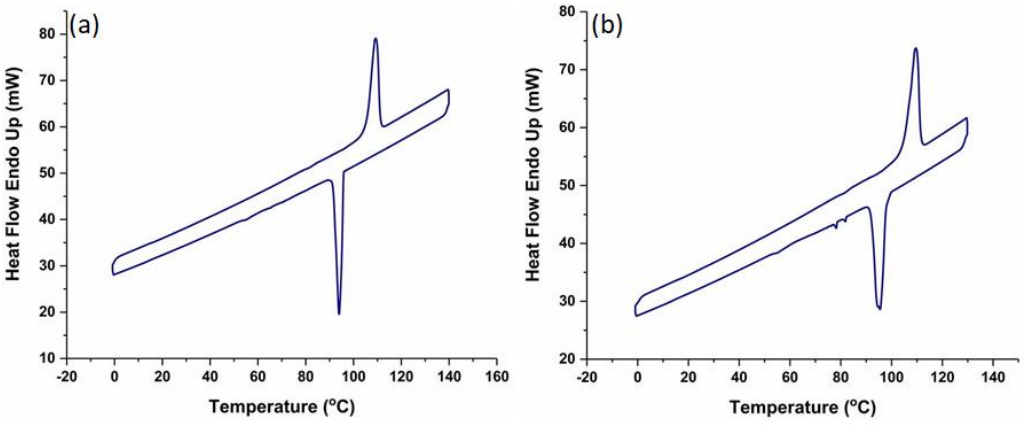

Figure 2G.3. DSC thermograms of **19d** (a) before irradiation and (b) after irradiation at 365 nm

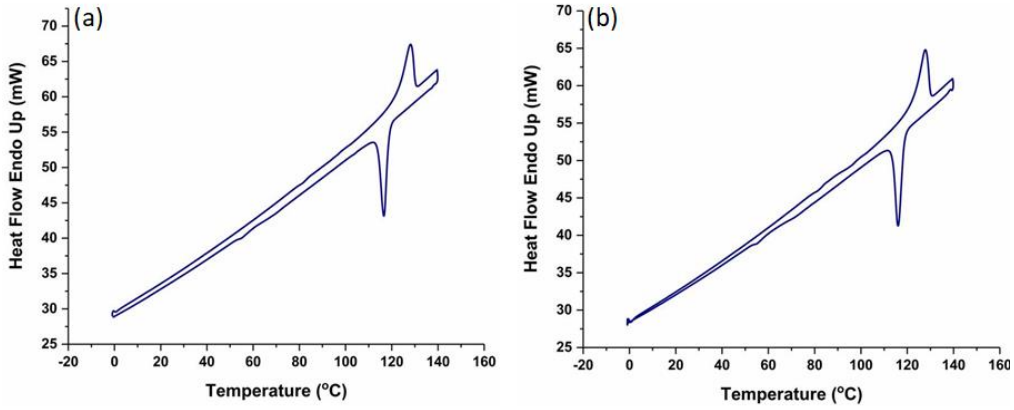

Figure 2G.4. DSC thermograms of **11d** (a) Before irradiation and (b) after irradiation at 365 nm

Light-induced phase transition (IR Data)

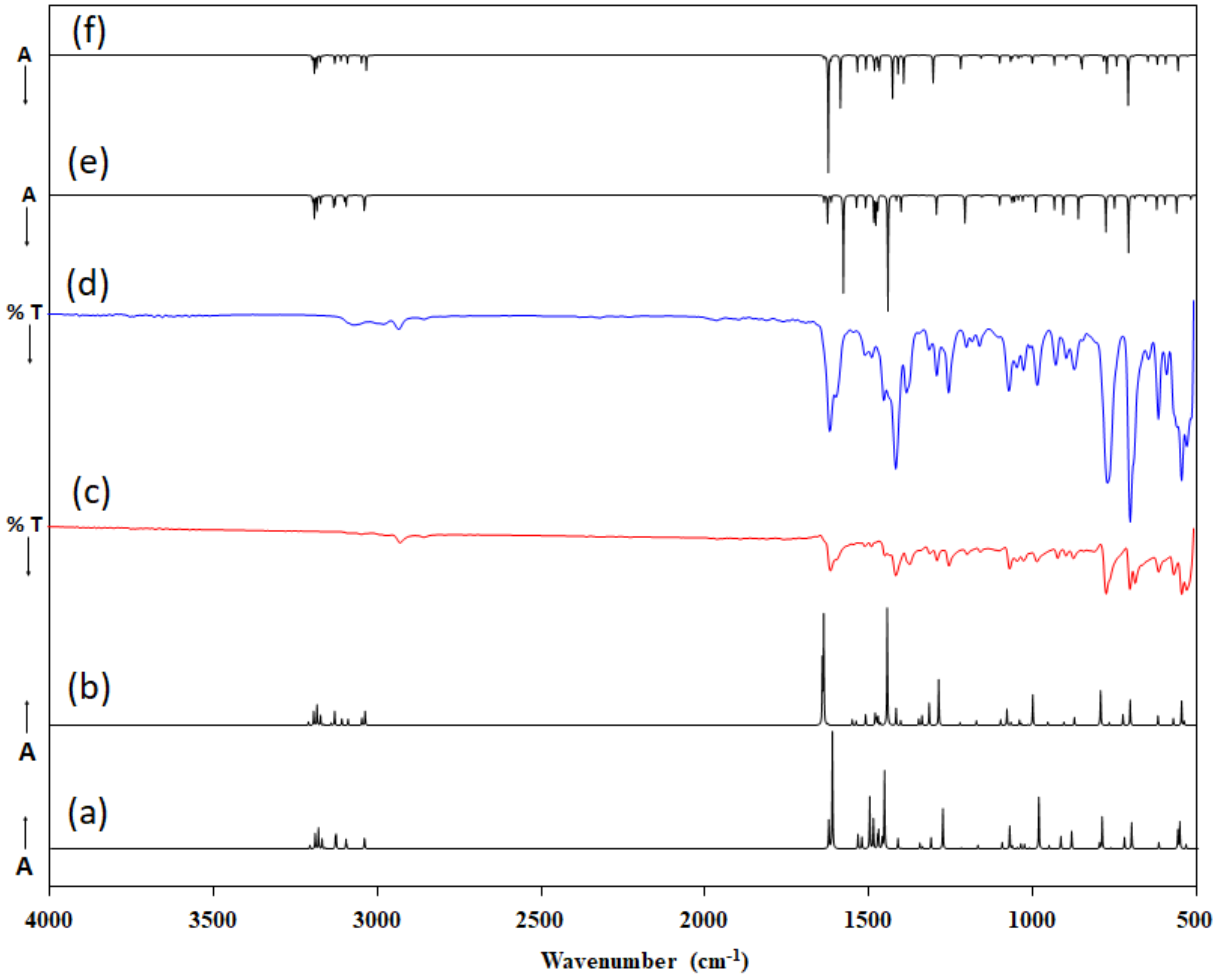

Figure 2G.5. Infrared spectral data for understanding the light-induced phase transition. Computed infrared spectra of **(*E*)-1d** of (a) O-N orientation and (b) N-O orientation; ATR spectral data of **1d** (c) before irradiation (as neat yellow solid) and (d) after irradiation with 365 nm (as molten red liquid); Computed infrared spectra of **(*Z*)-1d** of (e) O-N orientation and (f) N-O orientation. (Computations were performed at B3LYP/6-311G(d,p) level of theory and the frequencies are unscaled.)

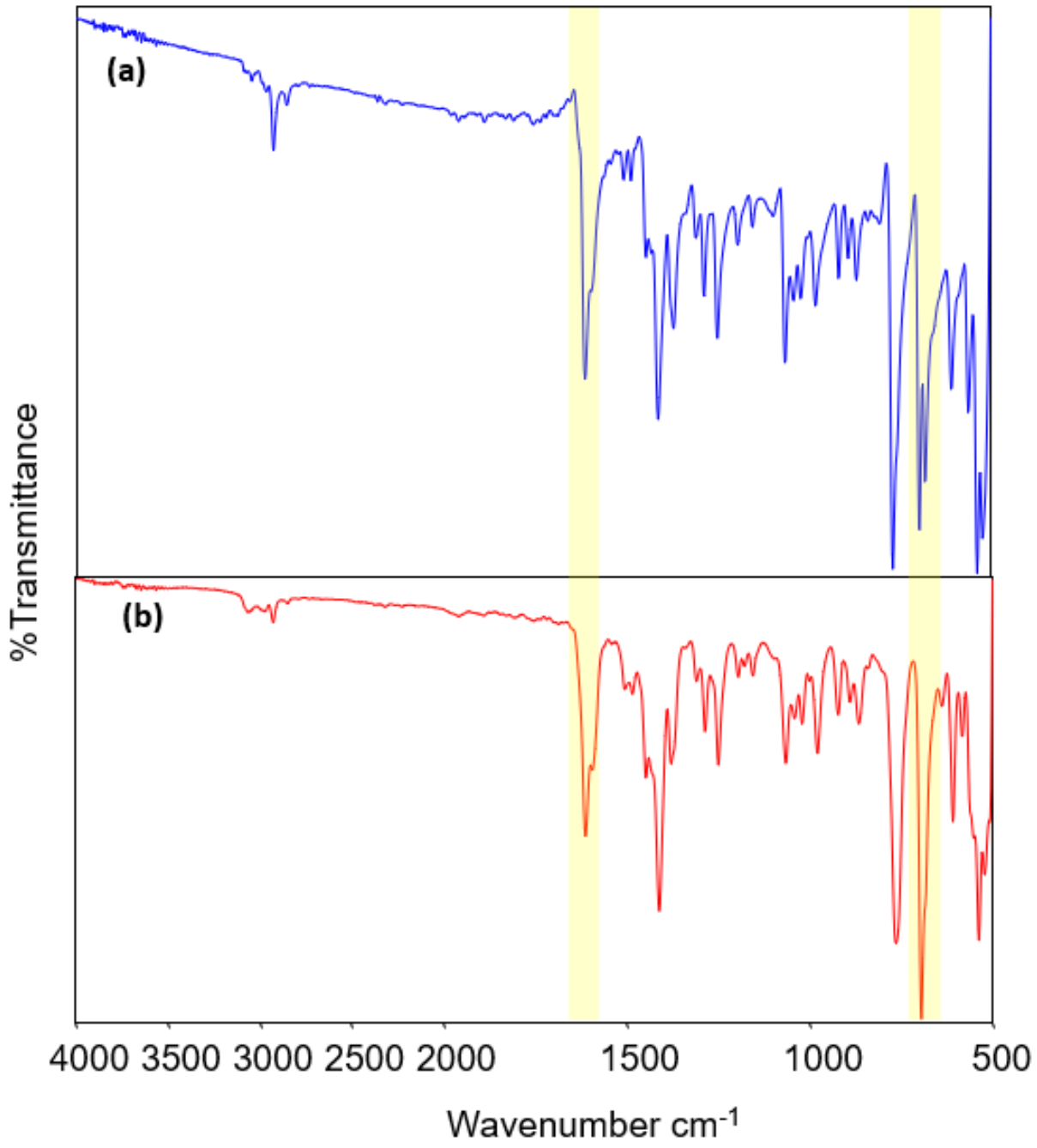

Figure 2G.6. Infrared spectral data for understanding the light-induced phase transition (a) before irradiation (as neat yellow solid) and (b) after irradiation with 365 nm.

Light-induced phase transition (NMR data)

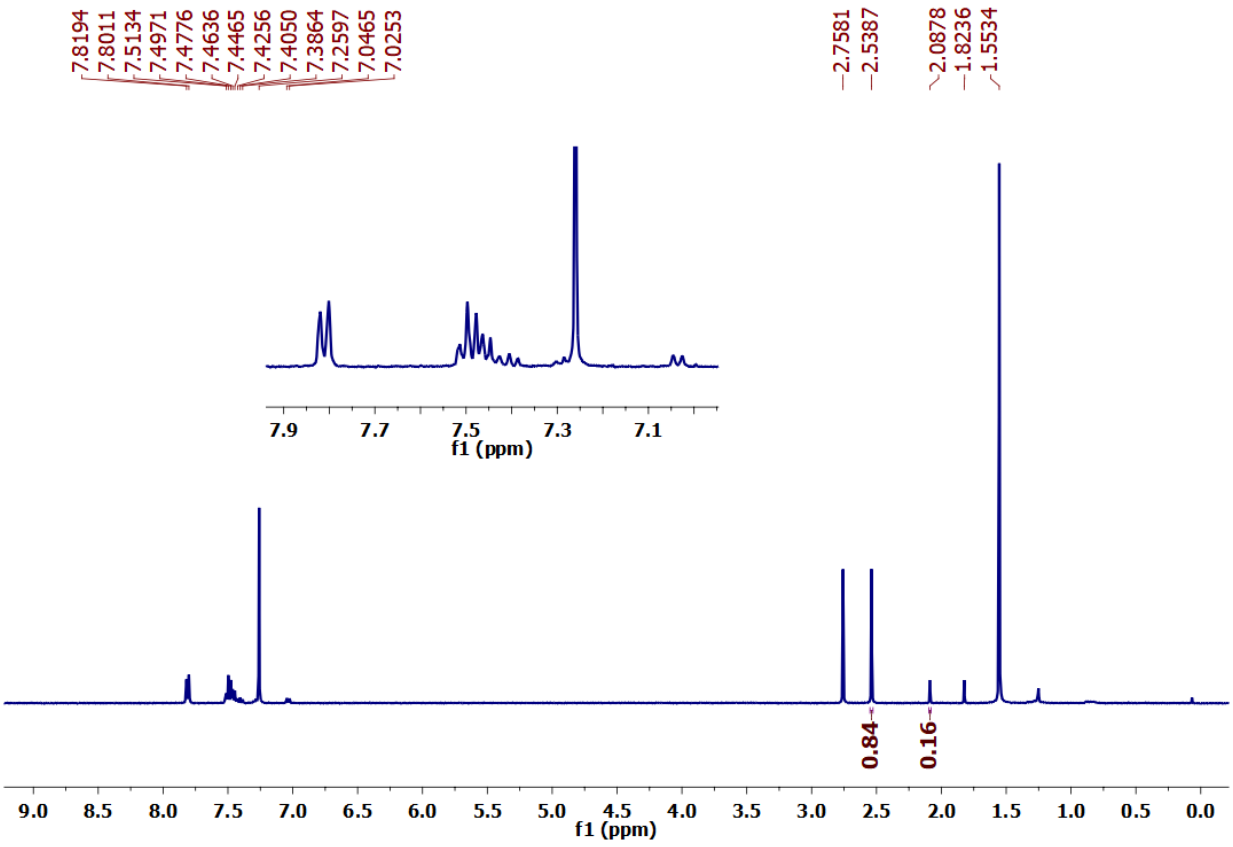

Figure 2G.7. ^{1}H-NMR of **1d** (in $CDCl_3$) after irradiation of the neat solid sample (approx. 4 mg for 30 sec) at 365 nm to obtain a red molten liquid. (Spectrum revealed the presence of 16% *Z*-isomer.)

Appendix 2H

Crystal data and structure refinement for compound 1d (CCDC Deposition Number 1937168)

Molecular formula	$C_{11}H_{11}N_3O$
Molecular weight	201.23
Temperature/K	200.0
Crystal System	monoclinic
Space group	P $2_1/n$
a/ Å	14.2797 (10)
b/ Å	4.6781 (2)
c/ Å	16.4528 (7)
α/°	90°
β/°	104.307° (5)
γ/ °	90°
Volume/ Å^3	1064.99 (10)
Z	4
ρ_{calc} g/cm^3	1.255
μ(mm^{-1})	0.084
F(000)	424
Crystal size	0.31×3×0.29
Radiation (MoKα)	MoKα (λ = 0.71073)
2 θ range for data collection/ °	5.12 to 65.5
Index ranges	-21≤h≤18, -6≤k≤7, -23≤l≤19
Reflections collected	9488
Independent Reflections	3629[R_{int} =0 .0350, R_{sigma} = 0.0415]
Data/restraints/parameters	3629/0/138
Goodness-of-fit on F^2	1.036
Final R indexes [I>=2σ (I)]	R_1 =0 .0648, wR_2 = 0.1708
Final R indexes [all data]	R_1 = 0.1034, wR_2 = 0.2120
Largest diff. peak hole/e Å^3	0.35-0.24

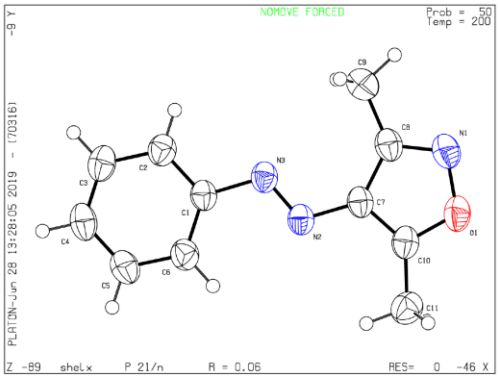

Appendix 2I

^{1}H and ^{13}C Characterisation data

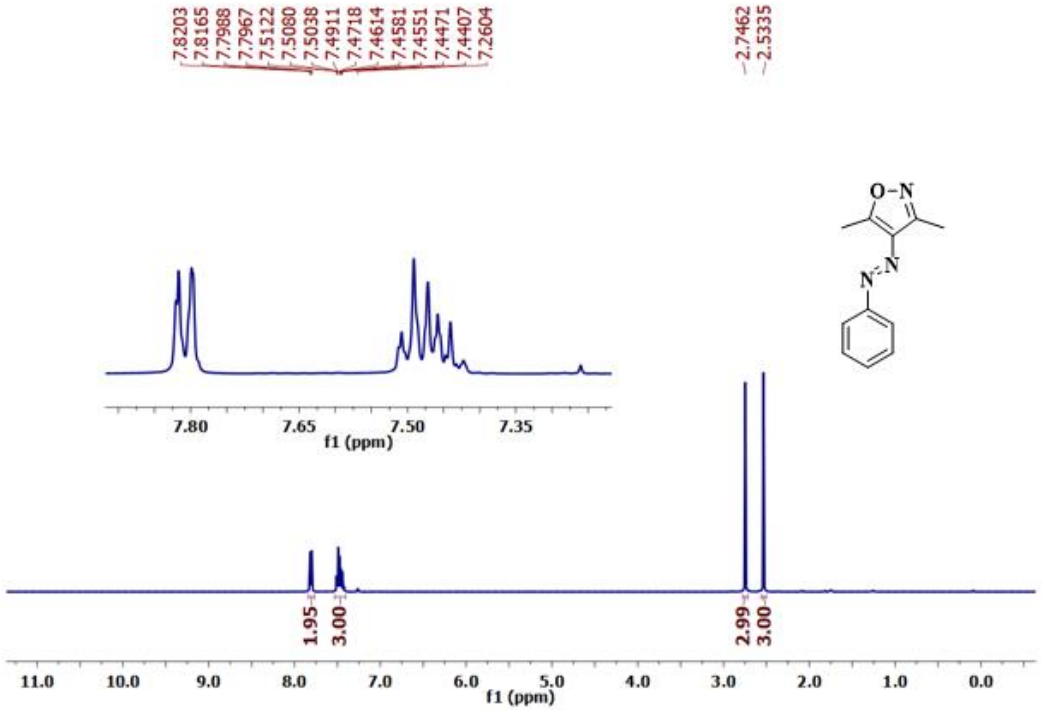

^{1}H NMR spectrum of (*E*)-3,5-dimethyl-4-(phenyldiazenyl)isoxazole **(1d)** in $CDCl_3$

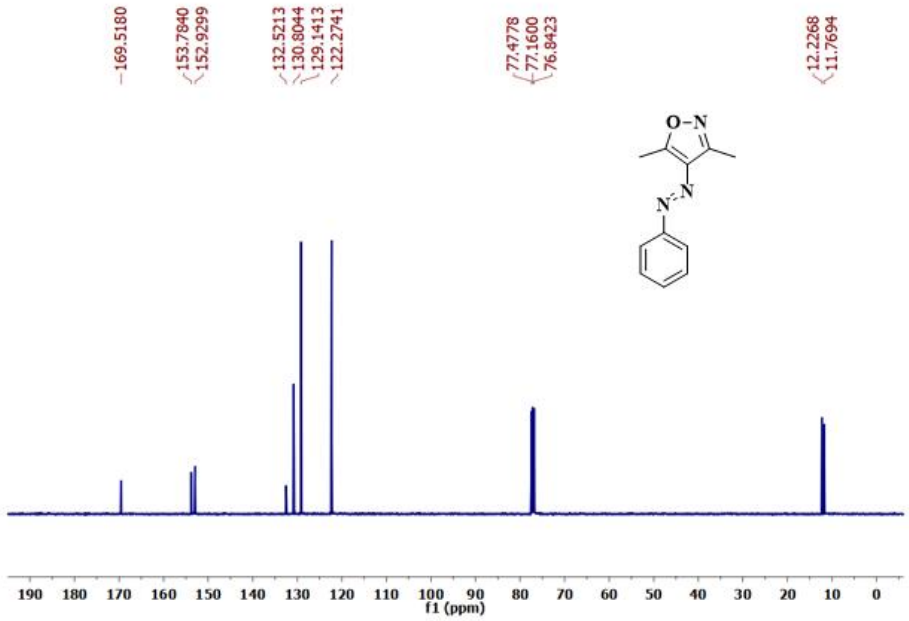

^{13}C NMR spectrum of (*E*)-3,5-dimethyl-4-(phenyldiazenyl)isoxazole **(1d)** in $CDCl_3$

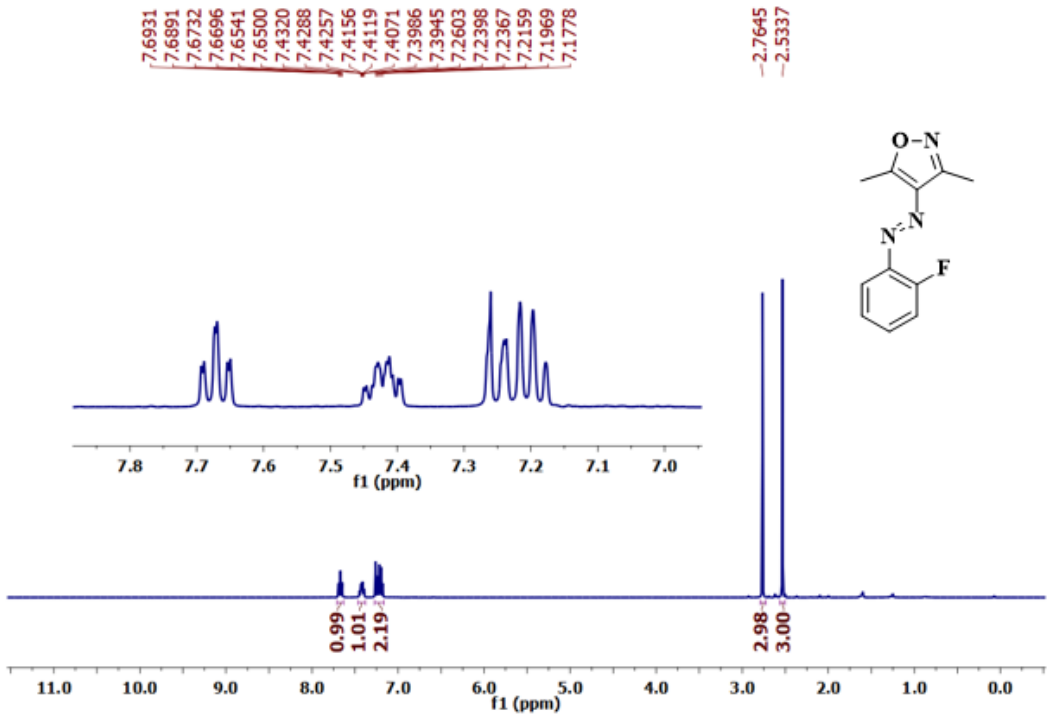

^{1}H NMR spectrum of (*E*)-4-((2-fluorophenyl)diazenyl)-3,5-dimethylisoxazole **(2d)** in $CDCl_3$

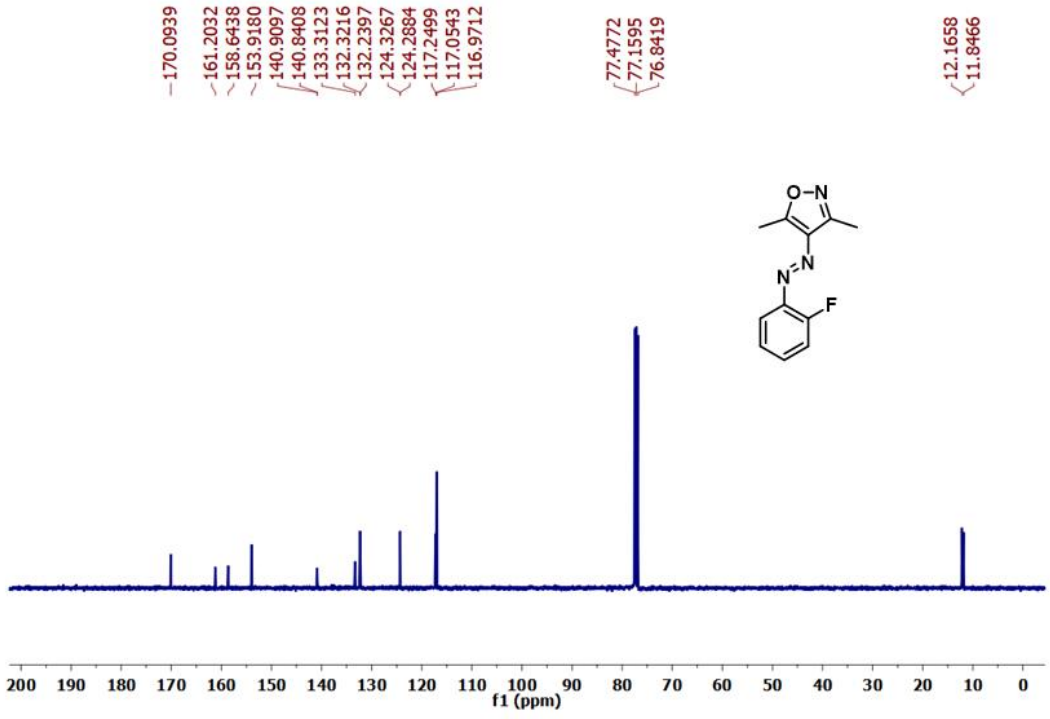

^{13}C NMR spectrum of (*E*)-4-((2-fluorophenyl)diazenyl)-3,5-dimethylisoxazole **(2d)** in $CDCl_3$

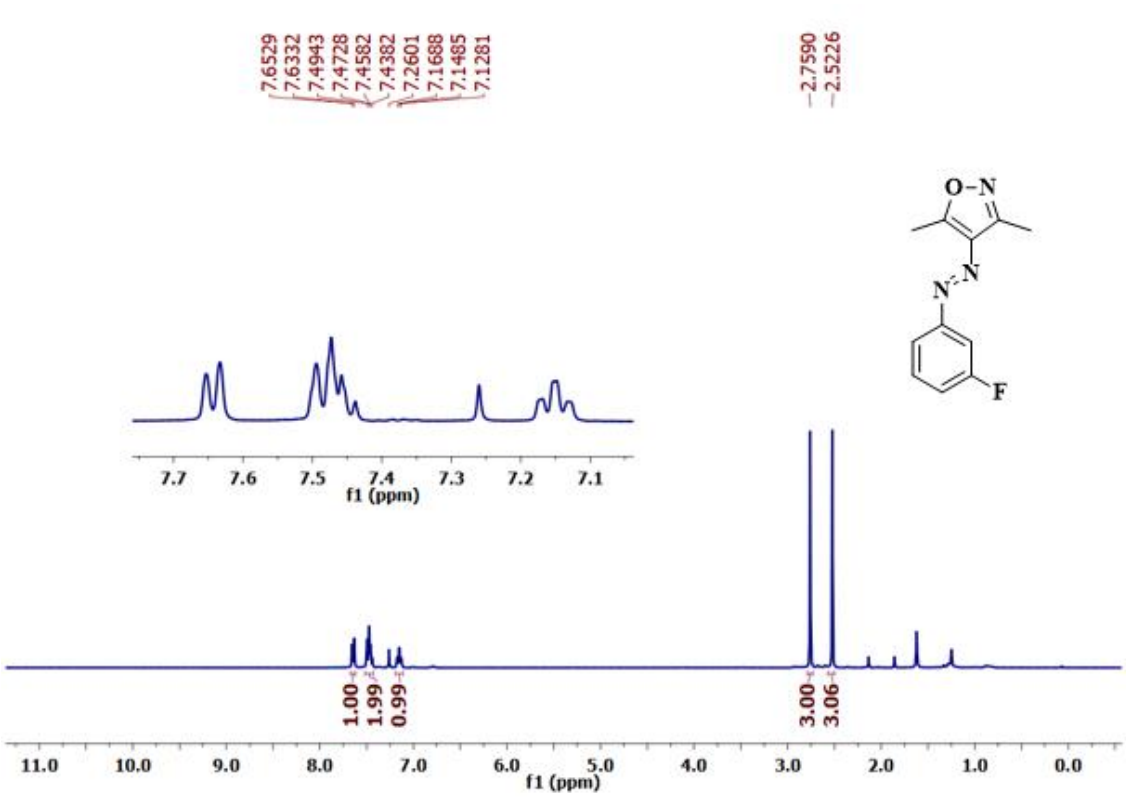

^{1}H NMR spectrum of (*E*)-4-((3-fluorophenyl)diazenyl)-3,5-dimethylisoxazole **(3d)** in $CDCl_3$

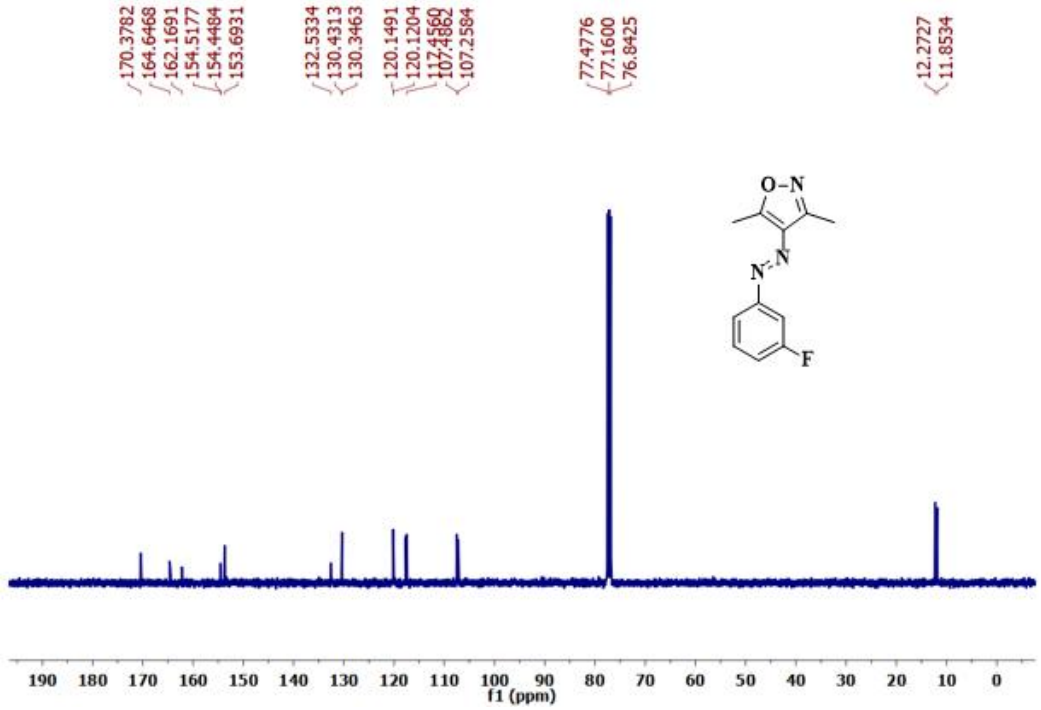

^{13}C NMR spectrum of (*E*)-4-((3-fluorophenyl)diazenyl)-3,5-dimethylisoxazole **(3d)** in $CDCl_3$

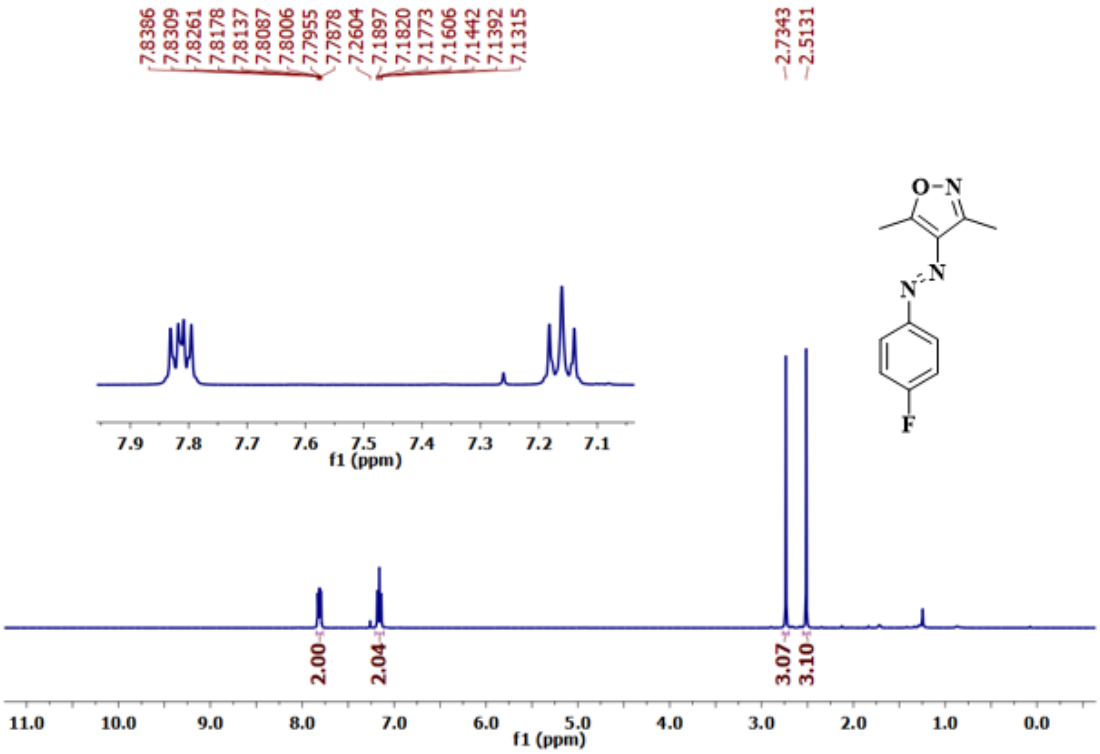

^{1}H NMR spectrum of (*E*)-4-((4-fluorophenyl)diazenyl)-3,5-dimethylisoxazole **(4d)** in $CDCl_3$

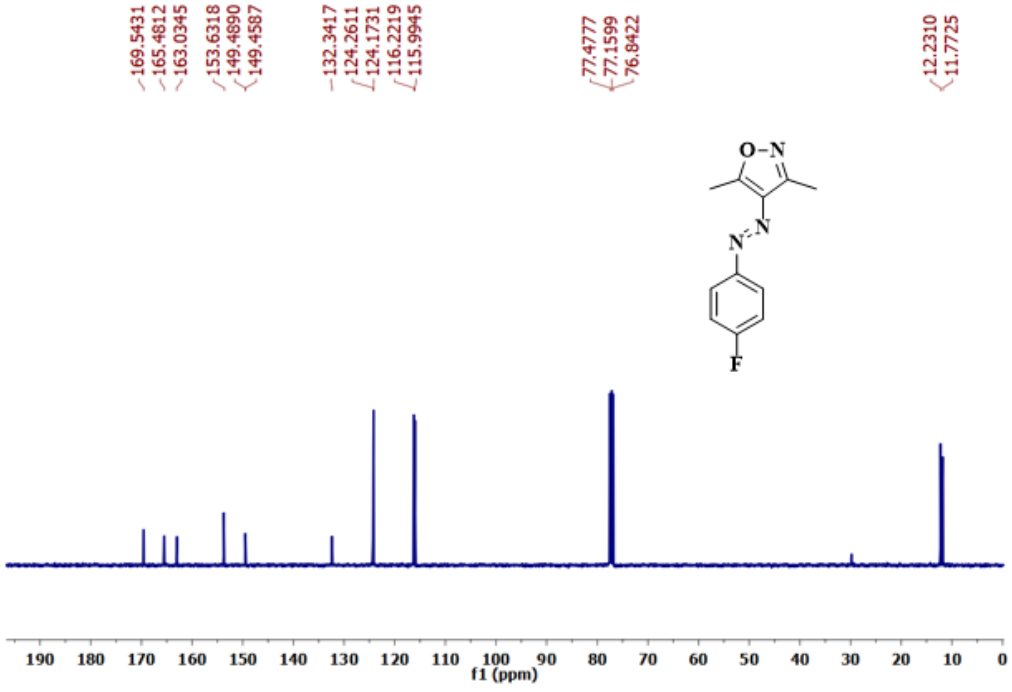

^{13}C NMR spectrum of (*E*)-4-((4-fluorophenyl)diazenyl)-3,5-dimethylisoxazole **(4d)** in $CDCl_3$

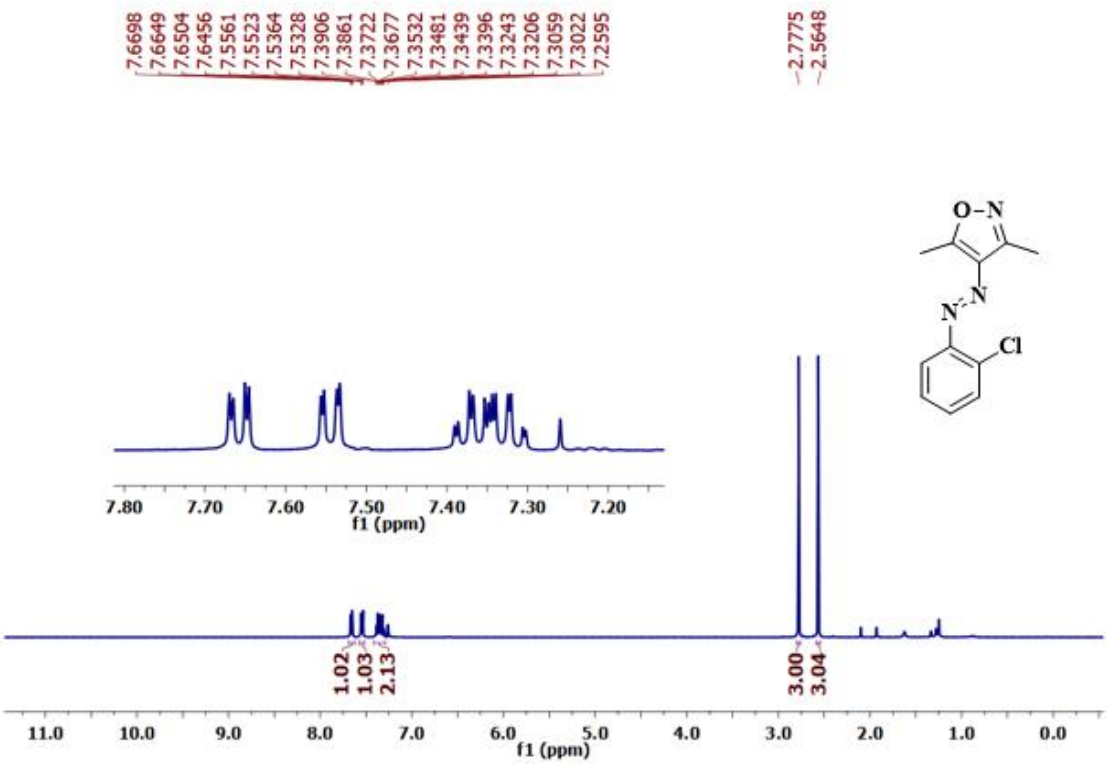

^{1}H NMR spectrum of (*E*)-4-((2-chlorophenyl)diazenyl)-3,5-dimethylisoxazole **(5d)** in $CDCl_3$

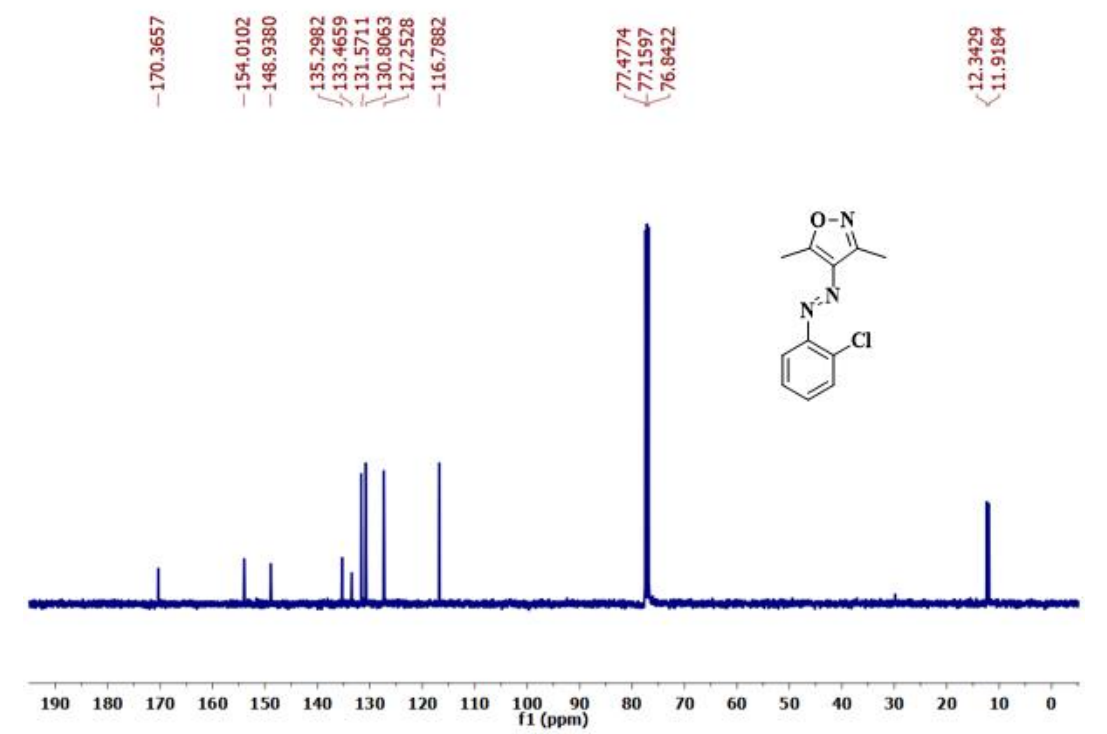

^{13}C NMR spectrum of (*E*)-4-((2-chlorophenyl)diazenyl)-3,5-dimethylisoxazole **(5d)** in $CDCl_3$

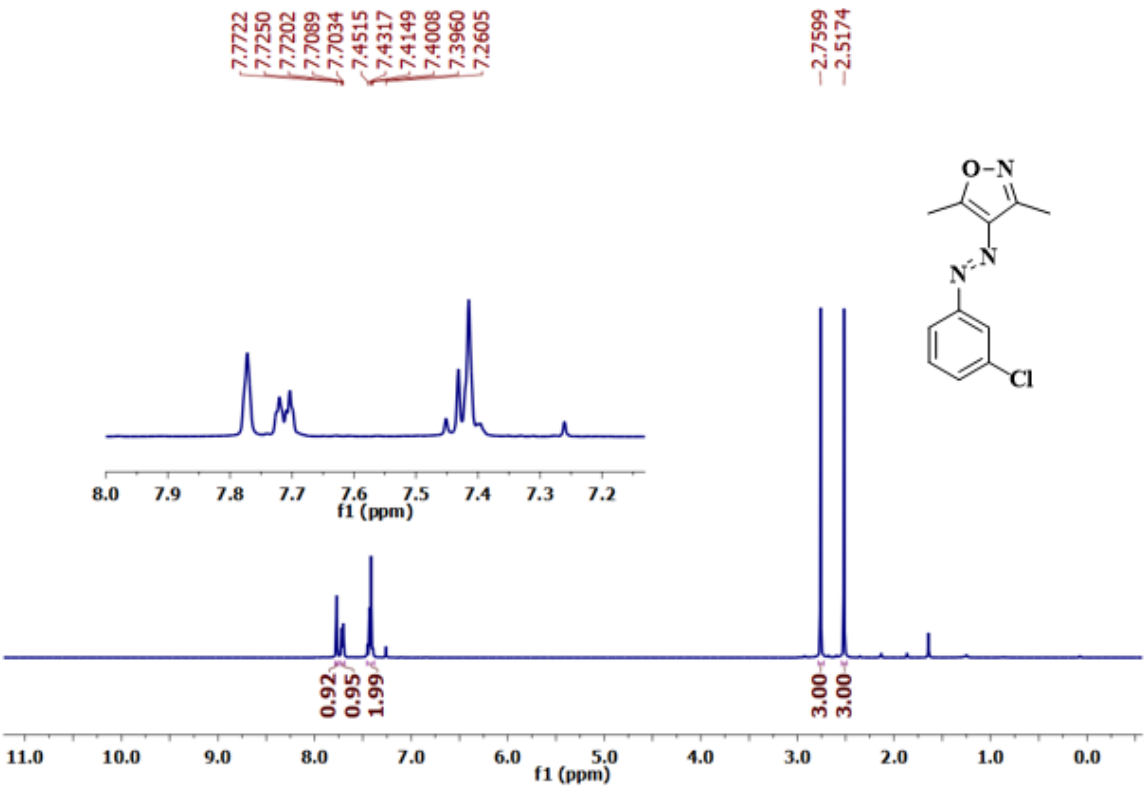

^{1}H NMR spectrum of (*E*)-4-((3-chlorophenyl)diazenyl)-3,5-dimethylisoxazole **(6d)** in $CDCl_3$

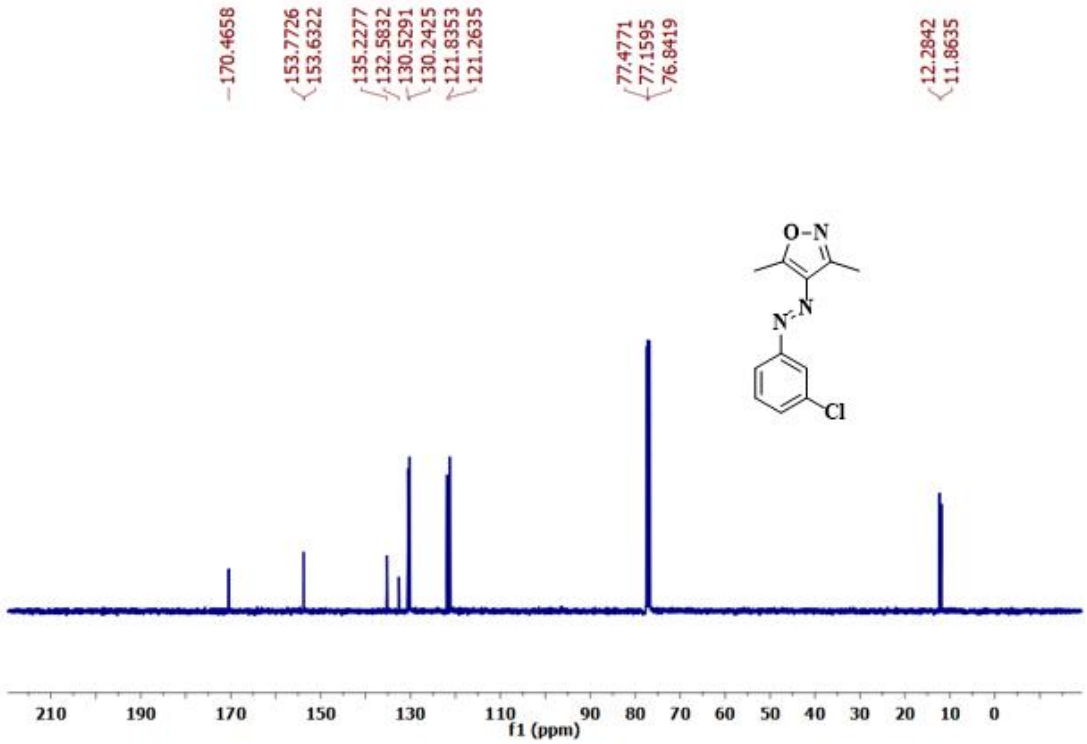

^{13}C NMR spectrum of (*E*)-4-((3-chlorophenyl)diazenyl)-3,5-dimethylisoxazole **(6d)** in $CDCl_3$

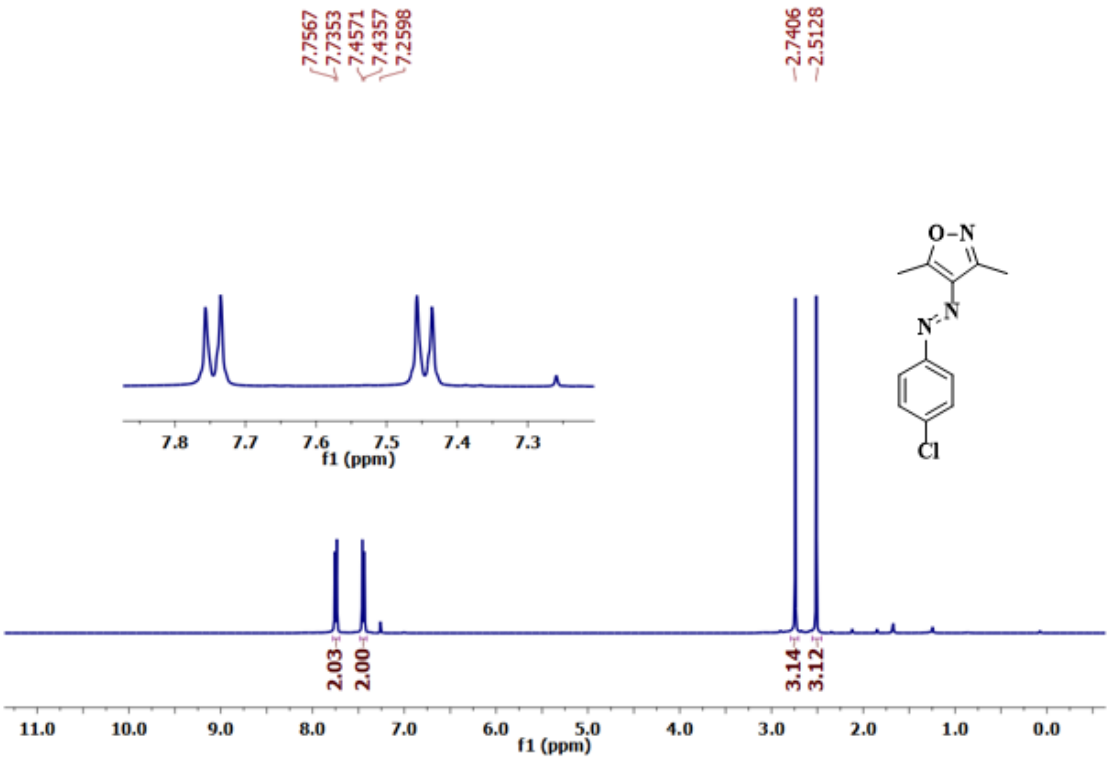

^{1}H NMR spectrum of (*E*)-4-((4-chlorophenyl)diazenyl)-3,5-dimethylisoxazole **(7d)** in $CDCl_3$

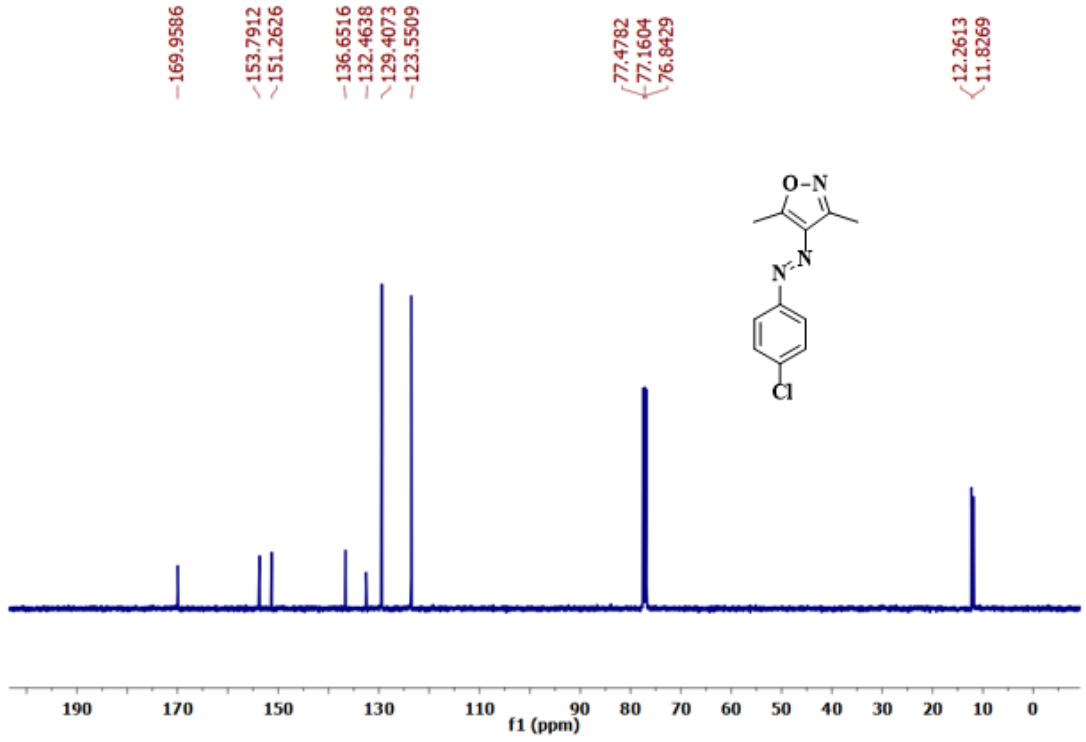

^{1}H NMR spectrum of (*E*)-4-((4-chlorophenyl)diazenyl)-3,5-dimethylisoxazole **(7d)** in $CDCl_3$

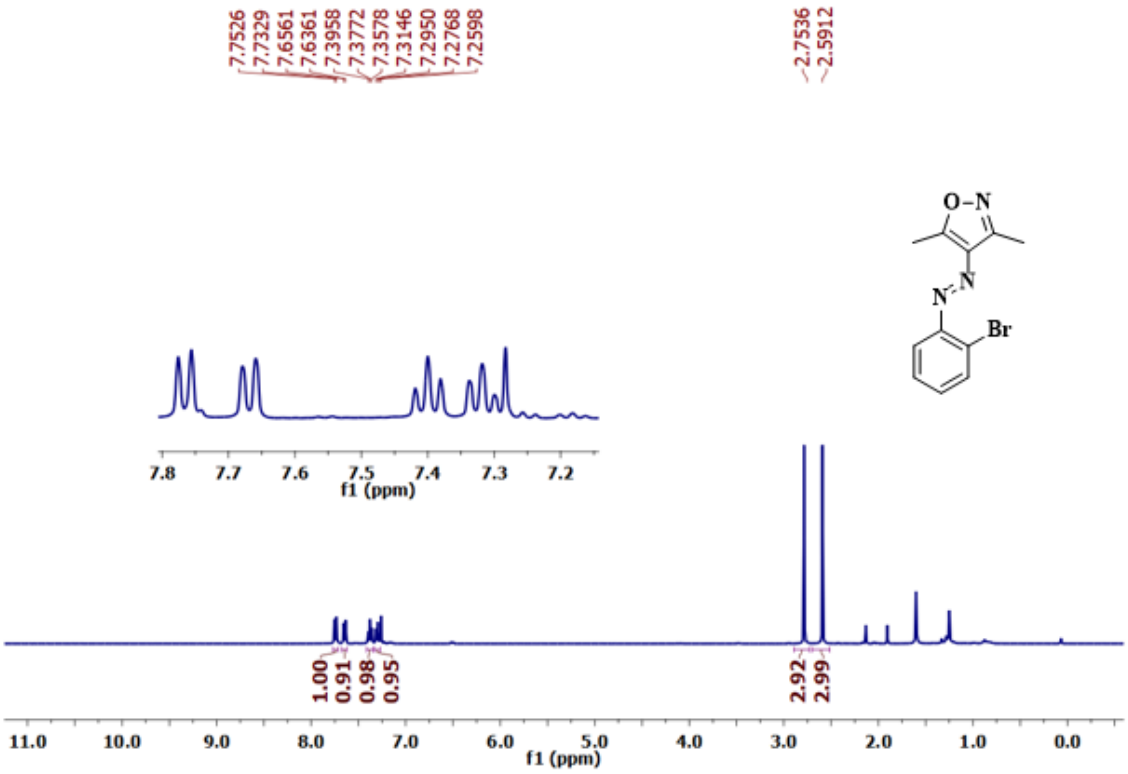

^{1}H NMR spectrum of (*E*)-4-((2-bromophenyl)diazenyl)-3,5-dimethylisoxazole **(8d)** in $CDCl_3$

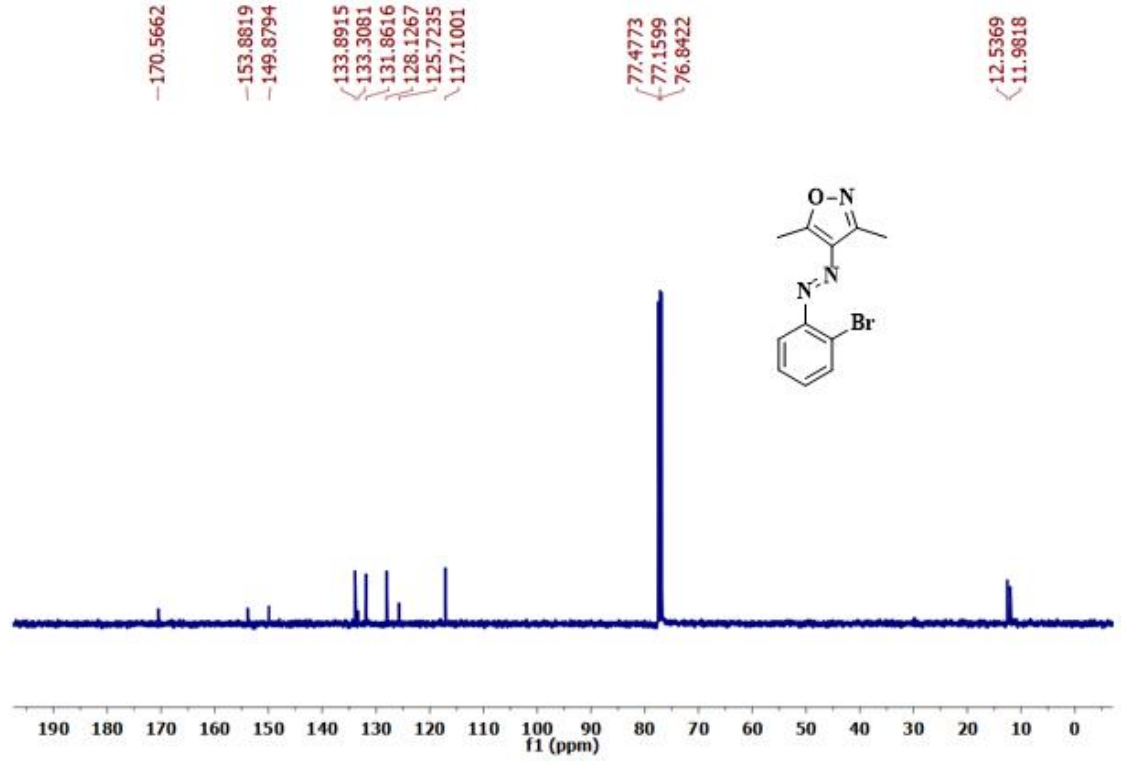

^{13}C NMR spectrum of (*E*)-4-((2-bromophenyl)diazenyl)-3,5-dimethylisoxazole **(8d)** in $CDCl_3$

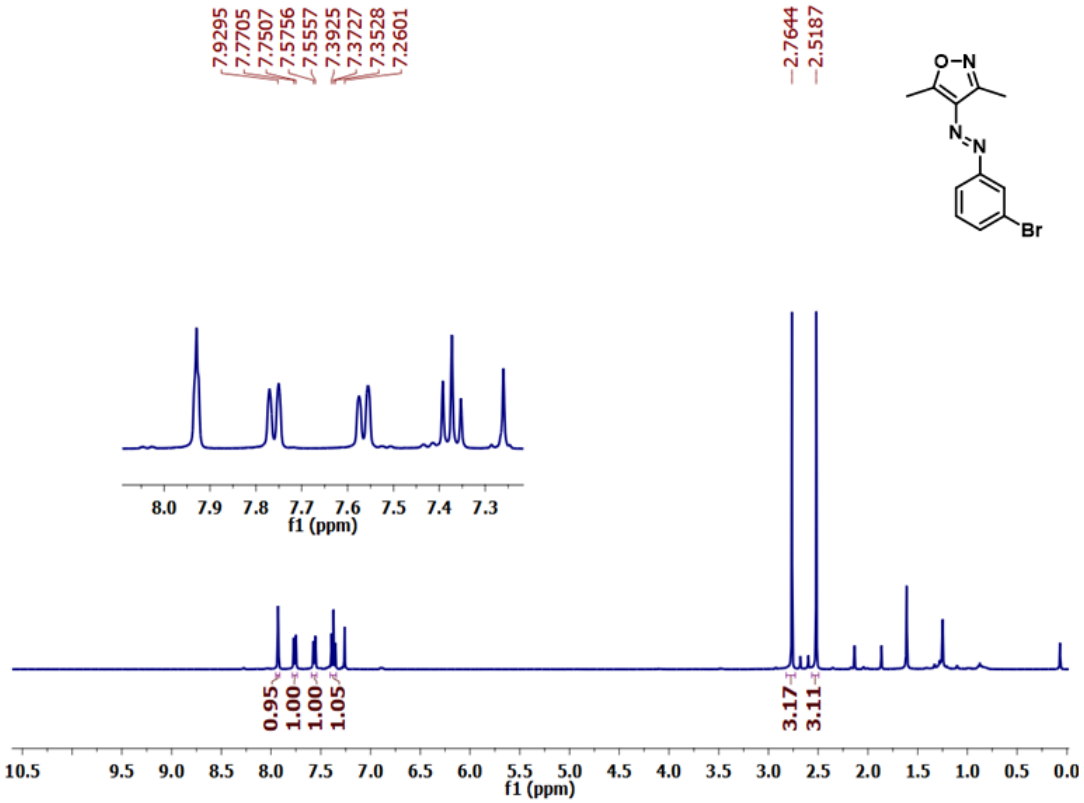

^{1}H NMR spectrum of (*E*)-4-((3-bromophenyl)diazenyl)-3,5-dimethylisoxazole **(9d)** in $CDCl_3$

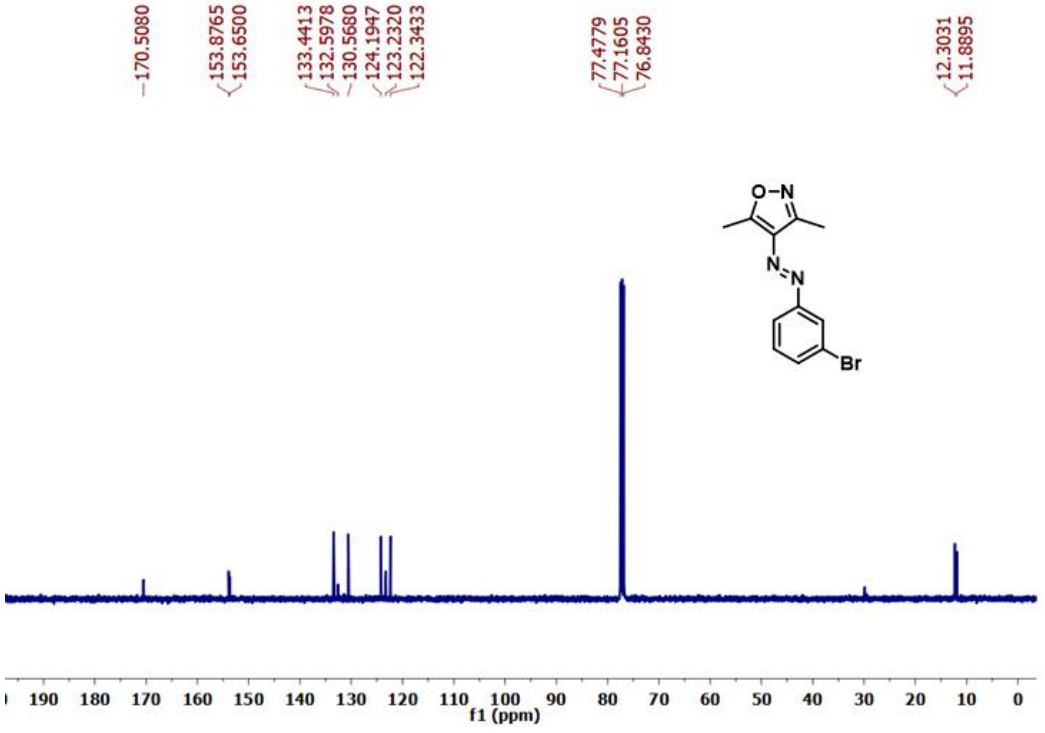

^{13}C NMR spectrum of (*E*)-4-((3-bromophenyl)diazenyl)-3,5-dimethylisoxazole **(9d)** in $CDCl_3$

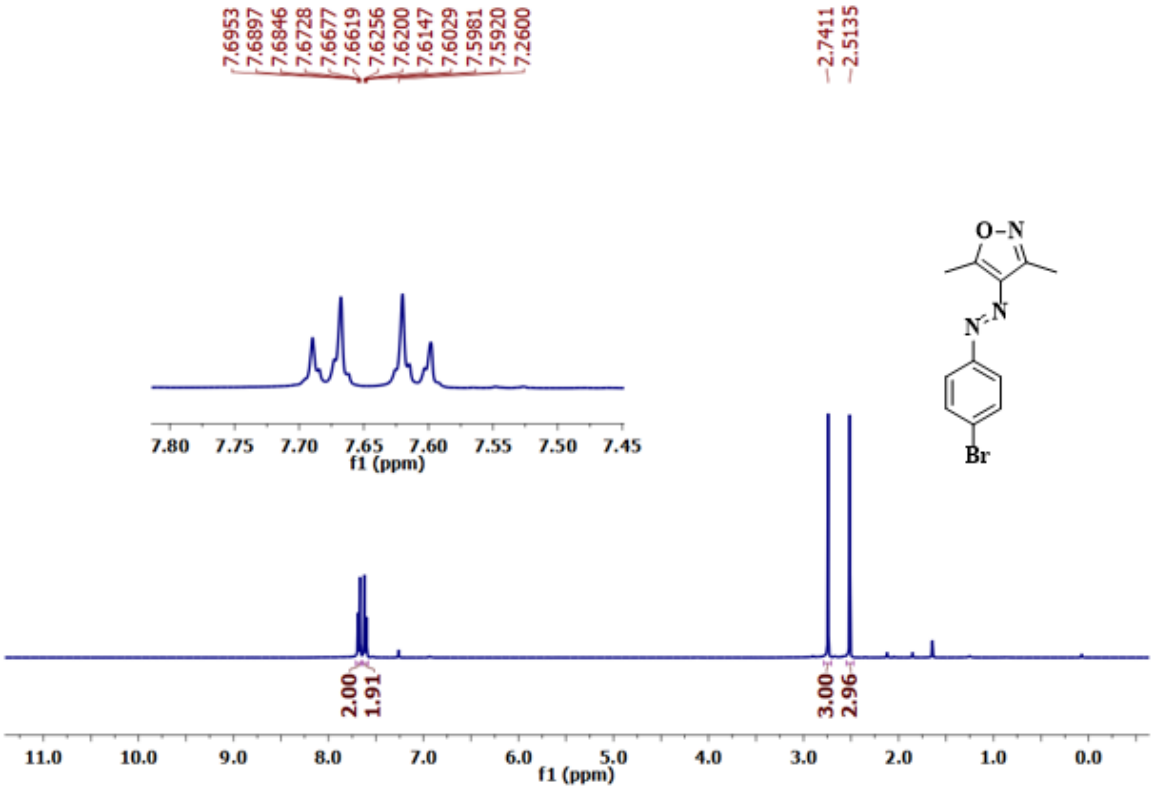

^{1}H NMR spectrum of (*E*)-4-((4-bromophenyl)diazenyl)-3,5-dimethylisoxazole **(10d)** in $CDCl_3$

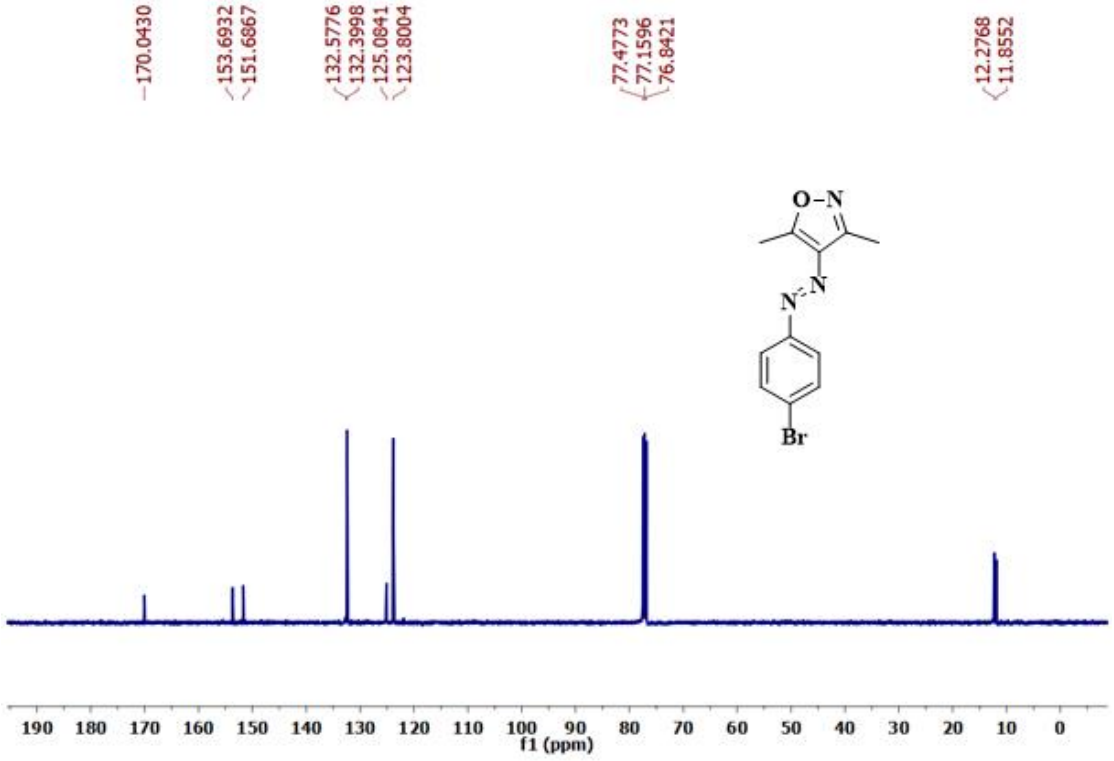

^{13}C NMR spectrum of (*E*)-4-((4-bromophenyl)diazenyl)-3,5-dimethylisoxazole **(10d)** in $CDCl_3$

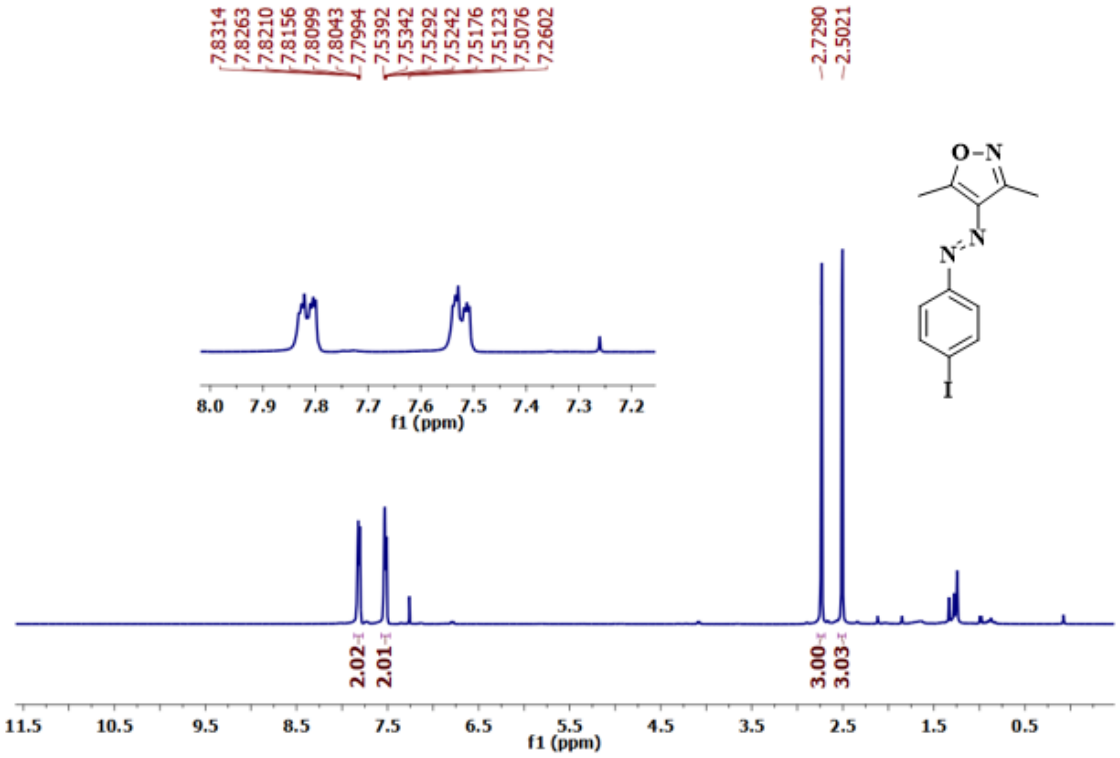

^{1}H NMR spectrum of (*E*)-4-((4-iodophenyl)diazenyl)-3,5-dimethylisoxazole **(11d)** in $CDCl_3$

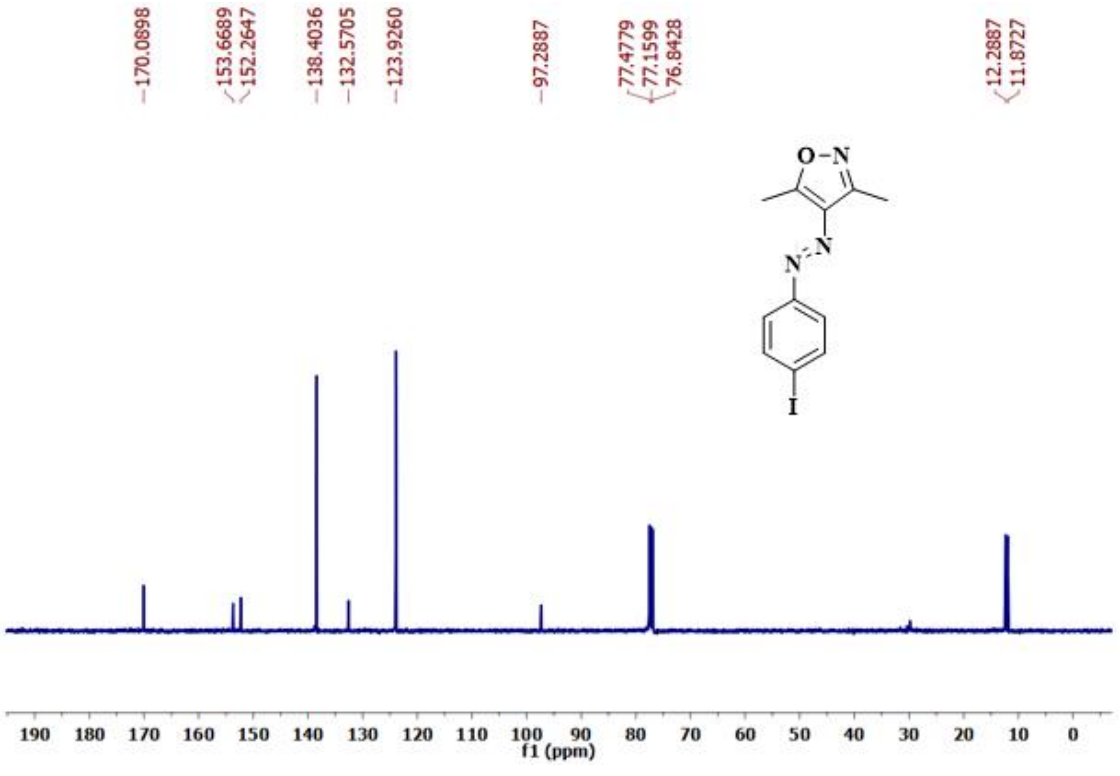

^{13}C NMR spectrum of (*E*)-4-((4-iodophenyl)diazenyl)-3,5-dimethylisoxazole **(11d)** in $CDCl_3$

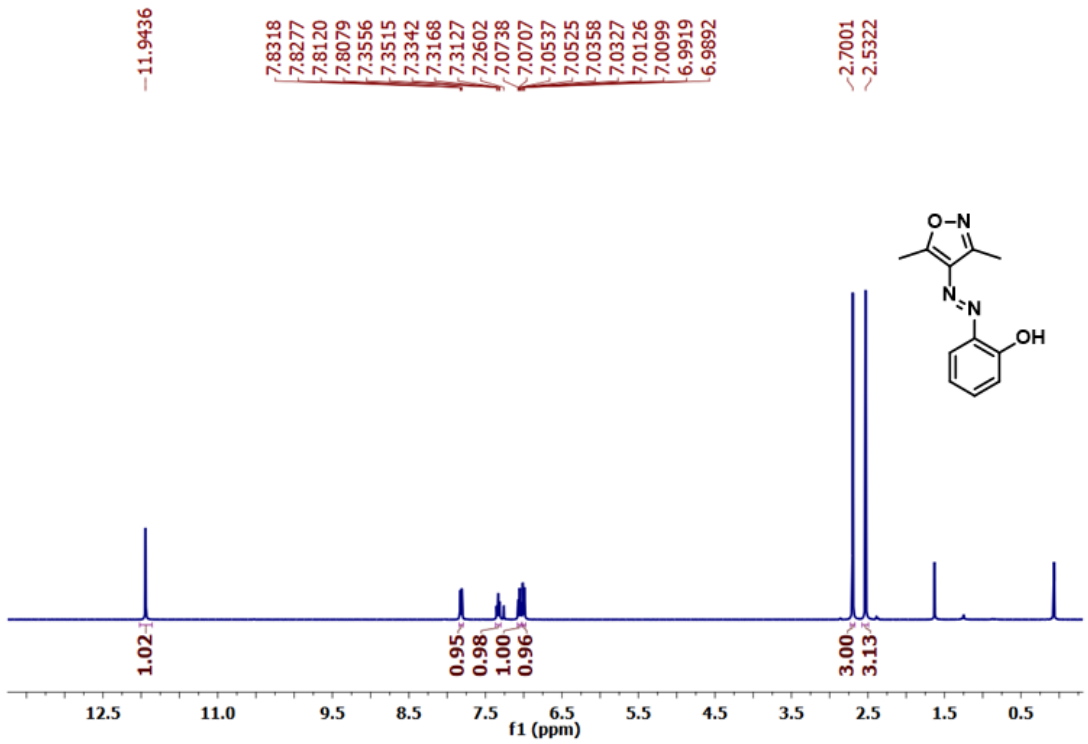

^{1}H NMR spectrum of (*E*)-2-((3,5-dimethylisoxazole-4-yl)phenol **(12d)** in $CDCl_3$

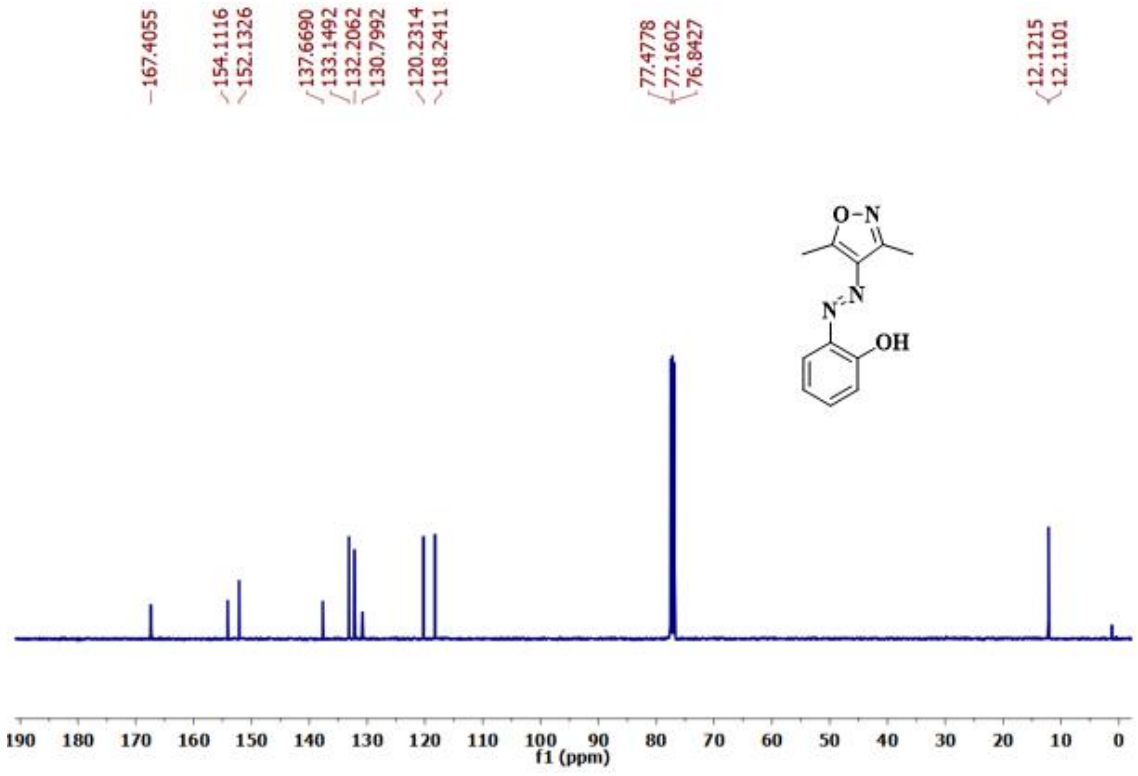

^{13}C NMR spectrum of (*E*)-2-((3,5-dimethylisoxazole-4-yl)phenol **(12d)** in $CDCl_3$

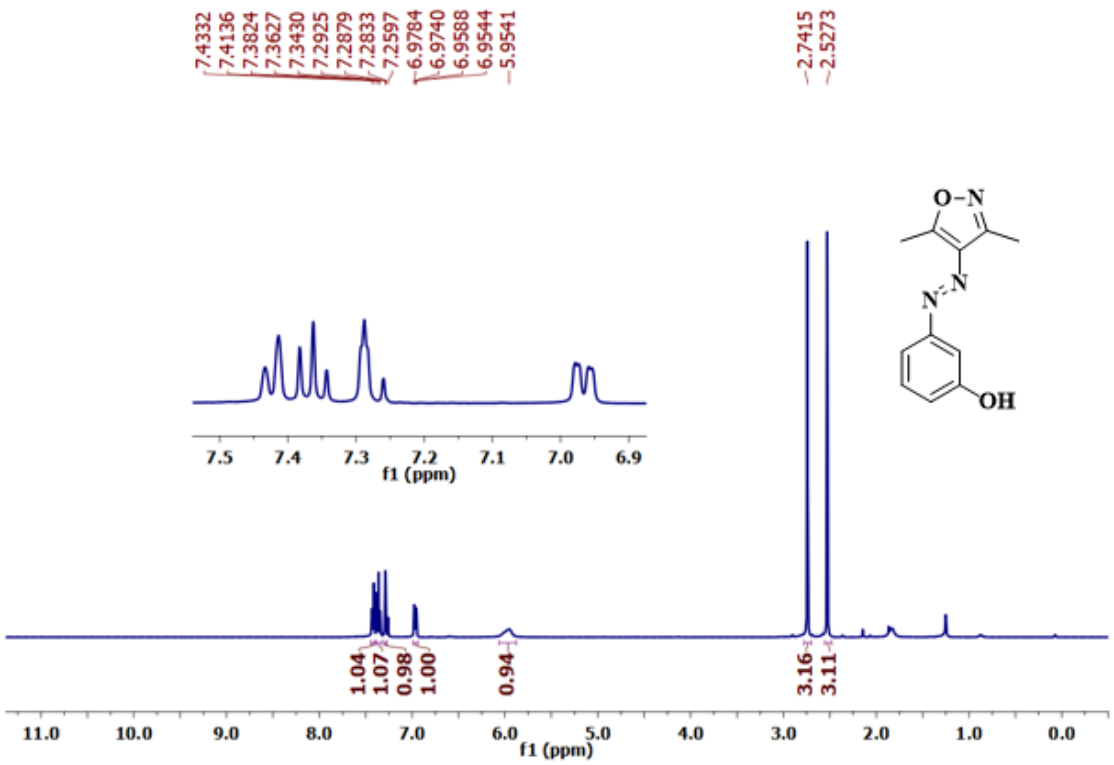

^{1}H NMR spectrum of (*E*)-3-((3,5-dimethylisoxazole-4-yl)phenol **(13d)** in $CDCl_3$

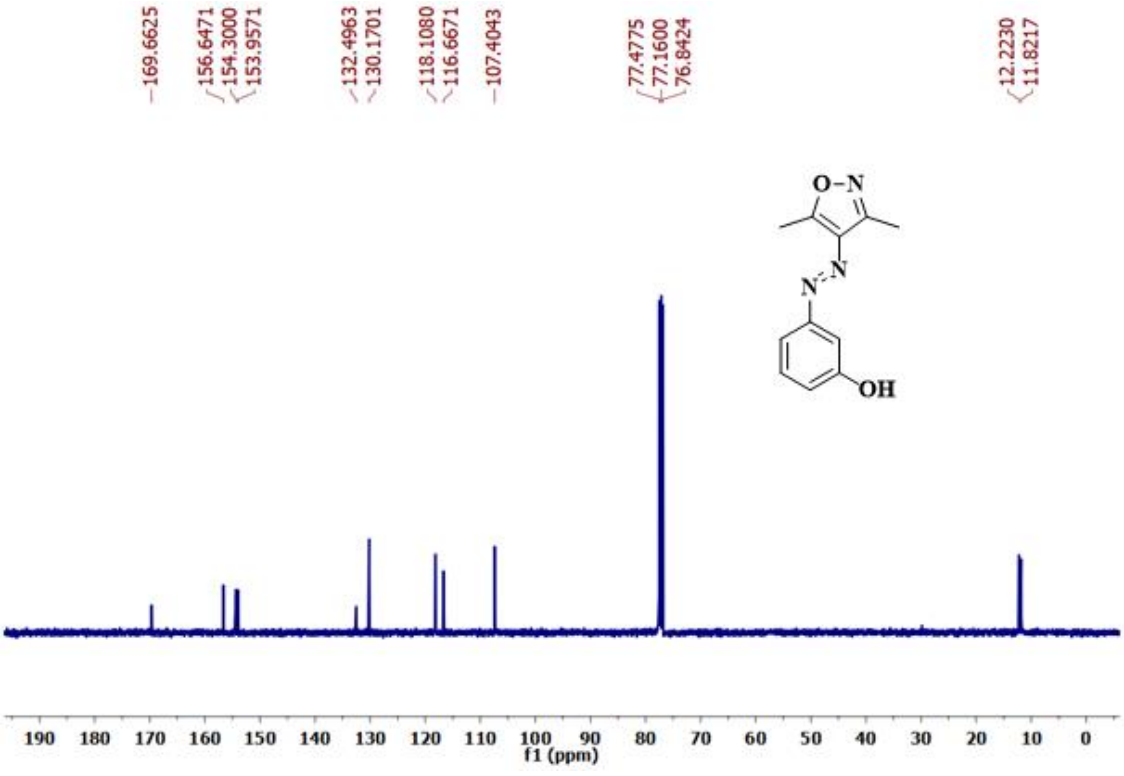

^{13}C NMR spectrum of (*E*)-3-((3,5-dimethylisoxazole-4-yl)phenol **(13d)** in $CDCl_3$

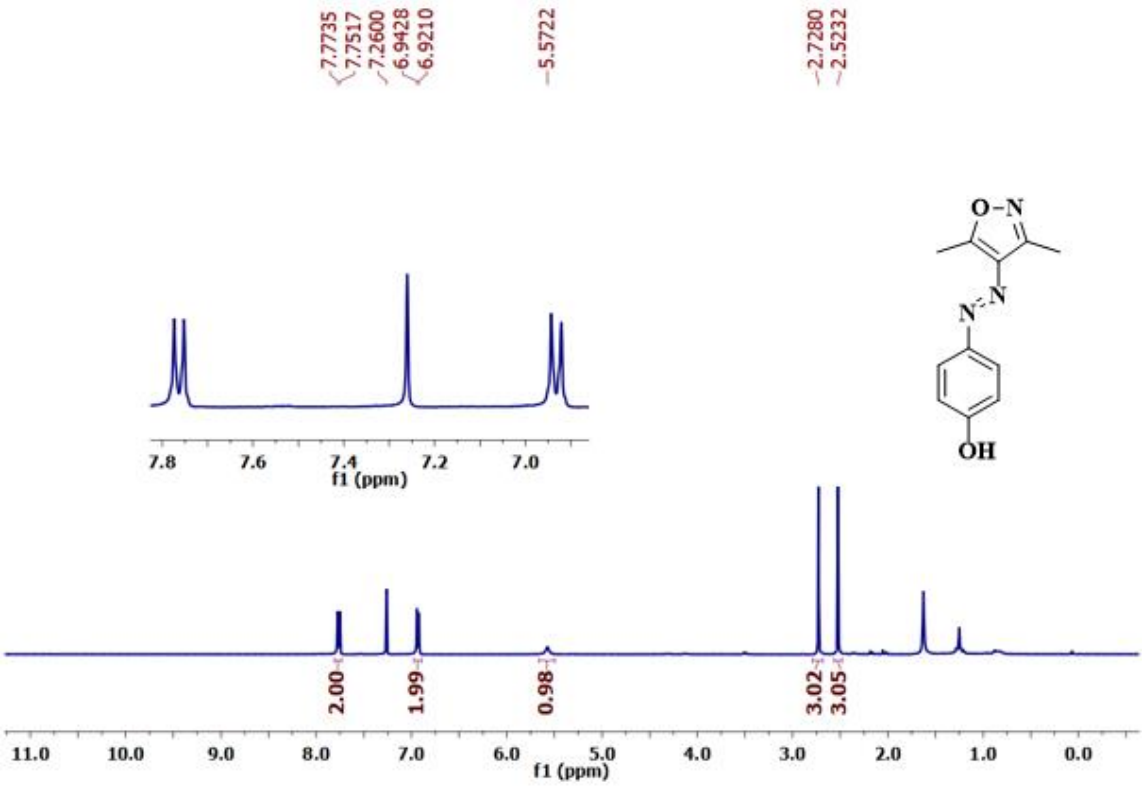

^{1}H NMR spectrum of (*E*)-4-((3,5-dimethylisoxazole-4-yl)phenol **(14d)** in $CDCl_3$

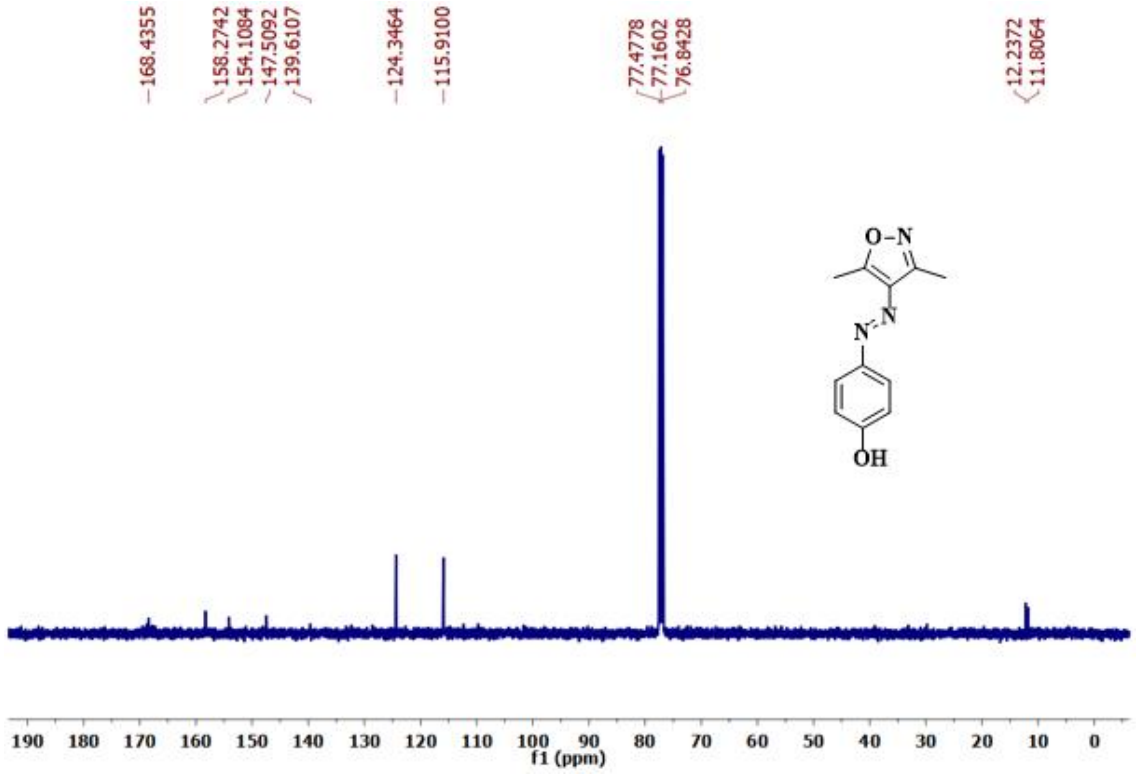

^{13}C NMR spectrum of (*E*)-4-((3,5-dimethylisoxazole-4-yl)phenol **(14d)** in $CDCl_3$

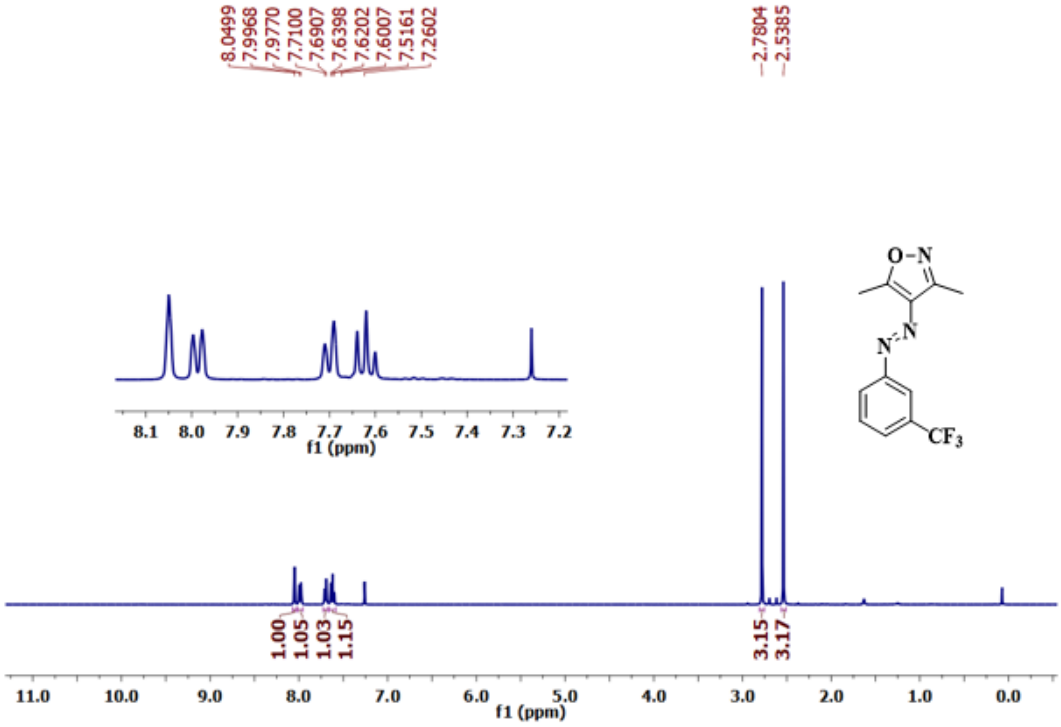

^{1}H NMR spectrum of (*E*)-3,5-dimethyl-4-((3-(trifluoromethyl)phenyl)diazenyl)isoxazole **(15d)** in $CDCl_3$

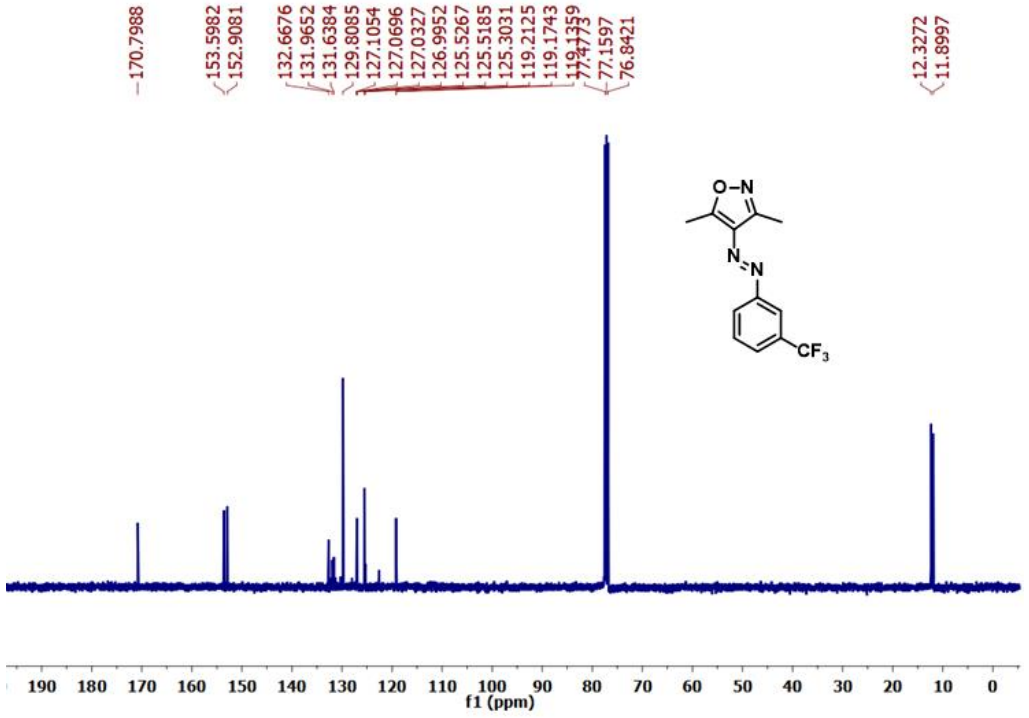

^{13}C NMR spectrum of (*E*)-3,5-dimethyl-4-((3-(trifluoromethyl)phenyl)diazenyl)isoxazole **(15d)** in $CDCl_3$

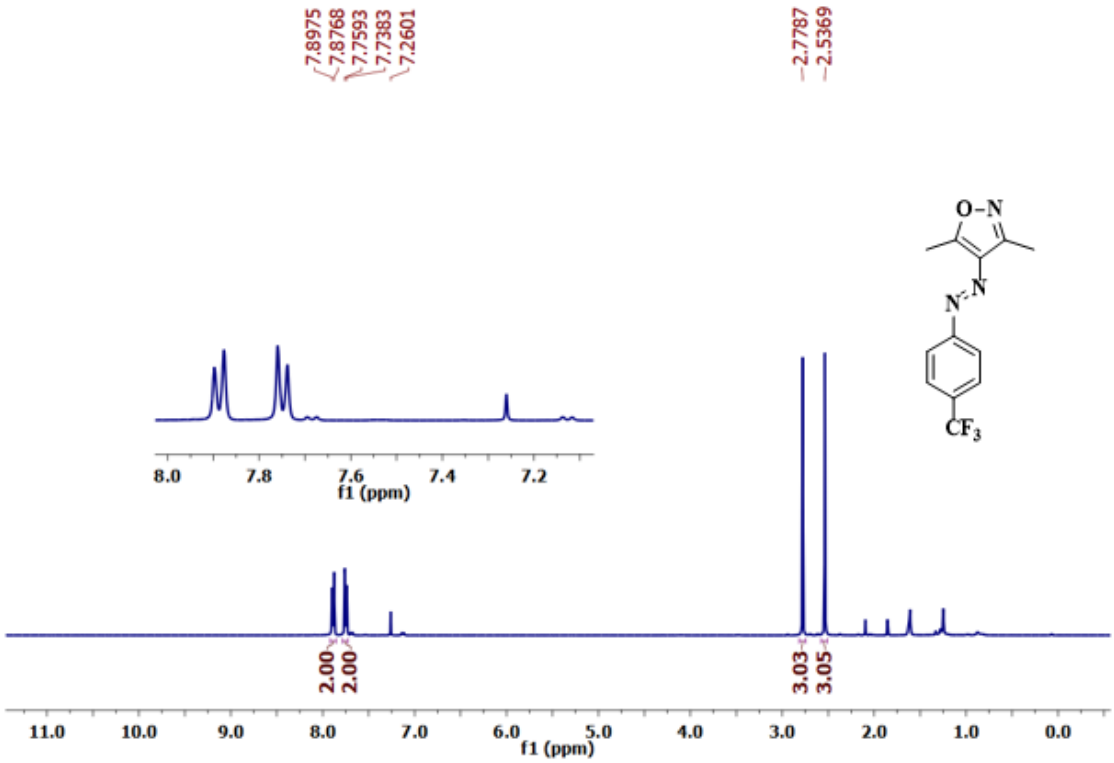

^{1}H NMR spectrum of (*E*)-3,5-dimethyl-4-((4-(trifluoromethyl)phenyl)diazenyl)isoxazole **(16d)** in $CDCl_3$

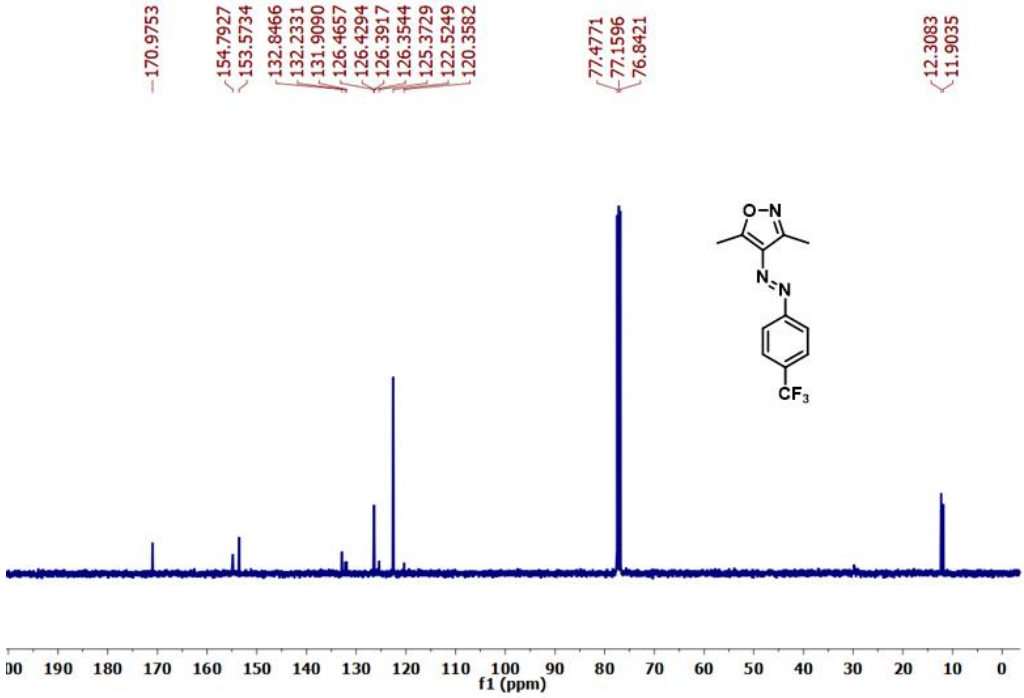

^{13}C NMR spectrum of (*E*)-3,5-dimethyl-4-((4-(trifluoromethyl)phenyl)diazenyl)isoxazole **(16d)** in $CDCl_3$

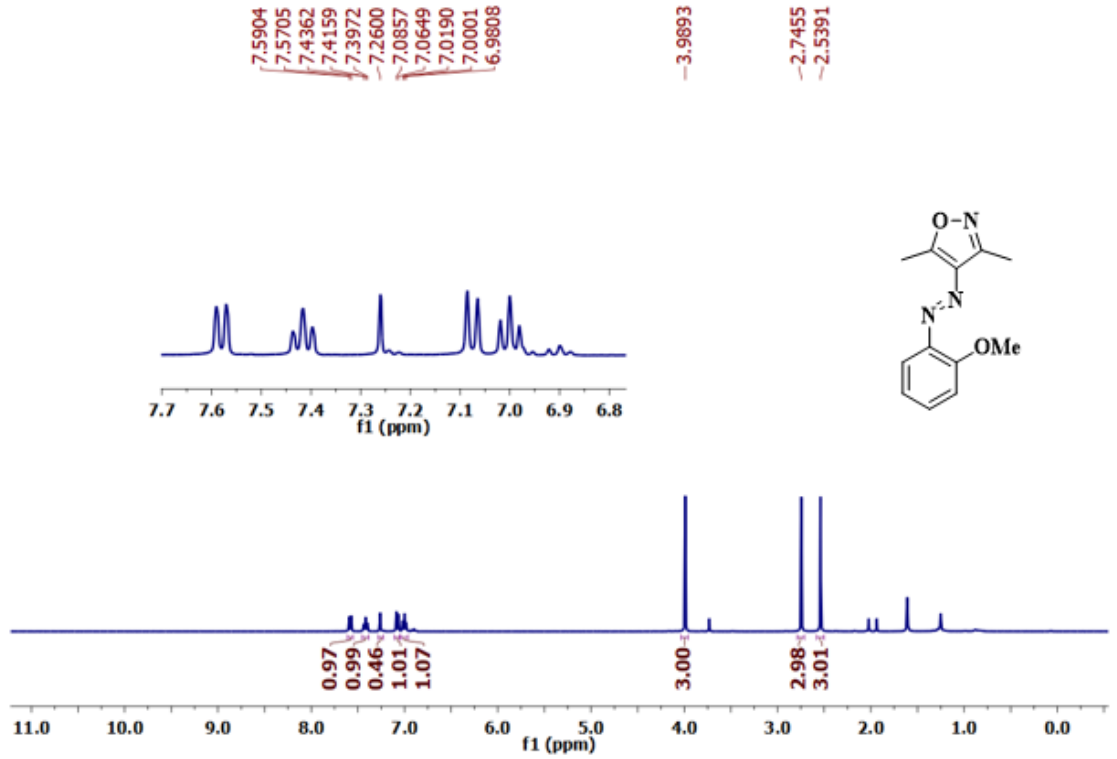

^{1}H NMR spectrum of (*E*)-4-((2-methoxyphenyl)diazenyl)-3,5-dimethylisoxazole **(17d)** in $CDCl_3$

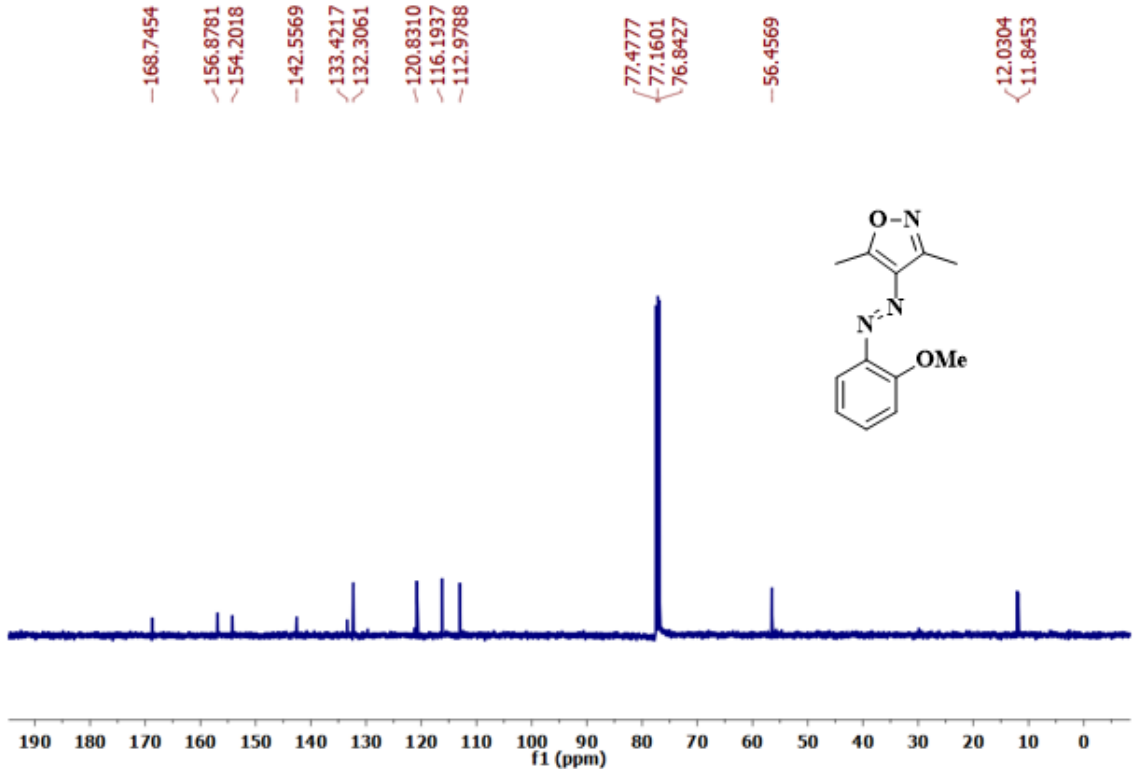

^{13}C NMR spectrum of (*E*)-4-((2-methoxyphenyl)diazenyl)-3,5-dimethylisoxazole **(17d)** in $CDCl_3$

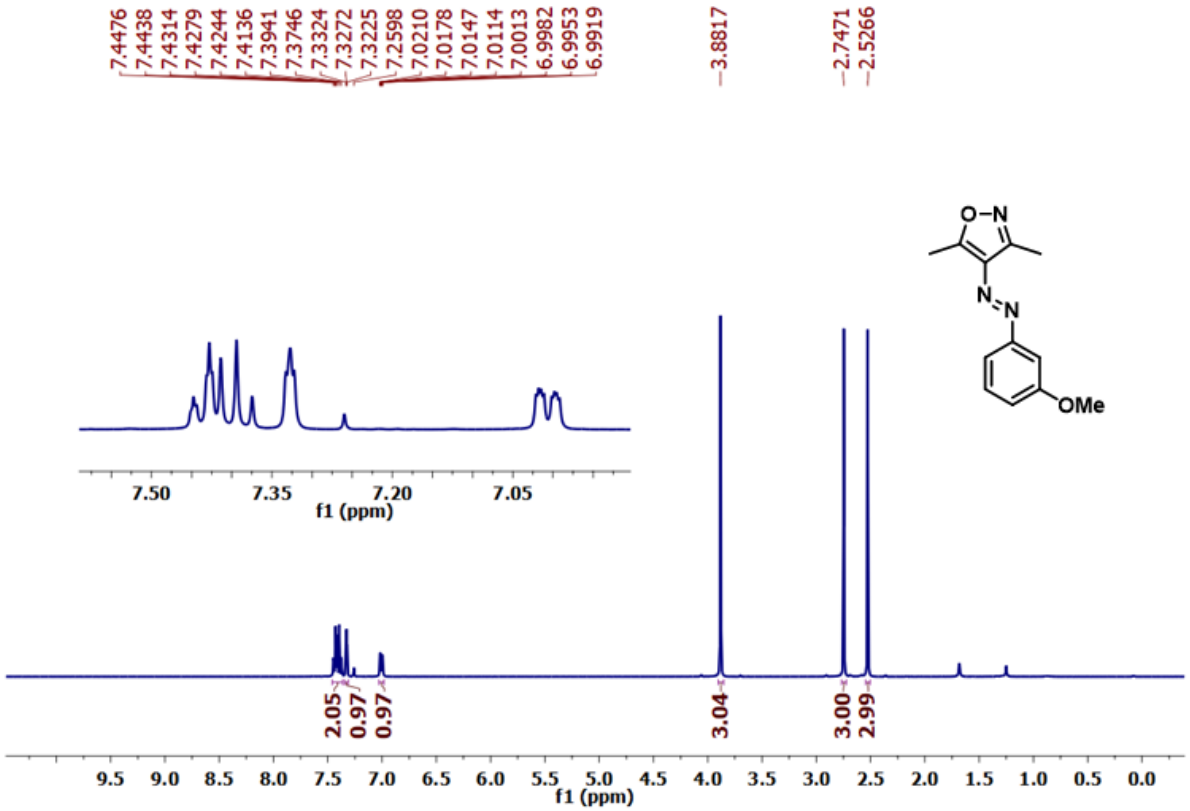

^{1}H NMR spectrum of (*E*)-4-((3-methoxyphenyl)diazenyl)-3,5-dimethylisoxazole **(18d)** in $CDCl_3$

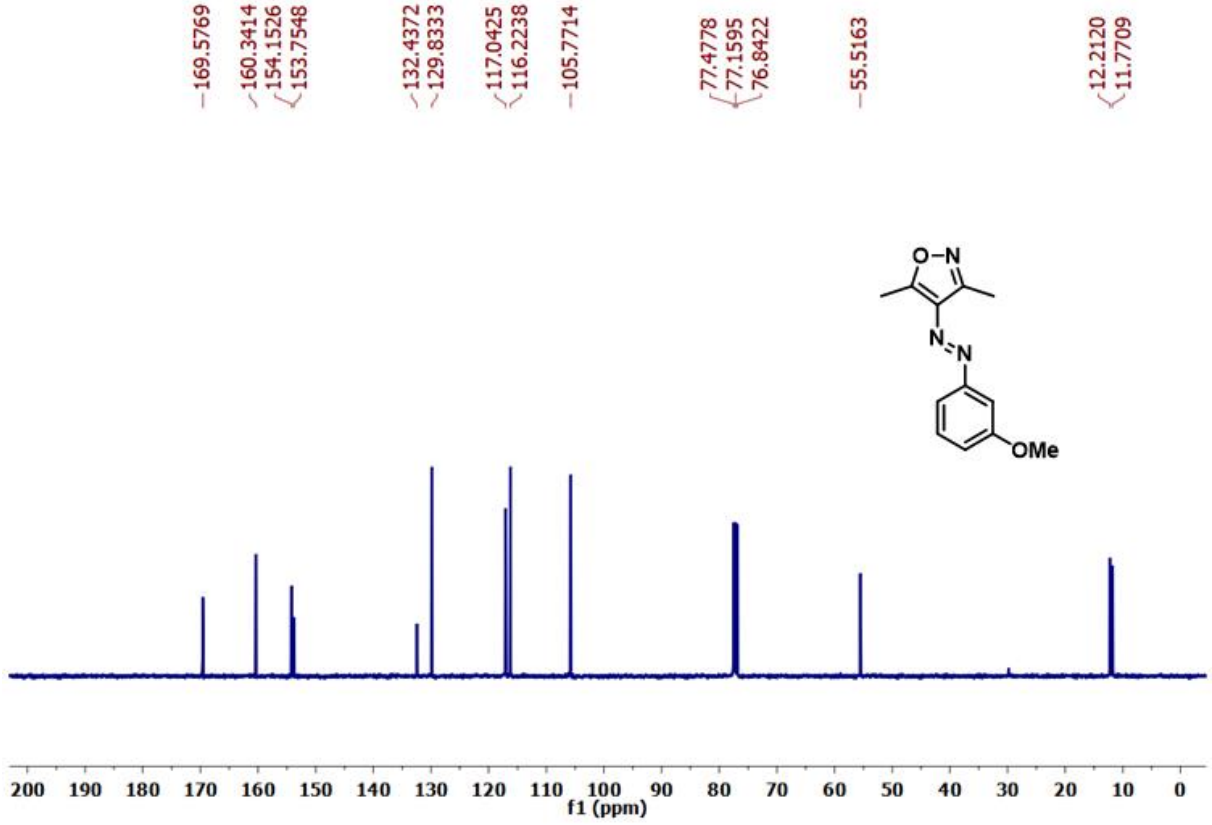

^{13}C NMR spectrum of (*E*)-4-((3-methoxyphenyl)diazenyl)-3,5-dimethylisoxazole **(18d)** in $CDCl_3$

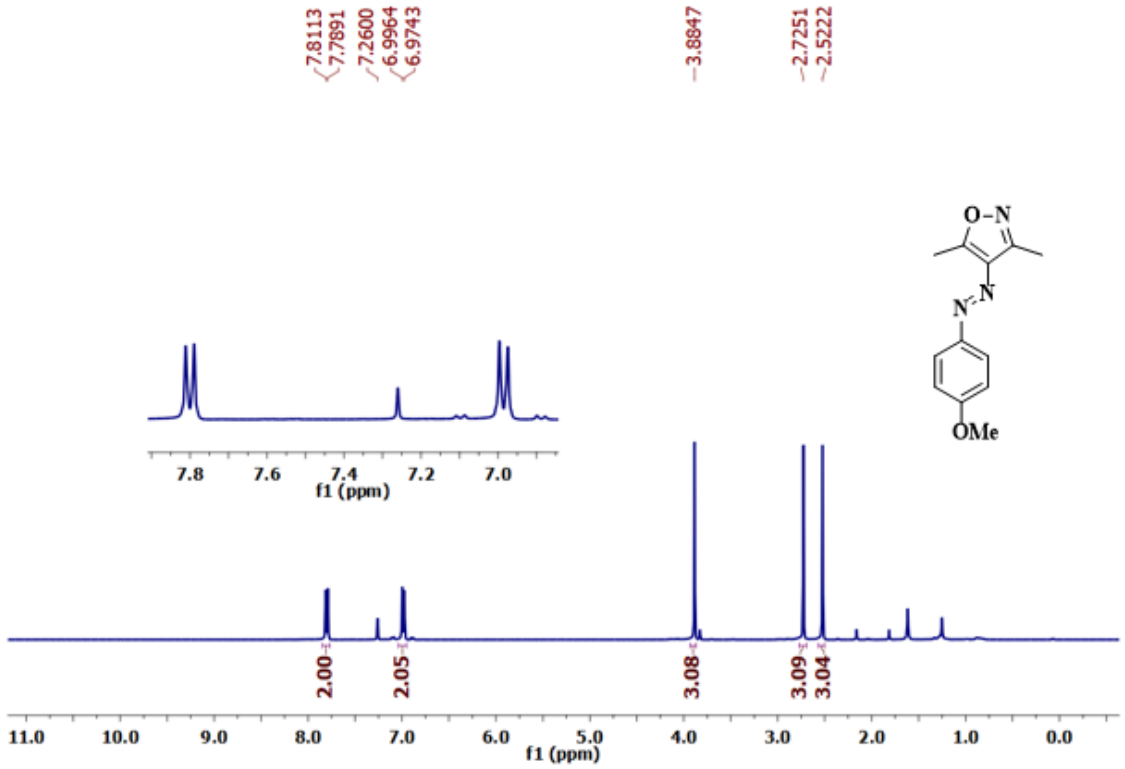

^{1}H NMR spectrum of (*E*)-4-((4-methoxyphenyl)diazenyl)-3,5-dimethylisoxazole **(19d)** in $CDCl_3$

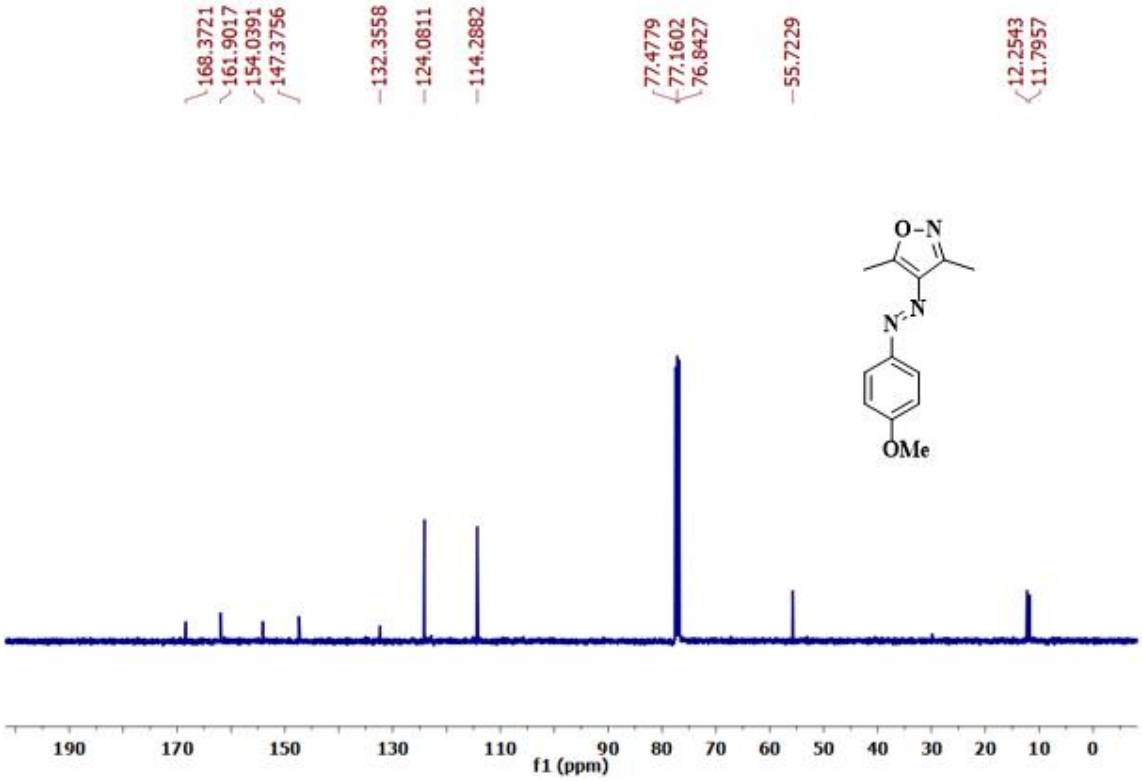

^{13}C NMR spectrum of (*E*)-4-((4-methoxyphenyl)diazenyl)-3,5-dimethylisoxazole **(19d)** in $CDCl_3$

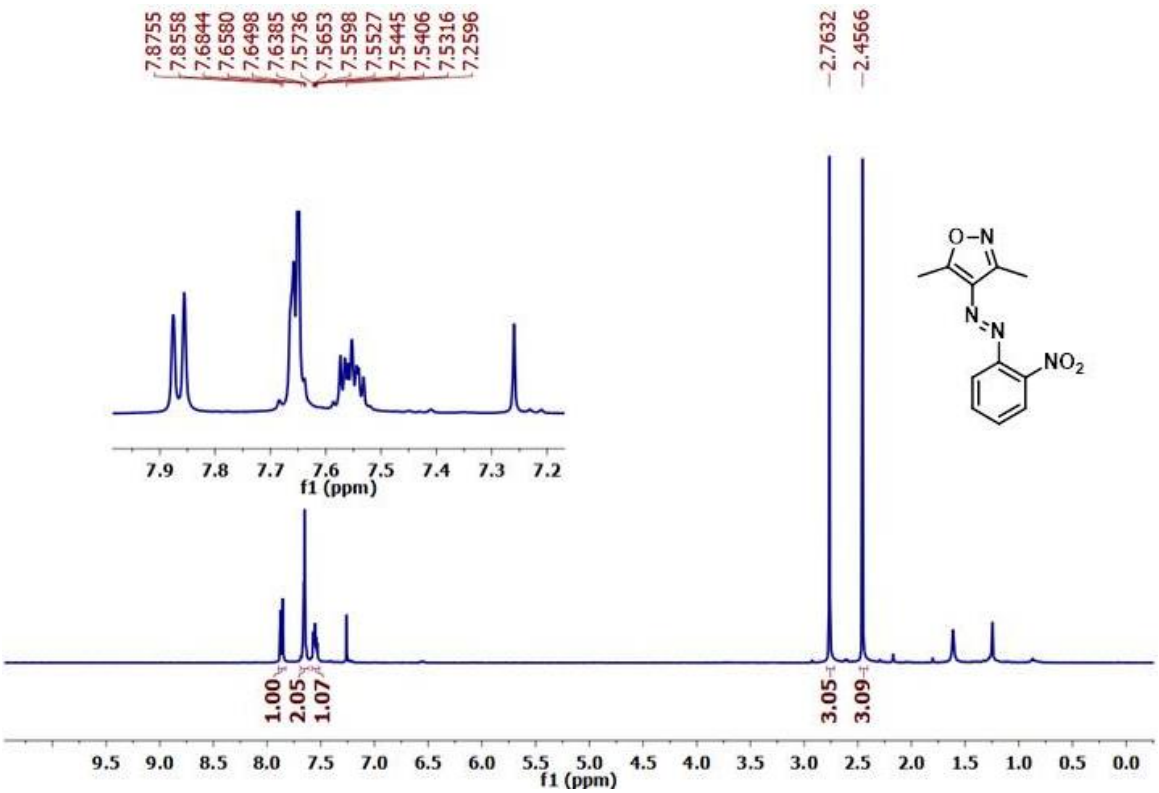

^{1}H NMR spectrum of (*E*)-3,5-dimethyl-4-((2-nitrophenyl)diazenyl)isoxazole **(20d)** in $CDCl_3$

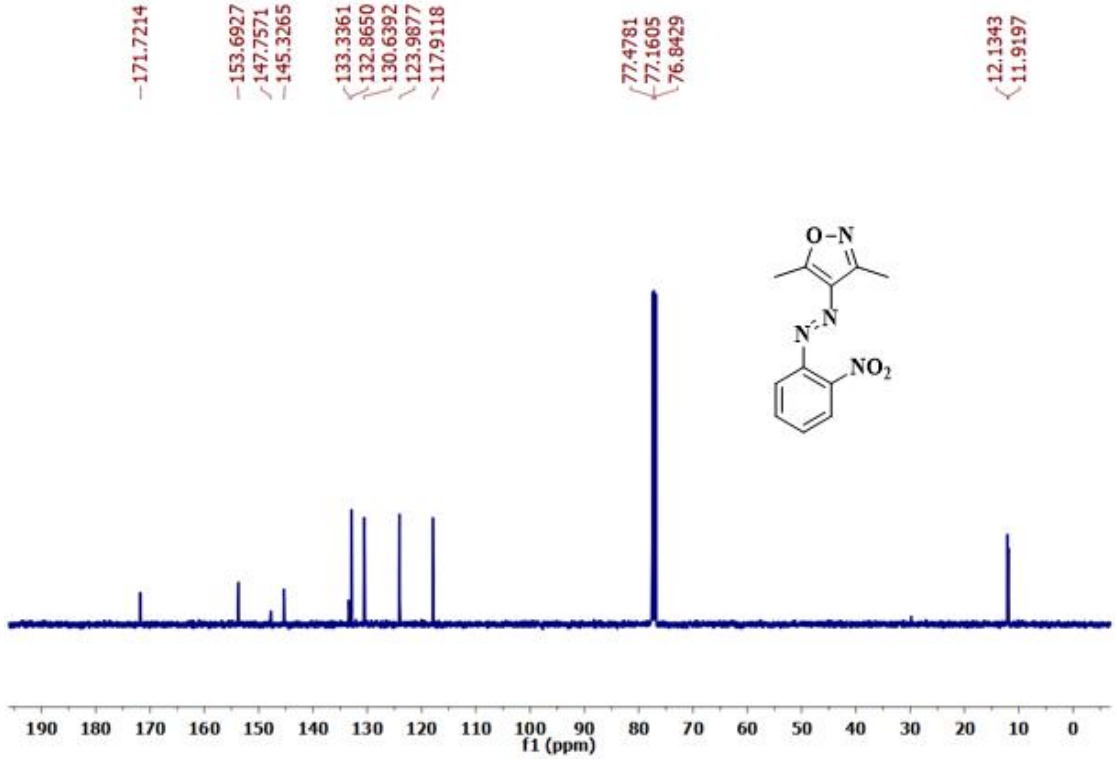

^{13}C NMR spectrum of (*E*)-3,5-dimethyl-4-((2-nitrophenyl)diazenyl)isoxazole **(20d)** in $CDCl_3$

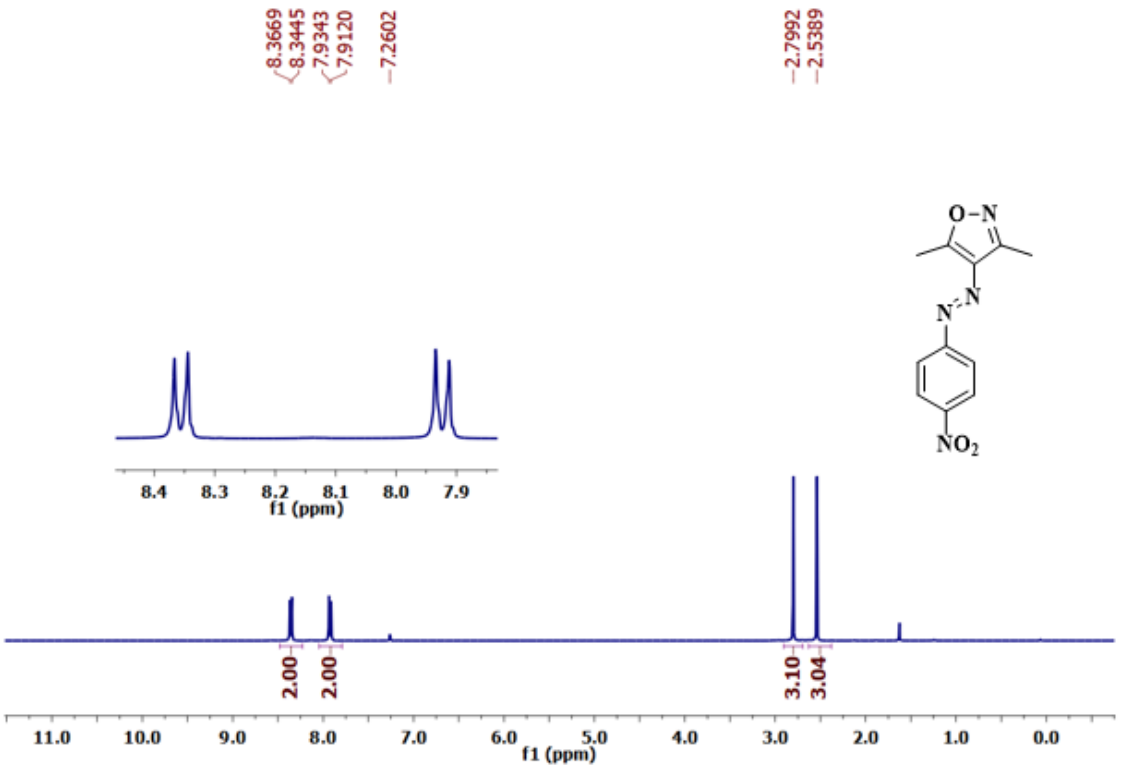

^{1}H NMR spectrum of (*E*)-3,5-dimethyl-4-((4-nitrophenyl)diazenyl)isoxazole **(21d)** in $CDCl_3$

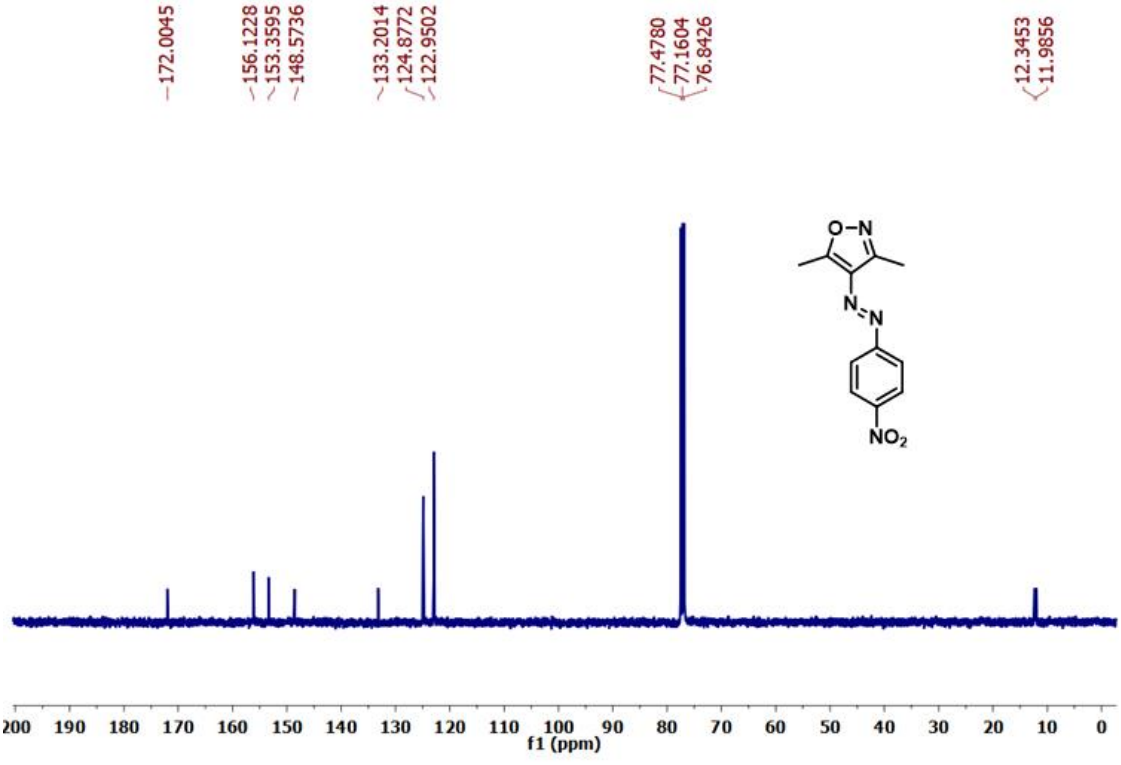

^{13}C NMR spectrum of (*E*)-3,5-dimethyl-4-((4-nitrophenyl)diazenyl)isoxazole **(21d)** in $CDCl_3$

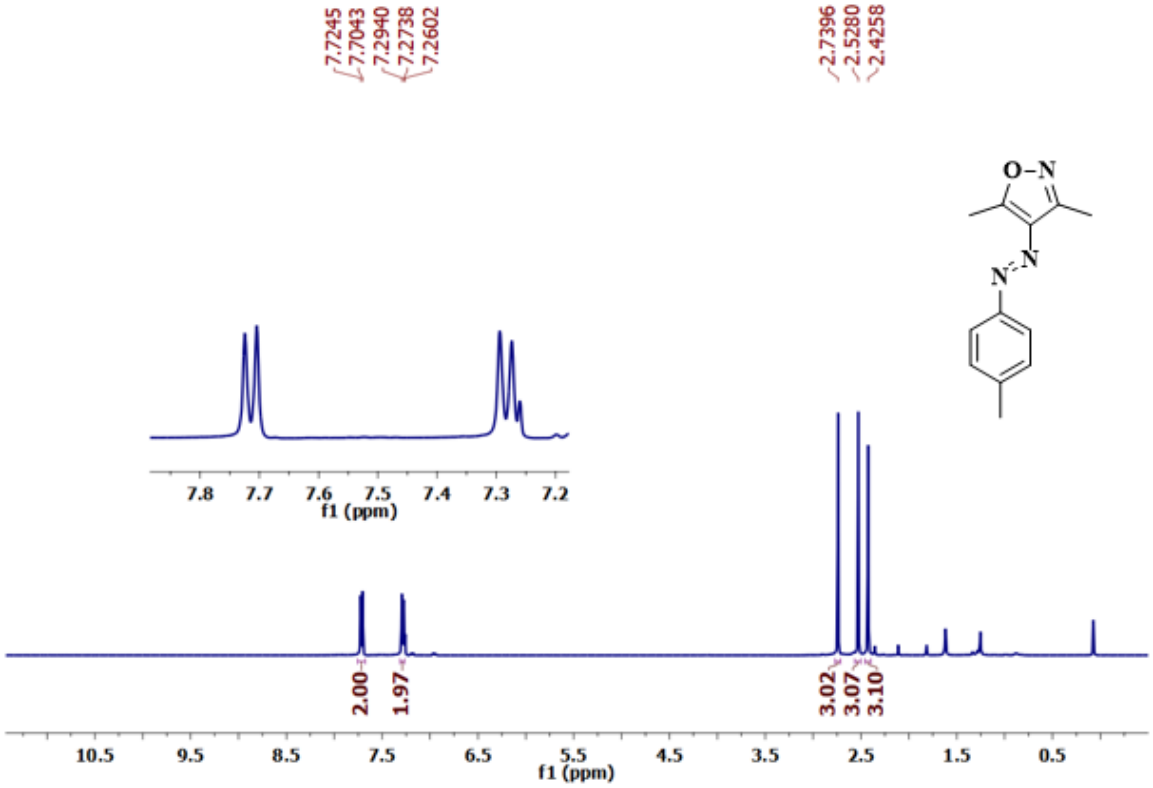

^{1}H NMR spectrum of (*E*)-3,5-dimethyl-4-(*p*-tolyldiazenyl)isoxazole **(22d)** in $CDCl_3$

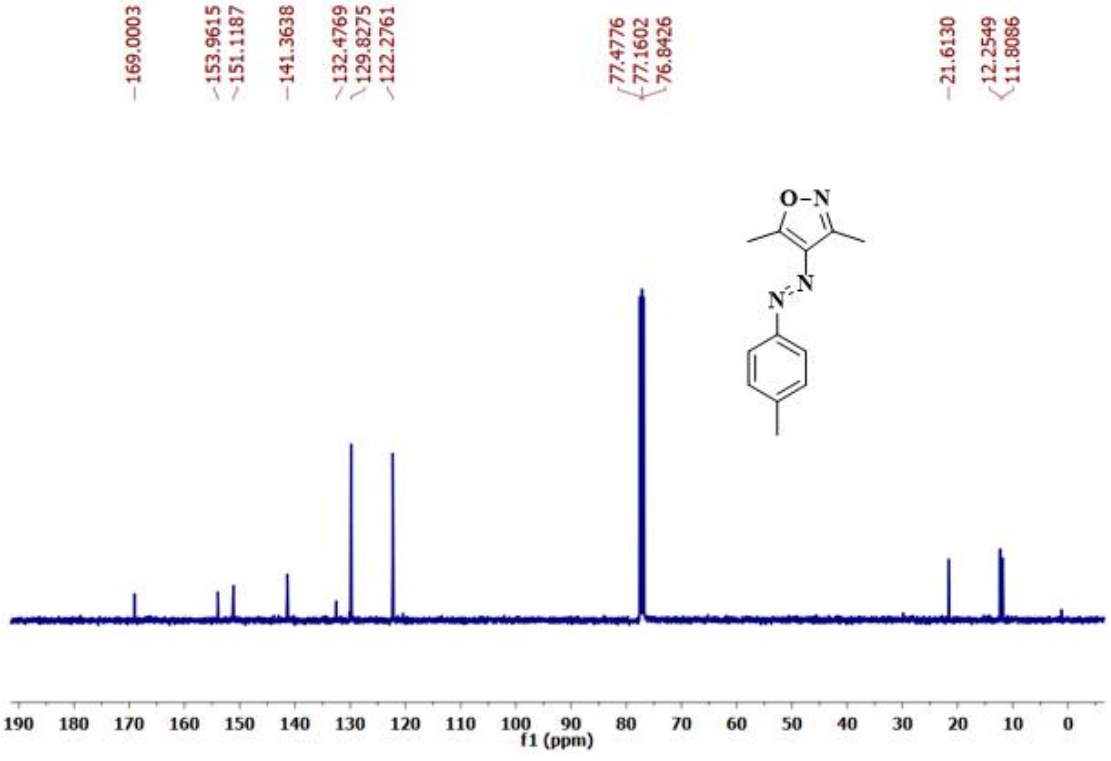

^{13}C NMR spectrum of (*E*)-3,5-dimethyl-4-(*p*-tolyldiazenyl)isoxazole **(22d)** in $CDCl_3$

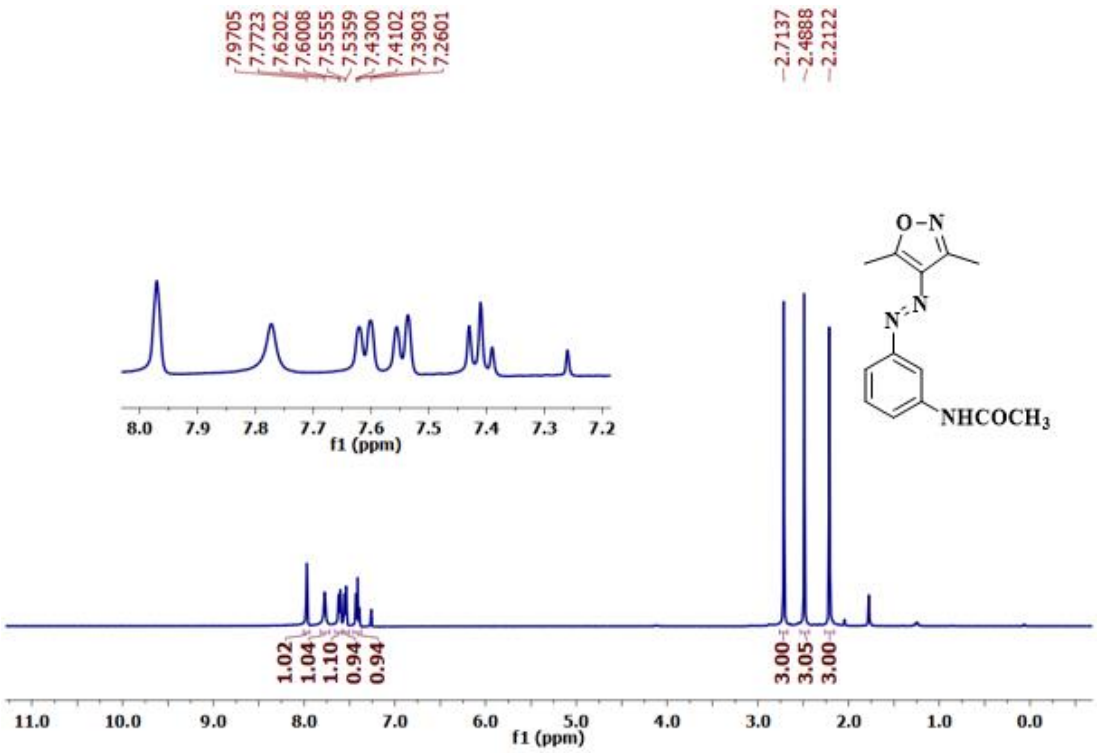

^{1}H NMR spectrum of (*E*)-*N*-(3-((3,5-dimethylisoxazol-4-yl)diazenyl)phenyl)acetamide **(23d)** in $CDCl_3$

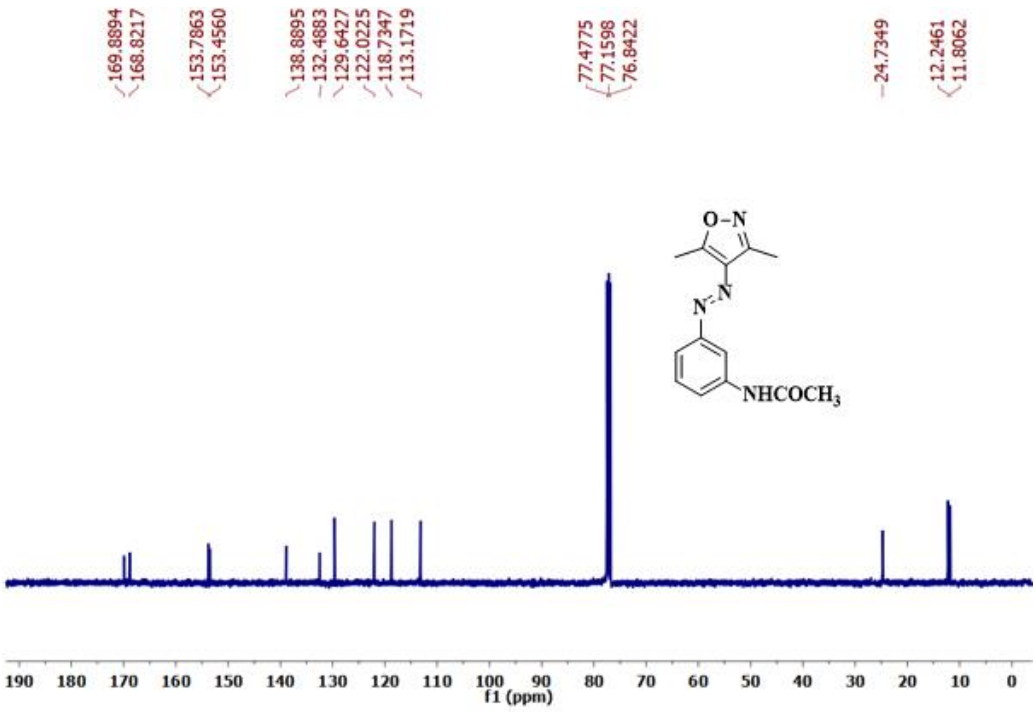

^{13}C NMR spectrum of (*E*)-*N*-(3-((3,5-dimethylisoxazol-4-yl)diazenyl)phenyl)acetamide **(23d)** in $CDCl_3$

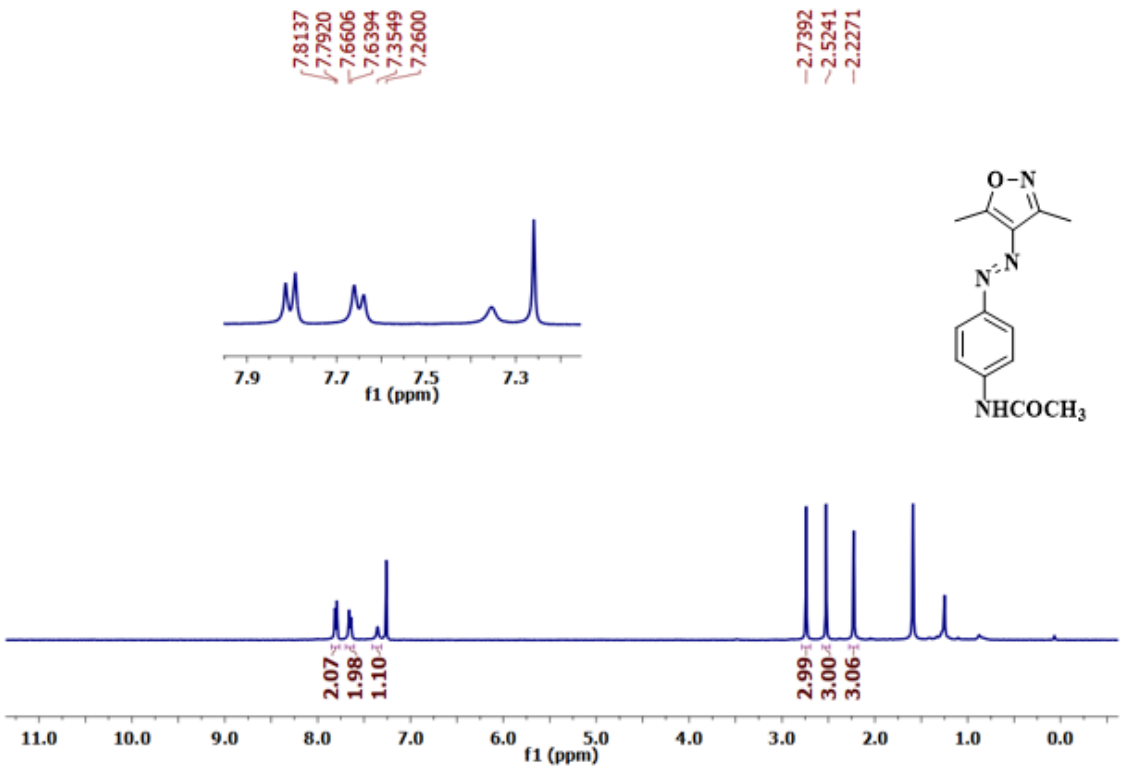

^{1}H NMR spectrum of (*E*)-*N*-(4-((3,5-dimethylisoxazol-4-yl)diazenyl)phenyl)acetamide **(24d)** in $CDCl_3$

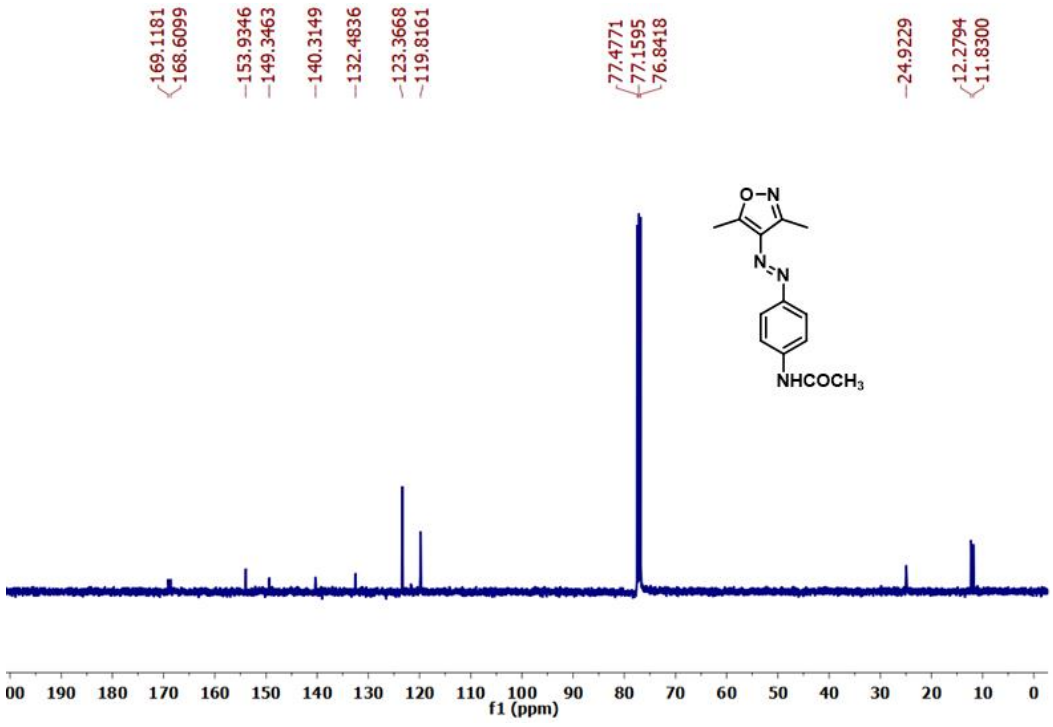

^{13}C NMR spectrum of (*E*)-*N*-(4-((3,5-dimethylisoxazol-4-yl)diazenyl)phenyl)acetamide **(24d)** in $CDCl_3$

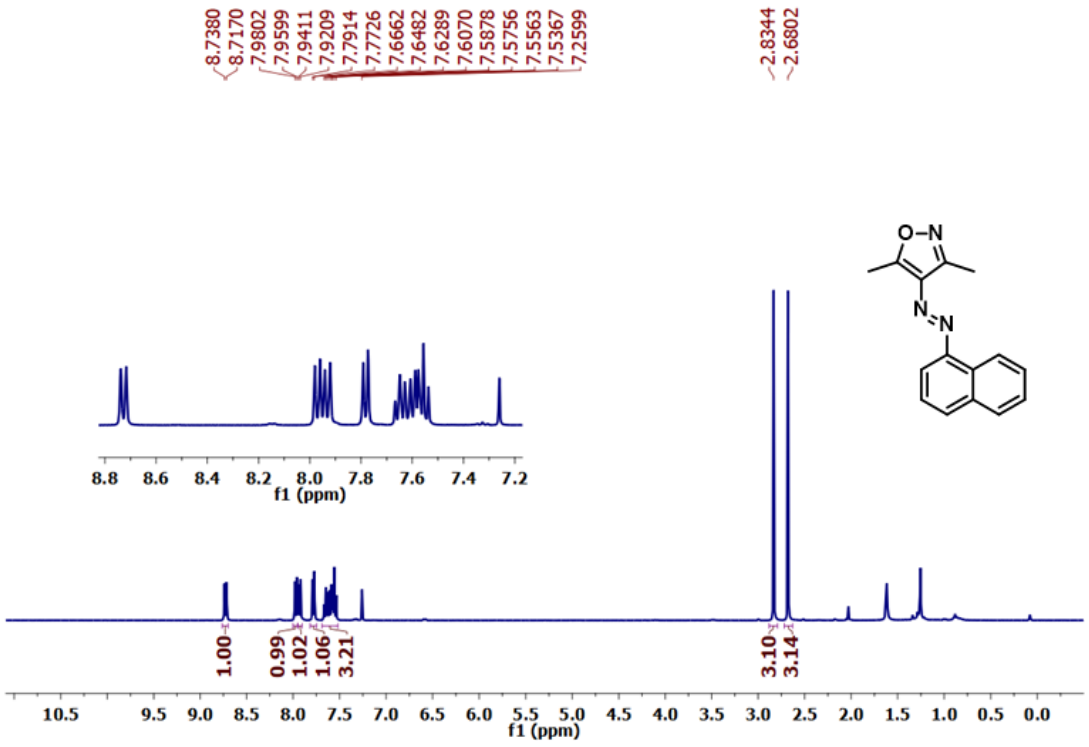

^{1}H NMR spectrum of (*E*)-3,5-dimethyl-4-(naphthalene-1-yldiazenyl)isoxazole **(25d)** in $CDCl_3$

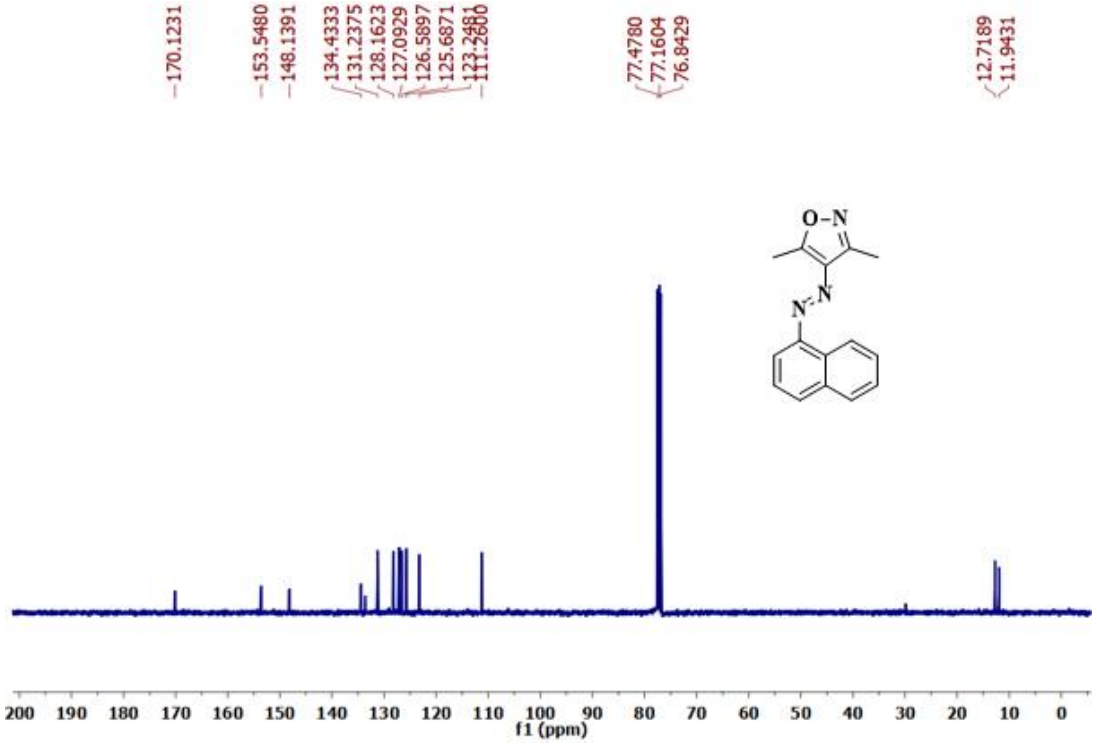

^{13}C NMR spectrum of (*E*)-3,5-dimethyl-4-(naphthalene-1-yldiazenyl)isoxazole **(25d)** in $CDCl_3$

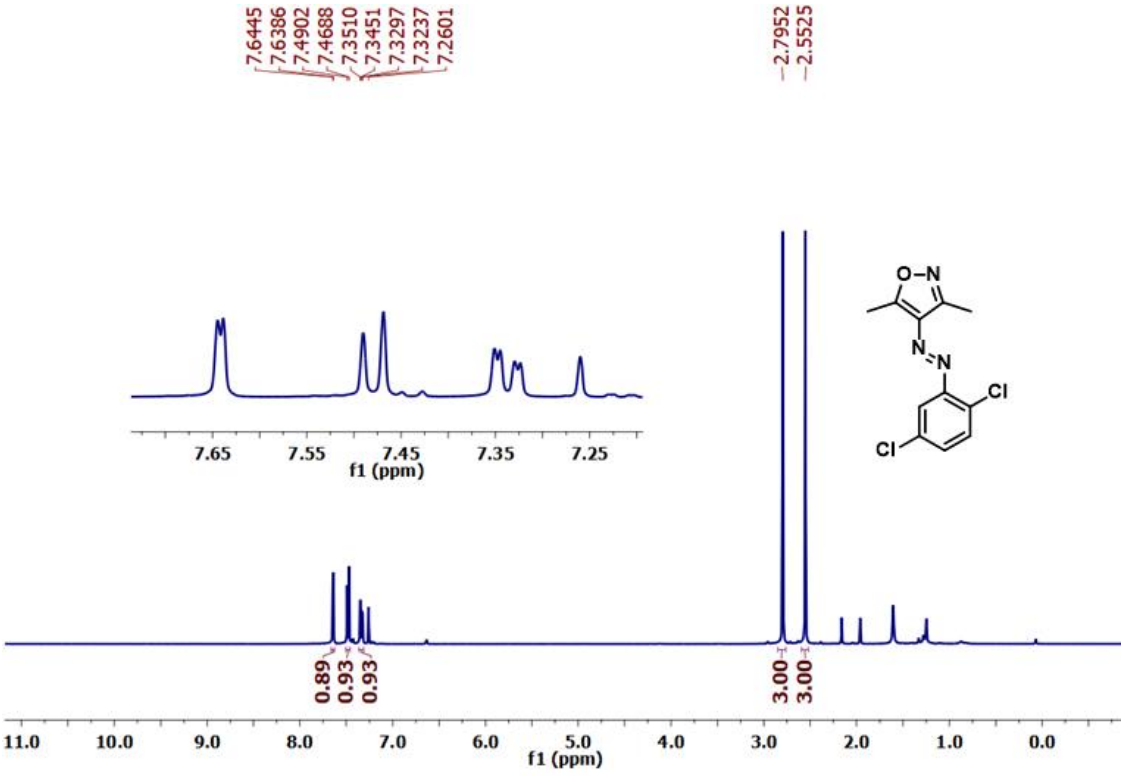

^{1}H NMR spectrum of (*E*)-4-((2,5-dichlorophenyl)diazenyl)-3,5-dimethylisoxazole **(26d)** in $CDCl_3$

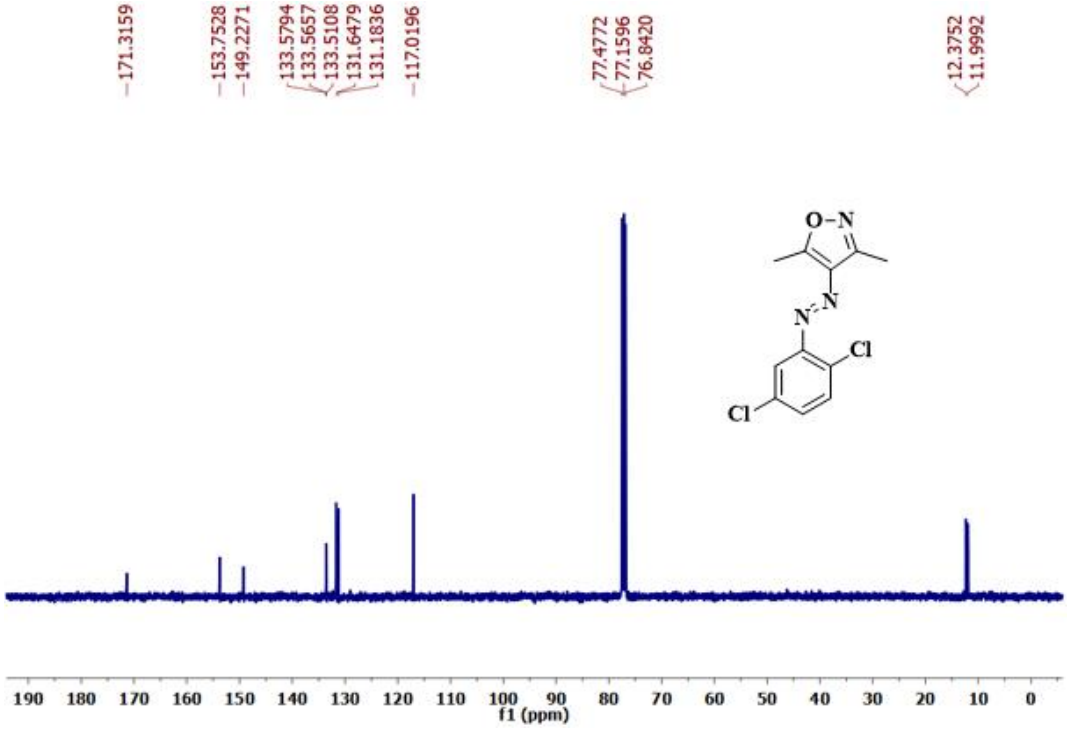

^{13}C NMR spectrum of (*E*)-4-((2,5-dichlorophenyl)diazenyl)-3,5-dimethylisoxazole **(26d)** in $CDCl_3$

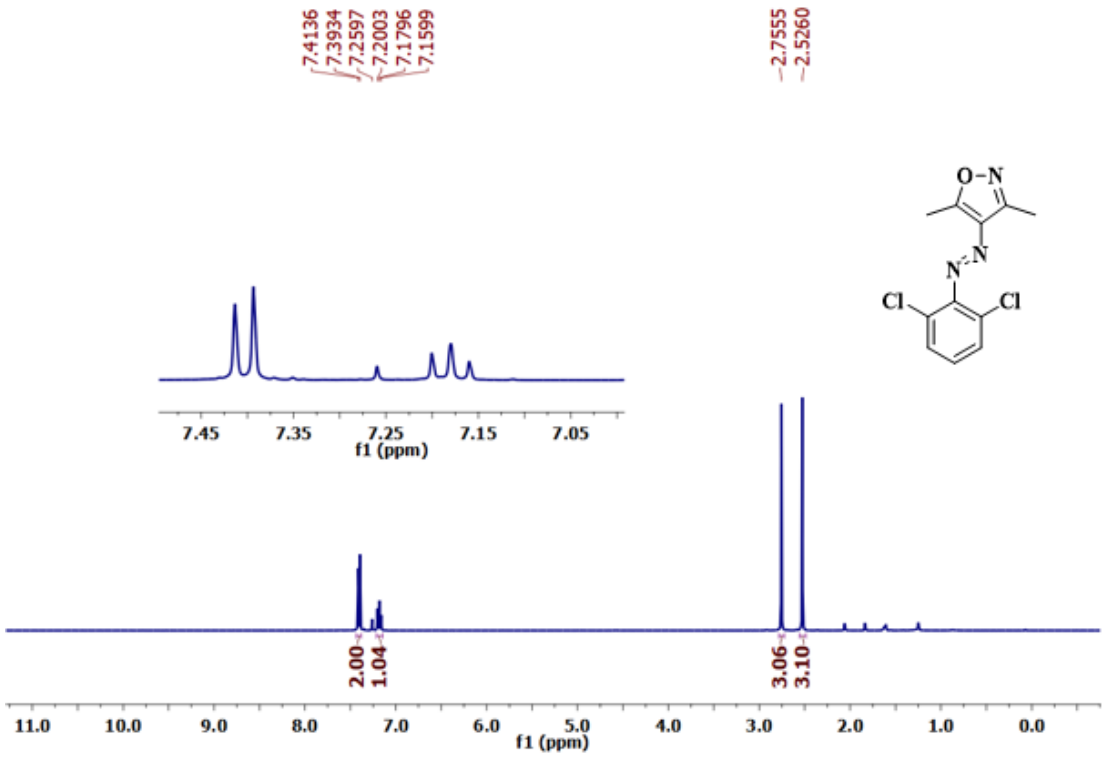

^{1}H NMR spectrum of (*E*)-4-((2,6-dichlorophenyl)diazenyl)-3,5-dimethylisoxazole **(27d)**

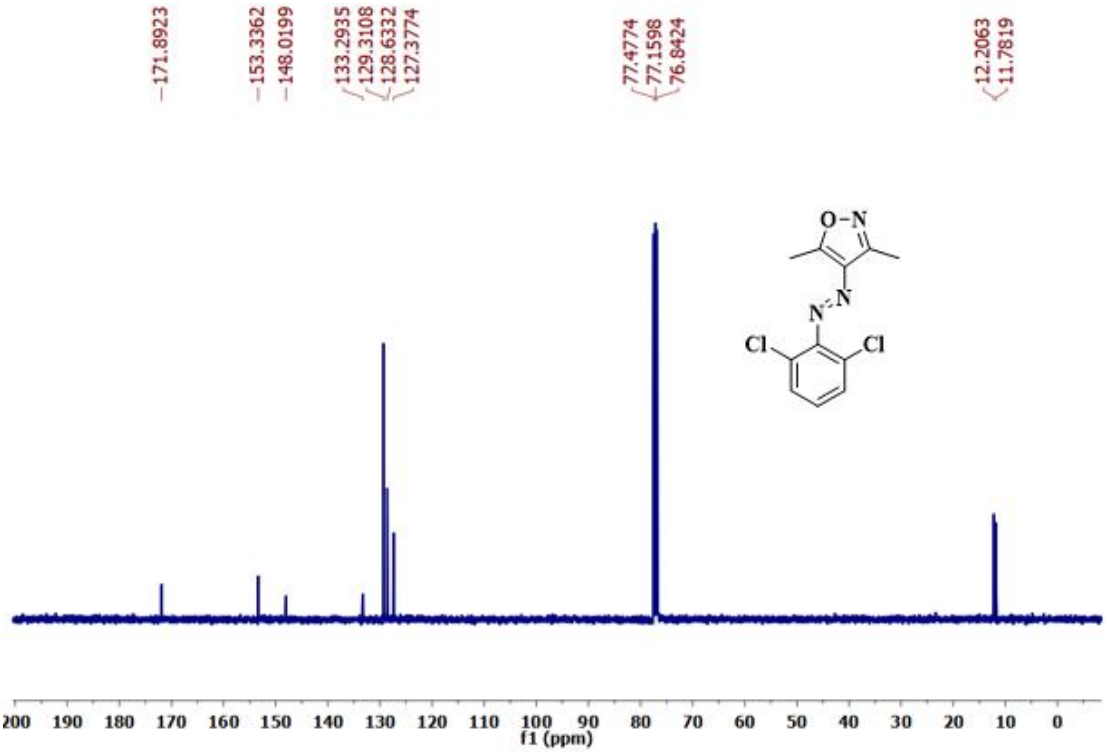

^{13}C NMR spectrum of (*E*)-4-((2,6-dichlorophenyl)diazenyl)-3,5-dimethylisoxazole **(27d)** in $CDCl_3$

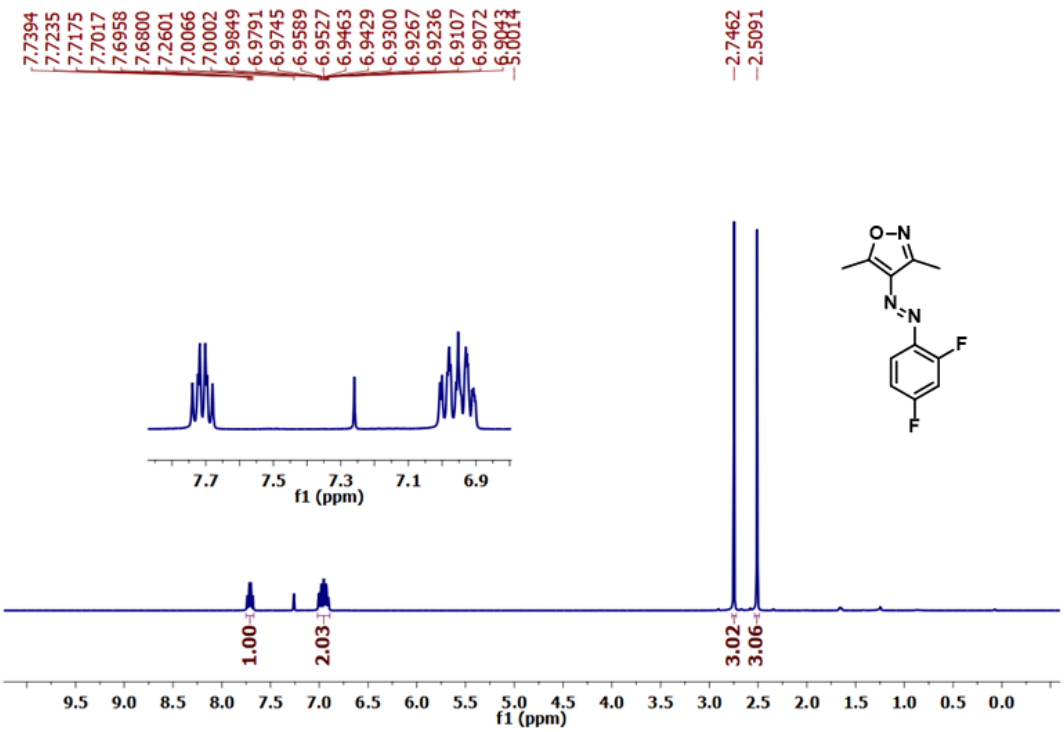

^{1}H NMR spectrum of (*E*)-4-((2,4-difluorophenyl)diazenyl)-3,5-dimethylisoxazole **(28d)** in $CDCl_3$

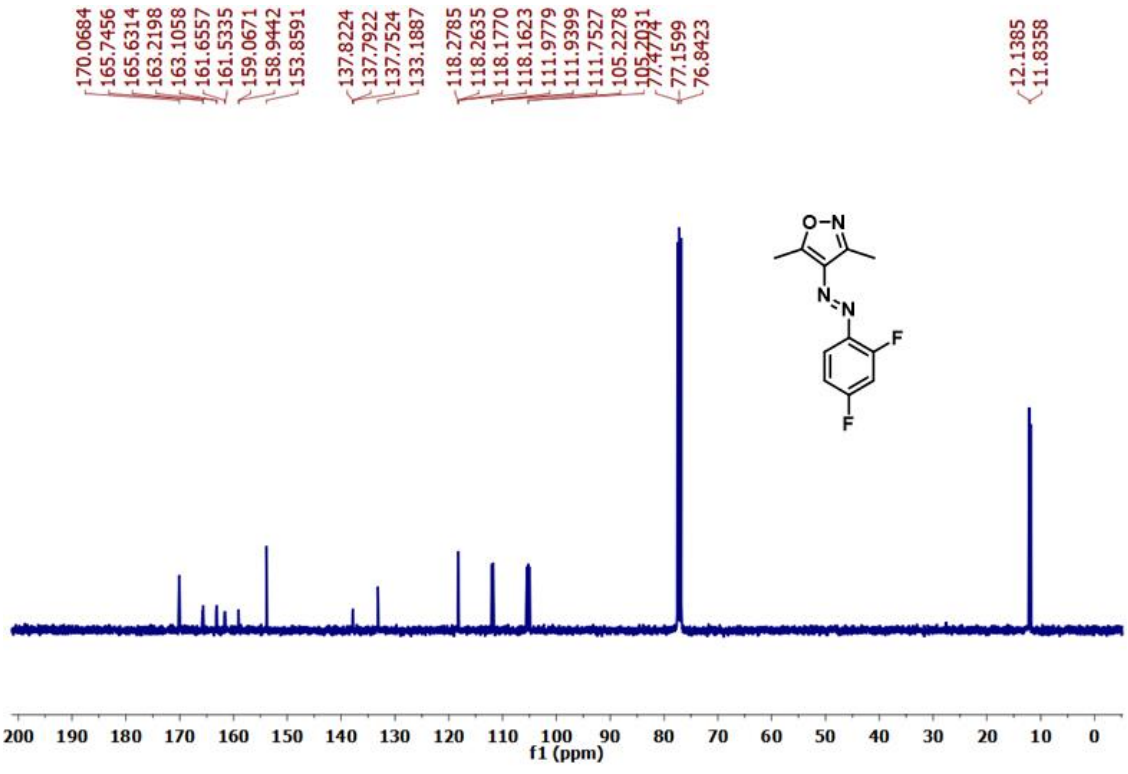

^{13}C NMR spectrum of (*E*)-4-((2,4-difluorophenyl)diazenyl)-3,5-dimethylisoxazole **(28d)** in $CDCl_3$

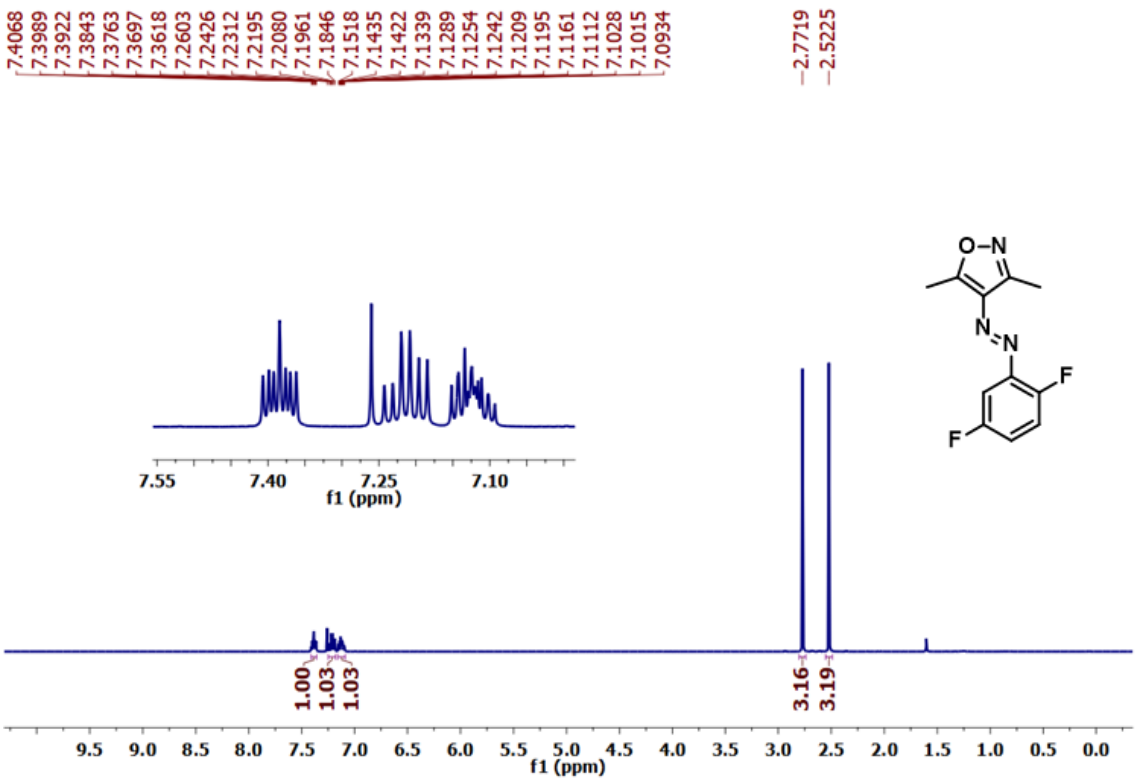

^{1}H NMR spectrum of (*E*)-4-((2,5-difluorophenyl)diazenyl)-3,5-dimethylisoxazole **(29d)** in $CDCl_3$

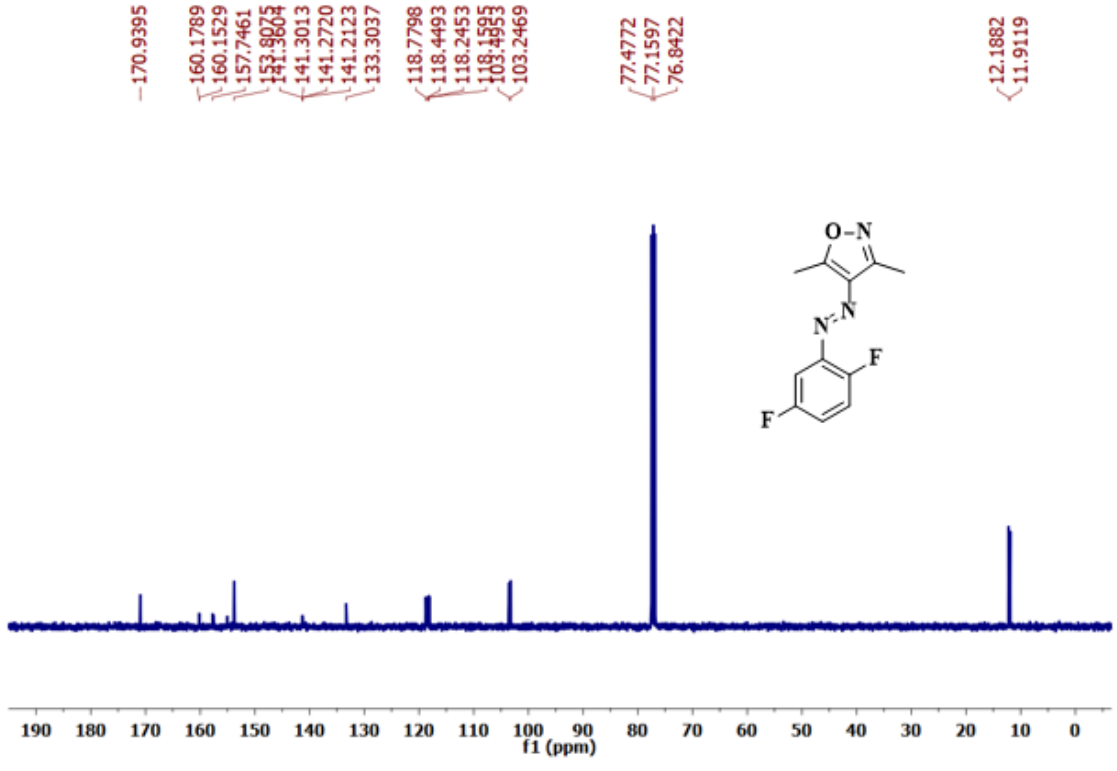

^{13}C NMR spectrum of (*E*)-4-((2,5-difluorophenyl)diazenyl)-3,5-dimethylisoxazole **(29d)** in $CDCl_3$

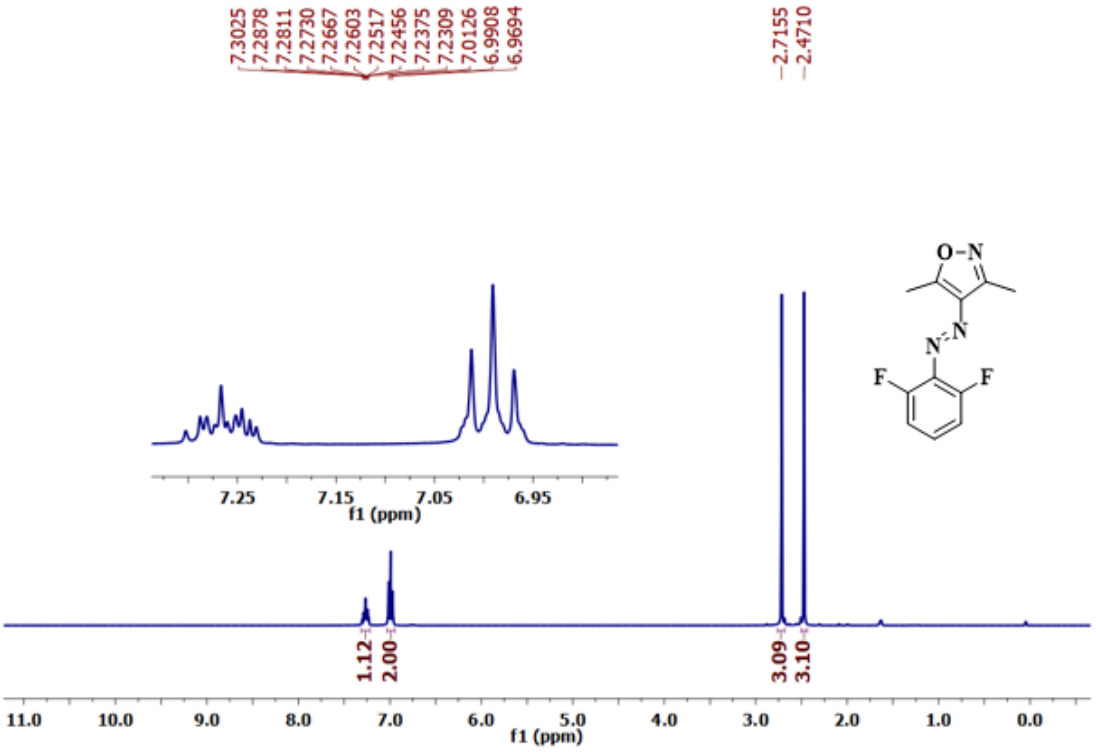

^{1}H NMR spectrum of (*E*)-4-((2,6-difluorophenyl)diazenyl)-3,5-dimethylisoxazole **(30d)** in $CDCl_3$

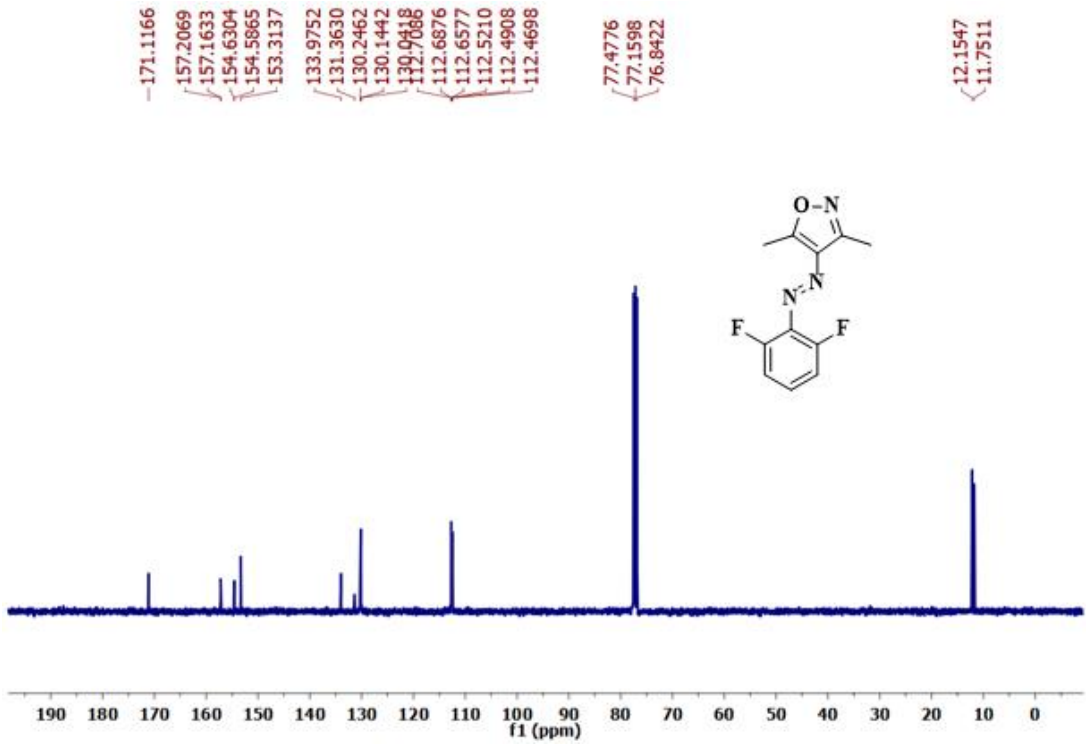

^{13}C NMR spectrum of (*E*)-4-((2,6-difluorophenyl)diazenyl)-3,5-dimethylisoxazole **(30d)** in $CDCl_3$

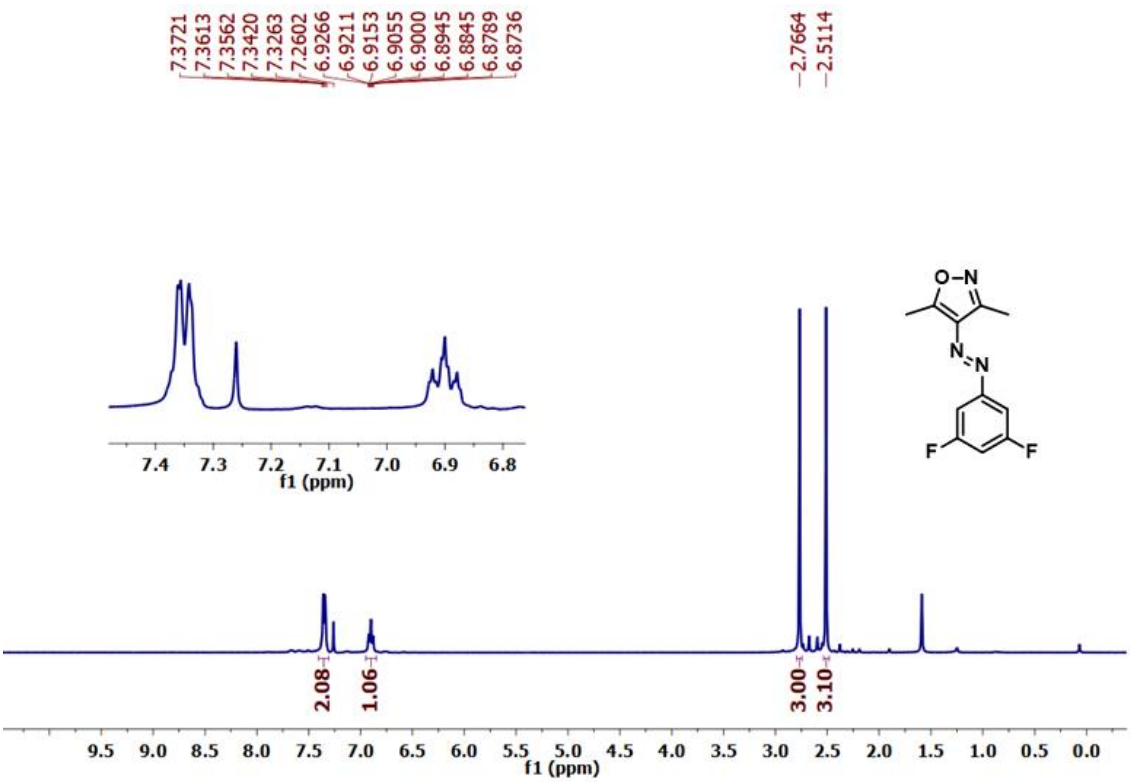

^{1}H NMR spectrum of (*E*)-4-((3,5-difluorophenyl)diazenyl)-3,5-dimethylisoxazole **(31d)** in $CDCl_3$

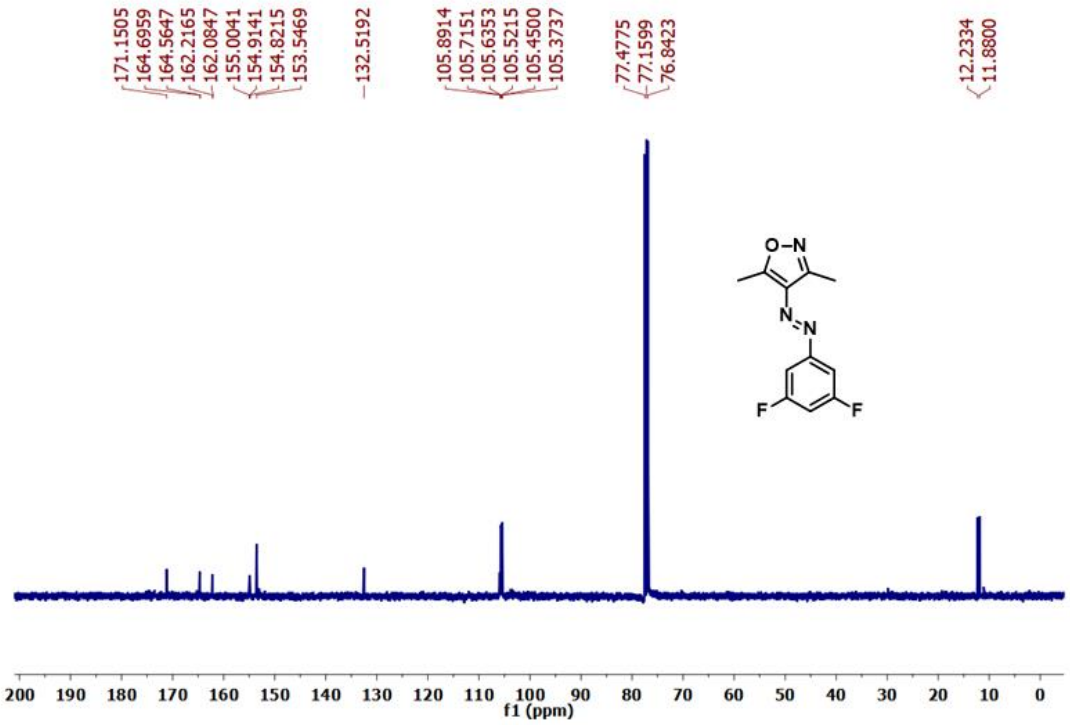

^{13}C NMR spectrum of (*E*)-4-((3,5-difluorophenyl)diazenyl)-3,5-dimethylisoxazole **(31d)** in $CDCl_3$

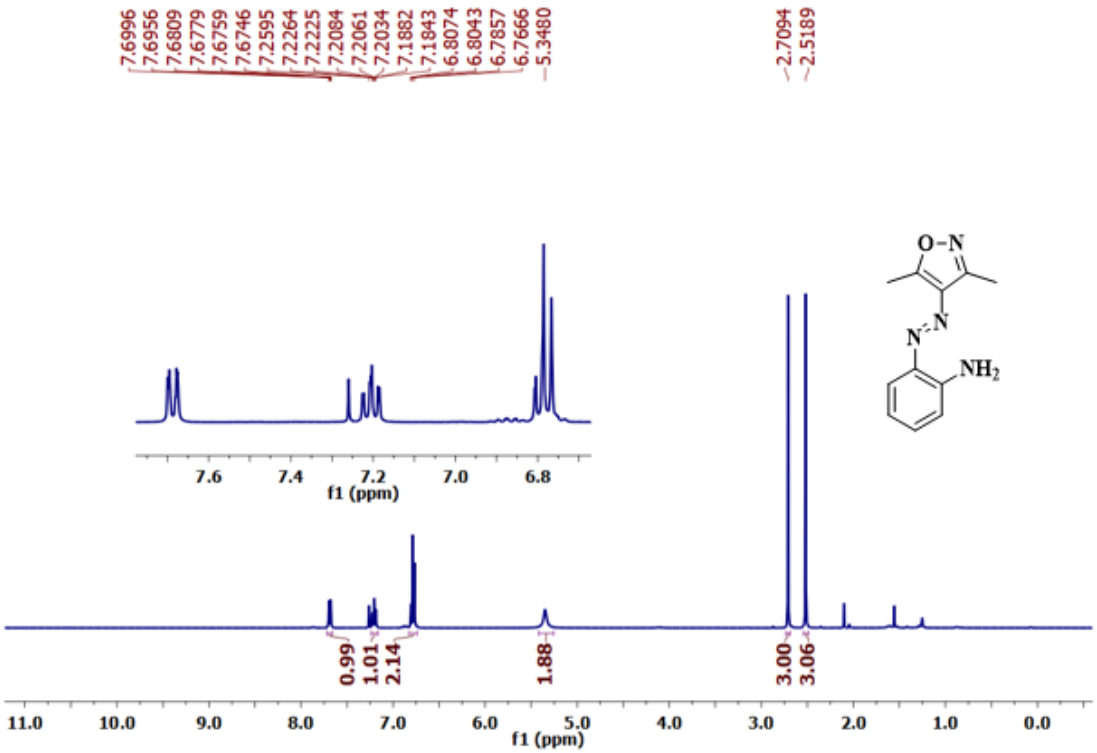

^{1}H NMR spectrum of (*E*)-2-((3,5-dimethylisoxazol-4-yl)diazenyl)aniline **(32d)** in $CDCl_3$

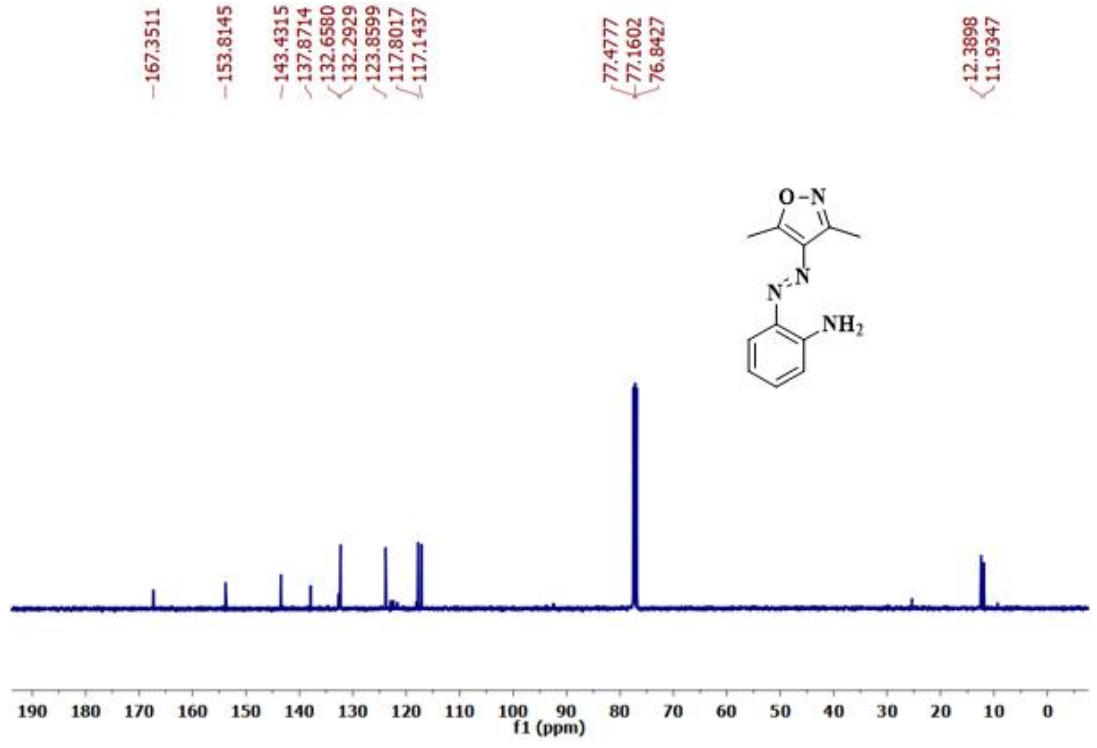

^{13}C NMR spectrum of (*E*)-2-((3,5-dimethylisoxazol-4-yl)diazenyl)aniline **(32d)** in $CDCl_3$

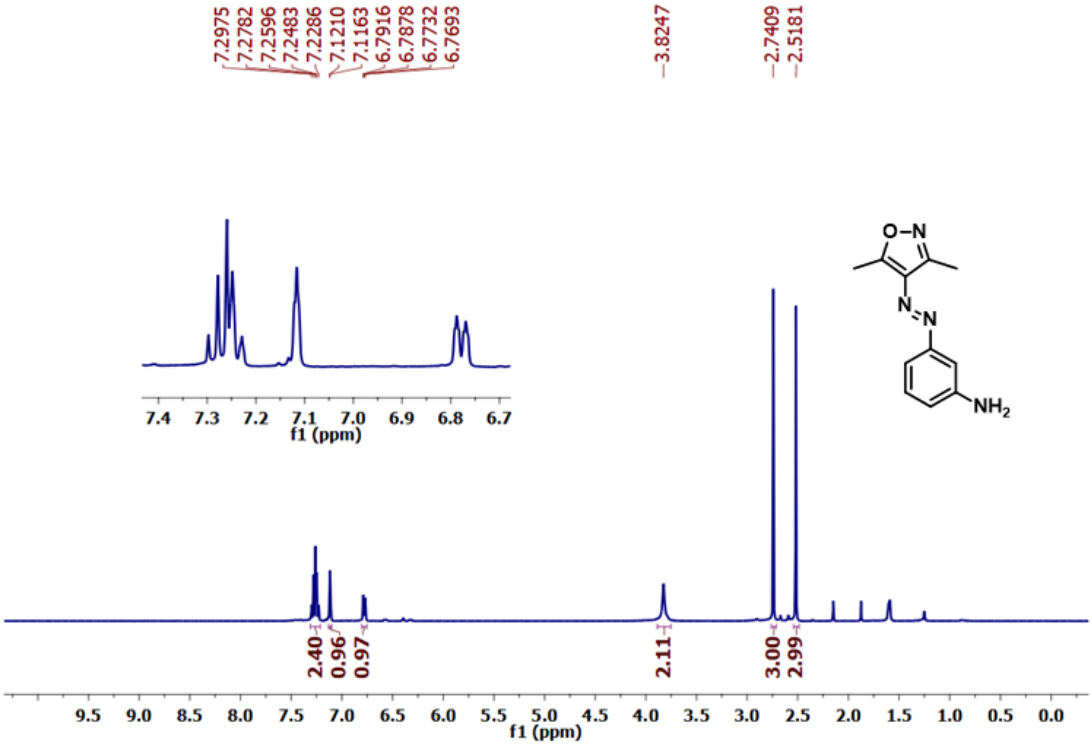

^{1}H NMR spectrum of (*E*)-3-((3,5-dimethylisoxazol-4-yl)diazenyl)aniline **(33d)** in $CDCl_3$

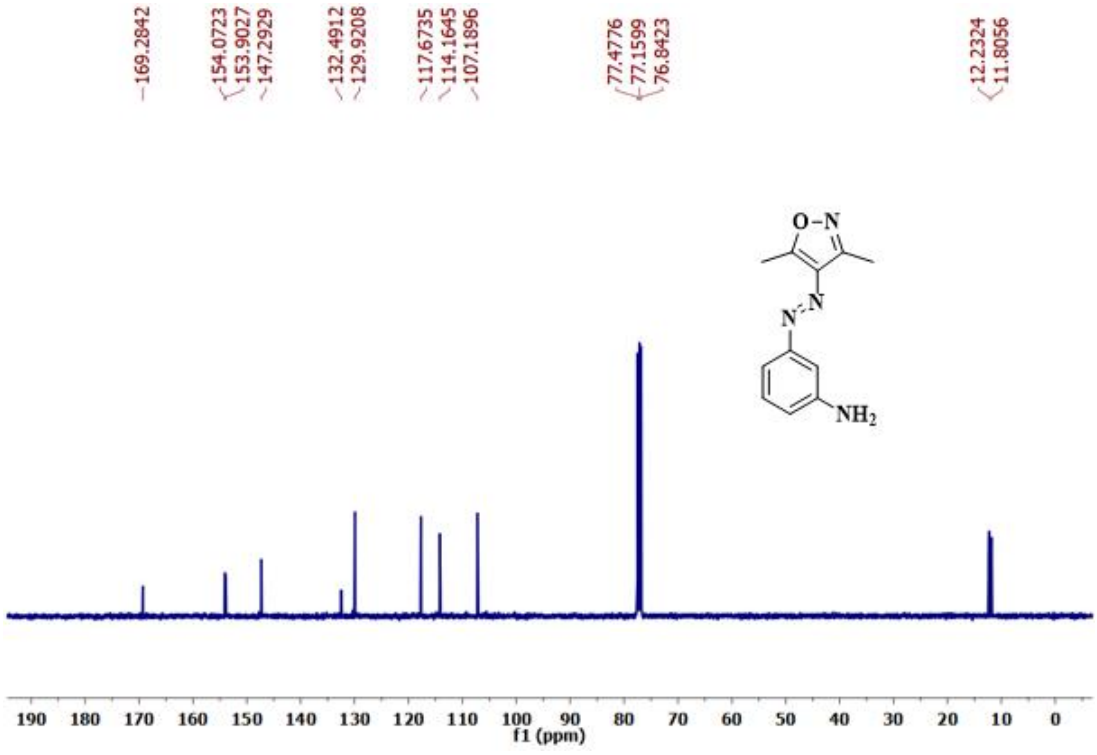

^{13}C NMR spectrum of (*E*)-3-((3,5-dimethylisoxazol-4-yl)diazenyl)aniline **(33d)** in $CDCl_3$

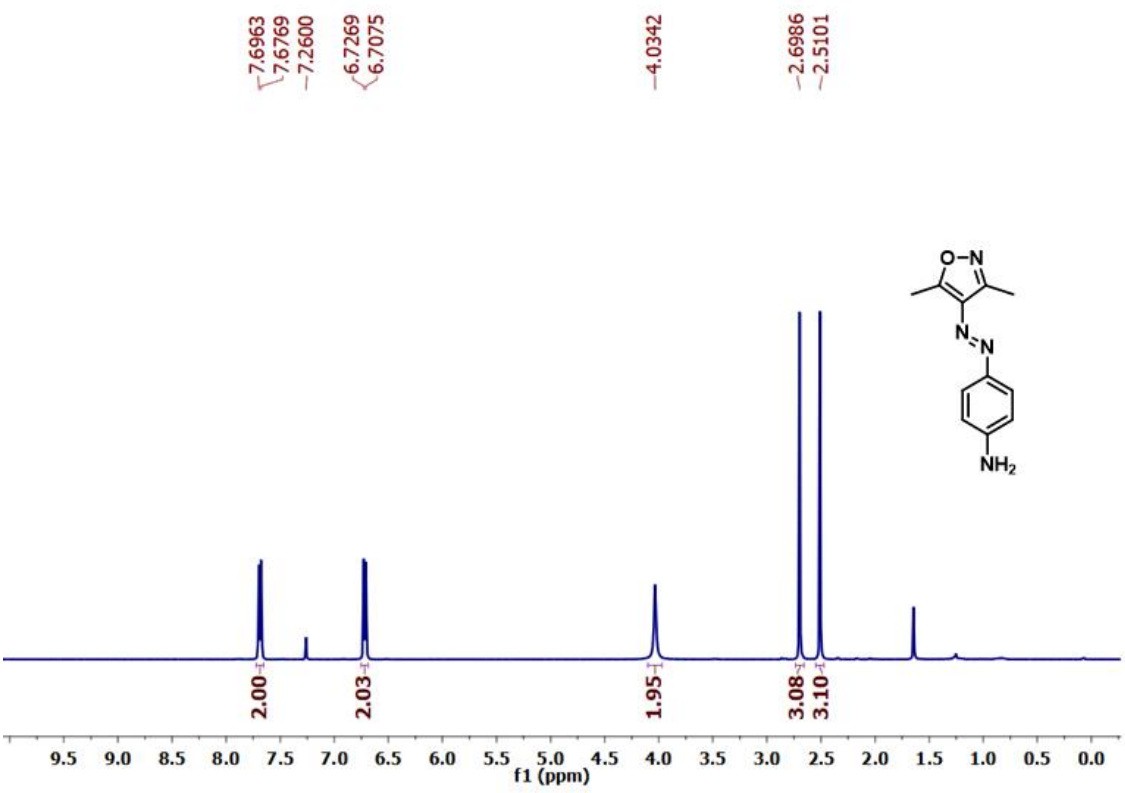

^{1}H NMR spectrum of (*E*)-4-((3,5-dimethylisoxazol-4-yl)diazenyl)aniline **(34d)** in $CDCl_3$

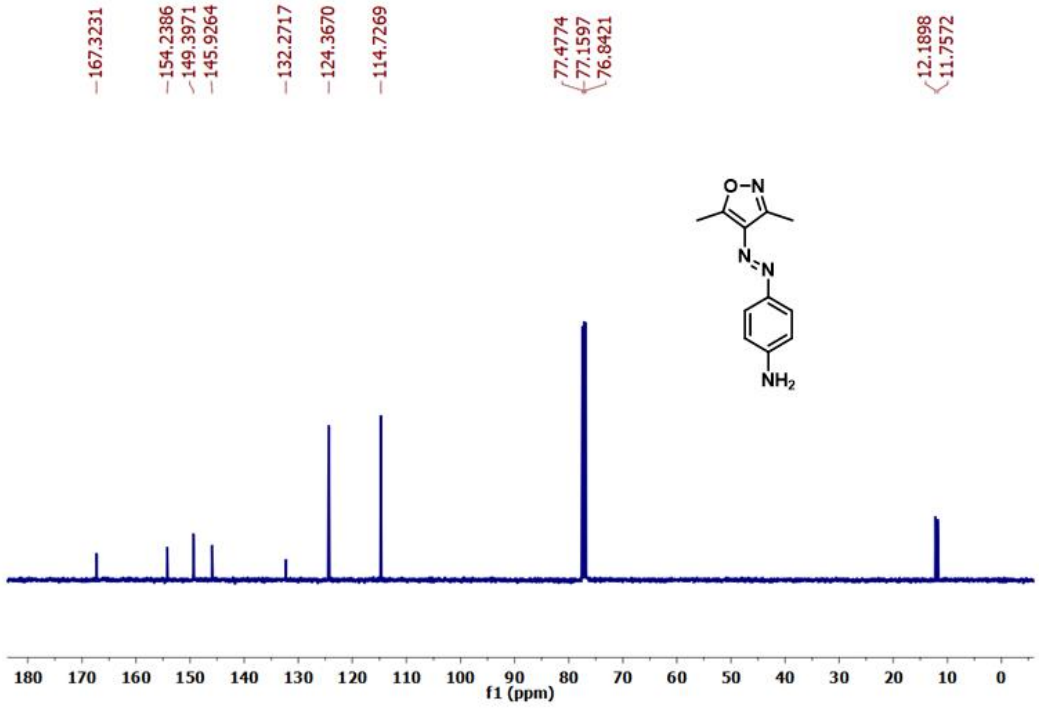

^{13}C NMR spectrum of (*E*)-4-((3,5-dimethylisoxazol-4-yl)diazenyl)aniline **(34d)** in $CDCl_3$

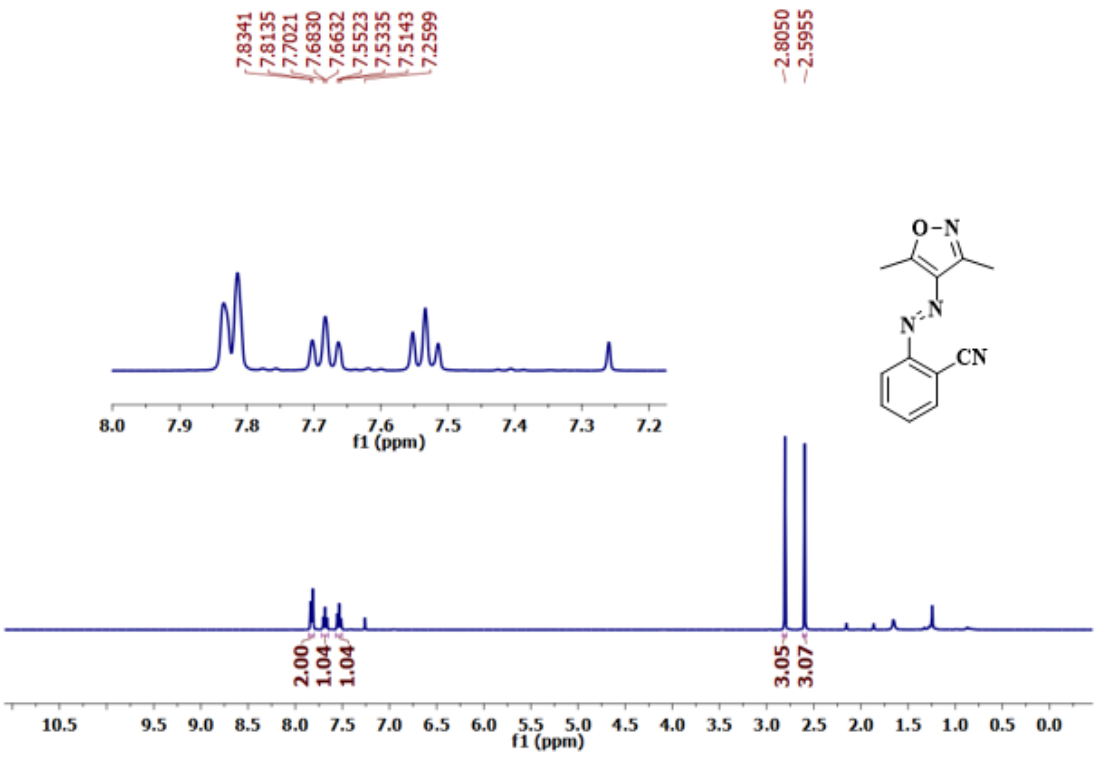

[1]H NMR spectrum of (*E*)-2-((3,5-dimethylisoxazol-4-yl)diazenyl)benzonitrile **(35d)** in $CDCl_3$

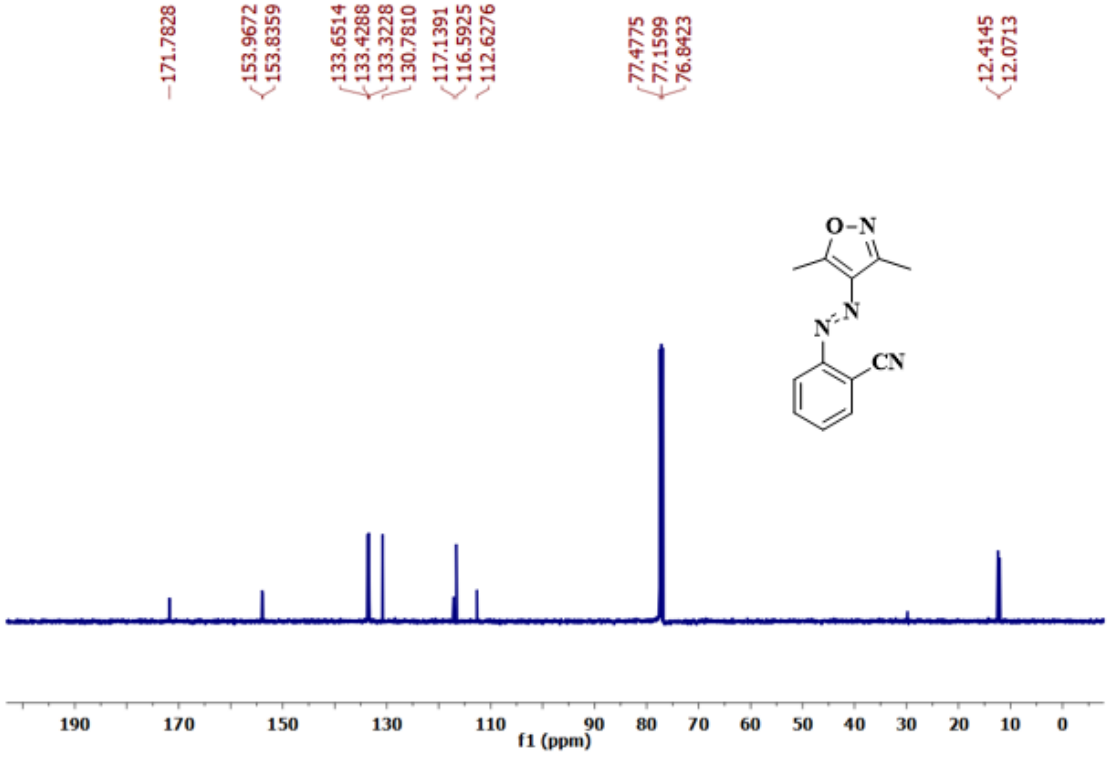

[13]C NMR spectrum of (*E*)-2-((3,5-dimethylisoxazol-4-yl)diazenyl)benzonitrile **(35d)** in $CDCl_3$

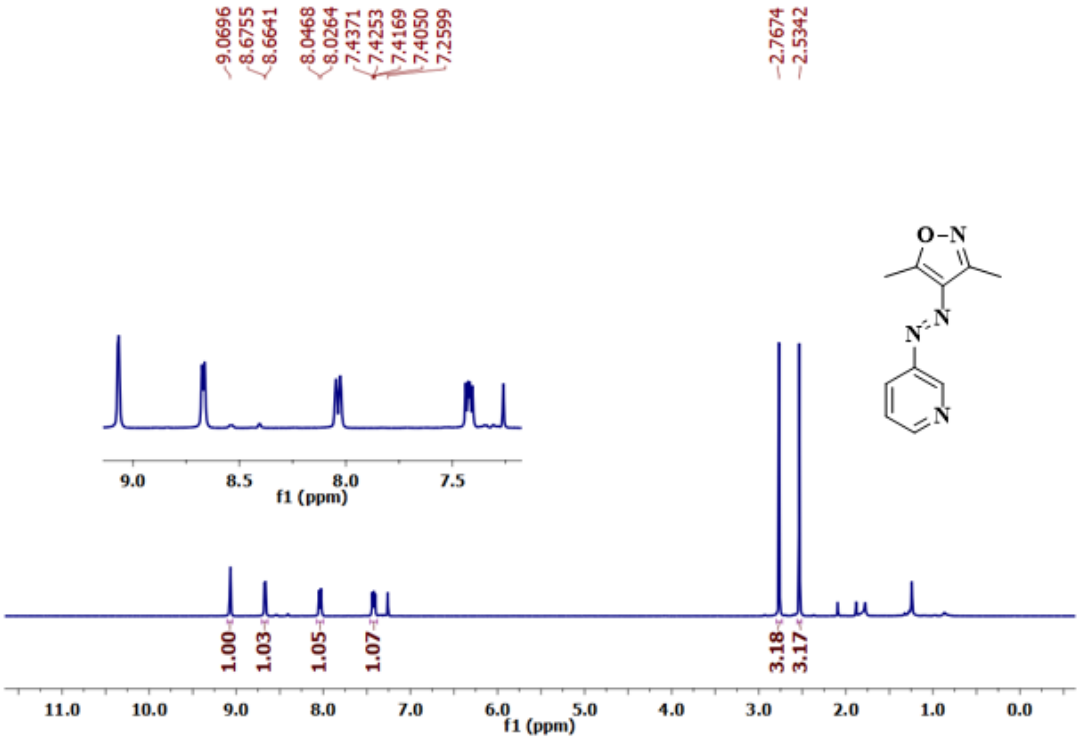

^{1}H NMR spectrum of (*E*)-3,5-dimethyl-4-(pyridin-3-yldiazenyl)isoxazole **(36d)** in $CDCl_3$

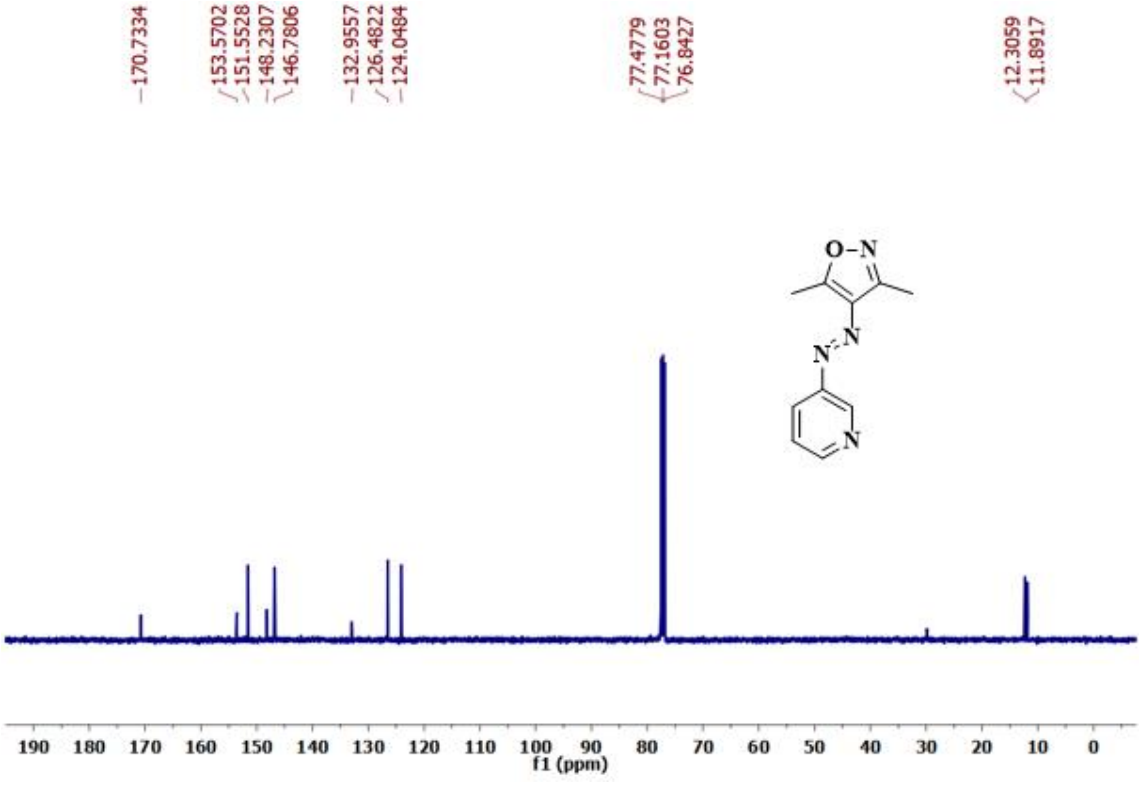

^{13}C NMR spectrum of (*E*)-3,5-dimethyl-4-(pyridin-3-yldiazenyl)isoxazole **(36d)** in $CDCl_3$

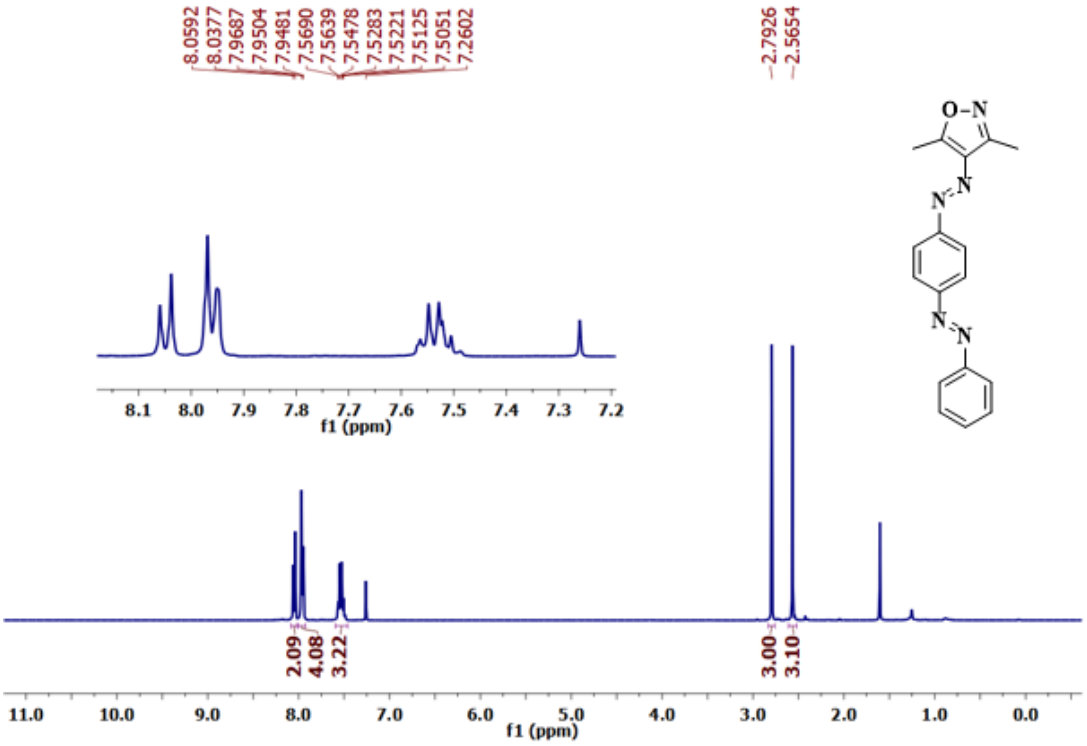

^{1}H NMR spectrum of 3,5-dimethyl-4-((*E*)-(4-((*E*)-phenyldiazenyl)phenyl)diazenyl)isoxazole **(37d)** in $CDCl_3$

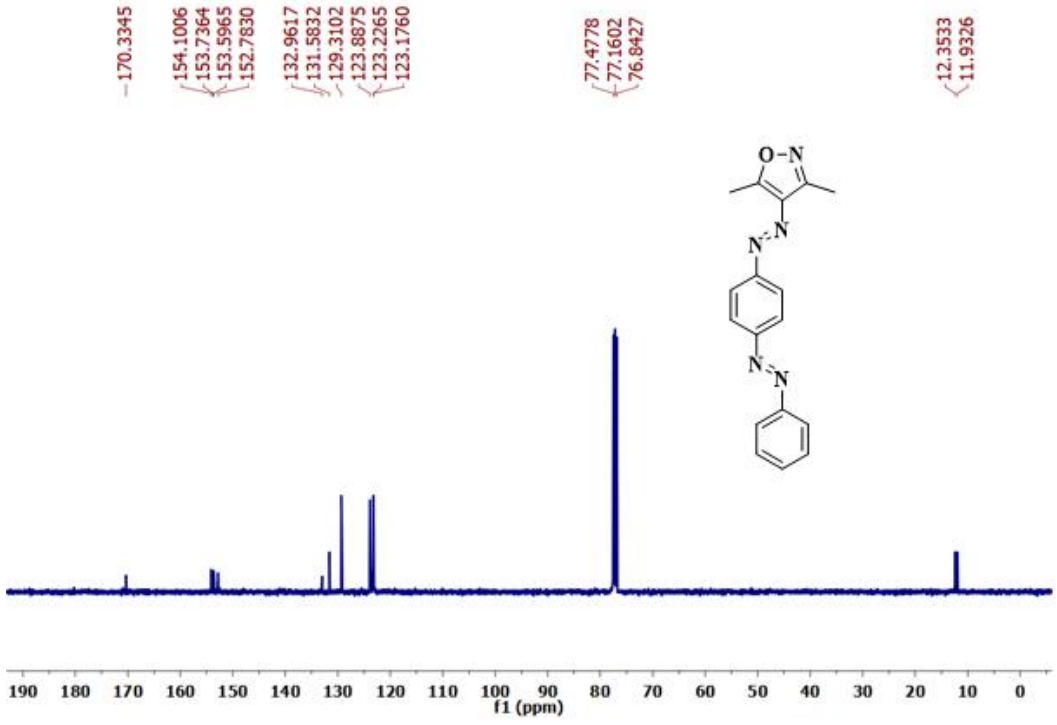

^{13}C NMR spectrum of 3,5-dimethyl-4-((*E*)-(4-((*E*)-phenyldiazenyl)phenyl)diazenyl)isoxazole **(37d)** in $CDCl_3$

Chapter 3. C_3-symmetric multiple arylazo-3,5-dimethylisoxazole incorporated benzene-1,3,5-tricarboxamides

3.1 Introduction

Recently multiazobenzene incorporated systems have gained major attention owing to their diverse properties and applications.[1] Diverse molecular designs are usually composed of a core part, spacer, or linker through which multiple azobenzenes are connected leading to various geometries or shapes such as linear,[2] branched,[3] and cyclic.[4] Among them, tripodal C_3-symmetric molecular systems have been explored extensively due to their easy synthesis, spectral simplification for spectroscopic characterization, and a variety of novel properties and applications. Molecules with more than one photoswitchable unit exist up to 2^n number of states and exhibit multiphotochromism.[1a] Another interesting feature of C_3-symmetric tripodal molecules is their unique design, where they are *meta* to each other leading to electronic decoupling between photoswitches.[3f,g] Thus, such systems have an advantage in enhanced photoswitching efficiency and reducing intermediate photoisomers. Because of their unique and programmed design, the C_3-symmetric systems can undergo self-assembly giving rise to various supramolecular architectures such as gels, LCs, etc.[5] Moreover, these supramolecular properties can be controlled reversibly by using light as a stimulus. Various attempts and approaches were utilized to improve their photoswitching efficiency and thermal properties at the molecular level. With the increasing interest in azoheteroarenes, possessing and since the literature on tripodal C_3-symmetric molecules incorporated with them are limited, we intended to utilize azoisoxazole-based photoswitches and functionalize them into C_3-symmetric designs.

Although factors controlling the multistate photoswitching are known to a reasonable extent, the corresponding knowledge in achieving bistability in the systems with two or more azo(hetero)arenes is highly desirable. Also, unraveling additional characteristics related to the multiazo(hetero)arenes such as solubility, concentration dependency, the thermal stability of the photoswitched states, photoswitching stability, wavelength of light for irradiation, etc. are equally pivotal in improving the design. However, systematic studies to establish structure-property relationships have not been carried out so far, particularly in achieving bistability and bringing applications prospects. In this regard, we have chosen six different C_3-symmetric photoswitchable systems (**Scheme 3.1**). All these target molecules have been designed in such a

way that they have the following features: (a) supramolecular assembly through hydrogen bonding and/or π–π stacking;[3c,6] (b) steric factors for disassembly through methyl groups at the linker or peripheral positions; (c) position of the azo group relative to the linker (*ortho*, *meta*, and *para*) in tuning the electronic coupling.

Through these investigations, we successfully synthesized and characterized six tripodal targets, and subjected them to extensive spectroscopic studies. Herein, we summarise the outcomes of those studies, in particular, tuning of photoswitching behavior, understanding the thermal stability of the metastable states, and potential application prospects through the factors associated with the designs.

3.2 Synthesis

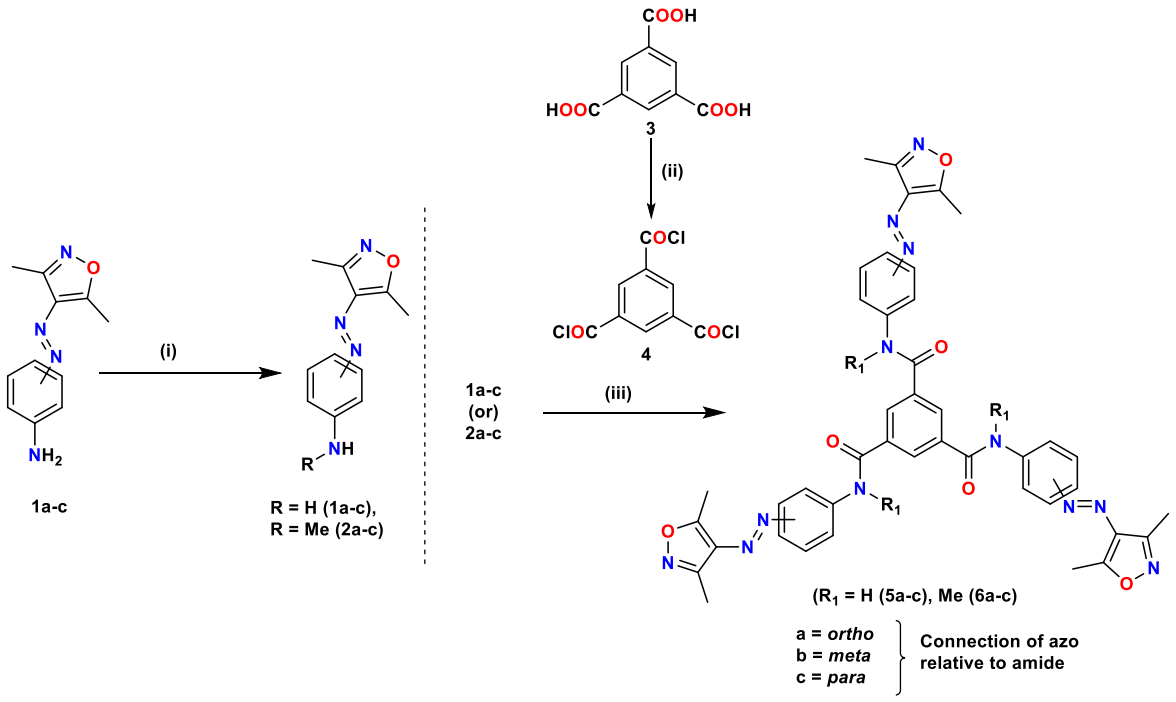

Scheme 3.1. Synthesis of the target molecules **5a-c** and **6a-c** (i) **1a-c**, HCHO, $NaCNBH_3$, MeOH, 1h, 0-5 ^oC, **2a**-67%, **2b**-75%, **2c**-85%; (ii) **3**, $SOCl_2$, cat. DMF, reflux, 4-5 h or PCl_5, toluene, reflux, 4-5 h, **4**; (iii) **4**, **1a-c**, pyridine, toluene, reflux, 4-5 h, **5a**-67%, **5b**-75%, **5c**-85%; or **4**, **2a-c**, Et_3N, DCE, rt, overnight, **6a**-33%, **6b**-68%, **6c**-20%.

We have synthesized all six tripodal targets using the procedures adopted from the literature (**Scheme 3.1**).[3c,7] For accessing the amide derivatives **5a-c** and **6a-c**, their corresponding amino 3,5-dimethylphenylazoisoxazoles (**1a-c**)[8] or the *N*-methylated amino phenylazo-3,5-dimethylisoxazoles analogs (**2a-c**)[5b] have been treated with the *in situ* generated

trimesoylchloride **4**, derived from trimesic acid **3**. All the molecules have been characterized using ^{1}H, ^{13}C-NMR, HRMS, IR, UV-vis, etc (**Experimental Section 3.9** and **Appendix 3D**).

3.3 Electronic spectral data and photochemical aspects

Foremost, we carried out UV-Vis spectroscopic studies for all the six tripodal targets **5a-c** and **6a-c**. Due to the azo chromophores, all the targets in their native state (*EEE*) exhibited strong π–π* absorption bands (**Figure 3.1a** and **Appendix 3A**). Also, the spectral data revealed that

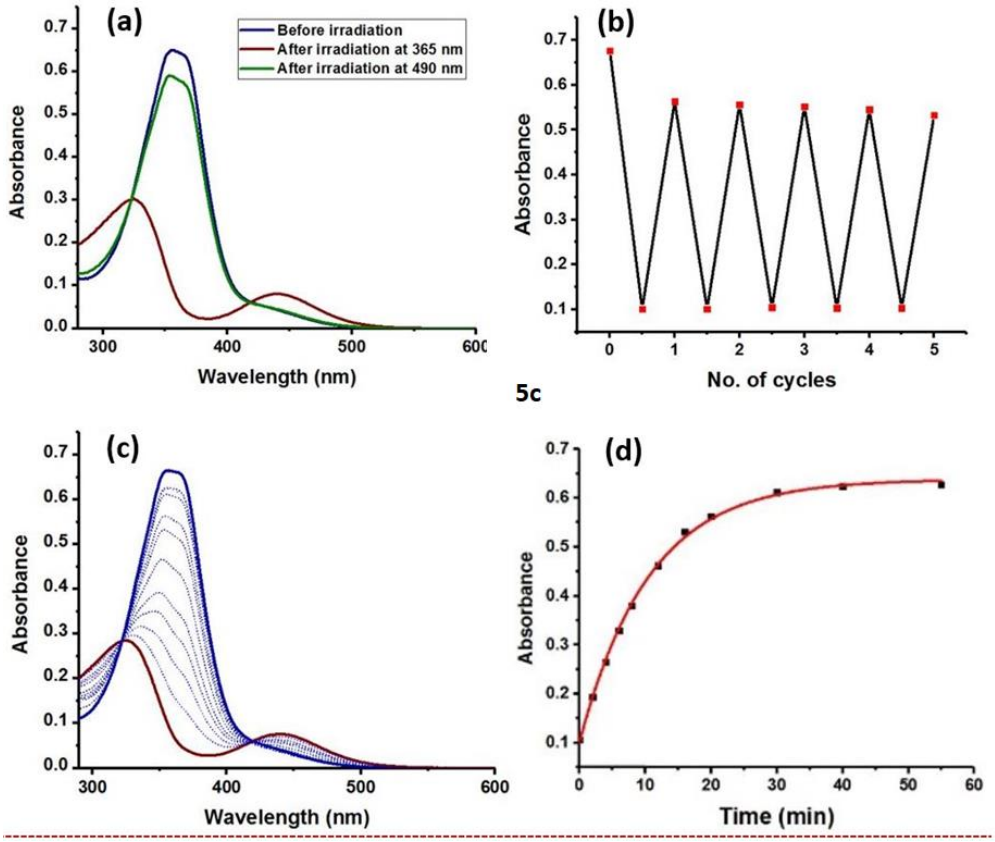

Figure 3.1. Representative data on the analysis of photoswitching in **5c**: (a) UV-Vis data depicting the wavelength-dependent photoisomerization in the forward and reverse isomerization sequence (in DMSO, 9.0 μM); (b) Photoswitching stability of **5c** over five cycles of forward and reverse isomerization indicating fatigue resistance; (c) Monitoring the thermal reverse isomerization kinetics using UV-Vis spectroscopy (in DMSO, 90 ± 2 ^{o}C); (d) The corresponding exponential growth curves of the native state.

n–π* absorption feature was silent. However, upon irradiation at 365 nm, π–π* band of *cis*-isomer was found to be blue-shifted and appeared with lower intensity, whereas the intensity of n-π* gained enhancement. The reverse *cis* to *trans* photoisomerization was performed using 490

nm light, which almost restored the native *trans* isomer, however, it was incomplete due to the attainment of PSS. Also, a significant influence on the orientation of the azo group was observed that imparts different properties to all the molecules. Apart from the contributions from the linkers through electronic effects, the shifts in the λ_{max} corresponding to the $\pi-\pi^*$ band signify the extent of π-conjugation. The targets with an azo group at a *para* position relative to the linker units have the maximum bathochromic shift, followed by *ortho* and then *meta*. Compared to benzene-1,3,5-tricarboxamide (BTA) *para* derivative **5c**, the corresponding *N*-methylated derivative **6c** render a strong blue shift in the $\pi-\pi^*$ absorption. In contrast, their *ortho* and *meta* analogs **6a,b** showed a slight red shift in the λ_{max} relative to the corresponding carboxamides **5a,b**, respectively.

Table 3.1. Absorption spectroscopic and photoswitching characteristics of the target compounds

S. No.	Compound	Electronic spectral data[a]				PSS composition (%*EEE*)[b]		
		Before switching		After photoswitching		Forward[c]	Reverse[d]	Conc. [μM]
		$\lambda_{max}/\pi-\pi^*$ (ε)	λ_{max}/ n-π^*	λ_{max}/ $\pi-\pi^*$	λ_{max}/n-π^*			
1	**5a**	322 (38273 ± 457)	-	271	432	64	70	17.3
2	**5b**	315 (48007 ± 673)	-	282	431	67	82	11.5
3	**5c**	354 (83089 ± 1077)	-	326	440	83	90	7.7
4	**6a**	325 (38419 ± 208)	-	-	440	74	90	15.3
5	**6b**	320 (45011 ± 662)	-	-	433	82	84	14.4
6	**6c**	338 (47541 ± 698)	-	303	436	81	94	11.7

[a]All the UV-Vis spectroscopic studies have been recorded in DMSO as a solvent; [b]The PSS compositions have been estimated using the literature procedure[7a]; [c]For all the forward isomerization step 365 nm LED; [d]For reverse photoisomerization wavelength of 490 nm have been used.

Interestingly, all the targets exhibited high molar absorptivity values indicating very intense π–π* absorption features (**Table 3.1** and **Appendix 3A**). Primarily this can be due to the presence of three phenylazoisoxazoles. Moreover, this trend is attributable to the substantial localization of the transitions at the azo groups. For the BTA derivatives **5a-c**, and their *N*-methylated analogs **6a-c**, the ε values have no particular dependency on the position of the azo group relative to the linker. However, in the *ortho* derivatives, the ε values were found to be lower, and similar. All the derivatives showed good to excellent photoswitching upon irradiation at 365 nm. The photoisomerization of *EEE*-isomers exhibited strong spectral changes accompanying the formation of the three potential photoisomers, *EEZ*, *EZZ*, and *ZZZ*. Since these isomeric species are indistinguishable based on absorption features, the exact composition is impossible to quantify using UV-vis spectroscopy. Apart from that, we observed an overlap of the π–π* absorption bands of the azo group with that of aromatic moieties upon photoisomerization (**Appendix 3A**). This is prominent in the cases of **6a,b**. However, in all those cases, enhancement in the intensity of the n–π* band confirmed the effective photoswitching towards *ZZZ*-isomer. For all the targets, we screened different wavelengths of light to induce the reverse isomerization step towards the native state whereby a wavelength of 490 nm was found to be suitable. Based on the observed spectral changes at their respective PSS, we have also estimated the fraction of molecules undergoing photoisomerization in the forward and reverse directions (**Table 3.1**). The method for estimation of PSS composition has been given in chapter 6. In general, the derivatives having a *para* connection (**5c** and **6c**) showed maximum photoswitching efficiency in both directions followed by *meta* (**5b** and **6b**) and then *ortho* (**5a** and **6a**) connected derivatives.

For selected derivatives **5c** and **6c**, the fatigue resistance has also been tested up to five cycles. All of them showed excellent reproducibility in the forward and reverse isomerization steps (**Figure 3A.3** and **Figure 3A.6** in **Appendix 3A**).

3.4 Quantification of photoisomers

For understanding bistability, the estimation of the individual photoisomers (PSS composition) for the forward and reverse isomerization steps is necessary. Towards this, we have conducted the photoswitching studies of all six targets in [D_6]DMSO (at mM concentration). Foremost, the wavelengths for photoswitching were optimized by following the spectral changes

in the UV-vis spectroscopic experiments, and the same wavelengths of light were used for NMR experiments. Since UV-vis spectroscopy is unable to distinguish between different photoisomers in multiazo(hetero)arene connected systems, the analysis of the PSS compositions has been carried out using ^{1}H-NMR spectroscopy (**Table 3.1** and **Appendix 3B**). For the majority of these targets, we identified a non-overlapping proton signal that can exhibit sequential shifts upon isomerization. For each system, the choice of the signal varies between core protons, methyl protons, and the *N*-H protons depending on the spectral overlap (**Table 3B.1** in **Appendix 3B)**. For photoswitching studies, a milli molar concentration sample in [D_6]DMSO solvent was used. For instance, the ^{1}H-NMR spectrum of **5c** was recorded before irradiation (**Figure 3.2**) to ensure only all-*trans*-isomer is present. Then the sample tube was irradiated at 365 nm to achieve PSS (for more details see materials and methods chapter 6). The signals corresponding to the residual *N*-H protons (*trans*-isomer) and newly appeared (*cis*-isomer) signals were integrated and normalized to give the percent composition of each isomer. The photoisomers *EEZ* and *EZZ* were present in ratios of 2:1 or 1:2 respectively at PSS. The signals of various photoisomers were also identified based on their shielding and deshielding effects. Similarly, reverse photoisomerization was performed using 490 nm light until a PSS is attained. Under this step, signals corresponding to the original all *trans*-isomer (*EEE*) regained in intensity along with other minor photoisomers, and integration of these signals gives the percent composition of photoisomers in PSS (**Figure 3.2**). The broadness and overlapping signals in **6a** hindered the quantification of the photoisomers, whereas the solubility issues in the reverse isomerization step did not allow us to estimate the PSS compositions in **5a**. Indeed, **6a** exhibited rotamers with many overlapping signals (**Figure 3B.4** in **Appendix 3B**).[9] In the case of **6b** and **6c,** we have chosen methyl protons of isoxazole. The individual photoisomers have been confirmed by following the kinetics of reverse photoisomerization in **6c** (**Figure 3B.7** in **Appendix 3B**). Among the systems for which we have obtained the PSS composition in the forward direction, **5c** and **6c** showed a maximum conversion of *ZZZ* isomers in the range of 82-91% (**Table 3.2**). Concerning the position of the azo group, the systems with *para* connections exhibited excellent isomerization conversions followed by *meta* connections. Comparatively the systems with *ortho* connections showed only a moderate isomerization.

Presumably, the longer wavelength π–π^* absorption and extended conjugation play a vital role in the effective forward isomerization of *para* derivatives. The converse holds for the

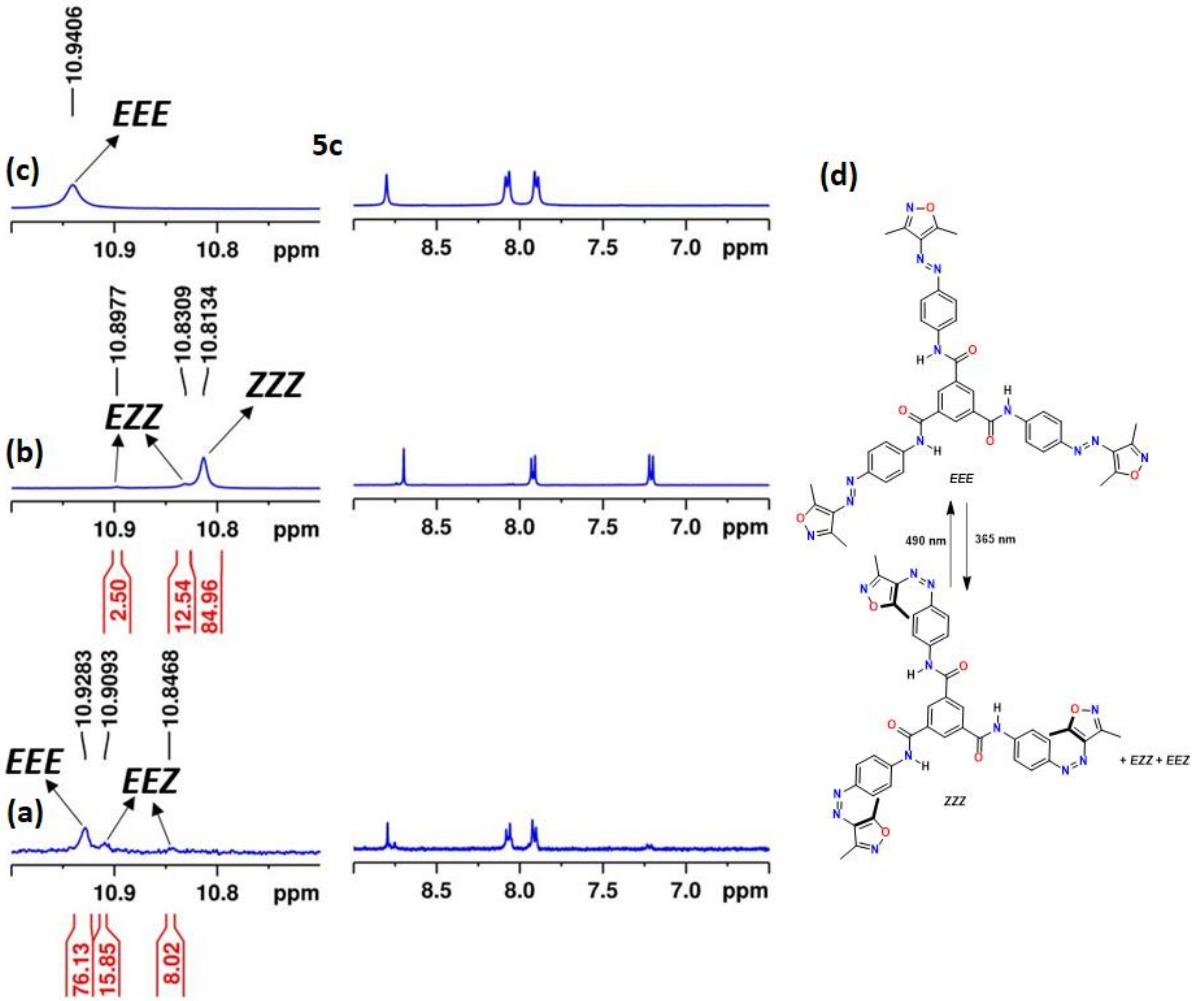

Figure 3.2. Representative data on the analysis of photoswitching in **5c**: (a) ^{1}H-NMR spectral analysis for the estimation of PSS compositions in forward and reverse isomerization (regions showing amide and aromatic region, in [D_6]DMSO, 2.26 mM): (a) before irradiation (*EEE*-isomer); (b) after irradiation at 365 nm/forward isomerization; (c) after irradiation at 490 nm/reverse isomerization (The individual photoisomers of the **5c** are indicated; poor solubility causes the low signal to noise ratio in "c"); (d) isomerization scheme indicating the structures of all individual isomers of **5c** (*EEE*, *EEZ*, *EZZ*, and *ZZZ*).

meta derivatives, and so exhibits slightly lower conversions, whereas, the tautomerism or steric effects are attributed to the poor isomerization conversions in the cases of *ortho* derivatives.[11] The *N*-methylation in the BTA derivatives influences the forward photoswitching only to a marginal extent in the cases of **6a-c**. Likewise, the estimation of PSS compositions in the reverse isomerization step revealed **5c** and **6c** as the best photoswitchable systems; however, they exhibit a moderate isomerization conversion towards the native *EEE*-isomers. Overall, **5c** and **6c** can be

Table 3.2. Estimation of PSS composition for forward and reverse isomerization steps of the selected targets using ^{1}H-NMR spectroscopy

S. No.	Compound	Conc. (mM)	λ (nm)	%Composition of individual isomers at PSS[a] ([D$_6$]DMSO)			
				EEE	***EEZ***	***EZZ***	***ZZZ***
1.	**5a**[c,d]	1.98	365	-	-	26	74
			490	[f]	[f]	[f]	[f]
2.	**5b**[b]	2.48	365	-	-	18	82
			490	41	43	16	-
3.	**5c**[b]	2.26	365	-	3	12	85
			490	76*	24	-	-
4.	**6b**[e]	7.79	365	-	-	25	75
			490	49	36	13	2
5.	**6c**[e]	4.16	365	-	-	10	90
			490	57	34	8	1

[a]Determined by using the normalized integral values of the signals corresponding to the four photoisomers based on the following protons: [b]Amide *N*-H, [c]Solubility increased after irradiation at 365 nm, [d]Benzene core-H, [e]Isoxazole-CH_3, Wavelength of irradiation: normal—forward; bold—reverse isomerization step (*poor solubility causes lower %*EEE*-isomer in the reverse isomerization step than actual), [f]Precipitates upon irradiation at 490 nm.

the best tripodal photoswitches in both forward and reverse directions, if *EEZ*-isomer is also taken into account for the quantification. The weak n-π* absorption features of the native state limit the complete reverse isomerization under irradiation conditions.

3.5 Solubility and concentration dependency in forward photoisomerization step

Solubility is a crucial parameter for the solution processing of the molecules for various applications and device fabrication. The majority of the targets were found to have reasonable solubility in different solvents. However, we observed the solubility issues in the cases of BTA derivatives with the azo groups attached at the *ortho* position relative to the linkers. In contrast, we observed better solubility for those systems with azo groups connected at *meta* or *para* positions. In general, the *N*-methylation of the carboxamide groups further enhances the solubility. Interestingly, in the cases of **5a** and **5c**, irradiation at 365 nm (forward

photoisomerization) improved the solubility, and on irradiating the solution enriched with the photoisomers at 490 nm induced precipitation.

Table 3.3. Concentration dependency in the photoswitching (forward isomerization step) in the selected target systems through PSS composition

S. No.	Compound	Conc. (mM)	λ (nm)	%Composition of individual isomers at PSS[a]			
				EEE	***EEZ***	***EZZ***	***ZZZ***
1		1.39		-	-	15	85
2		2.78		-	-	15	85
3	**5c**	4.16	365	-	-	15	85
4		6.94		-	-	15	85
5		11.1		-	-	16	84
6		1.39		-	2	9	89
7		2.78		-	2	9	89
8	**6c**	4.16	365	-	2	9	89
9		6.94		-	2	9	89
10		11.1		-	2	9	89

[a]PSS compositions have been measured at different concentrations of the samples after irradiation at 365 nm (until the PSS is attained) and the measurements were done using a ^{1}H-NMR spectrometer in [D_6]DMSO.

Selected targets **5c** and **6c** (those with azo groups connected at *para*-position) were tested for concentration dependency in the forward photoisomerization step, which showed no or negligible dependency upon varying the concentration up to 10 times. Indeed, Thiele's and Kim's group reported the importance of the concentrations in photoswitching efficiency. The possible supramolecular assembly through hydrogen bonding and π–π stacking has been accounted for limiting the isomerization conversions.[3c,5a,6d,e] Since the supramolecular interactions and assemblies can be hindered through the methyl groups, the derivatives such as **5c** and **6c**, did not show any effect of concentration on the forward isomerization conversions (**Table 3.3** and **Appendix 3C**). Notably, **5c** exhibited no concentration-dependent photoswitching, albeit possessing a BTA core, the moiety capable of forming supramolecular assembly through hydrogen bonding. Probably, the presence of two peripheral methyl groups in the isoxazole moiety either hinders the stacking or induces a weak assembly.

3.6 Thermal stability

Table 3.4. Kinetics data[a]

S. No.	Compound	Temp. (^{o}C)	Rate constant (min^{-1})	Half-life (min)	Conc. [μM]
1	**5a**	90 ± 2	$6.1x10^{-2} \pm 2.7x10^{-3}$	11	15.7
2	**5b**	90 ± 2	$2.7x10^{-2} \pm 6.8x10^{-4}$	26	13.0
3	**5c**	90 ± 2	$9.4x10^{-2} \pm 2.9x10^{-3}$	7	9.0
4	**6a**	90 ± 2	$6.6x10^{-2} \pm 4.6x10^{-3}$	11	17.9
5	**6b**	90 ± 2	$2.9x10^{-2} \pm 8.1x10^{-4}$	24	14.5
6	**6c**	90 ± 2	$4.8x10^{-2} \pm 1.1x10^{-3}$	14	13.7

[a]Rate constants and half-lives corresponding to the overall formation of *EEE*-isomer in each case, which was followed by UV-Vis spectroscopy in DMSO at the specified temperature;

To compare the thermal stability of the metastable states in all six targets, we have deduced the first-order formation constants of the native *EEE*-isomer from their respective photoswitched states. In this regard, we utilized UV-Vis spectroscopy and monitored the changes in the absorption corresponding to the λ_{max} of the π–π* band. Using the exponential growth of the *EEE*-isomer, we estimated the rate constants, and the half-life (**Table 3.4** and **Appendix 3A**). Indeed, all the derivatives exhibit higher thermal stability for the photoswitched states at room temperature, and so the isomerization rates were very slow. Hence, we performed the kinetics experiments at elevated temperatures. Interestingly, the rate constants measured by UV-Vis (overall formation rate constant) and ^{1}H-NMR spectroscopy (the average of normalized rate constants[2a,3d] of the individual steps) for **1b** (5.8×10^{-2} vs 8.3×10^{-2} min^{-1}) and **1c** (1.9×10^{-2} vs 2.6×10^{-2} min^{-1}) are quite comparable and exhibited a narrow difference.[10] This makes the comparison of the overall formation rates of the other targets quite useful in understanding the trends and also the influence of the design part on the thermal stability of the metastable states.

Based on the data, we observed that the systems with *meta* connections **(5b** and **6b)** of the azo groups relative to the linker units have longer half-lives and higher thermal stability of the photoswitched states (**Table 3.4**). In contrast, those with *ortho* (**5a** and **6a**) and *para* (**5c** and

6c) connections have lower half-lives. The thermal stability of the photoswitched states follows the order: *meta* > *ortho* > *para* in **5a-c** and *meta* > *para* > *ortho* after incorporation of *N*-methylation at the amide nitrogen in **6a-c** (**Table 3.4**).

3.7 Supramolecular studies

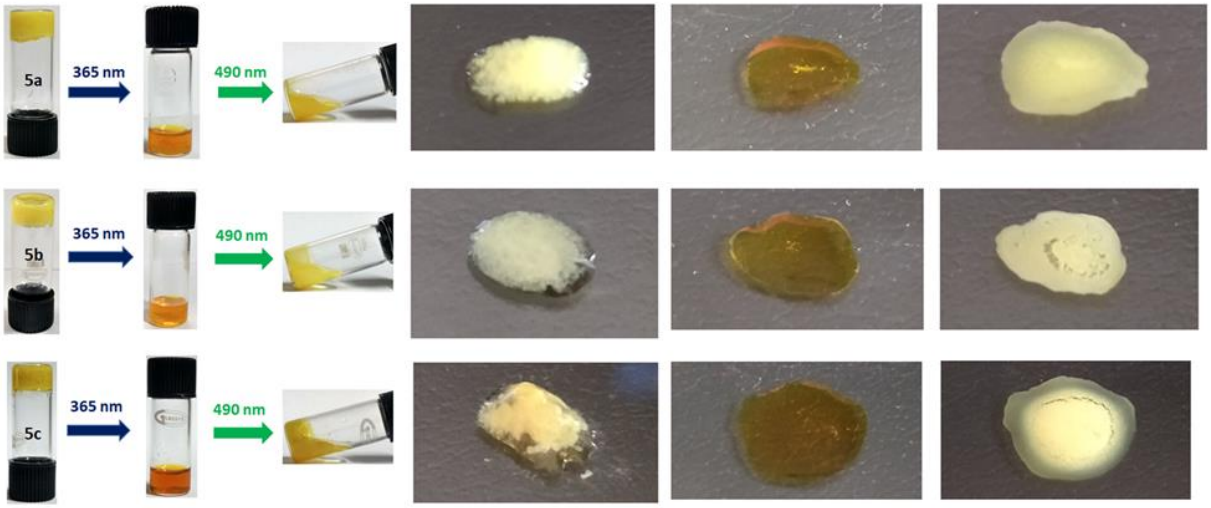

Figure 3.3. Photographs depicting the reversible photo-responsive sol-gel properties in **5a-c** (left) the samples of **5a-c** in DMF-H_2O (3:1); (Gel formation: For **5a**: 4.8 mM (0.4 wt%), reflux temperature; For **5b**: 9.6 mM (0.8 wt%), room temperature, and for **5c**: 4.3 mM (0.4 wt%), room temperature); All the three samples upon irradiation at 365 nm, attained sol form, whereas 490 nm irradiation resulted in partial gel; (right) The sol-gel changes have been monitored in a glass plate for all the three samples under the identical conditions.

The connection of phenylazo-3,5-dimethylisoxazole to the BTA core in **5a-c** led to an interesting situation, where the supramolecular assembly at the core through hydrogen bonding competes with the steric factor arising due to peripheral methyl groups towards disassembly. As a result, all these systems can be able to exhibit stimuli-responsive sol-gel phase transitions. The most striking aspect is the reversibility in the sol-gel formation in both directions by light. The derivative **5b-c** was heated to dissolve in DMF, and slowly cooled to room temperature, and water was added slowly to it. The solution turns into gel after standing for some time. However, in the case of **5a**, due to solubility issues at low temperature, it was heated to a higher temperature for dissolution and so, water was added without cooling it to room temperature to induce gelation. The gel-form in its native state collapsed to sol upon irradiation at 365 nm, whereas it reversed to a partial gel-form by irradiating at 490 nm light (**Figure 3.3)** Such photoresponsive reversible sol-gel phase transitions have been monitored by polarized optical

microscopy (POM) (**Figure 3.4**). The gel-form of the sample exhibited a birefringence pattern under POM, and upon irradiation at 365 nm light resulted in the sol-form. This can be monitored by the disappearance of birefringence due to the attainment of the isotropic phase. The process can be reversed by irradiation at 490 nm light which causes the reappearance of the birefringence. On the other hand, the systems with *N*-methylation at BTA cores **6a-c** did not exhibit such reversible sol-gel properties at all.

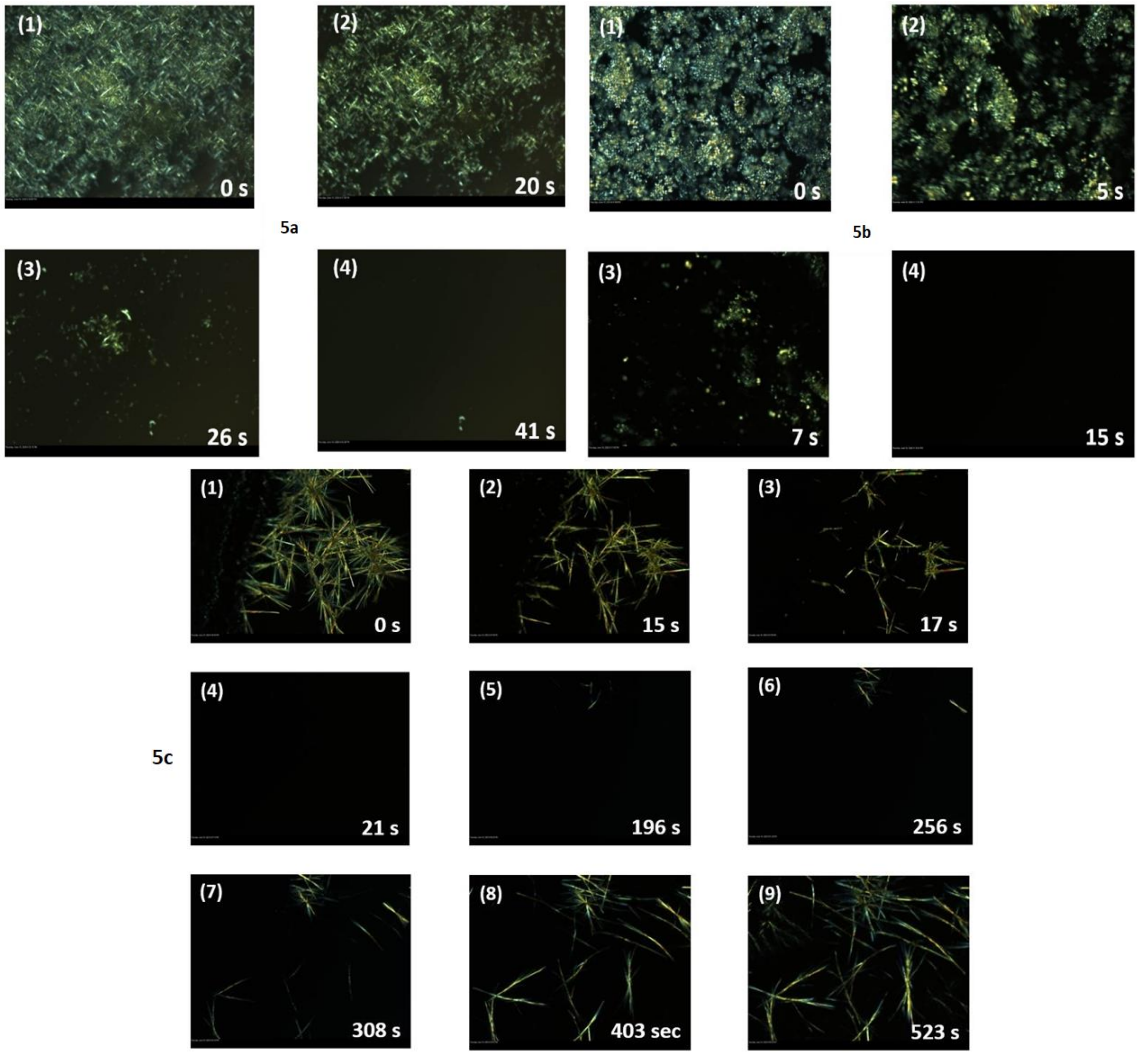

Figure 3.4. The polarized optical microscopic (POM) images for the reversible photo-responsive sol-gel properties in **5a-c** (magnification: x100): For **5a**: (1) - Before irradiation; (2-4) - After 365 nm irradiation (the time in seconds are indicated), For **5b**: (1) - Before irradiation; (2-4) - After 365 nm irradiation; For **5c**: (1) - Before irradiation; (2-4) - After 365 nm irradiation; and (5-9) after 490 nm irradiation.

3.8 Summary

Through this investigation, we have designed and synthesized six, C_3-symmetric tripodal multiple phenylazoisoxazole containing photoswitchable systems. Based on the studies, the following key outcomes have been envisaged:

(a) Albeit moderate to excellent photoswitching in the majority of the cases, the efficiency in the forward and reverse isomerization lies in the order (based on the orientation of the azo group): *para* > *meta* > *ortho*; Among the target systems, **5c** followed by **6c** showed the best photoswitching in both directions.

(b) The thermal stability of the metastable states strongly depends on the relative position of the azo group and follows the trend: *meta* > *ortho* > *para*.

(c) The *N*-methylation of the amides or the incorporation of phenylazoisoxazoles with methyl groups in the heterocycles improves the solubility, photoswitching efficiency, and also thermal stability of the metastable states.

Through these studies, we also demonstrated that subtle changes in the C_3-symmetric tripodal design can cause a variety of outcomes such as reversible photoresponsive sol-gel phase transitions. We are hopeful that these important conclusions will help design multiple azoheterocycles incorporated systems for a variety of applications in the future.

3.9 Experimental section

(*E*)-((3,5-dimethylisoxazol-4-yl)diazenyl)aniline (1a-c)[8]

The syntheses of **1a-c** have been performed based on the reported procedure adopted from the literature.

(*E*)-((3,5-dimethylisoxazol-4-yl)diazenyl)-*N*-methylaniline (2a-c)[5b]

Adopting a similar report, (*E*)-((3,5-dimethylisoxazol-4-yl)diazenyl)aniline **1a-c** (1.0 mmol) was dissolved in 30 ml of methanol and 0.5 ml of formaldehyde (37 wt % in water) solution was added to it. The reaction mixture was then stirred at 0 ^{o}C for half an hour. Sodium cyanoborohydride (3.0 mmol) was then portion-wise added to the reaction mixture over 45

minutes. The reaction was monitored by TLC. After completion of the reaction, the product was purified by column chromatography over basic alumina (Yield: **2a** = 38%, **2b** = 41%, **2c** = 36%).

(*E*)-2-((3,5-dimethylisoxazol-4-yl)diazenyl)-*N*-methylaniline (2a):

Orange solid, mp = 100-102 ^{o}C, ^{1}H NMR (400 MHz, $CDCl_3$): δ 2.52 (s, 3H), 2.69 (s, 3H), 2.99 (d, *J* = 3.1 Hz, 3H), 6.74-6.78 (m, 2H), 7.29-7.33 (td, *J* = 7.9, 1.2 Hz, 1H), 7.70-7.72 (dd, *J* = 8.3, 1.1 Hz, 1H), 7.74 (br, NH, 1H) ppm; ^{13}C (100 MHz, $CDCl_3$): δ 11.98, 12.24, 29.63, 111.45, 115.86, 127.77, 132.33, 132.70, 136.96, 144.58, 154.07, 166.03, ppm; HRMS-ESI: *m*/*z* $C_{12}H_{14}N_4O$ $[M+H]^+$ calc. 231.1246, obs. 231.1238; IR (ATR, cm^{-1}) 746, 1137, 1175, 1309, 1415, 1497, 1600, 2849, 2922, 3436.

(*E*)-3-((3,5-dimethylisoxazol-4-yl)diazenyl)-*N*-methylaniline (2b):

Orange solid, mp = 115-116 ^{o}C, ^{1}H NMR (400 MHz, $CDCl_3$): δ 2.53 (s, 3H), 2.74 (s, 3H), 2.91 (s, 3H), 3.90 (br, NH, 1H), 6.69-6.72 (ddd, *J* = 8.0, 2.4, 0.9 Hz, 1H), 7.03 (t, *J* = 2.1, 1H), 7.17-7.19 (ddd, *J* = 7.8, 1.8, 1.0 Hz, 1H), 7.29 (t, *J* = 7.9, 1H) ppm; ^{13}C (100 MHz, $CDCl_3$): δ 11.83, 12.23, 30.89, 104.70, 112.41, 115.36, 129.74, 132.53, 150.18, 153.98, 154.17, 169.08, ppm; HRMS-ESI: *m*/*z* $C_{12}H_{14}N_4O$ $[M+H]^+$ calc. 231.1246, obs. 231.1236; IR (ATR, cm^{-1}) 705, 783, 847, 1273, 1343, 1309, 1408, 1603, 2804, 2875, 2930, 2981, 3380, 3417.

(*E*)-4-((3,5-dimethylisoxazol-4-yl)diazenyl)-*N*-methylaniline (2c):

Orange solid, mp = 154-156 ^{o}C, ^{1}H NMR (400 MHz, $CDCl_3$) δ 2.52 (s, 3H), 2.70 (s, 3H), 2.92 (s, 3H), 4.20 (br, NH, 1H), 6.63 (d, *J* = 8.6, 2H), 7.73 (d, *J* = 8.9, 2H), ppm; ^{13}C (100 MHz, $CDCl_3$) δ 11.76, 12.20, 30.53, 111.90, 124.44, 132.28, 145.00, 151.71, 154.33, 166.78 ppm; HRMS-ESI: *m*/*z* $C_{12}H_{14}N_4O$ $[M+H]^+$ calc. 231.1246, obs. 231.1240; IR (ATR, cm^{-1}) 827, 1141, 1204, 1330, 1403, 1524, 1603, 2817, 2923, 3317, 3430.

General procedure for the synthesis of benzenetricarboxamide derivatives (5a-c)[5b]

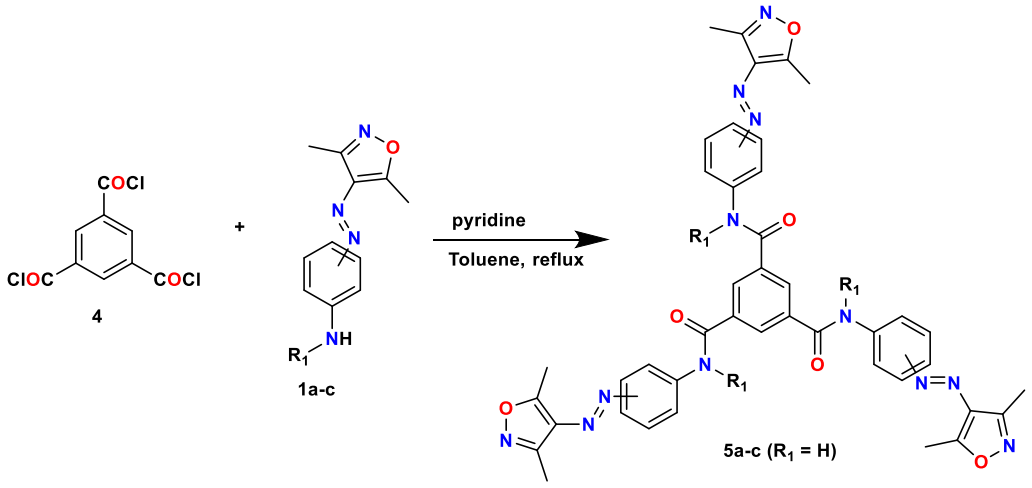

Trimesoyl chloride **4** was generated *in situ* from trimesic acid **3** (1.0 mmol) using PCl_5 (in excess) in dry toluene (20 ml) and refluxed for 4-5 hours. Trimesoyl chloride **4** thus formed, was transferred dropwise to a mixture containing **1a-c** (5.0 mmol) and pyridine (10.0 mmol) dissolved in dry toluene (30 ml) at 0 ^{o}C under inert conditions. The reaction mixture was refluxed for 2-3 hours. A yellow precipitate formed, was filtered, washed with water and methanol, and dried under vacuum for getting the pure product (Yield: **5a** = 67%, **5b** = 75%, and **5c** = 85%).

N^1,N^3,N^5-tris(2-((*E*)-(3,5-dimethylisoxazol-4-yl)diazenyl)phenyl)benzene-1,3,5-tricarboxamide (5a):

Yellow solid, mp = 221-222 ^{o}C, ^{1}H NMR (400 MHz, [D_6]DMSO): δ 2.31 (s, 9H), 2.74 (s, 9H), 7.36-7.40 (td, *J* = 8.2, 0.9 Hz, 3H), 7.59-7.64 (td, *J* = 8.0, 1.0 Hz, 3H), 7.72-7.74 (dd, *J* = 8.2, 1.1 Hz, 3H), 8.05 (d, *J* = 8.2 Hz, 3H), 8.83 (s, 3H), 10.58 (s, 3H) ppm; HRMS-ESI: *m/z* $C_{42}H_{36}N_{12}O_6$ $[M+H]^+$ calc. 805.2959, obs. 805.2975; IR (KBr pellet, cm^{-1}): 762, 1230, 1299, 1407, 1514, 1595, 1686, 2854, 2922.

N^1,N^3,N^5-tris(3-((*E*)-(3,5-dimethylisoxazol-4-yl)diazenyl)phenyl)benzene-1,3,5-tricarboxamide (5b):

Yellow solid, mp = 214-215 ^{o}C, ^{1}H NMR (400 MHz, [D_6]DMSO): δ 2.49 (s, 9H), 2.78 (s, 9H), 7.59-7.65 (m, 6H), 8.01-8.03 (dt, *J* = 7.5, 2.0 Hz, 3H), 8.35 (t, *J* = 1.7 Hz, 3H), 8.82 (s, 3H), 10.87 (s, 3H) ppm; ^{13}C (100 MHz, [D_6]DMSO): δ 11.45, 11.83, 113.37, 118.29, 122.77, 129.79,

130.17, 131.88, 135.35, 140.02, 152.71, 152.97, 164.77, 170.38 ppm; HRMS-ESI: *m/z* $C_{42}H_{36}N_{12}O_6$ $[M+H]^+$ calc. 805.2959, obs. 805.2967; IR (KBr pellet, cm^{-1}): 783, 977, 1248, 1407, 1482, 1546, 1600, 1663, 2854, 2927.

N^1,N^3,N^5-tris(4-((*E*)-(3,5-dimethylisoxazol-4-yl)diazenyl)phenyl)benzene-1,3,5-tricarboxamide (5c):

Yellow solid, mp = 226-227 ^oC, ^1H NMR (400 MHz, [D_6]DMSO) δ 2.47 (s, 9H), 2.76 (s, 9H), 7.90 (d, *J* = 8.4 Hz, 6H), 8.07 (d, *J* = 8.5 Hz, 6H), 8.80 (s, 3H), 10.94 (s, 3H), ppm; ^{13}C (100 MHz, [D_6]DMSO) δ 11.41, 11.81, 120.61, 123.01, 130.22, 131.79, 135.31, 141.64, 148.43, 153.05, 164.67, 169.52, ppm; HRMS-ESI: *m/z* $C_{42}H_{36}N_{12}O_6$ $[M+H]^+$ calc. 805.2959, obs. 805.2974; IR (KBr pellet, cm^{-1}): 843, 1155, 1248, 1306, 1535, 1600, 1660, 2854, 2928.

General procedure for the synthesis of *N*-methylated benzenetricarboxamide derivatives (6a-c)[7b]

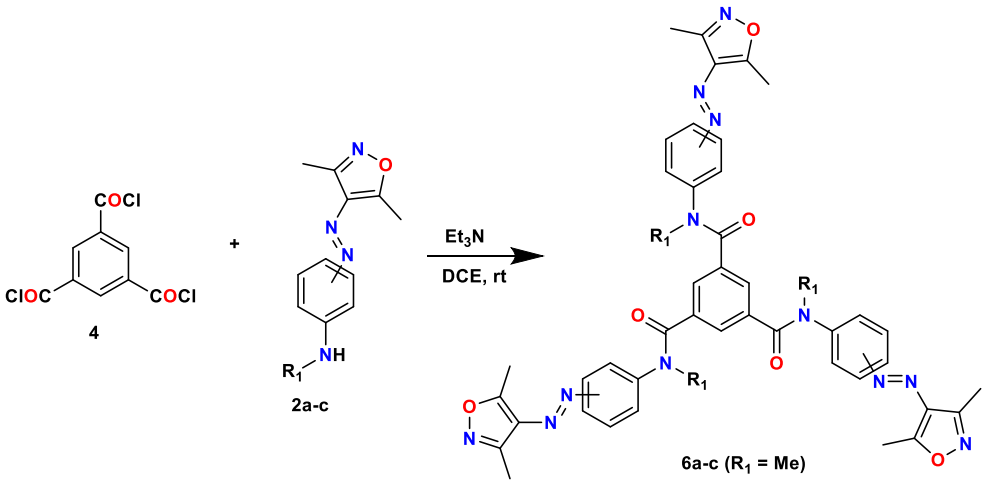

Trimesic acid **3** (1.0 mmol) was refluxed in $SOCl_2$ (5 ml) with a catalytic amount of DMF (50 µL). After the complete conversion of trimesic acid **3** to trimesoyl chloride **4**, $SOCl_2$ was evaporated. The *in situ* generated trimesoyl chloride was dissolved in dry DCE under a nitrogen atmosphere and transferred drop-wise into a separate three-neck RB flask containing the mixture of (*E*)-((3,5-dimethylisoxazol-4-yl)diazenyl)-*N*-methylaniline derivatives **(2a-c)** (3.3 mmol), triethylamine (0.5 mL) and dry DCE under nitrogen atmosphere at 0 ^oC. The reaction mixture was stirred overnight at room temperature. The precipitate formed was filtered and washed with ethanol to remove the starting materials (Yield: **6a** = 33%, 6**b** = 68%, and **6c** = 20%).

N^1,N^3,N^5-tris(2-((*E*)-(3,5-dimethylisoxazol-4-yl)diazenyl)phenyl)-N^1,N^3,N^5-trimethylbenzene-1,3,5-tricarboxamide (6a):

Yellow solid, mp = 181-182 ^{o}C, (Exists in two rotamer forms with overlapping signals at nearly 1:1 ratio) ^{1}H NMR (400 MHz, $CDCl_3$): δ 2.23-2.35 (m, 9H), 2.54-2.65 (m, 9H), 3.24 (s, 6H), 3.38 (s, 3H), 6.54-6.79 (m, 4H), 7.05-7.52 (m, 11H) ppm; ^{13}C (100 MHz, $CDCl_3$): δ 11.69, 11.79, 12.08, 12.30, 38.96, 39.06, 116.48, 127.83, 127.88, 128.12, 128.36, 128.71, 128.99, 129.34, 129.71, 130.13, 131.51, 131.80, 132.92, 133.02, 134.81, 134.92, 135.66, 142.16, 142.36, 142.64, 147.34, 147.40, 147.51, 152.89, 153.06, 168.72, 168.95, 169.39, 171.06, 171.47, 171.84 ppm; HRMS-ESI: *m*/*z* $C_{45}H_{42}N_{12}O_6$ $[M+H]^+$ calc. 847.3429, obs. 847.3464; IR (KBr pellet, cm^{-1}): 726, 774, 896, 1095, 1283, 1345, 1405, 1587, 1653, 2923, 3058.

N^1,N^3,N^5-tris(3-((*E*)-(3,5-dimethylisoxazol-4-yl)diazenyl)phenyl)-N^1,N^3,N^5-trimethylbenzene-1,3,5-tricarboxamide (6b):

Yellow solid, mp = 115-116 ^{o}C, ^{1}H NMR (400 MHz, $CDCl_3$): δ 2.51 (s, 9H), 2.74 (s, 9H), 3.37 (s, 9H), 6.62 (d, *J* = 5.6 Hz, 3H), 7.22 (t, *J* = 7.8 Hz, 3H), 7.30 (br, 3H), 7.50 (br, 3H), 7.61 (d, *J* = 7.9 Hz, 3H) ppm; ^{13}C (100 MHz, $CDCl_3$): δ 11.94, 12.31, 38.58, 119.58, 120.95, 129.12, 129.67, 130.48, 132.61, 135.56, 145.06, 153.52, 153.83, 168.67, 170.65, ppm; HRMS-ESI: *m*/*z* $C_{45}H_{42}N_{12}O_6$ $[M+H]^+$ calc. 847.3429, obs. 847.3469; IR (KBr pellet, cm^{-1}): 701, 796, 900, 979, 1107, 1273, 1351, 1408, 1591, 1650, 2854, 2926, 3067.

N^1,N^3,N^5-tris(4-((*E*)-(3,5-dimethylisoxazol-4-yl)diazenyl)phenyl)-N^1,N^3,N^5-trimethylbenzene-1,3,5-tricarboxamide (6c):

Yellow solid, mp = 227-228 ^{o}C, ^{1}H NMR (400 MHz, $CDCl_3$): δ 2.47 (s, 9H), 2.71 (s, 9H), 3.40 (s, 9H), 6.68 (d, *J* = 8.1 Hz, 6H), 7.15 (s, 3H), 7.74 (d, *J* = 8.1, 6H) ppm; ^{13}C (100 MHz, $CDCl_3$): δ 11.91, 12.35, 37.90, 123.16, 127.77, 130.41, 132.71, 135.99, 146.41, 150.66, 153.22, 168.86, 170.33, ppm; HRMS-ESI: *m*/*z* $C_{45}H_{42}N_{12}O_6$ $[M+H]^+$ calc. 847.3429, obs. 847.3469; IR (KBr pellet, cm^{-1}): 739, 849, 900, 978, 1104, 1283, 1412, 1496, 1597, 1654, 2854, 2919, 3056.

3.10 References

[1] a) F. Cisnetti, R. Ballardini, A. Credi, M. T. Gandolfi, S. Masiero, F. Negri, S. Pieraccini, G. P. Spada, *Chem. Eur. J.* **2004**, *10*, 2011–2021; b) A. Galanti, V. Diez-Cabanes, J. Santoro, M. Valášek, A. Minoia, M. Mayor, J. Cornil, P. Samorì, *J. Am. Chem. Soc.* **2018**, *140*, 16062–16070; c) K. Kreger, P. Wolfer, H. Audorff, L. Kador, N. Stingelin-Stutzmann, P. Smith, H.-W. Schmidt, *J. Am. Chem. Soc.* **2010**, *132*, 509– 516; d) L. M. Goldenberg, L. Kulikovsky, O. Kulikovska, J. Tomczyk, J. Stumpe, *Langmuir* **2010**, *26*, 2214–2217; e) J. Lee, S. Oh, J. Pyo, J.-M. Kim, J. H. Je, *Nanoscale* **2015**, *7*, 6457–6461; f) C. Probst, C. Meichner, H. Audorff, R. Walker, K. Kreger, L. Kador, H.-W. Schmidt, *J. Polym. Sci. Part B* **2016**, *54*, 2110–2117; g) X. Liu, X.-S. Luo, H.-L. Deng, W. Fan, S. Wang, C. Yang, X.-Y. Sun, S.-L. Chen, M.-H. Huang, *Chem. Mater.* **2019**, *31*, 5421–5430.

[2] a) D. Bléger, J. Dokić, M. V. Peters, L. Grubert, P. Saalfrank, S. Hecht, *J. Phys. Chem. B.* **2011**, *115*, 9930–9940; b) Á. Moneo, G. C. Justino, M. F. N. N. Carvalho, M. C. Oliveira, A. M. M. Antunes, D. Bléger, S. Hecht, J. P. Telo, *J. Phys. Chem. A.* **2013**, *117*, 14056−14064;

[3] a) J. Robertus, S. F. Reker, T. C. Pijper, A. Deuzeman, W. R. Browne, B. L. Feringa, *Phys. Chem. Chem. Phys.* **2012**, *14*, 4374–4382; b) J. Bahrenburg, C. M. Sievers, J. B. Schönborn, B. Hartke, F. Renth, F. Temps, C. Näther, D. Sönnichsen, *Photochem. Photobiol. Sci.* **2013**, *12*, 511–518; c) J. Kind, L. Kaltschnee, M. Leyendecker, C. M. Thiele, *Chem. Commun.* **2016**, *52*, 12506−12509; d) A. Galanti, J. Santoro, R. Mannancherry, Q. Duez, V. Diez-Cabanes, M. Valášek, J. D. Winter, J. Cornil, P. Gerbaux, M. Mayor, P. Samorì, *J. Am. Chem. Soc.* **2019**, *141*, 9273−9283; e) I. C.–Y. Hou, V. Diez-Cabanes, A. Galanti, M. Valášek, M. Mayor, J. Cornil, A. Narita, P. Samorì, K. Müllen, *Chem. Mater.* **2019**, *31*, 6979–6985; f) A. Galanti, V. Diez-Cabanes, J. Santoro, M. Valášek, A. Minoia, M. Mayor, J. Cornil, P. Samorì, *J. Am. Chem. Soc.* **2018**, *140*, 16062–16070; g) A. Galanti, J. Santoro, R. Mannancherry, Q. Duez, V. Diez-Cabanes, M. Valášek, J. D Winter, J. Cornil, P. Gerbaux, M. Mayor, P. Samorì, *J. Am. Chem. Soc.* **2019**, *141*, 9273–9283.

[4] a) R. Reuter, H. A. Wegner, *Chem. Eur. J.* **2011**, *17*, 2987–2995; b) R. Reuter, H. A. Wegner, *Org. Lett.* **2011**, *13*, 5908–5911; c) C. Slavov, C. Yang, L. Schweighauser, H. A. Wegner, A. Dreuw, J. Wachtveitl, *ChemPhysChem.* **2017**, *18*, 2137–2141; d) A. Vlasceanu, M. Koerstz, A. B. Skov, K. V. Mikkelsen, M. B. Nielsen, *Angew. Chem. Int. Ed.* **2018**, *57*, 6069–6072; e) A. H. Heindl, J. Becker, H. A. Wegner, *Chem. Sci.* **2019**, *10*, 7418–7425; n) A. H. Heindl, L. Schweighauser, C. Logemannb, H. A. Wegner, *Synthesis.* **2017**, *49*, 2632–2639.

[5] a) S. Lee, S. Oh, J. Lee, Y. Malpani, Y-S. Jung, B. Kang, J.Y. Lee, K. Ozasa, T. Isoshima, S. Y. Lee, M. Hara, D. Hashizume, J. M. Kim, *Langmuir.* **2013**, *29*, 5869−5877; b) S. Devi, I. Bala, S. P. Gupta, P. Kumar, S. K. Pal, S. Venkataramani, *Org. Biomol. Chem.* **2019**, *17*, 1947–1954; c) M. Pfletscher, C. Wölper, J. S. Gutmann, M. Mezger, M. Giese, *Chem. Commun.* **2016**, *52*, 8549–8552.

[6] a) Y-J. Choi, D-Y. Kim, M. Park, W-J. Yoon, Y. Lee, J-K. Hwang, Y-W. Chiang, S-W. Kuo, C-H. Hsu, K-U. Jeong, *ACS Appl. Mater. Interfaces.* **2016**, *8*, 9490−9498; b) Y. Huang, D-H. Kim, *Nanoscale*, **2012**, *4*, 6312−6317; d) R. Reuter, H. A. Wegner, *Chem. Commun.*, **2013**, *49*, 146–148; e) M. Yamauchi, K. Yokoyama, N. Aratani, H. Yamada, S. Masuo, *Angew. Chem. Intl. Ed.* **2019**, *58*, 14173–14178; *Angew. Chem.* **2019**, *131*, 14311–14316; f) I. Abe, M. Hara, T. Seki, S. J. Cho, M. Shimizu, K. Matsuura, H-K. Cheong, J. Y. Kim, J. Oh, J. Jung, M. Han, *J. Mater. Chem. C.* **2019**, *7*, 2276–2282.

[7] a) S. Devi, A. K. Gaur, D. Gupta, M. Saraswat, S. Venkataramani, *ChemPhotoChem* **2018**, *2*, 806–810; b) K. Yano, Y. Itoh, F. Araoka, G. Watanabe, T. Hikima, T. Aida, *Science* **2019**, *363*, 161–165.
[8] P. Kumar, A. Srivastava, C. Sah, S. Devi, S. Venkataramani, *Chem*. *Eur*. *J*. **2019**, *25*, 11924–11932.
[9] Apart from **6a**, the other *N*-methylated amide derivatives **6b,c** exhibited broadening in the *N*-methyl proton signals. On the other hand, the quantification has been made using the isoxazole methyl proton signals in **6b,c**. The data is available as **Appendix 3B**.
[10] D. Gupta, A. K. Gaur, P. Kumar, H. Kumar, A. Mahadevan, S. Devi, S. Roy, S. Venkataramani, *Chem*. *Eur*. *J*. **2021**, *27*, 3463–3472.
[11] H. M. D. Bandara, S. C. Burdette, *Chem*. *Soc*. *Rev*. **2012**, *41*, 1809–1825.

Appendix 3A

Analysis of photoswitching and thermal stability aspects using UV-Vis spectroscopy

Photoswitching studies have been analyzed in the solution phase using UV-vis spectroscopy.

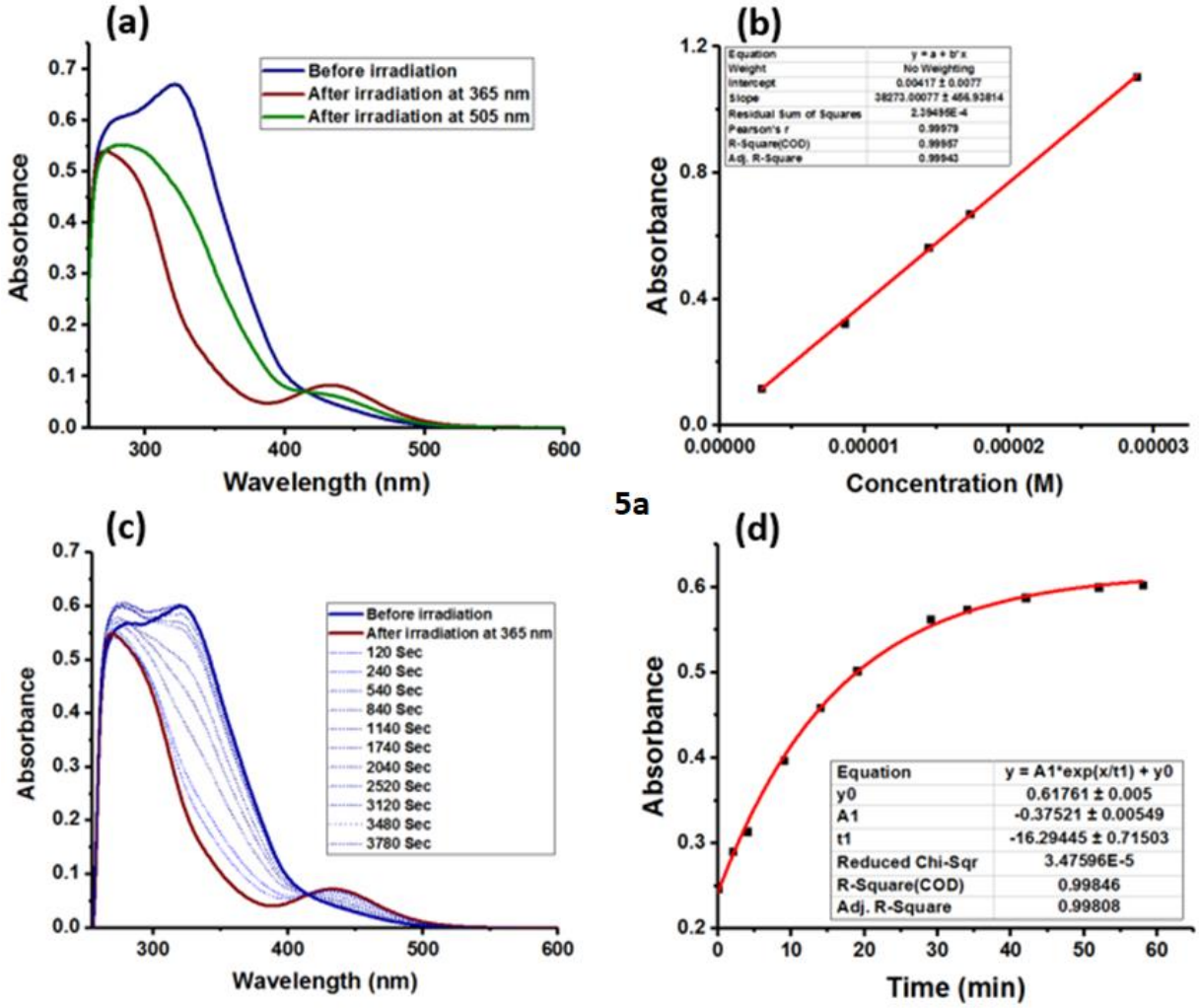

Figure 3A.1. Photoswitching and thermal stability aspects **5a** (a) Forward and reverse isomerization (DMSO, 17.3 μM); (b) Estimation of molar extinction coefficient (in DMSO) for the π−π* absorption; (c) Stepwise thermal reverse isomerization kinetics measurements of **5a** (UV-Vis spectroscopic monitoring of the 15.7 μM solution at 90 ^{o}C); (d) First order thermal reverse isomerization kinetics plot and exponential fit of **5a** (15.7 μM solution at 90 ^{o}C).

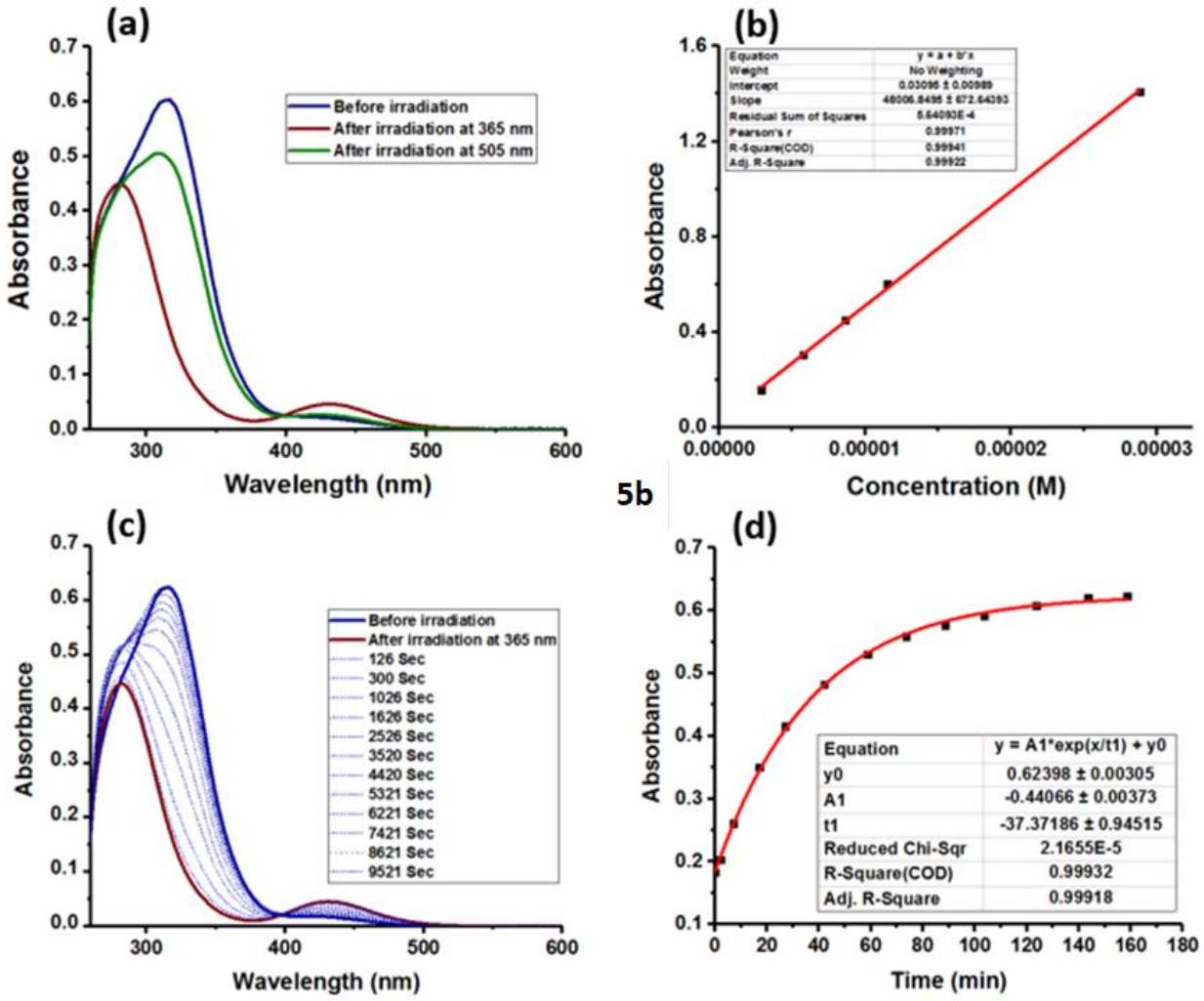

Figure 3A.2. Photoswitching and thermal stability aspects **5b** (a) Forward and reverse isomerization (DMSO, 11.5 μM); (b) Estimation of molar extinction coefficient (in DMSO) for the π−π* absorption; (c) Stepwise thermal reverse isomerization kinetics measurements of **5b** (UV-Vis spectroscopic monitoring of the 13.0 μM solution at 90 ^{o}C); (d) First order thermal reverse isomerization kinetics plot and exponential fit of **5b** (13.0 μM solution at 90 ^{o}C).

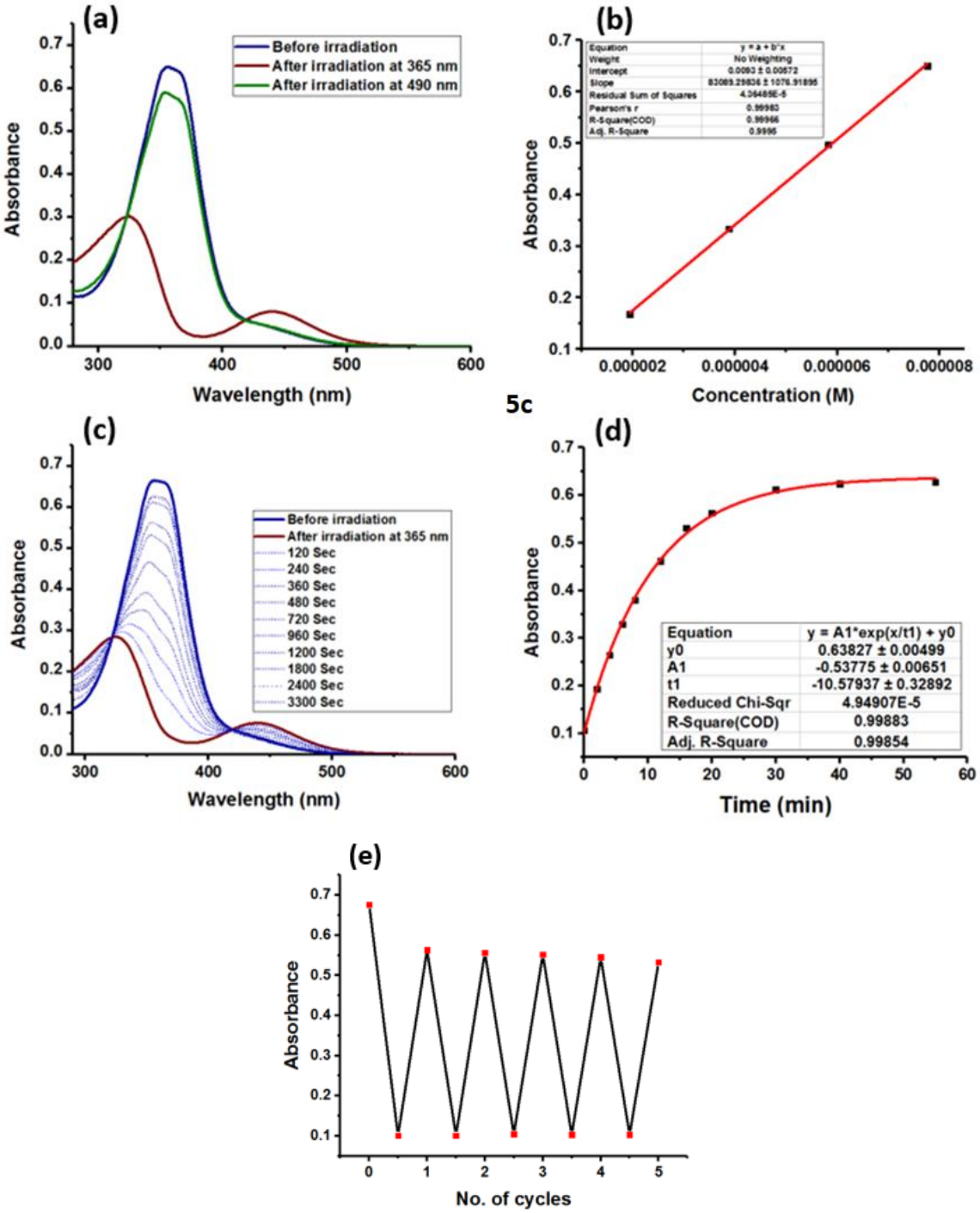

Figure 3A.3. Photoswitching and thermal stability aspects **5c** (a) Forward and reverse isomerization (DMSO, 7.7 μM); (b) Estimation of molar extinction coefficient (in DMSO) for the π−π* absorption; (c) Stepwise thermal reverse isomerization kinetics measurements of **5c** (UV-Vis spectroscopic monitoring of the 9.0 μM solution at 90 ^{o}C); (d) First order thermal reverse isomerization kinetics plot and exponential fit of **5c** (9.0 μM solution at 90 ^{o}C), (e) Photoswitching stability test up to five cycles of **5c** in DMSO (forward isomerization step: 365 nm; reverse isomerization step: 490 nm).

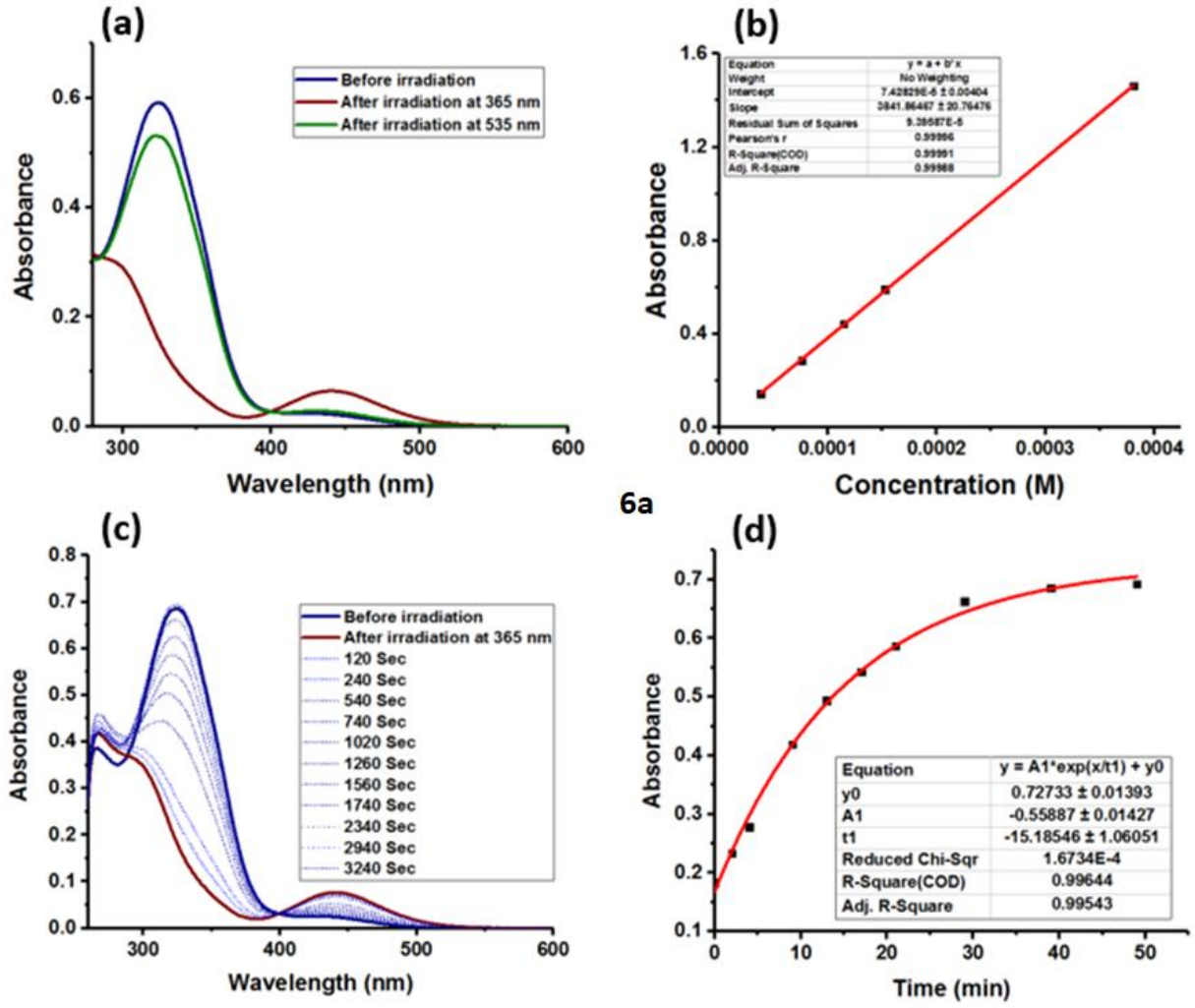

Figure 3A.4. Photoswitching and thermal stability aspects **6a** (a) Forward and reverse isomerization (DMSO, 15.3 μM); (b) Estimation of molar extinction coefficient (in DMSO) for the π−π* absorption; (c) Stepwise thermal reverse isomerization kinetics measurements of **6a** (UV-Vis spectroscopic monitoring of the 17.9 μM solution at 90 ^{o}C); (d) First order thermal reverse isomerization kinetics plot and exponential fit of **6a** (17.9 μM solution at 90 ^{o}C).

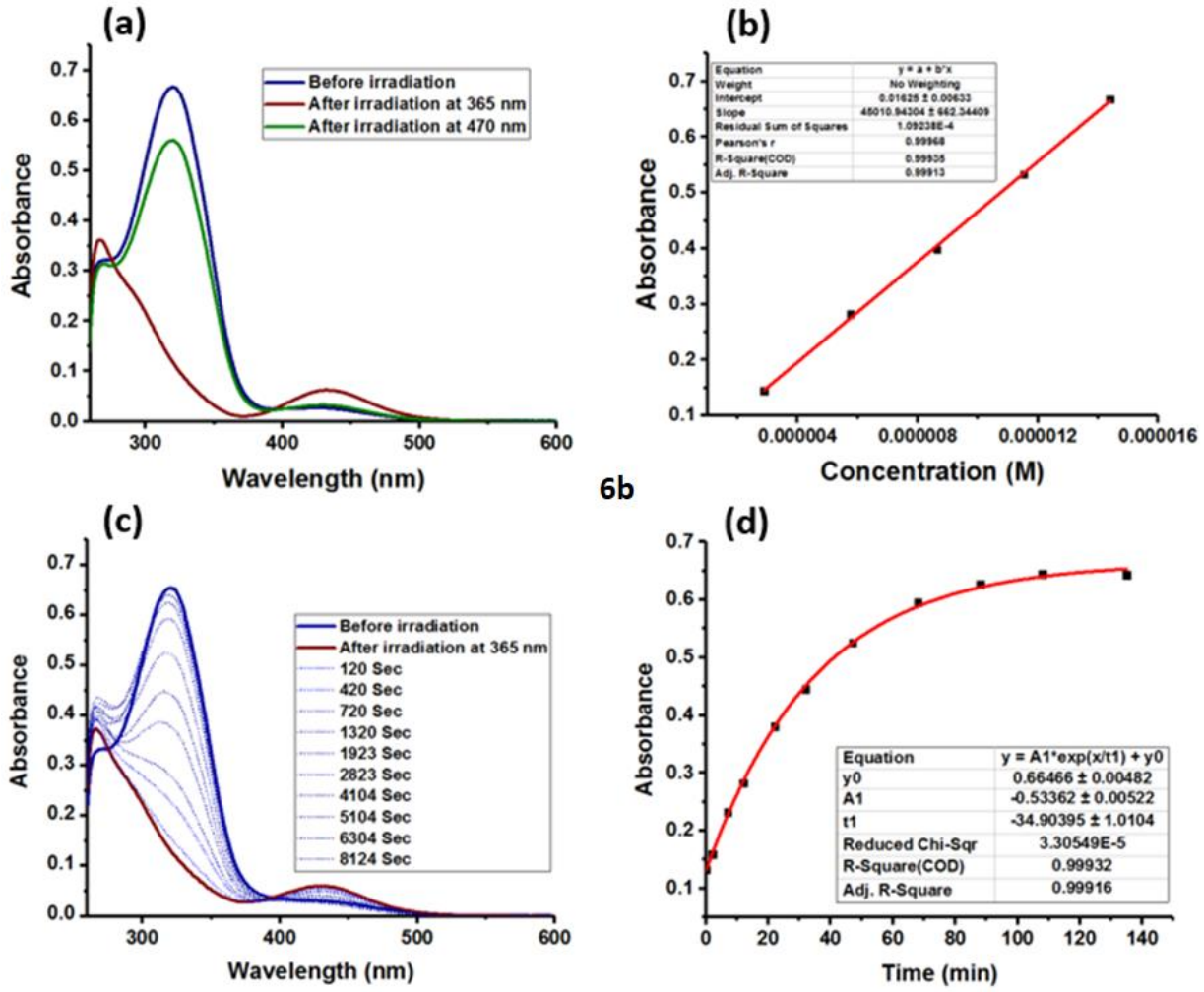

Figure 3A.5. Photoswitching and thermal stability aspects **6b** (a) Forward and reverse isomerization (DMSO, 14.4 μM); (b) Estimation of molar extinction coefficient (in DMSO) for the π−π* absorption; (c) Stepwise thermal reverse isomerization kinetics measurements of **6b** (UV-Vis spectroscopic monitoring of the 14.5 μM solution at 90 ^{o}C); (d) First order thermal reverse isomerization kinetics plot and exponential fit of **6b** (14.5 μM solution at 90 ^{o}C).

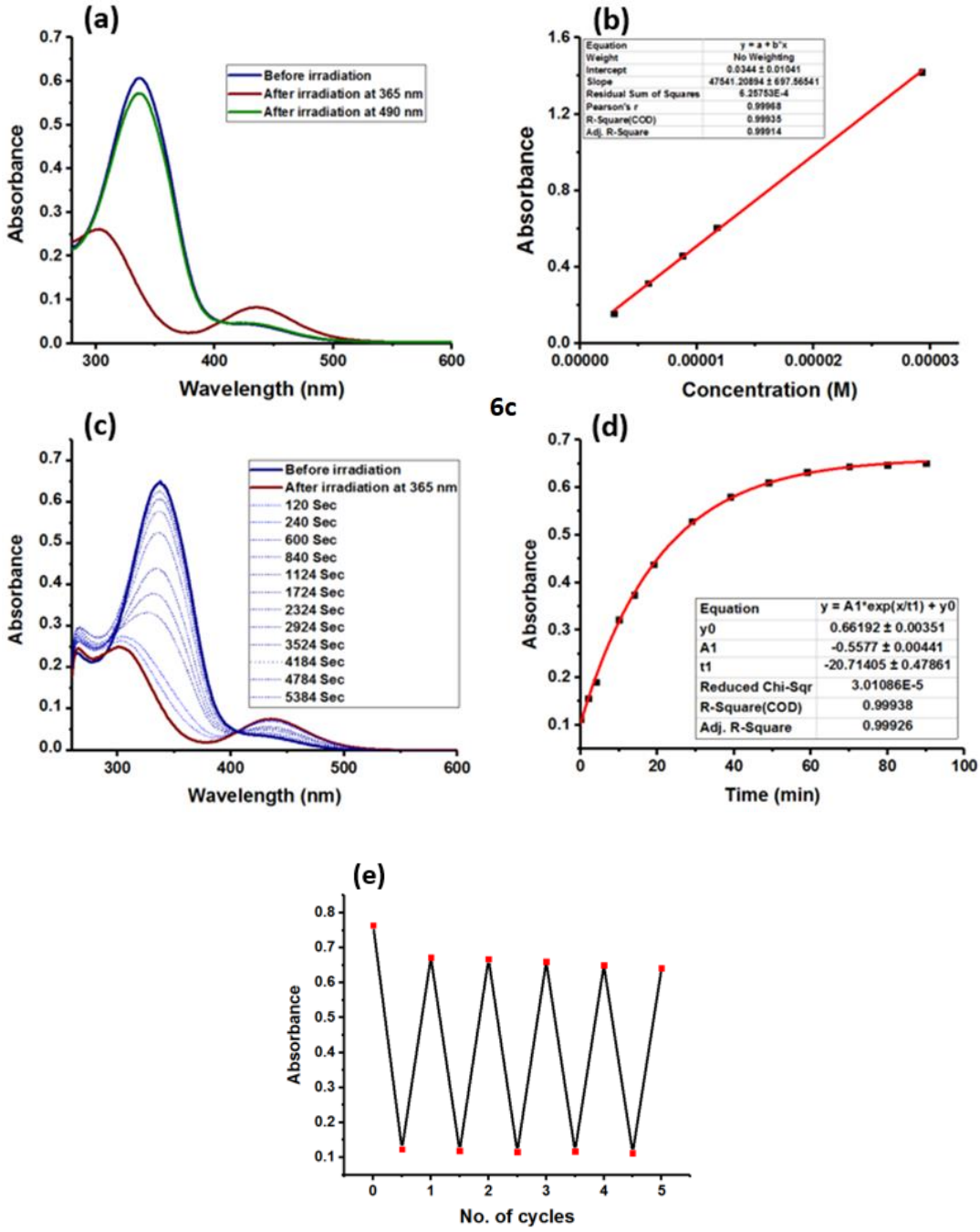

Figure 3A.6. Photoswitching and thermal stability aspects **6c** (a) Forward and reverse isomerization (DMSO, 11.7 μM); (b) Estimation of molar extinction coefficient (in DMSO) for the π−π* absorption; (c) Stepwise thermal reverse isomerization kinetics measurements of **6c** (UV-Vis spectroscopic monitoring of the 13.7 μM solution at 90 ^{o}C); (d) First order thermal reverse isomerization kinetics plot and exponential fit of **6c** (13.7 μM solution at 90 ^{o}C), (e) Photoswitching stability test up to five cycles of **6c** in DMSO (forward isomerization step: 365 nm; reverse isomerization step: 490 nm).

Appendix 3B

For the forward and reverse photoisomerization steps in the individual targets, the composition at their respective PSS has been estimated by using the ^{1}H-NMR spectroscopic techniques and normalized integral values.

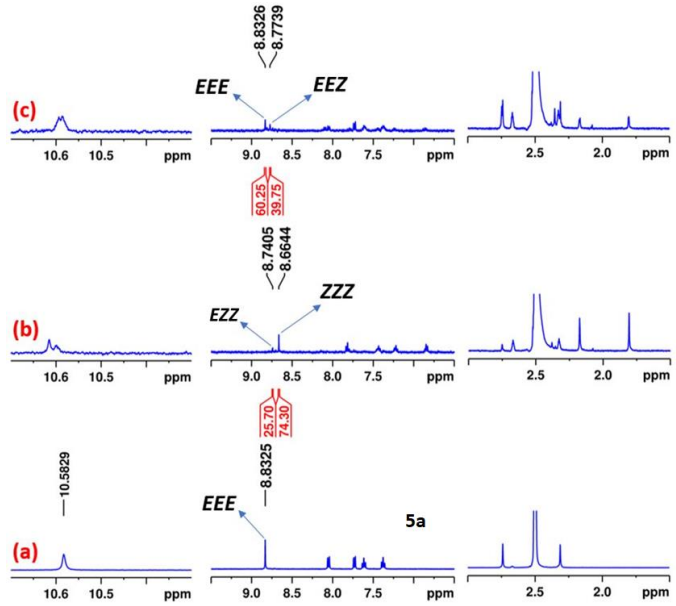

Figure 3B.1. PSS composition in **5a** ([D_6]DMSO, 1.98 mM) (a) Before irradiation; (b) After irradiation at 365 nm; (c) After irradiation at 490 nm (For forward and reverse isomerization steps, PSS composition has been estimated using the normalized integral values of signals due to the benzene core C-H protons)

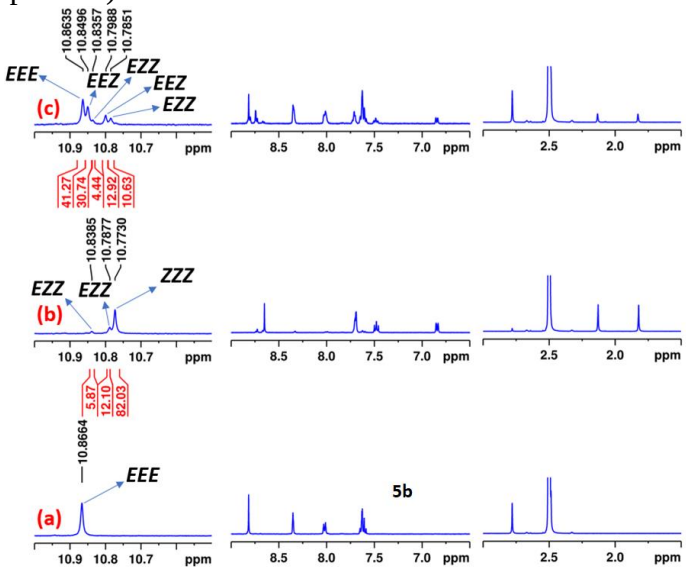

Figure 3B.2. PSS composition in **5b** ([D_6]DMSO, 2.48 mM) (a) Before irradiation; (b) After irradiation at 365 nm; (c) After irradiation at 490 nm (For forward and reverse isomerization steps, PSS composition has been estimated using the normalized integral values of signals due to the amide *N*-H protons)

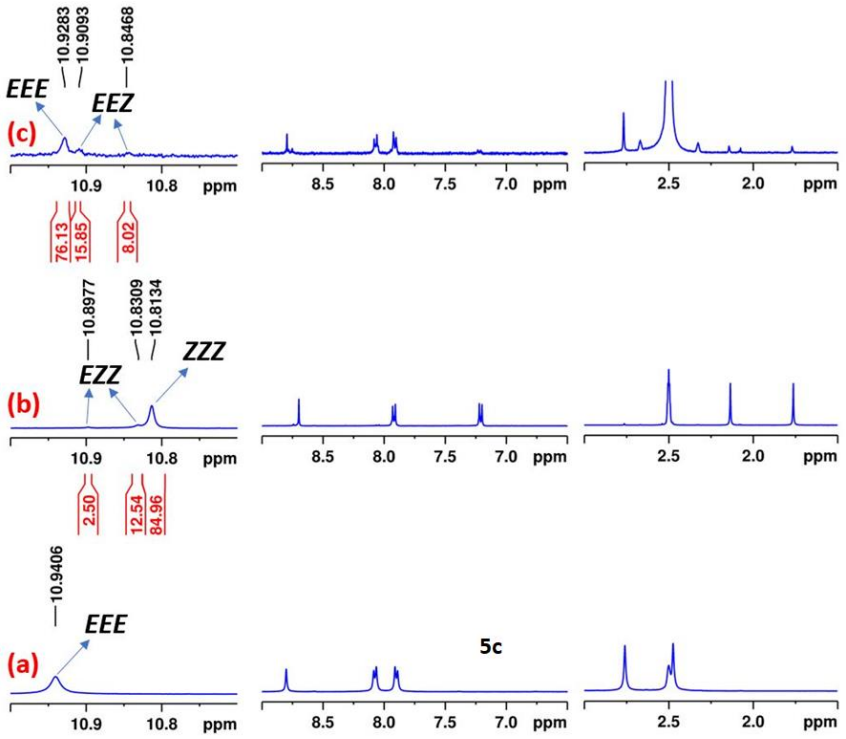

Figure 3B.3 PSS composition in **5c** ([D_6]DMSO, 2.26 mM) (a) Before irradiation; (b) After irradiation at 365 nm; (c) After irradiation at 490 nm (For forward and reverse isomerization steps, PSS composition has been estimated using the normalized integral values of signals due to the amide *N*-H protons)

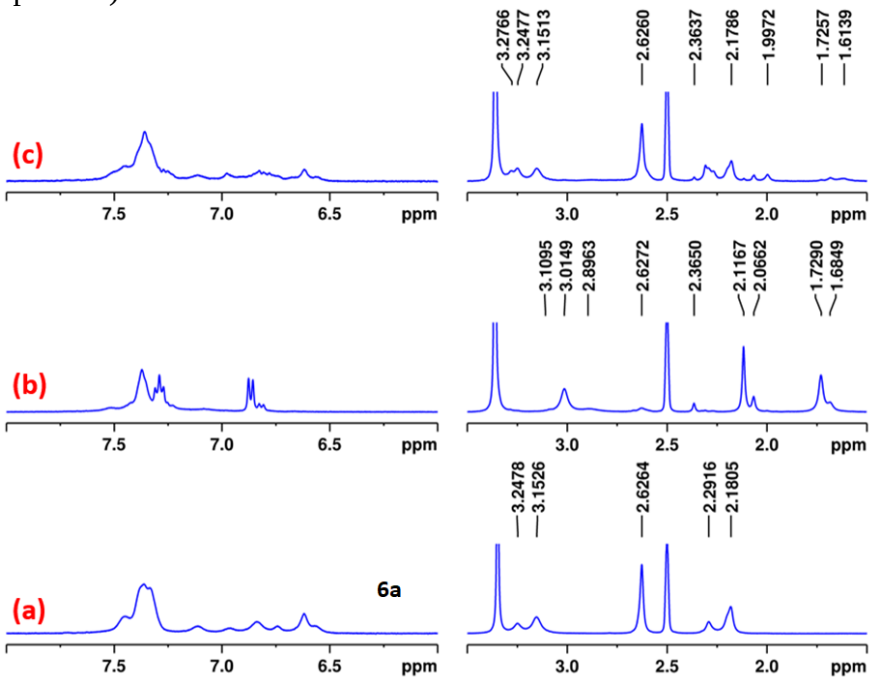

Figure 3B.4. PSS composition in **6a** ([D_6]DMSO, 2.26 mM) (a) Before irradiation; (b) After irradiation at 365 nm; (c) After irradiation at 490 nm (For forward and reverse isomerization steps, PSS composition has not been estimated due to overlapping of signals).

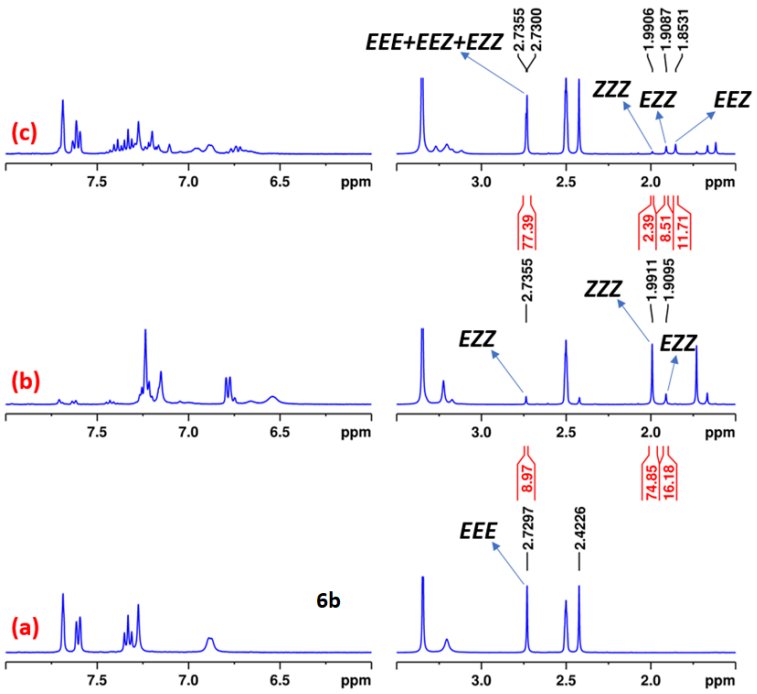

Figure 3B.5. PSS composition in **6b** ([D_6]DMSO, 7.79 mM) (a) Before irradiation; (b) After irradiation at 365 nm; (c) After irradiation at 490 nm (For forward and reverse isomerization steps, PSS composition has been estimated using the normalized integral values of signals due to the isoxazole-CH_3 protons)

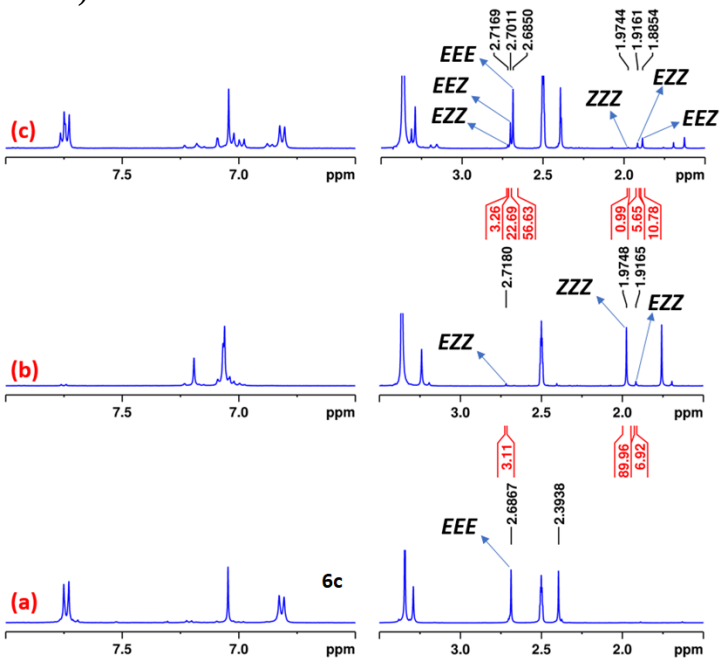

Figure 3B.6. PSS composition in **6c** ([D_6]DMSO, 4.16 mM) (a) Before irradiation; (b) After irradiation at 365 nm; (c) After irradiation at 490 nm (For forward and reverse isomerization steps, PSS composition has been estimated using the normalized integral values of signals due to the isoxazole-CH_3 protons.

Table 3B.1 PSS composition for forward and reverse isomerization steps of the target systems estimated by using ^{1}H-NMR spectroscopy

S. No.	Comp.	Conc. (mM)	λ (nm)	%Composition of individual isomers at PSS[a]				Proton Signal	Chemical Shift of individual photoisomers (δ, ppm)			
				EEE	*EEZ*	*EZZ*	*ZZZ*		*EEE*	*EEZ*	*EZZ*	*ZZZ*
1	**5a**[b]	1.98	365	-	-	26	74	Benzene core	-	-	8.7405	8.6644
			490	[c]	[c]	[c]	[c]		8.8326	8.7739	-	-
2	**5b**	2.48	365	-	-	18	82	Amide *N*-H	-	-	10.8385, 10.7877 (1:2)	10.7730
			490	41	43	16	-		10.8635	10.8496, 10.7988 (2:1)	10.8357, 10.7851 (1:2)	-
3	**5c**	2.26	365	-	3	12	85	Amide *N*-H	-	10.8977	10.8309	10.8134
			490	76	24	-	-		10.9283	10.9093, 10.8468 (2:1)	-	-
4	**6a**[c]	15.58	365	-	-	-	-	Amide *N*-Me	-	-	-	-
			490	-	-	-	-		-	-	-	-
5	**6b**	7.79	365	-	-	25	75	Isoxazole-3,5-dimethyl	-	-	2.7355, 1.9095 (1:2)	1.9911
			490	49	36	13	2		2.7355*, 2.7300*	2.7355*, 2.7300*, 1.8531	2.7355*, 2.7300*, 1.9087	1.9906
6	**6c**	4.16	365	-	-	10	90	Isoxazole-3,5-dimethyl	-	-	2.7180, 1.9165 (1:2)	1.9748
			490	57	34	8	1		2.6850	2.7011, 1.8854 (2:1)	2.7169*, 1.9161 (1:2)	1.9744

All the measurements are done in [D_6]DMSO; [a]unable to be determined due to poor solubility and/or overlapping signals;[b]solubility increased after irradiation at 365 nm; [c]unable to be determined due to rotamers; (*Common signal).

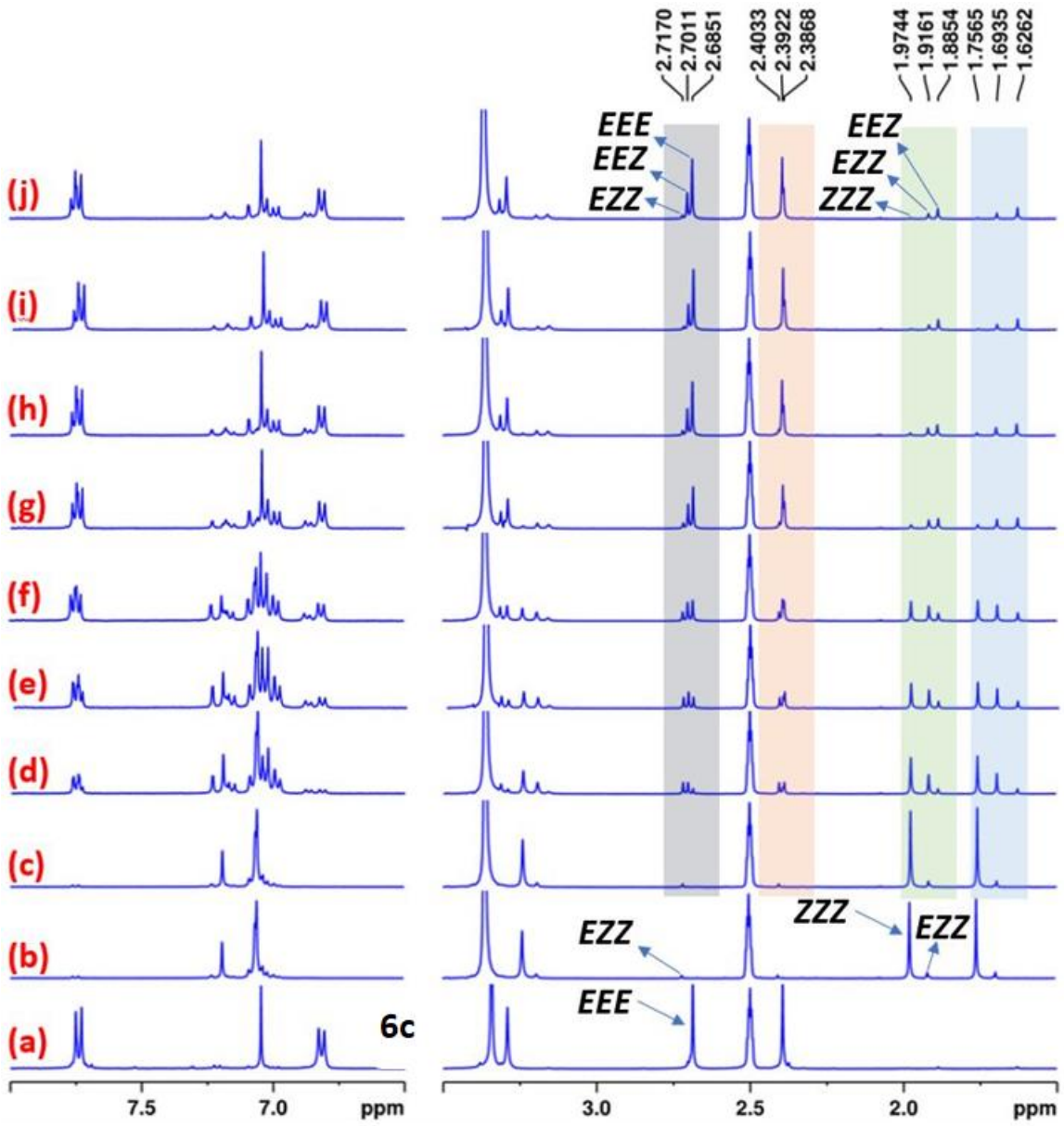

Figure 3B.7. Representative spectral stack for identification and the assignment of individual photoisomers in **6c** (a) Before irradiation; (b) After irradiation at 365 nm to enrich *ZZZ*-isomer; After irradiation of the sample at 490 nm for (c) 3 min; (d) 5 min; (e) 9 min; (f) 19 min; (g) 29 min; (h) 41 min; (i) 56 min; (j) 76 mins.

Appendix 3C

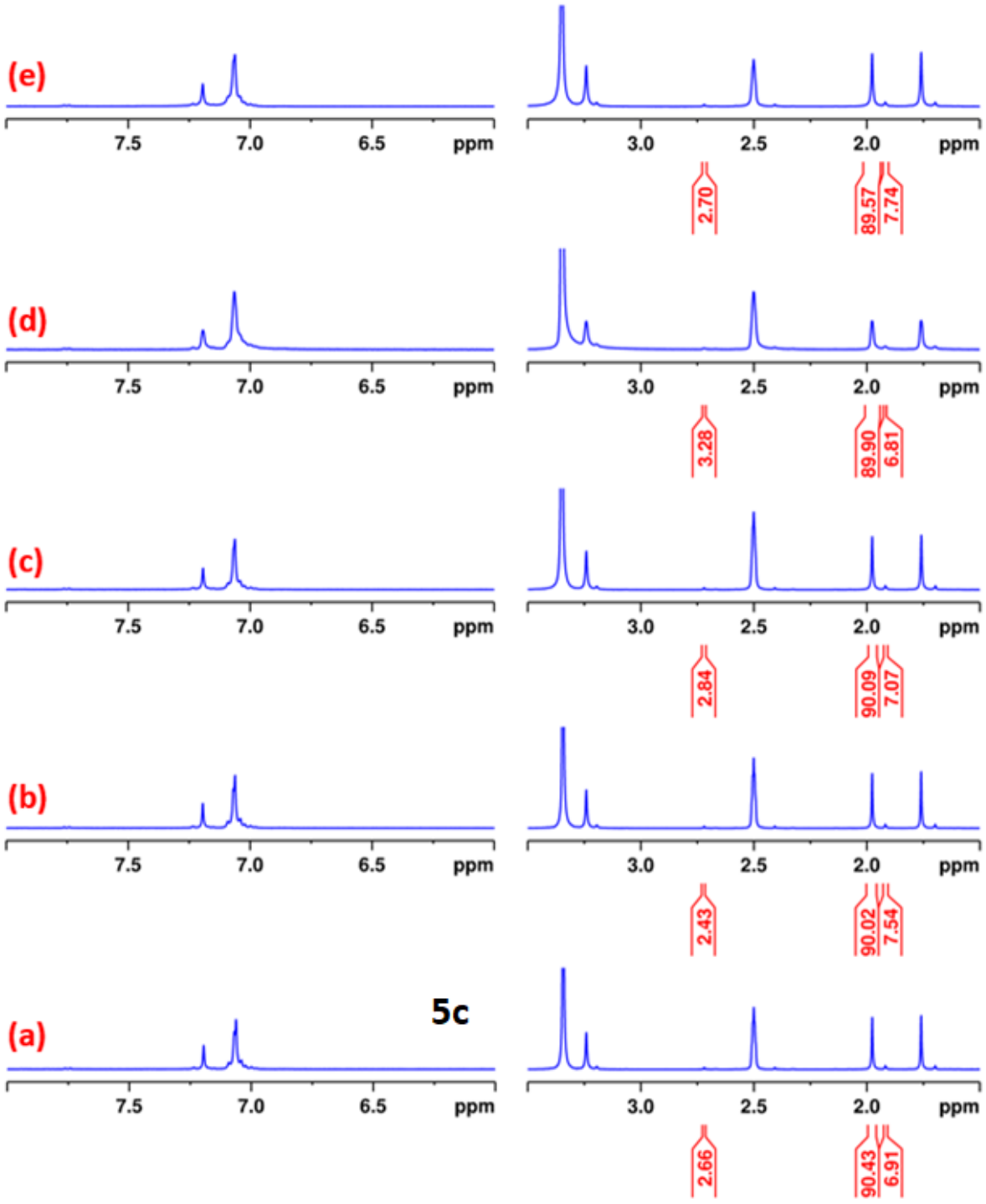

Figure 3C.1. Stacking plots depicting the studies on the concentration dependency of **5c** in the forward isomerization step (at different concentrations in [D_6]DMSO the samples have been irradiated at 365 nm to attain PSS).

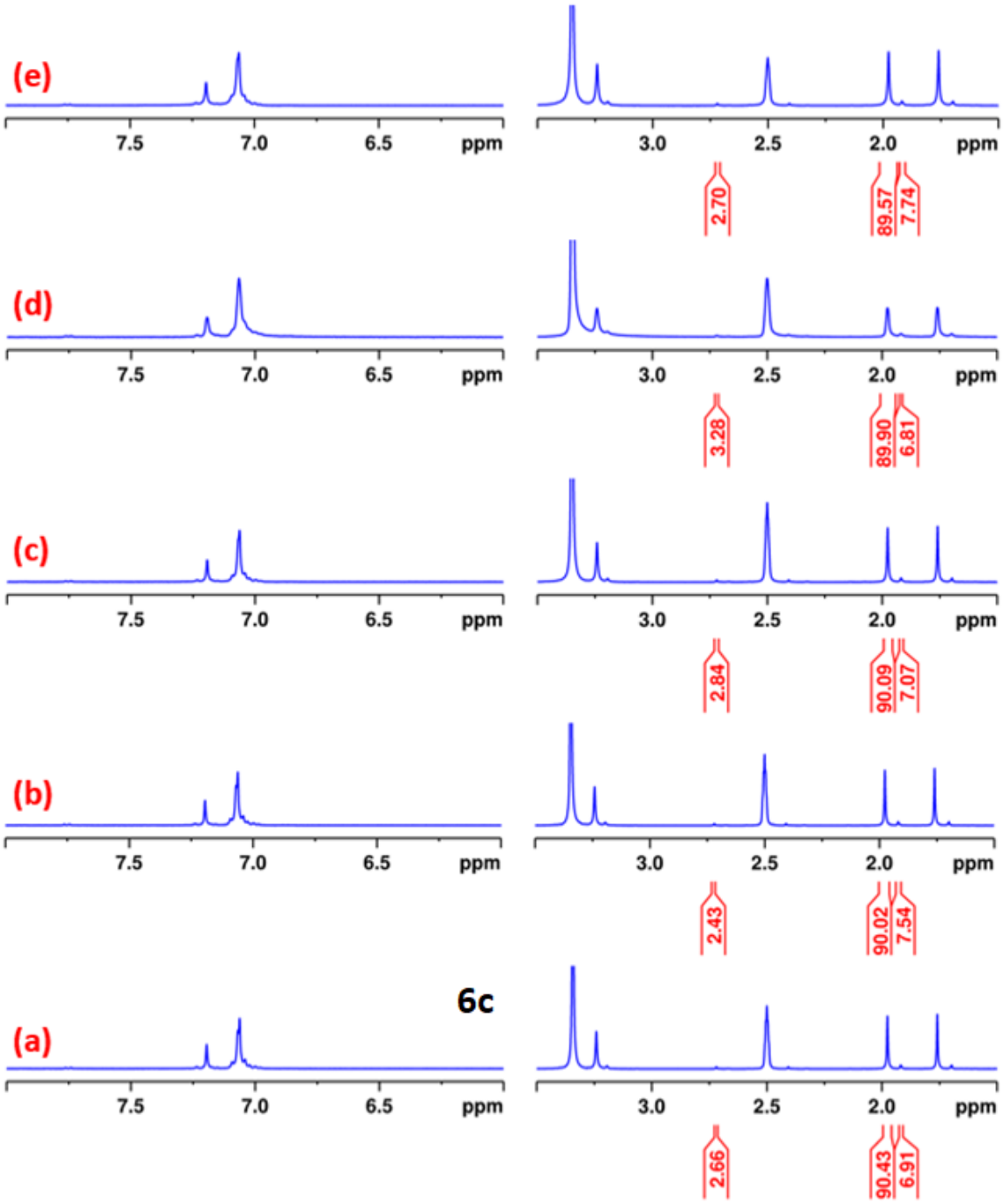

Figure 3C.2. Stacking plots depicting the studies on the concentration dependency of **6c** in the forward isomerization step (at different concentrations in [D_6]DMSO the samples have been irradiated at 365 nm to attain PSS).

Appendix 3D

Compound characterization (^{1}H and ^{13}C-NMR) data

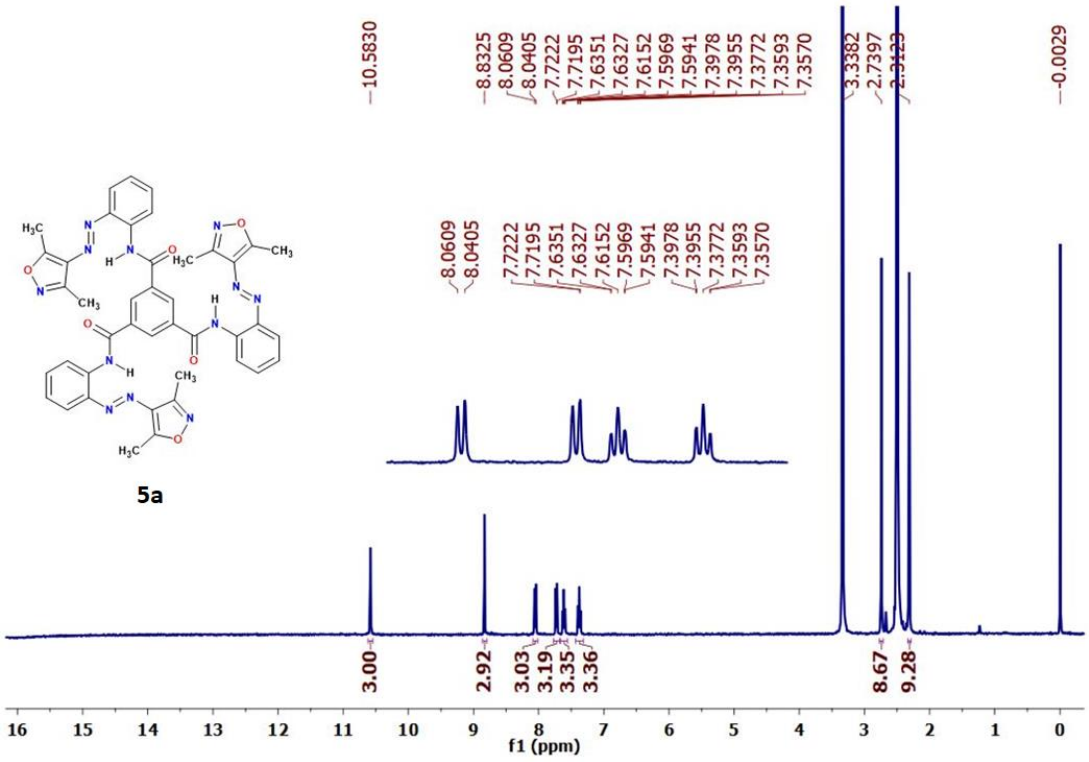

^{1}H NMR spectrum of **5a** in [D_6]DMSO

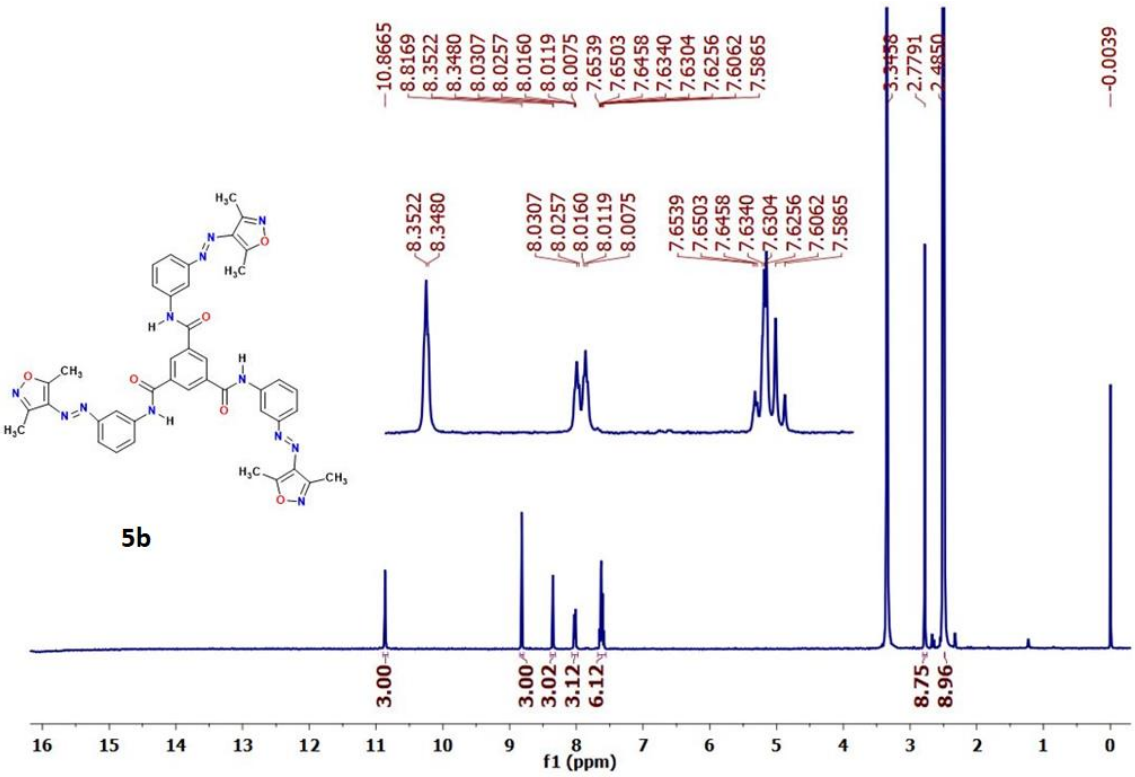

^{1}H NMR spectrum of **5b** in [D_6]DMSO

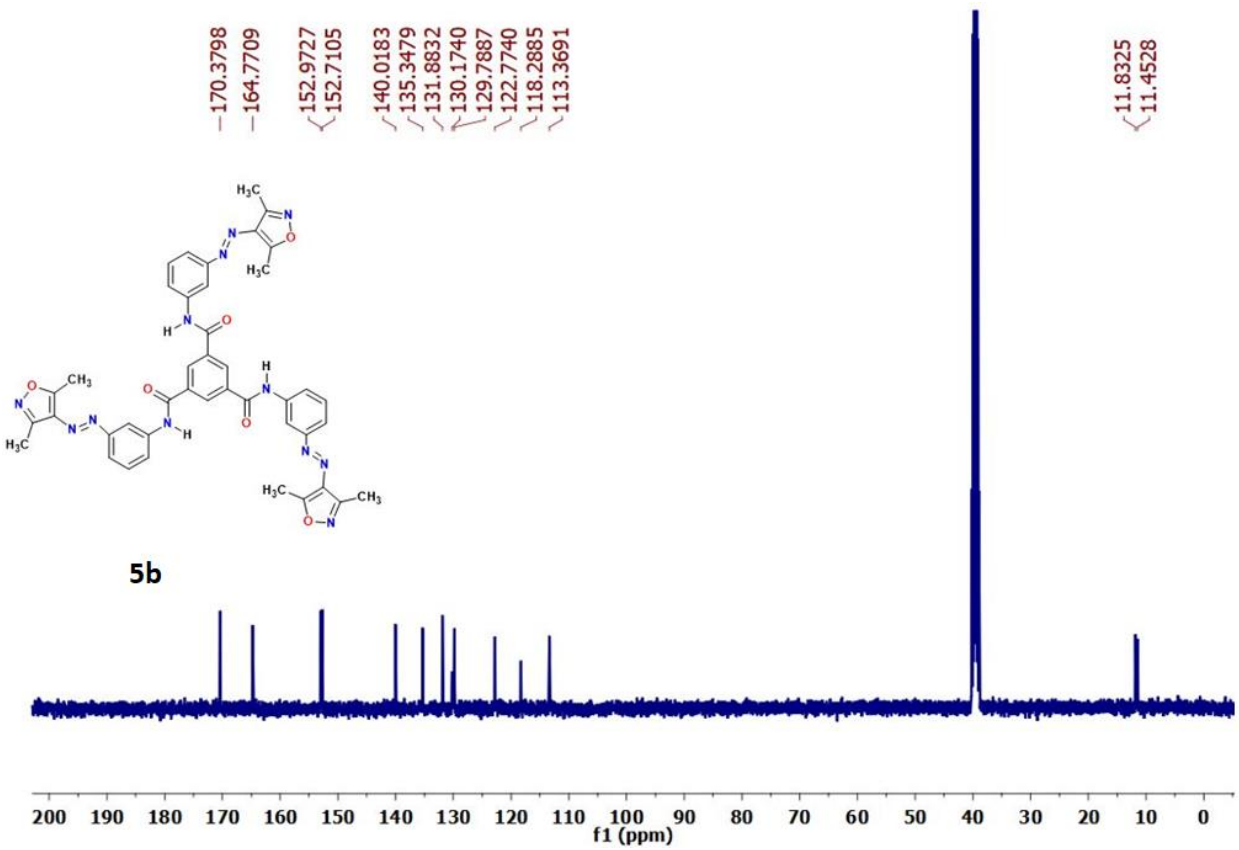

^{13}C NMR spectrum of **5b** in [D_6]DMSO

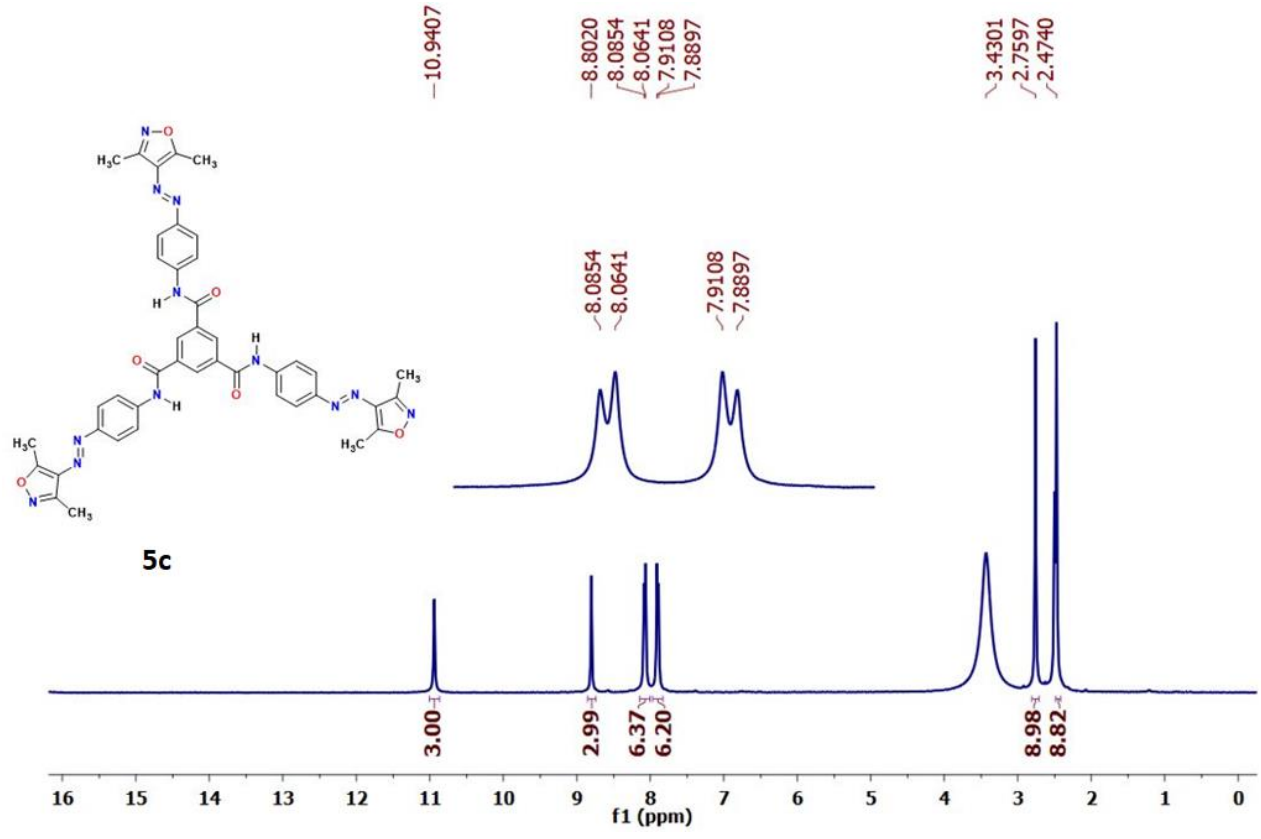

^{1}H NMR spectrum of **5c** in [D_6]DMSO

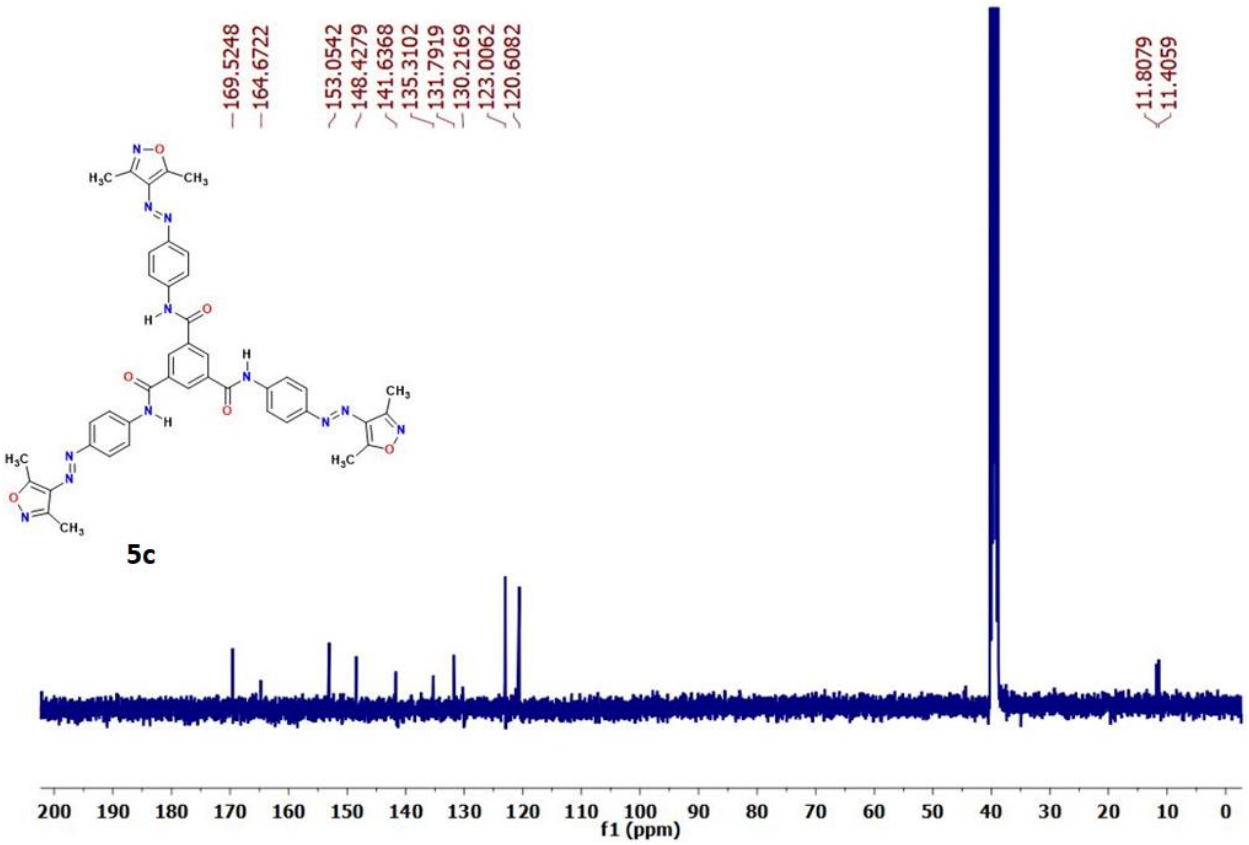

^{13}C NMR spectrum of **5c** in [D_6]DMSO

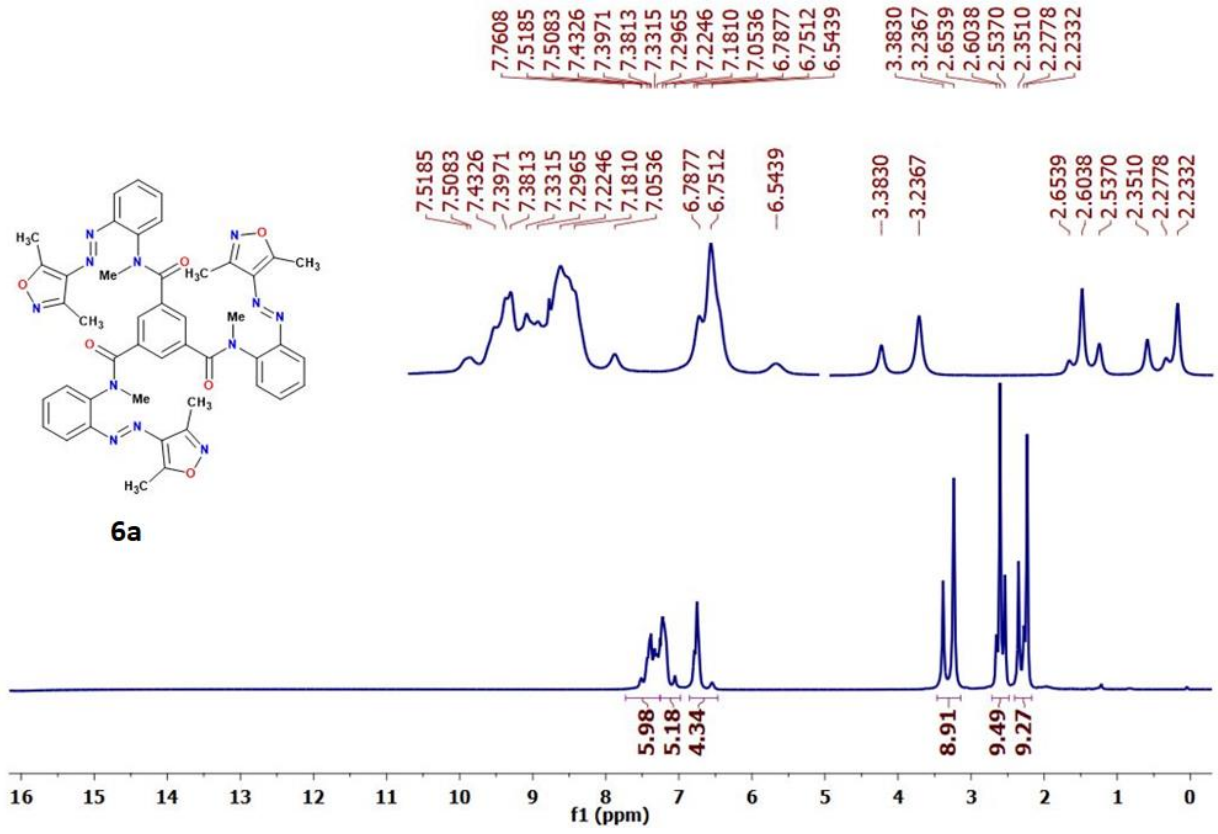

^{1}H NMR spectrum of **6a** in $CDCl_3$

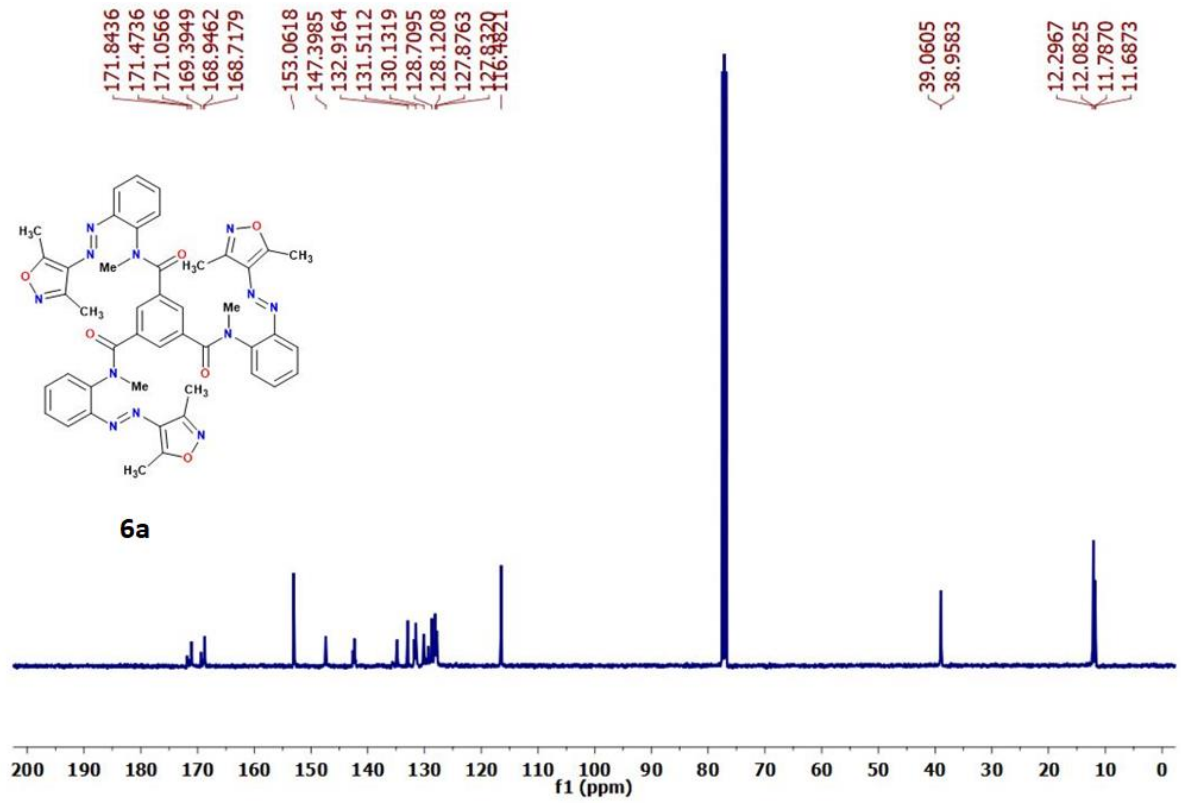

^{13}C NMR spectrum of **6a** in $CDCl_3$

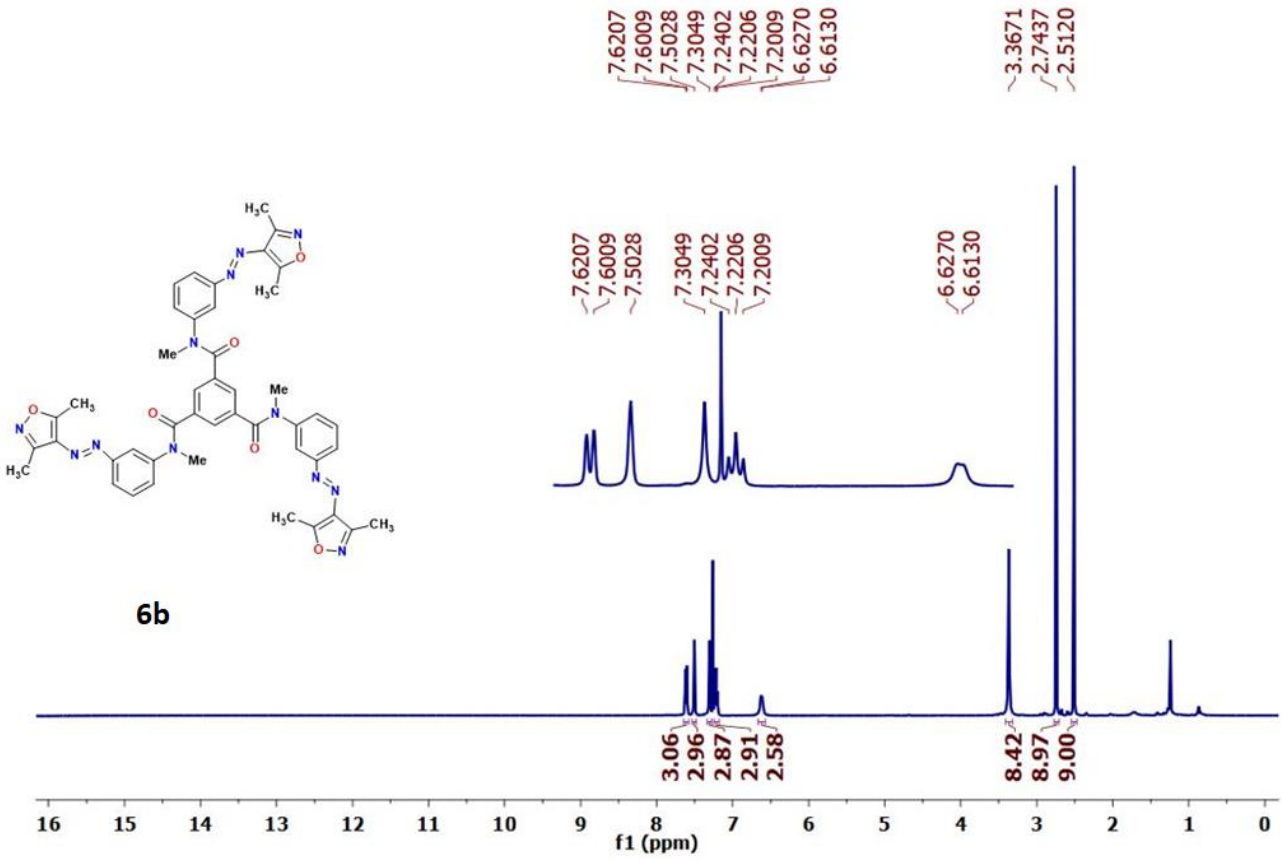

^{1}H NMR spectrum of **6b** in $CDCl_3$

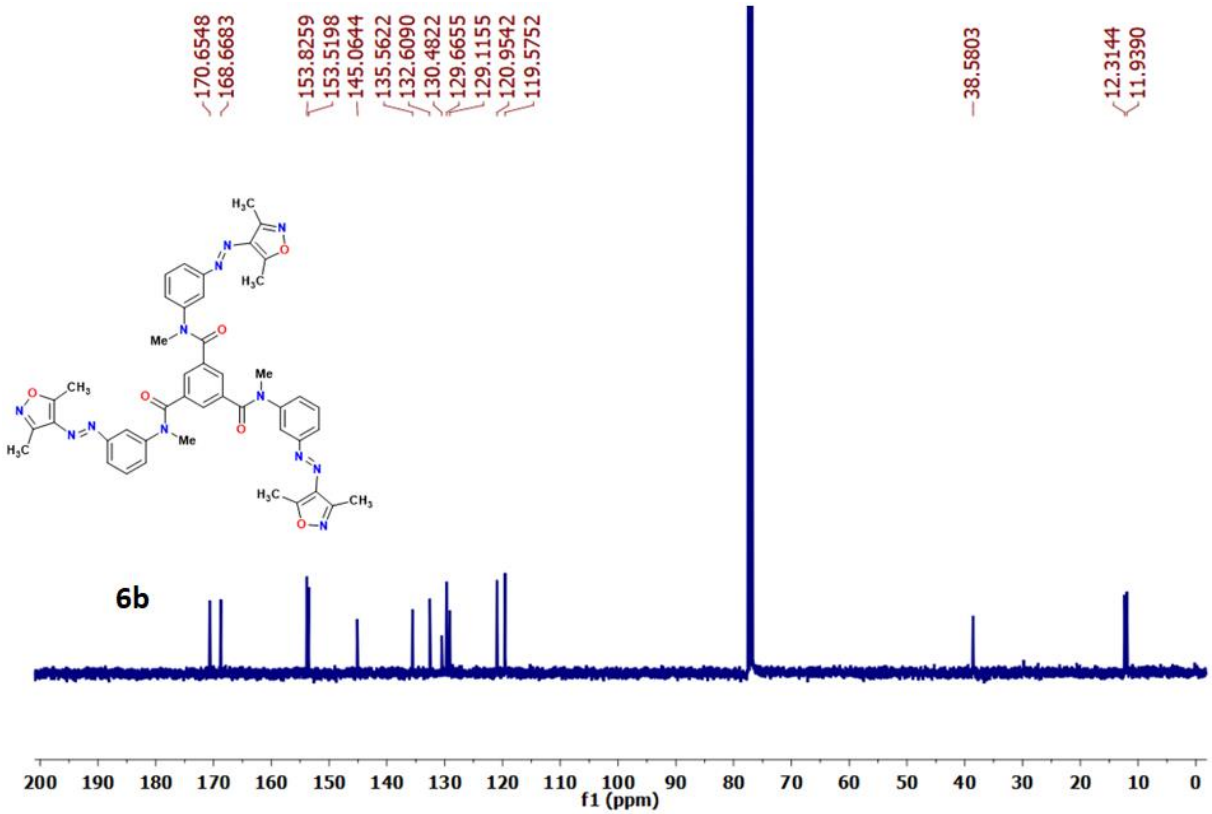

^{13}C NMR spectrum of **6b** in $CDCl_3$

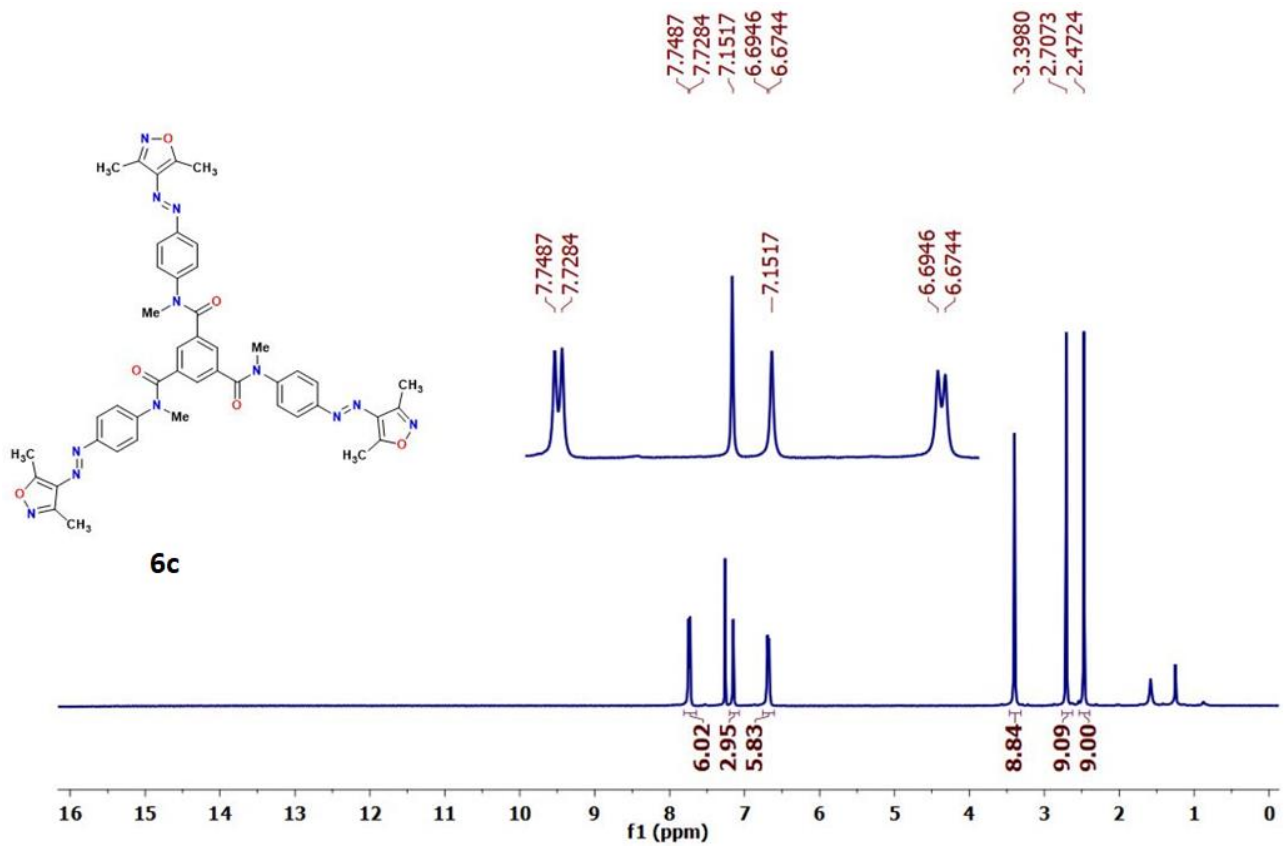

^{1}H NMR spectrum of **6c** in $CDCl_3$

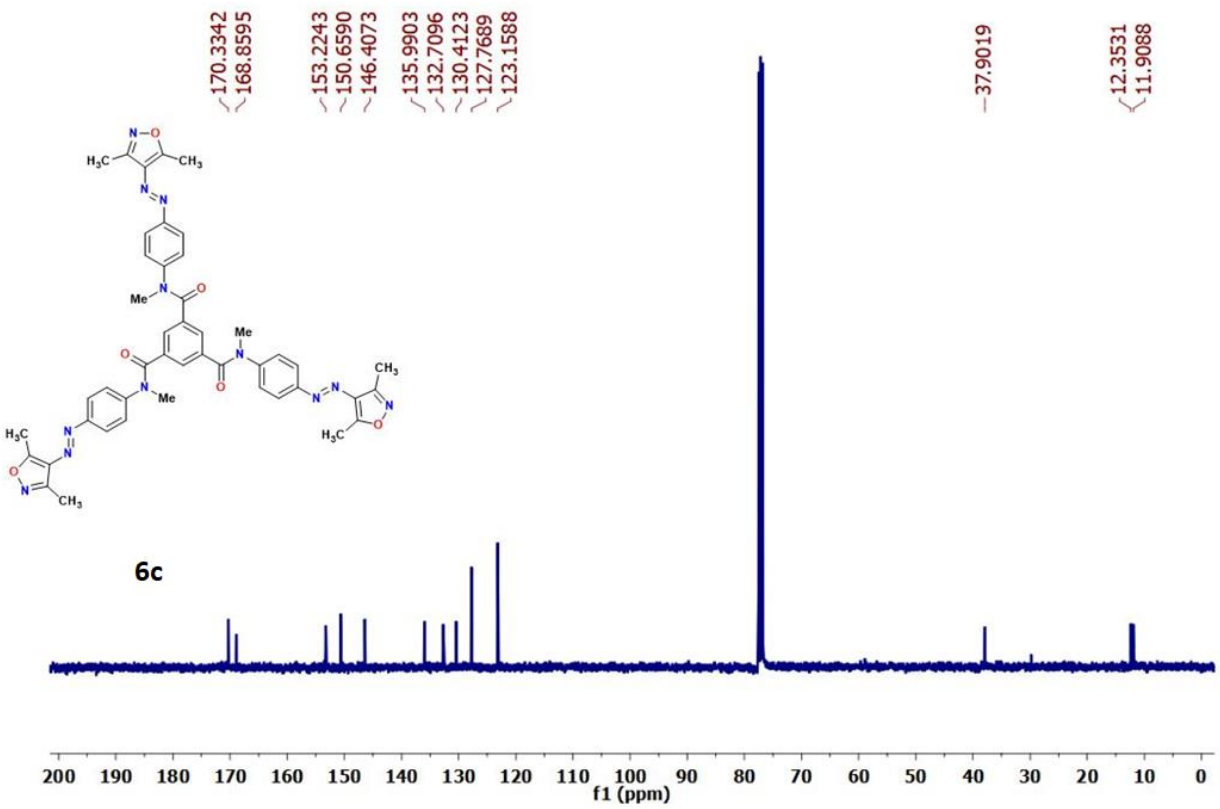

^{13}C NMR spectrum of **6c** in $CDCl_3$

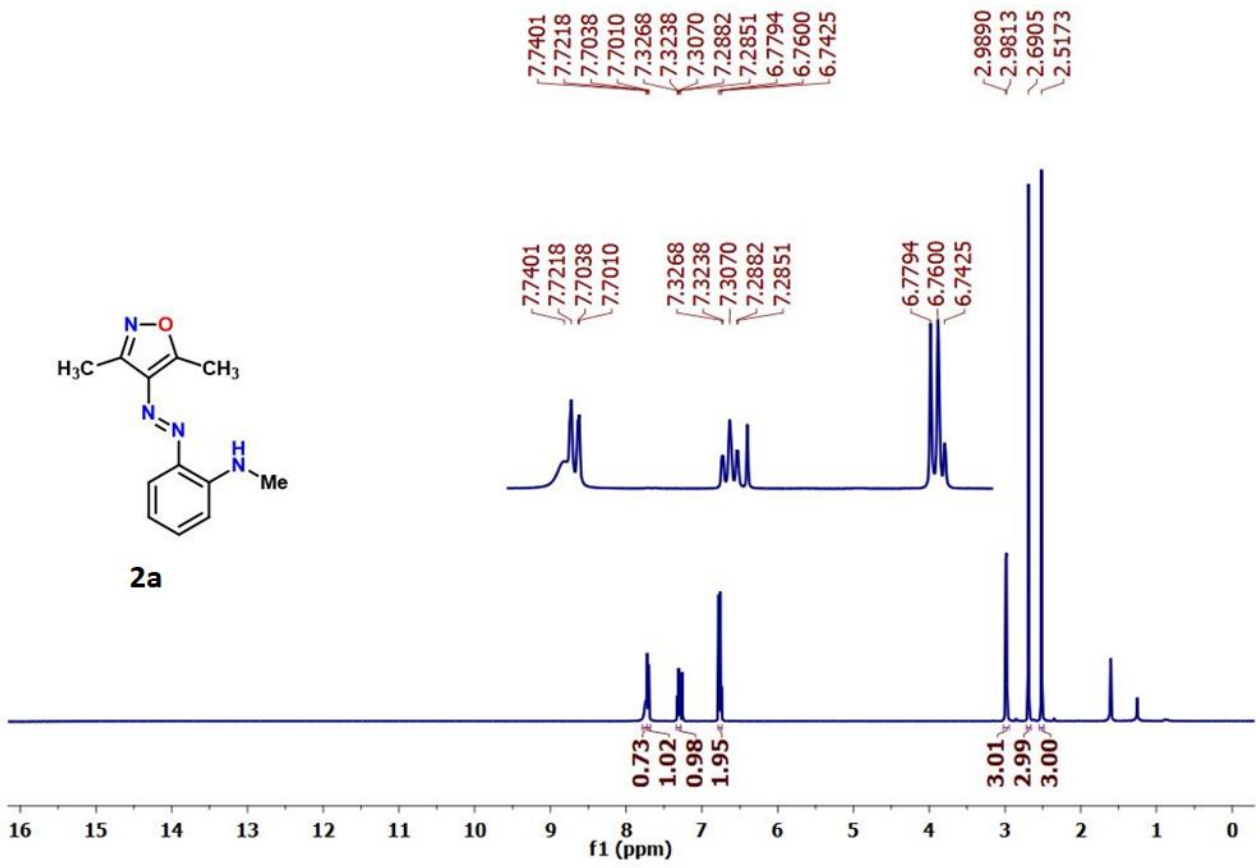

^{1}H NMR spectrum of **2a** in $CDCl_3$

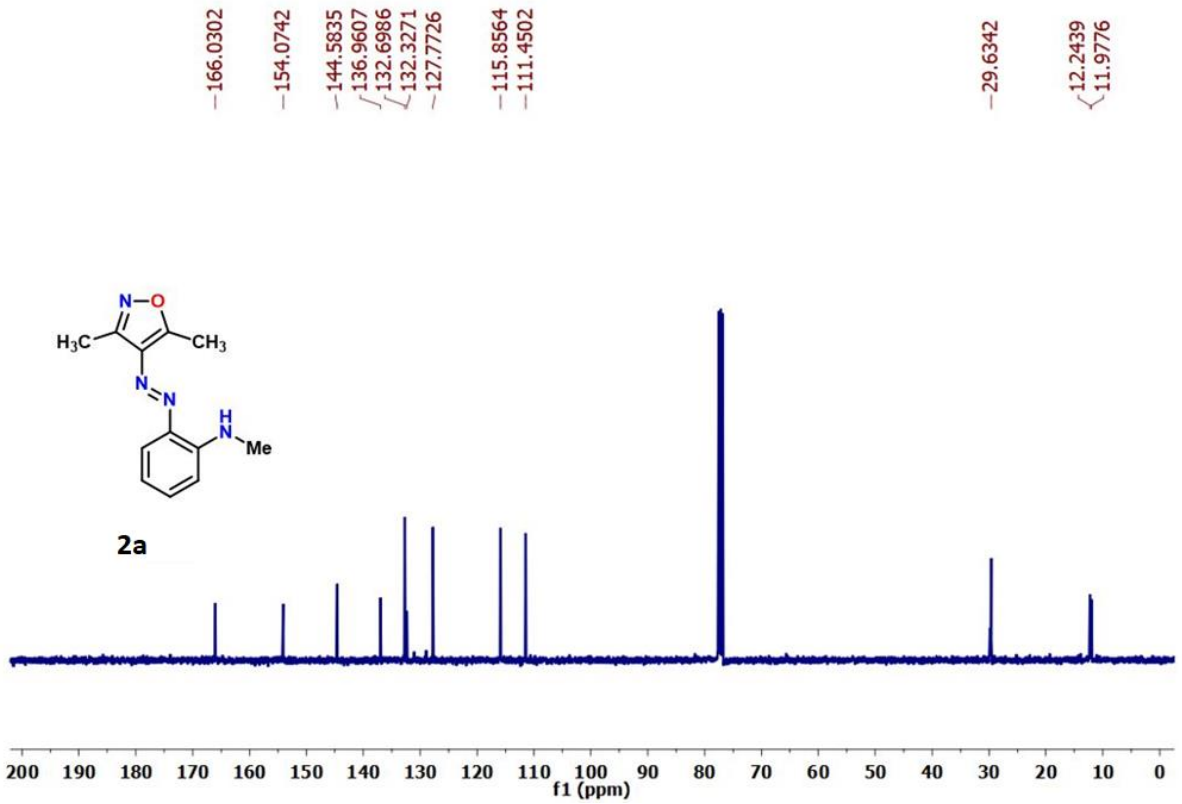

^{13}C NMR spectrum of **2a** in $CDCl_3$

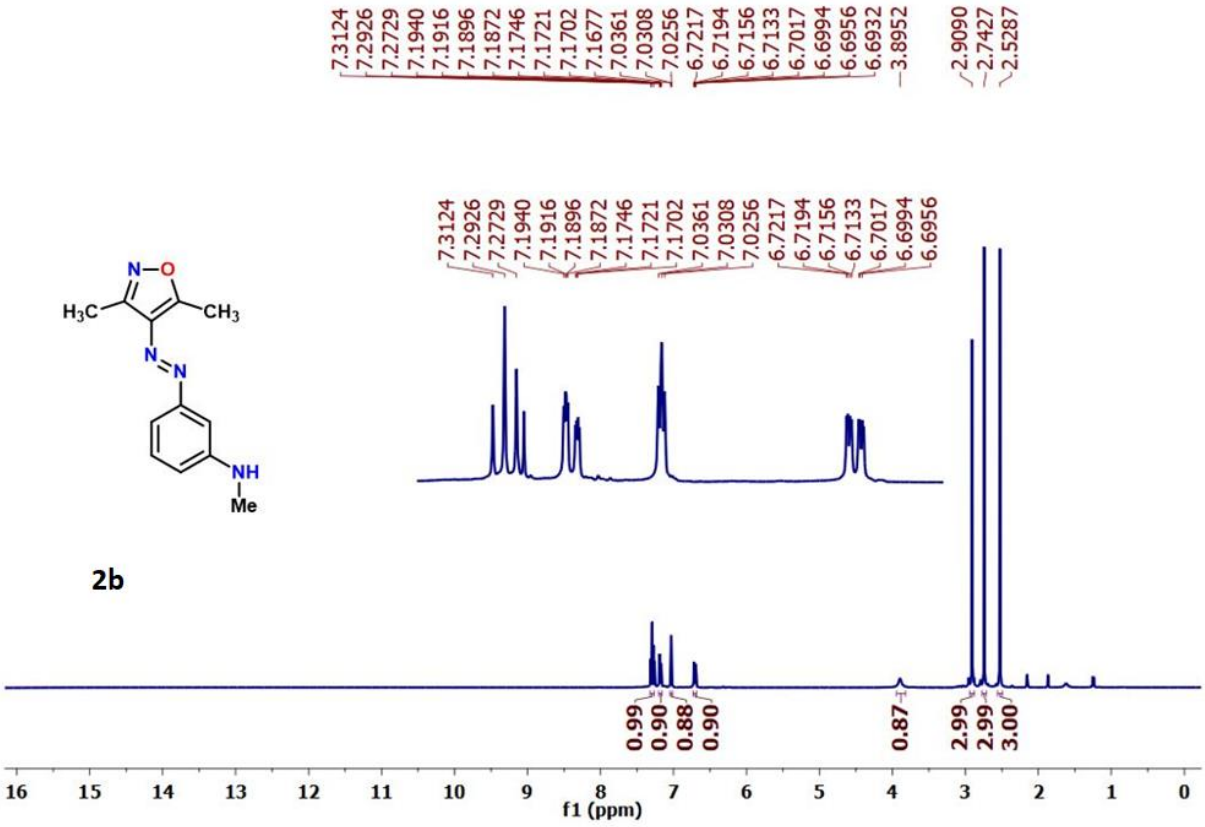

^{1}H NMR spectrum of **2b** in $CDCl_3$

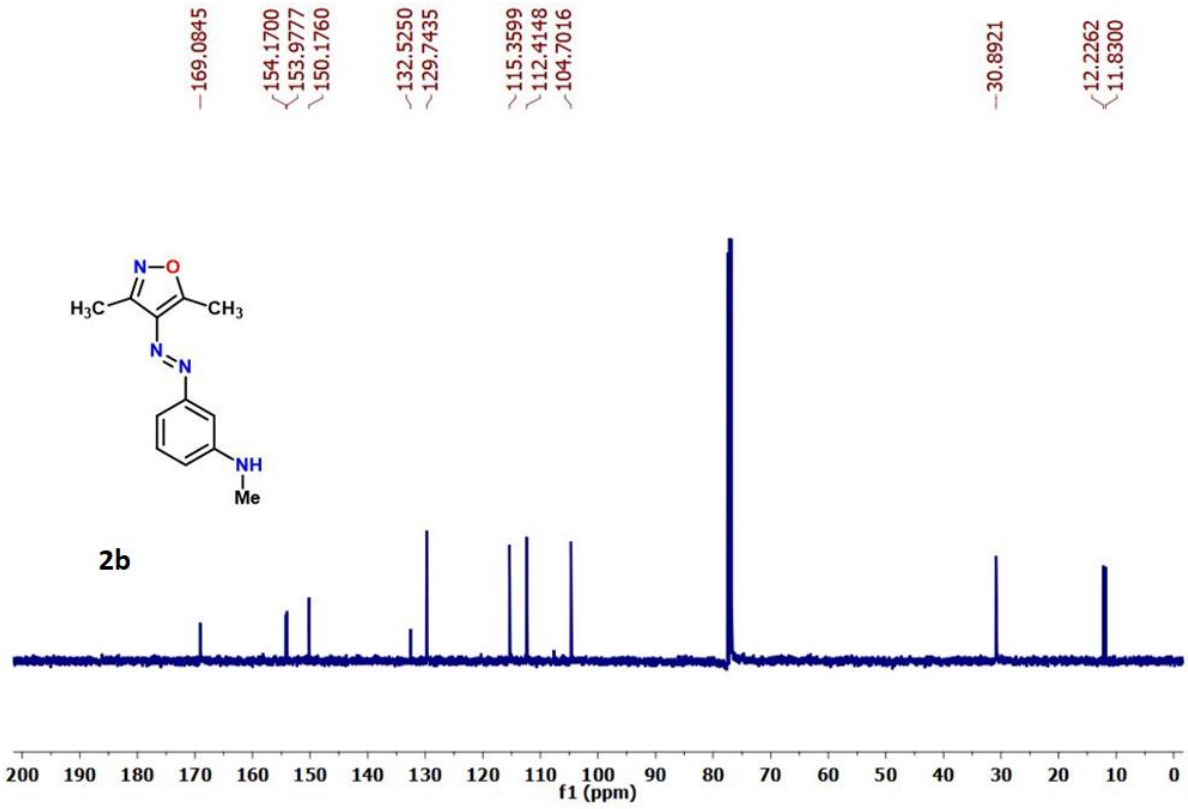

^{13}C NMR spectrum of **2b** in $CDCl_3$

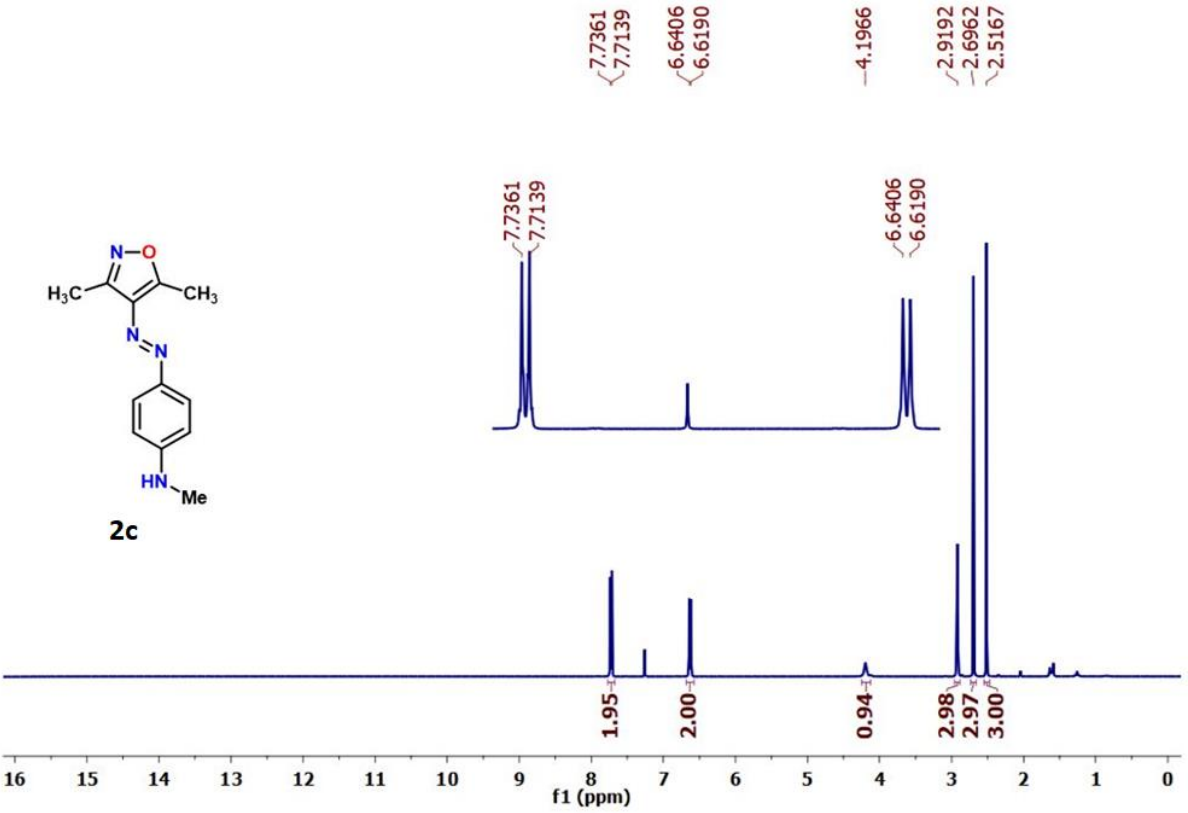

^{1}H NMR spectrum of **2c** in $CDCl_3$

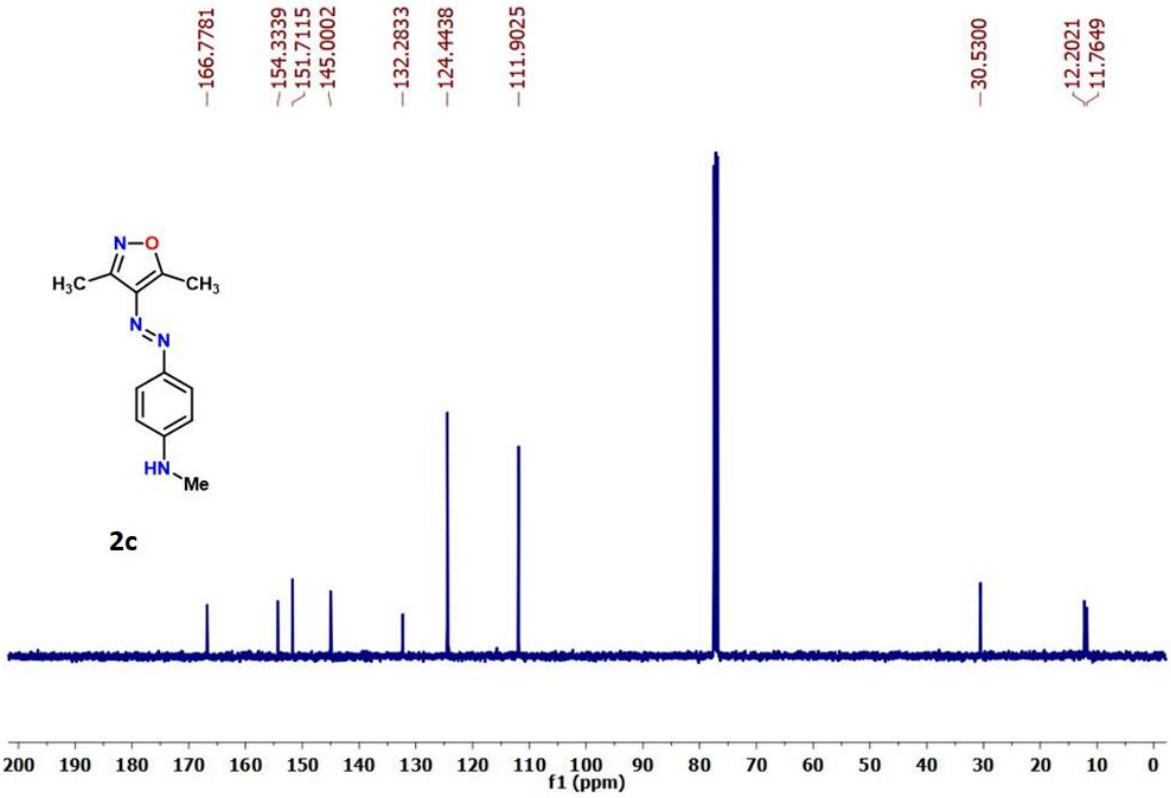

^{13}C NMR spectrum of **2c** in $CDCl_3$

Chapter 4. Arylazoisoxazole based reversibly photoswitchable discotic liquid crystals

4.1 Introduction

Smart materials or stimuli-responsive materials are interesting as they can change their property in a controlled and reversible manner under the influence of external stimuli.[1] Such materials can be designed and made at the molecular level, however, bringing stimuli responsiveness at the macroscopic level is quite challenging. One way of introducing such effects can be done using the controlled supramolecular assembly of stimuli-responsive molecules. In this regard, LC materials with photoresponsive groups are gaining importance.[2] Where the reversible *E-Z* isomerization of azobenzenes and the geometrical changes associated with their photoswitching play a significant role. Additionally, they modulate the LC properties ranging from partial to complete mesophase changes (ordered LC phase to isotropic phase).

In this regard, various roles and connection strategies of azobenzenes were explored.[3] Additionally, linear, branched or bent, tripodal, and pillararene-like architectural distinctions in the connections have also been investigated with a wide range of property changes.[4] Imparting photoresponsiveness to the LCs possessing fluidity and long-range directional order can control the functions like grating, photoalignment, polarization changes, photomechanical properties, actuators, solid surface properties, bimesomorphism, etc. by light or temperature.[3b,4f,5] Despite great success in controlling properties through the introduction of azobenzenes in a wide variety of LCs, the corresponding light-driven modulation in the domains of DLCs is surprisingly explored only to a limited extent.[7,3b,4f,6] In contrast to the widely explored photoresponsive alignment of calamitic nematic phases, the alignment of relatively viscous nematic phase formed by disc-shaped molecules i.e. discotic nematic (N_D) is a slow and challenging process. This work presents DLC photoalignment strategy that can offer a novel guideline to understanding the orientation mechanism of DLCs at a molecular level, leading not only to comprehending the anisotropic physical properties of DLCs but also to the fabrication of unique molecular devices for next-generation photonic and electronic devices.

The benzene-1,3,5-tricarboxamide (BTA) core accessible through simple synthetic sequences using trimesic acid can be an excellent supramolecular synthon that can engender DLCs.[7,8] Because the resulting C_3-symmetric design can be expected to show interesting LC

properties with columnar assemblies, we decided to incorporate azobenzene and azoheteroarene units to introduce reversible photoswitching, accompanied by changes in the mesophase.

4.2 Design, synthesis, and exploring LC properties of BTA-based photoswitchable alkoxyazobenzene incorporated systems

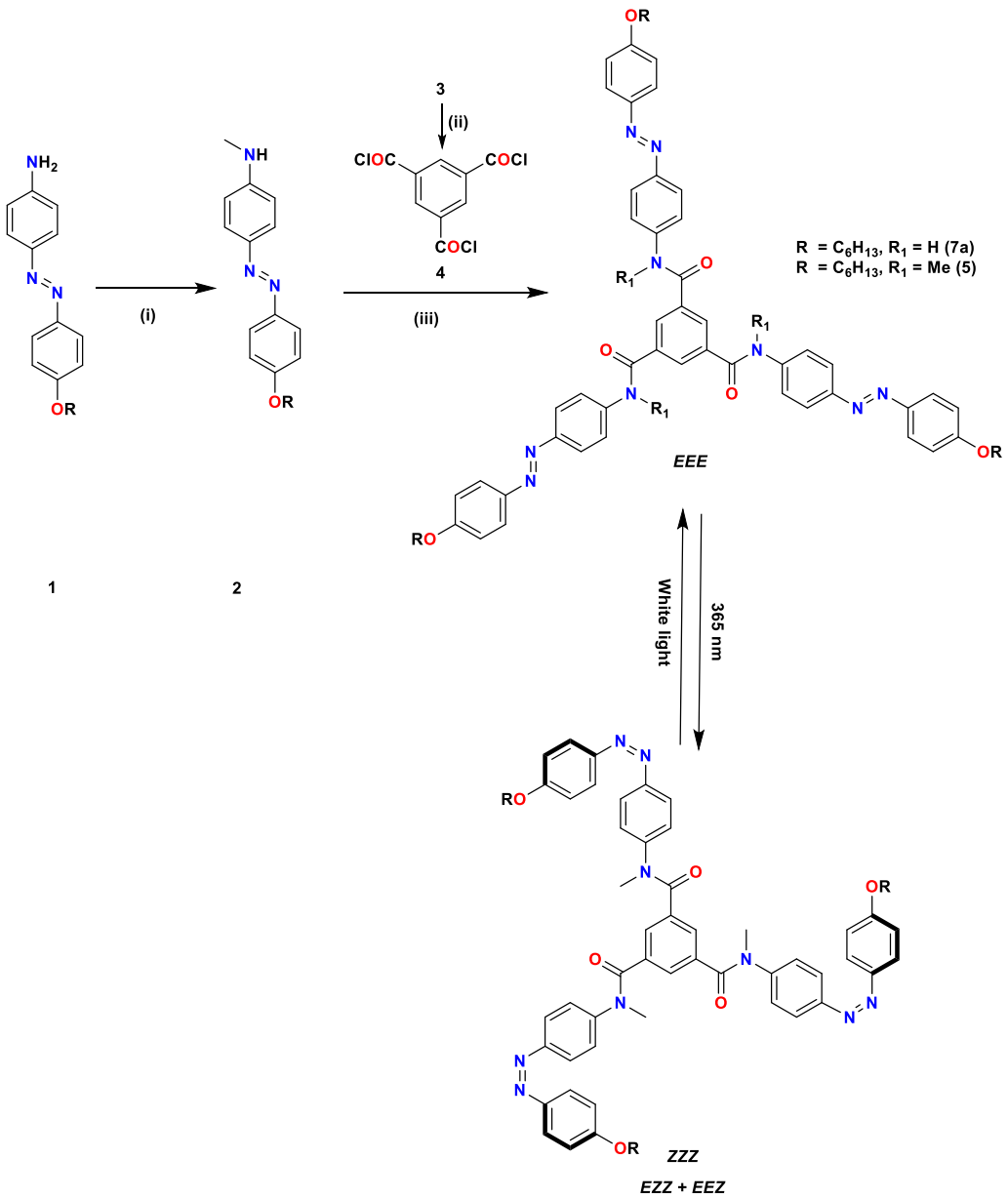

Scheme 4.1. Synthesis of target compound **5** and its photoisomerization channel. (i) **2**, HCHO, $NaCNBH_3$, MeOH, 0 °C, 2 h, **2**-32%; (ii) trimesic acid (**3**), PCl_5, toluene, reflux, **4**; (iii) **4**, pyridine, toluene, rt, **5**-40%.

Despite the reports of multi-azobenzene incorporated LC molecules, the corresponding derivatives leading to photoswitchable discotic LCs are scarce. In this regard, in our group, we designed a BTA core based on three alkoxyazobenzene functionalized

derivatives, which showed discotic LCs properties at room temperature.[7] These derivatives showed reversible and good to excellent photoswitching in solution as well as in LC thin film state. Yet, the LC state remains unaffected after irradiation with light. For comparison, an *N*-methylated analog of C_6 alkyl chain-containing molecule has been synthesized. The *N*-methylation of aminoazobenzene **1** was performed through a reductive amination strategy using formaldehyde and sodium cyanoborohydride at 0 ^{o}C, which was further reacted with *in situ* generated trimesyl chloride to obtain the target compound **5**. Both compounds **2** and **5** were characterized using ^{1}H NMR, ^{13}C NMR, IR, and HRMS spectroscopy (**Scheme 4.1**, **Experimental Section 4.8,** and **Appendix 4G**).

4.2.1 Analysis of photoswitching using UV-Vis and NMR spectroscopy

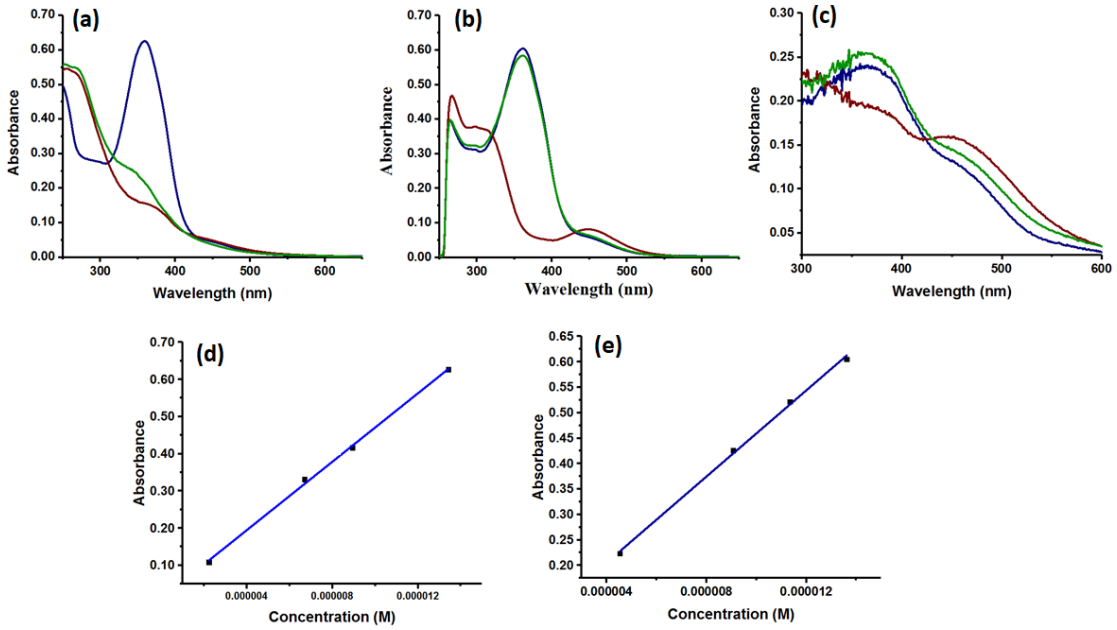

Figure 4.1. (a) Analysis of photoswitching behavior of **5** in $CHCl_3$ (13.4 μM); (b) Analysis of photoswitching behavior of **5** in DMSO (13.6 μM); (c) Analysis of photoswitching behavior in the solid state for **5** in KBr medium; (d) Estimation of molar extinction coefficient (ε = 46021 M^{-1} cm^{-1}) at of **5**-*EEE* in $CHCl_3$; (e) Estimation of molar extinction coefficient (ε = 42372 M^{-1} cm^{-1}) at of **5**-*EEE* in DMSO; The spectrum in blue trace corresponds to **5**-*EEE*, and the one in the red trace is recorded after irradiation at 365 nm. The green trace represents the reverse photoisomerization step after irradiation at 505 nm.

The target molecule **5** was subjected to photoswitching and followed by UV-vis spectroscopy. In this regard, the solutions of **5** in $CHCl_3$ and DMSO in micromolar concentrations were used. In $CHCl_3$, target **5** was found to photoswitch from the native state, however, the reverse photoisomerization step was not observed. On contrary, in DMSO target **5** was found to switch reversibly and very efficiently; at 365 nm, it isomerized from native to the photoswitched state, whereas the irradiation at 505 nm led to a reversal of the native state.

The molar absorption coefficient was also estimated for compound **5** in $CHCl_3$ and DMSO (**Figure 4.1d,e**).

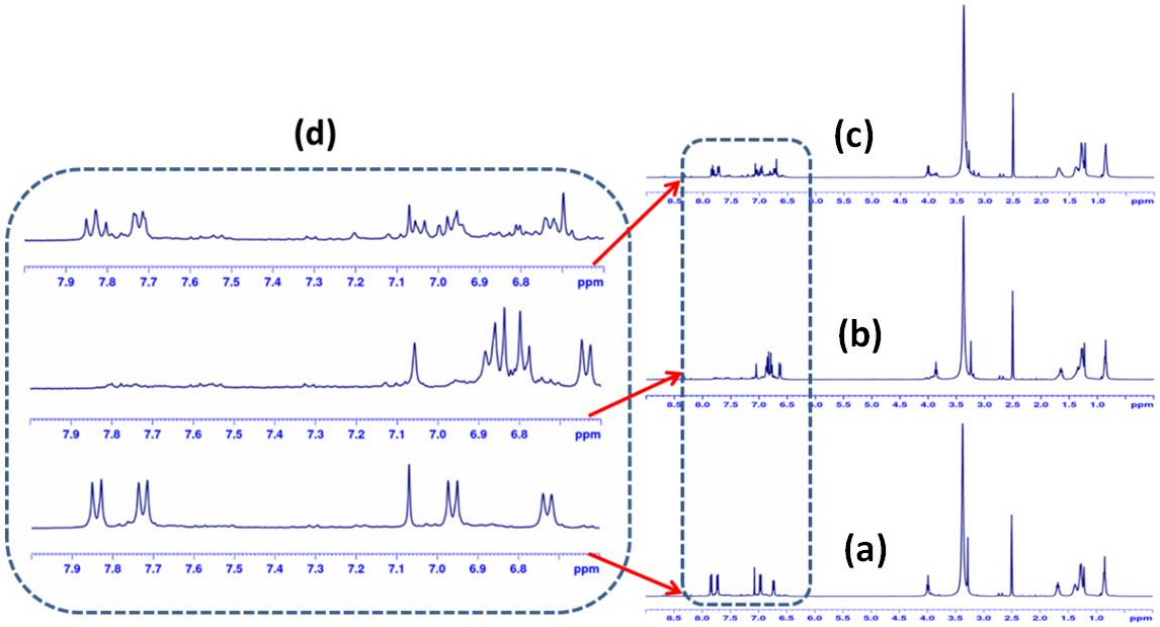

Figure 4.2. ^{1}H NMR spectra of **5**-*EEE* (8.4 mM in [D_6]DMSO) (a) before irradiation; (b) after irradiating with 365 nm UV light for 90 minutes; (c) after irradiating with the 505 nm light corresponding to the reverse isomerization step; (d) Zoomed region corresponds to the aromatic protons (as an insert).

The target compound was also photoswitched reversibly in the solid state as well (**Figure 4.1c**). The photoswitching was also followed by using the ^{1}H NMR spectroscopy. Upon irradiation at 365 nm, all the aromatic and *N*-methyl protons showed an upfield shift with near quantitative isomerization. However, the reverse isomerization led to a mixture of photoisomers (**Figure 4.2**).

4.2.2 POM and XRD studies

After getting compound **5,** we checked its mesomorphic properties by polarized optical microscope (POM) and X-ray diffraction (XRD) techniques. From the combined information by POM and XRD techniques, it was found that the columnar mesomorphic behavior was missing in the *N*-methylated derivative while its analogous compound **7a** showed Col_r and Col_h LC behavior.[7] This behavior was expected as in the tricarboxamides derivatives, the columnar LC behavior is driven by the intermolecular H-bonding which is absent in the *N*-methylated derivative. As **5** is not exhibiting any columnar assembly, due to disordered or amorphous structure. Still, we checked the texture of **5** under the microscope whether it's changing or not after the irradiation with 365 nm UV light. But we didn't

observe any changes in the texture under a microscope. Hence the only difference in compounds **7a** and **5** is that the compound is exhibiting well-defined columnar mesomorphic behavior and **5** is showing some disordered structure (because of a less sharp small angle peak). This result indicates the important role of amide *N*-H in self-assembly, which leads to columnar assembly. This motivated us to modify the existing molecular design so that we can reversibly control mesophase in the presence of amide *N*-H as a linker.

Taking a cue from the previous design, we intended to connect a photoswitch at the peripheral position. In this regard, the BTA core was tethered with the photoswitches through flexible alkyl spacers to assist supramolecular assembly. Equally, such designs can provide sufficient free volume to induce morphological changes upon *trans*/*cis* isomerization. Indeed, the resulting tripodal design offers enormous opportunities to tune the properties and, more importantly, the light-modulated DLC behavior that can be conceived at room temperature.

Herein, we report the design and synthesis of three target molecules (**1a-c**) and their investigations (**Scheme 4.2**). Extensive spectroscopic studies have been carried out to understand the photoswitching properties and the stability of the photoswitched states of these targets. DLC properties and their modulation by light have been investigated using differential scanning calorimetry (DSC), polarized optical microscopy (POM), and X-ray diffraction (XRD) studies. To evaluate the effect of photoswitching in the modulation of LC behavior, POM and atomic force microscopic (AFM) studies were also carried out. The details of the investigations in bringing "On and off" control of the DLC properties by light are discussed.

4.3 Design and synthesis

To design a molecule exhibiting DLC properties, we have chosen the BTA core and alkoxy side chains. The BTA core has an excellent propensity to form the columnar assembly through hydrogen bonding across amide groups. However, we focused on the conformational tunability of the molecular structure from a disclike to a rodlike shape by employing the rod-shaped phenylazo-3,5-dimethylisoxazole units at the periphery. Additionally, phenylazo-3,5-dimethylisoxazole photoswitch contributes to the light responsiveness of the desired targets. The choice of this particular unit is also due to its efficient photoswitching in both directions, the excellent thermal stability of the photoswitched state, solid-state photoswitching, and ease of synthesis.[9] More importantly, such phenylazo-3,5-dimethylisoxazole systems exhibited reversible light-induced phase transition due to the presence of weak intermolecular

interactions in the native state. Besides that, the tether (alkoxy groups) length has been varied to impart changes in the mesomorphic properties of the target DLCs. Based on this, three

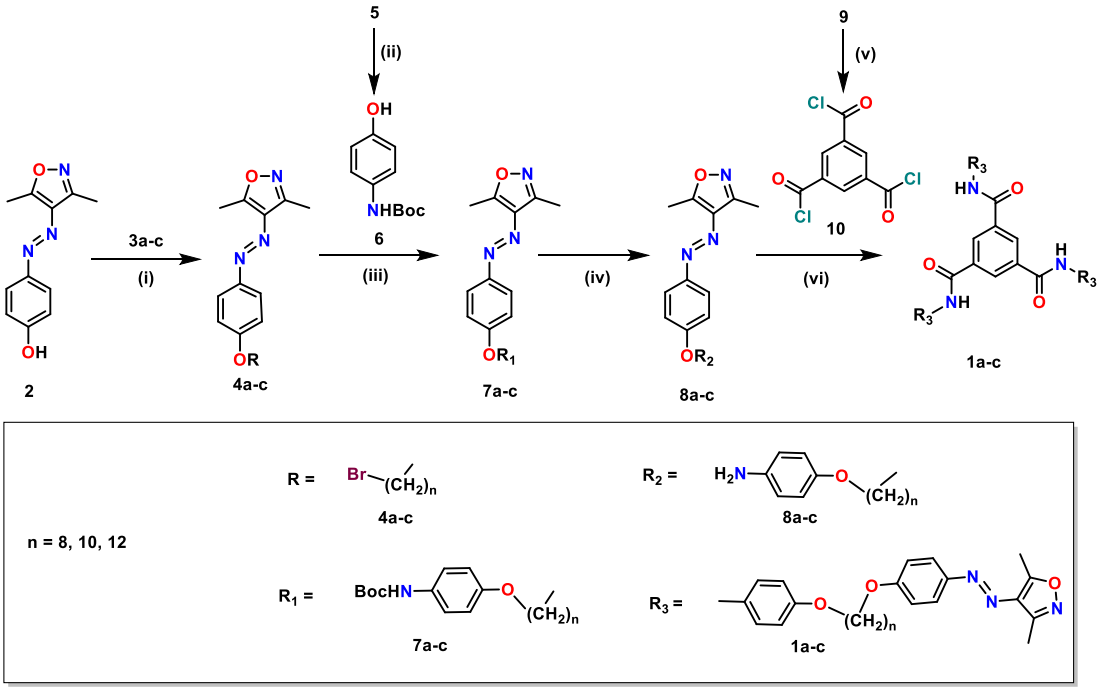

Scheme 4.2. Synthesis of the target molecules **1a-c**, (i) **2,** Br-$(CH_2)_n$-Br **3a-c**, K_2CO_3, DMF, 60 ^oC, 1 h, **4a**-57%, **4b**-57%, **4c**-60%; (ii) 4-amino phenol **5**, di-tert-butyl dicarbonate, Et_3N, THF, rt, overnight, **6**-68%; (iii) **6**, **4a-c**, K_2CO_3, cat. KI, CH_3CN, overnight, **7a**-85%, **7b**-78%, **7c**-88%; (iv) **7a-c**, DCM:TFA (6:1), 0 ^oC to rt, 4 h, **8a**-32%, **8b**-28%, **8c**-29%; (v) Trimesic acid **9**, $SOCl_2$, cat. DMF, reflux, 4-5 h; (vi) **10**, **8a-c**, Et_3N, dry DCE, rt, 12 h, **1a**-59%, **1b**-54 %, **1c**-76%.

target molecules **1a-c** have been considered synthetic targets. The synthesis of desired target molecules (**1a-c**) has been performed in multiple steps, starting from the *p*-hydroxyphenylazo-3,5-dimethylisoxazole **2**, which is synthesized by a reported procedure (**Scheme 4.2**).[9a] Hydroxy group has been alkylated by reacting with dibromoalkanes of different carbon chains (C_8, C_{10}, C_{12}) **3a-c** for getting the products **4a-c**. The hydroxy group of *N*-Boc protected 4-aminophenol **6** has further substituted the free bromine present at the terminal position in the presence of potassium carbonate and a catalytic amount of potassium iodide to form **7a-c**. This step gives free amines (**8a-c**) after completion of the deprotection of Boc in the presence of trifluoroacetic acid (TFA). These molecules (**8a-c**) have been functionalized into the benzenetricarboxamides (**1a-c**) by reacting with the *in situ* generated trimesoyl chloride **10**. The characterization of all the molecules has been performed by using ^1H, ^{13}C-NMR, HRMS, IR, UV-vis, etc (**Experimental Section 4.8** and **Appendix 4G**).

4.4 Photoswitching studies of the targets

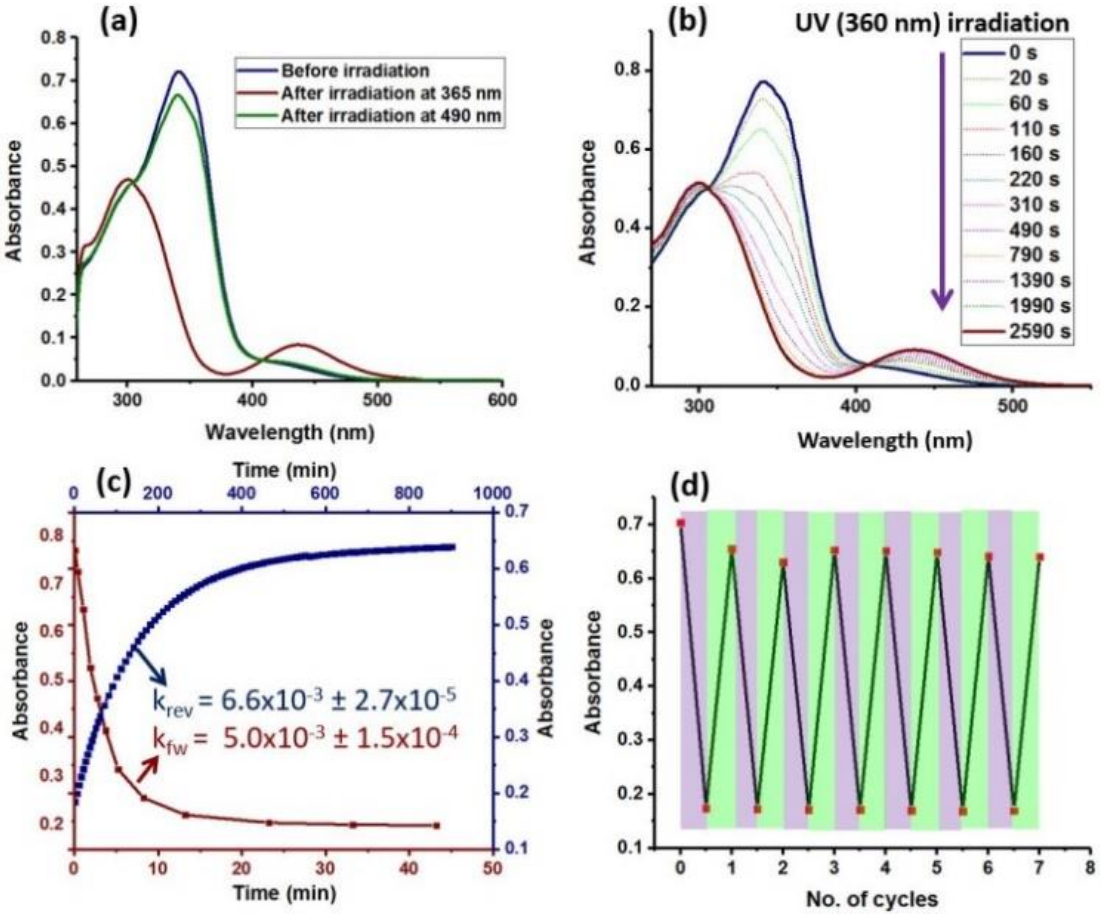

Figure 4.3. Analysis of UV-vis spectroscopic studies of **1a** (a) Photoswitching behavior of **1a** (10.8 μM, DMSO); (b) Forward (*EEE* to *ZZZ*) photoisomerization kinetics spectral data of **1a** (11.5 μM, DMSO) recorded at different intervals of irradiation time at 360 nm (50 μw power LED) at rt; (k_{fw} is estimated in s^{-1}, whereas k_{rev} is expressed in min^{-1}); (c) Kinetics plots of thermal reverse isomerization (8.5 μM, DMSO, blue trace) at 60 °C and photochemical forward isomerization (11.5 μM, DMSO, brown trace) at 360 nm and 25 °C of **1a**; (d) Photoisomerization stability experiment. (The irradiation at 365 and 490 nm lights have been alternatively used in the forward and reverse isomerization steps, respectively). For the kinetics and photoisomerization stability experiments, the absorptions at λ_{max} = 341 nm have been followed.

It has been observed that electronic spectral properties are independent of alkoxy spacer chain length in **1a-c**. The λ_{max} at 341 nm is common for all three compounds **1a-c**, which has been attributed to the π–π* absorption band. The λ_{max} corresponding to the n–π* band was unclear due to low intensity. Similarly, the photoswitched state $\lambda_{\pi-\pi*}$ values are quite similar, and more importantly, the n–π* band is intense. On the other hand, molar absorptivity values for **1a-c** have been estimated to be 67061, 62421, and 66107 M^{-1} cm^{-1}, respectively, which are quite similar. The molecules incorporated with three photoswitchable units in a C_3-symmetric

manner in principle can exhibit multiple photoisomers that include the *EEE*- (native state), *EEZ*-, *EZZ*-, and *ZZZ*- (all-*cis*) isomers. Since UV-vis spectroscopy has limitations in

Table 4.1. Electronic spectroscopic data and PSS composition estimated using UV-vis and NMR spectroscopy

Compound	Electronic spectral data[a] from UV-vis spectroscopy							NMR spectral data			
	Before irradiation		After irradiation		PSS composition in terms of conversion of *EEE* isomer[b,c,d]			PSS composition			
	λ_{max}/ π–π* (ε)	λ_{max}/ n-π*	λ_{max}/ π–π*	λ_{max}/ n-π*	Forward %*EEE*	Reverse %*EEE*	Conc. [μM]	λ (nm)	%*EEE*	%*ZZZ*	Conc. (mM)
1a	341 (67061 ± 702)	-	301	437	76	92	10.8	365 **490**	3 79	97 21	7.3
1b	341 (62421 ± 515)	-	301	437	75	96	11.6	365 **490**	2 84	98 16	1.2
1c	341 (66107 ±1054)	-	300	437	75	95	10.4	365 **490**	18 [d]	82 [d]	1.5

[a]All the data have been estimated in DMSO; [b]The PSS composition has been estimated based on the ref [10]; [c]The forward and reverse steps may have some amount of *EEZ* and *EZZ* isomers at PSS. [d]Due to poor solubility, the PSS composition for the reverse isomerization step in **1c** was not estimated.

distinguishing and quantifying the individual photoisomers, we utilized the ^{1}H-NMR spectroscopy in this regard. All three samples of the targets **1a-c** have been subjected to photoswitching experiments at mM concentrations in [D_6]DMSO and followed by using ^{1}H-NMR spectroscopy (**Figure 4.4, Table 4.1, Appendix 4B**). Interestingly, an excellent photoswitching from all-*trans* (*EEE*) isomer was observed exhibiting a near quantitative conversion to all-*cis* isomer at 365 nm irradiation conditions (%*ZZZ*-isomer at PSS: **1a**- 97%, **1b**- 98%, **1c**- 82%). On the other hand, the reverse photoisomerization at 490 nm was incomplete, although nearly 80% of the native state has been reverted. Due to the solubility issue upon reverse photoswitching, we could not estimate the PSS for **1c**. Surprisingly, we did not observe any signal attributed to the other photoisomers, *EEZ*-, and *EZZ*-isomers. We performed additional experiments to gain further insights into these two intermediate photoisomers. The irradiated sample of **1a** in [D_6]DMSO after enrichment of all-*cis* isomer has been subjected to reverse isomerization step under both photochemical (at 490 nm irradiation) and thermal (at room temperature) conditions. Upon following the changes in the spectral features at different intervals of time, we did not see any additional signals (**Figure 4B.4** and **Figure 4B.5** in **Appendix 4B**). Presumably, the location of the photoswitches

(terminal position) and alkoxy tether (flexibility of the spacer) make the phenylazo-3,5-dimetyhlisoxazoles behave like independent photoresponsive units. The lack

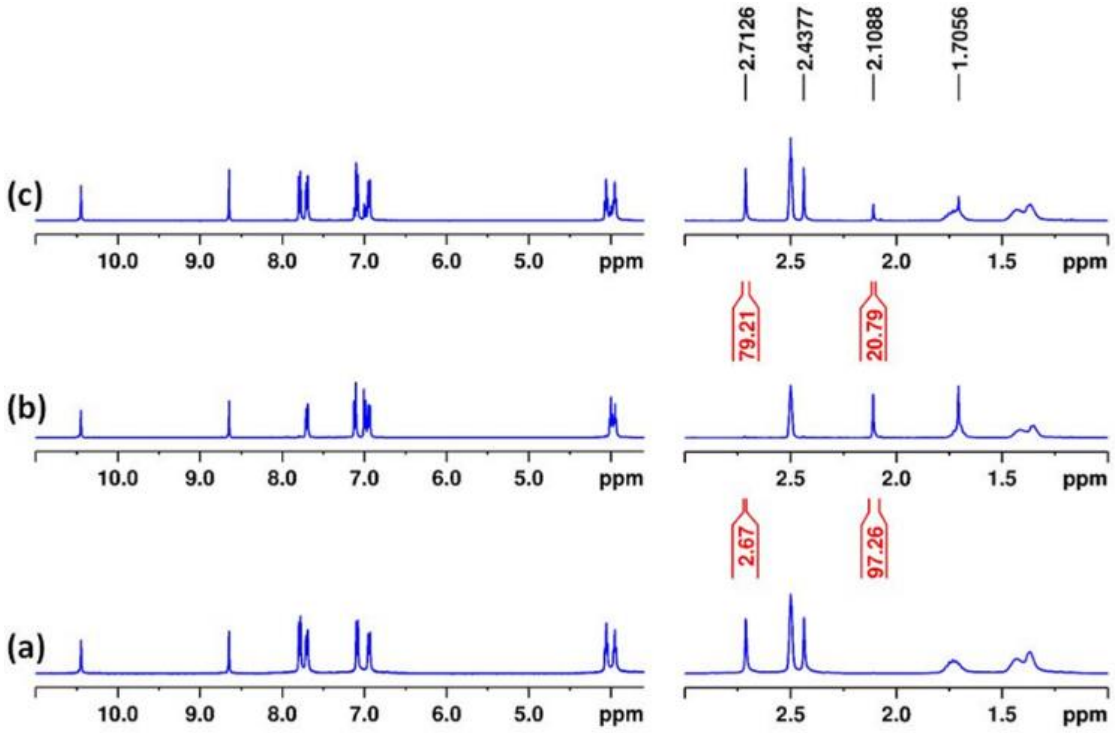

Figure 4.4. Analysis of photoswitching for the target (**1a**) using ^{1}H-NMR (7.3 mmol, [D_6]DMSO) (a) Before irradiation; (b) after irradiation at 365 nm, and (c) after irradiation at 490 nm. (The normalized integral values due to the signals corresponding to methyl protons are indicated).

of electronic coupling between the three photoswitches could be responsible for this. Interestingly, all three targets exhibited excellent photoswitching in the solid state too (**Appendix 4C**).

4.5 Thermal stability of the photoswitched states and photoisomerization rates

The reverse isomerization steps of azo photoswitches are thermally enabled even under dark. Indeed, their thermal isomerization rates limit their practical utility. Previously, we reported that the unsubstituted phenylazo-3,5-dimethylisoxazole at room temperature is more stable at the *Z*-isomeric state with an estimated half-life of 45.5 days in [D_6]DMSO.[9a] Hence, the thermal stability of photoswitched states of **1a-c** is expected to be high. In this regard, we performed the thermal reverse isomerization kinetics experiments of **1a-c** in DMSO at higher temperatures (60, 70, 80, and 90 ^{o}C), and the rates have been estimated by using UV-vis spectroscopic studies. All the photoswitched states in targets **1a-c** exhibited an exponential growth of the native state (**Figure 4.3c** and **Appendix 4D**). Rate constants have

been estimated from first-order kinetic plots. Indeed, the rate constants of all the three targets **1a-c** at 80 °C have been estimated to be 6.1×10^{-2} min^{-1} (**Table 4D.1** in **Appendix 4D**),

Table 4.2. Activation parameters associated with the thermal reverse isomerization step in **1a-c** (in DMSO)

Compound	E_a	$\Delta G^{\ddagger}$ (298K)	$\Delta H^{\ddagger}$	$\Delta S^{\ddagger}$
1a	$105.2 \pm 2.5^{[a]}$ $25.1 \pm 0.6^{[b]}$	$96.4 \pm 3.3^{[a]}$ $23.0 \pm 0.8^{[b]}$	$102.3 \pm 2.5^{[a]}$ $24.5 \pm 0.6^{[b]}$	$19.8 \pm 7.2^{[c]}$ $4.7 \pm 1.7^{[d]}$
1b	$103.5 \pm 2.0^{[a]}$ $24.7 \pm 0.5^{[b]}$	$96.0 \pm 2.8^{[a]}$ $22.9 \pm 0.7^{[b]}$	$100.6 \pm 2.1^{[a]}$ $24.0 \pm 0.5^{[b]}$	$15.3 \pm 5.9^{[c]}$ $3.7 \pm 1.4^{[d]}$
1c	$104.1 \pm 1.6^{[a]}$ $24.9 \pm 0.4^{[b]}$	$96.2 \pm 1.8^{[a]}$ $23.0 \pm 0.4^{[b]}$	$101.2 \pm 1.2^{[a]}$ $24.2 \pm 0.3^{[b]}$	$16.7 \pm 4.6^{[c]}$ $4.0 \pm 1.1^{[d]}$

$^{[a]}$kJ mol^{-1}; $^{[b]}$kcal mol^{-1}; $^{[c]}$J K^{-1}; $^{[d]}$cal K^{-1}.

which is marginally faster than that of 4-methoxyphenylazo-3,5-dimethylisoxazole exhibited a rate constant of 2.3×10^{-2} min^{-1}.[9a] Once again, this indicates the independent nature of the photoswitches. Hence, we utilized the kinetics data photoswitches. Hence, we utilized the kinetics data measured at variable temperatures in determining the activation parameters (E_a, $\Delta H^{\ddagger}$, $\Delta S^{\ddagger}$, and $\Delta G^{\ddagger}$) using Arrhenius and Eyring plots (**Table 4.2** and **Appendix 4D**). The similarity in these data for **1a-c** indicated a negligible effect of alkyl chain length variation in the thermal stability of the photoswitched states. Moreover, the activation parameters confirm the excellent thermal stability of the photoswitched states in the solution phase.

We have also followed the forward isomerization (*E*-*Z*) kinetics of the targets **1a-c** under photochemical conditions (at 360 nm). Again, we observed first-order kinetics with *ZZZ*-isomer's fast exponential growth (**Figure 4.3b-c, Table 4D.2,** and **Figure 4D.4-4D.6** in **Appendix 4D**). Moreover, the forward isomerization rates are also found to be quite similar for all three target molecules.

4.6 Self-assembly behavior and light-induced mesophase changes

Before studying the mesogens' self-assembly and thermal behavior of **1a-c**, their thermal stability was determined by the thermogravimetric analysis (TGA) to ensure their stability throughout the mesomorphic temperature range. The decomposition temperatures (213-223 °C) corresponding to 5 wt% loss are far greater than their isotropic temperatures

(110-124 °C), suggesting their high thermal stability (**Table 4.3** and **Figure 4E.1** in **Appendix 4E**). The phase transition behaviors in compounds **1a-c** are established by careful microscopic observations as listed in **Table 4.3**. In the case of all the derivatives, when a virgin sample was carefully observed under POM upon heating, a phase transition from solid amorphous (S) to mesophase (M) was noted by the presence of shearable birefringence which then followed by the disappearance of birefringence in an isotropic phase. On cooling back from isotropic liquid, the reappearance of shearable birefringence is observed at the temperatures indicated in **Table 4.3** which retains up to room temperature. In all cases, solid to mesophase transition can be observed in DSC endotherms (**Figure 4E.2** in **Appendix 4E**) while mesophase to isotropic (I) transition (vice-versa) could not be detected in thermograms though repeatedly perceived by microscopic observations. In continuation to the first cycle, the second or further heating and cooling cycles exhibit room temperature mesophase, and even in DSC, unlike the first heating cycle, no observable peaks corresponding to solid to mesophase transition were observed. The isogyre (maltese) textures[11] were obtained by shearing the optically isotropic homeotropic regions of compounds **1b** and **1c,** indicative of an orientational defect in the assembly (**Figure 4E.3** in **Appendix 4E** and **Figure 4.5c**, respectively), while for **1a**, non-specific texture (**Figure 4E.3a** in **Appendix 4E**) was obtained.

Table 4.3. Thermal behavior of compounds **1a-c**

C	**Heating**	**Cooling**	$\mathbf{T_d}$ [c]
1a	S_1 (119.7[a]) S_2 160.0[b] (158.8[a]) N_D 166.0[b] I [N_D 162[b] I]	I 128.8[b] N_D [I 130[b] N_D]	220
1b	S 112.4[b] (114.3[a]) N_D 124.4[b] I [N_D 125[a] I]	I 121[b] N_D [I 120[b] N_D]	223
1c	S 118.6[b] (119.5[a]) N_D 131.7[b] I [N_D 134.4[b] I]	I 123[b] N_D [I 128.5[b] N_D]	213
[a] Phase transition temperatures (in °C) obtained by DSC (rate 10 °C/min) and [b] by POM (rate 3 °C/min) and double brackets enclosed the second heating/cooling cycle. [c] decomposition temperatures (in °C) corresponding to 5 % weight loss. Abbreviations: S - Solid amorphous phase, N_D - discotic nematic liquid crystalline phase, I - isotropic phase.			

The XRD patterns of compounds **1a, 1b,** and **1c** were carried out for investigating the structural assembly. For the X-ray measurements, the samples were prepared by heating the compounds to their respective isotropic temperatures and then filled into a 0.7 um thick

(diameter) glass capillary through capillary action. All the compounds **1a-c** in their mesophase temperature range showed only one reflection in the small-angle region with *d*-spacing 28.73 Å, 29.71 Å, and 30.72 Å, respectively, and a broad halo in the wide-angle regime (**Table 4.4, Figure 4.5a** and **Figure 4E.4** in **Appendix 4E**). The wide-angle broad peak is indicative of the occurrence of the LC phase and appears due to the correlated flexible alkyl chains. Based on the observed XRD patterns and POM observations, two types of structures are possible, one is smectic or lamellar assembly and the other is discotic nematic. To assign the exact mesophase structure, the correlation length ((ξ)) corresponding to the small-angle region peak was calculated for each compound. The correlation lengths provide information about the number of correlated discs in the mesophase which in turn indicates ordering within the mesophases. The correlation length of 35.04 Å, 36.65 Å, and 54.40 Å were calculated[12] in the case of **1a**, **1b,** and **1c**, respectively (**Figure 4E.5** in **Appendix 4E**), which correspond to about 1.22, 1.23, and 1.77 number of correlated discs (**Figure 4E.5b** in **Appendix 4E**). The correlation length (ξ) was calculated using Scherrer's equation $\xi = [k*2\pi]/[(\Delta q)]$. Here, k is the shape factor whose typical value is 0.89, λ is the wavelength of the incident X-ray, q is the scattering vector ($q = 4\pi\sin\theta/\lambda$), θ is the maximum of the reflection, and Δq is the broadening in q at half of the maximum intensity. The Δq is calculated from the fitting of the diffraction peaks by Lorentzian profiles. The ratio of the ξ and corresponding *d*-spacings gives a realization of correlation length in terms of correlated units of length scale *d*. These low values of correlation lengths point to only the next neighbor

Table 4.4. Variation of *d*-spacings in the phases of **1a-c**[a]

Compound	Phase	Small-angle peak (Å)[b]	Wide-angle peak (Å)[c]
1a	N_D	28.73	4.52 (**h_a**)
1b	N_D	29.71	4.65 (**h_a**)
1c	N_D	30.72	4.76 (**h_a**)

[a]*d*-spacings presented in the table are at 25 °C. [b]Small-angle peak corresponds to the average molecular separation of correlated discs. [c]Wide-angle peak, **h_a** represents the fluid chain-chain correlation.

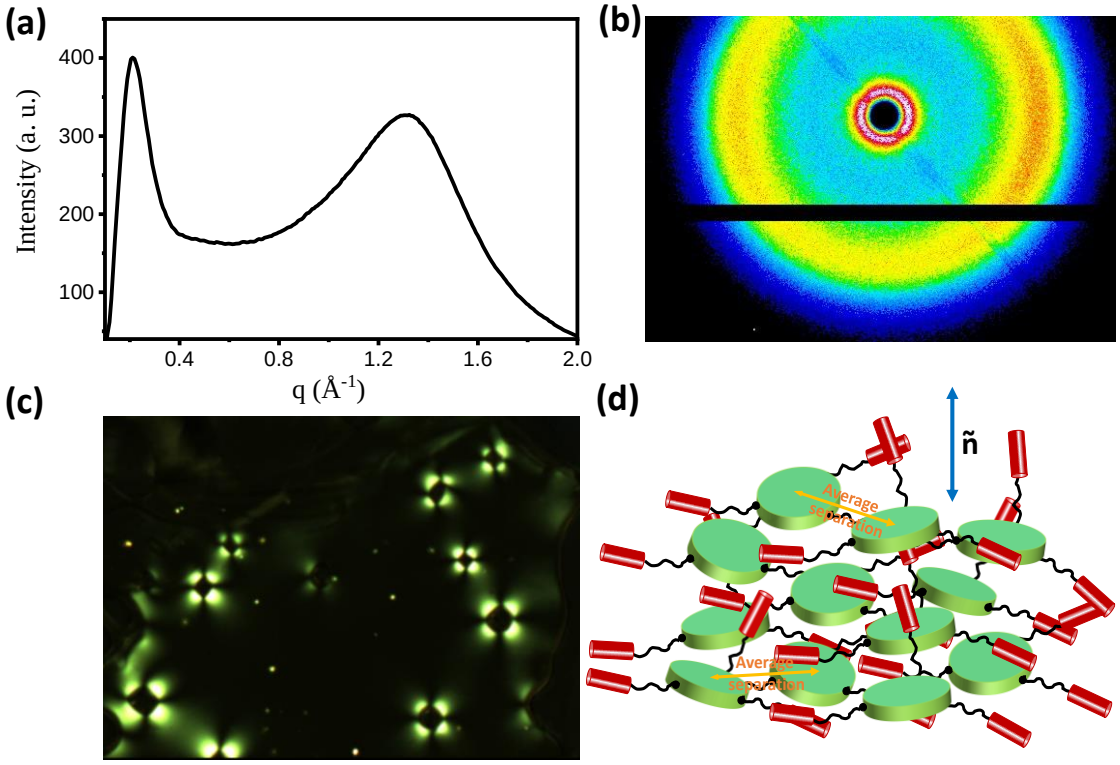

Figure 4.5. (a) 1D and (b) 2D X-ray diffraction pattern of compound **1c** in the mesophase at 25 °C (on cooling). (c) POM image of compound **1c** at 47.5 °C recorded upon cooling the mesophase with a scan rate of 10 °C/min (magnification: ×200). (d) A schematic representation of the assemblies of molecules in the discotic nematic (N_D) phase aligns with the director, ñ. correlations and indicate the presence of short-range ordered intermolecular assembly. The combined information obtained from the XRD patterns, low correlation length, and maltese-cross textures led to the assignment of the discotic nematic phase for 1a-c compounds.[13,14]

Due to the anisotropic optical nature of the LC materials, any morphological variation in molecular assembly can be monitored by the resulting change in their optical appearance under POM.[15] For instance, upon illumination of the UV light at 25 °C, after a few seconds (5 s), transmittance through a pair of crossed polarizers, with the LC cell positioned between them, is reduced due to loss of birefringence of the sample,[16] indicating an anchoring transition from the initial random to a homeotropic alignment of the LCs since then light is no longer absorbed. Interestingly, the birefringence recovers back to almost the original intensity after illuminating the sample with the irradiation at 490 nm, suggesting the reversibility of the mesophase. To demonstrate the photochemical robustness of compound **1c**, we performed a test over 6 photoswitching cycles, by alternative irradiation at 365 and 490 nm, which showed negligible degradation of its photoisomerization response (**Figure 4.6** and **Figure 4E.6** in **Appendix 4E**). Additionally, we performed a small-angle X-ray scattering (SAXS) experiment before and after irradiation with UV light (**Figure 4.6e**). Interestingly, it can be

noted that the small angle peak intensity got decreased after irradiating the sample with 365 nm light. Also, the full width at half maxima (FWHM) becomes wider upon irradiation with 365 nm light. Both these factors i.e. the reduction of peak intensity and the increment in FWHM after shining the sample with the UV light are an indication of the weakening of the regular arrangement of the molecular self-assembly in the mesophase.

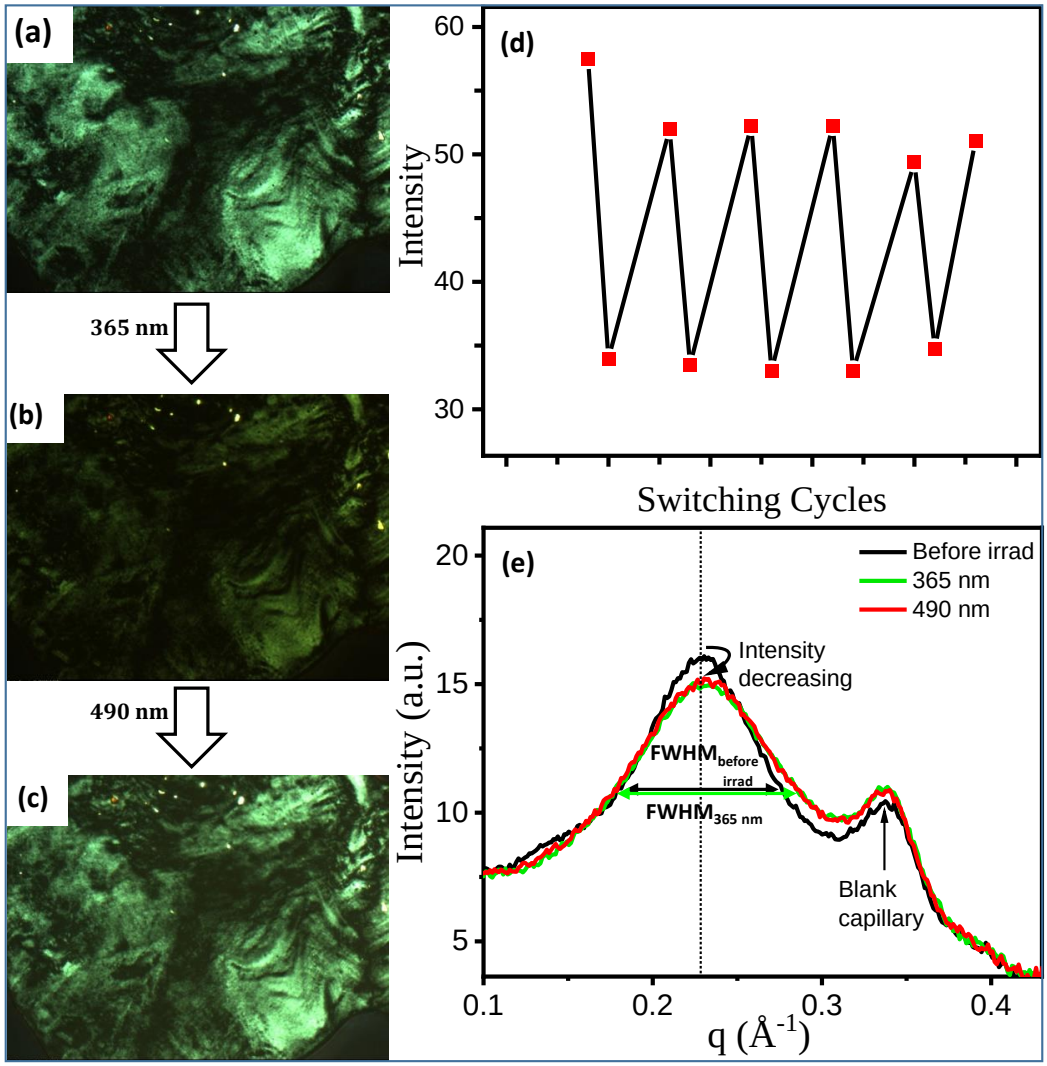

Figure 4.6. Photoswitching behavior using POM (at 25 °C): optical microscopic images of compound **1c** (magnification: x100) (a) Reversibility of bright and dark states due to the changes in the discotic smectic LC mesophase over six cycles. (The images have been obtained using POM by alternatively irradiating between 365 and 490 nm of a sample). (b) Transmittance Intensity versus no. of cycles plot showing that up to 5 cycles, the reduction, and increment in the birefringence intensity remain almost constant (intensity calculated through Image J software). (c) Photoswitching behavioral study by SAXS measurements of compound **1c** at 25 °C.

Furthermore, the morphological changes driven by the perturbation in the self-assembly of the benzene-1,3,5-tricarboxamide (BTA) appended phenylazo-3,5-dimethylisoxazole

photoswitches upon irradiation with UV light were investigated by AFM studies (**Figure 4.7**). For the thin-film photoresponse and surface property studies, we have chosen compound 1c with longer spacers. Toward this end, to ensure that all the molecules are in their thermodynamically stable *EEE*-state, we spin-coated the non-irradiated solution of the compound 1c (in toluene, 0.6 mM) on top of a silicon wafer. The AFM image recorded for the native state sample shown in **Figure 4.7a** displays the bright features corresponding to molecular aggregates with an average height of 12 nm.

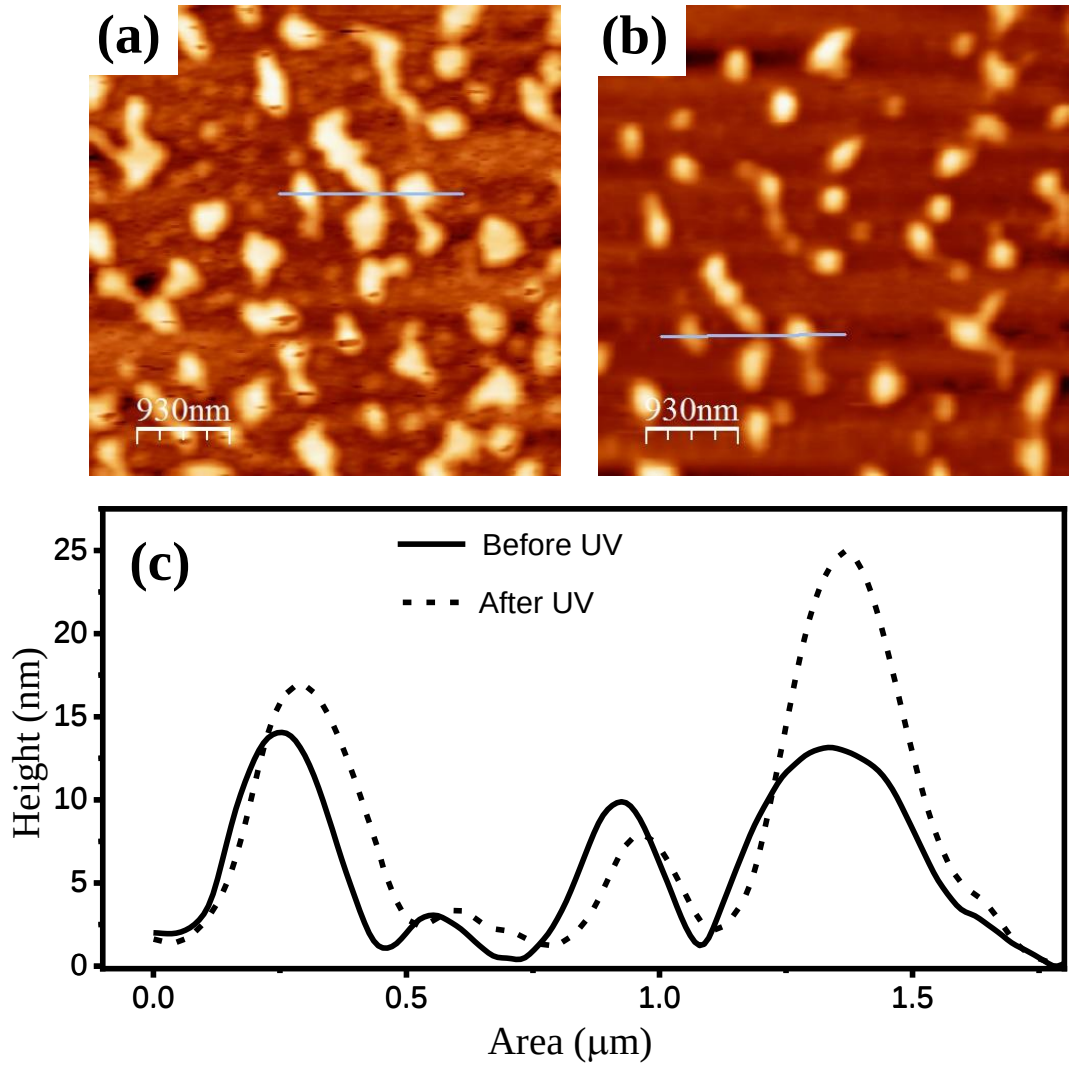

Figure 4.7. Morphological changes of thin-film of compound **1c** after *in-situ* irradiation with 365 nm UV-light as monitored by using AFM technique: (a) before irradiation; (b) after irradiation; (c) Height traces graph showing an increase in height after irradiating the thin-film with 365 nm light. The thin film was prepared by spin-coating an mM solution of **1c** in toluene.

After the *in-situ* irradiation of the sample with UV light (365 nm), a relative increase in height of molecular aggregates was observed (**Figure 4.7c**). At this juncture, we cannot provide an unequivocal and comprehensive insight into the conformation adopted by the

phenylazo-3,5-dimethylisoxazole units. However, careful image analysis revealed that each of the native state domains extended over the large area (**Figure 4.7a**) have shrunk in the photoswitched state (**Figure 4.7b**) that are most likely indicative of a different tilt[16] of the aliphatic spacer groups as well as phenylazo-3,5-dimethylisoxazole units. The height profile of the different domains (**Appendix 4F**) before and after irradiation revealed an increase in the molecular height after the *in-situ* irradiation of the sample.

All this evidence unambiguously confirms the light-induced mesophase changes in our discotic nematic systems **1a-c**. Based on the XRD studies, the core parts of the target molecules have been identified as discotic stacks forming a supramolecular assembly through hydrogen bonding and π–π stacking, whereas the existence of weakly interacting phenylazoisoxazoles has been modeled at the peripheral positions. Since the phenylazo-3,5-dimethylisoxazole photoswitches are known for light-induced phase transition, the 365 nm irradiation can potentially cause the weakening of such interactions and a concomitant repulsive interaction between the *Z*-isomers of the photoswitches. Presumably, the impact of such a localized change associated with phenylazo-3,5-dimethylisoxazole magnified into a macroscopic change to the supramolecular assembly that leads to the mesophase changes. More importantly, such changes did not influence the core part at all, which can be inferred from the reversal of the mesophase upon irradiation at 490 nm that converts the *Z*-isomer back to the native state. Thus, the reversible *E*-*Z* photoisomerization at the phenylazo-3,5-dimethylisoxazole alone controls the target systems mesophases.

4.7 Summary

In summary, we have successfully synthesized DLCs based on benzene-1,3,5-tricarboxamide (BTA) functionalised with phenylazo-3,5-dimethylisoxazole photoswitchable units at the periphery. A series of three such compounds (**1a-c**) with varying flexible alkyl linkers were synthesized and characterized and their mesomorphic and photoswitching properties were comprehensively investigated. All three C_3-symmetric molecular structures assembled to form discotic nematic mesophase. The modulation of light-induced reversible photoswitching has been effectively achieved using the photoswitches at the peripheral position. The solution phase studies of **1a-c** revealed an effective bidirectional photoswitching and also excellent thermal stability of the photoswitched states, which has been extended to the thin film/LC state. Remarkably, such LC assembly rendered light controlled reversible “on and off” or “bright and dark” states that have been demonstrated by

using the POM. Using AFM, changes in the height profile of the LC assembly upon switching have been confirmed. All these studies established them as reversibly light-modulated DLC smectic materials.

4.8 Experimental section

Procedure for synthesis of (*E*)-4-((4-alkoxyphenyl)diazenyl)aniline (2)

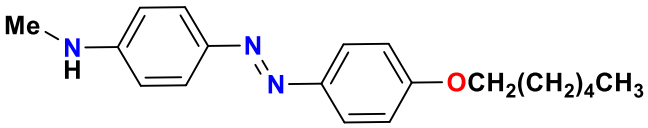

To compound **2** (100 mg, 0.32 mmol) dissolved in 15 ml methanol in a 50 ml round bottom flask, formaldehyde solution (37 %) (0.4 mmol) was added. At 0 °C, the solution was stirred for 30 minutes and $NaCNBH_3$ (0.51 mmol) is added portion-wise over 1 hour. The reaction completion was checked by TLC. The solvent was evaporated under a vacuum and the product was extracted by using ethylacetate. The extracted organic layer was washed with brine solution, dried with anhydrous sodium sulfate and evaporated to dryness, and subjected to purification by column chromatography. (Eluent: ethylacetate:n-hexane, 1:19); Orange Solid, 2 h, Yield = 32 %, M.P = 111-113 ^{o}C.

(*E*)-4-((4-(hexyloxy)phenyl)diazenyl)-*N*-methylaniline: (2)

^{1}H NMR (400 MHz, $CDCl_3$) δ (ppm) 0.90-0.93 (t, *J* = 6.2 Hz, 3H), 1.35-1.37 (m, 4H), 1.44-1.51 (m, 2H), 1.77-1.84 (m, 2H), 2.91 (s. 3H), 4.00-4.03 (t, *J* = 6.6 Hz, 2H), 4.16 (br s, 1H, -NH-CH_3), 6.64-6.66 (d, *J* = 8.8 Hz, 2H), 6.96-6.98 (d, *J* = 8.9 Hz, 2H), 7.80-7.84 (m, 4H); ^{13}C NMR (100 MHz, $CDCl_3$) δ (ppm) 14.11, 22.74, 25.84, 29.34, 30.56, 31.72, 68.40, 112.01, 114.73, 123.98, 124.85, 144.81, 147.30, 151.47, 160.67; HRMS (ESI) m/z $[M+H]^+$-calcd for $C_{19}H_{25}N_3O$, theoretical 312.2076; found 312.2064; IR (ATR, cm^{-1}) 3364, 2956, 2935, 2923, 2907, 2868, 2851, 2821, 1599, 1578, 1521, 1498, 1464, 1430, 1394, 1338, 1320, 1275, 1239, 1156, 1142, 1109, 1057, 1026, 988, 825, 800, 63, 724, 640, 619, 541, 506.

General procedure for the synthesis of long chain triamide (5)

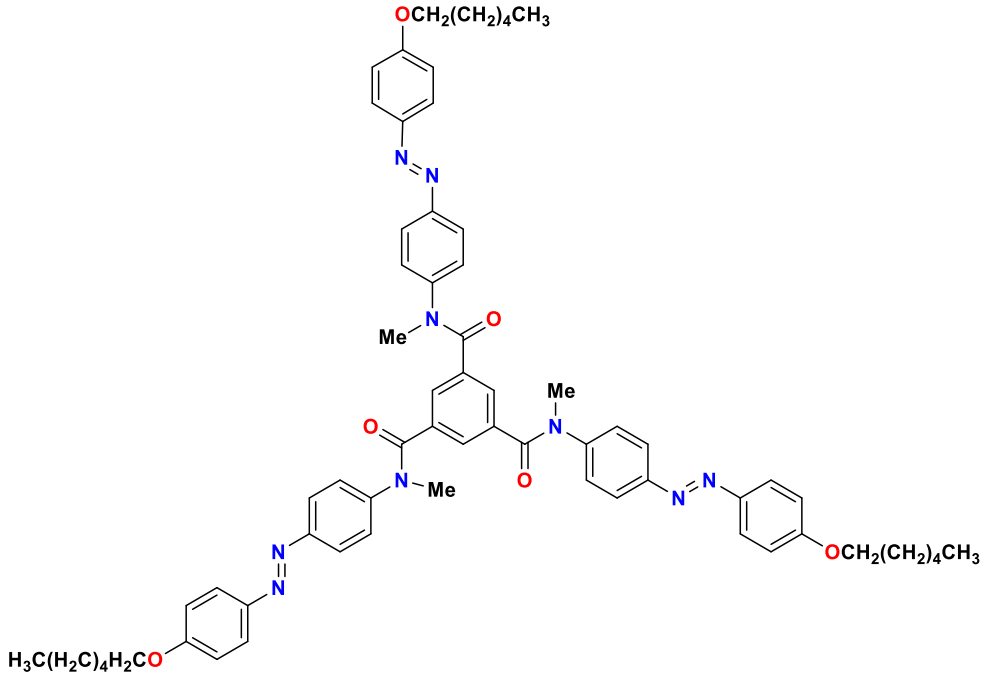

The synthetic procedure has been adopted from the literature.[10b] To the trimesic acid (0.05 g, 0.24 mmol) in a two-neck round bottom flask dry toluene (25 mL) was added under the argon atmosphere. To the insoluble reaction mixture, PCl_5 (0.25 gm, 1.2 mmol) was added in portions. After the complete addition of PCl_5, the reaction mixture was refluxed up to the formation of a transparent reaction mixture. (Note: The trimesylchloride is highly sensitive to moisture) A mixture of **2** (0.354 g, 1.2 mmol), pyridine (0.19 g, 2.4 mmol), and dry toluene (50 mL) have been taken in a two-neck round bottom flask and stirred for ten minutes under argon atmosphere and cooled to 0 ^{o}C. Now trimesyl chloride solution in toluene from the previous stage of the reaction was carefully transferred into this reaction mixture. The reaction mixture was then allowed to stir at room temperature and the reaction was monitored by TLC. After the completion of the reaction, the toluene was evaporated in a rotavap. Then the crude product was purified by column chromatography on silica gel (EtOAc:n-hexanes = 40:60) to obtain a pure product as dark orange color solids. **5**- orange solid, 10 h, Yield = 40%, M. P.= 173-174 °C.

***N*^{1},*N*^{3},*N*^{5}-*tris*(4-((*E*)-(4-(hexyloxy)phenyl)diazenyl)phenyl)-*N*^{1},*N*^{3},*N*^{5}-trimethylbenzene-1,3,5-tricarboxamide (5):**

^{1}H NMR (400 MHz, [D_6]DMSO) δ (ppm) = 0.83-0.87 (t, J = 6.7 Hz, 9H), 1.25-1.28 (m, 12H), 1.34-1.39 (m, 6H), 1.65-1.70 (m, 6H), 3.28 (s, 9H), 3.97-4.00 (t, J = 6.5 Hz, 6H), 6.72-

6.74 (d, J = 8.4 Hz, 6H), 6.95-6.97 (d, J = 9.0 Hz, 6H), 7.07 (s, 3H), 7.72-7.74 (d, J = 8.6 Hz, 6H), 7.83-7.85 (d, J = 8.9 Hz, 6H).

^{1}H NMR (400 MHz, $CDCl_3$) δ (ppm) = 0.89 (t, J = 6.9 Hz, 9H), 1.31-1.34 (m, 12H), 1.42-1.45 (m, 6H), 1.73-1.80 (m, 6H), 3.37 (s, 9H), 3.94-3.97 (t, J = 6.5 Hz, 6H), 6.54-6.56 (d, J = 8.2 Hz, 6H), 6.84-6.86 (d, J = 8.9 Hz, 6H), 7.12 (s, 3H), 7.85-7.87 (d, J = 8.6 Hz, 6H), 7.94-7.96 (d, J = 8.9 Hz, 6H); ^{13}C NMR (100 MHz, $CDCl_3$) δ(ppm) = 169.08, 161.99, 150.60, 146.70, 145.80, 136.25, 129.77, 127.63, 125.03, 123.78, 114.74, 68.40, 37.68, 31.47, 29.73, 29.12, 25.68, 22.61, 13.95; HRMS (ESI) m/z $[M+H]^+$ calcd for $C_{66}H_{75}N_9O_6$ 1090.5919, found 1090.5968; IR (ATR, cm^{-1}) 2953, 2925, 2856, 1649, 1595, 1574, 1495, 1468, 1455, 1379, 1347, 1300, 1251, 1138, 1105, 1009, 935,897, 839, 769, 732, 703, 682, 581, 561, 516, 505.

Synthesis of 1a-c target compounds

General procedure for the synthesis of 4a-c

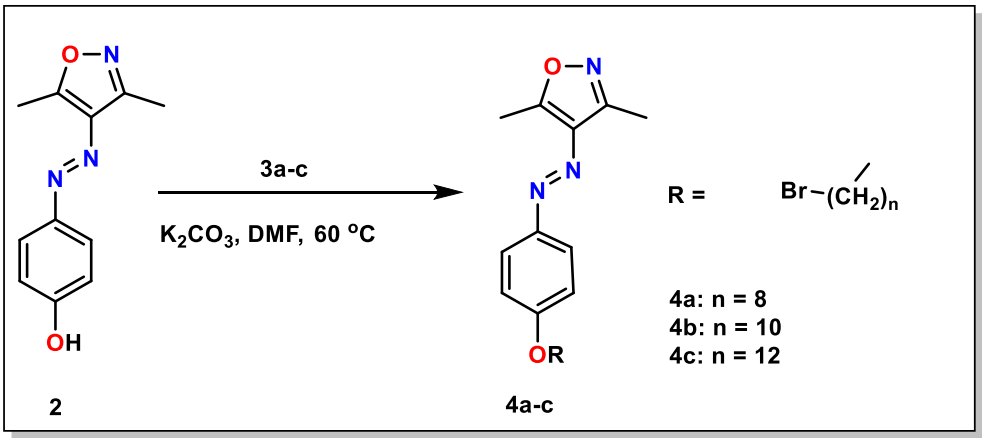

A modified procedure has been used based on the literature report.[7] A flask was charged with 4-hydroxy phenylazo-3,5-dimethylisoxazole **(2)** (1.13 g, 5.2 mmol), and potassium carbonate (1.08 g, 7.8 mmol) dissolved in DMF (20 ml). The dibromoalkanes (7.8 mmol) **(3a-c)** were added to the reaction mixture and heated at 60 ^{o}C for an hour. Reaction progress was monitored by TLC. The reaction mixture was poured into ice-cold water. The resulting yellow ppt. obtained was filtered and washed with water. The precipitate was further dissolved in ethyl acetate, dried over anhydrous sodium sulfate, and further concentrated in a rotary evaporator. The pure product is obtained after performing column chromatography in 2-4% ethyl acetate-hexane mixture on silica gel. **4a**-yellow solid, Yield =

57%, M.P = 62-64 ^{o}C, **4b**- yellow Solid, Yield = 57%, M.P = 68-70 ^{o}C, **4c**- yellow Solid, Yield = 60%, M.P = 72-74 ^{o}C.

Synthesis of *tert*-butyl (4-hydroxyphenyl)carbamate 6[17]

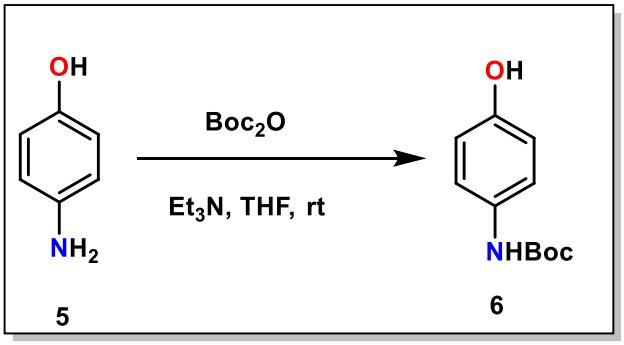

4-Aminophenol **(5)** (0.10 g, 0.9 mmol), di-tert-butyl dicarbonate (diboc) (0.24 g, 1.1 mmol), and triethylamine (0.3 ml, 1.8 mmol) were dissolved in 5 ml THF and stirred overnight at room temperature and followed by TLC. After completion, the reaction mixture was concentrated in a rotary evaporator and further purified by column chromatography in 10-12% ethyl acetate-hexane mixture. **6**-light brown solid, Yield = 68%, M.P = 151-153 ^{o}C.

General procedure for the synthesis of 7a-c

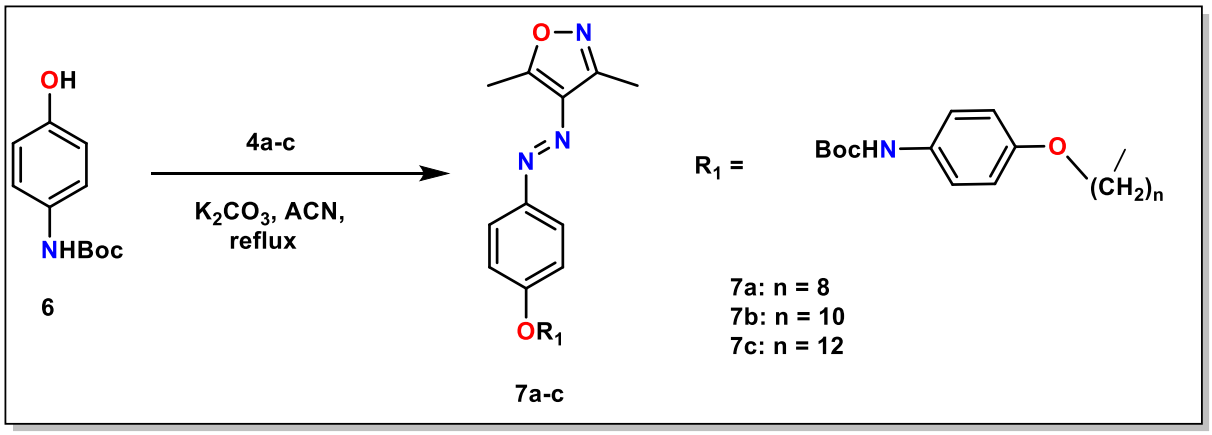

The synthetic procedure has been adopted from the literature.[18] The BOC protected 4-aminophenol **(6)** (0.47 g, 2.2 mmol), potassium carbonate (0.39 g, 2.8 mmol), a catalytic amount of potassium iodide, and **4a-c** (1.14 g, 2.8 mmol) were dissolved in acetonitrile (15 ml) and refluxed overnight and monitored by TLC. After completion of the reaction, the precipitate obtained was filtered and washed with water and acetonitrile. **7a**-yellow Solid,

Yield = 85%, M.P = 138-140 ^{o}C, **7b**- yellow Solid, Yield = 78%, M.P = 130-132 ^{o}C, **7c**- yellow Solid, Yield = 88%, M.P = 148-150 ^{o}C.

General procedure for the synthesis of 8a-c[18]

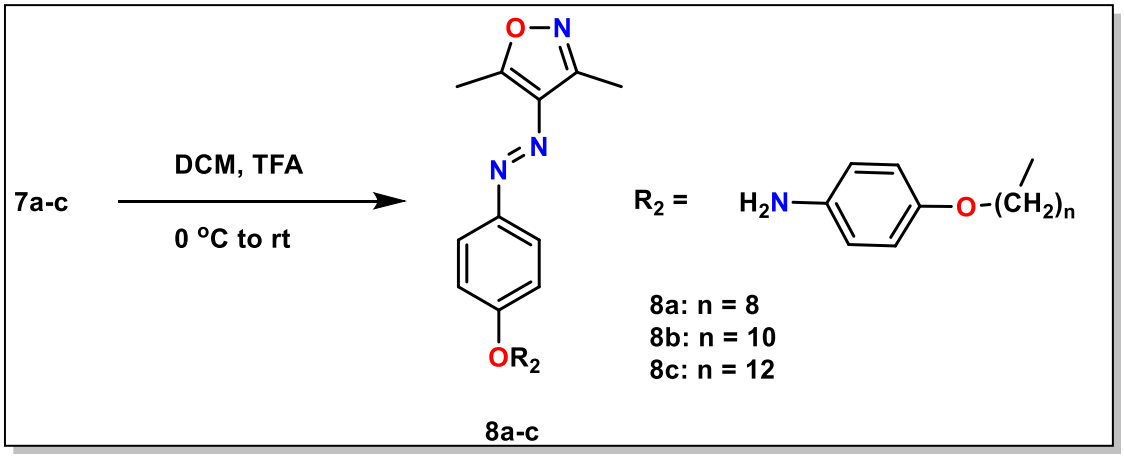

The products **(7a-c)** (4.00 g, 7.5 mmol) were dissolved in 6:1 ratio of dichloromethane (DCM) and trifluoroacetic acid (TFA) (150 ml) and stirred at 0 ^{o}C and then at rt for 4 hours. Reaction progress was monitored by TLC. After completion, the reaction mixture was neutralized with 5% aq. NaOH. The organic layer was separated, washed with brine solution, and dried over anhydrous sodium sulphate. This was concentrated in a rotary evaporator and further purified by column chromatography by using 15-20% ethyl acetate-hexane on basic alumina. **8a**-brownish yellow Solid, Yield = 32%, M.P = 101-103 ^{o}C, **8b**- brownish yellow Solid, Yield = 28%, M.P = 102-104 ^{o}C, **8c**- brownish yellow Solid, Yield = 29%, M.P = 110-112 ^{o}C.

General procedure for the synthesis of 1a-c

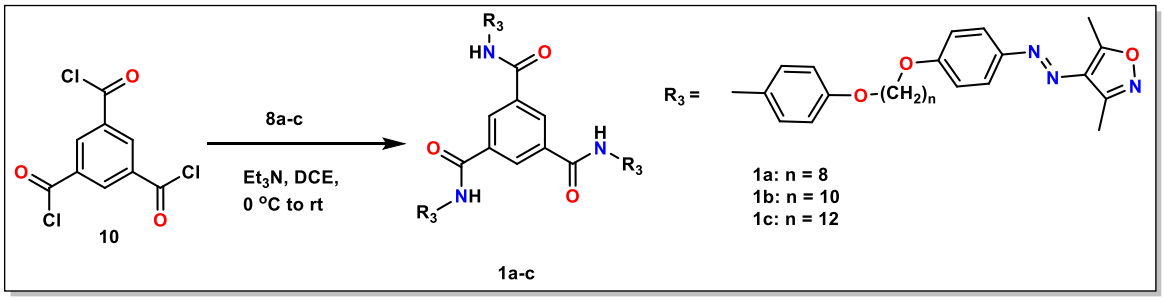

The target molecules **(1a-c)** have been synthesized based on a reported procedure.[19] Trimesoyl chloride **(10)** has been prepared from trimesic acid **(9)** (0.09 g, 0.4 mmol) using thionyl chloride in the presence of a catalytic quantity of DMF under reflux conditions until a

transparent homogeneous mixture was formed. Then the excess thionyl chloride was distilled off. Under inert and dry conditions, the previous step products (**8a-c**) (1.7 mmol) were dissolved in dry 1,2-dichloroethane (DCE) (30 ml) and triethylamine (0.3 ml, 2.2 mmol) and stirred at 0 ^{o}C. The *in situ* prepared trimesoyl chloride (**10**) was carefully dissolved in dry DCE (10 ml), and dropwise added into the reaction mixture by maintaining the temperature at 0 ^{o}C and stirred overnight at rt. The reaction progress was monitored by TLC. After completion, the reaction mixture was precipitated out by the addition of methanol. For obtaining the pure product, the precipitate obtained was filtered off, washed with MeOH, and then diethyl ether and dried under vacuum. **1a**-brownish yellow Solid, Yield = 59%, M.P = 117-119 ^{o}C, **1b**- brownish yellow Solid, Yield = 54%, M.P = 110-112 ^{o}C, **1c**- yellow Solid, Yield = 76%, M.P = 121-123 ^{o}C.

Characterization data:

(*E*)-4-((4-((8-Bromooctyl)oxy)phenyl)diazenyl)-3,5-dimethylisoxazole (4a)

^{1}H NMR (400 MHz, $CDCl_3$) δ (ppm) 7.78 (d, *J* = 8.8 Hz, 2H), 6.97 (d, *J* = 8.8 Hz, 2H), 4.02 (t, *J* = 6.5 Hz, 2H), 3.42 (t, *J* = 6.8 Hz, 2H), 2.72 (s, 3H), 2.52 (s, 3H), 1.90 – 1.78 (m, 4H), 1.52 – 1.42 (m, 4H), 1.38 (br, 4H); ^{13}C NMR (100 MHz, $CDCl_3$) δ (ppm) 168.26, 161.46, 153.97, 147.12, 132.30, 124.03, 114.71, 68.33, 34.14, 32.85, 29.28, 29.24, 28.78, 28.18, 26.02, 12.24, 11.76; HRMS (ESI) m/z $[M+H]^+$- calcd. for $C_{19}H_{26}BrN_3O_2$ 408.1287, found 408.1257; IR (ATR, cm^{-1}) 2937, 2924, 2853, 1599, 1579, 1407, 633.

(*E*)-4-((4-((10-Bromodecyl)oxy)phenyl)diazenyl)-3,5-dimethylisoxazole (4b)

^{1}H NMR (400 MHz, $CDCl_3$) δ (ppm) 7.79 (d, *J* = 8.8 Hz, 2H), 6.97 (d, *J* = 8.8 Hz, 2H), 4.02 (t, *J* = 6.5 Hz, 2H), 3.41 (t, *J* = 6.8 Hz, 2H), 2.72 (s, 3H), 2.52 (s, 3H), 1.89 – 1.78 (m, 4H), 1.51 – 1.39 (m, 4H), 1.31 (br, 8H); ^{13}C NMR (100 MHz, $CDCl_3$) δ (ppm) 168.26, 161.49, 153.98, 147.14, 132.30, 124.03, 114.71, 68.39, 34.21, 32.90, 29.54, 29.46, 29.43, 29.27, 28.85, 28.25, 26.10, 12.25, 11.76; HRMS (ESI) m/z $[M+H]^+$- calcd. for $C_{21}H_{30}BrN_3O_2$ 436.1600, found 436.1616; IR (ATR, cm^{-1}) 2934, 2919, 2849, 1594, 1498, 1405, 640.

(*E*)-4-((4-((12-Bromododecyl)oxy)phenyl)diazenyl)-3,5-dimethylisoxazole (4c)

^{1}H NMR (400 MHz, $CDCl_3$) δ (ppm) 7.78 (d, *J* = 8.9 Hz, 2H), 6.97 (d, *J* = 8.9 Hz, 2H), 4.02 (t, *J* = 6.5 Hz, 2H), 3.40 (t, *J* = 6.9 Hz, 2H), 2.72 (s, 3H), 2.52 (s, 3H), 1.88 – 1.78 (m, 4H), 1.51 – 1.40 (m, 8H), 1.29 (br, 12H); ^{13}C NMR (100 MHz, $CDCl_3$) δ (ppm) 168.21, 161.52,

153.92, 147.07, 132.30, 124.03, 114.73, 68.43, 34.20, 32.93, 29.64 (2C), 29.62, 29.53, 29.48, 29.29, 28.87, 28.27, 26.11, 12.22, 11.76; HRMS (ESI) m/z $[M+H]^+$- calcd. for $C_{23}H_{34}BrN_3O_2$ 464.1913, found 464.1898; IR (ATR, cm^{-1}) 2936. 2917, 2849, 1499, 1404, 641.

***tert*-Butyl (4-hydroxyphenyl)carbamate (6)**

^1H NMR (400 MHz, $CDCl_3$) δ (ppm) 7.12 (d, *J* = 7.9 Hz, 2H), 6.70 (d, *J* = 8.6 Hz, 2H), 6.41 (br, 1H, -O<u>H</u>), 6.13 (br, 1H, -*N*<u>H</u>), 1.50 (s, 9H); ^{13}C NMR (100 MHz, $CDCl_3$) δ (ppm) 153.84, 152.29, 130.81, 121.69, 115.89, 80.66, 28.51; HRMS (ESI): m/z $[M-H]^+$- calcd. for $C_{11}H_{15}NO_3$ 208.0974, found 208.0964; IR (ATR, cm^{-1}) 3386, 3360, 2987, 2976, 2929, 1696, 1515, 628.

***tert*-Butyl(*E*)-(4-((8-(4-((3,5-dimethylisoxazol-4-yl)diazenyl)phenoxy)octyl)oxy)phenyl)carbamate (7a)**

^1H NMR (400 MHz, $CDCl_3$) δ (ppm) 7.79 (d, *J* = 8.6 Hz, 2H), 7.23 (br, 2H), 6.97 (d, *J* = 8.7 Hz, 2H), 6.82 (d, *J* = 8.7 Hz, 2H), 6.33 (br, 1H, -*N*<u>H</u>), 4.03 (t, *J* = 6.4 Hz, 2H), 3.92 (t, *J* = 6.4 Hz, 2H), 2.72 (s, 3H), 2.52 (s, 3H), 1.85 – 1.73 (m, 4H), 1.50 (s, 9H), 1.47 (br, 4H), 1.40 (br, 4H); ^{13}C NMR (100 MHz, $CDCl_3$): δ (ppm) 168.31, 161.54, 155.31, 154.07, 153.31, 147.20, 132.35, 131.36, 124.08, 120.63, 114.96, 114.77, 80.36, 68.42, 68.35, 29.43, 29.40, 29.29, 28.50 (2C), 26.10, 26.08, 12.27, 11.80; HRMS (ESI) m/z $[M+H]^+$- calcd. for $C_{30}H_{40}N_4O_5$ 537.3077, found 537.3051; IR (ATR, cm^{-1}) 2936, 2917, 2849, 1499, 1404, 1243, 1148, 1022, 839, 641.

***tert*-Butyl(*E*)-(4-((10-(4-((3,5-dimethylisoxazol-4-yl)diazenyl)phenoxy)decyl)oxy)phenyl)carbamate (7b)**

^1H NMR (400 MHz, $CDCl_3$) δ (ppm) 7.79 (d, *J* = 9.0 Hz, 2H), 7.24 (d, *J* = 8.4 Hz, 2H), 6.97 (d, *J* = 9.0 Hz, 2H), 6.82 (d, *J* = 9.0 Hz, 2H), 6.33 (br, 1H, -*N*<u>H</u>), 4.02 (t, *J* = 6.5 Hz, 2H), 3.91 (t, *J* = 6.6 Hz, 2H), 2.72 (s, 3H), 2.52 (s, 3H), 1.85 – 1.72 (m, 4H), 1.50 (s, 9H), 1.47 – 1.40 (m, 4H), 1.34 (br, 8H); ^{13}C NMR (100 MHz, $CDCl_3$) δ (ppm) 168.21, 161.52, 155.28, 154.00, 153.30, 147.15, 132.30, 131.36, 124.03, 120.57, 114.92, 114.73, 80.27, 68.42, 68.36, 29.57, 29.45 (2C), 29.38, 29.27, 28.46 (2C), 26.11, 26.09, 12.20, 11.73; HRMS (ESI) m/z $[M+H]^+$ calcd. for $C_{32}H_{44}N_4O_5$ 565.3390, found 565.3380; IR (ATR, cm^{-1}) 3346, 2919, 2847, 1689, 1597, 1521.

***tert*-Butyl(*E*)-(4-((12-(4-((3,5-dimethylisoxazol-4-yl)diazenyl)phenoxy)dodecyl)oxy)phenyl)carbamate (7c)**

^{1}H NMR (400 MHz, $CDCl_3$) δ (ppm) 7.79 (d, *J* = 8.8 Hz, 2H), 7.23 (br, 2H), 6.97 (d, *J* = 8.8 Hz, 2H), 6.82 (d, *J* = 8.8 Hz, 2H), 6.35 (br, 1H, -*N*H), 4.02 (t, *J* = 6.5 Hz, 2H), 3.91 (t, *J* = 6.6 Hz, 2H), 2.72 (s, 3H), 2.52 (s, 3H), 1.85 – 1.71 (m, 4H), 1.50 (s, 9H), 1.47 – 1.40 (m, 4H), 1.30 (br, 12H); ^{13}C NMR (100 MHz, $CDCl_3$): δ (ppm) 168.27, 161.55, 155.32, 154.04, 153.29, 147.18, 132.34, 131.33, 124.06, 120.54, 114.94, 114.76, 80.32, 68.47, 68.42, 29.69 (3C), 29.52 (2C), 29.42, 29.32, 28.50 (2C), 26.15 (2C), 12.27, 11.79; HRMS (ESI) m/z $[M+H]^+$- calcd. for $C_{34}H_{48}N_4O_5$ 593.3703, found 593.3698; IR (ATR, cm^{-1}) 3345, 2921, 2849, 1687, 1597, 1517.

(*E*)-4-((8-(4-((3,5-Dimethylisoxazol-4-yl)diazenyl)phenoxy)octyl)oxy)aniline (8a)

^{1}H NMR (400 MHz, $CDCl_3$): δ (ppm) 7.79 (d, *J* = 9.0 Hz, 2H), 6.97 (d, *J* = 9.0 Hz, 2H), 6.74 (d, *J* = 8.8 Hz, 2H), 6.64 (d, *J* = 8.8 Hz, 2H), 4.03 (t, *J* = 6.5 Hz, 2H), 3.88 (t, *J* = 6.5 Hz, 2H), 2.72 (s, 3H), 2.52 (s, 3H), 1.85 – 1.71 (m, 4H), 1.53 – 1.44 (m, 4H), 1.42 – 1.39 (m, 4H); ^{13}C NMR (100 MHz, $CDCl_3$): δ (ppm) 168.27, 161.47, 153.96, 152.34, 147.08, 139.78, 132.27, 124.01, 116.50, 115.65, 114.70, 68.64, 68.36, 29.48, 29.40, 29.38, 29.24, 26.09, 26.03, 12.19, 11.72; HRMS (ESI) m/z $[M+H]^+$- calcd. for $C_{25}H_{32}N_4O_3$ 437.2553, found 437.2539; IR (ATR, cm^{-1}) 2934, 2858, 1596, 1512.

(*E*)-4-((10-(4-((3,5-Dimethylisoxazol-4-yl)diazenyl)phenoxy)decyl)oxy)aniline (8b)

^{1}H NMR (400 MHz, $CDCl_3$) δ (ppm) 7.79 (d, *J* = 8.2 Hz, 2H), 6.97 (d, *J* = 8.3 Hz, 2H), 6.74 (d, *J* = 7.9 Hz, 2H), 6.62 (d, *J* = 7.9 Hz, 2H), 4.01 (t, *J* = 5.8 Hz, 2H), 3.87 (t, *J* = 6.1 Hz, 2H), 3.40 (br, 2H, –*N*H$_2$), 2.71 (s, 3H), 2.52 (s, 3H), 1.82 – 1.72 (m, 4H), 1.46 (br, 4H), 1.34 (br, 8H); ^{13}C NMR (100 MHz, $CDCl_3$) δ (ppm) 168.19, 161.45, 153.90, 152.26, 147.07, 139.91, 132.20, 123.98, 116.40, 115.60, 114.66, 68.63, 68.36, 29.54 (2C), 29.47, 29.45, 29.41, 29.23, 26.11, 26.05, 12.18, 11.69; HRMS (ESI) m/z $[M+H]^+$ calcd. for $C_{27}H_{36}N_4O_3$ 465.2866, found 465.2850; IR (ATR, cm^{-1}) 3448, 3363, 2936. 2921, 2852, 1615, 1594.

(*E*)-4-((12-(4-((3,5-Dimethylisoxazol-4-yl)diazenyl)phenoxy)dodecyl)oxy)aniline (8c)

^{1}H NMR (400 MHz, $CDCl_3$) δ (ppm) 7.79 (d, *J* = 8.9 Hz, 2H), 6.97 (d, *J* = 9.0 Hz, 2H), 6.74 (d, *J* = 8.8 Hz, 2H), 6.63 (d, *J* = 8.8 Hz, 2H), 4.02 (t, *J* = 6.6 Hz, 2H), 3.87 (t, *J* = 6.6 Hz, 2H), 3.42 (br, 2H, –*N*H$_2$), 2.72 (s, 3H), 2.52 (s, 3H), 1.81 (p, *J* = 6.7 Hz, 2H), 1.73 (p, *J* = 6.7 Hz,

2H), 1.51 – 1.41 (m, 4H), 1.29 (br, 12H); ^{13}C NMR (100 MHz, $CDCl_3$) δ (ppm) 168.25, 161.48, 154.04, 152.36, 147.14, 139.84, 132.33, 124.05, 116.52, 115.73, 114.76, 68.78, 68.47, 29.69 (4C), 29.55 (2C), 29.51, 29.31, 26.19, 26.13, 12.24, 11.78; HRMS (ESI): m/z $[M+H]^+$ calcd. for $C_{29}H_{40}N_4O_3$ 493.3179, found 493.3158**;** IR (ATR, cm^{-1}) 3448, 3360, 2937, 2919, 2851, 1616, 1594.

***N*^{1},*N*^{3},*N*^{5}-tris(4-((8-(4-((*E*)-(3,5-Dimethylisoxazol-4-yl)diazenyl)phenoxy)octyl)oxy)phenyl)benzene-1,3,5-tricarboxamide (1a)**

^{1}H NMR (400 MHz, $CDCl_3$) δ (ppm) 8.49 (s, 3H, partly exchanged), 8.44 (s, 3H), 7.77 (d, *J* = 9.0 Hz, 6H), 7.54 (d, *J* = 8.6 Hz, 6H), 6.96 (d, *J* = 9.0 Hz, 6H), 6.86 (d, *J* = 8.8 Hz, 6H), 4.03 (t, *J* = 6.5 Hz, 6H), 3.93 (t, *J* = 6.5 Hz, 6H), 2.71 (s, 9H), 2.51 (s, 9H), 1.80 (sep, *J* = 6.6 Hz, 12H), 1.52 – 1.37 (m, 24H); ^{13}C NMR (125 MHz, $CDCl_3$) δ (ppm) 168.77, 164.93, 160.16, 156.43, 152.95, 146.35, 135.89, 132.32, 130.70, 128.63, 125.65, 124.06, 122.41, 114.74, 68.39, 68.30, 29.48, 29.44, 29.41, 29.28, 26.12, 26.09, 12.21, 11.75; HRMS (ESI) m/z $[M+H]^+$ calcd. for $C_{84}H_{96}N_{12}O_{12}$ 1465.7349, found 1465.7301; IR (ATR, cm^{-1}) 3277, 2935, 2854, 1650, 1602, 1515, 1244, 833.

***N*^{1},*N*^{3},*N*^{5}-tris(4-((10-(4-((*E*)-(3,5-Dimethylisoxazol-4-yl)diazenyl)phenoxy)decyl)oxy)phenyl)benzene-1,3,5-tricarboxamide (1b)**

^{1}H NMR (400 MHz, $CDCl_3$) δ (ppm) 8.43 (br, 6H), 7.77 (d, *J* = 9.0 Hz, 6H), 7.51 (d, *J* = 8.9 Hz, 6H), 6.96 (d, *J* = 9.0 Hz, 6H), 6.86 (d, *J* = 9.0 Hz, 6H), 4.02 (t, *J* = 6.5 Hz, 6H), 3.92 (t, *J* = 6.5 Hz, 6H), 2.71 (s, 9H), 2.51 (s, 9H), 1.79 (sep, *J* = 6.6 Hz, 12H), 1.52 – 1.42 (m, 12H), 1.35 (br, 24H); ^{13}C NMR (100 MHz, $CDCl_3$) δ (ppm) 168.20, 165.35, 161.44, 156.25, 153.92, 147.10, 135.92, 132.23, 130.85, 128.37, 123.99, 122.30, 114.65, 114.61, 68.35, 68.25, 29.64 (2C), 29.58, 29.49, 29.46, 29.28, 26.17, 26.11, 12.16, 11.68; HRMS (ESI) m/z $[M+H]^+$ calcd. for $C_{90}H_{108}N_{12}O_{12}$ 1549.8288, found 1549.8334; IR (ATR, cm^{-1}) 3286, 2919, 2848, 1644, 1597, 1509, 1238, 822.

***N*^{1},*N*^{3},*N*^{5}-tris(4-((12-(4-((*E*)-(3,5-Dimethylisoxazol-4-yl)diazenyl)phenoxy)dodecyl)oxy)phenyl)benzene-1,3,5-tricarboxamide (1c)**

^{1}H NMR (400 MHz, $CDCl_3$) δ (ppm) 8.43 (s, 3H), 8.32 (br, 3H), 7.77 (d, *J* = 8.9 Hz, 6H), 7.51 (d, *J* = 8.8 Hz, 6H), 6.96 (d, *J* = 8.9 Hz, 6H), 6.86 (d, *J* = 8.9 Hz, 6H), 4.02 (t, *J* = 6.6 Hz, 6H), 3.93 (t, *J* = 6.5 Hz, 6H), 2.71 (s, 9H), 2.51 (s, 9H), 1.79 (sep, *J* = 6.6 Hz, 12H), 1.51

– 1.43 (m, 12H), 1.31 (br, 36H); ^{13}C NMR (125 MHz, $CDCl_3$) δ (ppm) 168.25, 164.87, 161.55, 156.49, 154.06, 147.20, 135.92, 132.34, 130.62, 128.61, 124.07, 122.41, 114.76 (2C), 68.47, 68.38, 29.75 (2C), 29.73, 29.71, 29.63, 29.53, 29.47, 29.33, 26.21, 26.16, 12.21, 11.76; HRMS (ESI) m/z $[M+H]^+$ calcd. for $C_{96}H_{120}N_{12}O_{12}$ 1633.9227, found 1633.9308; IR (ATR, cm^{-1}) 3288, 2917, 2850, 1646, 1602, 1511, 1244, 822.

4.9 References

[1] a) P. Xie, R. Zhang, *J. Mater. Chem.* **2005**, *15*, 2529; b) Z. Yang, Z. Liu, L. Yuan, Asian *J. Org. Chem.* **2021**, *10*, 74; c) J. S. M. Lee, H. Sato, *Nat. Chem.* **2020**, *12*, 584; d) Y.–S. Meng, T. Liu, *Acc. Chem. Res.* **2019**, *52*, 1369; e) Z. L. Pianowski. *Chem. Eur. J.* **2019**, *25*, 5128.

[2] a) H. K. Bisoyi, Q. Li, *Chem. Rev.* **2016**, *116*, 15089−15166; b) H.−K. Lee, A. Kanazawa, T. Shiono, T. Ikeda, T. Fujisawa, M. Aizawa, B. J. Lee, *Appl. Phys.* **1999**, *86*, 5927−5934; c) S. Tazuke, S. Kurihara, T. Ikeda, *Chem. Lett.* **1987**, *16*, 911−914; d) A. Shishido, O. Tsutsumi, A. Kanazawa, T. Shiono, T. Ikeda, N. Tamai, *J. Am. Chem. Soc.* **1997**, *119*, 7791−7796; e) J. Garcia-Amoros, A. Szymczyk, D. Velasco, *Phys. Chem. Chem. Phys.* **2009**, *11*, 4244−4250; f) D. Tanaka, H. Ishiguro, Y. Shimizu, K. Uchida, *J. Mater. Chem.* **2012**, *22*, 25065−25071; g) N. Zettsu, T. Ogasawara, R. Arakawa, S. Nagano, T. Ubukata, T. Seki, *Macromolecules* **2007**, *40*, 4607−4613; h) H. Yu, A. Shishido, T. Ikeda, *Appl. Phys. Lett.* **2008**, *92*, 103117.

[3] a) G. Lee, R. J. Carlton, F. Araoka, N. L. Abbott, H. Takezoe, *Adv. Mater.* **2013**, *25*, 245–249; b) K. Kreger, P. Wolfer, H. Audorff, L. Kador, N. Stingelin-Stutzmann, P. Smith, H-W. Schmidt, *J. Am. Chem. Soc.* **2010**, *132*, 509–516; c) M. Pfletscher, S. Hölscher, C. Wölper, M. Mezger, M. Giese, *Chem. Mater.* **2017**, *29*, 8462–8471; d) M. Pfletscher, C. Wölper, J. S. Gutmann, M. Mezgerd, M. Giese, *Chem. Commun.* **2016**, *52*, 8549–8552.

[4] a) S. Pan, M. Ni, B. Mu, Q. Li, X.-Y. Hu, C. Lin, D. Chen, L. Wang, *Adv. Funct. Mater.* **2015**, *25*, 3571–3580; b) P. Wolfer, K. Kreger, H.-w. Schmidt, N. Stingelin, P. Smith, *Mol. Cryst. Liq. Cryst.* **2012**, *562*, 133–140; c) P. Wolfer, H. Audorff, K. Kreger, L. Kador, H.-W. Schmidt, N. Stingelin, P. Smith, *J. Mater. Chem.* **2011**, *21*, 4339–4345; d) D. Tanaka, H. Ishiguro, Y. Shimizu, K. Uchida, *J. Mater. Chem.* **2012**, *22*, 25065–25071; e) Y. Zhou, M. Xu, T. Li, Y. Guo, T. Yi, S. Xiao, F. Li, C. Huang, *J. Colloid Interface Sci.* **2008**, *321*, 205–211; f) A. Stracke, J. H. Wendorff, D. Goldmann, D. Janietz, *Liq. Cryst.* **2000**, *27*, 1049–1057.

[5] a) Y.-J. Choi, D-Y. Kim, M. Park, W.-J. Yoon, Y. Lee, J.-K. Hwang, Y.-W. Chiang, S.-W. Kuo, C.-H. Hsu, K.-U. Jeong, *ACS Appl. Mater. Interfaces* **2016**, *8*, 9490−9498; b) K. Ichimura, *Chem. Rev.* **2000**, *100*, 1847–1873; c) S. V. Serak, N. V. Tabiryan, G. Assanto, *Mol. Cryst. Liq. Cryst.* **2012**, *559*, 202–213.

[6] a) M. Sperner, N. Tober, H. Detert, *Eur. J. Org. Chem.* **2019**, 4688–4693; b) W. P. Silva, E. Girotto, H. Gallardo, R. Cristiano, *J. Mol. Liq.* **2020**, *307*, 112944; c) Y. Norikane, Y. Hirai, M. Yoshida, *Chem. Commun.* **2011**, *47*, 1770–1772; d) T. Hegmann, J. Kain, S. Diele, B. Schubet, H. Bögel, C. Tschierske, *J. Mater. Chem.* **2003**, *13*, 991–1003; e) M. T. Allen, K. D. M. Harris, B. M. Kariuki, K. Kumari, J. A. Preece, S. Diele, D. Lose, T. Hegmann, C. Tschierske, *Liq. Cryst.* **2000**, *16*, 6701.

[7] S. Devi, I. Bala, S. P. Gupta, P. Kumar, S. K. Pal, S. Venkataramani, *Org. Biomol. Chem.* **2019**, *17*, 1947–1954.

[8] a) T. Wöhrle, I. Wurzbach, J. Kirres, A. Kostidou, N. Kapernaum, J. Litterscheidt, J. C. Haenle, P. Staffeld, A. Baro, F. Giesselmann, S. Laschat, *Chem. Rev.* **2016**, *116*, 1139−1241; b) A. Eremin, *Liq. Cryst. Rev.* **2020**, *8*, 29–43; c) L. Hines, K. Petersen, G. Z. Lum, and Metin Sitti, *Adv. Mater.* **2017**, 29, 1603483; d) T. J. White, D. J. Broer, *Nat. Mater.* **2015**, *14*, 1087−1098.

[9] a) P. Kumar, A. Srivastava, C. Sah, S. Devi, S. Venkataramani, *Chem. Eur. J.* **2019**, *25*, 11924−11932; b) L. Kortekaas, J. Simke, D. Kurka B. J. Ravoo, *ACS Appl. Mater. Interfaces* **2020**, *12*, 32054–32060.

[10] a) K. Ghebreyessus, S. M. Cooper, *Organometallics* **2017**, *36*, 3360–3370; b) S. Devi, A. K. Gaur, D. Gupta, M. Saraswat, S. Venkataramani, *ChemPhotoChem* **2018**, *2*, 806.

[11] a) W. Li, J. Zhang, J. B. Li, M. Zhang, L. Wu, *Chem*. *Commun*. **2009**, 5269–5271; b) I. Bala, H. Singh, V. R. Battula, S. P. Gupta, J. De, S. Kumar, K. Kailasam, S. K. Pal, *Chem*. *Eur*. *J*. **2017**, *23*, 14718–14722.

[12] R.B. Zhang, G. Ungar, X. Zeng, Z. Shen, *Soft Matter* **2017**, *13*, 4122-4131

[13] a) A. Concellón, R. Termine, A. Golemme, P. Romero, M. Marcos, J. L. Serrano, *J. Mater*. *Chem*. *C* **2019**, *7*, 2911: b) A. Concellón, M. Marcos, P. Romero, J. L. Serrano, R. Termine, A. Golemme, *Angew*. *Chem*. *Int*. *Ed*. **2017**, *129*, 1279.

[14] Y. Yu, T. Ikeda, *J. Photochem. Photobiol.* **2004**, *5*, 247–265.

[15] M. Moriyama, N. Mizoshita, T. Kato, *Polymer journal* **2004**, *36*, 661–664.

[16] D. Bléger, A. Ciesielski, P. Samorì, S. Hecht, *Chem. Eur. J.* **2010**, *16*, 14256–14260.

[17] Z. Li, R. Huang, H. Xu, J. Chen, Y. Zhan, X. Zhou, H. Chen, B. Jiang, *Org*. *Lett*. **2017**, *19*, 4972.

[18] C. Shepherd, E. Hadzifejzovic, F. Shkal, K. Jurkschat, J. Moghal, E. M. Parker, M. Sawangphruk, D. R. Slocombe, J. S. Foord, M. G. Moloney, *Langmuir* **2016**, *32*, 7917.

[19] D. Gupta, A. K. Gaur, P. Kumar, H. Kumar, A. Mahadevan, S. Devi, S. Roy and S. Venkataramani, *Chem*. *Eur*. *J*. **2021**, *27*, 3463.

Appendix 4A

Analysis of photoswitching behavior of (1a-c) using UV-vis spectroscopy

Photoswitching studies of all three derivatives **(1a-c)** have been performed in a common solvent DMSO at room temperature. Their molar absorption coefficients (ε) have been estimated corresponding to their π–π^* absorption maxima. Also, photoisomerization stability experiments have been performed up to several cycles.

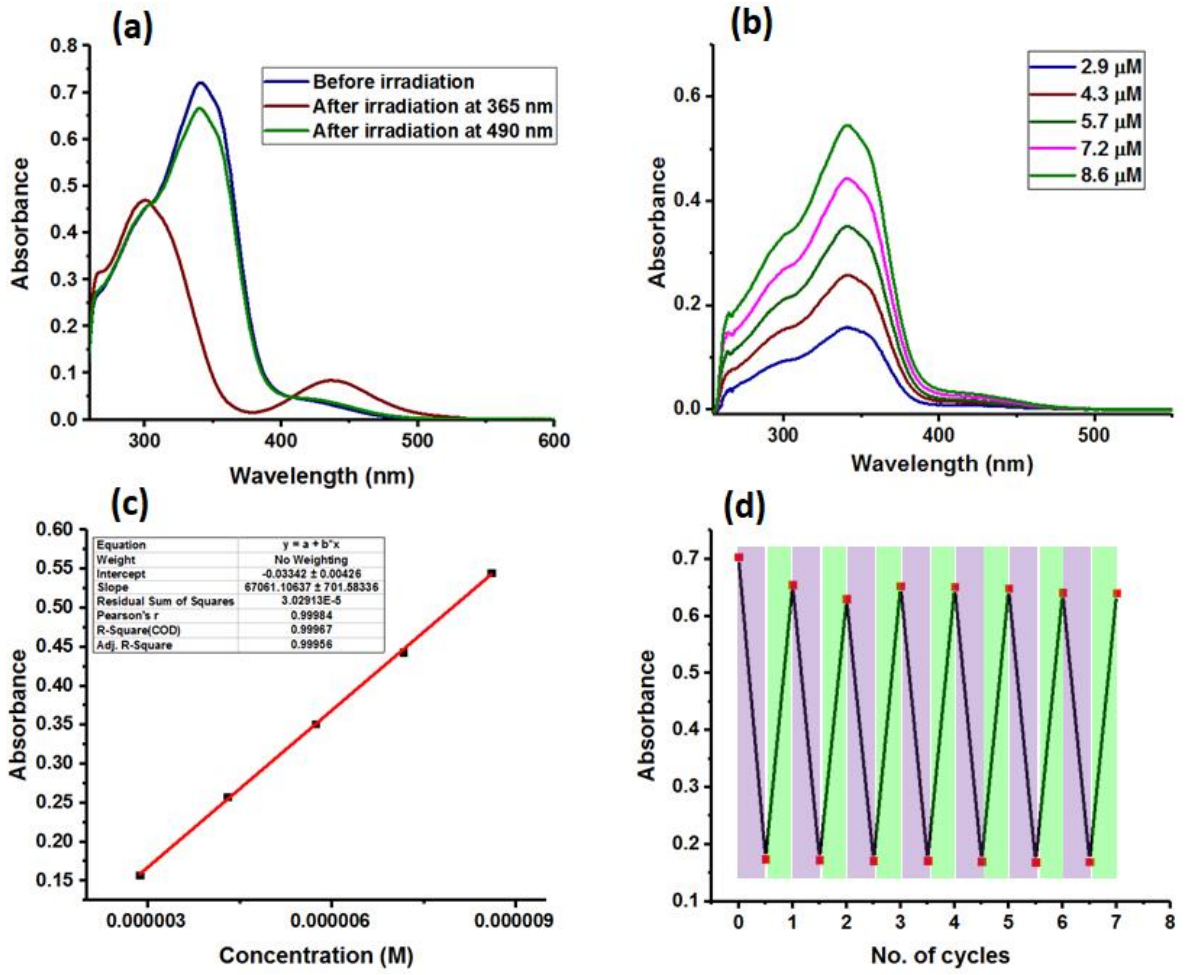

Figure 4A.1. Analysis of photoswitching in the target **1a** using UV-vis spectroscopy; (a) Absorption spectra of **1a** during the forward and reverse isomerization steps; (b) Absorption spectra of **1a** at various concentrations; (c) Estimation of molar absorption coefficient corresponding to the π–π^* absorption band; (d) Photoswitching stability experiment; (Alternative irradiation at 365 and 490 nm irradiation in the forward and reverse isomerization steps, respectively).

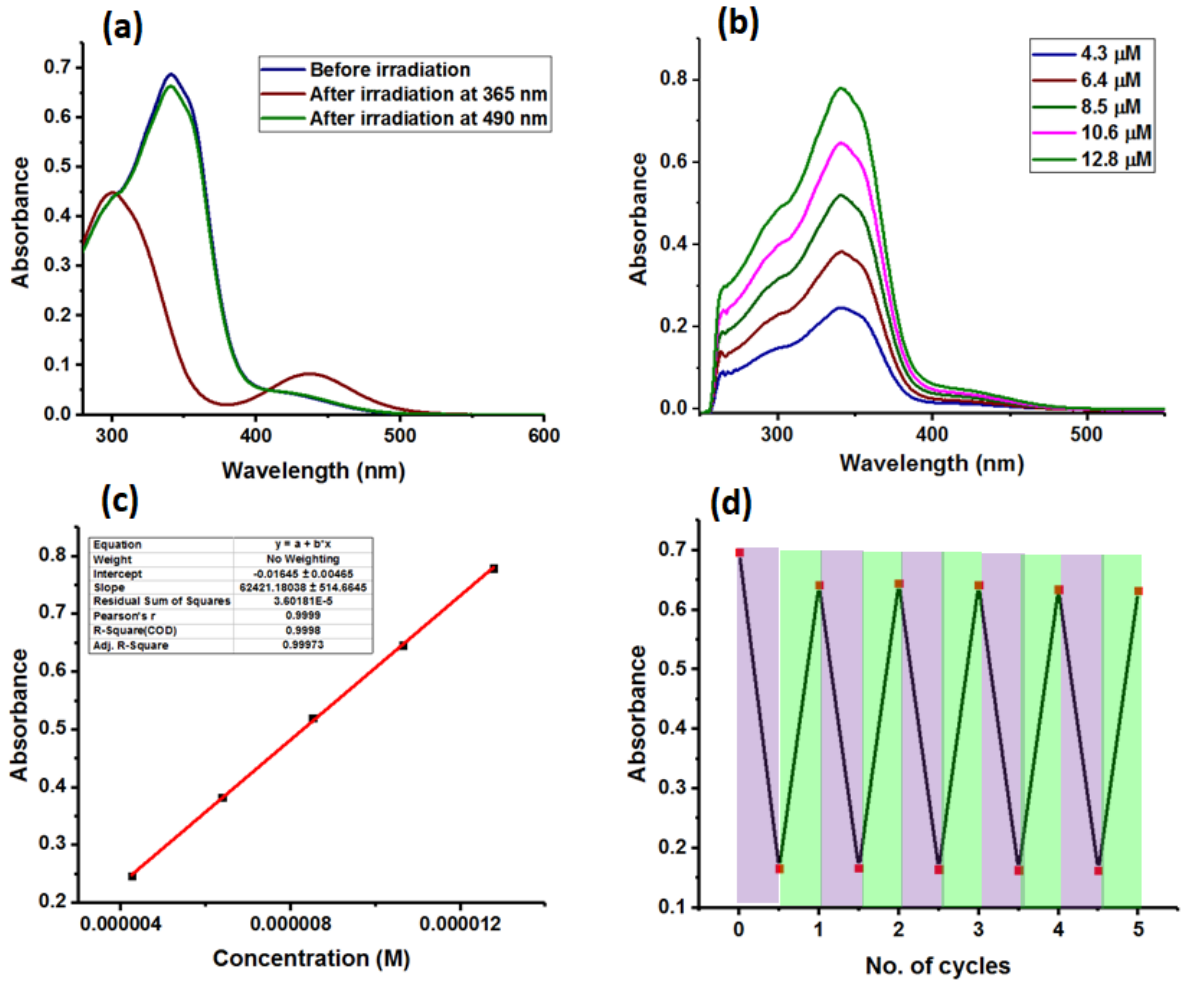

Figure 4A.2. Analysis of photoswitching in the target **1b** using UV-vis spectroscopy; (a) Absorption spectra of **1b** during the forward and reverse isomerization steps; (b) Absorption spectra of **1a** at various concentrations; (c) Estimation of molar absorption coefficient corresponding to the π–π^* absorption band; (d) Photoswitching stability experiment; (Alternative irradiation at 365 and 490 nm irradiation in the forward and reverse isomerization steps, respectively).

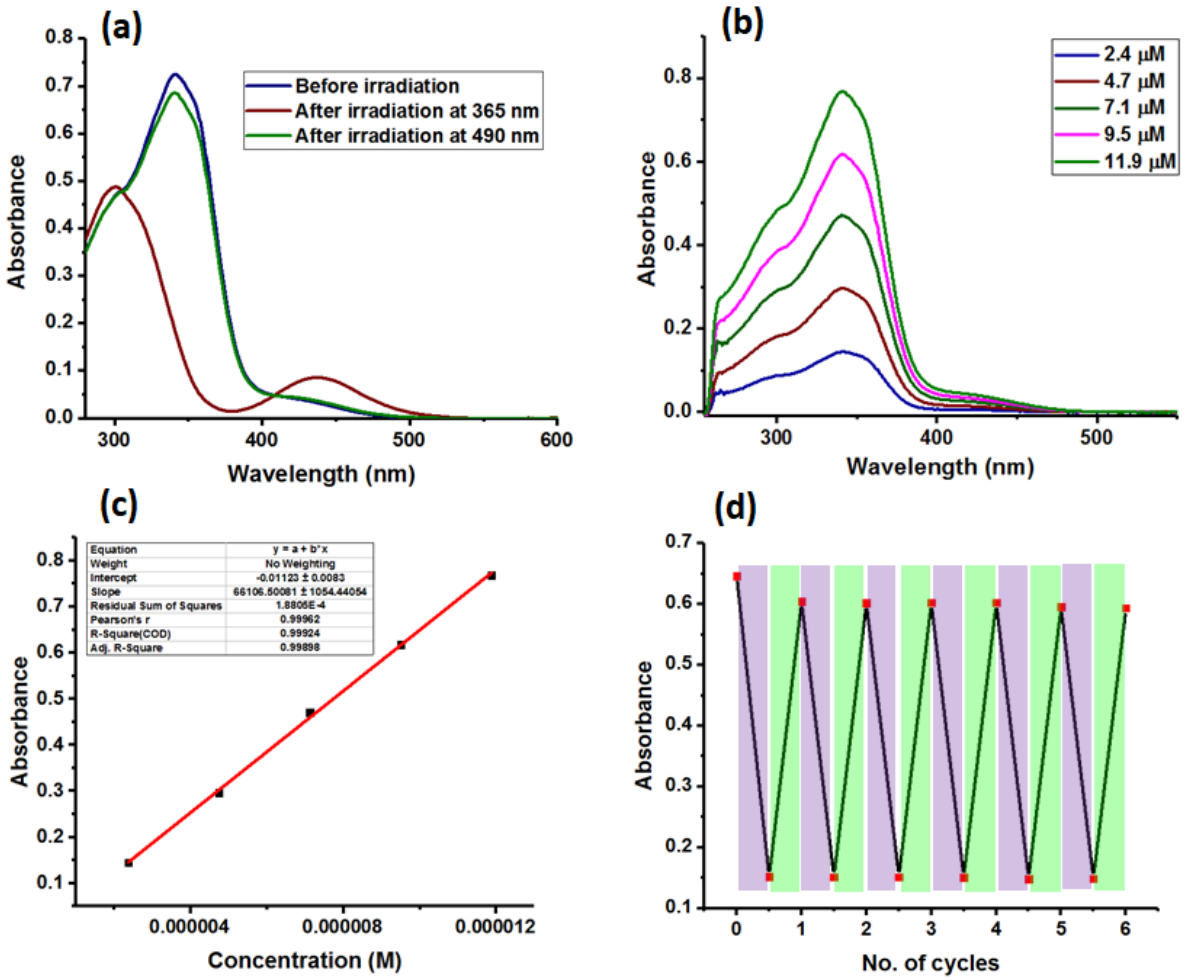

Figure 4A.3. Analysis of photoswitching in the target **1c** using UV-vis spectroscopy; (a) Absorption spectra of **1c** during the forward and reverse isomerization steps; (b) Absorption spectra of **1a** at various concentrations; (c) Estimation of molar absorption coefficient corresponding to the π–π^* absorption band; (d) Photoswitching stability experiment; (Alternative irradiation at 365 and 490 nm irradiation in the forward and reverse isomerization steps, respectively).

Appendix 4B

Analysis of photoswitching using ^{1}H NMR spectroscopy

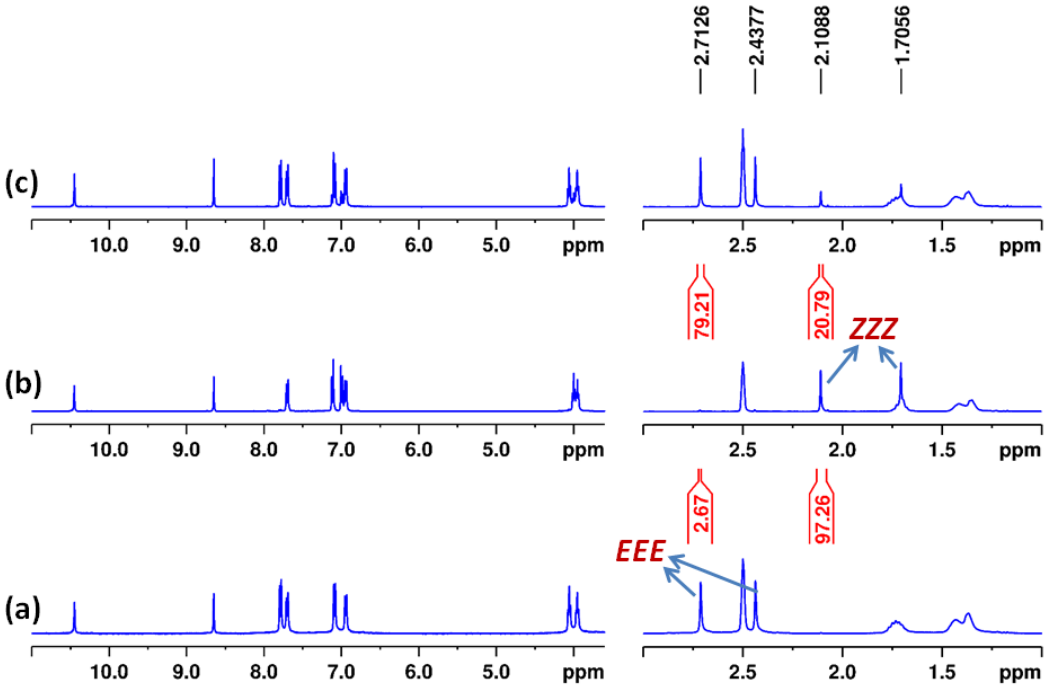

Figure 4B.1. Analysis of Photoswitching in the target **1a** (7.3 mmol, in [D_6]DMSO); (a) before irradiation; (b) after irradiation at 365 nm, and (c) after irradiation at 490 nm.

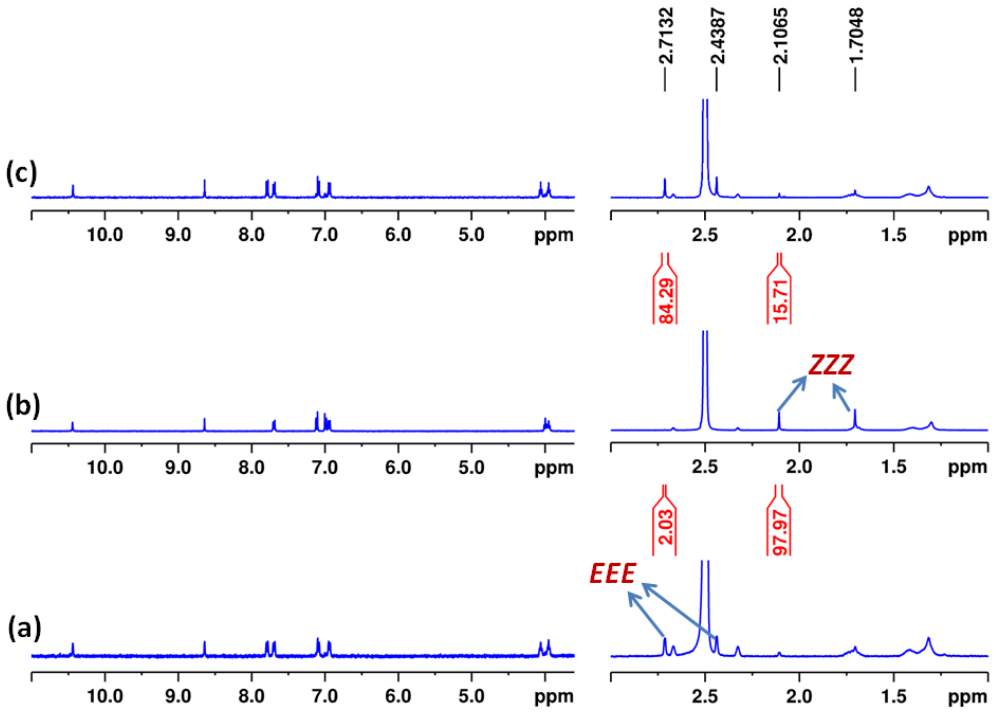

Figure 4B.2. Analysis of Photoswitching of the target **1b** (1.2 mmol, in [D_6]DMSO); (a) before irradiation, (b) after irradiation at 365 nm, and (c) after irradiation at 490 nm.

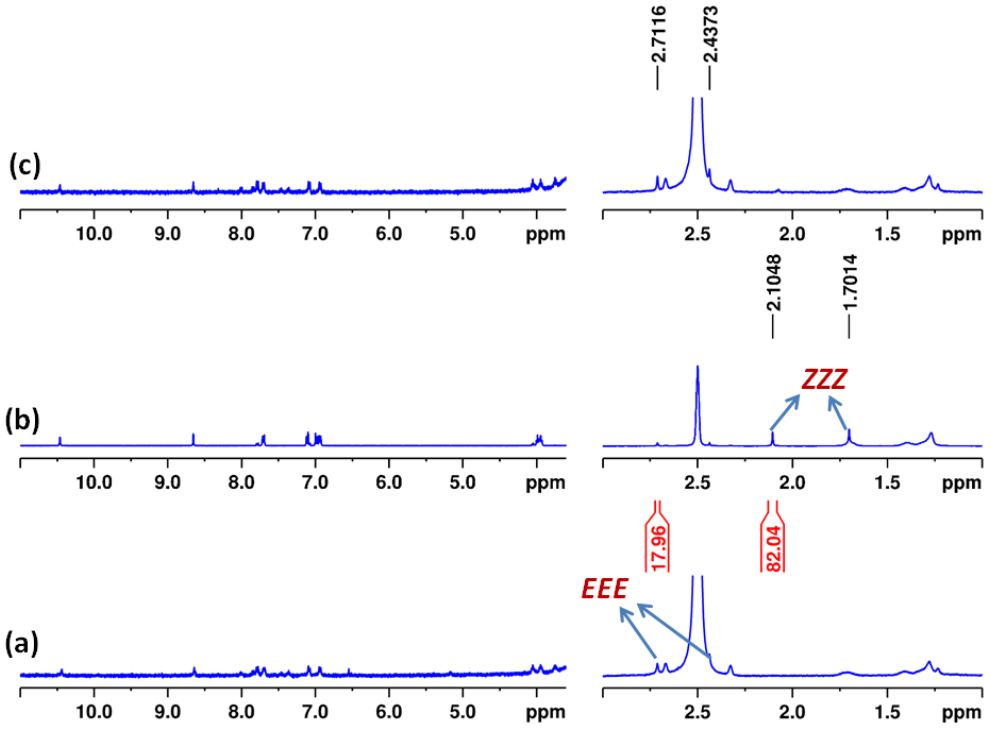

Figure 4B.3. Analysis of Photoswitching of the target **1c** (1.5 mM**,** in [D_6]DMSO); (a) before irradiation; (b) after irradiation at 365 nm, and (c) after irradiation at 490 nm; (Note: The spectral resolution is limited by the poor solubility in the native state, however, on heating or under forward isomerization step, i.e. irradiation at 365 nm the solubility increases).

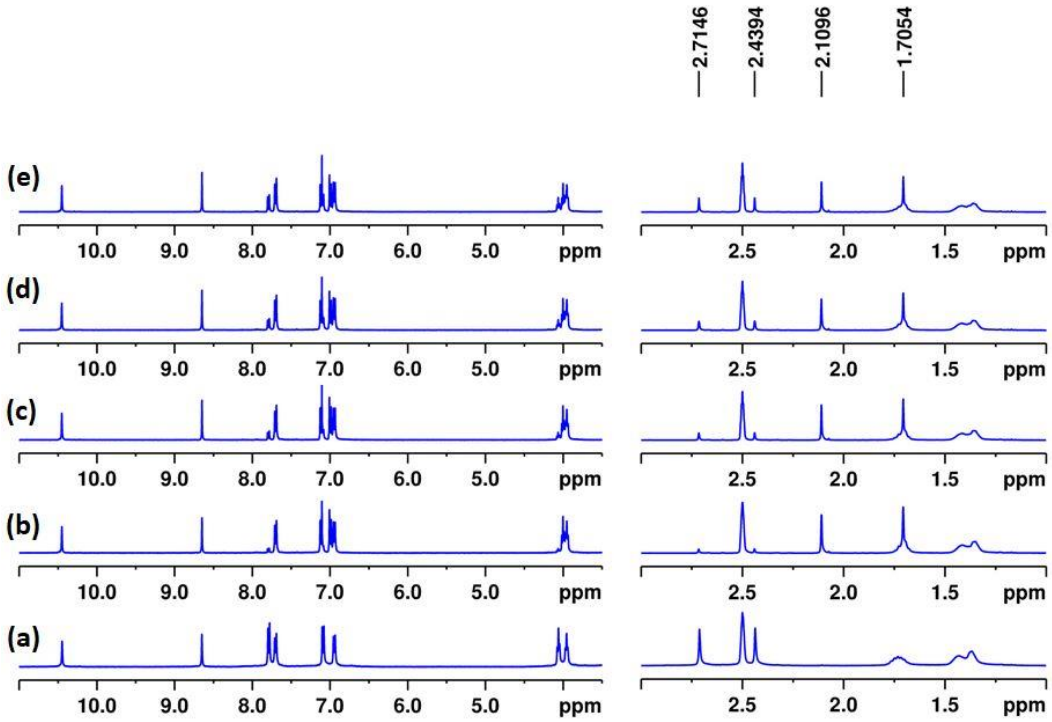

Figure 4B.4. Photochemical reverse isomerisation in **1a** (7.3 mM, 25 ^{o}C, [D_6]DMSO); (a) before irradiation; (b) after irradiation at 365 nm, and after irradiation at 490 nm for (c) 2 min (d) 5 min, and (e) 15 min.

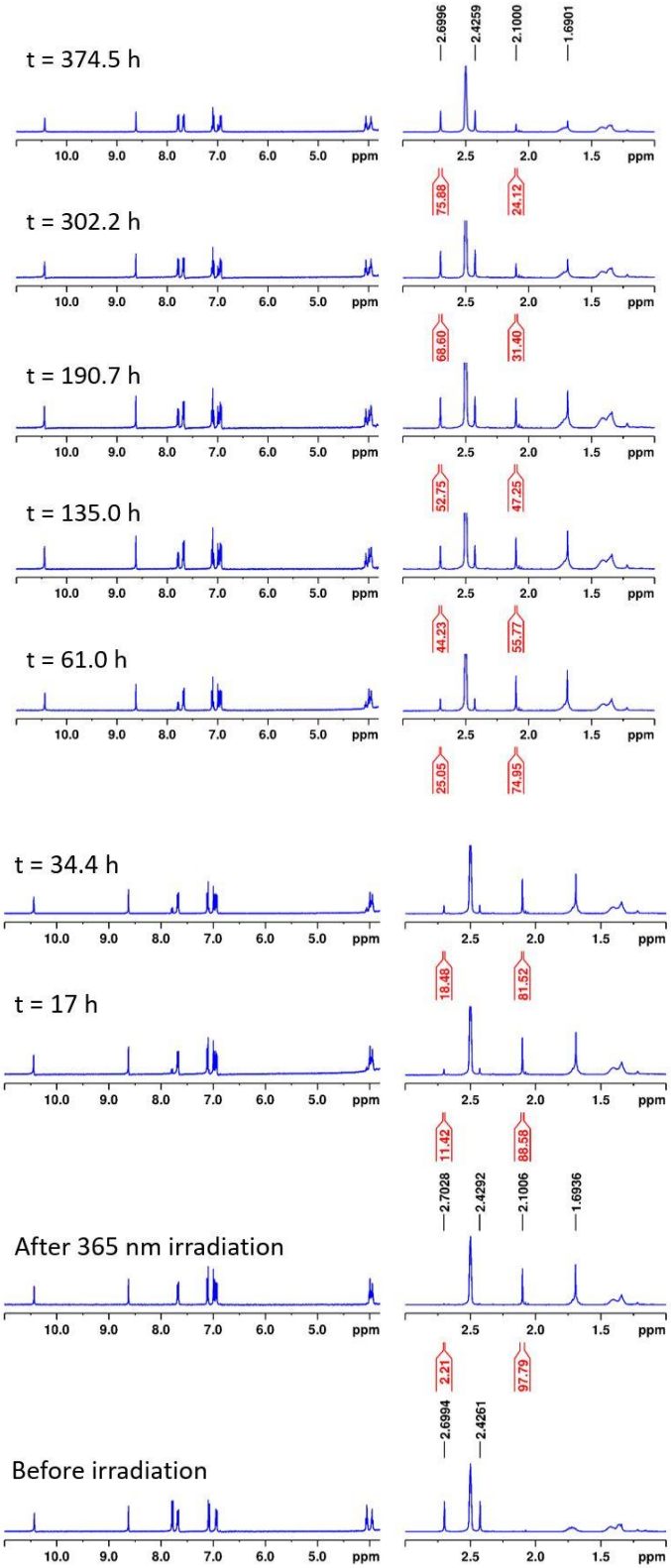

Figure 4B.5. Thermal reverse isomerization in **1a** (5.2 mM, 25 ^{o}C, [D_6]DMSO), (From bottom to top): Before irradiation, after irradiation at 365 nm, and the reverse isomerization at different intervals of time (the times are indicated; the normalized integral values due to the signals corresponding to methyl protons are indicated).

Appendix 4C

Photoswitching of 1a-c in solid state

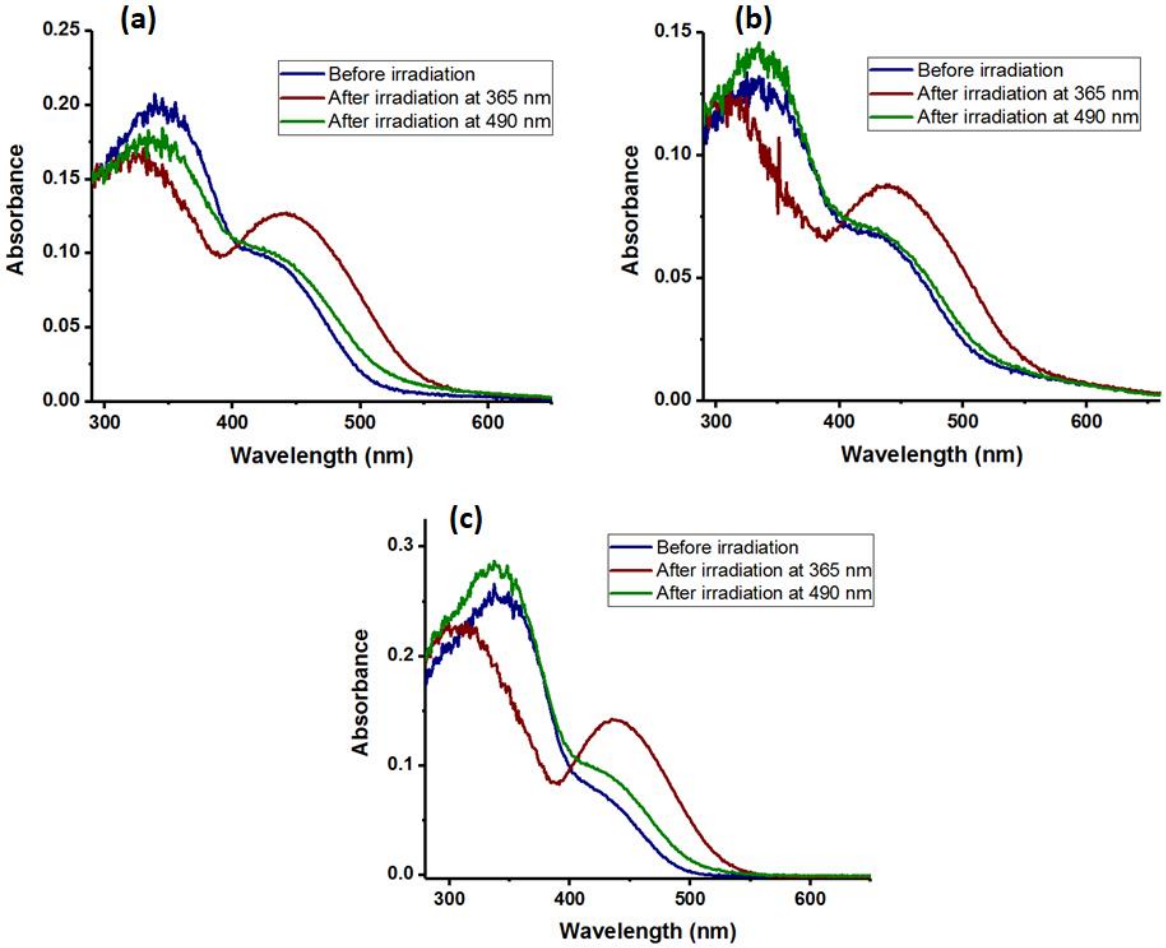

Figure 4C.1. Analysis of solid-state photoswitching in the targets **1a-c** using UV-vis spectroscopy (in KBr medium); (a) **1a**; (b) **1b**, and (c) **1c**.

Appendix 4D

Kinetics data

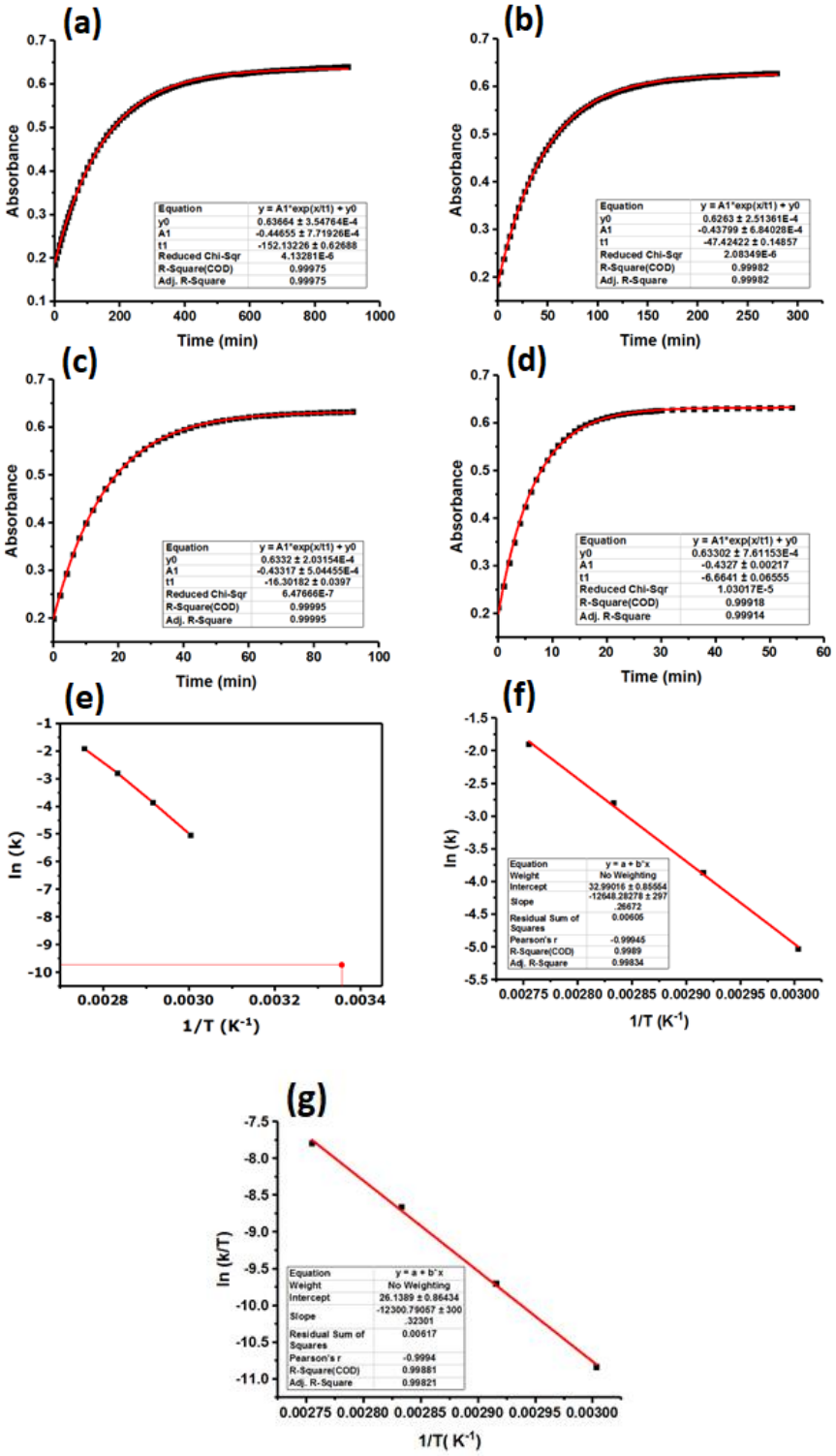

Figure 4D.1. First order thermal reverse isomerization kinetics plots for **1a** (8.5 μM, DMSO) at (a) 60 ^{o}C; (b) 70 ^{o}C; (c) 80 ^{o}C; (d) 90 ^{o}C; (e) Arrhenius plot after extrapolated to 25 ^{o}C; (f) Arrhenius plot; (g) Eyring plot.

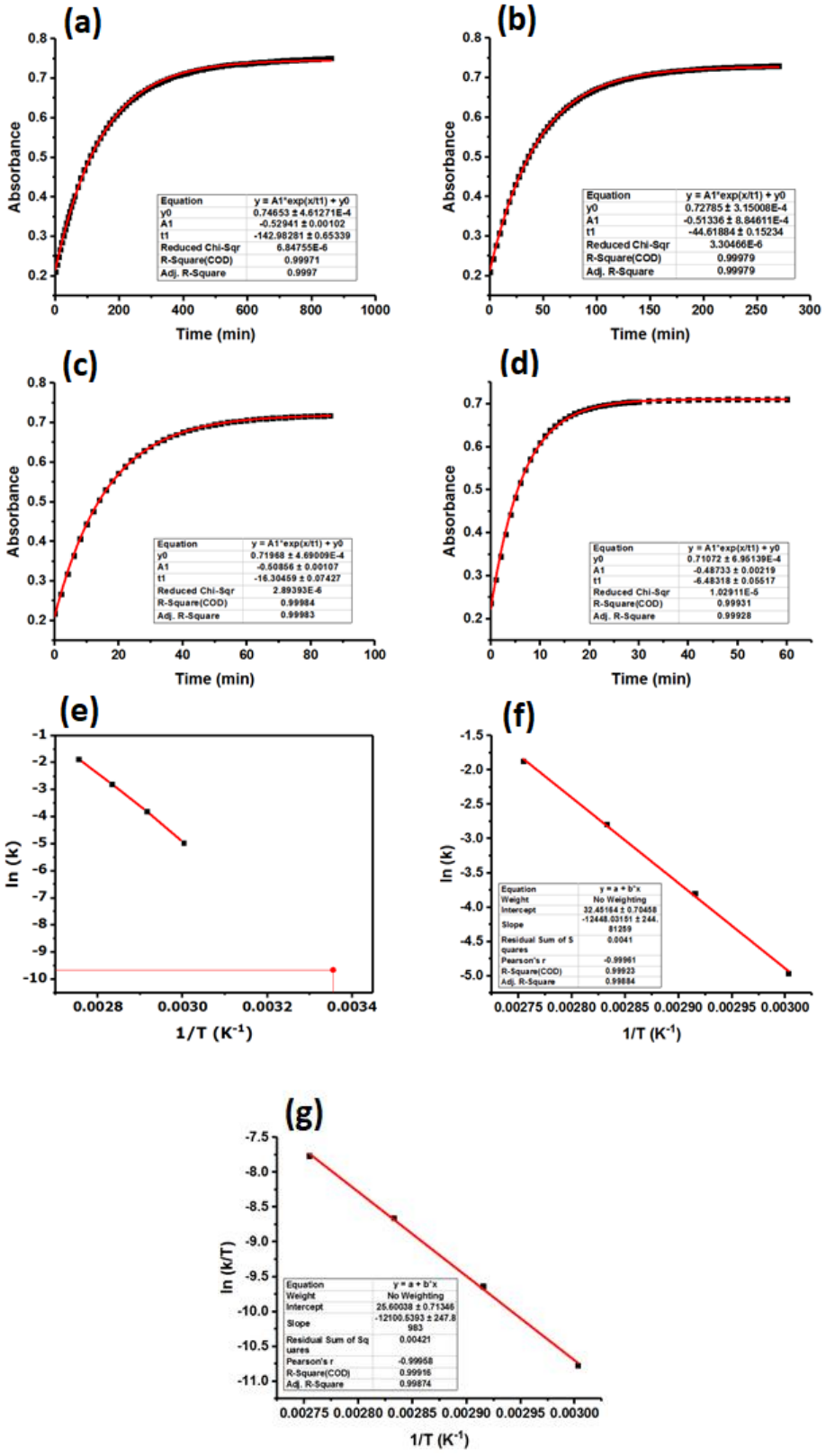

Figure 4D.2. First order thermal reverse isomerization kinetics plot for **1b** (10.3 μM, DMSO) at (a) 60 ^{o}C; (b) 70 ^{o}C; (c) 80 ^{o}C; (d) 90 ^{o}C; (e) after extrapolated to 25 ^{o}C; (f) Arrhenius plot; (g) Eyring plot.

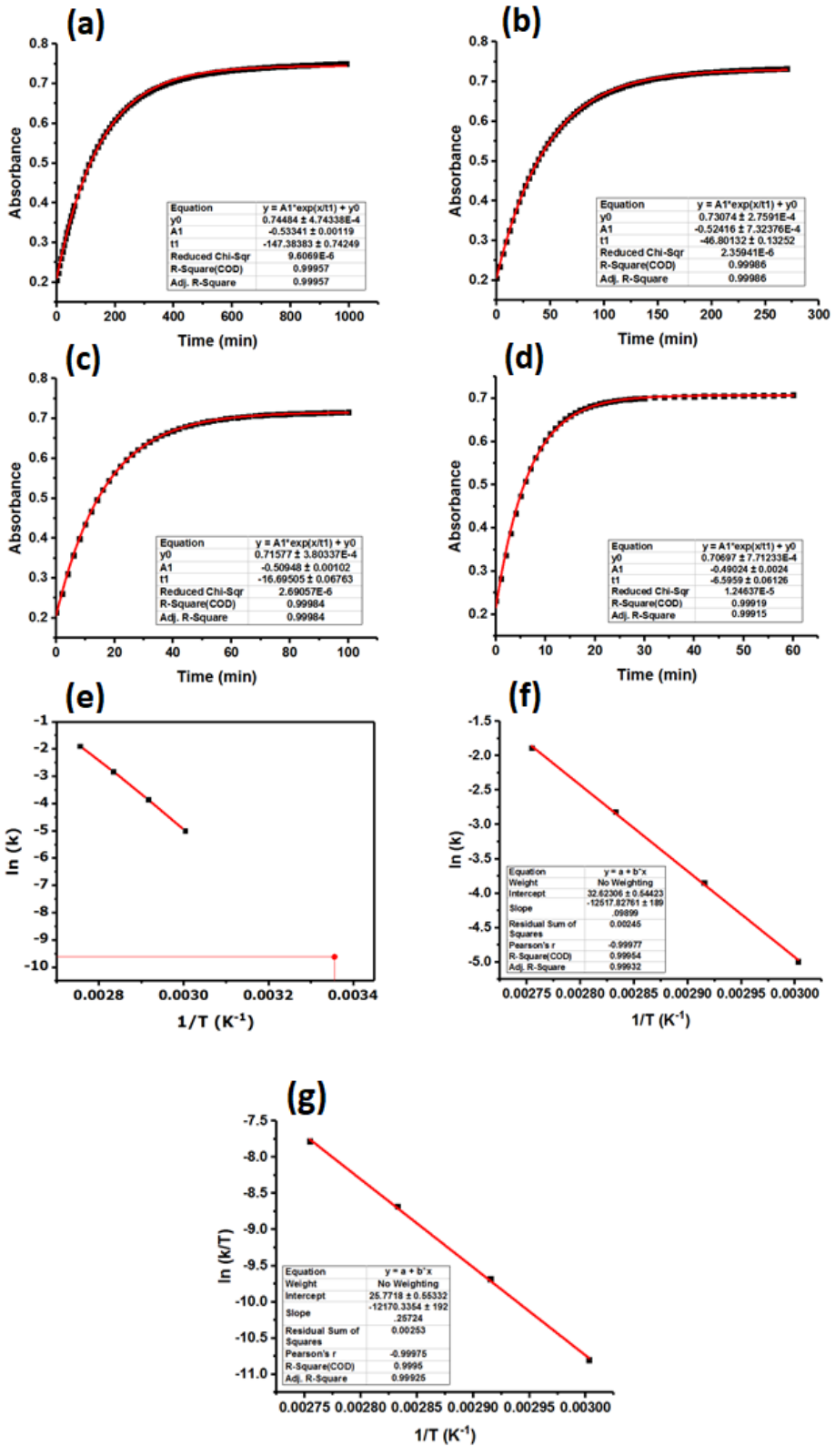

Figure 4D.3 First order thermal reverse isomerization kinetics plot for **1c** (9.7 μM, DMSO) at (a) 60 ^{o}C; (b) 70 ^{o}C; (c) 80 ^{o}C; (d) 90 ^{o}C; (e) after extrapolated to 25 ^{o}C; (f) Arrhenius plot; (g) Eyring plot.

Table 4D.1. Thermal reverse isomerization kinetics data

S. No.	Compound	Temperature (^{o}C)	Rate constant (min^{-1})	Half-life (min)	Conc. [μM]
1	**1a**	90	$1.5 \times 10^{-1} \pm 1.5 \times 10^{-3}$	5	8.5
		80	$6.1 \times 10^{-2} \pm 1.5 \times 10^{-4}$	11	8.5
		70	$2.1 \times 10^{-2} \pm 6.6 \times 10^{-5}$	33	8.5
		60	$6.6 \times 10^{-3} \pm 2.7 \times 10^{-5}$	106	8.5
		25	6.0×10^{-5}	8[a]	-
2	**1b**	90	$1.5 \times 10^{-1} \pm 1.3 \times 10^{-3}$	5	10.3
		80	$6.1 \times 10^{-2} \pm 2.8 \times 10^{-4}$	11	10.3
		70	$2.2 \times 10^{-2} \pm 7.7 \times 10^{-5}$	31	10.3
		60	$7.0 \times 10^{-3} \pm 3.2 \times 10^{-5}$	99	10.3
		25	6.4×10^{-5}	7.5[a]	-
3	**1c**	90	$1.5 \times 10^{-1} \pm 1.4 \times 10^{-3}$	5	9.7
		80	$6.0 \times 10^{-2} \pm 2.4 \times 10^{-4}$	12	9.7
		70	$2.1 \times 10^{-2} \pm 6.1 \times 10^{-5}$	32	9.7
		60	$6.8 \times 10^{-3} \pm 3.4 \times 10^{-5}$	102	9.7
		25	6.7×10^{-5}	7.2[a]	-

[a]estimated in days

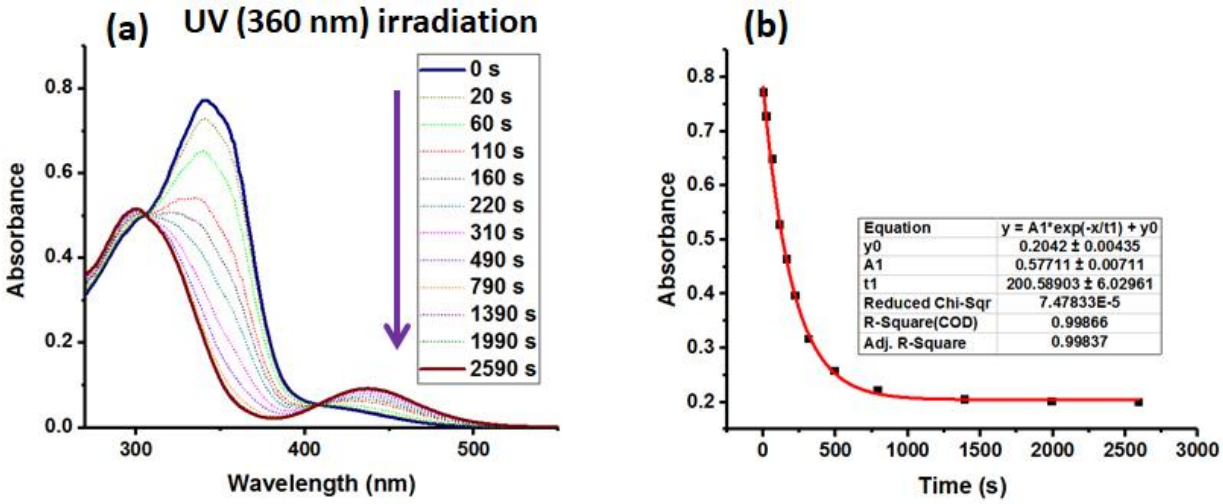

Figure 4D.4. Photochemical forward isomerization kinetics experiment in **1a** (11.5 μM, DMSO); (a) Forward (*EEE* to *ZZZ*) photoisomerization spectral data of **1a** recorded at different intervals of irradiation time at 360 nm (50 μW power LED) at rt; (b) First order exponential decay of *EEE*-isomer. (Monitored at λ_{max} = 341 nm)

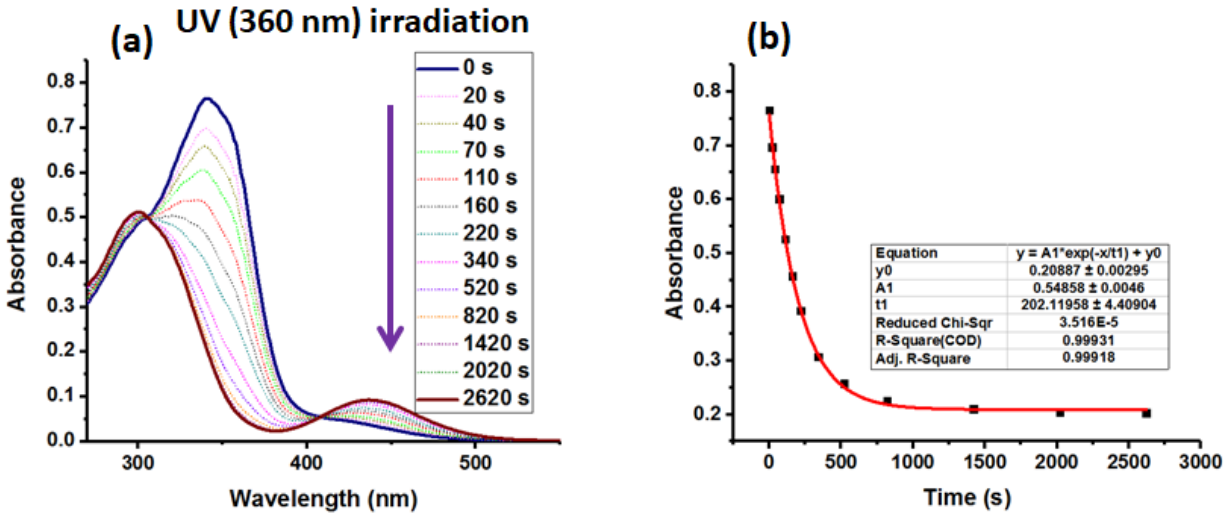

Figure 4D.5. Photochemical forward isomerization kinetics experiment in **1b** (12.3 μM, DMSO); (a) Forward (*EEE* to *ZZZ*) photoisomerization spectral data of **1b** recorded at different intervals of irradiation time at 360 nm (50 μW power LED) at rt; (b) First order exponential decay of *EEE*-isomer. (Monitored at λ_{max} = 341 nm).

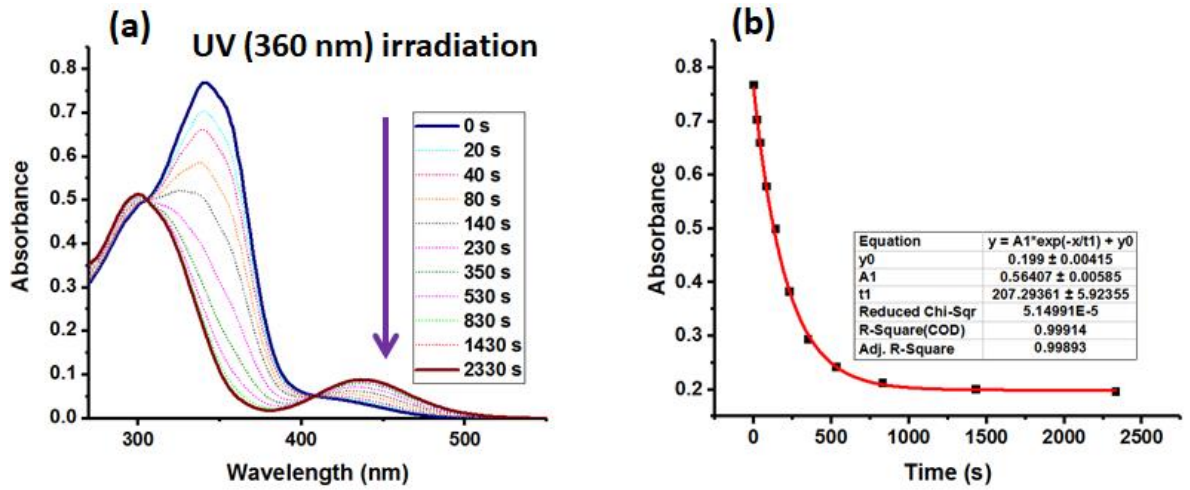

Figure 4D.6. Photochemical forward isomerization kinetics experiment in **1c** (11.5 μM, DMSO); (a) Forward (*EEE* to *ZZZ*) photoisomerization spectral data of **1c** recorded at different intervals of irradiation time at 360 nm (50 μW power LED) at rt; (b) First order exponential decay of *EEE*-isomer. (Monitored at λ_{max} = 341 nm).

Table 4D.2. Photochemical forward isomerization first-order kinetics data

S. No.	Compound	Temperature (^oC)	Rate constant (s^{-1})	Half-life (s)	Conc. [μM]
1	**1a**	25	$5.0 \times 10^{-3} \pm 1.5 \times 10^{-4}$	139	11.5
2	**1b**	25	$5.0 \times 10^{-3} \pm 1.1 \times 10^{-4}$	140	12.3
3	**1c**	25	$4.8 \times 10^{-2} \pm 1.4 \times 10^{-4}$	144	11.5

Appendix 4E

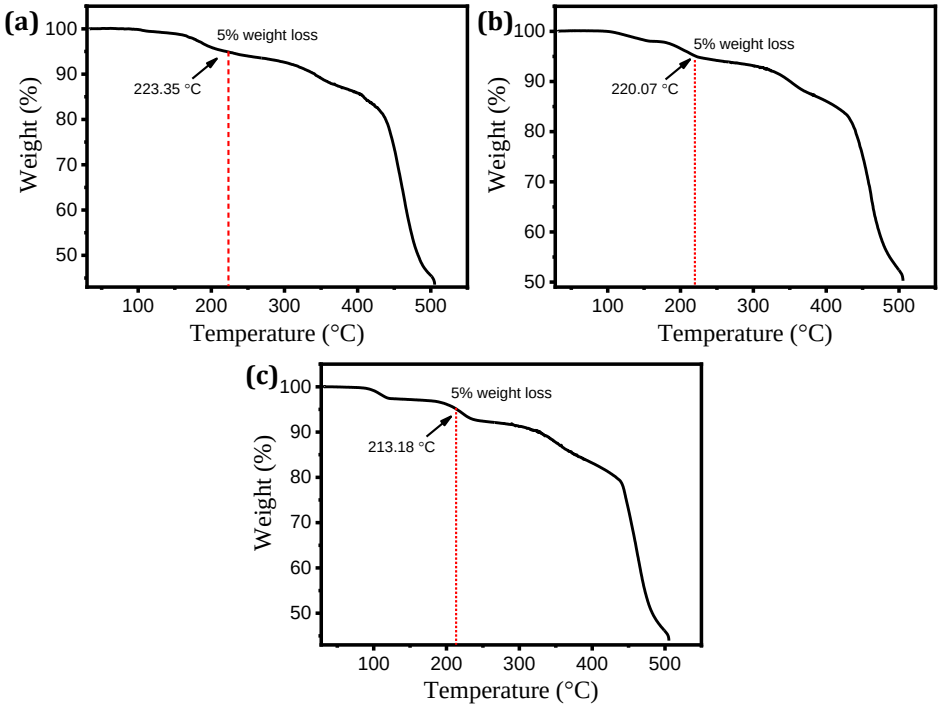

Figure 4E.1. Thermogravimetric analysis (TGA) curves for the targets (a) **1a**; (b) **1b**, and (c) **1c**.

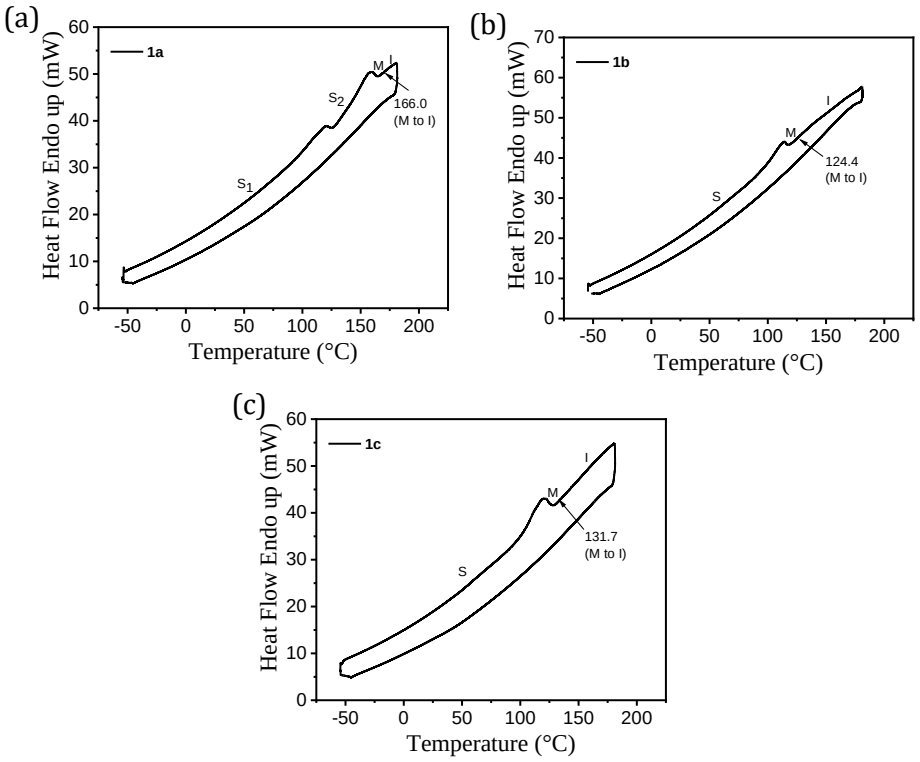

Figure 4E.2. DSC thermogram of compounds (a) **1a**; (b) **1b**, and (c) **1c** on heating as well as on cooling (first heating cycle, scan rate: 10 °C/min).

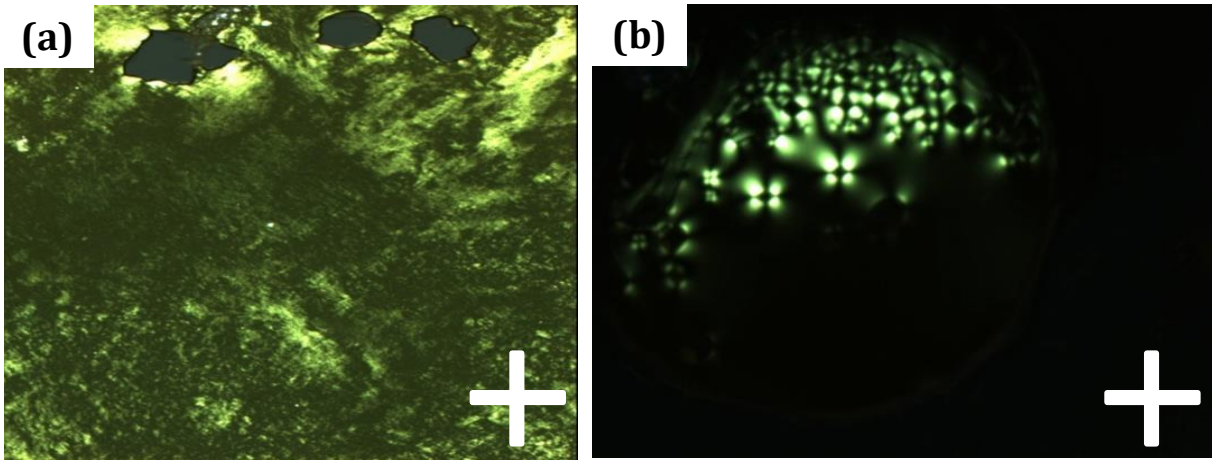

Figure 4E.3. Optical micrographs of compounds (a) **1a** at 75.3 °C and (b) **1b** at 45.3 °C recorded upon cooling the sample from the isotropic liquid (scan rate: 10 °C/min, ×200).

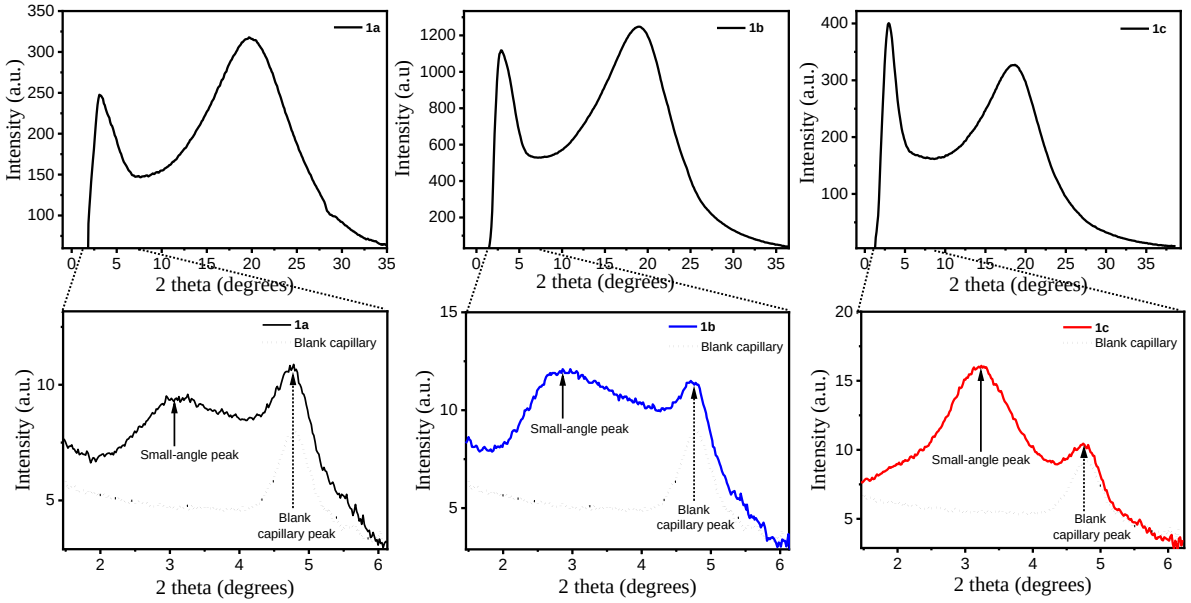

Figure 4E.4. Upper row shows the wide-angle XRD patterns of compounds **1a-c** at 25 °C and the below row displays their corresponding small-angle diffraction patterns. Note: In small angle, XRD data the blank capillary peak becomes prominent due to the loss of peak intensity at larger sample-detector distances (or smaller scattering angles).

Calculation of correlation length

The correlation length (ξ) was calculated using Scherrer's equation ξ = [k*2π]/[(Δq)]. Here, k is the shape factor whose typical value is 0.89, λ is the wavelength of the incident X-ray, q is the scattering vector (q = 4πsinθ/λ), θ is the maximum of the reflection, and Δq is the broadening in q at half of the maximum intensity. The Δq is calculated from the fitting of the diffraction peaks by Lorentzian profiles. The ratio of the ξ and corresponding *d*-spacings gives a realization of correlation length in terms of correlated units of length scale *d*.

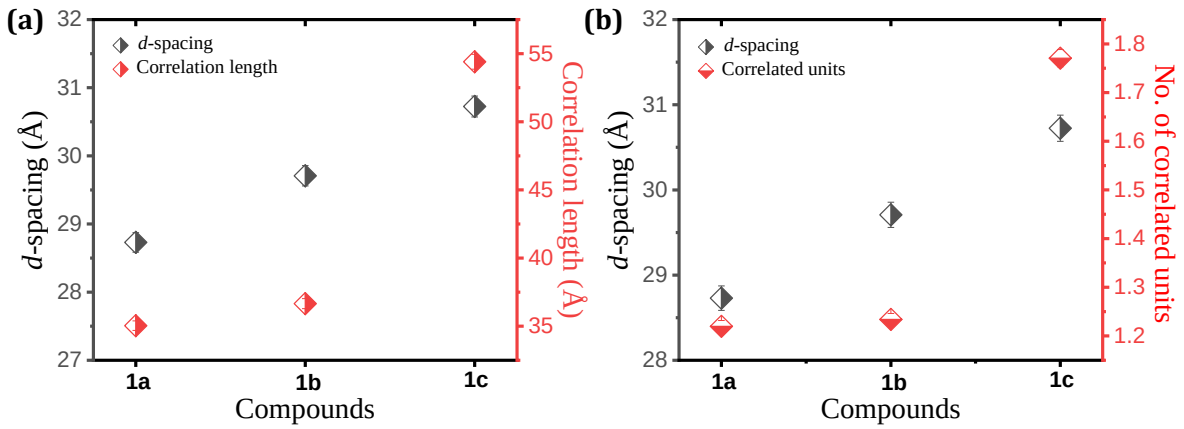

Figure 4E.5. Variation of (a) correlation length (ξ) and (b) number of correlated units with *d*-spacing corresponding to the (10) peak for compounds **1a-c**.

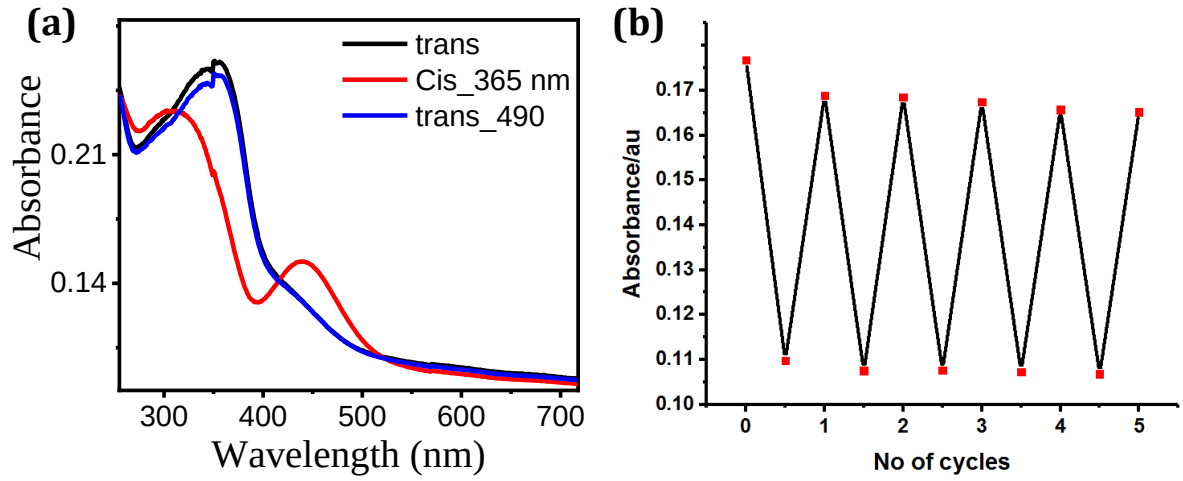

Figure 4E.6. Analysis of photoswitching in LC phase of **1c** using UV-vis spectroscopic studies: (a) absorption spectral changes before irradiation (black trace), after irradiation at 365 nm UV light (red trace), and after reverse photoswitching by irradiation at 490 nm light (blue trace). (b) Photoisomerization stability experiment. (Alternative irradiation at 365 and 490 nm irradiation in the forward and reverse isomerization steps, respectively; The plot depicts that up to 5 cycles the absorption intensity remains almost constant indicating fatigue resistance)

Appendix 4F

Atomic force microscopic (AFM) studies

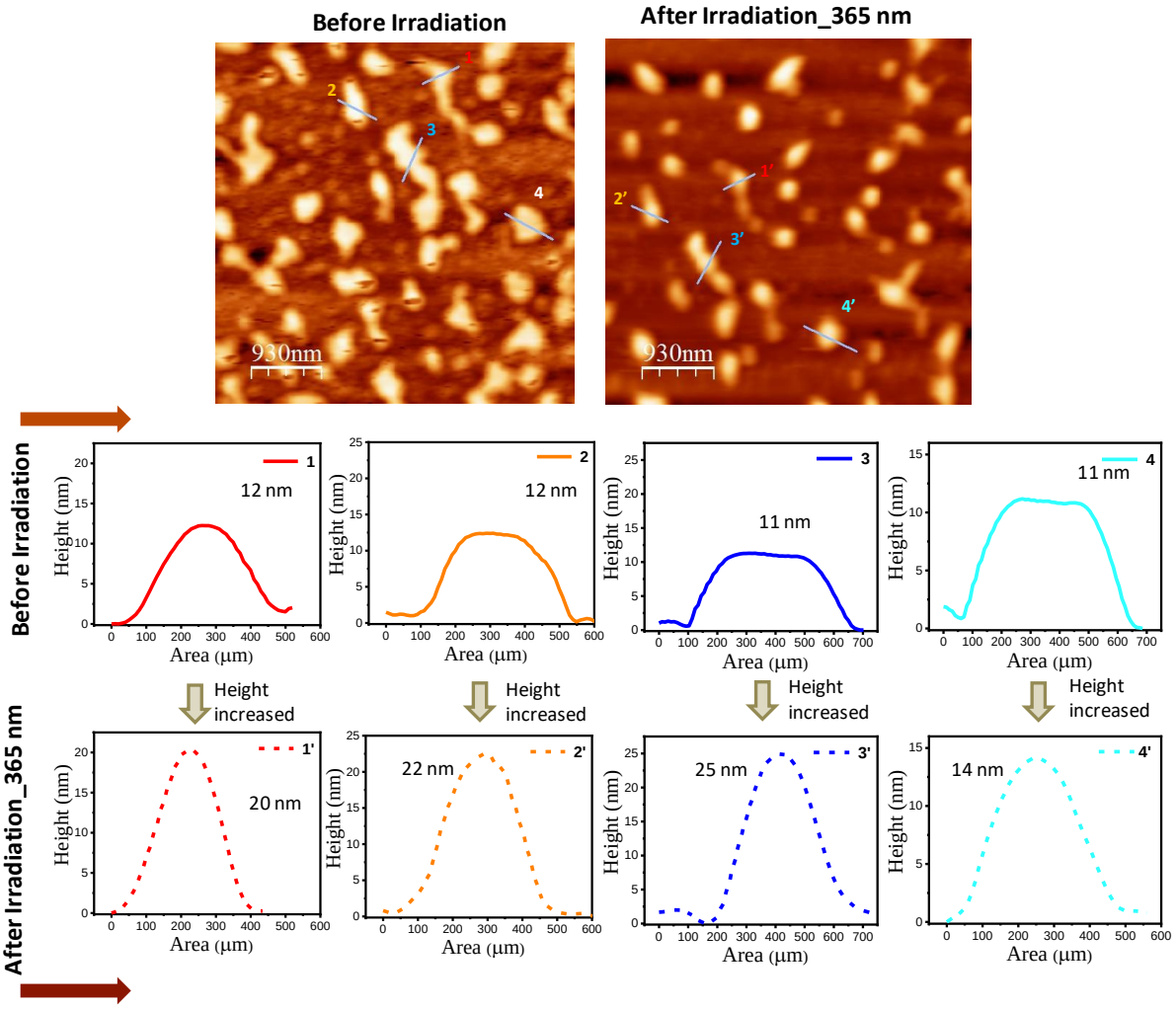

Figure 4F.1. Morphological changes of thin-film of compound **1c** after *in-situ* irradiation at 365 nm UV-light as monitored by using AFM technique. Height traces graph showing increase in height after irradiating the thin-film with 365 nm light at different areas marked as 1, 2, 3, 4 (before irradiation) and 1′, 2′, 3′, 4′ (after irradiation). Thin-film was prepared by spin-coating a micromolar solution of 1c in toluene.

Appendix 4G

NMR Spectral data

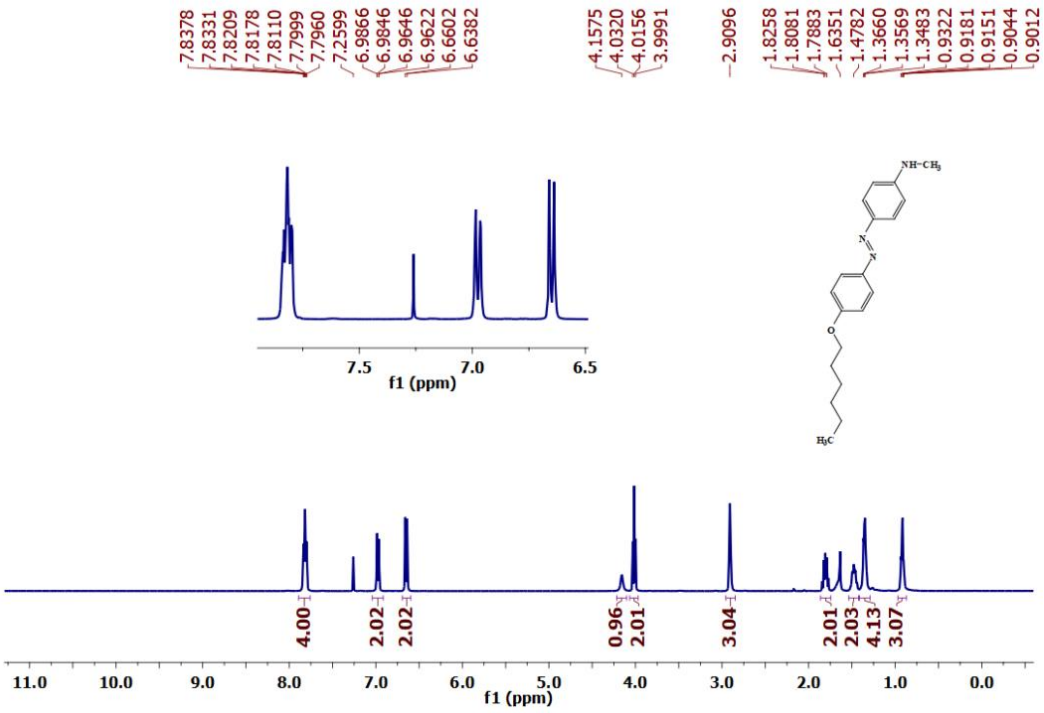

^{1}H NMR spectrum of (*E*)-4-((4-(hexyloxy)phenyl)diazenyl)-*N*-methylaniline **(2)** in $CDCl_3$.

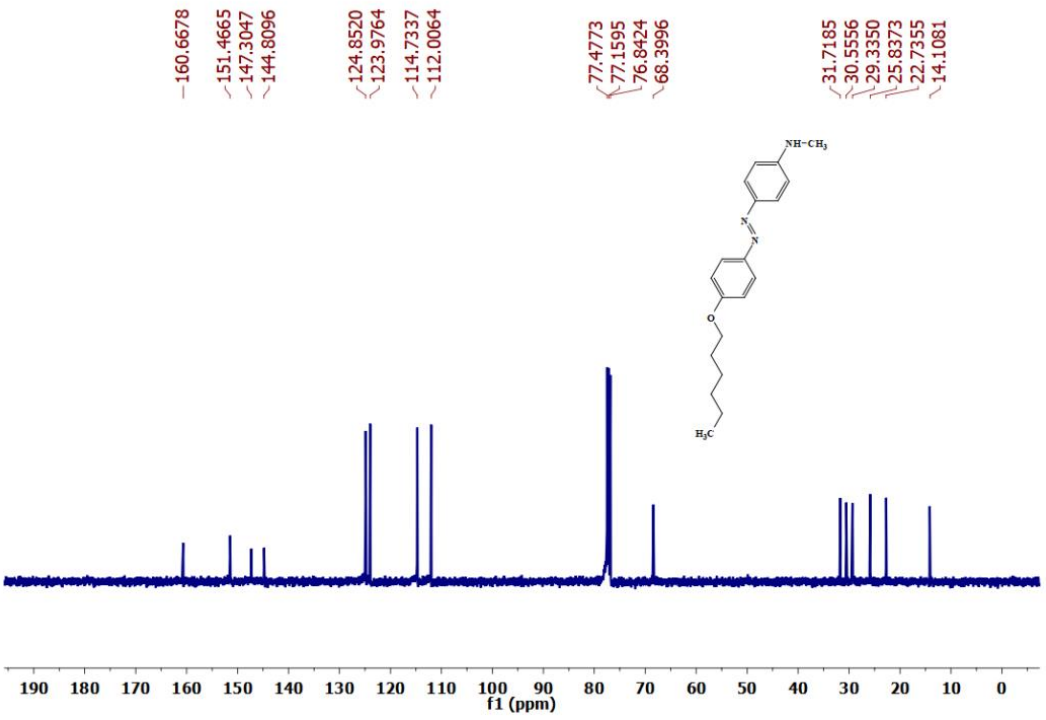

^{13}C NMR spectrum of (*E*)-4-((4-(hexyloxy)phenyl)diazenyl)-*N*-methylaniline **(2)** in $CDCl_3$.

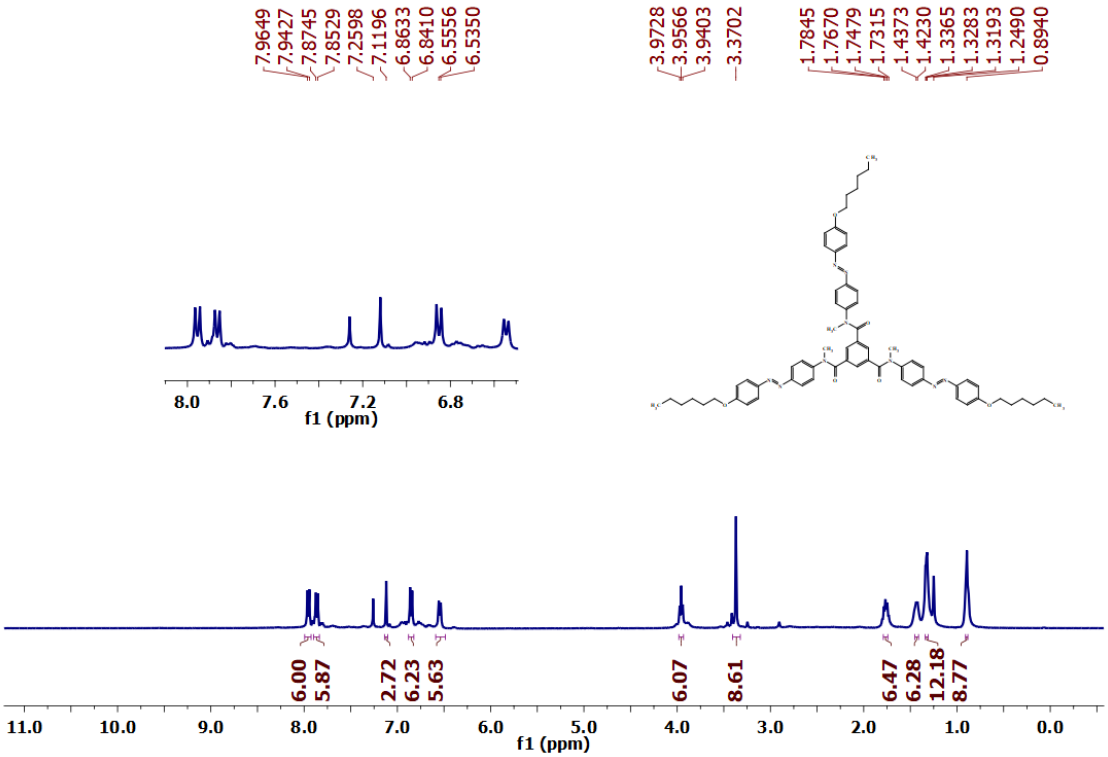

^{1}H NMR spectrum of N^{1},N^{3},N^{5}-tris(4-((*E*)-(4-(hexyloxy)phenyl)diazenyl)phenyl)-N^{1},N^{3},N^{5}-trimethylbenzene-1,3,5-tricarboxamide (**6**) in $CDCl_3$.

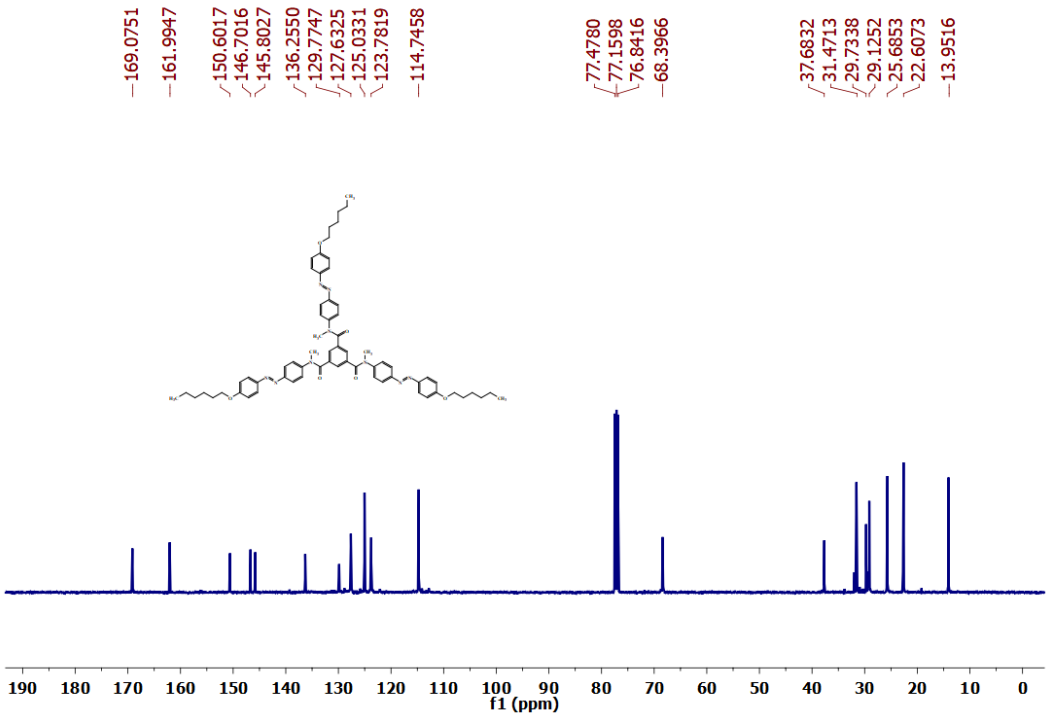

^{13}C NMR spectrum of N^{1},N^{3},N^{5}-tris(4-((*E*)-(4-(hexyloxy)phenyl)diazenyl)phenyl)-N^{1},N^{3},N^{5}-trimethylbenzene-1,3,5-tricarboxamide (**6**) in $CDCl_3$.

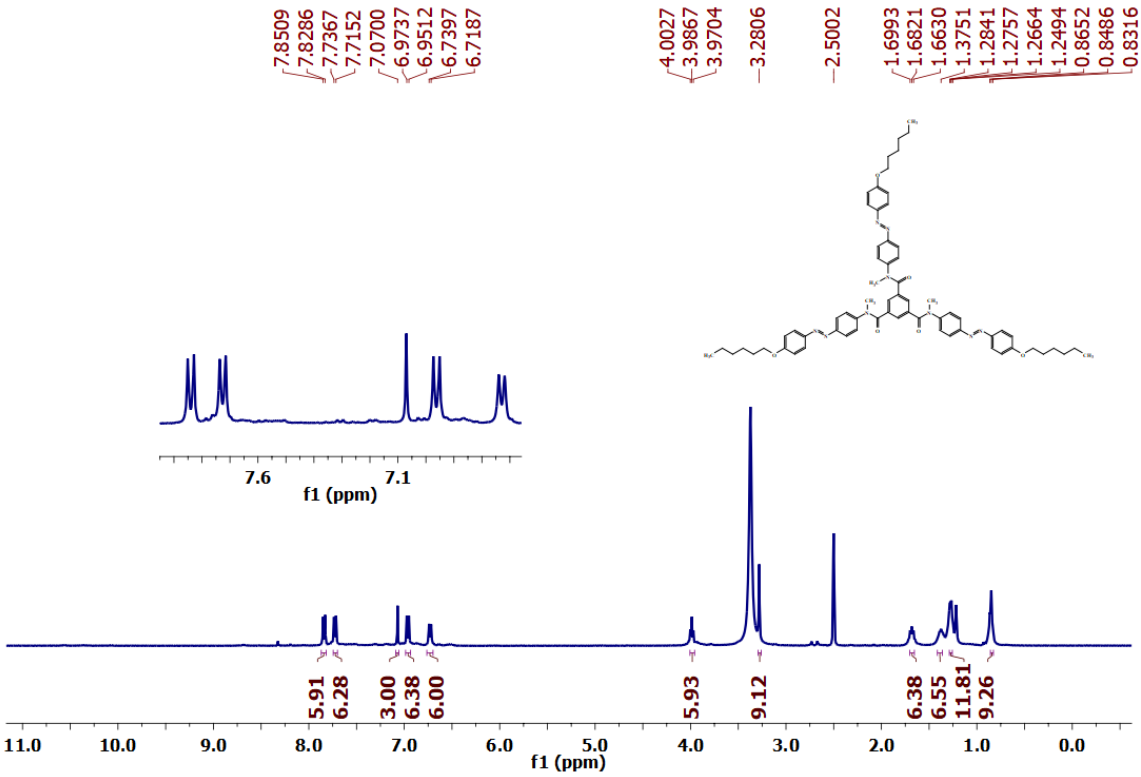

^{1}H NMR spectrum of N^1,N^3,N^5-tris(4-((*E*)-(4-(hexyloxy)phenyl)diazenyl)phenyl)-N^1,N^3,N^5-trimethylbenzene-1,3,5-tricarboxamide (**6**) in [D_6]DMSO.

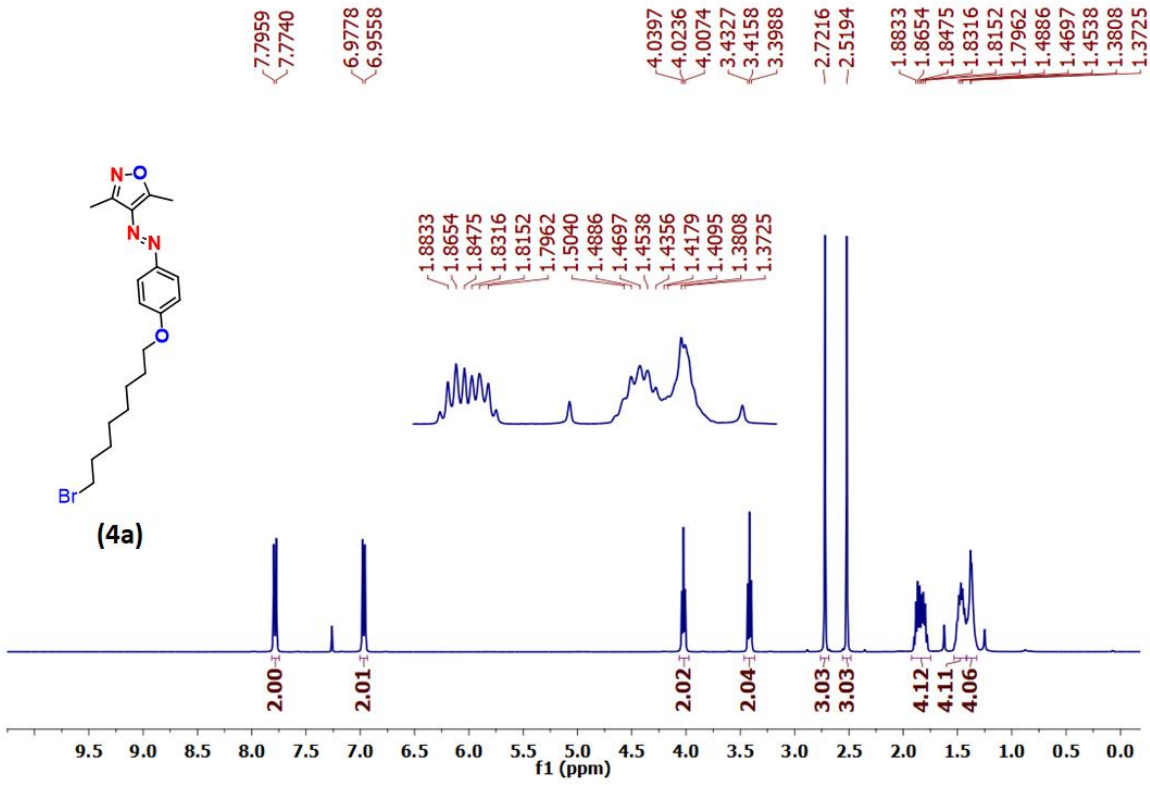

^{1}H NMR spectrum of (*E*)-4-((4-((8-bromooctyl)oxy)phenyl)diazenyl)-3,5-dimethylisoxazole **(4a)** in $CDCl_3$

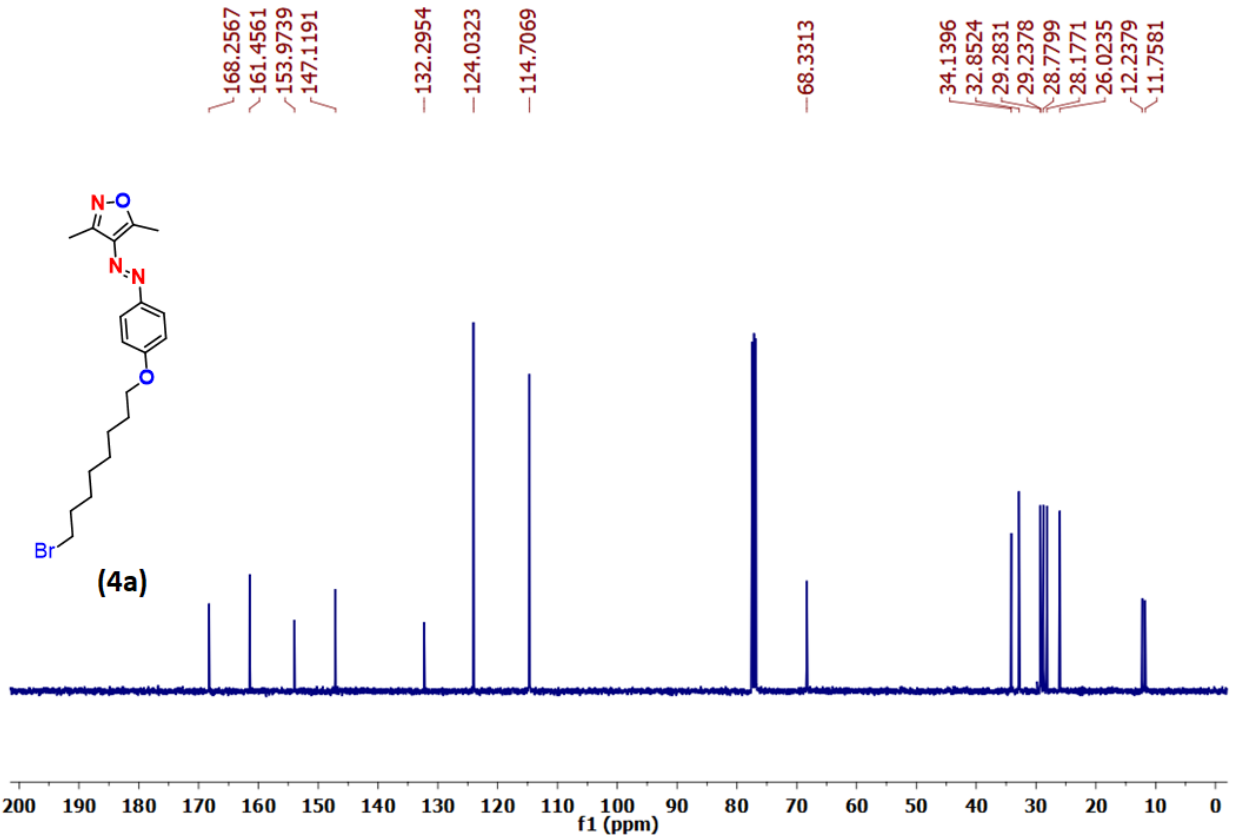

^{13}C NMR spectrum of (*E*)-4-((4-((8-bromooctyl)oxy)phenyl)diazenyl)-3,5-dimethylisoxazole **(4a)** in $CDCl_3$

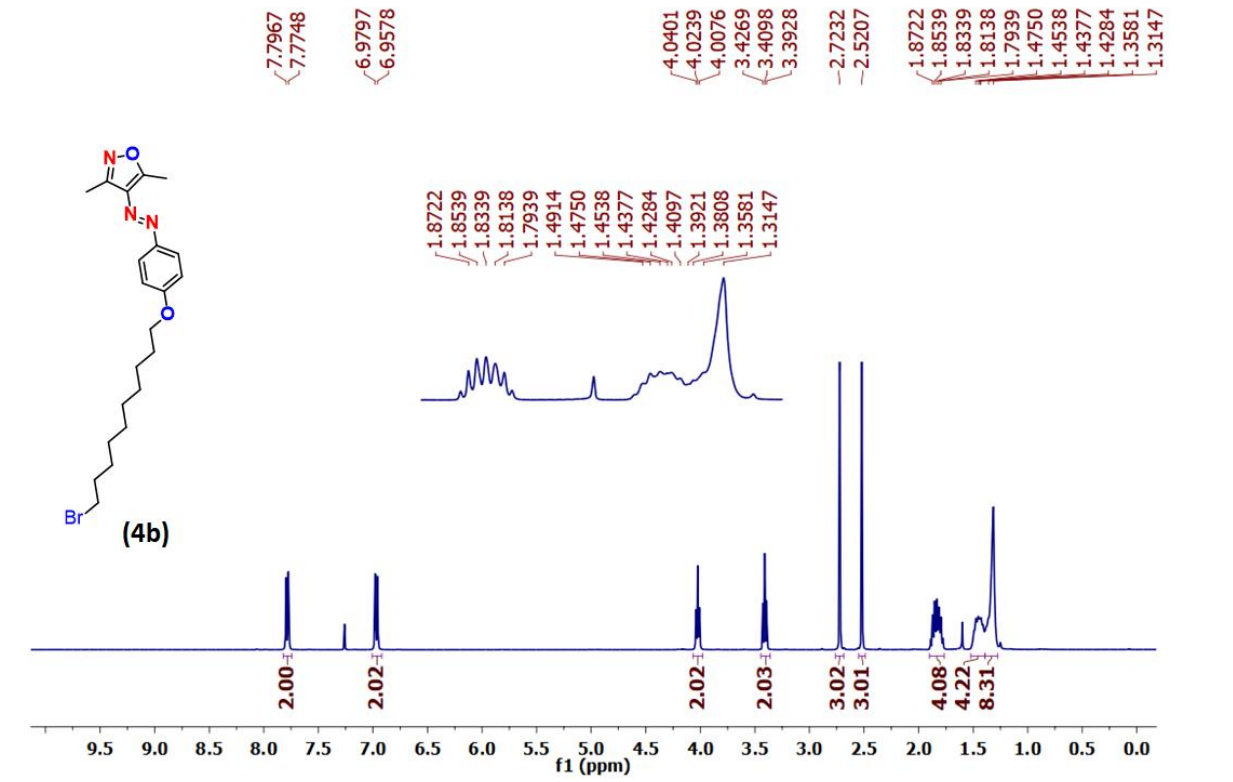

^{1}H NMR spectrum of (*E*)-4-((4-((10-bromodecyl)oxy)phenyl)diazenyl)-3,5-dimethylisoxazole **(4b)** in $CDCl_3$

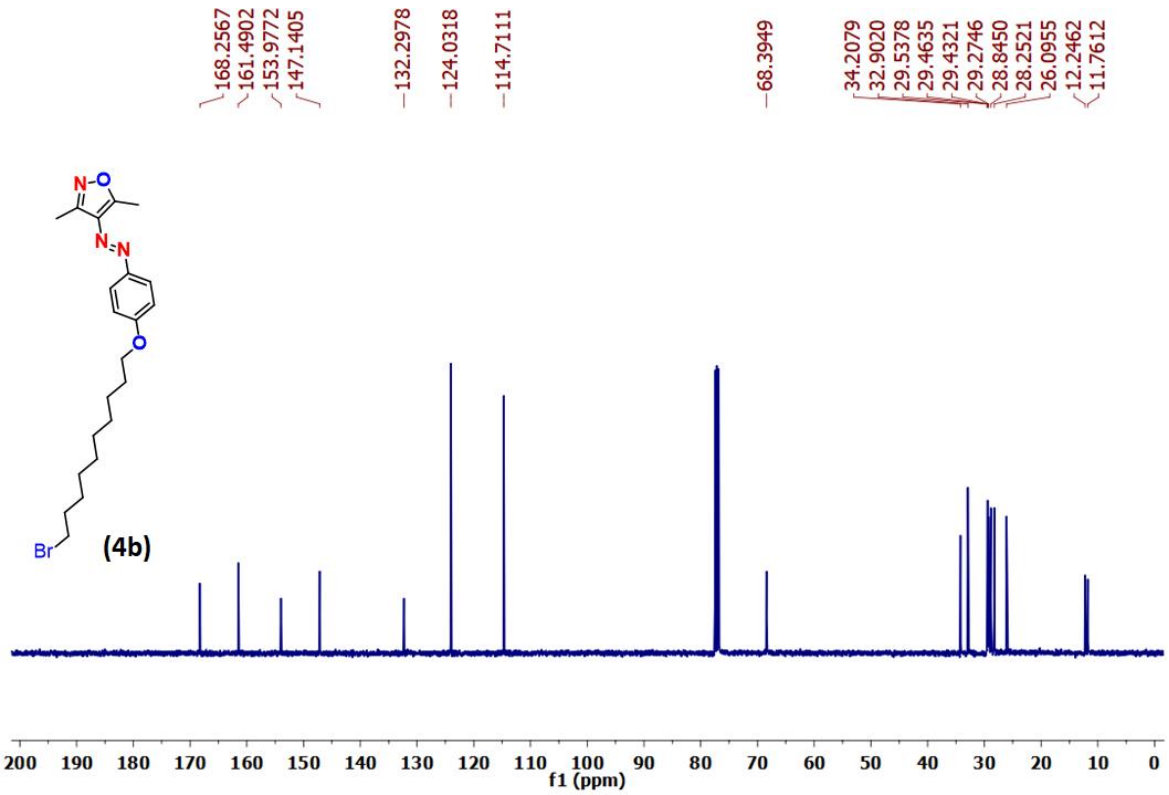

^{13}C NMR spectrum of (*E*)-4-((4-((10-bromodecyl)oxy)phenyl)diazenyl)-3,5-dimethylisoxazole **(4b)** in $CDCl_3$

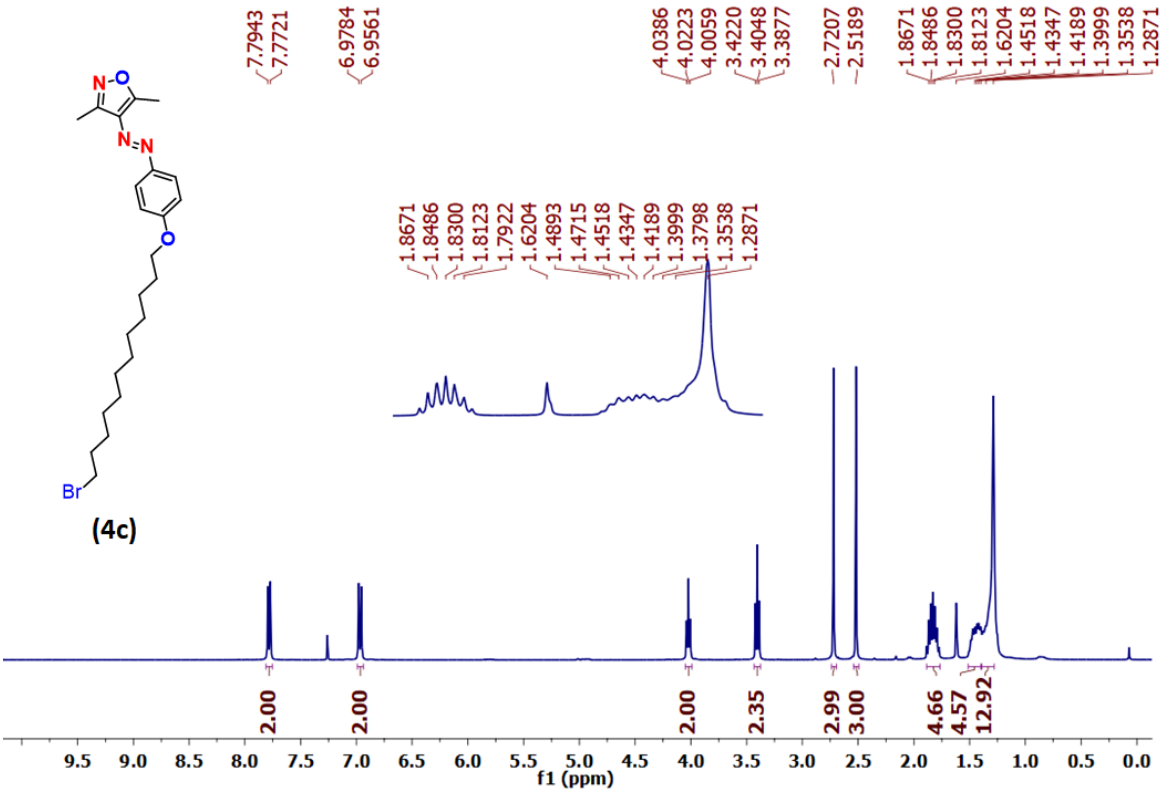

^{1}H NMR spectrum of (*E*)-4-((4-((12-bromododecyl)oxy)phenyl)diazenyl)-3,5-dimethylisoxazole **(4c)** in $CDCl_3$

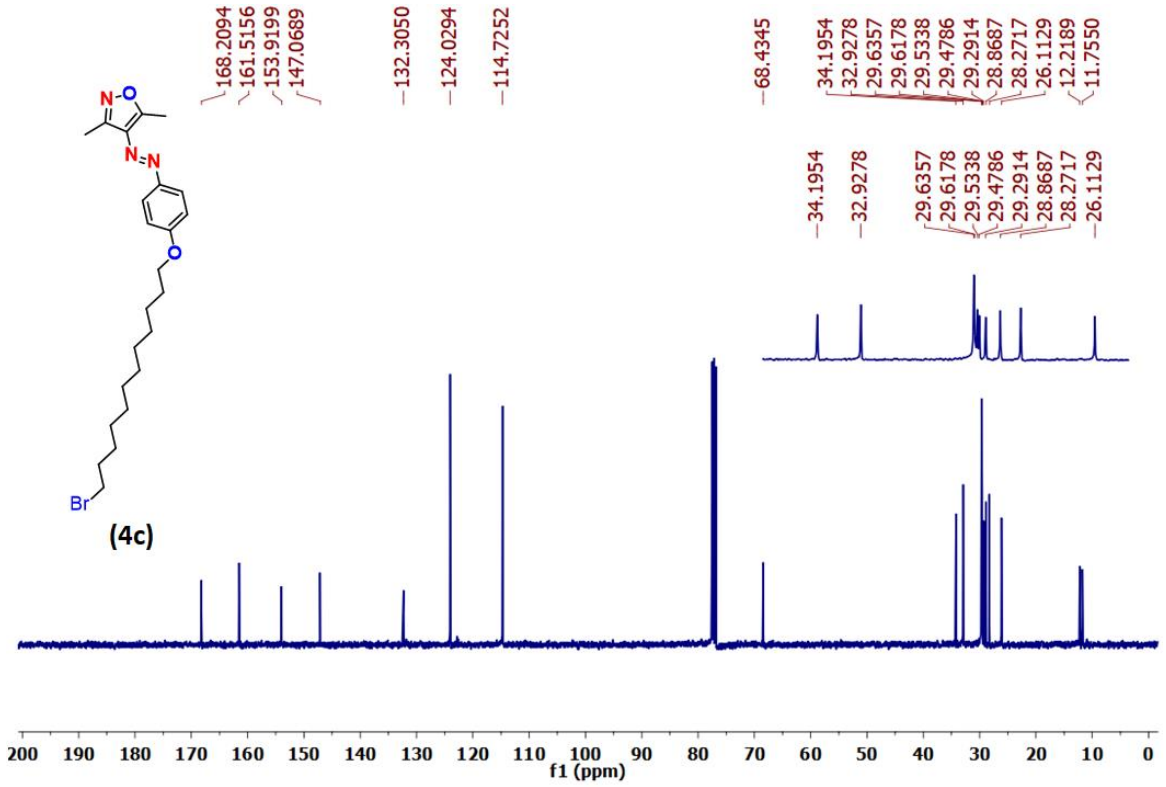

^{13}C NMR spectrum of (*E*)-4-((4-((12-bromododecyl)oxy)phenyl)diazenyl)-3,5-dimethylisoxazole **(4c)** in $CDCl_3$

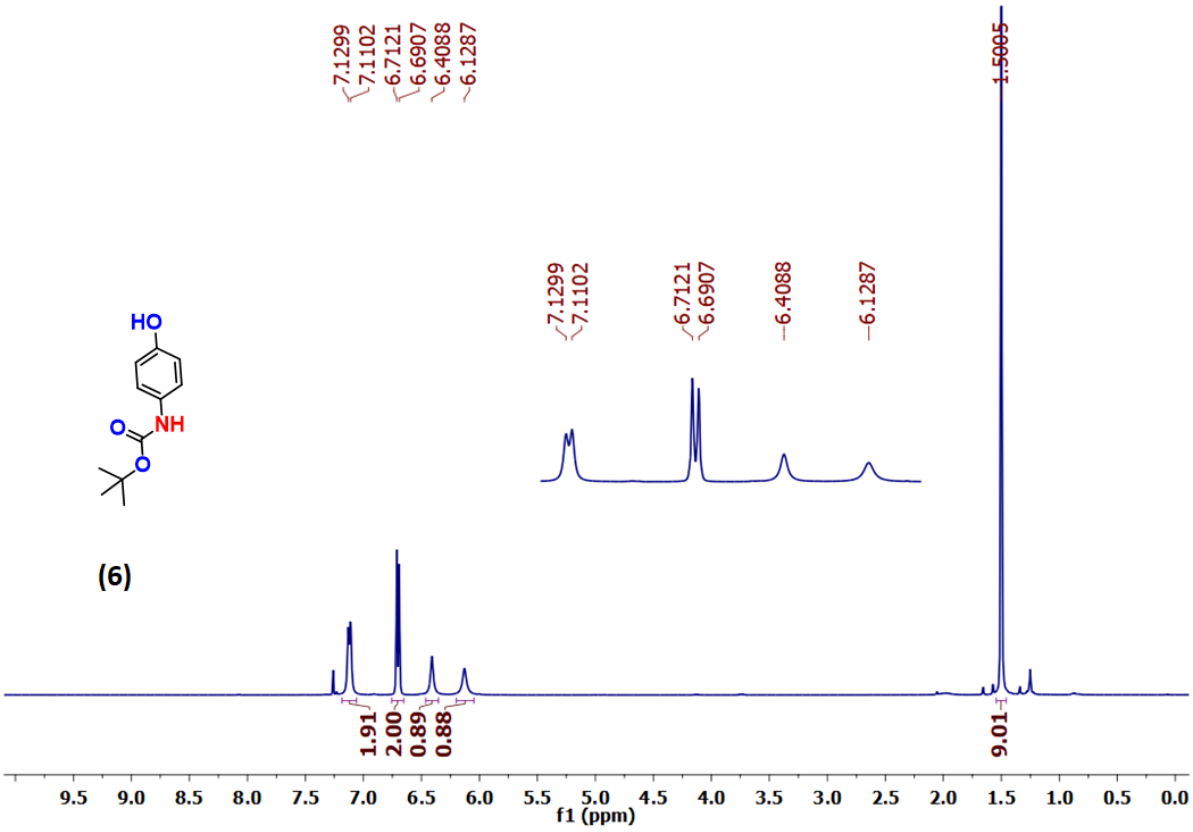

^{1}H NMR spectrum of tert-butyl (4-hydroxyphenyl)carbamate **(6)** in $CDCl_3$

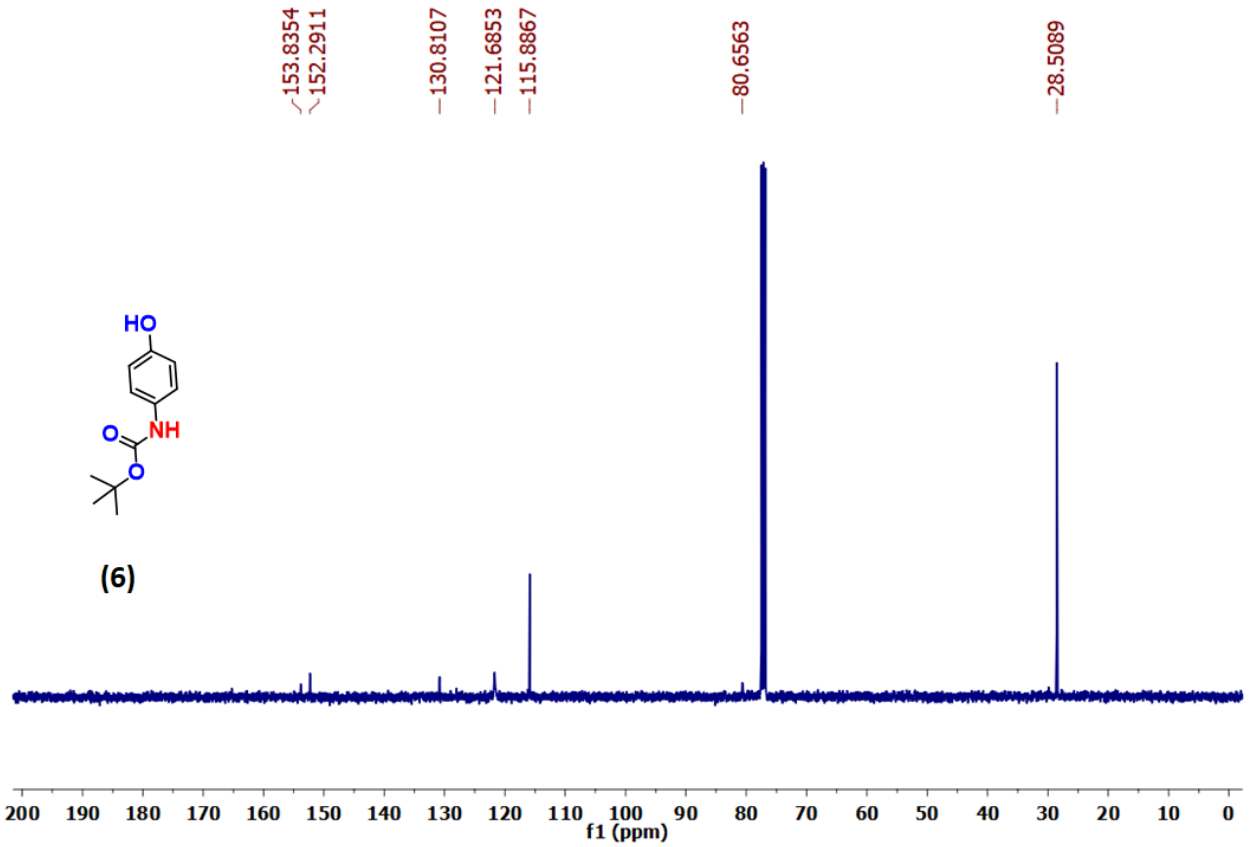

^{13}C NMR spectrum of tert-butyl (4-hydroxyphenyl)carbamate **(6)** in $CDCl_3$

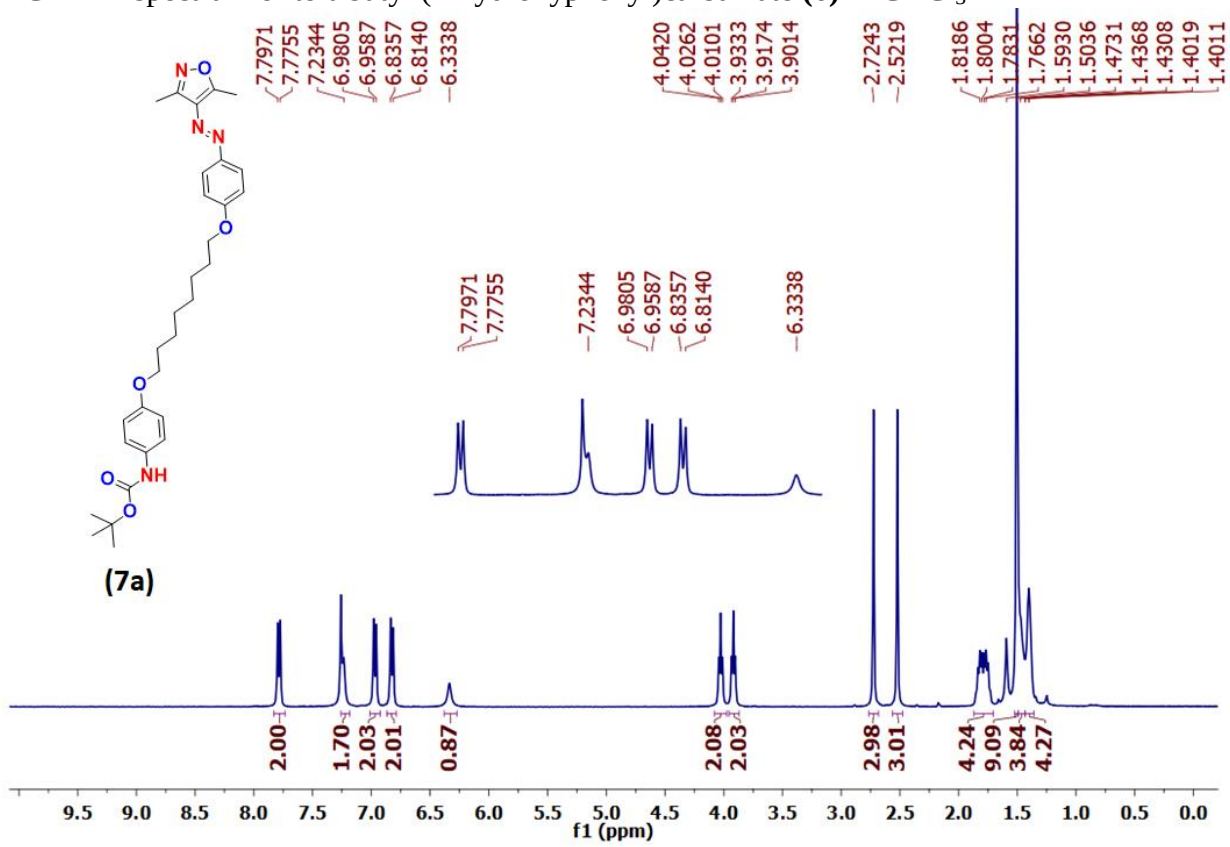

^{1}H NMR spectrum of tert-butyl (E)-(4-((8-(4-((3,5-dimethylisoxazol-4-yl)diazenyl)phenoxy)octyl)oxy)phenyl) **(7a)** in $CDCl_3$

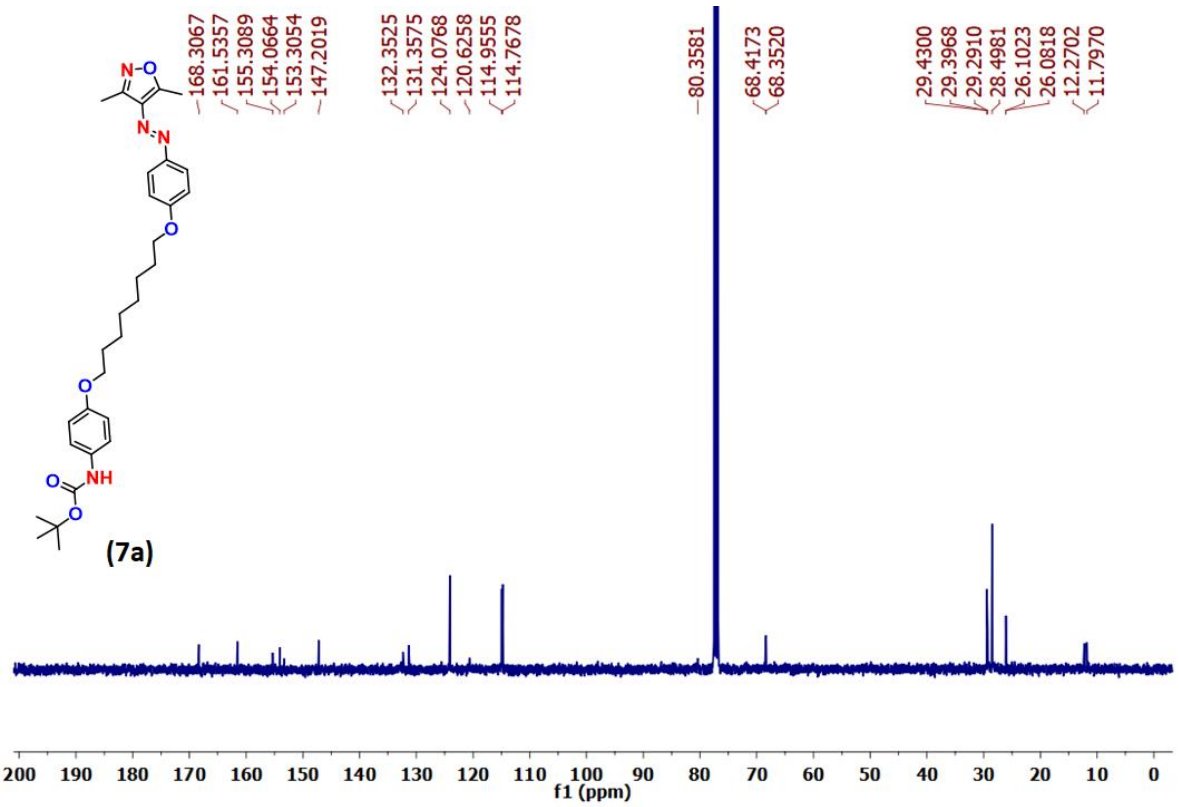

^{13}C NMR spectrum of tert-butyl (E)-(4-((8-(4-((3,5-dimethylisoxazol-4-yl)diazenyl)phenoxy)octyl)oxy)phenyl) **(7a)** in $CDCl_3$

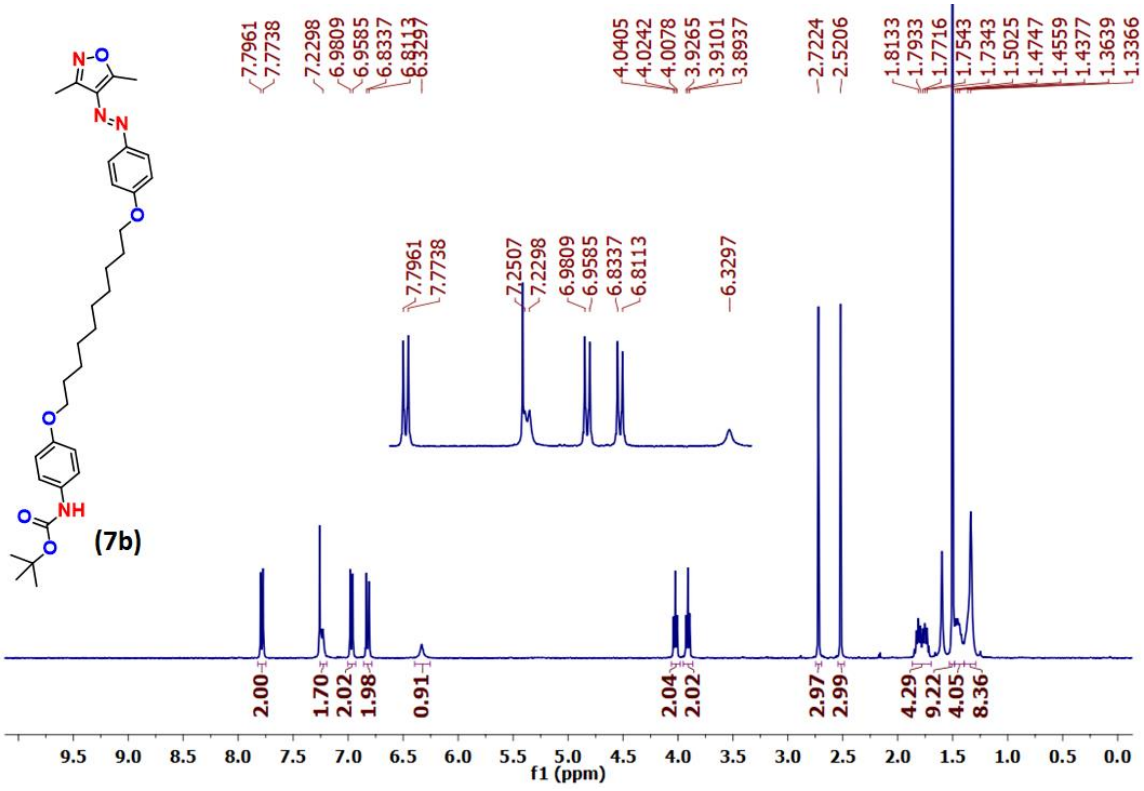

^{1}H NMR spectrum of tert-butyl (E)-(4-((10-(4-((3,5-dimethylisoxazol-4 yl)diazenyl)phenoxy)decyl)oxy)phenyl)carbamate **(7b)** in $CDCl_3$

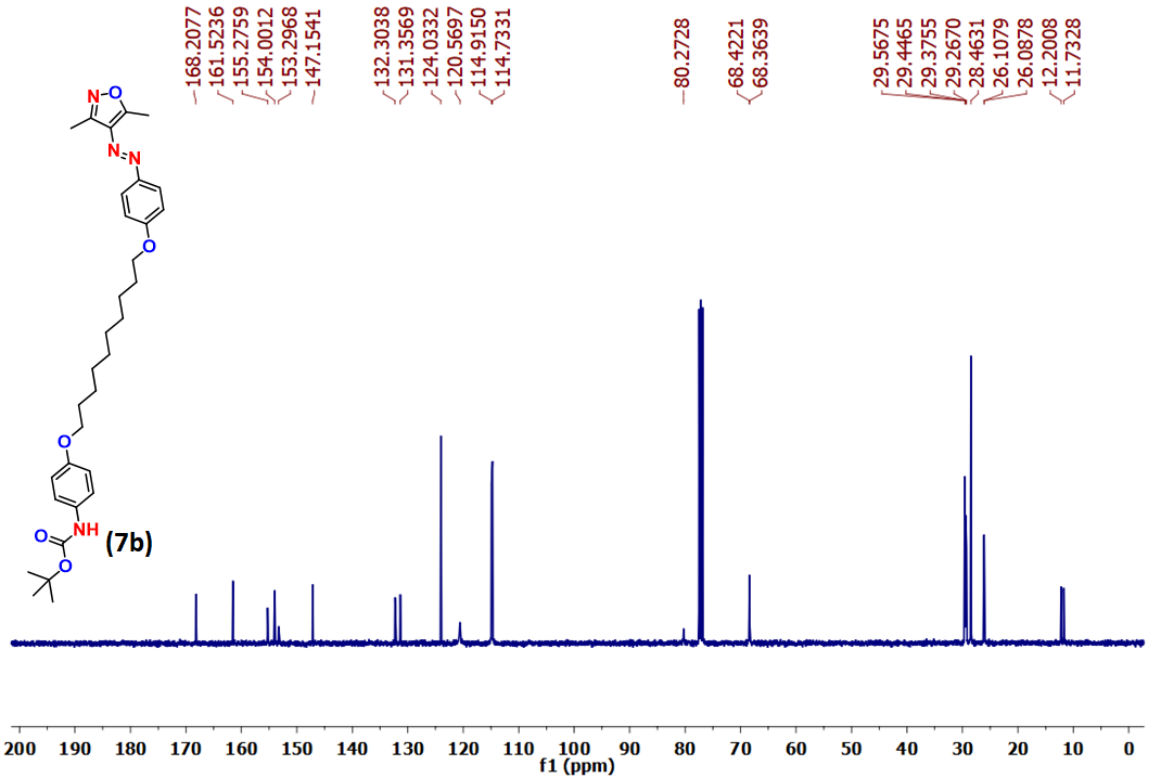

^{13}C NMR spectrum of tert-butyl (E)-(4-((10-(4-((3,5-dimethylisoxazol-4-yl)diazenyl)phenoxy)decyl)oxy)phenyl)carbamate **(7b)** in $CDCl_3$

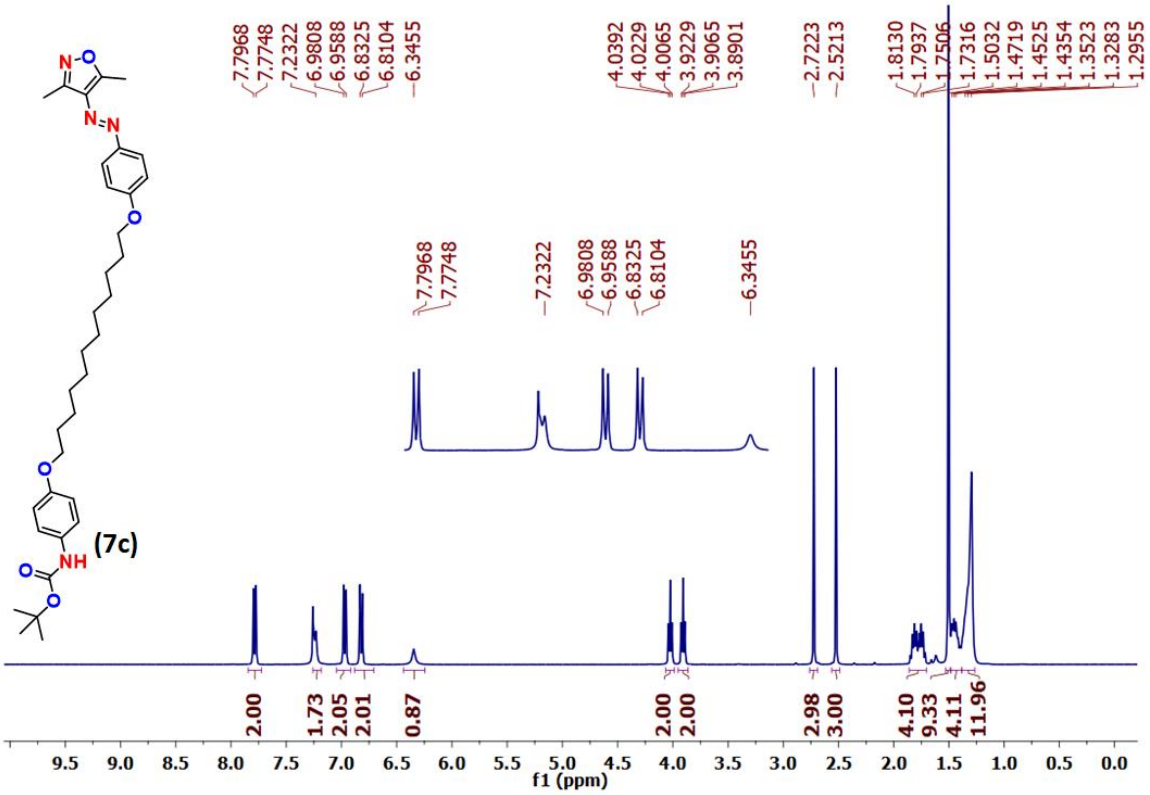

^{1}H NMR spectrum of tert-butyl (*E*)-(4-((12-(4-((3,5-dimethylisoxazol-4-yl)diazenyl)phenoxy)dodecyl)oxy)phenyl)carbamate **(7c)** in $CDCl_3$

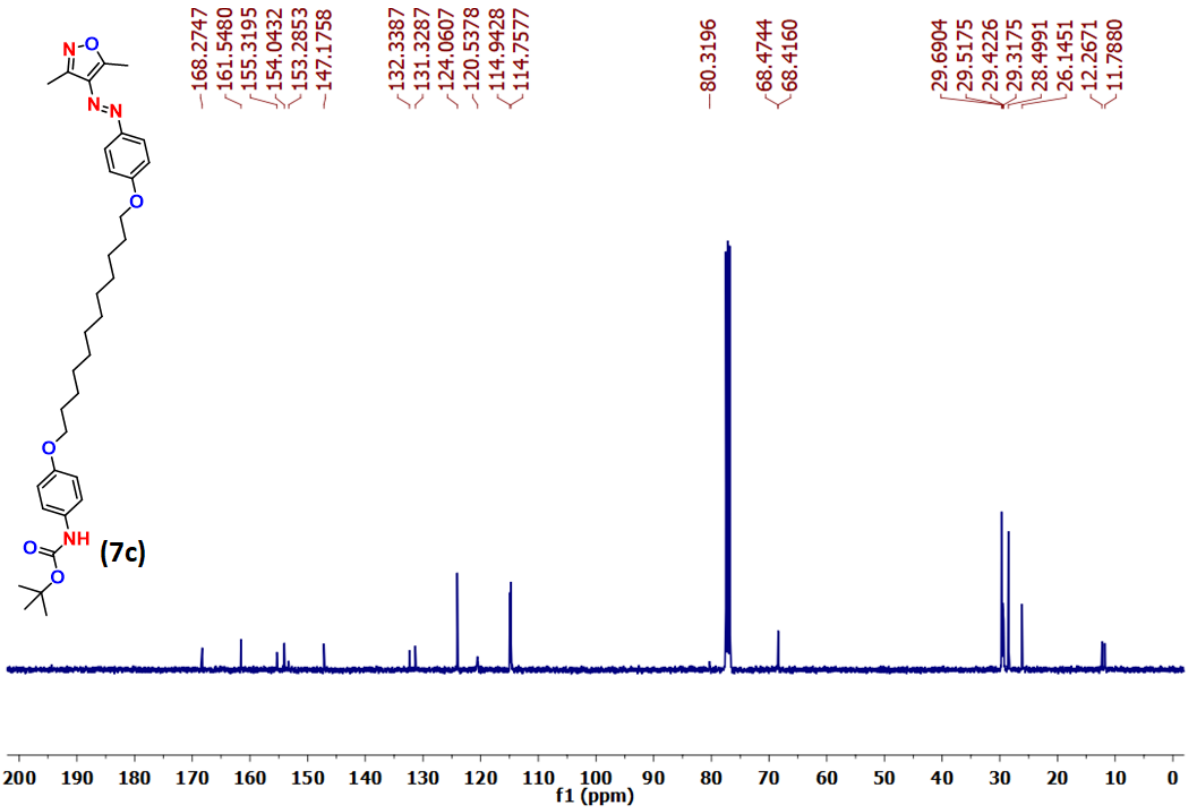

^{13}C NMR spectrum of tert-butyl (*E*)-(4-((12-(4-((3,5-dimethylisoxazol-4-yl)diazenyl)phenoxy)dodecyl)oxy)phenyl)carbamate **(7c)** in $CDCl_3$

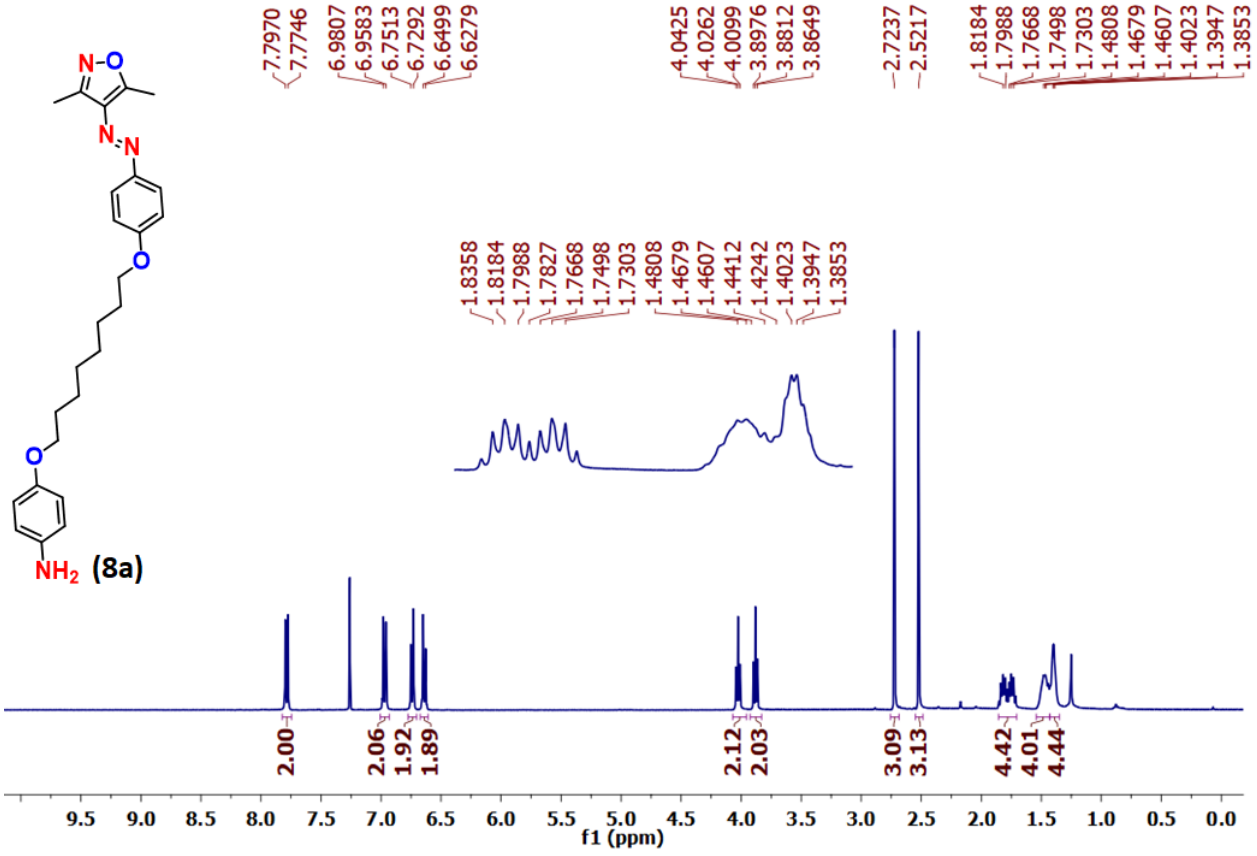

^{1}H NMR spectrum of (*E*)-4-((8-(4-((3,5-dimethylisoxazol-4-yl)diazenyl)phenoxy)octyl)oxy)aniline **(8a)** in $CDCl_3$

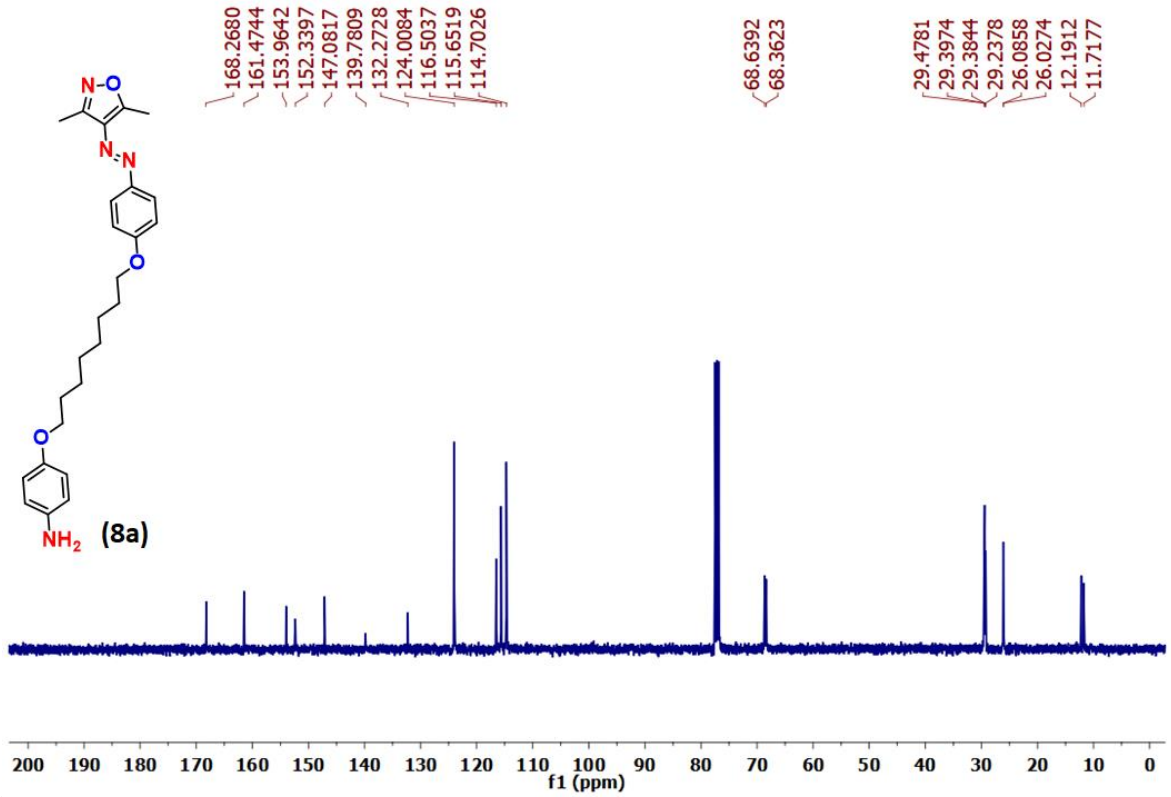

^{13}C NMR spectrum of (*E*)-4-((8-(4-((3,5-dimethylisoxazol-4-yl)diazenyl)phenoxy)octyl)oxy)aniline **(8a)** in $CDCl_3$

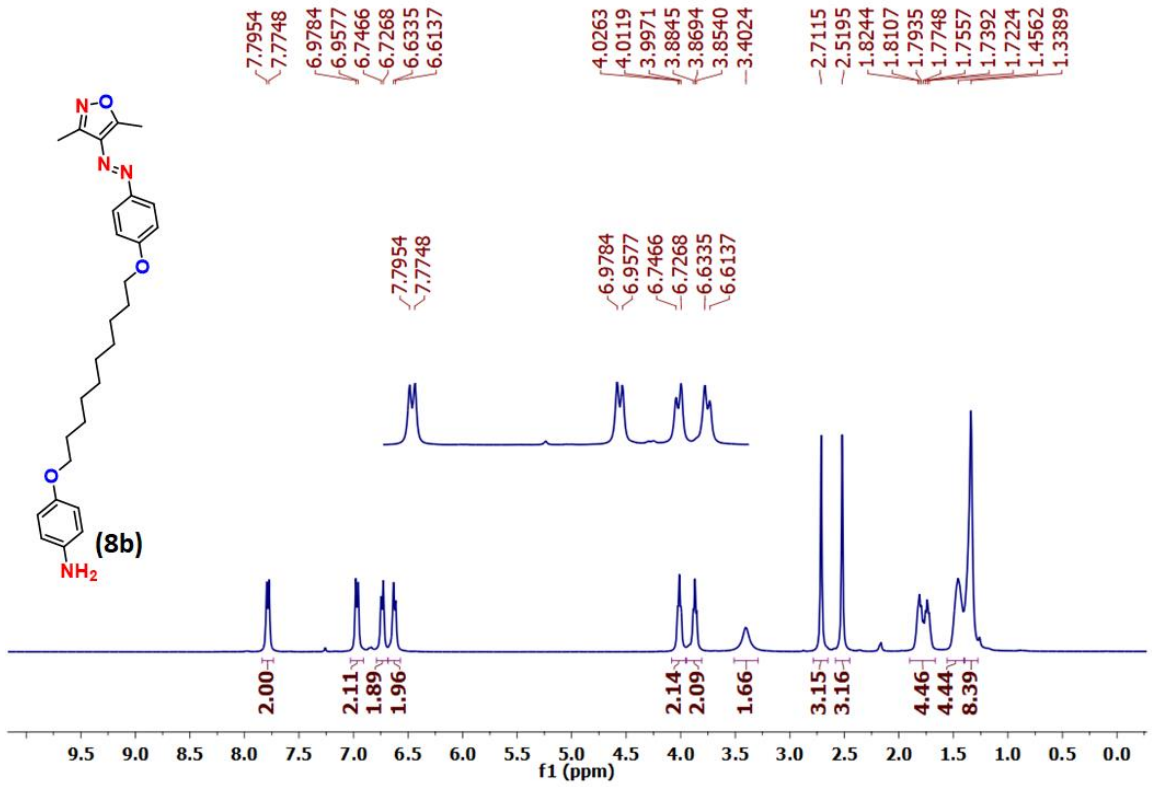

^{1}H NMR spectrum of (*E*)-4-((10-(4-((3,5-dimethylisoxazol-4-yl)diazenyl)phenoxy)decyl)oxy)aniline **(8b)** in $CDCl_3$

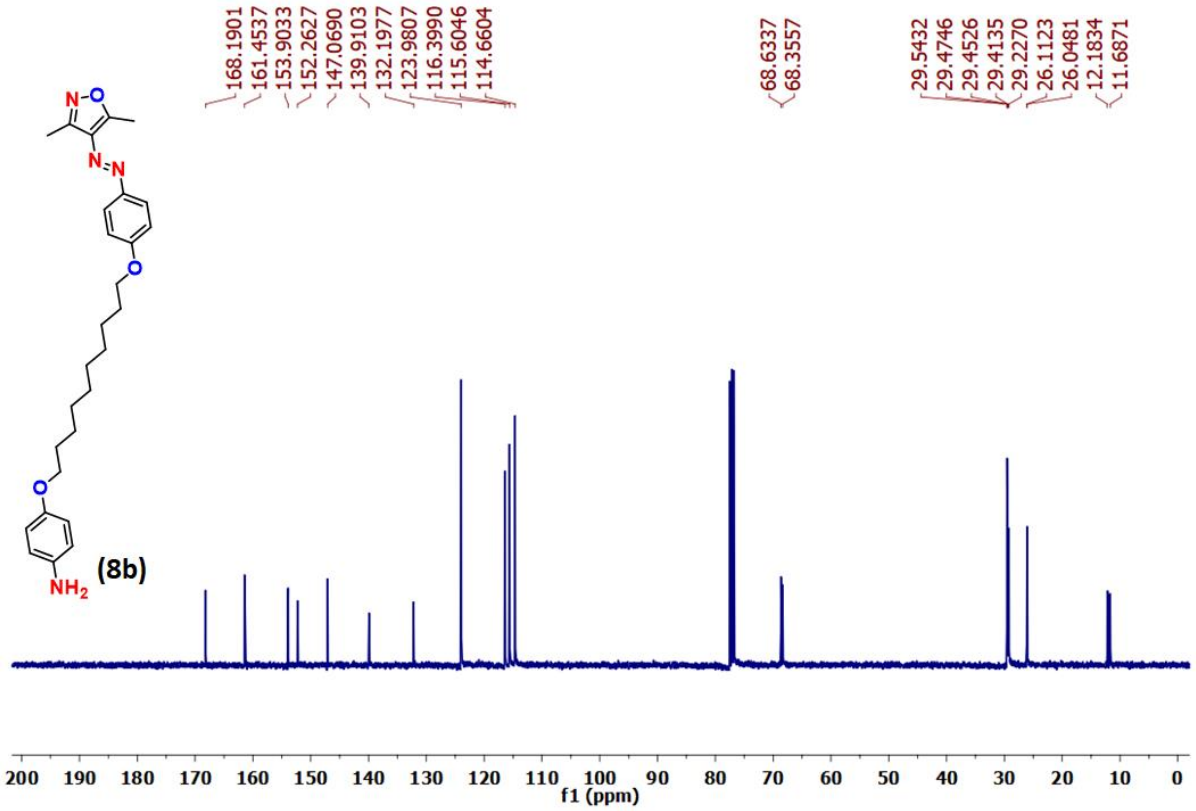

^{13}C NMR spectrum of (*E*)-4-((10-(4-((3,5-dimethylisoxazol-4-yl)diazenyl)phenoxy)decyl)oxy)aniline **(8b)** in $CDCl_3$

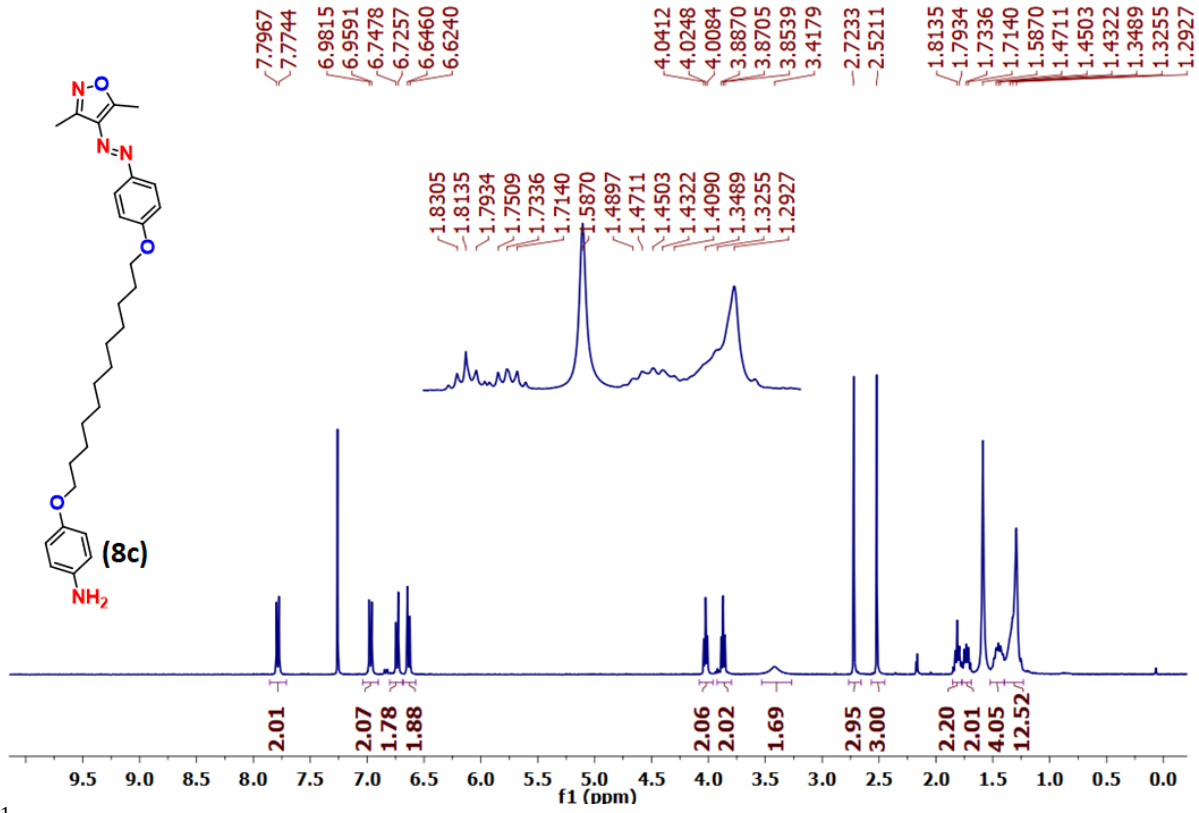

^{1}H NMR spectrum of (*E*)-4-((12-(4-((3,5-dimethylisoxazol-4-yl)diazenyl)phenoxy)dodecyl)oxy)aniline **(8c)** in $CDCl_3$

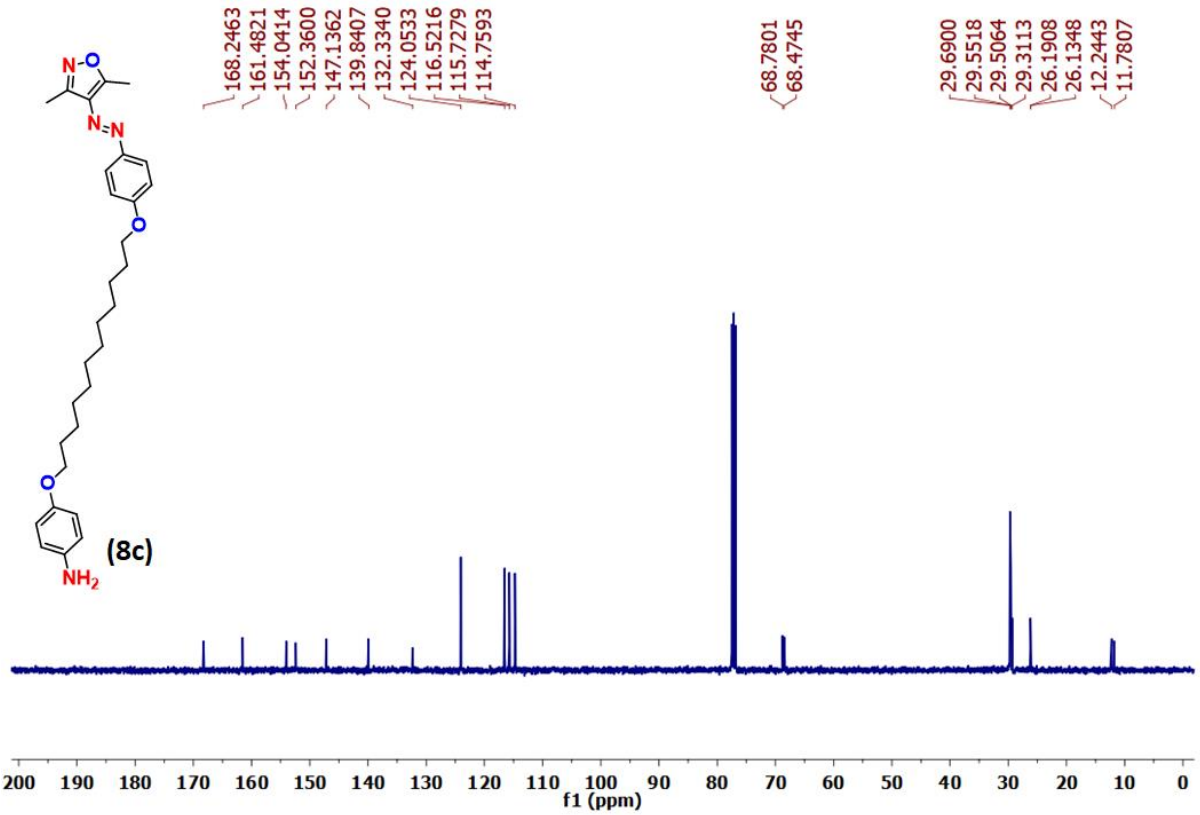

^{13}C NMR spectrum of (*E*)-4-((12-(4-((3,5-dimethylisoxazol-4-yl)diazenyl)phenoxy)dodecyl)oxy)aniline **(8c)** in $CDCl_3$

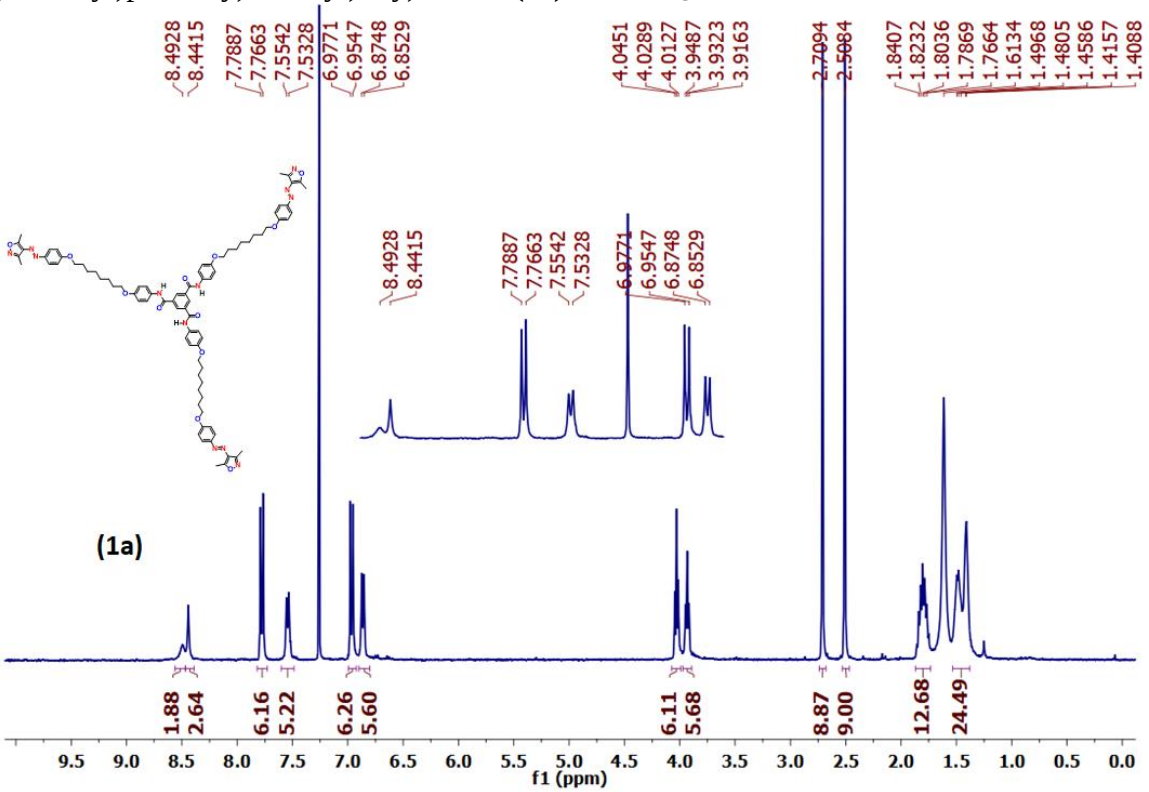

^{1}H NMR spectrum of N^{1},N^{3},N^{5}-tris(4-((8-(4-((*E*)-(3,5-dimethylisoxazol-4-yl)diazenyl)phenoxy)octyl)oxy)phenyl)benzene-1,3,5-tricarboxamide **(1a)** in $CDCl_3$

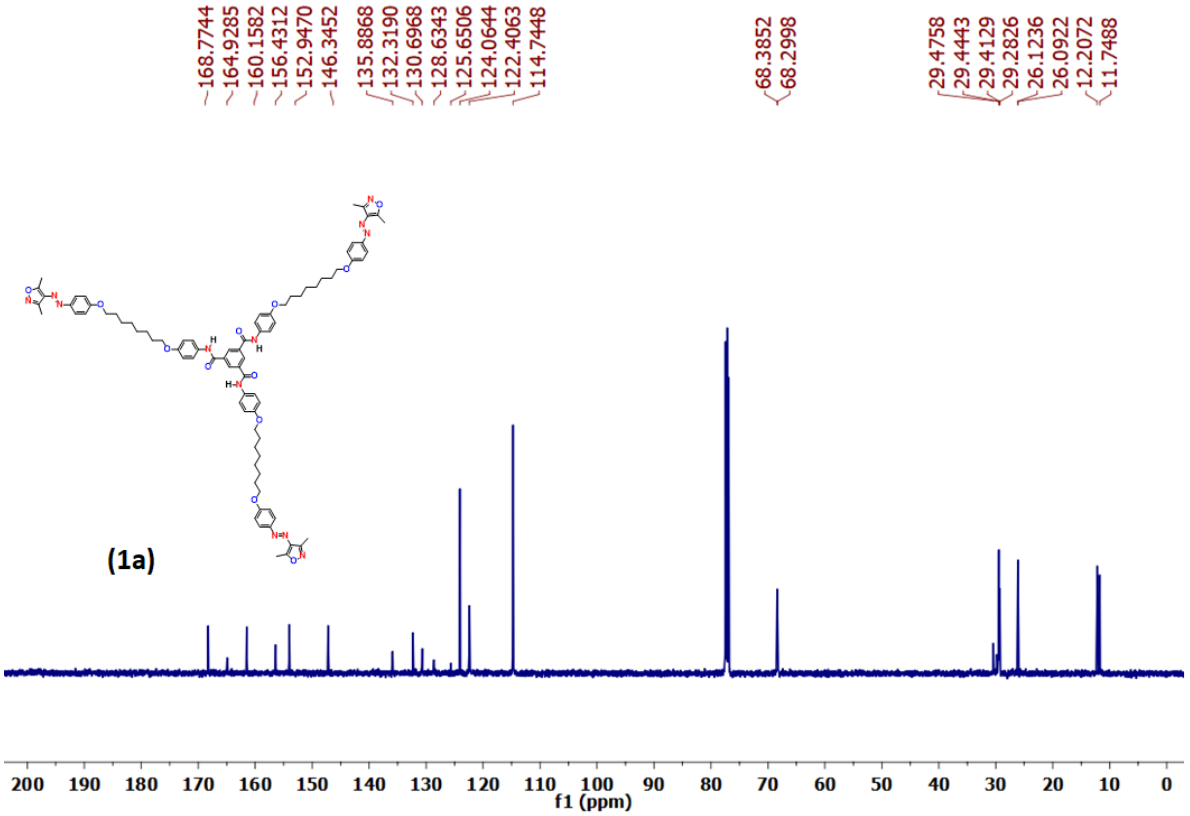

^{13}C NMR spectrum of N^1,N^3,N^5-tris(4-((8-(4-((*E*)-(3,5-dimethylisoxazol-4-yl)diazenyl)phenoxy)octyl)oxy)phenyl)benzene-1,3,5-tricarboxamide **(1a)** in $CDCl_3$

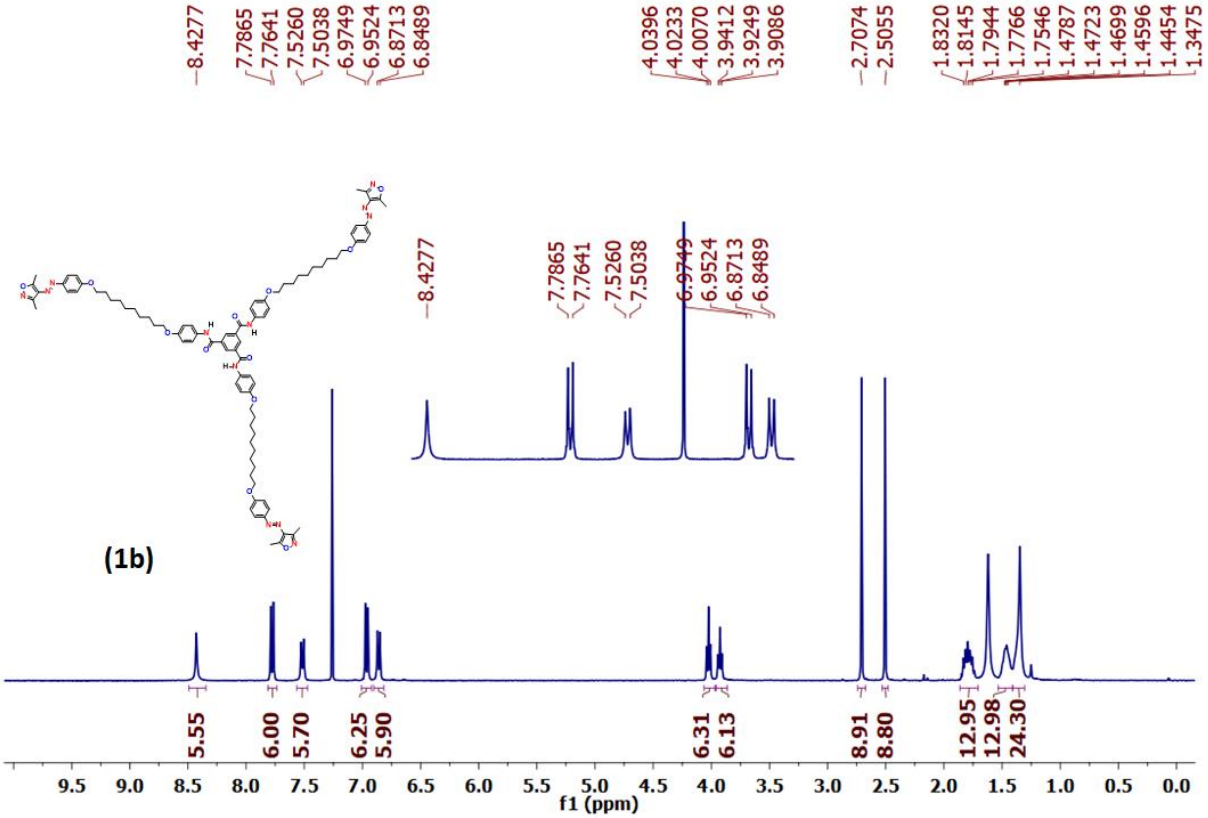

^{1}H NMR spectrum of N^1,N^3,N^5-tris(4-((10-(4-((*E*)-(3,5-dimethylisoxazol-4-yl)diazenyl)phenoxy)decyl)oxy)phenyl)benzene-1,3,5-tricarboxamide **(1b)** in $CDCl_3$

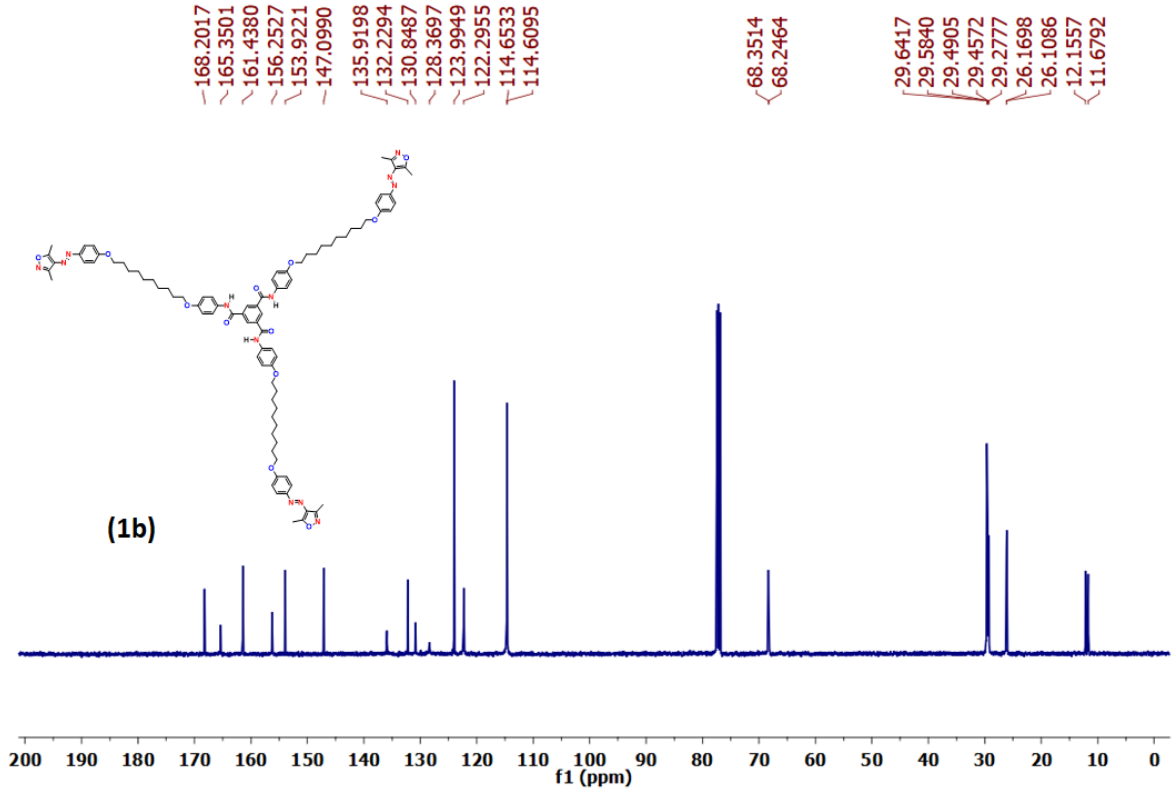

^{13}C NMR spectrum of N^1,N^3,N^5-tris(4-((10-(4-((*E*)-(3,5-dimethylisoxazol-4-yl)diazenyl)phenoxy)decyl)oxy)phenyl)benzene-1,3,5-tricarboxamide **(1b)** in $CDCl_3$

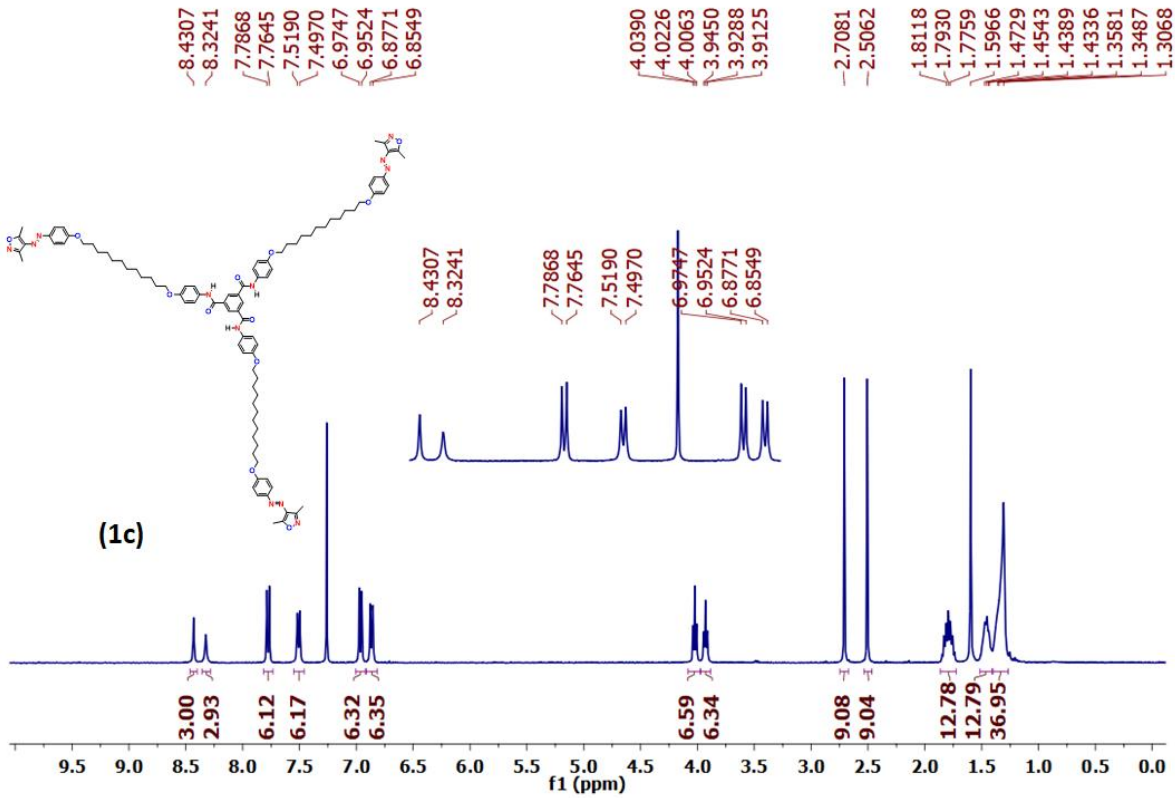

^{1}H NMR spectrum of N^1, N^3, N^5-tris(4-((12-(4-((*E*)-(3,5-dimethylisoxazol-4-yl)diazenyl)phenoxy)dodecyl)oxy)phenyl)benzene-1,3,5-tricarboxamide **(1c)** in $CDCl_3$

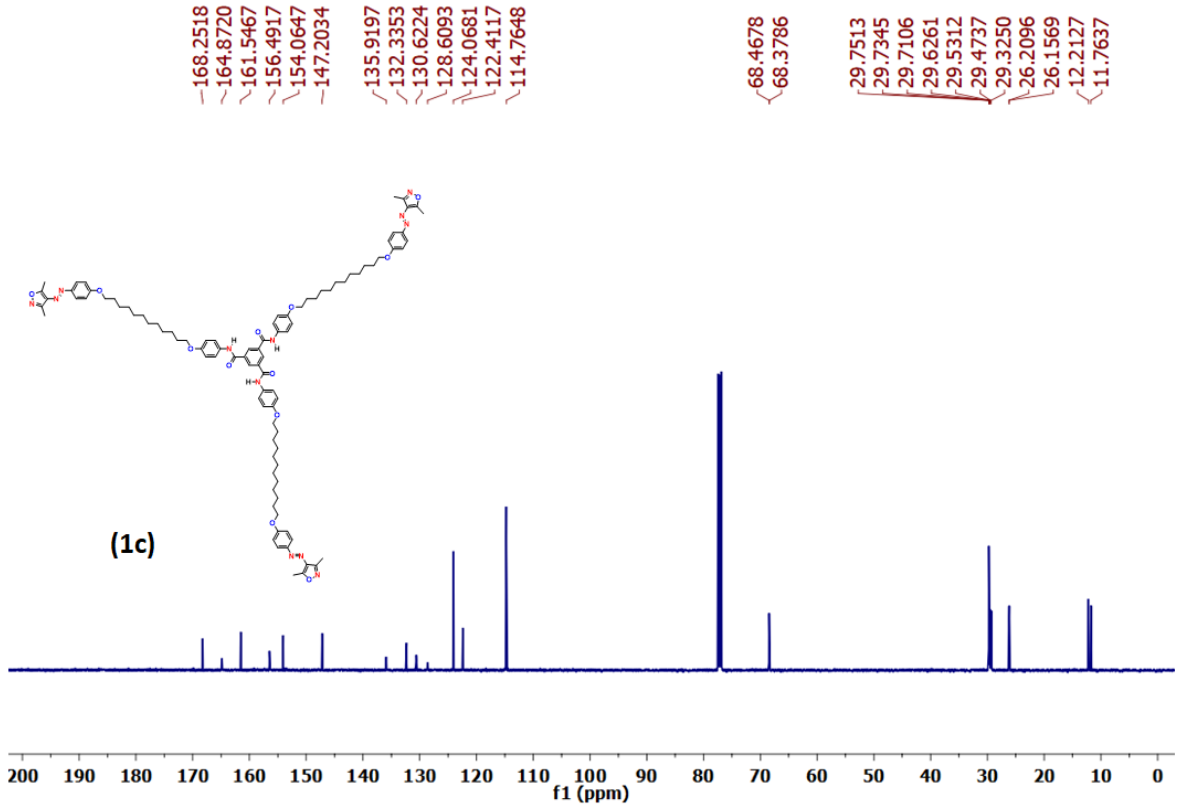

^{13}C NMR spectrum of N^1, N^3, N^5-tris(4-((12-(4-((E)-(3,5-dimethylisoxazol-4-yl)diazenyl)phenoxy)dodecyl)oxy)phenyl)benzene-1,3,5-tricarboxamide **(1c)** in $CDCl_3$

Chapter 5. Conclusions and Perspectives

5.1 Introduction

Photoswitches – species exhibiting bistability – undergo structural or geometrical changes in response to light of appropriate wavelengths.[1] Due to the difference in properties, they can be useful in diverse applications. Azobenzenes are one of the primitive photoswitches that have widespread applications due to their robustness, stability, ease of synthesis, and high photostability. In general, they reversibly switch between *trans* and *cis* isomeric states by light.[2] The changes in the molecular shapes and geometry of the two isomers, lead to variation in the physical properties such as dipole moment, melting points, refractive index, redox potential, etc.[2] Interestingly, the *cis* isomer relaxes slowly back to the native *trans* isomeric state at room temperature even under dark which limits the usefulness of the azobenzenes. High thermal stability of *cis* isomer is needed for certain applications such as data storage. Equally, completeness of photoswitching or quantitative isomerization is another important factor for enhancing their application potential. Despite their high popularity, azobenzene suffers from incomplete photoswitching and low thermal stability of *cis* isomer. On the other hand, continuous efforts have been made, and strategies such as *ortho*-fluorination were adopted to improve the photoswitching efficiency and tuning the thermal stability of *cis* isomers.[3] An alternative approach is the introduction of heterocycles, in particular with five-membered ring systems in the design that has been popularly utilized in recent times. The resulting azoheterocycles with different heterocycles have been synthesized using simple, economical, and high-yielding synthetic methods, which offered an improved photoswitching property and tunable *cis* isomer stability and several application prospects.[4] In this regard, we have attempted to utilize a new class of azoheteroarene, namely arylazo-3,5-dimethylisoxazole. Through this thesis contribution, we report the fundamental, supramolecular, and LCs-based aspects using the simple and their benzene-1,3,5-tricarboxamide (BTA) core-based derivatives of arylazo-3,5-dimethylisoxazole photoswitches.

5.2 Arylazo-3,5-dimethylisoxazole photoswitches

In the first chapter, the fundamental aspects of arylazo-3,5-dimethylisoxazole photoswitches have been discussed. Using a simple synthetic strategy, a library of 37 mono and disubstituted arylazo-3,5-dimethylisoxazole derivatives have been generated in good to excellent yields. Photoswitching studies of all the derivatives were carried out in solution phase and solid-state and followed by various spectroscopic techniques. Overall good to

excellent and reversible photoswitching in solution as well as in solid state with contrasting color changes were observed. Also, the *cis* (*Z*) isomeric state of these derivatives showed high thermal stability which makes this class of photoswitches highly interesting. UV-vis and NMR spectroscopic data revealed **1d** (no substitution, in $CDCl_3$, $\%Z_{PSS\text{-}E\text{-}Z}$ = 59, $\%E_{PSS\text{-}Z\text{-}E}$ = 76, in [D_6]DMSO, $\%Z_{PSS\text{-}E\text{-}Z}$ = 84, $\%E_{PSS\text{-}Z\text{-}E}$ = 77),, **4d** (4-F, in [D_6]DMSO, $\%Z_{PSS\text{-}E\text{-}Z}$ = 80, $\%E_{PSS\text{-}Z\text{-}E}$ = 82),), **9d** (3-Br, in [D_6]DMSO, $\%Z_{PSS\text{-}E\text{-}Z}$ = 89, $\%E_{PSS\text{-}Z\text{-}E}$ = 76) and **19d** (4-OMe, in [D_6]DMSO, $\%Z_{PSS\text{-}E\text{-}Z}$ = 98, $\%E_{PSS\text{-}Z\text{-}E}$ = 92) as the best photoswitches among all the 37 derivatives, whereas a high thermal stability of *cis* (*Z*) isomer up to 45 days in case of **1d** isomer at room temperature was estimated. Interestingly, a majority of this class of photoswitches exhibited a partial light-induced phase transition from solid to liquid, whereas compound **1d** underwent complete photo melting with contrasting color changes. This interesting phenomenon makes these photoswitches suitable for patterned crystallization, which has been demonstrated by molding the molten liquid into the text 'IISER'. Another salient feature is the substitutions such as *ortho* hydroxy group can also allow the derivative

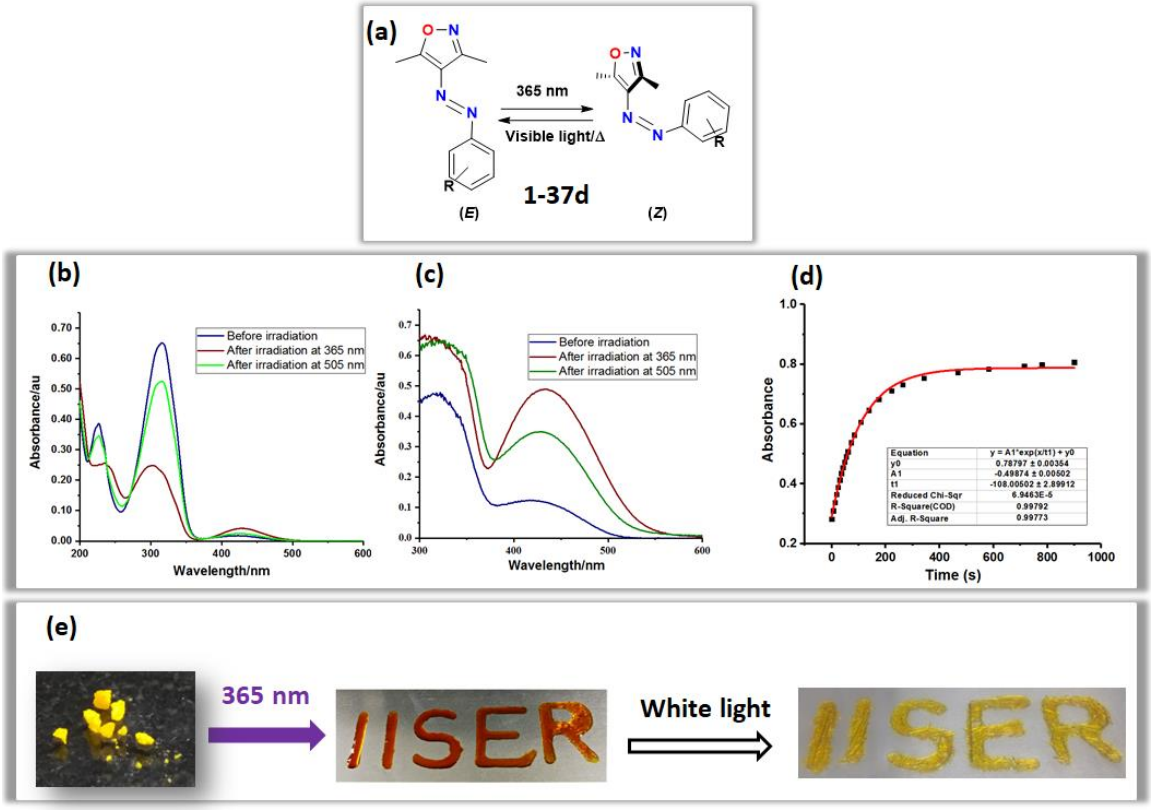

Figure 5.1. (a) Arylazo-3,5-dimethylisoxazole photoswitches, (b) photoswitching in solution phase, (c) photoswitching in solid-state, (d) thermal reverse isomerization kinetics plot, (e) light-induced phase transition and demonstration of patterned crystallization.

to undergo photoisomerization instead of tautomerization, which usually inhibits the photoisomerization in the case of azobenzene analogs. All these interesting properties make them useful photoswitches for many applications.

5.3 C_3-Symmetric multiple arylazo-3,5-dimethylisoxazole incorporated benzene-1,3,5-tricarboxamides

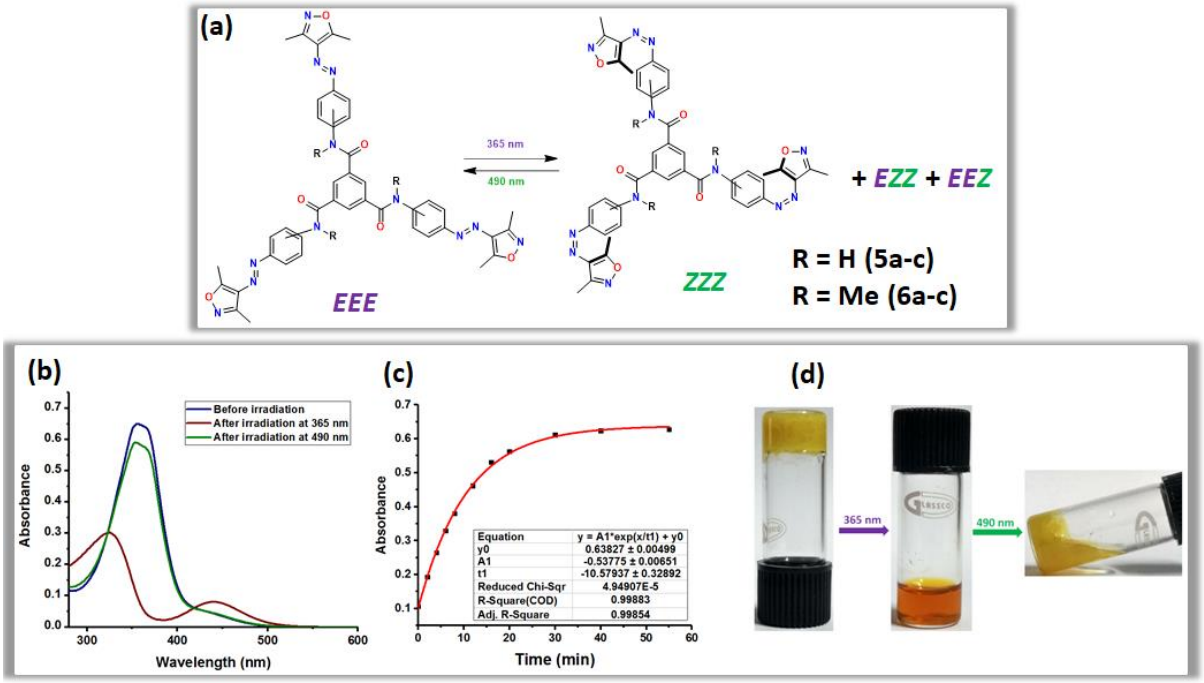

Figure 5.2. (a) Photoswitching in tripodal C_3-symmetric arylazoisoxazole based BTA derivatives, (b) photoswitching, (c) thermal reverse isomerization kinetics of photoisomerized state, (d) reversible gel to the sol phase transition.

Having seen a variety of interesting properties of arylazoisoxazole photoswitches, we were motivated to functionalize them further into C_3-symmetric tricarboxamides derivatives and to understand the design-property relationship. The amino derivatives of phenylazoisoxazole were not the best photoswitches. This is mainly attributed to the possible tautomerism that usually enables fast thermal reverse isomerization step. However, upon functionalizing them into amide derivatives in a C_3-symmetric tripodal architecture, the photoswitching efficiency is expected to improve. In this regard, three isomeric aminophenylazo-3,5-dimethylisoxazole derivatives (**1a-c**) and their *N*-methylated analogs (**2a-c**) were systematically functionalized into tripodal derivatives, **5a-c**, and **6a-c**, respectively. The derivatives **5a-c** showed poor solubility presumably due to hydrogen bonding and π–π stacking, however, the corresponding *N*-methylated derivatives exhibited more solubility. All six derivatives exhibited good to excellent and reversible photoswitching

and high thermal stability of the all-*cis*-isomeric state. The photoswitching efficiency was found to follow the order *para* > *meta* > *ortho*. Whereas the thermal stability of photoswitched states (*ZZZ*-isomers) followed a general trend *meta* > *ortho* > *para*. Another interesting property observed was light-induced reversible gel to sol phase transition in the molecules **5a-c**, which is not observed in the case of **6a-c**.

These results showed us the importance of H-bonding at the core part, which is absent in *N*-methylated **6a-c** in supramolecular assemblies. The resulting C_3-symmetric arylazoisoxazole functionalized designs and their supramolecular self-assembly property leave the possibility of many other important applications such as host-guest complexation, LCs, etc after some minor modifications.

5.4 Arylazoisoxazole based reversibly photoswitchable discotic liquid crystals

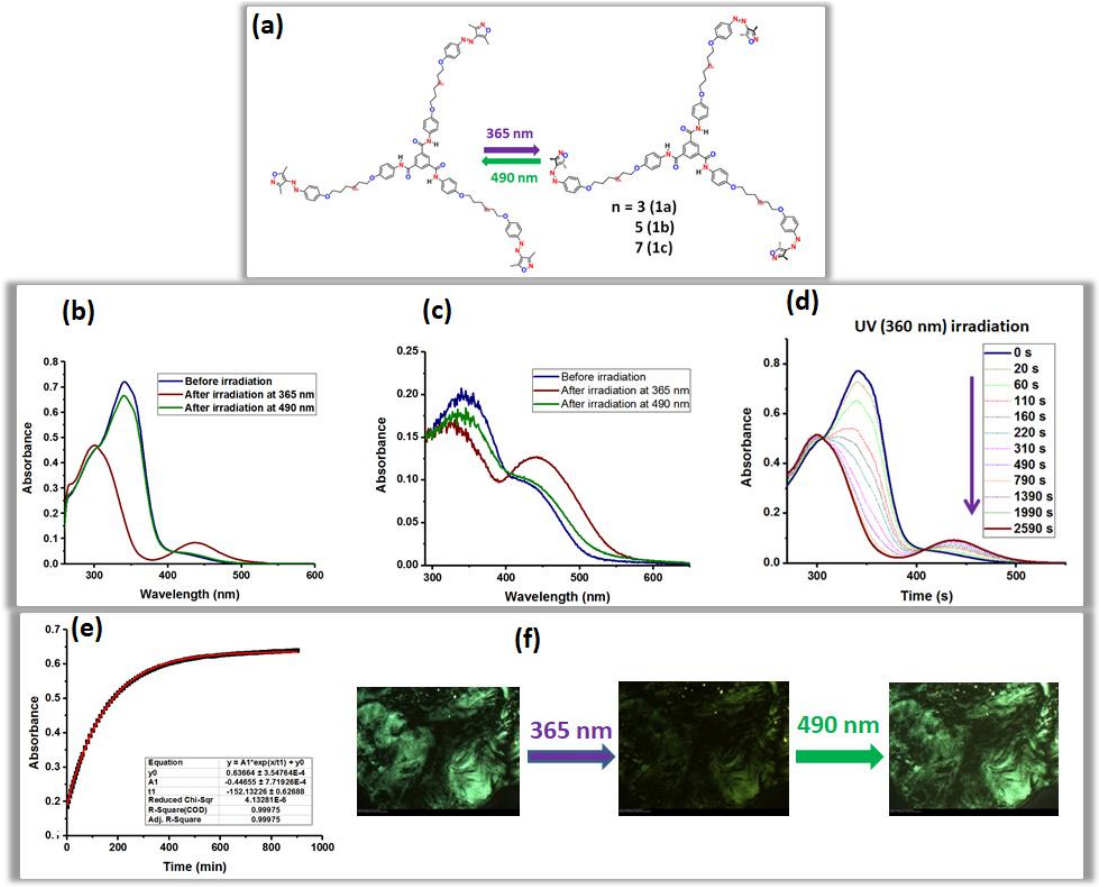

Figure 5.3. (a) Photoswitching in tripodal C_3-symmetric arylazoisoxazole based photoswitchable LCs, (b) photoswitching in solution state, (c) photoswitching in solid- state, (d) kinetics of *trans* to *cis* photoisomerization, (e) thermal reverse isomerization kinetics of photoisomerized state, (f) light-induced reversible LC phase modulation by POM (magnification: x100).

The third chapter deals with a similar C_3-symmetric tripodal scaffold with the BTA core decorated with the arylazo-3,5-dimethylisoxazole photoswitches at the peripheral positions. We intended to have a BTA core that can stack through hydrogen bonding and π-stacking, whereas the long alkoxy tether connecting the core and the photoswitches will provide flexibility in obtaining LC properties. Besides that, the photoswitches were connected purposefully to control the resulting mesophase by light. Three target molecules **1a-c**, which differ in the length of alkyl spacer (number of carbons = 8, 10, and 12) were synthesized in good yields and characterized by various spectroscopic techniques. All three molecules **1a-c** showed discotic LC property in lamellar assembly, confirmed from POM, DSC, and XRD studies. The analysis of photoswitching using UV-vis spectroscopy of target molecules **1a-c** showed excellent and reversible photoisomerization in solution, solid, and LC states. The kinetics studies of the all-*cis* to all-*trans* thermal isomerization step confirmed high thermal stability of photoswitched states, whereas kinetics of all-*trans* to all-*cis* photoisomerization at room temperature showed a faster rate. Surprisingly, photochromic units were found to behave independently (noninteracting nature), which was confirmed by NMR spectroscopic analysis of photoswitching, and thermal and photochemical reverse isomerization studies. Interestingly, when photoswitching was performed in the LC state and followed by POM, we observed changes in the intensity of birefringence (bright and dark), which was found to be reversible. These results were further supported by AFM studies where height profiles were found to be changed after irradiation with UV light. Thus, we have successfully designed and developed molecular systems with azoheteroarene-based LCs that can be reversibly tuned by light.

5.5 Perspectives

In perspective, we have developed a new class of photoswitchable arylazoisoxazoles with exciting properties and high application potential. Good to excellent and reversible photoswitching efficiency in solution (particularly in DMSO) and interestingly in solid-state as well as light-induced phase transition make these photoswitches highly suitable for various applications. Indeed, the properties such as light-induced phase transition already made ways for photomodulated adhesive materials, energy storage materials, etc.[5] Also, photoswitching in solid-state makes them useful for the fabrication of devices. Furthermore, the high *cis*-isomeric thermal stability of these photoswitches can be exploited for long-term optical data storage. Based on the literature reports on some of the azoheteroarenes, their thermal stability

further can be improved by replacing both the methyl groups of isoxazole units with hydrogen.

Since arylazoisoxazoles showed excellent photoswitching and related characteristics, their multistate C_3-symmetric derivatives also emerged as excellent photoswitchable molecular materials for solution phase (DMSO) and solid-state applications. Despite a moderate light control, such molecules showed photoswitching in a bulk phase that leads to modulating supramolecular properties such as sol-gel phase transition and mesophase changes by light. To achieve full control over these properties, further design modification is necessary.

So far we have studied their C_3-symmetric derivatives; these photoswitches further leave the possibility of functionalization into various designs. The properties of arylazoisoxazole photoswitches can further be tuned for a particular application of interest. Since these molecules absorb in the UV region, their absorption wavelength can further be tuned towards the visible region by proper substitutions. These photoswitches are still in the beginning stage of their use in various applications.

5.6 References

[1] a) H. Bouas-Laurent, H. Dürr, *Pure Appl. Chem.* **2001**, *73*, 639–665; b) M. Irie, *Chem. Rev.* **2000**, *100*, 1683–1684.

[2] H. M. D. Bandara, S. C. Burdette, *Chem. Soc. Rev.* **2012**, *41*, 1809–1825; b) G. S. Hartley, R. J. W. Le Fèvre, *J. Chem. Soc.* **1939**, 531–535.

[3] D. Bléger, J. Schwarz, A. M. Brouwer, S. Hecht, *J. Am. Chem. Soc.* **2012**, *134*, 20597–20600.

[4] a) C. E. Weston, R. D. Richardson, P. R. Haycock, A. J. P. White, M. J. Fuchter, *J. Am. Chem. Soc.* **2014**, *136*, 11878−11881; b) J. Calbo, C. E. Weston, A. J. P. White, H. S. Rzepa, J. Contreras-García, M. J. Fuchter, *J. Am. Chem. Soc.* **2017**, *139*, 1261−1274; c) C. E. Weston, A. Kramer, F. Colin, O. Yildiz, M. G. J. Baud, F.-J. Meyer-Almes, M. J. Fuchter, *ACS Infect. Dis.* **2017**, *3*, 152−161; d) J. Broichhagen, J. A. Frank, N. R. Johnston, R. K. Mitchell, K. Šmid, P. Marchetti, M. Bugliani, G. A. Rutter, D. Trauner, D. J. Hodson, *Chem. Commun.* **2015**, *51*, 6018–6021.

[5] a) L. Kortekaas, J. Simke, D. W. Kurka, B. J. Ravoo, *ACS Appl. Mater. Interfaces* **2020**, *12*, 32054–32060; b) L. Kortekaas, J. Simke, N. B. Arndt, M. Böckmann, N. L. Doltsinis, B. J. Ravoo, *Chem. Sci.* **2021**, *12*, 11338−1346; c) Z.-Y. Zhang, Y. He, Z. Wang, J. Xu, M. Xie, P. Tao, D. Ji, K. Moth-Poulsen, T. Li, *J. Am. Chem. Soc.* **2020**, *142*, 12256−12264.

Chapter 6. Materials and methods

6.1 Synthesis

Solvent and reagents were purchased from commercially available sources such as Sigma Aldrich, TCI, Avra, Rankem, Promochem, CIL, etc., which were used without further purification. For anhydrous condition reactions dry solvents such as 1,2-dichloroethane (DCE), toluene, acetonitrile, THF, etc., were obtained from MBRAUN solvent purification system (MB-SPS) and further stored on molecular sieves. N_2 or Ar gases were used for anhydrous condition reactions. Hexane is distilled for column chromatography. UV-vis spectroscopic studies were performed using solvents of spectroscopic or HPLC grade.

Reaction progress was monitored by thin-layer chromatography (TLC) purchased from Merck Silica gel 60 F_{254} TLC plates and visualized in a UV chamber (λ = 254 nm). Compounds were purified on a silica gel (mesh size 100-200 Å or 60-120 Å) or neutral/basic alumina using n-hexane/ethyl acetate as an eluent.

6.2 Photoswitching and Characterisation

Nuclear Magnetic Resonance (NMR) spectroscopy: ^{1}H and ^{13}C NMR spectra of all the compounds were carried out on a Bruker Avance-III 400 MHz spectrometer at 400 MHz and 100 MHz, respectively, or a Bruker Avance Neo 500 MHz spectrometer (or 125 MHz for ^{13}C), which are indicated appropriately. The chemical shift (δ) values are reported in parts per million (ppm) and coupling constant (*J*) in hertz (Hz), respectively. The signal multiplicities were abbreviated as follows: s-singlet, d-doublet, t-triplet, q-quartet, p-pentet, sep-septet, dd-doublet of doublets, dt (doublet of triplets), br-broad, m-multiplet, etc. For calibration residual solvent signals were used as internal standard (^{1}H NMR: $CDCl_3$ = 7.26 ppm, [D_6]DMSO = 2.50 ppm; ^{13}C NMR: $CDCl_3$ = 77.16 ppm, [D_6]DMSO = 39.52 ppm).

High-resolution mass spectrometry (HRMS): HRMS was recorded on a Waters Synapt G2-Si Q-TOF mass spectrometer under the electrospray ionization (ESI) method in positive and negative modes.

FT-IR spectroscopy: Infrared spectra (IR) were recorded on a Bruker Alpha spectrometer in transmittance mode using a ZnSe Attenuated Total Reflectance (ATR) assembly or on a Perkin Elmer Spectrum FT-IR spectrometer as a KBr pellet and reported in cm^{-1}.

Melting points (MPs): MPs were recorded on a Stuart SMP20 melting point apparatus which are uncorrected.

UV-vis spectroscopy, photoswitching, kinetics studies, and light sources used:

Analysis of photoswitching and kinetics studies of all the azo-compounds were carried out using a UV-vis spectrophotometer either a Cary 5000 UV-Vis-NIR or a Cary 60 spectrophotometer of Agilent technology equipped with a Peltier cell assembly as a temperature controller. In most of the cases, for *trans* (*E*) to *cis* (*Z*) photoisomerization light of 365 nm wavelength, whereas for reverse *cis* (*Z*) to *trans* (*E*) photoisomerization, light of CFL bulb of 35 W, 470 nm, 490 nm, and 505 nm wavelengths have been used. The torch of 365 nm (Convoy S2+) was purchased from commercial sources, whereas visible range wavelengths such as 470 nm, 490nm, 505 nm, etc were used from the LED light source (Applied Photophysics, SX/LED with a bandwidth of 20 nm). For photoswitching studies irradiation was performed either in a quartz cuvette of 1 cm path length or quartz NMR tubes from Sigma Aldrich until photostationary states (PSSs) was reached.

Polarised optical microscopy (POM): POM studies were performed on a Nikon Eclipse LV100POL polarising microscope provided with a Linkam heating stage (LTS 420). All images were captured using a Q-imaging camera.

Differential scanning calorimetric (DSC) studies: DSC studies were performed using a Perkin Elmer DSC 8000 coupled to a controlled liquid nitrogen accessory (CLN 2) with a heating and cooling scan rate of 10 °C min^{-1}.

X-ray diffraction small/wide angle (XRD) studies: XRD studies were carried out using Cu Kα (λ=1.54 Å) radiation from a source (GeniX 3D, Xenocs) operating at 50 kV and 0.6 mA. The diffraction patterns were collected on a two-module Pilatus detector. Single crystal X-ray diffraction data were collected using a Rigaku XtaLAB mini diffractometer equipped with a Mercury375 M CCD detector.

Atomic force microscopy (AFM): AFM studies were performed on Innova atomic force microscopy using NanoDrive (v8.03) software. The AFM images were processed and analyzed using WSxM software. The height profiles were plotted using Origin 8.

Thermogravimetric analysis data (TGA): TGA experiments were scanned in the temperature range 25 to 500 ^{o}C (range of heating: 10 ^{o}C min^{-1}) under a nitrogen atmosphere on a Shimadzu DTG-60H instrument.

6.3 Photoswitching and phase transition studies using polarized optical microscopy (POM)

The light-induced phase transition from solid to liquid was performed using POM. A small amount of compound **1d** was taken on a glass slide, which showed birefringence under an optical microscope before irradiation. The sample was irradiated at 365 nm light and the process of solid to amorphous liquid phase transition was visualized under a polarized microscope by the disappearance of birefringence into a dark isotropic liquid. This process was captured in the form of images or video.

The reversible gel-sol phase transition process was followed by a polarized optical microscope (POM) in compound **5a-c**. The image of gel was recorded before irradiation by taking a small amount of gel from the vial which showed birefringence. Then, 365 nm light was irradiated and gel to sol phase transition was followed by the disappearance of birefringence into dark amorphous liquid. The reverse process of sol to gel was followed under the irradiation of 490 nm light with the reappearance of birefringence. The whole process was captured under a polarized microscope.

Similarly, light-induced liquid crystalline phase modulation was also followed by POM where we put a small amount of compound **1c** on the top of a glass slide, which is heated up to isotropic temperature and then slowly cooled up to room temperature. During cooling mesophase was obtained where we observed isogyre type of textures on shearing and image was captured. These textures were irradiated at 365 nm light continuously and changes were recorded in the form of images or video. For reverse photoisomerization, the sample was irradiated at 490 nm light and the textures appearance was visualized and captured.

6.4 Photoswitching: UV-vis spectroscopic studies

For solution-state photoswitching studies, first of all, the absorbance of native *trans* isomer was recorded in a quartz cuvette of 1 cm path length under dark. Then irradiation was performed under dark conditions at room temperature using UV or visible light and absorbance were recorded repeatedly until PSS (no further spectral change) was reached. Similarly for reverse photoisomerization, the cuvette was irradiated at an appropriate

wavelength of visible light using LEDs. The wavelength for the reverse photoisomerization step was optimized based on the spectral changes until PSS was attained.

Solid-state UV-vis studies were performed using a DRS assembly. The sample was mixed with KBr powder approx. 1 or 2:100 ratios and then made into fine powder. KBr powder was used as blank for baseline. Then the experiment was performed in absorbance mode. First of all, an un-irradiated sample was scanned in UV-vis range (800 nm to 400 nm) to get the absorbance of *trans*-isomer then the same sample was irradiated at 365 nm wavelength until PSS was reached to get the absorbance spectrum of *cis*-isomer. Similarly, reverse photoisomerization was performed for the same sample using visible light range wavelengths.

6.5 Photoswitching: ^{1}H NMR spectroscopic studies

Photoswitching studies were followed by ^{1}H NMR spectroscopy by performing the experiments using an NMR tube of quartz. Firstly, we recorded the ^{1}H NMR of the native sample (*trans* isomeric state) at mM concentrations. Wherever necessary, low concentrations of samples were preferred for such studies to reduce inner filtration effects. The *trans* to *cis* photoisomerization was followed by irradiating the sample with UV light externally in dark and the spectral recording was done immediately after introducing the NMR sample into the instrument. The irradiation steps were continued and recordings were performed at different intervals of time such that PSS was attained. Similarly, reverse photoisomerization was performed using wavelengths of the visible light region. The choice of wavelengths was optimized before the NMR experiments.

6.6 Kinetics studies: UV-vis spectroscopic studies

For kinetics studies of *cis* to *trans* thermal reverse isomerization at variable temperatures, the sample was irradiated until it reaches the PSS. The externally irradiated sample was then introduced inside the spectrophotometer carefully without being exposed to ambient light. The attainment of PSS was confirmed by recording absorbance maxima at different intervals of time until it reached a constant value. Then the cuvette containing solution is immediately introduced into the instrument and using kinetics mode, the recordings were started. In a manual recording of kinetics, a cuvette used to be introduced into the UV-Vis spectrophotometer, and at regular intervals of time, the changes in the absorbances were recorded. For higher temperature kinetics two different methods were adopted: (a) a thermostat with a water bath was used for heating the sample; before recording, the cuvette

was cooled up to room temperature using ice cold water; (b) a Peltier temperature controller connected to the UV-Vis spectrophotometer was used for pre-set and accurate temperatures and for following variable temperature kinetics. Similarly, the kinetics of the *trans*-to-*cis* photoisomerization step was also performed by using a selected light source.

6.7 Kinetics studies: ^{1}H NMR spectroscopic studies

Similarly, the thermal reverse isomerization kinetics was performed using ^{1}H NMR spectroscopy. The sample was irradiated in a quartz NMR sample tube using 365 nm UV light, and the sample was introduced immediately into the NMR instrument, and the spectra were recorded. PSS was confirmed by repeating the irradiation sequences until no further changes in spectral data. The kinetics mode of recording was done by keeping the sample tube in a thermostat for different intervals of time. The normalized integral values corresponding to the *cis* and *trans* isomers were used for the kinetics plot.

6.8 Differential scanning calorimetric (DSC) studies

DSC studies of *cis* and *trans* isomers were recorded to obtain the phase transition temperatures. Firstly, a DSC scan of *trans* isomer was performed in its native solid state without irradiation; then an irradiated sample of similar weight (in a different pan) was irradiated with UV light for a sufficiently long time and it was scanned in a DSC instrument at a scan rate of 10 ^{o}C/min.

6.9 Infrared spectroscopic (IR) studies of phase transition

We recorded the IR spectra of native solid (*trans*-isomer) using ATR mode; then the sample was irradiated on top of the ZnSe crystal at 365 nm wavelength of light until it completely photo melts, which was followed by IR spectroscopy.

6.10 Estimation of PSS composition and error analysis

(a) UV-vis spectroscopic studies

The estimation of the percentage of PSS composition of *cis* and *trans* isomers in the solution state was performed using UV-vis spectroscopy. The following equation was used in this regard.[1]

$$\%cis = \frac{A_{trans} - A_{cis}}{A_{trans}} \times 100 \quad \text{.......} \quad (1)$$

or $\%cis = \left(1 - \frac{A_{cis}}{A_{trans}}\right) \times 100$

Where A_{trans} is the absorbance corresponding to the *trans*-isomer at λ_{max}, A_{cis} is the absorbance corresponding to the *cis*-isomer at the same wavelength of absorption estimated at PSS.

For the estimation of PSS composition in the solid state, the following expression was used. Using the same expression PSS composition of reverse photoisomerization was also estimated.

$$\%\text{conversion of } EEE\text{-isomer} = \left(1 - \frac{A_{n-\pi^*} \text{ absorption before irradiation}}{A_{n-\pi^*} \text{absorption after irradiation}}\right) \times 100$$

Where $A_{n\text{-}\pi^*}$ is the absorption of *trans* and *cis*-isomer at λ_{max} (n to π^*) of *trans*-isomer. The error in PSS estimation using UV-vis spectroscopy was found up to 5%.[1b]

(b) ^{1}H-NMR spectroscopic studies

A milli molar concentration solution was prepared in a quartz NMR tube and was subjected to the recording of the ^{1}H NMR spectrum before irradiation. Then the NMR sample tube was irradiated at 365 nm and a spectrum was recorded immediately. Irradiation and spectral recording steps were repeated until a PSS was attained. Then the direct integration of the peaks of *trans* and *cis*-isomers was followed by the normalization of selected non-overlapping signals corresponding to those isomers that give the PSS composition of both isomers. Similar studies were done for reverse photoisomerization and kinetics studies as well.

In our analysis of NMR experimental data using integral values, we did not account for error. However, to minimize the error, we considered the following:

1. We have chosen one type of signal during the forward and reverse isomerization steps.
2. We have also attempted to use those signals whose overlap is minimal so that a clear integration can be made and normalized to obtain the %conversions.
3. The samples were continuously irradiated such that a photostationary state (PSS) is reached, which was followed by ^{1}H-NMR. This way, we ensured that no further isomerization is possible. Also, the experiments were repeated for reproducibility.

4. For a few cases, the signal-to-noise ratio cannot be improved any further owing to the poor solubility. Particularly, during the reverse photoisomerization step, the conversion into *EEE*-isomer is accompanied by precipitation. In the solution containing the native state (*EEE*-isomer), this situation can be overcome by heating to dissolve the sample; whereas it is not possible under photoirradiation (reverse photoisomerization) conditions.
5. Along the line, the normalized integration values have been estimated using the basic version of the software (TopSpin). Moreover, we did not perform the line-shape simulations or deconvolution procedures, which are critical for minimizing the error during quantification for close-lying signals.
6. Based on repeated measurements in certain cases (or during the attainment of PSS), we observed a marginal error of 2-3% in the normalized integral values.[1b]

6.11 Thermal reverse isomerization kinetics

Thermal reverse isomerization kinetics of *cis* to *trans* isomerization was followed by either using UV-vis or NMR spectroscopy. Since *cis*-isomer is thermodynamically less stable it spontaneously converts into the thermodynamically more stable *trans*-isomer at room temperature. Kinetics of *cis* to *trans* thermal reverse isomerization follow first-order exponential decay. Thermal stability of *cis*-isomer can be understood by the comparison of rate constant or half-life. For higher temperature kinetics studies DMSO as a solvent was chosen due to its aprotic nature and high boiling point. The following equations have been used for the first-order exponential decay of *cis*-isomer or growth of *trans*-isomer.

The rate constant has been calculated using the following first-order rate equation:

$$[A] = [A]_o e^{-kt} \quad \text{..... (1)}$$

Half-life was estimated from the rate constant using the following equation

$$t_{1/2} = \frac{0.693}{k} \quad \text{..... (2)}$$

The activation parameters for the *cis* to *trans* thermal reverse isomerization step were obtained using variable temperature kinetics plots. Rate constants obtained from these plots were utilized to plot Eyring and Arrhenius plots.

Eyring equation

$$k = \frac{k_B T}{h} e^{\left(\frac{-\Delta G^{\ddagger}}{RT}\right)} \quad \text{..... (3)}$$

$$k = \frac{k_B T}{h} e^{\left(\frac{\Delta S^{\ddagger}}{R}\right)} e^{\frac{-\Delta H^{\ddagger}}{RT}} \quad \text{..... (4)}$$

The linear form of the Eyring equation (**equation 5**) was used for the estimation of activation parameters, enthalpy of activation ($\Delta H^{\ddagger}$), and entropy of activation ($\Delta S^{\ddagger}$). The slope $-(\Delta H^{\ddagger}/R)$ of ln(k/T) vs 1/T plot gives the value of ($\Delta H^{\ddagger}$) whereas the intercept ($\ln(k_B/h) + \Delta S^{\ddagger}/R$) gives the value of ($\Delta S^{\ddagger}$).

The linear form of the equation

$$\ln\left(\frac{k}{T}\right) = -\left(\frac{\Delta H^{\ddagger}}{R}\right)\left(\frac{1}{T}\right) + \left(ln\left(\frac{k_B}{h}\right) + \frac{\Delta S^{\ddagger}}{R}\right) \text{.....(5)}$$

The linear form of the Arrhenius equation (**equation 8**) was used for the estimation of activation energy (Ea). The slope (–Ea/R) of ln (k) vs (1/T) plot gives the value of activation energy (Ea).

Arrhenius equation

$$k = A\, e^{\left(\frac{-E_a}{RT}\right)} \text{ ..... (6)}$$

$$lnk = lnA - \frac{E_a}{RT} \text{ ..... (7)}$$

$$lnk = -\frac{E_a}{R}\left(\frac{1}{T}\right) + lnA \text{ .... (8)}$$

The first-order exponential fitting of plots was used for estimation of error in rate constant and half-life using Origin software. The error estimation in activation parameters was performed according to the literature reports.[1b, 2]

6.12 References:

[1] K. Ghebreyessus, S. M. Cooper, *Organometallics* **2017**, *36*, 3360–3370; b) C. E. Weston, R. D. Richardson, P. R. Haycock, A. J. P. White, M. J. Fuchter, *J. Am. Chem. Soc.* **2014**, *136*, 11878–11881; c) S. Devi, A. K. Gaur, D. Gupta, M. Saraswat, S. Venkataramani, *ChemPhotoChem* **2018**, *2*, 806–810.

[2] G. Lente, I. Fábián, A. J. Poë, *New J. Chem.* **2005**, *29*, 759-760.

Copyright permissions for published work(s):

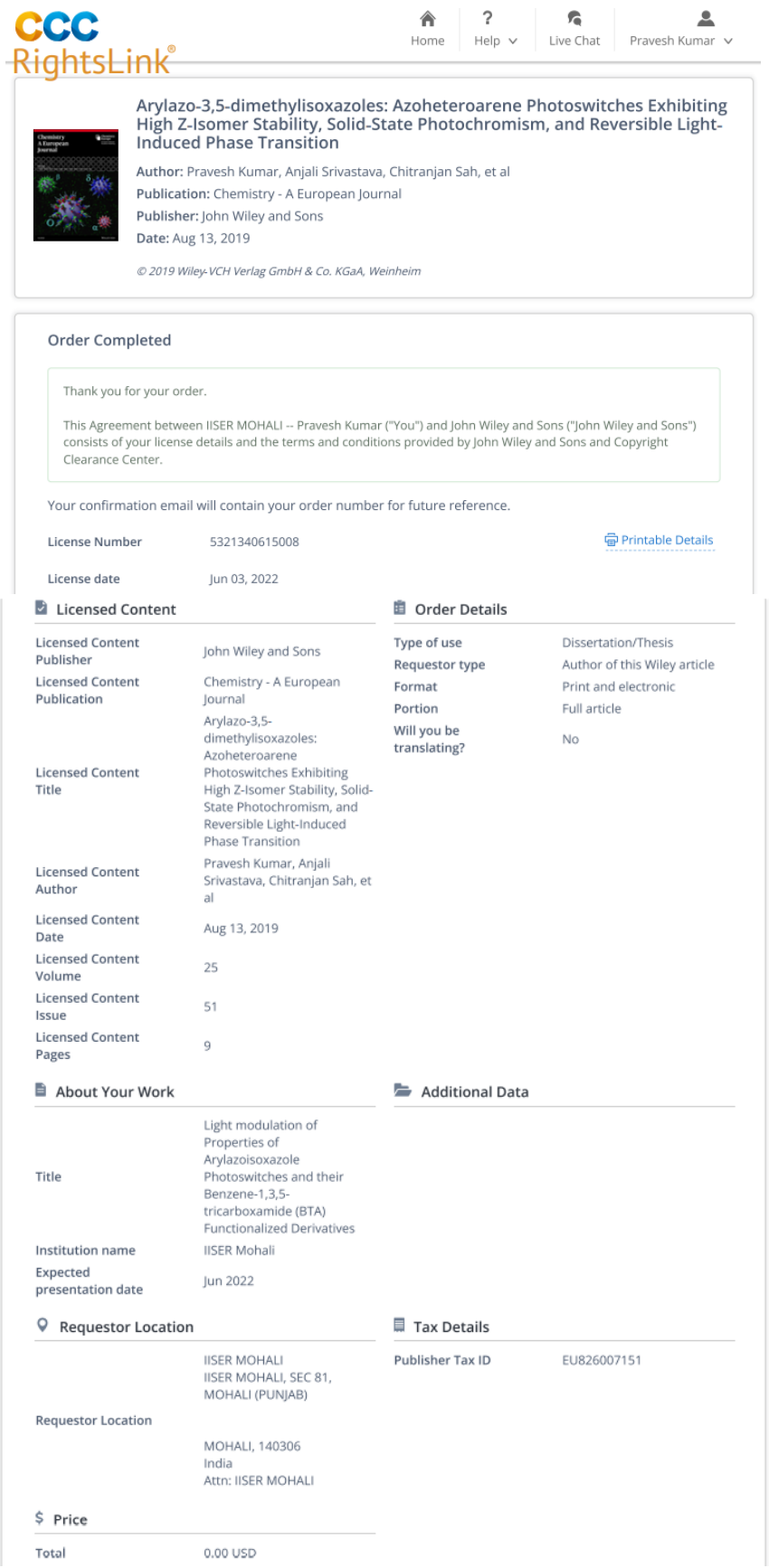

CCC RightsLink

Home | Help | Live Chat | Pravesh Kumar

Arylazo-3,5-dimethylisoxazoles: Azoheteroarene Photoswitches Exhibiting High Z-Isomer Stability, Solid-State Photochromism, and Reversible Light-Induced Phase Transition

Author: Pravesh Kumar, Anjali Srivastava, Chitranjan Sah, et al
Publication: Chemistry - A European Journal
Publisher: John Wiley and Sons
Date: Aug 13, 2019

© 2019 Wiley-VCH Verlag GmbH & Co. KGaA, Weinheim

Order Completed

Thank you for your order.

This Agreement between IISER MOHALI -- Pravesh Kumar ("You") and John Wiley and Sons ("John Wiley and Sons") consists of your license details and the terms and conditions provided by John Wiley and Sons and Copyright Clearance Center.

Your confirmation email will contain your order number for future reference.

Printable Details

License Number	5321340615008
License date	Jun 03, 2022

Licensed Content

Licensed Content Publisher	John Wiley and Sons
Licensed Content Publication	Chemistry - A European Journal
Licensed Content Title	Arylazo-3,5-dimethylisoxazoles: Azoheteroarene Photoswitches Exhibiting High Z-Isomer Stability, Solid-State Photochromism, and Reversible Light-Induced Phase Transition
Licensed Content Author	Pravesh Kumar, Anjali Srivastava, Chitranjan Sah, et al
Licensed Content Date	Aug 13, 2019
Licensed Content Volume	25
Licensed Content Issue	51
Licensed Content Pages	9

Order Details

Type of use	Dissertation/Thesis
Requestor type	Author of this Wiley article
Format	Print and electronic
Portion	Full article
Will you be translating?	No

About Your Work

Title	Light modulation of Properties of Arylazoisoxazole Photoswitches and their Benzene-1,3,5-tricarboxamide (BTA) Functionalized Derivatives
Institution name	IISER Mohali
Expected presentation date	Jun 2022

Additional Data

Requestor Location

Requestor Location	IISER MOHALI IISER MOHALI, SEC 81, MOHALI (PUNJAB) MOHALI, 140306 India Attn: IISER MOHALI

Tax Details

Publisher Tax ID	EU826007151

Price

Total	0.00 USD

Tuning of Bistability, Thermal Stability of the Metastable States, and Application Prospects in the C3-Symmetric Designs of Multiple Azo(hetero)arenes Systems

Author: Sudha Devi, Saonli Roy, Sugumar Venkataramani, et al
Publication: Chemistry - A European Journal
Publisher: John Wiley and Sons
Date: Jan 15, 2021

Order Completed

Thank you for your order.

This Agreement between IISER MOHALI -- Pravesh Kumar ("You") and John Wiley and Sons ("John Wiley and Sons") consists of your license details and the terms and conditions provided by John Wiley and Sons and Copyright Clearance Center.

Your confirmation email will contain your order number for future reference.

License Number	5321350218529
License date	Jun 03, 2022

Printable Details

Licensed Content

Licensed Content Publisher	John Wiley and Sons
Licensed Content Publication	Chemistry - A European Journal
Licensed Content Title	Tuning of Bistability, Thermal Stability of the Metastable States, and Application Prospects in the C3-Symmetric Designs of Multiple Azo(hetero)arenes Systems
Licensed Content Author	Sudha Devi, Saonli Roy, Sugumar Venkataramani, et al
Licensed Content Date	Jan 15, 2021
Licensed Content Volume	27
Licensed Content Issue	10
Licensed Content Pages	10

Order Details

Type of use	Dissertation/Thesis
Requestor type	Author of this Wiley article
Format	Print and electronic
Portion	Full article
Will you be translating?	No

About Your Work

Title	Light modulation of Properties of Arylazoisoxazole Photoswitches and their Benzene-1,3,5-tricarboxamide (BTA) Functionalized Derivatives
Institution name	IISER Mohali
Expected presentation date	Jun 2022

Additional Data

Requestor Location

Requestor Location	IISER MOHALI IISER MOHALI, SEC 81, MOHALI (PUNJAB) MOHALI, 140306 India Attn: IISER MOHALI

Tax Details

Publisher Tax ID	EU826007151

Price

Total	0.00 USD

Pravesh Kumar
Indian Institute of Science Education and Research (IISER) Mohali, India
pkpanwar88@gmail.com **ph16040@iisermohali.ac.in** **+91-8894071889**

PhD Chemistry

08/2018–07/2021 **CSIR-Senior Research Fellow**
Indian Institute of Science Education and Research (IISER) Mohali, India

08/2016–07/2018 **CSIR-Junior Research Fellow**
Indian Institute of Science Education and Research (IISER) Mohali, India

Education

07/2009–06/2011 Master of Science (Chemistry), Gurukula Kangri University, Haridwar (Uttarakhand), India

07/2006–06/2009 Bachelor of Science, Guru Nanak Khalsa College, Yamunanagar (Hariyana)
Affiliated to Kurukshetra University, Kurukshetra (Hariyana), India
Majors: Biochemistry (Specialization), Chemistry, Zoology

Academic Achievements

- Qualified **CSIR-NET** (**National Eligibility Test**) Conducted by CSIR–UGC June 2012. All India Rank – **034**.
- Qualified **GATE** (**Graduate Aptitude Test in Engineering**) Chemistry–2013. All India Rank **– 811**.
- Qualified **CSIR-JRF** (**Junior Research Fellowship**) Conducted by CSIR–UGC December 2015. All India Rank – **064**.

Technical Skills

- Experience in target-oriented organic synthesis, cross-coupling reactions, and functionalization strategies
- Handled air/moisture sensitive reagents/reactions and milligram/gram scale reactions.
- Experience in the purification of various products using distillation, recrystallization, and column chromatography techniques.
- Expertise in softwares such as Chemdraw**,** TopSpin**,** SciFinder**,** Origin etc.

Instruments Handled

- PerkinElmer DSC8000 Differential Scanning Calorimetry (DSC)
- Nikon Eclipse LV100POL Polarized Optical Microscope (POM)
- Agilent Cary 5000 and Cary 60 Ultraviolet-visible (UV-vis) spectrophotometer
- Horiba Scientific Fluoromax spectrofluorometer 4
- Perkin Elmer Spectrum Two Fourier Transform-Infrared (FT-IR) Spectrometer

- Bruker Alpha Attenuated total reflectance (ATR) –Infrared Spectrometer
- Bruker Avance III 400 MHz NMR Nuclear Magnetic Resonance (NMR) spectrometer
- Waters SYNAPT G2S High Definition Mass Spectrometer (HDMS) with ESI mode

Personal Skills

- Experience in the poster, oral presentations**,** and manuscript writing.
- Good communication skills, self-motivated, creative, well organized
- A good team worker with leadership qualities.
- Proficiency in Mother Tongue Hindi (Reading, writing, and speaking) and English (Reading, writing, and speaking).

Teaching contributions

Indian Institute of Science Education and Research (IISER) Mohali (Teaching Assistant) (2017-18) for undergraduate Chemistry courses

- Assisted in the CHM211 & CHM112 laboratory courses for the BS-MS students. Roles and responsibilities: To demonstrate the experiments to a small group and assist them to execute the experiments; troubleshoot the experiments and address questions; evaluation of lab records and assist the instructors in grading.
- Co-guided master thesis students (Amal Sam Sunny year 2018-19 and Roshan Nasare 2021-22)
- Mentored undergraduate students during summer internships and mentored junior colleagues.